METALS, SUPERCONDUCTORS

Anomaly in the conductivity of shock-compressed nickel at a pressure of ~23 GPa

V. V. Komissarov and M. N. Pavlovskiĭ

All-Russian Scientific-Research Institute of Experimental Physics, 607190 Sarov, Russia
(Submitted June 4, 1998)
Fiz. Tverd. Tela (St. Petersburg) **41**, 369–371 (March 1999)

In the pressure range 14–35 GPa we have measured the resistance of shock-compressed nickel. Its abrupt decrease at ~23 GPa is noted, and the boundaries of the existence of this anomaly (±1 GPa) are determined. It is shown that the observed anomaly can be linked with a structural rearrangement of the electron shells of nickel. © *1999 American Institute of Physics.* [S1063-7834(99)00103-3]

Experimental information about the properties of materials existing in a compressed state is of great interest from a practical as well as a scientific point of view. However, while the thermodynamic properties of matter at high pressures have been examined in some detail, information about the kinematic properties (viscosity, thermal conductivity, electrical conductivity, etc.) is quite scant. Therefore, new information about them, in particular their electrical conductivity at high pressures, is of especial value.

The present paper reports results of measurements of the electrical conductivity of shock-compressed nickel in the pressure range 14–35 GPa. In the scientific literature such data are lacking. Nickel samples were compressed with the aid of strong shock waves formed by ignition of an explosive charge. The use of shock waves makes it possible to perform measurements at pressures where the use of static pressures becomes problematic or is simply impossible.

A diagram of the experiment is shown in Fig. 1. The nickel sample (grade NP-2, GOST 492-73) in the form of a segment of wire of diameter 0.03 mm and length ~7 mm was cemented in place with the help of epoxy resin between two disks of reference material (aluminum, copper, monocrystalline LiF, CsI, and NaCl, fluoroplast-4, etc.) in which the pressure of the shock-wave front was known in advance. The samples were loaded with a planar, stationary shock wave. The shock front in the reference materials, as the experimental results showed, had a nearly ''table-shaped'' single-wave configuration. When the nickel samples were themselves used as the reference material, they were isolated by sheets of mica ~0.03 mm thick.

The technique used to determine the electrical conductivity of the shock-compressed nickel samples is described in Refs. 1 and 2. A feed voltage was applied to the nickel samples for ~10 μs leading up to the instant of arrival of the shock wave. Each nickel sample had four identical leads, which made it possible to determine its resistance R in the compressed state without having to take account of the resistance of the leads. One pair of leads served as the voltage leads. The signal was recorded with the help of the second pair of leads and fed directly to the the deflecting system of oscillographs of the type S9-4 and S9-8. One of the oscillograms obtained in these experiments is shown in Fig. 1. The electrical conductivity of the shock-loaded nickel samples R was calculated from the formula $R=R_0 z/z_0$, where R_0 is the initial resistance of the nickel sample, equal to ~$I\Omega$, and z_0 and z are the excursions on the oscillogram. Results of the experiments are plotted in Fig. 2 in the coordinates $(R-R_0)/R_0=f(P)$,[1)] where they are compared with data[3] on the electrical conductivity of nickel under conditions of static compression. The higher position of the dependence of shock-compressed nickel in comparison with the corresponding dependence for static compression is a result of the fact that for shock loading higher nickel temperatures are reached than for static compression. As can be seen from Fig. 2, the dependence $(R-R_0)/R_0=f(P)$ for shock-loaded nickel at ~23 GPa has a segment characterized by an abrupt drop of the resistance followed by an equally dramatic rebound.

To obtain additional information on the behavior of shock-compressed nickel in the pressure region of interest, we recorded the structure of the profile of the shock front propagating through a massive nickel plate with the help of a manganese pressure sensor.[2,4] A diagram of these experiments is shown in Fig. 3. A manganese pressure sensor of thickness ~0.03 mm having the shape of a flat bifilar spiral with outer diameter ~4.5 mm[2,5] was cemented with epoxy resin between two nickel disks of thickness 6 and 8 mm and isolated from them by sheets of mica ~0.05 mm thick. To make more complete use of the working area of the oscillograph screen and improve the accuracy of the measurements, ~I μs after switching on the recording instruments we fed a rectangular voltage pulse with an amplitude around 10 V to the deflecting system of the S9-4 oscillographs thereby shifting the beam to its baseline position.[2,5] One of the oscillograms recorded in this series of measurements is shown in Fig. 3. The pressure of shock-loading the nickel and correspondingly the manganese sensor (P) was determined from a measurement of the resistance R_M of the manganese sensor in its compressed state $R_M=R_{M_0}(z_0-z_1+z)\,z_0^{-1}$, where R_{M_0} is the initial resistance of the manganese sensor, equal

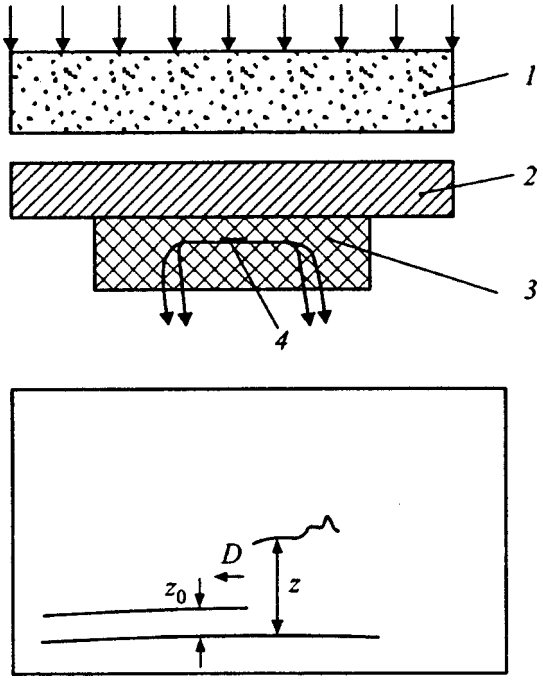

FIG. 1. Diagram of the experiment and oscillogram measuring the conductivity of shock-compressed nickel. *1* — explosive charge of diameter 120 mm, *2* — copper or aluminum screen of thickness 10 mm, *3* — reference material, *4* — nickel sample with copper leads. Frequency of the scaling sine wave in the oscillogram 5 MHz, shock load pressure of the reference material (NaCl) 26.2 GPa.

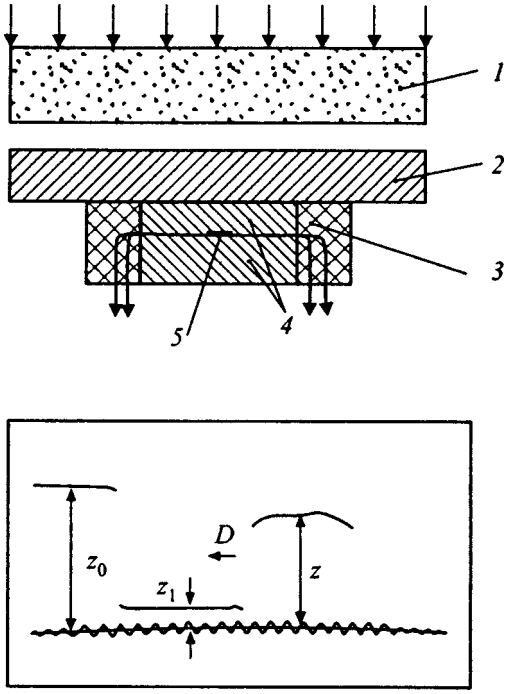

FIG. 3. Diagram of the experiment and oscillogram for revealing the profile of the compression front in nickel. *1* — explosive charge of diameter 120 mm, *2* — aluminum screen of thickness 10 mm, *3* — epoxy resin, *4* — nickel sample, *5* — manganese pressure sensor. Frequency of scaling sine wave in oscillogram 5 MHz.

to $\sim 1.5\,\Omega$, and z_0, z_1, and z are the amplitudes of the deflections of the beam on the oscillogram in Fig. 3. In the transformation from R_M/R_{M_0} to P we used the dependence of the resistance of manganese on the shock-loading pressure $P=f(R_M/R_{M_0})$ from Ref. 4. The results of this series of measurements showed that the shock front in nickel at shock-loading pressures of 24.5−30 GPa has a nearly ''table-shaped'' profile. The calculated decrease in the nickel resistance at ~ 23 GPa is not accompanied, consequently, by a noticeable decrease in its specific volume, which would lead to a splitting of the shock front propagating through the nickel sample as is observed during polymorphic phase transitions.[2,5] This apparently also explains the fact that in studies of the shock-compressibility of nickel[6,7] no salient point is observed in its shock adiabat.

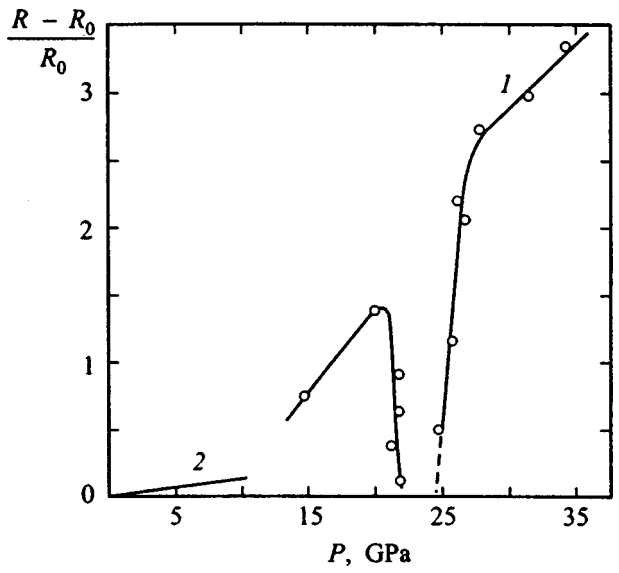

FIG. 2. Variation of the electrical resistance of nickel as a function of shock load pressure for shock compression (*1*) and for static compression[3] (*2*).

From the measurements reported here we have confirmed an abrupt decrease in the electrical resistance of shock-compressed nickel at pressures of ~ 23 GPa and have determined the narrow boundaries of existence of this anomaly. The recorded anomaly cannot be due to the occurrence of a polymorphic phase transition in nickel during shock compression. It is probable, as has been suggested, that the recorded anomaly is connected in some way with a structural rearrangement of nickel electron shells during compression.[8]

The authors express their gratitude to A. B. Medvedev and R. F. Trunin for their interest in this work and helpful discussions of this work.

[1)] The error in the determination of the pressure and of the relative difference $(R-R_0)/R_0$ was $\sim \pm 3\%$.

[1] M. N. Pavlovskiĭ, Zh. Éksp. Teor. Fiz. **73**, *1(7)*, 237 (1977) [Sov. Phys. JETP **46**, 122 (1977)].
[2] M. N. Pavlovskiĭ and V. V. Komissarov, Zh. Éksp. Teor. Fiz. **98**, *5(11)*, 1746 [*sic*] (1990) [Sov. Phys. JETP **71**, [*sic*] (1990)].
[3] *Handbook of Physical Quantities* [in Russian] (Energoizdat, Moscow, 1991), p. 443.

[4] M. N. Pavlovskiĭ and V. V. Komissarov, Zh. Éksp. Teor. Fiz. **83**, *6(12)*, 2146 (1982) [Sov. Phys. JETP **56**, 1244 (1982)].
[5] L. V. Al'tshuler, M. N. Pavlovskiĭ, and V. V. Komissarov, Zh. Éksp. Teor. Fiz. **106**, *4(10)*, 1136 (1994) [JETP **79**, 616 (1994)].
[6] L. V. Al'tshuler, A. A. Bakanova, and R. F. Trunin, Zh. Eksp. Teor. Fiz. **42**, *1*, 91 (1962) [Sov. Phys. JETP **15**, 65 (1962)].
[7] M. Raĭs, R. Mak-Kuin, and Dzh. Uolsh, in *Dynamical Studies of Solids under High Pressures* [Russian translation] (Mir, Moscow, 1965), p. 55.
[8] P. V. Bridgman, in *Solids under Pressure*, edited by W. Paul and D. Warschauer (McGraw-Hill, New York, 1963).

Translated by Paul F. Schippnick

Nature of soft vibrational modes in metallic glasses

V. M. Manichev*) and E. A. Gusev

Russian Scientific Center ''Kurchatov Institute,'' 123182 Moscow, Russia
(Submitted July 17 1998)
Fiz. Tverd. Tela (St. Petersburg) **41**, 372–379 (March 1999)

A general theory of vibrational excitations in metallic glasses is presented, based on the disclination model of the structure of solids with local icosahedral symmetry. The representation of nonorthogonal plane waves is used, which allows one to separate the diagonal terms in the Hamiltonian, and also the terms describing scattering of these waves by fluctuations of the density and the force constants, and by topological structure fluctuations. We have derived and solved the Dyson equation for the Green's function. We have obtained an analytical expression for the density of vibrational states of the glass. The nature of the soft vibrational modes is discussed. It is shown that these modes are resonant modes, whose presence is due to the fluctuations of the density and the force constants. Special attention is given to the role of forward scattering and the nature of the spatial variation in the amplitude of the given modes.
 [S1063-7834(99)00203-8]

At present an analytical theory of vibrational excitations in real three-dimensional metallic glasses is lacking. Whereas there is at least a formal analytical solution of the problem in the one-dimensional case,[1] in the three-dimensional case there are only the results of computer modeling.[2,3] A calculation of the vibrational spectrum of the so-called ''Polytope 120,'' an example of ideal icosahedral packing of the three-dimensional sphere S^3 (Refs. 4 and 5), is a beautiful mathematical problem, too distantly related to the vibrational spectrum of real glasses and consequently not capable of explaining the characteristic features of observed spectra. In particular, it would be pointless to formulate the problem of soft modes or localization within the framework of such an approach. On the other hand, it is specifically the ''excess'' soft modes, whose presence at frequencies $\omega \sim 0.1\omega_D$ (ω_D is the Debye frequency) has been detected in all metallic glasses (see the review in Ref. 2), that are presently the least understood region of the vibrational spectrum. Obviously, the solution of the given problem is directly connected to the solution of the problem of an analytical calculation of the spectrum, i.e., to the possibility of an analytical calculation of the eigenvalue spectrum of the dynamical matrix of the glass. The main complication here is the absence in the cellular representation of a simple type of basic ideal crystal lattice in the theory of disordered alloys and incommensurate crystals. Here, in contrast to crystals, the phase functions $e^{i\mathbf{k}\mathbf{r}_i}$, where $\mathbf{r}_i$ is the equilibrium position of the ith atom, do not form an orthogonal transformation basis, and the formal transformation to the $\mathbf{k}$ representation for the displacements and momenta does not preserve the canonical form of the equations of motion.[6] On the other hand, in inelastic neutron scattering studies the initial excited vibrational state is a plane wave.[7] The solution of the problem is to use functions which have been bi-ortho-normalized with respect to the indicated phase functions.[8] It will be shown below that such an approach, while preserving the canonical form of the equations of motion, allows one to separate the diagonal terms in the Hamiltonian describing plane-wave excitations from the nondiagonal terms describing scattering of these waves by fluctuations in the density and force constants, and also by topological structure fluctuations. Under sufficiently general assumptions, the given scattering problem allows an exact solution, which makes it possible to find the Green's function and, correspondingly, the spectrum of vibrational excitations. In the concluding section we show that the indicated problem of soft vibrational modes is solved within the framework of the proposed theory.

1. TOPOLOGICAL PROPERTIES OF THE STRUCTURE OF METALLIC GLASSES

A fundamental parameter of any model of the structure of a metallic glass is the coordination number Z. The spatial correlation of the coordination numbers is formalized in the disclination model of a glass.[9,10] In the case of an ''ideal'' monoatomic structure $Z=12$ for atoms with an icosahedral environment and $Z=14, 15, 16$ for atoms located at the centers of the Frank–Casper base polyhedra.[11] Atoms with $Z=14, 15, 16$ form a connected (in general, simply-connected) linear structure called the disclination network (a network of ''negative'' disclinations) or, in the Frank–Casper terminology, a ''basic skeleton.''[12] From the point of view of the disclination model, the structures of metallic glasses, quasicrystals, and Frank–Casper crystalline phases differ only in the nature of the spatial ordering of the disclinations.[11] In metallic glasses the disclinations are disordered, in Frank–Casper phases they form a crystal-like periodic structure with long-range translational order,[13] in quasicrystals the disclinations form complicated hierarchical structures[14] with the type of hierarchy of non-intersecting dodecahedral networks in icosahedral quasicrystals.[15] The best-known Frank–Casper phases consist of atoms whose coordination numbers take on only two values: thus, for example, in the $A15$ phase besides the atoms with $Z=12$ only

atoms with $Z=14$ are present, with $Z=15$ in the $C15$ phase, and with $Z=16$ in the Laves phase.[13] (In exotic phases with complicated disclination structure all of the enumerated types of atoms are present.) The relative number of atoms with $Z=12, 14$, and 16 in icosahedral quasicrystals is 63:7:30 (Ref. 15). Thus it may be expected that an ''ideal'' monoatomic glass is formed from atoms of two main types: $Z=12$ and another type, whose coordination number depends on the nature of the interatomic forces. The remaining types ($Z=14$ and $Z=15$, for example, if $Z=16$ is the dominant type) can be considered as ''impurities'' or topological fluctuations in the disclination network. A ''nonideal'' or unrelaxed monoatomic structure leads to coordination numbers $Z=13, 11, 10, 9$, and 8, due to the presence of so-called ''positive'' disclinations.[9] The appearance of ''positive'' disclinations is compensated by an identical additional number of ''negative'' disclinations so that the total density of disclinations, taking their sign into account, remains constant. Such a different disclination structure arises in real multicomponent glasses. In this case, atoms of one type preferentially occupy well-defined sites. Thus, for example, the atoms of metalloids, having comparatively small dimensions, occupy for the most part sites with low coordination numbers. Despite such a diversity of structure, the distribution over coordination numbers in this case has two distinct peaks.[16] Thus, while avoiding unnecessary complications, we arrive at the following simplified dynamical model. With the vibrational dynamics in mind, we divide all the atoms into two main classes (the A atoms and B atoms) and one ''impurity'' class (the C atoms). Although the main criterion for dividing the atoms into classes in our model is the coordination number of the specific atom, the above-indicated correlation between the type of atom and its coordination number also allows us to characterize each class by a definite mass of the atom that is representative of the class and by a definite set of force constants. Note that the given correlation is obviously not strict and, as will become clear below, is not obligatory for the calculations that are to follow. Nevertheless, it can be helpful both for comparison with experimental data and for their interpretation. On the other hand, deviations from the indicated correspondence can be taken into account both within the framework of the approach laid out below and with the help of known methods such as the coherent potential approximation, developed for systems with substitutional disorder.

2. HAMILTONIAN AND GREEN'S FUNCTION IN THE REPRESENTATION OF NONORTHOGONAL PLANE WAVES

In the harmonic approximation, the Hamiltonian of the vibrational excitations has the standard form

$$H=\sum_n \sum_{i_n} \frac{(P^\alpha_{i_n})^2}{2M_{i_n}}+\sum_{i_c} \frac{(P^\alpha_{i_c})^2}{2M_{i_c}} + \frac{1}{2}\sum_n \sum_{n'} \sum_{i_n} \sum_{i_{n'}} (A^{\alpha\beta}_{i_n i_{n'}}+\Delta A^{\alpha\beta}_{i_n i_{n'}})u^\alpha_{i_n}u^\beta_{i_{n'}} + \sum_n \sum_{i_n} \sum_{i_c} B^{\alpha\beta}_{i_n i_c}u^\alpha_{i_n}w^\beta_{i_c}+\frac{1}{2}\sum_{i_c} \sum_{i'_c} C^{\alpha\beta}_{i_c i'_c}w^\alpha_{i_c}w^\beta_{i'_c}. \quad (1)$$

Here $u^\alpha_{i_n}$ and $P^\alpha_{i_n}$ are the Cartesian components of the displacement and the momentum of the i_nth atom of the nth class ($n=A,B$) whose equilibrium position $\mathbf{r}_{i_n}$, and M_{i_n} is its mass. The quantities corresponding to the C atoms have the index i_c. Since it will not cause any misunderstandings in the discussion that follows, to simplify the notation we will take doubly occurring Greek indices to indicate summation without explicitly writing down the summation sign.

The force constants satisfy the usual relations

$$\sum_{n'} \sum_{i_{n'}} (A^{\alpha\beta}_{i_n i_{n'}}+\Delta A^{\alpha\beta}_{i_n i_{n'}})+\sum_{i_c} B^{\alpha\beta}_{i_n i_c}=0, \quad (2)$$

$$\sum_{n'} \sum_{i_{n'}} B^{\alpha\beta}_{i_c i_{n'}}+\sum_{i'_c} C^{\alpha\beta}_{i_c i'_c}=0. \quad (3)$$

The constants $\Delta A^{\alpha\beta}_{i_n i_{n'}}$ describe the influence of the C atoms. They are given a separate notation for convenience so as to fulfill the relation

$$\sum_{n'} \sum_{i_{n'}} A^{\alpha\beta}_{i_n i_{n'}}=0, \quad (4)$$

describing the hypothetical situation when the coordination number takes only two values. Without loss of generality, we significantly simplify the purely formal form of the results that are to follow, in particular relations (16)–(18), by adopting a diagonal form for the matrix $C^{\alpha\beta}_{i_c i'_c}$:

$$C^{\alpha\beta}_{i_c i'_c}=C_{i_c}\delta_{i_c i'_c}\delta^{\alpha\beta}. \quad (5)$$

Diagonality in the subscripts implies the absence of a direct interaction of the C atoms, which is fulfilled for a low concentration of the latter. We write the matrices $\Delta A^{\alpha\beta}_{i_n i_{n'}}$ and $B^{\alpha\beta}_{i_c i_{n'}}$ in the form[17]:

$$B^{\alpha\beta}_{i_n i_c}=B_{i_c} f(r_{i_n}-r_{i_c})\,\delta^{\alpha\beta}, \quad (6)$$

$$\Delta A^{\alpha\beta}_{i_n i_{n'}}=\sum_{i_c} A_{i_c} f(r_{i_n}-r_{i_c})f(r_{i_{n'}}-r_{i_c})\,\delta^{\alpha\beta}. \quad (7)$$

Equations (2)–(4) in this case give

$$B_{i_c}=-\frac{C_{i_c}}{\sum_n \sum_{i_n} f(r_{i_n}-r_{i_c})}, \quad (8)$$

$$A_{i_c}=\frac{C_{i_c}}{\sum_n \sum_{n'} \sum_{i_n} \sum_{i_{n'}} f(r_{i_n}-r_{i_c})f(r_{i_{n'}}-r_{i_c})}. \quad (9)$$

Proportionality of all the force matrices $\delta^{\alpha\beta}$ leads to a scalar model which in explicit form will be used only in the following section since in the derivation of the general relations of the given section it leads only to insignificant simplifications.

We are interested in the structure of the spectral density function $g(\omega)$, which is defined in terms of the Green's function in the cellular representation

$$g(\omega)=-\frac{2\omega}{3\pi N}\,\mathrm{Im\,Tr}\,MG(\omega+i\varepsilon),\quad \varepsilon\to+0. \tag{10}$$

Here N is the total number of atoms.

We will use the causal Green's function

$$G^{\alpha\beta}_{i_n i_{n'}}(t)=-i\langle T(u^{\alpha}_{i_n}(t)u^{\beta}_{i_{n'}}(0))\rangle, \tag{11}$$

where T is the T-ordering operator and $\langle\ldots\rangle$ denotes averaging over the ground state of the system. The Fourier transforms of these functions in time satisfy the following equations:

$$M_{i_n}\omega^2 G^{\alpha\beta}_{i_n i_{n'}}(\omega)=\delta^{\alpha\beta}_{nn'}\delta_{i_n i_{n'}}+\sum_{n''}\sum_{i_{n''}}(A^{\alpha\gamma}_{i_n i_{n''}}+\Delta A^{\alpha\gamma}_{i_n i_{n''}})G^{\gamma\beta}_{i_{n''} i_{n'}}(\omega)+\sum_{i_c}B^{\alpha\gamma}_{i_n i_c}G^{\gamma\beta}_{i_c i_{n'}}(\omega), \tag{12}$$

$$M_{i_c}\omega^2 G^{\alpha\beta}_{i_c i'_c}(\omega)=\delta^{\alpha\beta}\delta_{i_c i'_c}+\sum_{n}\sum_{i_n}B^{\alpha\gamma}_{i_c i_n}G^{\gamma\beta}_{i_n i'_c}(\omega)+\sum_{i''_c}C^{\alpha\gamma}_{i_c i''_c}G^{\gamma\beta}_{i''_c i'_c}(\omega), \tag{13}$$

$$M_{i_n}\omega^2 G^{\alpha\beta}_{i_n i_c}(\omega)=\sum_{n'}\sum_{i_{n'}}(A^{\alpha\gamma}_{i_n i_{n'}}+\Delta A^{\alpha\gamma}_{i_n i_{n'}})G^{\gamma\beta}_{i_{n'} i_c}(\omega)+\sum_{i'_c}B^{\alpha\gamma}_{i_n i'_c}G^{\gamma\beta}_{i'_c i_c}(\omega), \tag{14}$$

$$M_{i_c}\omega^2 G^{\alpha\beta}_{i_c i_n}(\omega)=\sum_{n'}\sum_{i_{n'}}B^{\alpha\gamma}_{i_c i_{n'}}G^{\gamma\beta}_{i_{n'} i_n}(\omega)+\sum_{i'_c}C^{\alpha\gamma}_{i_c i'_c}G^{\gamma\beta}_{i'_c i_n}(\omega). \tag{15}$$

Using condition (5) on the $C^{\alpha\beta}_{i_c i'_c}$ and the equality $G^{\alpha\beta}_{i_n i_c}(\omega)=G^{\beta\alpha}_{i_c i_n}(\omega)$, where the latter is a consequence of commutativity of displacements, we at once obtain

$$G^{\alpha\beta}_{i_c i_n}(\omega)=\frac{1}{M_{i_c}}\frac{\sum_{n'}\sum_{i_{n'}}B^{\alpha\gamma}_{i_c i_{n'}}G^{\gamma\beta}_{i_{n'} i_n}(\omega)}{\omega^2-\omega^2_{i_c}}, \tag{16}$$

$$G^{\alpha\beta}_{i_c i'_c}(\omega)=\frac{\delta^{\alpha\beta}\delta_{i_c i'_c}}{M_{i_c}(\omega^2-\omega^2_{i_c})}+\frac{\sum_{n}\sum_{i_n}\sum_{n'}\sum_{i_{n'}}B^{\alpha\gamma}_{i_c i_n}B^{\beta\delta}_{i_c i_{n'}}G^{\gamma\delta}_{i_n i_{n'}}(\omega)}{M_{i_c}M_{i'_c}(\omega^2-\omega^2_{i_c})(\omega^2-\omega^2_{i'_c})}, \tag{17}$$

$$M_{i_n}\omega^2 G^{\alpha\beta}_{i_n i_{n'}}(\omega)=\delta^{\alpha\beta}_{nn'}\delta_{i_n i_{n'}}+\sum_{n''}\sum_{i_{n''}}(A^{\alpha\gamma}_{i_n i_{n''}}+D^{\alpha\gamma}_{i_n i_{n''}})G^{\gamma\beta}_{i_{n''} i_{n'}}(\omega), \tag{18}$$

where $\omega^2_{i_c}=C_{i_c}/M_{i_c}$,

$$D^{\alpha\beta}_{i_n i_{n'}}(\omega)=\sum_{i_c}\frac{M_{i_c}\omega^2_{i_c}\omega^2}{\omega^2-\omega^2_{i_c}}\times\frac{f(r_{i_n}-r_{i_c})f(r_{i_{n'}}-r_{i_c})}{\sum_{n}\sum_{n'}\sum_{i_n}\sum_{i_{n'}}f(r_{i_n}-r_{i_c})f(r_{i_{n'}}-r_{i_c})}\delta^{\alpha\beta}.$$

Let us proceed now to the mixed (**k**,**r**) representation[18] by introducing the collective variables $U^{\alpha}_{n}(\mathbf{k})$ and $P^{\alpha}_{n}(\mathbf{k})$ for the atoms of the classes A and B while treating the C atoms in the cellular representation. In the representation of nonorthogonal plane waves[8] we have

$$u^{\alpha}_{i_n}=\frac{1}{\sqrt{N_n}}\sum_{\mathbf{k}}U^{\alpha}_{n}(\mathbf{k})e^{i\mathbf{k}\mathbf{r}_{i_n}}, \tag{19}$$

$$P^{\alpha}_{i_n}=\frac{1}{\sqrt{N_n}}\sum_{\mathbf{k}}P^{\alpha}_{n}(\mathbf{k})\psi^{*}_{n\mathbf{k}}(\mathbf{r}_{i_n}), \tag{20}$$

where N_n is the number of atoms of type n and $\psi^{*}_{n\mathbf{k}}(\mathbf{r}_{i_n})$ is the set of functions that are bi-ortho-normalized with respect to the $e^{i\mathbf{k}\mathbf{r}_{i_n}}$ and satisfy the relations

$$\frac{1}{N_n}\sum_{i_n}e^{i\mathbf{k}\mathbf{r}_{i_n}}\psi^{*}_{n\mathbf{k}'}(\mathbf{r}_{i_n})=\delta_{\mathbf{k}\mathbf{k}'}, \tag{21}$$

$$\frac{1}{N_n}\sum_{\mathbf{k}}e^{i\mathbf{k}\mathbf{r}_{i'_n}}\psi^{*}_{n\mathbf{k}}(\mathbf{r}_{i_n})=\delta_{\mathbf{r}_{i_n}\mathbf{r}_{i'_n}}. \tag{22}$$

We assume that in their **k** values all the states are contained within a sphere of radius $k_0=(3N\pi^2/V)^{1/3}$, where V is the total volume of the system. The Hamiltonian in the (**k**,**r**) representation has the form

$$H=\frac{1}{2}\sum_{n}\sum_{\mathbf{k}}P^{\alpha}_{n}(\mathbf{k})\dot{U}^{\alpha}_{n}(\mathbf{k})+\frac{1}{2}\sum_{n}\sum_{n'}\sum_{\mathbf{k}}\sum_{\mathbf{k}'}\Phi^{\alpha\beta}_{nn'}(\mathbf{k},\mathbf{k}')U^{\alpha}_{n}(\mathbf{k})U^{\beta}_{n'}(\mathbf{k}')+\frac{1}{2}\sum_{n}\sum_{n'}\sum_{\mathbf{k}}\sum_{\mathbf{k}'}\left(\frac{1}{\sqrt{N_n N_{n'}}}\times\sum_{i_n}\sum_{i_{n'}}\Delta A^{\alpha\beta}_{i_n i_{n'}}e^{i\mathbf{k}\mathbf{r}_{i_n}}e^{i\mathbf{k}'\mathbf{r}_{i_{n'}}}\right)\times U^{\alpha}_{n}(\mathbf{k})U^{\beta}_{n'}(\mathbf{k}')+\sum_{i_c}\frac{(P^{\alpha}_{i_c})^2}{2M_{i_c}}+\sum_{n}\sum_{\mathbf{k}}\sum_{i_c}\left(\frac{1}{\sqrt{N_n}}\sum_{i_n}B^{\alpha\beta}_{i_n i_c}e^{i\mathbf{k}\mathbf{r}_{i_n}}\right)U^{\alpha}_{n}(\mathbf{k})w^{\beta}_{i_c}+\frac{1}{2}\sum_{i_c}\sum_{i'_c}C^{\alpha\beta}_{i_c i'_c}w^{\alpha}_{i_c}w^{\beta}_{i'_c}, \tag{23}$$

where

$$\Phi_{nn'}^{\alpha\beta}(\mathbf{k},\mathbf{k}')=\frac{1}{\sqrt{N_nN_{n'}}}\sum_{i_n}\sum_{i_{n'}}A_{i_ni_{n'}}^{\alpha\beta}e^{i\mathbf{k}\mathbf{r}_{i_n}}e^{i\mathbf{k}'\mathbf{r}_{i_{n'}}},$$

and the dot above $U_n^\alpha(\mathbf{k})$ as usual denotes differentiation with respect to t. Using the relation

$$\dot{U}_n^\alpha(\mathbf{k})=\frac{P_n^\alpha(-\mathbf{k})}{\overline{M_n}}-\sum_{\mathbf{k}'\neq\mathbf{k}}\dot{U}_n^\alpha(\mathbf{k}')\,\frac{1}{N_n}\times\sum_{i_n}\frac{M_{i_n}}{\overline{M_n}}e^{-i(\mathbf{k}-\mathbf{k}')r_{i_n}},$$

the first term of the given Hamiltonian can be rewritten in the form

$$T=\frac{1}{2}\sum_n\sum_{\mathbf{k}}\frac{P_n^\alpha(\mathbf{k})P_n^\alpha(-\mathbf{k})}{\overline{M_n}}-\frac{1}{2}\sum_n\sum_{\mathbf{k}}\sum_{\mathbf{k}'}M_n(-\mathbf{k},\mathbf{k}')P_n^\alpha(\mathbf{k})\dot{U}_n^\alpha(\mathbf{k}'),$$

where

$$M_n(\mathbf{k},\mathbf{k}')=\frac{1}{N_n}\sum_{i_n}\frac{M_{i_n}}{\overline{M_n}}e^{i(\mathbf{k}+\mathbf{k}')r_{i_n}}(1-\delta_{\mathbf{k},-\mathbf{k}'}),$$

$$\overline{M_n}=\frac{1}{N_n}\sum_{i_n}M_{i_n}.$$

In the zeroth-approximation Hamiltonian H_0 we separate out the terms that are diagonal in $\mathbf{k}$ in the full Hamiltonian H:

$$H_0=\frac{1}{2}\sum_n\sum_{\mathbf{k}}\frac{P_n^\alpha(\mathbf{k})P_n^\alpha(-\mathbf{k})}{\overline{M_n}}+\frac{1}{2}\sum_n\sum_{n'}\sum_{\mathbf{k}}\Phi_{nn'}^{\alpha\beta}(\mathbf{k},-\mathbf{k})U_n^\alpha(\mathbf{k})U_{n'}^\beta(-\mathbf{k}).\tag{24}$$

The zeroth-order Hamiltonian H_0 leads to the following equation for the eigenvalues:

$$\overline{M_n}\omega^2U_n^\alpha(\mathbf{k})-\sum_{n'}\Phi_{nn'}^{\alpha\beta}(-\mathbf{k},\mathbf{k})U_{n'}^\beta(\mathbf{k})=0.\tag{25}$$

Since $A_{i_ni_{n'}}^{\alpha\beta}=A_{nn'}^{\alpha\beta}(\mathbf{r}_{i_n}-\mathbf{r}_{i_{n'}})$, the functions $\Phi_{nn'}(-\mathbf{k},\mathbf{k})$ can be rewritten in the following form:

$$\Phi_{nn'}^{\alpha\beta}(-\mathbf{k},\mathbf{k})=\frac{1}{\sqrt{N_nN_{n'}}}\sum_{i_n}\sum_{i_{n'}}A_{i_ni_{n'}}^{\alpha\beta}e^{-i\mathbf{k}(\mathbf{r}_{i_n}-\mathbf{r}_{i_{n'}})}=\frac{\sqrt{N_nN_{n'}}}{V}\int A_{nn'}^{\alpha\beta}(\mathbf{r})g_{nn'}(\mathbf{r})e^{-i\mathbf{k}\mathbf{r}}d\mathbf{r},\tag{26}$$

where $g_{nn'}(\mathbf{r})$ is the partial pairwise correlation function.

Thus, Eq. (25), whose solutions we denote as $\omega^2=\omega_s^2(\mathbf{k})\equiv\omega_\xi^2$, $\xi\equiv(\mathbf{k},s)$, $-\xi\equiv(-\mathbf{k},s)$ leads to an equation of sixth degree in ω^2 in which all of the coefficients are expressed in terms of functions which are known in principle: derivatives of the interatomic potentials and partial pairwise correlation functions (with allowance for the above remark about correlation of the type of atom and its coordination number).

We define the Green's function $G_{\xi\xi'}(t)$ in the $\mathbf{k}$ representation with the help of the creation a_ξ and annihilation a_ξ^+ operators, introduced in the standard way

$$U_n^\alpha(\mathbf{k})=\sum_S\sqrt{\frac{\hbar}{2\overline{M_n}\omega_\xi}}e_n^\alpha(\xi)(a_\xi+a_{-\xi}^+),\tag{27}$$

$$P_n^\alpha(\mathbf{k})=-i\sum_S\sqrt{\frac{\hbar\omega_\xi\overline{M_n}}{2}}e_n^{\alpha*}(\xi)(a_{-\xi}-a_\xi^+),\tag{28}$$

$$G_{\xi,\xi'}(t)=-i\langle T(A_\xi(t)A_{\xi'}(0))\rangle.\tag{29}$$

Here $A_\xi=a_\xi+a_{-\xi}^+$, and $e_n^\alpha(\xi)$ are the polarization vectors satisfying the relations

$$\sum_n e_n^\alpha(\xi)e_n^{\alpha*}(\xi')=\delta_{SS'},$$

$$\sum_S e_n^\alpha(\xi)e_{n'}^{\beta*}(\xi)=\delta_{nn'}^{\alpha\beta}.\tag{30}$$

The Green's function in the two representations are linked by the obvious relation

$$G_{i_ni_{n'}}^{\alpha\beta}(\omega)=\frac{1}{2\sqrt{\overline{M_n}\overline{M_{n'}}}\sqrt{N_nN_{n'}}}\times\sum_{\xi_1}\sum_{\xi_2}\frac{G_{\xi_1,-\xi_2}(\omega)}{\sqrt{\omega_{\xi_1}\omega_{\xi_2}}}e_n^\alpha(\xi_1)e_{n'}^{\beta*}(\xi_2)\times e^{i\mathbf{k}_1\mathbf{r}_{i_n}}e^{-i\mathbf{k}_2\mathbf{r}_{i_{n'}}}.\tag{31}$$

We substitute this relation into Eq. (18) and multiply the resulting equation by

$$\frac{1}{N_{n'}\sqrt{N_n\overline{M_n}}}e_n^{\alpha*}(\xi)e_{n'}^\beta(\xi')\psi_{n'\mathbf{k}'}^*(\mathbf{r}_{i_{n'}})e^{-i\mathbf{k}\mathbf{r}_{i_n}}$$

and sum over n, n', i_n, and $i_{n'}$. Employing conditions of orthogonality (21) and (30), we obtain the following equation in $G_{\xi_1,\xi_2}(\omega)$:

$$\omega^2\sum_n\sum_{i_n}\frac{M_{i_n}}{N_n\overline{M_n}}\sum_{\xi_1}\frac{G_{\xi_1,-\xi'}(\omega)}{2\sqrt{\omega_{\xi_1}\omega_{\xi'}}}e_n^{\alpha*}(\xi)e_n^\alpha(\xi_1)\times e^{i\mathbf{k}_1\mathbf{r}_{i_n}}e^{-i\mathbf{k}\mathbf{r}_{i_n}}=\delta_{\xi\xi'}+\sum_{\xi_1}\frac{1}{2\sqrt{\omega_{\xi_1}\omega_{\xi'}}}(\Phi_{-\xi\xi_1}+D_{-\xi\xi_1})G_{\xi_1,-\xi'}(\omega).\tag{32}$$

Here

$$\Phi_{\xi_1\xi_2}=\sum_n\sum_{n'}\frac{e_n^\alpha(\xi_1)e_{n'}^\beta(\xi_2)}{\sqrt{\overline{M_n}\overline{M_{n'}}}}\frac{1}{\sqrt{N_nN_{n'}}}\times\sum_{i_n}\sum_{i_{n'}}A_{i_ni_{n'}}^{\alpha\beta}e^{i\mathbf{k}_1\mathbf{r}_{i_n}}e^{i\mathbf{k}_2\mathbf{r}_{i_{n'}}},$$

$$D_{\xi_1\xi_2}=\sum_n \sum_{n'} \frac{e_n^{\alpha}(\xi_1)e_{n'}^{\beta}(\xi_2)}{\sqrt{\overline{M_n M_{n'}}}} \frac{1}{\sqrt{N_n N_{n'}}} \times \sum_{i_n} \sum_{i_{n'}} D_{i_n i_{n'}}^{\alpha\beta} e^{i\mathbf{k}_1\mathbf{r}_{i_n}} e^{i\mathbf{k}_2\mathbf{r}_{i_{n'}}}.$$

Taking into account that $\Phi_{-\xi\xi}$ is the matrix of eigenvalues of the Hamiltonian H_0 in the **k** representation and, consequently, $\Phi_{-\xi\xi}=\omega_\xi^2$, we obtain the following Dyson equation in the **k** representation:

$$G_{\xi,-\xi'}(\omega)=\frac{2\omega_\xi}{\omega^2-\omega_\xi^2}\delta_{\xi\xi'}+\frac{2\omega_\xi}{\omega^2-\omega_\xi^2}V_\xi^0 G_{\xi,-\xi'}(\omega) + \frac{2\omega_\xi}{\omega^2-\omega_\xi^2}\sum_{\xi_1\neq\xi} V_{-\xi\xi_1} G_{\xi_1,-\xi'}(\omega) - \omega^2\frac{2\omega_\xi}{\omega^2-\omega_\xi^2}\sum_{\xi_1\neq\xi} M_{-\xi\xi_1} G_{\xi_1,-\xi'}(\omega). \tag{33}$$

Here

$$V_\xi^0=\frac{D_{-\xi\xi}}{2\omega_\xi}, \quad V_{-\xi\xi_1}=\frac{\Phi_{-\xi\xi_1}+D_{-\xi\xi_1}}{2\sqrt{\omega_\xi\omega_{\xi_1}}},$$

$$M_{-\xi\xi_1}=\sum_n \sum_{i_n} \frac{M_{i_n}}{2N_n\overline{M_n}\sqrt{\omega_\xi\omega_{\xi_1}}} e^{-i\mathbf{k}\mathbf{r}_{i_n}} e^{i\mathbf{k}_1\mathbf{r}_{i_n}} e_n^{\alpha *}(\xi) \times e_n^{\alpha}(\xi_1).$$

Since the operators a_ξ and a_ξ^+ diagonalize H_0

$$H_0=\sum_\xi \hbar\omega_\xi\left(a_\xi^+ a_\xi+\frac{1}{2}\right),$$

and the corresponding Green's function is equal to

$$G_{\xi,\xi'}^0(\omega)\equiv G_\xi^0(\omega)\delta_{\xi,-\xi'} = \frac{2\omega_\xi}{\omega^2-\omega_\xi^2+i\varepsilon}\delta_{\xi,-\xi'}, \quad \xi\to+0,$$

the Dyson equation (33) takes the form

$$G_{\xi,-\xi'}(\omega)=G_\xi^0\delta_{\xi\xi'}+G_\xi^0\sum_{\xi_1}\tilde{V}_{-\xi\xi_1}G_{\xi_1,-\xi'}(\omega). \tag{34}$$

Here

$$\tilde{V}_{-\xi\xi_1}=V_\xi^0\delta_{\xi\xi_1}+(V_{-\xi\xi_1}-\omega^2 M_{-\xi\xi_1})(1-\delta_{\xi\xi_1}).$$

Note that the given equation can also be derived with the aid of the standard diagrammatic technique[19]: the problem with Hamiltonian (23) can be reduced to a problem of scattering in an external field.

Since it follows from the explicit form of $\Phi_{\xi\xi_1}$, $D_{\xi\xi_1}$, and $M_{\xi\xi_1}$ that the kernel $\tilde{V}_{-\xi\xi_1}$ is degenerate

$$\tilde{V}_{-\xi\xi_1}=\sum_i v_i(-\xi)v_i(\xi_1), \tag{35}$$

the solution of Eq. (34) is easily found:

$$G_{\xi,-\xi'}(\omega)=G_\xi^0\delta_{\xi\xi'}+G_\xi^0 G_{\xi'}^0 \times\sum_{i,j} v_i(-\xi)[\hat{I}-\hat{W}(\omega)]_{ij}^{-1}v_j(\xi'), \tag{36}$$

where the elements of the matrix $\hat{W}(\omega)$ have the following form:

$$W_{ij}(\omega)=\sum_\xi G_\xi^0 v_i(\xi)v_j(-\xi).$$

The first term on the right-hand side of equality (36) describes the unrenormalized vibrational states in the form of plane waves, and the second term describes waves scattered by fluctuations of the density (the matrix $M_{\xi\xi_1}$), the force constants (the matrix $\Phi_{\xi\xi_1}$), and the topology (the matrix $D_{\xi\xi_1}$). Two results of scattering is renormalization of the starting spectrum and formation of localized and resonance states. The Green's function (36) is an exact solution of the problem of determining the vibrational spectrum in the harmonic approximation. Formally, the number of terms in the sum (35) is a macroscopic quantity of order zN, where z is the number of neighbors interacting with an atom. However, as will be shown below, the kernel (35) can be represented as the sum of only a few terms.

3. NATURE OF THE SOFT MODES

As is well known,[18] in the case of a crystal the appearance of excess modes and a resonance peak in the low-energy part of the spectrum ($\omega\leqslant 0.1\omega_D$) is due mainly to the presence of very heavy impurities ($M_c/M>10$) or impurities which are weakly bound with the lattice. Let us investigate the behavior, in this energy region, of the spectral density of the glass. In what follows, we will everywhere adhere to the scalar model and assume all atoms of all types to be identical with masses equal to M. In this case $\Phi_{-\mathbf{k}\mathbf{k}_1}$ can be written in the following form:

$$\Phi_{-\mathbf{k}\mathbf{k}_1}=\frac{1}{MN}\sum_i\sum_{i'} A_{ii'}e^{-i\mathbf{k}(\mathbf{r}_i-\mathbf{r}_{i'})}e^{i(\mathbf{k}_1-\mathbf{k})\mathbf{r}_{i'}} = \frac{N}{V}\int\frac{A_{ii'}(r)}{M}g(r)e^{-i\mathbf{k}\mathbf{r}}d\mathbf{r}\left(\frac{1}{N}\sum_i e^{i\mathbf{q}\mathbf{r}}\right) = -\omega_{\mathbf{k}}^2\frac{S_{\mathbf{q}}}{N}, \tag{37}$$

where $S_{\mathbf{q}}=(1/N)\Sigma_i e^{i\mathbf{q}\mathbf{r}}$ and $\mathbf{q}=\mathbf{k}_1-\mathbf{k}$. Further, $S_{\mathbf{q}}S_{\mathbf{q}}^*=NS(\mathbf{q})$, where $S(\mathbf{q})$ is the structure factor, which for a glass depends only on the magnitude of $\mathbf{q}$ and has the form

$$S(q)=1+\frac{N}{V}\int g(r)\frac{\sin(qr)}{qr}4\pi r^2 dr. \tag{38}$$

Since $g(r)\to 1$ as $r\to\infty$, $S(q)$ has a δ-function peak in the limit $q\to 0$. The height of this peak $\simeq N$, and its characteristic width $\sim 1/L$, where L is a characteristic scale on the order of the size of the system ($L^3\simeq V$). Since neighboring states are separated in k by an interval that is also $\sim 1/L$, there is

strong scattering with vanishingly small momentum transfer, which we will refer to below as forward scattering. In an ideal crystal, with accuracy to inverse lattice vectors that are unimportant here the exact relation $S(\mathbf{q})=N\delta_{\mathbf{q},0}$ is fulfilled and scattering is absent. In a glass, the indicated forward scattering is described in the potential $\tilde{V}_{-\mathbf{kk}_1}$ by a contribution proportional to $\Sigma_{\mathbf{\Delta}}\delta_{\mathbf{q},\mathbf{\Delta}}$, where Δ is a small quantity of order $1/L$. This, in turn, makes the following contribution to the Green's function:

$$G_{-\mathbf{kk}}+\frac{1}{2}\sum_{\mathbf{\Delta}}\frac{\partial}{\partial\mathbf{k}}(G_{-\mathbf{kk}})\mathbf{\Delta}.$$

The second term of this sum is of order $(kL)^{-1}\ll 1$ and can be discarded. Therefore, in what follows, we take forward scattering into account in a form proportional to $N\delta_{\mathbf{q},0}$. As a result, we have

$$S_{\mathbf{q}}=s_0N\delta_{\mathbf{q},0}+s(q)e^{i\varphi(q)}. \tag{39}$$

Here the choice of the origin determines the zero value of the phase of the singular term. The numerical factor s_0, describing the forward scattering, characterizes the deviation of the singular part of the structure factor from the exact δ function of an ideal crystal ($s_0\leqslant 1$), and $s(q)$ is a function that behaves similarly to the nonsingular part of the structure factor over the entire region of variation of q, i.e., it is comparatively small for small q and of the order of unity for $q\geqslant k_0$. Since $\varphi(0)=0$, the phase is small for small q and, consequently, the imaginary part of $S_{\mathbf{q}}$ is also small. In addition, as can be seen from relation (39), forward scattering plays the main role in the formation of the spectrum at small ω (small k of the starting spectrum) and the q dependence of the nonsingular part of relation (39) can be neglected. Restoring the symmetric form (in $\mathbf{k},\mathbf{k}_1$) of the nonsingular part of $\Phi_{-\mathbf{kk}_1}$ [it can be obtained explicitly by considering an analogous relation for $\Phi_{-\mathbf{kk}_1}\Phi^*_{-\mathbf{kk}_1}$ instead of relation (37)], we have

$$\Phi_{-\mathbf{kk}_1}=-s_0\omega_{\mathbf{k}}^2\delta_{\mathbf{k},\mathbf{k}_1}-\frac{s}{N}\omega_{\mathbf{k}}\omega_{\mathbf{k}_1}. \tag{40}$$

Analogous considerations lead to the following form for the remaining terms of the scattering potential:

$$D_{-\mathbf{kk}_1}=\frac{\omega_c^2\omega^2}{\omega^2-\omega_c^2}c\,\delta_{\mathbf{k},\mathbf{k}_1}+\frac{\omega_c^2\omega^2}{\omega^2-\omega_c^2}\frac{c}{N}, \tag{41}$$

$$\omega^2M_{-\mathbf{kk}_1}=s_0\omega^2\delta_{\mathbf{k},\mathbf{k}_1}+\frac{s}{N}\omega^2. \tag{42}$$

In the solution of the Dyson equation, it is convenient to take forward scattering into account separately. This being the case, only two functionally distinct terms remain in the sum (35). As a result, in the low-frequency region we have the following expression for the Green's function:

$$G_{\mathbf{kk}_1}\simeq P_{\mathbf{k}}\delta_{\mathbf{k},\mathbf{k}_1}+\frac{P_{\mathbf{k}}P_{\mathbf{k}_1}v(-\mathbf{k})v(\mathbf{k}_1)}{1-\sum_{\mathbf{k}'}P_{\mathbf{k}'}v(-\mathbf{k}')v(\mathbf{k}')}. \tag{43}$$

Here

$$P_{\mathbf{k}}=\frac{G_{\mathbf{k}}^0}{1-G_{\mathbf{k}}^0V_{\mathbf{kk}}},$$

$$V_{\mathbf{kk}}=\frac{1}{2\omega_{\mathbf{k}}}\left(-s_0\omega_{\mathbf{k}}^2-s_0\omega^2+\frac{\omega_c^2\omega^2}{\omega^2-\omega_c^2}c\right),$$

$$v(-\mathbf{k})v(\mathbf{k}_1)=\frac{1}{N\sqrt{\omega_{\mathbf{k}}\omega_{\mathbf{k}_1}}}\left(-s\omega_{\mathbf{k}}\omega_{\mathbf{k}_1}-s\omega^2+\frac{\omega_c^2\omega^2}{\omega^2-\omega_c^2}c\right).$$

Hence it is clear that the renormalization of the starting spectrum in this region is due mainly to forward scattering and is defined by the equation

$$1-G_{\mathbf{k}}^0V_{\mathbf{kk}}=0, \tag{44}$$

while the resonant frequencies are found by solving the generalized Lifshits equation

$$\mathrm{Re}\left(1-\sum_{\mathbf{k}'}P_{\mathbf{k}'}v(-\mathbf{k}')v(\mathbf{k}')\right)=0. \tag{45}$$

Using the Debye approximation for the starting spectrum ($3\omega^2/\omega_D^3$), we obtain the following expressions for the resonant frequency ω_R and spectral density for $\omega\ll\omega_D$:

$$\omega_R^2=\frac{\omega_D^2}{3}\frac{(1-s_0)(1-s_0-s)}{(1+s_0)(1+2s)}\left\{1-\frac{2+s_0}{1+s_0}c\right\}, \tag{46}$$

$$g(\omega)=g_0(\omega)+\Delta g(\omega), \tag{47}$$

where

$$g_0(\omega)=3\left(1+\frac{2+3s_0}{2(1+s_0)}c\right)\frac{(1+s_0)^{1/2}}{(1-s_0)^{3/2}}\frac{\omega^2}{\omega_D^3},$$

$$\Delta g(\omega)=\frac{1}{2\pi}\left(1+\frac{2-s_0}{2(1+s_0)}c\right)\frac{s^2}{(1-s_0^2)(1+2s)}\times\frac{\Gamma\omega^4}{(\omega^2-\omega_R^2)^2+(\Gamma\omega^3)^2},$$

$$\Gamma=\frac{\pi(1+2s-s_0)}{2(1+2s)(1+s_0)^{1/2}(1-s_0)^{3/2}}.$$

These functions, along with the starting spectrum, are plotted in Fig. 1. First of all, note the renormalization of the starting spectrum, due mainly to forward scattering. In this regard, notice also that as $s_0\to 1\,\omega_R\to 0$, i.e., the larger the difference between the singular term of the structure factor and the δ function of an ideal crystal, the more strongly the starting spectrum is renormalized and the lower the characteristic frequency of the resonant modes lies. The factor $1-s_0$ defining this behavior owes its existence to fluctuations of the force constants, i.e., to the first term on the right-hand side of Eq. (40). [In an ideal crystal ($s_0=s=0$) expression (46) formally gives $\omega_R^2=\omega_D^2/3$ and the resonance at low frequencies is absent.] Here the corrections due to the presence of the C at-

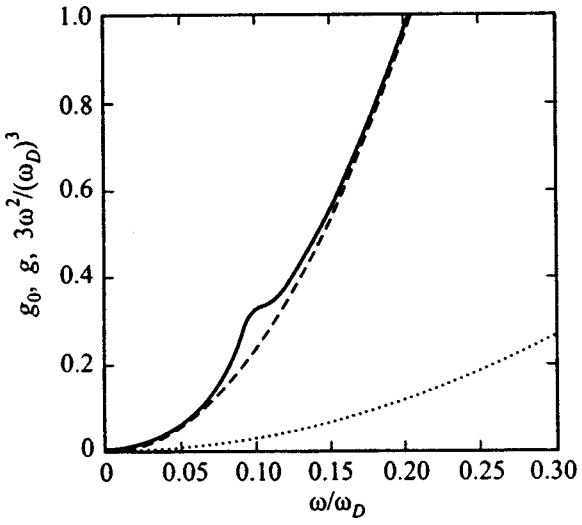

FIG. 1. Density of vibrational states for $\omega \ll \omega_D$, $s_0=0.7$, and $s=0.1$: g_0 (dashed curve) and g (solid curve). The dotted curve plots the starting spectrum $3\omega^2/(\omega_D)^3$.

oms, i.e., due to strong topological fluctuations, are small. However, these are the fluctuations that lead to a decrease in the so-called participation coefficient of the atoms in the given modes. Indeed, let us consider the spatial variation of the amplitude of a resonant mode near an isolated C atom located at the origin. Toward this end, we introduce in the coordinate representation the Green's function $\tilde{G}_{ii'}(\omega)$ satisfying the equation

$$M\omega^2\tilde{G}_{ii'}(\omega)=\delta_{ii'}+\sum_{i''} A_{ii''}\tilde{G}_{i''i'}(\omega). \tag{48}$$

We then obtain the following relation between the amplitude of the resonant mode at the site $\mathbf{r}_i$ and the amplitude of this mode w_0 at the C atom in question:

$$u_i=-M\omega_R^2\tilde{G}_{i0}w_0.$$

Employing relation (31) between the Green's functions in the two representations, we obtain the solution (43), in which we must eliminate that part of the scattering potential due to the C atoms, and also the value of the resonant frequency (46)

$$u_i\simeq \frac{\pi(1-s_0)^2}{4(1+s_0)}\,\frac{\cos(\pi\sqrt{1-s_0}r_i/\sqrt{3a})}{r_i}\,aw_0, \tag{49}$$

where a is the interatomic distance. Despite the slow Coulomb falloff in the amplitude, its value is already small at the nearest neighbor to the C atom: $u_i/w_0 \ll 1$, which, of course, leads to the decrease in the participation coefficient observed at the given frequencies.[3]

Let us make some concluding remarks. First of all, in this work we have shown that, in agreement with recent experimental data,[20,21] the presence of low-frequency excess modes can be understood in terms of the harmonic approximation. Further, the geometrical basis of the model lies in the division of the atoms into classes based on their coordination number, which formally leads to the unrenormalized optical modes even in a single-component glass. The actual existence of such modes depends, obviously, on the nature of the scattering in the high-frequency region of the spectrum and depends strongly on the actual composition of the glass. Nevertheless, the formal possibility of observing them in glasses which are nearly single-component, follows from the proposed approach. In addition, the geometrical basis (disclination model) is not obligatory in the treatment of the low-frequency resonances. Indeed, we have in fact shown that the main reason for the appearance of the low-frequency resonances in a glass is the strong fluctuations of the density and force constants while the low participation coefficient is due to the relatively high amplitude of the given modes in the strong topological fluctuations. Such a formulation, of course, does not depend on the details of the geometrical description of the structure of the glass.

The authors would like to thank V. A. Borodin and P. V. Vladimirov for numerous discussions of the structure of glasses, and also V. N. Peregudov for a discussion of various aspects of quasiparticle excitations.

This work was supported by the Russian Fund for Fundamental Research (Grant No. 97-02-16529).

*)E-mail:manichev@dni.polyn.kiae.su

[1] K. Ishii, Prog. Theor. Phys. Suppl. No. 53, 77 (1973).
[2] J. Hafner, in *Glassy Metals I*, edited by H.-J. Güntherodt and H. Beck (Springer, Berlin, 1981), p. 93.
[3] J. Hafner, M. Krajčí, and M. Windisch, J. Non-Cryst. Solids **192 & 193**, 212 (1995).
[4] M. Widom, Phys. Rev. B **34**, 756 (1986).
[5] M. A. Fradkin, Zh. Éksp. Teor. Fiz. **93**, 1442 (1987) [Sov. Phys. JETP **66**, 822 (1987)].
[6] J. M. Ziman, *Models of Disorder: The Theoretical Physics of Homogeneously Disordered Systems* (Cambridge University Press, Cambridge, 1979), Ch. 11.
[7] J.-B. Suck and H. Rudin, in *Glassy Metals II*, edited by H. Beck and H.-J. Güntherodt (Springer, Berlin, 1983), p. 217.
[8] G. J. Morgan, J. Phys. C **1**, 347 (1968).
[9] D. Nelson, Phys. Rev. B **28**, 5515 (1983).
[10] V. M. Manichev, Zh. Éksp. Teor. Fiz. **108**, 1446 (1995) [JETP **81**, 793 (1995)].
[11] D. Nelson and F. Spaepen, Solid State Phys. **42**, *1*, 1 (1989).
[12] F. C. Frank and J. S. Kasper, Acta Crystallogr. **11**, 184 (1958).
[13] F. C. Frank and J. S. Kasper, Acta Crystallogr. **12**, 483 (1959).
[14] J. F. Sadoc and N. Rivier, Philos. Mag. B **55**, 537 (1987).
[15] V. A. Borodin and V. M. Manichev, Phys. Rev. B **54**, 15 747 (1996).
[16] P. Gaskell, in *Glassy Metals II*, edited by H. Beck and H.-J. Güntherodt (Springer, Berlin, 1983), p. 5.
[17] A. M. Kosevich, JETP Lett. **1**, 146 (1965).
[18] I. M. Lifshits, Usp. Fiz. Nauk **83**, No. 4, 617 (1964) [Sov. Phys. Usp. **7**, 549 (1965)].
[19] V. M. Manichev and E. A. Gusev, J. Non-Cryst. Solids **232–234** (1998).
[20] J.-B. Suck, J. Non-Cryst. Solids **205–207**, 592 (1996).
[21] J.-B. Suck, Mater. Sci. Eng., A **226–228**, 479 (1997).

Translated by Paul F. Schippnick

Electrical properties of chromium films

G. M. Abramova and G. S. Patrin*)

Krasnoyarsk State University, 660041 Krasnoyarsk, Russia

N. I. Kiselev and G. A. Petrakovskiĭ

L. V. Kirenskiĭ Institute of Physics, 660036 Krasnoyarsk, Russia
(Submitted July 17, 1998; accepted for publication September 3, 1998)
Fiz. Tverd. Tela (St. Petersburg) **41**, 380–382 (March 1999)

We have investigated experimentally the influence of a constant electric current on the magnitude and temperature dependence of the resistance of chromium films prepared by vacuum-thermal condensation. The results are interpreted in terms of the Fröhlich conductivity model. [S1063-7834(99)00303-2]

In recent years, coherent states of conduction electrons in solids have been received great interest, in particular, in the guise of the phenomenon of Fröhlich conductivity[1] observed in the slip region of charge density waves (CDW's) and spin density waves (SDW's) and manifested in the nonlinear growth of the conductivity in electric fields E larger than some threshold value E_c. For this mechanism, as follows from Ref. 2, the critical field E_c can be approximated by

$$eE_c(2\pi/Q)=(\Sigma^2/E_F)\varepsilon^4 10^6, \tag{1}$$

where e is the charge of the electron, Q is the wave vector of the CDW (SDW), E_F is the Fermi energy, Σ is the dielectric gap of the CDW (SDW), and $\varepsilon\sim 1$. Estimates of the critical separation field of the spin density waves for chromium (Néel temperature $T_N\cong 312$ K, Ref. 3) based on Eq. (1) give $E_c\sim 16$ mV/cm. The critical separation current corresponding to E_c is given by

$$I_c=(l/R)E_c, \tag{2}$$

where l is the distance between contacts and R is the resistance of the metal. For bulk samples of chromium $R\sim 10^5\,\Omega$ and for $l\approx 0.5$ cm the separation current $I_c\approx 800$ A. However, in chromium films the resistance R grows by several orders of magnitude as the film thickness is decreased.[4] In view of this it may be expected that in chromium films for realistically attainable values of the transport current the Fröhlich conductivity regime is realized. For example, for $R=50\,\Omega$ one gets $I_c=1.28\times 10^{-4}$ A.

The present paper reports results of a study of the electrical properties of chromium films as functions of the transport current flowing through the sample.

Chromium films of thickness $d=700$ and 1040 Å were prepared by vacuum-thermal condensation on a glass substrate. The substrate temperature was $T=180\,^\circ$C. Electrolytic chromium of purity 99.99% or higher was used. The electrical resistance was measured by the four-probe potentiometric method at constant current in the temperature range $T=77-350$ K and current range $I=10^{-5}-10^{-1}$ A with an accuracy of $\pm 10^{-6}\,\Omega$. The temperature of the samples was monitored by a chromel–alumel thermocouple. The current–voltage characteristics (CVC's) at $T=78$ and 300 K were measured in the fixed-current regime for the current in the range $I=10^{-5}-7\times 10^{-3}$ A. The film thickness and its chemical composition were determined by x-ray fluorescence analysis, and the lattice parameters and phase composition—by x-ray structure analysis.

Figure 1 plots the temperature dependence of the resistance $R(T)$, measured for different values of the constant current, for a chromium film of thickness $d=1040$ Å. The points plotted in the inset for $T=78$ K were taken from the CVC's. The results of the measurements of $R(T)$ for $I=10^{-3}$ A in the temperature range $T=200-300$ K (inset to Fig. 1) agree with the data in the literature for thin chromium films[4] ($d=14-50$ Å) and bulk samples.[5] A weakly expressed anomaly in $R(T)$ is observed in the region of $T_{an}=280$ K. Below $T=200$ K the temperature dependence of the conductivity of the investigated chromium films differs substantially from that of the bulk samples,[5] but is similar to that observed in chromium alloys (e.g., Cr–Fe and Cr–V, Ref. 6). It is clear from Fig. 1 that the magnitude and temperature dependence of the resistance of chromium films in the temperature region $T\sim 78$ K depends substantially on the magnitude of the current at which the measurements were made. For currents $I<10^{-3}$ A, $R(T=78\,\text{K})$ exceeds $R(T=300\,\text{K})$ by almost 10%. Thus, for $I=10^{-5}$ A the ratio $R(T=78\,\text{K})/R(T=300\,\text{K})=1.095$.

Figure 2 plots the dependence of the resistance on the transport current, calculated from the current–voltage curves. We found that the CVC's of the investigated chromium films at $T=300$ K obey Ohm's law up to $I\approx 4\times 10^{-2}$ A and are hysteresis-free. The $R(I)$ dependence corresponding to the given current–voltage curve is plotted by curve *1* in Fig. 2. As follows from the experiment, the growth of the resistance at higher currents is associated with Joule heating of the sample. At $T=78$ K, as the current is increased the resistance falls abruptly in the current region $I=10^{-4}-10^{-3}$ A by almost 9% [curve *2* in Fig. 2(a)], after which a stepped falloff is observed up to $I\sim 10^{-1}$ A, with drops no greater than 1% [curve *2* in Fig. 2(b)]. The behavior of the CVC's and of $R(I)$ did not depend on the polarity of

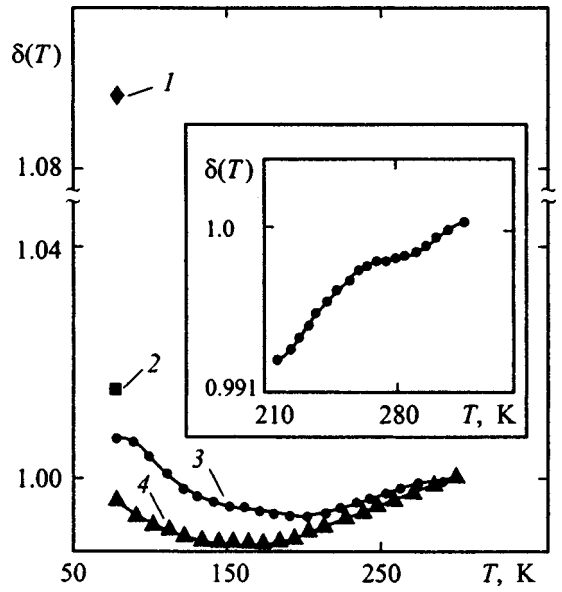

FIG. 1. Temperature dependence of the relative resistance $\delta(T)=R(T)/R(T=300\,\mathrm{K})$ for different values of the transport current. I (A): *1* — 10^{-4}, *2* — 4×10^{-4}, *3* — 10^{-3}, *4* — 7×10^{-2}. Inset plots the dependence $\sigma(T)$ for $I=10^{-3}$ A in the high-temperature region.

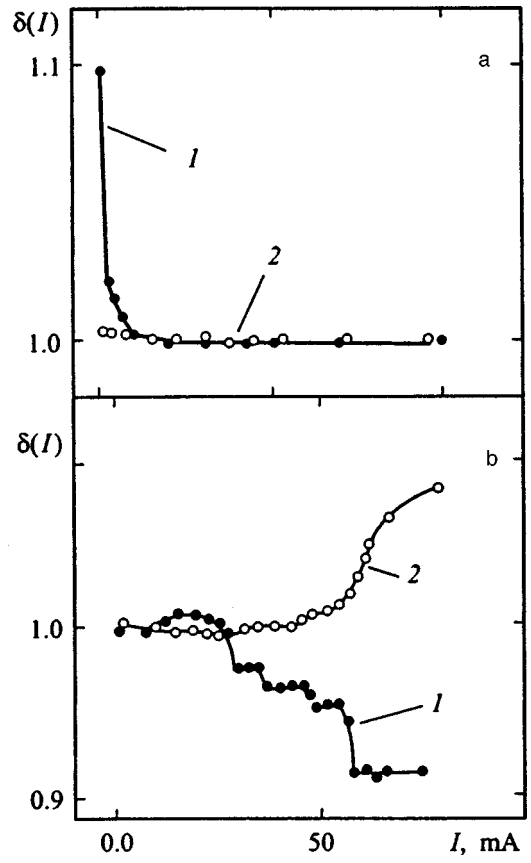

FIG. 2. Dependence of the relative resistance $\delta(I)=R(I)/R(I=10^{-3}\,\mathrm{A})$ on the transport current. $I=10^{-5}-10^{-3}$ A (a) and $10^{-3}-8\times10^{-2}$ A (b). $T=300$ (*1*) and 78 K (*2*).

the current; however, hysteresis was observed in the ''increase–decrease'' current cycle. These results were reproduced in all succeeding experiments.

The experimental value of the current at which the abrupt drop in $R(I)$ was observed was $I_J=10^{-4}$ A. A smoother decrease in $R(I)$ was observed up to $I=3.4\times10^{-2}$ A, after which the resistance grew weakly and then remained constant up to $I\approx10^{-3}$ A. Above this value a falling segment of $R(I)$ is again observed [Fig. 2(b)]. The estimates based on Eq. (1) for the investigated films give the value $I_c=6.8\times10^{-2}$ A, which is comparable with the experimental value I_J.

X-ray structure analysis of the films revealed the presence of an ultradispersed phase of chromium oxides. Chromium films with this type of phase composition, prepared by vacuum-arc sputtering, were discussed in Refs. 7 and 8. Note that quite a number of works have been dedicated to the problem of the formation of an oxide layer on the surface of chromium films (see, e.g., Refs. 7–9). According to the results of these works, the surface layer of the films consists of a mixture of metallic chromium and its oxides. The thickness of such a layer is equal to $t=15-150$ Å, depending on the method of preparation. The resistivity of the surface layer is given by the expression

$$(1/\sigma_0)=\rho_m^0 C_m^0\{1-(\mu_f/\mu_c)^n\}^{-1}, \tag{3}$$

where ρ_m^0 is the resistivity of the metal, C_m^0 is the concentration of the metal in the layer, μ_f is the concentration of the oxide phase, and μ_c is the critical concentration of oxide for the percolation mechanism of conductivity; the parameter $n\sim1-2$ (Ref. 8).

It is well known[10] that, using four-probe measurement, the conductivity of the sample is given by

$$\sigma=\sigma_0+\sigma_v Z. \tag{4}$$

Here Z is depth into the sample, measured from its surface, σ_0 is the surface conductivity [in the given case it is given by formula (3)], and σ_v is the bulk conductivity. Since the thickness of the conducting layer in which the electric field and current density are still uniform is much larger than the film thickness ($t\sim0.2$ cm, Ref. 11), it may be assumed that the entire volume of the film ($d=1040$ Å) contributes to the conductivity while the temperature dependence of the resistance is mainly determined by the conductivity of metallic chromium. This conclusion is supported by the dependence plotted in the inset to Fig. 1.

It was shown in Ref. 8 that the presence of a 15–20% oxide phase in Ni–Cr films increases the resistance twofold in comparison to the value characteristic of the metal. (Unfortunately, works dedicated to the electrical properties of chromium films have not indicated the value of the current at which the measurements were performed.) In our case, the resistance of the film at $T=300$ K, for a current $I=10^{-3}$ A, was $R=1.225\times10^{-4}\,\Omega$, which exceeds by two orders of magnitude the resistance of bulk samples of chromium.

Since at temperatures above the temperature of the resistance anomaly [Fig. 2(a)] no noticeable changes were observed in the resistance of the films, considered as a function of the current, the nature of the observed nonlinear effects in the low-temperature region can be associated with the presence of a SDW state, e.g., as a manifestation of Fröhlich

conductivity due to slip of the spin density wave.[1]

The experimental results obtained here allow one to conclude that the electrical properties of chromium films of the given thickness depend substantially on the magnitude of the transport current. To come to an unambiguous conclusion about the mechanisms responsible for the observed peculiarities in the electrical conductivity of chromium films, a detailed study of the dependence of the electrical properties on the conditions of preparation as well as the thickness is required.

The authors express their gratitude to G. V. Bondarenko for x-ray fluorescence analysis and A. D. Vasil'ev for x-ray structure measurements of the samples.

*)E-mail: pat@iph.krasnoyarsk.ru

[1] S. N. Artemenko and A. F. Volkov, Usp. Fiz. Nauk **166**, No. 4, 434 (1996).
[2] P. A. Lee and T. M. Rice, Phys. Rev. B **19**, 3970 (1979).
[3] N. I. Kulikov and V. V. Tugushev, Usp. Fiz. Nauk **144**, No. 4, 643 (1984) [Phys. Usp. **27**, 954 (1984)].
[4] J. A. J. Lourens, S. Arajs, H. F. Helbig, L. Cheriet, and El-Sayed A. Mehanna, J. Appl. Phys. **63**, 4282 (1988).
[5] Y. Ishikova, S. Ikeda, and Ch. Akiba, J. Phys. Soc. Jpn. **39**, No. 3, 823 (1975).
[6] V. Yu. Galkin, Fiz. Met. Metalloved. **77**, No. 2, 5 (1994).
[7] A. Ya. Vovk and A. V. Filatov, Metallofiz. Noveĭshie Tekhnol. **20**, No. 1, 17 (1998).
[8] H. Bartuch, H. Dintner, and A. Nimmrichter, Thin Solid Films **116**, No. 3, 211 (1984).
[9] K. Shanker and P. H. Holloway, Thin Solid Films **105**, No. 4, 293 (1983).
[10] N. F. Kovtonyuk and Yu. A. Kontsevoĭ, *Measurement of Parameters of Semiconductor Materials* [in Russian] (Metallurgiya, Moscow, 1970), 429 pp.
[11] H. R. Kokabi, I. Provost, and G. Desgardin, Rev. Sci. Instrum. **64**, No. 6, 1549 (1993).

Translated by Paul F. Schippnick

Radiation-induced changes in the atomic structure of grain boundaries in tungsten

E. I. Lugovskaya and T. I. Mazilova

Scientific-Research and Design Institute of Vacuum Machine Building, 310109 Khar'kov, Ukraine
(Submitted April 23, 1998; accepted for publication September 4, 1998)
Fiz. Tverd. Tela (St. Petersburg) **41**, 383–385 (March 1999)

Field-ion microscopy is used to study changes in the structure of the grain boundaries induced by intergrain adsorption of point defects created by ion bombardment of tungsten bicrystals. It is found that irradiation at temperatures below the threshold of grain-boundary relaxation causes a local expansion of the boundaries. Computer simulation using molecular dynamics shows that intergrain adsorption of vacancies can lead to the formation of three-dimensional grain-boundary structures. © *1999 American Institute of Physics.* [S1063-7834(99)00403-7]

In *fcc* metals characterized by low stacking-fault energies, splitting of the dislocations at the block walls leads to the formation of complex three-dimensional configurations ($3D$ structures). At the large-angle boundaries in these materials in a number of cases formation of $3D$ structures with splitting of the dislocations in closest packed planes intersecting the boundaries was also observed.[1–3] Large-angle grain boundaries in *fcc* metals characterized by high stacking-fault energies, as was shown in earlier studies using field-ion microscopy,[4,5] are localized two-dimensional lattice defects. In the present work we show that, at temperatures below the grain-boundary relaxation threshold, adsorption of radiation defects at large-angle grain boundaries in tungsten is accompanied by the formation of metastable $3D$ structures characterized by an increased stacking-fault energy.

The experiments were performed using a field-ion microscope with the samples cooled to 21–80 K. As the imaging gas we used helium at a pressure of $10^{-2}-10^{-3}$ Pa. Bicrystalline needle-like specimens with radii of curvature about $20-100$ nm were prepared by electrochemical etching from a tungsten wire with mean diameter of the grains (fibers) equal to 250 nm.

The samples were bombarded with helium ions formed by the passage of an auto-electron current. The intensity of ion bombardment was determined using relations derived in Ref. 6. When the ions were formed at distances r less than $10r_0$ from the tip, where r_0 is the radius of the tip, bombardment proceeded from the conical region of formation of the ion flux, and when they were formed at larger distances r bombardment proceeded from a cylindrical region coaxial with the specimen. In the present work the electric field strength E in the auto-electron regime was $(4-5)\times 10^7$ V/cm during bombardment. For $r_0<100$ nm, the ions formed at $r<10r_0$ have an energy below the displacement threshold. As a consequence, the main contribution to the generation of point defects comes from ions formed in a comparatively distant cylindrical region. For the cylindrical region the ion energy distribution is Maxwellian,[7] similar to the energy distribution in Tokamak-type plasma setups, with mean energy equal to eEr_0, where e is the charge of the electron. Thus, when needlelike specimens are bombarded by ions formed by the interaction of auto-electrons with atoms of the imaging gas, the action of the low-energy component of the plasma on the first wall of nuclear reactors is imitated.

Radiation-induced changes in the atomic structure of the grain boundaries were investigated in the temperature interval $750-1000$ K, in which the interstitial atoms and vacancies are mobile and processes of grain-boundary relaxation are suppressed in tungsten.[8,9] Some of the specimens were bombarded at temperatures of $1070-1200$ K. The mean ion energy of the ion flux bombarding this group of specimens lay in the interval $200-350$ eV. The total helium ion fluxes lay in the range $10^{16}-5\times 10^{17}$ ion/cm^2. Analysis of the series of ion-microscope images taken during field ablation showed that the inner regions of the microcrystals do not contain lattice defects that could be responsible for preferential adsorption of one of the different types of point defects. In light of the small dimensions of the microcrystallites, we can neglect processes of recombination of point defects. In this approximation, the maximum calculated total flux of interstitial atoms and vacancies onto the grain boundaries in the surface layer of the bicrystals was 8×10^{17} cm^{-2}.

As a result of helium-ion bombardment at total fluxes of 5×10^{16} ion/cm^2 and above, formation of segments of the grain boundaries characterized by anomalously large values of the width of the region with increased stacking-fault energy was observed. The width of the region of preferential field ablation of the atoms at the large-angle boundaries grew by two- to threefold, reaching values of $1.0-1.2$ nm. Figures 1(a)–(c) show a series of field-ion-microscope images of a segment of the surface of a tungsten bicrystal bombarded by a helium-ion flux of 7×10^{16} ion/cm^2 with a mean ion energy of 250 eV. Images of the boundary in the segment of the mating of the (211) faces of adjacent grains A and B were taken sequentially after ablation of the bombarded crystal to a depth of 10, 12, and 14 nm [Figs. 1(a)–(c)]. In Fig. 1(d) the dashed lines demarcate a segment of the boundary of enhanced thickness, which can be related to $3D$ structures. These microphotographs also illustrate the characteristic inhomogeneity of the structure of boundaries in bombarded tungsten: the $3D$ structure was observed only on one facet of

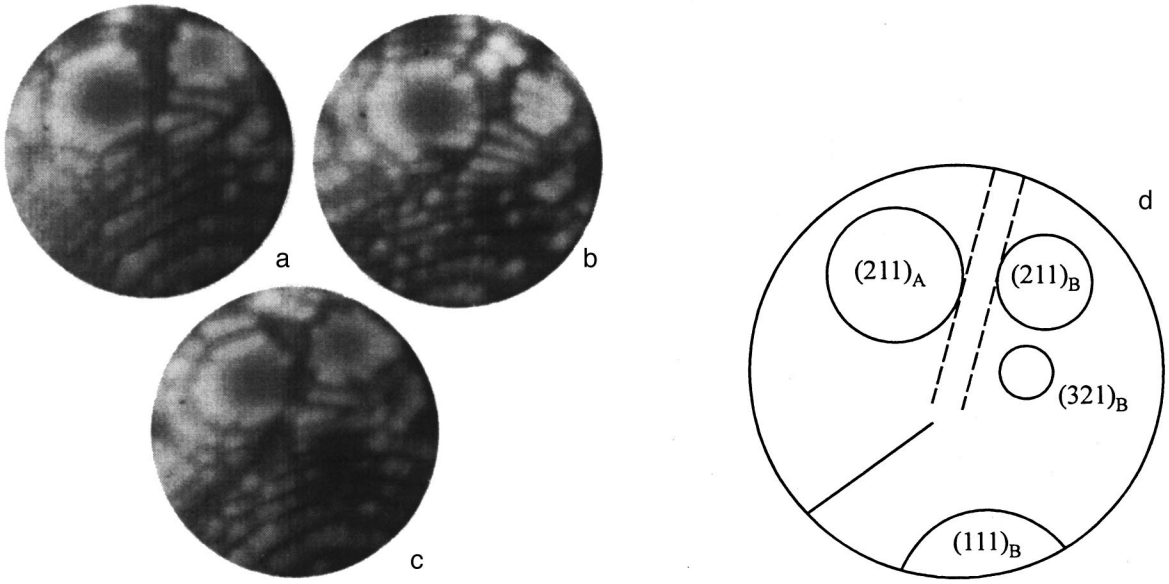

FIG. 1. Field ion microscope images of a tungsten bicrystal bombarded by a helium ion flux 7×10^{16} ion/cm^2 with mean energy 250 eV. Images a–c were obtained after ablation of the bombarded crystal to a depth of 10, 12, and 14 nm, respectively. The dashed lines in diagram d demarcate a segment of the boundary with 3*D* structure, and the solid line indicates the position of a two-dimensional facet.

the grain-boundary ledge. Calculation of the lowering of the field-ablation energy Q in these segments, based on the model of image forces,[10] gives $\Delta Q/Q=8.5\times10^{-2}$. Expansion of the large-angle grain boundaries during bombardment at temperatures above 1100 K was not observed. This may be connected with the occurrence of processes of grain-boundary relaxation.

These data show that as a result of intergrain adsorption, the point defects not only annihilate each other, but also induce substantial changes in the structure of the grain boundaries. Comparison with the results of a study of the evolution of the structure of the grain boundaries as a result of intergrain adsorption of helium[7,11] and interstitial atoms[12] suggests that the more mobile interstitial atoms wind up at the free surface during intergrain adsorption, resulting in an enrichment of the grain boundaries by vacancies. In this case, the vacancy component of the radiation-defect flux may be responsible for the observed expansion of the boundaries. With this in mind, we performed a computer simulation of the evolution of the structure of the grain boundaries induced

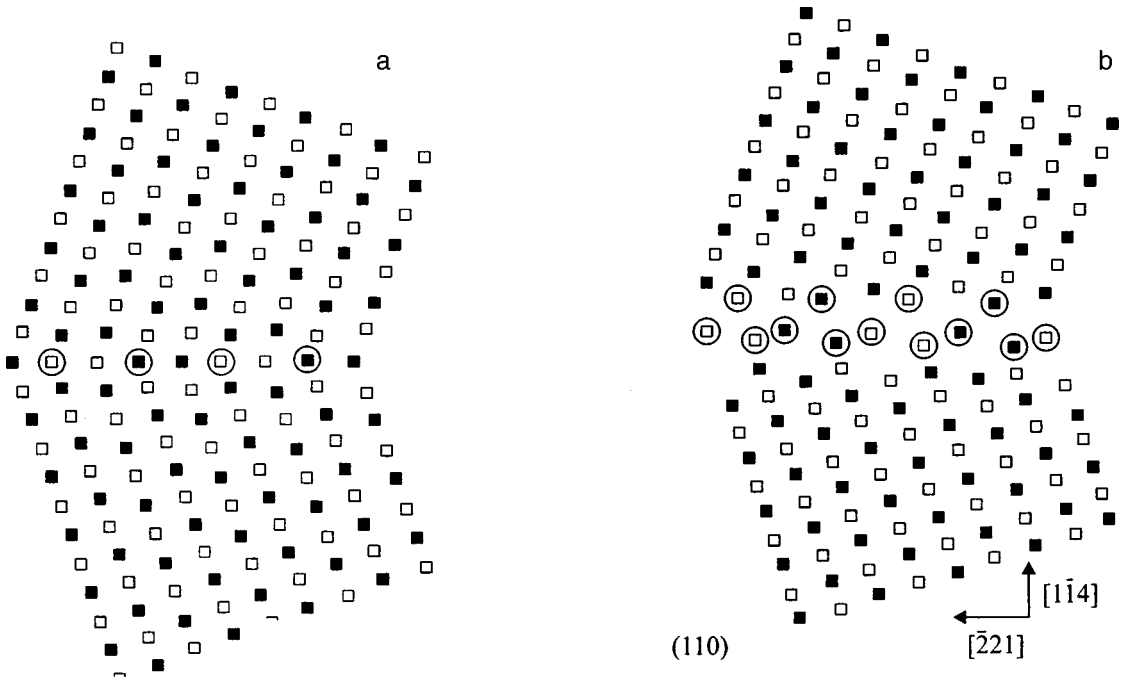

FIG. 2. Atomic configurations of an equilibrium symmetric $\Sigma9(114)$ boundary (a) and this same boundary after adsorption of two monolayers of vacancies (b).

by the adsorption of several monolayers of vacancies. The model crystallite consisted of 840 interacting and 504 boundary atoms. On the outer {110} faces we prescribed periodic boundary conditions, and on the remaining faces we prescribed flexible boundary conditions. The bicrystal consisted of 40 atomic planes {114}, parallel to the $\Sigma 9$, 38.9°, {110} boundary. The computer simulation employed molecular dynamics with a central pairwise potential.[13,14] Adsorption of a monolayer of vacancies was simulated by removal of a {114} atomic layer from the region of the nucleus of the boundary.

Results of the computer simulation of the evolution of the structure at the grain boundaries are shown in Fig. 2. The initial boundary was characterized by a high degree of localization of the stacking-fault energy. The largest stacking-fault energy is observed in the partly coalesced[13,15] {114} planes in the nucleus of the boundary [Fig. 2(a)]. The maximum energy corresponding to a {114} sublattice shifted during coalescence is equal to 0.70 eV/atom. The atoms with large excess energy are denoted in Fig. 2 by circles whose radius is proportional to the stacking-fault energy. With distance from the geometrical center of the boundary the stacking-fault energy falls exponentially with a scale factor in the exponential equal to $2.5\,\mathrm{nm}^{-1}$. The formation at the boundary of two vacancy layers leads to a change in the character of the stacking-fault energy distribution. The excess energy at the level 0.5 ± 0.2 eV/atom is observed in three atomic {114} layers [Fig. 2(b)], and only beyond the limits of this $3D$ structure does the exponential falloff of the stacking-fault energy occur. As a result, the specific surface energy of the boundary is raised to $3.0\,\mathrm{J/m}^2$, near the specific surface energy of the single crystals.[1] It is significant that such $3D$ structures, despite the significant increase in the stacking-fault energy as in the case of *fcc* metals,[1–3] are metastable: stable to dilational and shear grain-boundary deformations. The excess stacking-fault energy per atom of the $3D$ layer is significantly less than the formation energy of the vacancies in tungsten (3.9 eV), and its formation can be vouchsafed by the liberation of the energy of the vacancies during their intergrain adsorption.

ACKNOWLEDGMENTS

In conclusion, we would like to express our deep gratitude to V. S. Boĭko and I. M. Mikhaĭlovskiĭ for helpful discussions.

[1] A. P. Sutton and R. W. Ballufi, *Interfaces in Crystalline Materials* (Clarendon Press, Oxford, 1995), 819 pp.
[2] F. Ernst, M. W. Finnis, D. Hofmann, T. Muschik, U. Schonberger, D. Wolf, and M. Methfessel, Phys. Rev. Lett. **69**, 620 (1992).
[3] D. Wolf and K. L. Merkle, *Materials Interfaces*, edited by D. Wolf and S. Yip (Chapman & Hall, London, 1992), p. 87.
[4] D. G. Brandon, B. Ralph, S. Ranganathan, and M. S. Wald, Acta Metall. **12**, No. 7, 813 (1964).
[5] R. I. Garber, Zh. I. Dranova, and I. M. Mikhaĭlovskiĭ, Zh. Éksp. Teor. Fiz. **54**, 714 (1968) [Sov. Phys. JETP **27**, 381 (1968)].
[6] P. A. Bereznyak and V. V. Slezov, Radiotekh. Elektron. **17**, No. 2, 354 (1972).
[7] P. A. Bereznyak, O. A. Velikodnaya, V. I. Gerasimenko, Zh. I. Dranova, and I. M. Mikhaĭlovskiĭ, Vopr. Atom. Nauki i Tekhniki. Fizika radiatsionnykh povrezhdeniĭ i radiatsionnoe materialovedenie, *1(61)*, 41 (1994).
[8] A. S. Lazarenko, I. M. Mikhailovskij, V. B. Rabukhin, and O. A. Velikodnaja, Acta Metall. Mater. **43**, No. 2, 639 (1995).
[9] V. V. Kirsanov, A. L. Suvorov, and Yu. V. Trushin, *Processes of Radiation Defect Formation in Metals* [in Russian] (Énergoatomizdat, Moscow, 1985), 272 pp.
[10] E. W. Muller and T. T. Tsong, *Field Ion Microscopy* (American Elsevier Publishing Company, New York, 1969).
[11] V. I. Gerasimenko, I. M. Mikhaĭlovskiĭ, I. M. Neklyudov, A. A. Parkhomenko, and O. A. Velikodnaya, Zh. Tekh. Fiz. **68**, No. 7, 64 (1998) [Tech. Phys. **43**, 803 (1998)].
[12] Zh. I. Dranova and I. M. Mikhaĭlovskiĭ, Fiz. Met. Metalloved. **26**, No. 1, 33 (1984).
[13] P. A. Bereznyak, O. A. Velikodnaya, T. I. Mazilova, and I. M. Mikhaĭlovskiĭ, Pis'ma Zh. Tekh. Fiz. **59**, No. 8, 515 (1994) [Tech. Phys. Lett. **59**, 542 (1994)].
[14] V. V. Pokropivnyĭ, Metallofizika i Noveĭshie Tekhnologii **18**, No. 2, 38 (1996).
[15] T. I. Mazilova and I. M. Mikhailovskii, Crystallogr. Rep. **42**, No. 5, 729 (1997).

Translated by Paul F. Schippnick

Shape of the magnetic resonance line in a thin film on the surface of an anisotropic superconductor

S. A. Efremova and S. L. Tsarevskiĭ*)

Kazan' State University, 420008 Kazan', Russia
(Submitted June 17, 1998)
Fiz. Tverd. Tela (St. Petersburg) **41**, 386–388 (March 1999)

The shape of the EPR line in a thin ($=\lambda/2$, where λ is the London penetration depth of the magnetic field in the superconductor) paramagnetic film deposited on the surface of an anisotropic superconductor is calculated in an oblique magnetic field with allowance for the inhomogeneity of the local magnetic field of the Abrikosov vortex lattice. It is shown that, as the tilt angle of the external magnetic field is varied, the shape of the EPR line changes noticeably. This fact can give additional information about the superconductor parameters (the symmetry type of the vortex lattice and the anisotropy parameter of the superconductor).
 [S1063-7834(99)00503-1]

At present, the method of observation of the electron paramagnetic resonance (EPR)[1–3] and nuclear magnetic resonance (NMR)[4] of a magnetic marker on the surface of a high-temperature superconductor (HTSC) is widely used to study the penetration of a magnetic field into a superconductor and the transition to the superconducting state. In EPR studies, a film of the free radical diphenyl picrylhydrazyl (DPPH) deposited on the surface of the superconductor is often used as the magnetic marker[1,3] while silicone is usually used in NMR studies.[4] In either case, the variation of the inhomogeneous line width of the magnetic resonance as a function of temperature is tracked as the sample transitions to the superconducting state or to the vortex state as the external uniform field is swept. Such experiments allow one to estimate the penetration depth of the magnetic field in the superconductor λ and the local macroscopic magnetization of the sample. However, if a thin film ($\leqslant 1000$ Å) of controllable thickness is used as the EPR or NMR marker, then it is possible to obtain significantly richer information about the parameters of the superconductor from an analysis of the line shape of the magnetic resonance. The present paper reports results of a calculation of the line shape of the magnetic resonance in a thin magnetic film of calibrated thickness ($\cong 0.5\lambda$) deposited on the surface of an anisotropic superconductor, in a magnetic field that is tilted relative to the surface of the superconductor. It is well known that in an external field **H** ($H_{c1}<H<H_{c2}$, where H_{c1} and H_{c2} are the critical fields) in a type-II superconductor a two-dimensional Abrikosov vortex lattice is formed. The authors of Ref. 5 obtained analytical expressions for the Fourier components

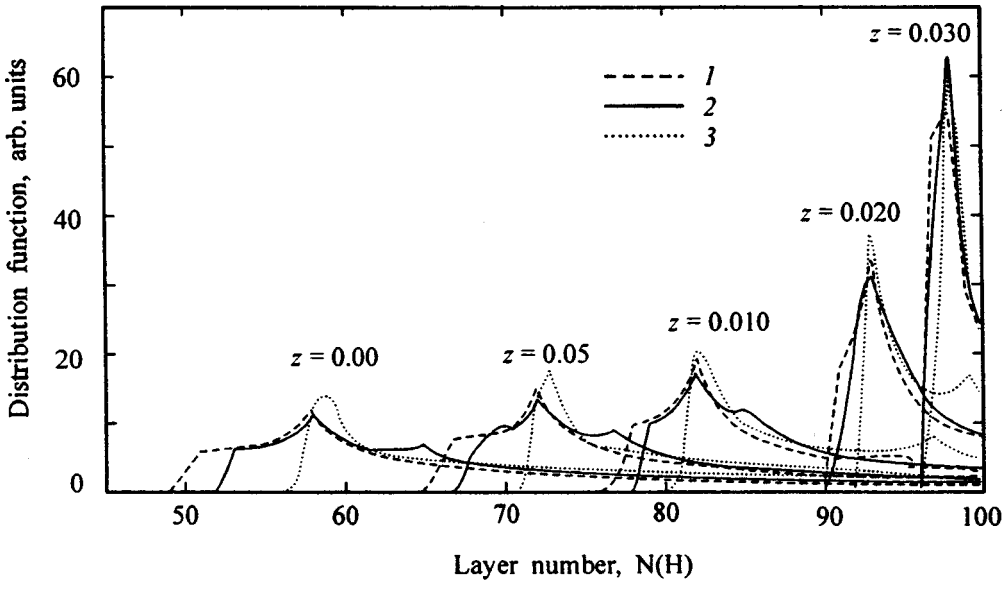

FIG. 1. Distribution function $\rho(h,z,\theta)$ of the local magnetic field **h** in the unit cell of the vortex lattice above the surface of the superconductor (in arbitrary units) for $\theta=0$ (*1*), $\pi/6$ (*2*), and $\pi/3$ (*3*). Field values are plotted along the abscissa in the units $100\,(h-h_{\min})/(H-h_{\min})$. $H=2$, $h_{\min}=1.8767$.

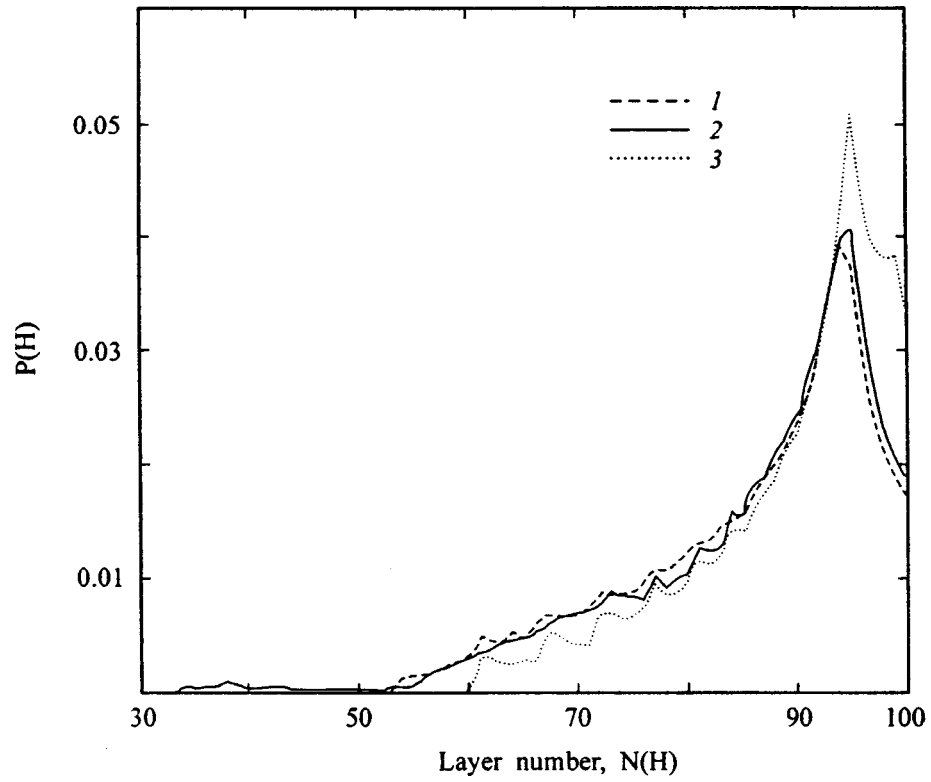

FIG. 2. Dependence of the absorption energy P on the magnetic field and the tilt angle θ. $\theta=0$ (*1*), $\pi/6$ (*2*), $\pi/3$ (*3*). Labelling of the abscissa the same as in Fig. 1.

of the local magnetic field **h** above the surface of the superconductor in an oblique magnetic field on the basis of a solution of the London equations. A picture of the magnetic field at assorted distances z above the surface of the superconductor can be gained using the inverse Fourier transform. To analyze the shape of the resonance line requires a quite detailed picture of the magnetic field in the unit cell of the vortex lattice for a representative set of distances above the surface of the superconductor. This depends on both the number of points into which the unit cell of the vortex lattice is divided and at which $\mathbf{h}(\mathbf{r})$ is calculated (we used 512×512 points) and also the number of such portraits as a map of h (there were 100). On the basis of these maps it is possible to obtain the density distribution function $\rho(h,z,\theta)$ of the local magnetic field within a narrow layer $z,z+dz$ above the surface of the superconductor (θ is the angle between the normal to the surface, parallel to the **c** axis, and the uniform magnetic field **H**).[5] By way of an example, Fig. 1 plots $\rho(h,z,\theta)$ for various θ and z. The calculations were performed for the HTSC Y–Ba–Cu–O with anisotropy parameter $\Gamma=25$ in a field $H=2$ (in units of Φ_0/λ^2). The field is plotted along the abscissa in units of $100(h-h_{\min})/(H-h_{\min})$, where $h_{\min}=1.8767$ is the minimum value of the local magnetic field in the interior of the superconductor.[5] As can be seen from Fig. 1, in oblique magnetic fields the line shape $\rho(h,z,\theta)$ becomes complicated by the appearance of an additional peak. This is due to the fact that, an additional saddle point with a different field value appears in the distribution of the local magnetic field in the immediate vicinity above the surface of the superconductor. The height of the peaks and their relative positions for a given tilt angle θ and height z, of course, depend on the symmetry type of the vortex lattice and the anisotropy parameter of the superconductor Γ. Calculations show that a nonuniform field quite rapidly becomes uniform, already at a distance $\simeq0.5$ (measured in units of λ). Thus, to determine the characteristics of a nonuniform field of Abrikosov vortices using an EPR marker it is necessary to use films of a specific thickness, less than 0.5. The power of the variable magnetic field absorbed by the resonant spins located in a narrow layer above the surface is proportional to $\int_0^d\rho(h,z,\theta)dz$, where d is the film thickness. It should also be noted that each resonant spin has its own absorption curve possessing, as a rule, a Lorentzian line shape and defining the homogeneous absorption width Δ. The power of the variable magnetic field absorbed by all the resonant spins, considered as a function of the external magnetic field H and the angle θ, is equal to

$$P(H,\theta)=C\int_{-\infty}^{\infty}dh\,\frac{\Delta}{\Delta^2+(H-h)^2}\int_0^d dz\,\rho(h,z,\theta). \qquad (1)$$

The constant C is defined by the normalization requirement $\int P(H,\theta)dH=1$.

Figure 2 plots the EPR lines $P(H,\theta)$ calculated according to Eq. (1) for the paramagnetic marker DPPH deposited on the surface of the HTSC, $d=0.5$, $\Delta=2$ [in units of $(H-h_{\min})/100$], for three values of θ.

As can be seen from Fig. 2, the line shape of the EPR marker varies quite noticeably with variation of the tilt angle of the external magnetic field, which makes it possible to

extract more detailed information about the local magnetic field of the superconductor (e.g., the symmetry type of the vortex lattice, the anisotropy parameter Γ, etc.).

*)E-mail: Sergey.Tsarevskii@ksu.ru

[1] B. Rakvin, P. Pozek, and A. Dulcic, Solid State Commun. **72**, 199 (1989).
[2] A. A. Romanyukha, Yu. N. Shvachko, and B. B. Ustinov, Usp. Fiz. Nauk **161**, No. 10, 37 (1991) [Sov. Phys. Usp. **34**, 862 (1991)].
[3] R. I. Khasanov, Yu. M. Vashakidze, and Yu. I. Talanov, Physica C **218**, No. 1–2, 51 (1993).
[4] Y. Maniva, T. Mituhashi, K. Muzoguchi, and K. Kurne, Physica C **175**, No. 3–4, 401 (1991).
[5] S. A. Efremova and S. L. Tsarevskiĭ, Fiz. Tverd. Tela (St. Petersburg) **39**, 1935 (1997) [Phys. Solid State **39**, 1729 (1997)].

Translated by Paul F. Schippnick

Comparative analysis of the effect of La and Co on the superconductivity and energy-band spectrum of $YBa_2Cu_3O_y$ for different oxygen contents

V. É. Gasumyants, E. V. Vladimirskaya, M. V. Elizarova

St. Petersburg State Technical University, 195251 St. Petersburg, Russia

I. B. Patrina

Institute of Silicate Chemistry, Russian Academy of Sciences, 195155 St. Petersburg, Russia
(Submitted June 25, 1998)
Fiz. Tverd. Tela (St. Petersburg) **41**, 389–394 (March 1997)

Temperature dependences of the resistivity and Seebeck coefficient of $Y(Ba_{1-x}La_x)_2Cu_3O_y$ and $YBa_2Cu_{3-x}Co_xO_y$ samples ($x=0-0.25$) have been measured under maximum sample saturation with oxygen, as well as following their anneal in an oxygen-deficient atmosphere. The $T_c(x)$ dependences for as-prepared samples were found to pass through a maximum at $x=0.05$, which persists after annealing for $Y(Ba_{1-x}La_x)_2Cu_3O_y$ and disappears for $YBa_2Cu_{3-x}Co_xO_y$. A phenomenological model of the band spectrum in normal phase has been used to determine the parameters of the conduction band and of the carrier system, and to analyze their variation with the dopant type and content, as well as with annealing. Despite the differences observed in the $T_c(x)$ dependence, the critical temperatures for all the sample series studied were found to correlate with the conduction-band effective width. The mechanism of the effect of impurities on the band-structure parameters and the reasons for the different influence of annealing on the properties of $Y(Ba_{1-x}La_x)_2Cu_3O_y$ and $YBa_2Cu_{3-x}Co_xO_y$ are discussed. [S1063-7834(99)00603-6]

It is known that the state of the oxygen subsystem determines to a considerable extent both the properties of the normal phase and the critical temperature T_c in the $YBa_2Cu_3O_y$ system. In addition to annealing the sample in an oxygen-deficient atmosphere, the oxygen content and distribution in the lattice can be affected by doping it with various heterovalent impurities. The pattern of variation of $YBa_2Cu_3O_y$ properties when the chain copper is replaced by $3d$ metals (Fe, Co, Al), and when rare-earth elements are substituted for barium is basically the same, although in the first case it is copper that is replaced which, besides oxygen, is assumed to be responsible for the properties of the normal phase. It appeared of interest to carry out a comparative quantitative analysis of the effect of the above two types of substitution on the characteristics of the normal state in order to reveal the part played by various lattice sites in the formation of the band responsible for conduction.

We use an analysis of transport coefficients to solve this problem in normal phase based on the model of electronic transport in HTSC materials,[1] which permits one to determine quantitative band-structure parameters and to analyze the trends in its transformation observed when doping with different impurities.[1–3] We chose cobalt and lanthanum, respectively, for the impurities to substitute for copper and barium. The first of them substitutes for copper in $YBa_2Cu_{3-x}Co_xO_y$ within a broad concentration range only at the chain sites,[4,5] and the second is widely used in studies of the effect of barium substitution because of their ionic radii being close in magnitude (for Ba, $r_i=1.35$ Å, and for La, $r_i=1.33$ Å). Both impurities have a higher valence than that of the elements they replace, which results in an increase of oxygen content with increasing doping level.[4,6–9] A characteristic feature of the $YBa_2Cu_{3-x}Co_xO_y$ and $YBa_{2-x}La_xCu_3O_y$ systems is that for low concentrations of both impurities T_c slightly increases with x, to be followed by its sharp decrease.[4,8–11] It was pointed out[8] that the maximum in the $T_c(x)$ dependence at small x for $YBa_{2-x}La_xCu_3O_y$ is observed in samples with the highest possible extent of orthorhombic distortion, for which reason the presence of this maximum is associated with additional filling by oxygen of the O(1) sites. The transformation of the temperature dependences of resistivity[8–10,12–15] and of the Seebeck coefficient[13,16,17] with increasing content both of cobalt and lanthanum is basically similar to that observed in the case of increasing oxygen deficiency. Note that, as shown in our earlier work,[17] the $YBa_{2-x}La_xCu_3O_y$ system exhibits, despite the nonmonotonic pattern of the $T_c(x)$ dependence, a correlation between the band-structure parameters and T_c, which was previously found to be characteristic of the $YBa_2Cu_3O_y$ system with other types of substitution.

This has stimulated the present comparative study of the effect of cobalt and lanthanum on the superconductivity, transport properties in the normal phase, and band-structure parameters of $YBa_2Cu_{3-x}Co_xO_y$ ($x=0-0.25$) and $YBa_{2-x}La_xCu_3O_y$ ($x=0-0.5$). In order to obtain more detailed information on the mechanism of the impurity effect, on the reasons for the nonmonotonic pattern of the $T_c(x)$ dependence, and on the nature of the relation between the band-structure parameters and superconducting properties of the Y–Ba–Cu–O compounds, the influence of additional

TABLE I. Unit cell parameters in as-prepared $Y(Ba_{1-x}La_x)_2Cu_3O_y$ samples and oxygen content before (y_1) and after (y_2) annealing.

x	a, Å	b, Å	$a-b$, Å	c, Å	y_1	y_2
0.00	3.822	3.885	0.063	11.670	6.95	6.86
0.025	3.820	3.894	0.074	11.655	6.98	6.89
0.05	3.823	3.895	0.072	11.630	6.99	6.92
0.10	3.819	3.890	0.071	11.650	7.03	6.96
0.15	3.828	3.879	0.051	11.640	7.10	7.02
0.20	3.857	3.857	0	11.600	7.14	7.04
0.25	3.853	3.853	0	11.580	7.17	7.06

off-stoichiometry in oxygen was also investigated for both systems.

1. SAMPLE CHARACTERISTICS

$YBa_{2-x}La_xCu_3O_y$ ($x=0-0.5$) and $YBa_2Cu_{3-x}Co_xO_y$ ($x=0-0.25$) ceramic samples were prepared by the standard solid-phase synthesis. The final treatment included annealing in an oxygen flow at $T=450\,^\circ$C for 10 h. All samples were shown by x-ray diffraction to be single phase with an accuracy not worse than 1%. To reflect the percentage relation between the substituting and substituted element, we used for the chemical formulas $Y(Ba_{1-x}La_x)_2Cu_3O_y$ ($x=0-0.25$) and $YBa_2Cu(2)_2Cu(1)_{1-x}Co_xO_y$ ($YBa_2Cu_{3-x}Co_xO_y$) ($x=0-0.25$), because lanthanum can occupy in $YBa_2Cu_3O_y$ two equivalent barium sites, whereas cobalt can substitute for copper only in the Cu(1) site. The cell parameters determined from x-ray diffraction measurements to within $\pm 0.001-0.002$ are listed in Tables I and II. At $x=0.025$, the $Y(Ba_{1-x}La_x)_2Cu_3O_y$ system exhibits the largest orthorhombic distortion $b-a$, while for $YBa_2Cu_{3-x}Co_xO_y$ the $b-a$ parameter is the same for $x=0$ and 0.05. The $Y(Ba_{1-x}La_x)_2Cu_3O_y$ compound transfers to trigonal symmetry near $x=0.2$, and $YBa_2Cu_{3-x}Co_xO_y$, near $x=0.10$, which is in agreement with literature data.[4,6,8,9,15,18] The extra oxygen deficiency was achieved by combined annealing of samples of both series in vacuum at $T=450\,^\circ$C for 2 h. The oxygen content was determined by iodometric titration to within $\pm 0.01-0.02$. The oxygen indices y for all four series are listed in Tables I and II. An increase in doping level gives rise to an increase of y, and after annealing the oxygen content decreased by 0.07–0.1.

TABLE II. Unit cell parameters in as-prepared $YBa_2Cu_{3-x}Co_xO_y$ samples and oxygen content before (y_1) and after (y_2) annealing.

x	a, Å	b, Å	$a-b$, Å	c, Å	y_1	y_2
0.0	3.822	3.880	0.058	11.698	6.98	6.88
0.05	3.831	3.889	0.058	11.682	7.00	6.90
0.10	3.865	3.872	0.007	11.661	7.02	6.92
0.15	3.869	3.869	0	11.676	7.04	6.94
0.20	3.872	3.872	0	11.669	7.05	6.95
0.25	3.874	3.874	0	11.666	7.06	6.95

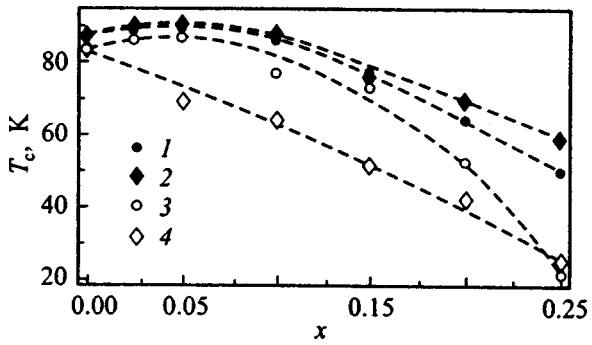

FIG. 1. Critical temperature vs impurity content for (*1,3*) $Y(Ba_{1-x}La_x)_2Cu_3O_y$ and (*2,4*) $YBa_2Cu_{3-x}Co_xO_y$ compounds. *1,2* — as-prepared sample series; *3,4* — sample series with reduced oxygen content.

2. EXPERIMENTAL RESULTS

We measured temperature dependences of the resistivity and Seebeck coefficient on all series of samples within the $T=T_c-300$ K range by the technique described elsewhere.[16]

The temperature dependences of resistivity follow the pattern typical of the $YBa_2Cu_3O_y$ system. For three series, the values of ρ decrease linearly with decreasing temperature, and the slope of the $\rho(T)$ curves decreases with increasing impurity content. An exclusion from this rule is the series of $YBa_2Cu_{3-x}Co_xO_y$ samples with an extra oxygen deficiency, where one observes for $x\geqslant 0.15$ a transition to semiconducting behavior of $\rho(T)$ in the low-temperature domain.

Figure 1 presents T_c vs impurity concentration plots for all four series derived from resistivity measurements. Both as-prepared sample series exhibit a maximum in the $T_c(x)$ dependence at $x=0.05$. Note that the lattice undergoes a maximum orthorhombic distortion near this impurity concentration, and the oxygen content approaches the closest to the stoichiometry value $y=7$, which implies the maximum ordering in the oxygen subsystem (see Tables I and II). Further increase of the impurity concentration results in a monotonic decrease of the critical temperature. After annealing in an oxygen-deficient atmosphere, the maximum in the $T_c(x)$ dependence for the $Y(Ba_{1-x}La_x)_2Cu_3O_y$ system remains at the same lanthanum concentration, whereas in $YBa_2Cu_{3-x}Co_xO_y$ T_c falls off monotonically with increasing x throughout the concentration range covered.

The temperature dependences of the Seebeck coefficient for $Y(Ba_{1-x}La_x)_2Cu_3O_y$ and $YBa_2Cu_{3-x}Co_xO_y$ are displayed in Figs. 2 and 3. They exhibit all the features characteristic of the $YBa_2Cu_3O_y$ system, viz. an extended region at high temperatures where $S(T)\approx$ const (for samples only slightly deviating from stoichiometry) and a maximum in $S(T)$ at $T=120-200$ K. As the impurity content increases, the Seebeck coefficient grows substantially in absolute magnitude, the maximum in the $S(T)$ dependence broadens and shifts toward higher temperatures. The decrease in oxygen content brought about the expected increase in the absolute value of the Seebeck coefficient for both systems, but the shape of the $S(T)$ curves and the pattern of their transformation with increasing doping level did not undergo any

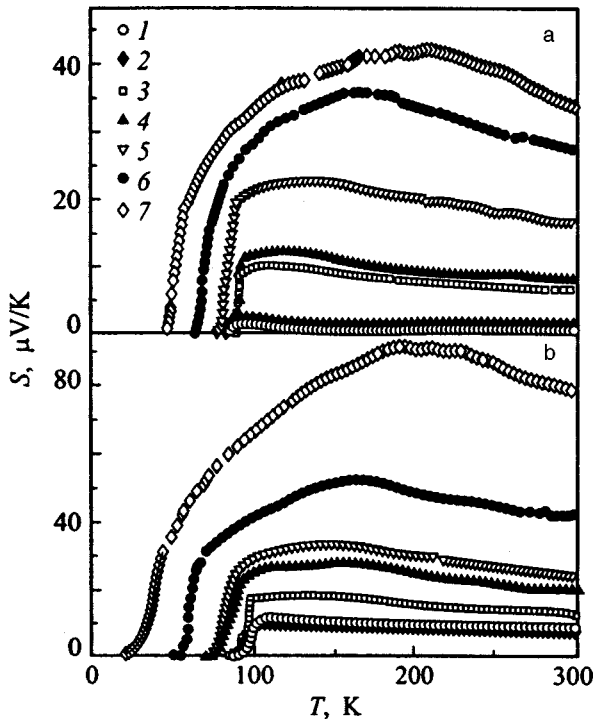

FIG. 2. Temperature dependences of the Seebeck coefficient for $Y(Ba_{1-x}La_x)_2Cu_3O_y$. a — as-prepared samples, b — series with reduced oxygen content. x: *1* — 0, *2* — 0.025, *3* — 0.05, *4* — 0.1, *5* — 0.15, *6* — 0.2, *7* — 0.25.

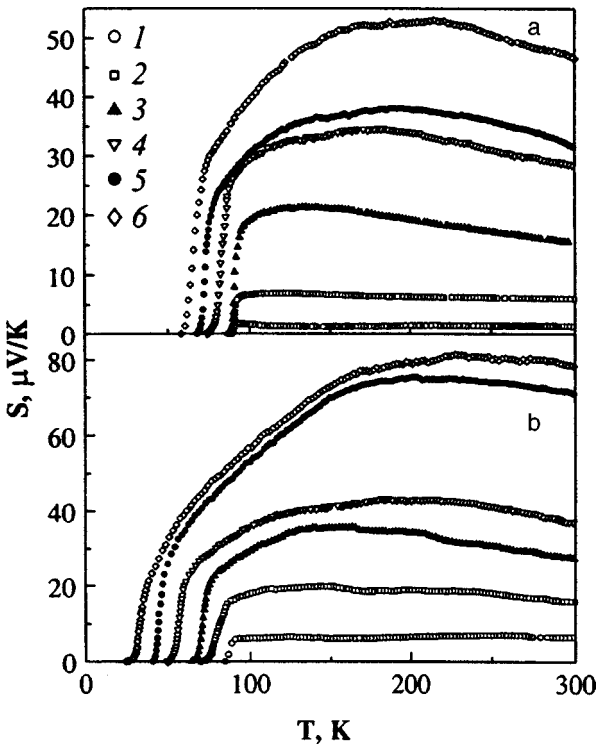

FIG. 3. Temperature dependences of the Seebeck coefficient for $YBa_2Cu_{3-x}Co_xO_y$. a — as-prepared samples, b — series with reduced oxygen content. x: *1* — 0, *2* — 0.05, *3* — 0.1, *4* — 0.15, *5* — 0.2, *6* — 0.25.

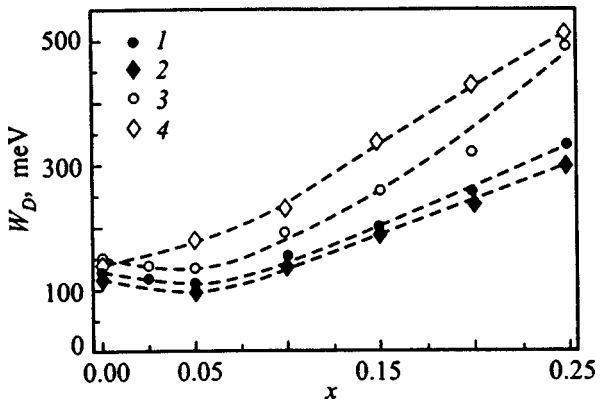

FIG. 4. Total effective conduction-band width vs doping level in (*1,3*) $Y(Ba_{1-x}La_x)_2Cu_3O_y$ and (*2,4*) $YBa_2Cu_{3-x}Co_xO_y$ compounds. *1,2* — as-prepared samples; *3,4* — sample series with reduced oxygen content.

noticeable changes. Thus the behavior of $S(T)$ in $Y(Ba_{1-x}La_x)_2Cu_3O_y$ and $YBa_2Cu_{3-x}Co_xO_y$ samples with increasing doping level is similar to that observed[2] in $YBa_2Cu_3O_y$ with increasing oxygen deficiency.

3. ANALYSIS OF THE RESULTS AND CONCLUSIONS

The results obtained were analyzed within the phenomenological model of electronic transport in normal phase (narrow-band model), which was described in detail in our previous publications.[1,2] A quantitative comparison of calculations with the experimental data presented in the preceding Section has permitted determination of the three main model parameters characterizing band structure and the carrier system, namely, the effective width of the conduction band W_D and the interval of delocalized states W_σ, as well as the electron filling of the band F, which is equal to the ratio of the number of electrons n to the number of band states N. We are now going to analyze the concentration dependences of these parameters for the samples studied.

As for the band filling F, it grows nearly linearly in all four sample series with impurity concentration (for the as-prepared samples, from 0.5 to 0.543 and 0.565, and for the annealed ones, from 0.51 to 0.565 and 0.579 for the samples doped with lanthanum and cobalt, respectively). This means that the La → Ba and Co → Cu(1) heterovalent substitutions do not bring about complete compensation of the excess positive charge through increasing oxygen content, and that the number of carriers (holes) in the band decreases. In the $YBa_2Cu_{3-x}Co_xO_y$ system, F increases more than in $Y(Ba_{1-x}La_x)_2Cu_3O_y$ for the corresponding substitution levels, which can be attributed to a lower degree of compensation of the excess positive charge by the extra oxygen (see Tables I and II).

Figure 4 presents the effective conduction-band width W_D calculated as a function of doping level for all the sample series studied. In the $Y(Ba_{1-x}La_x)_2Cu_3O_y$ system, one immediately sees a weak minimum in the $W_D(x)$ dependence at $x=0.05$ for samples both with a high and a reduced oxygen index. A similar pattern is observed with the first series of $YBa_2Cu_{3-x}Co_xO_y$ samples as well, but in this compound a decrease in oxygen content results in a disappear-

ance of the minimum in the $W_D(x)$ dependence to make it monotonically rising throughout the cobalt range studied. The width of the interval of delocalized states W_σ varies with increasing impurity content similar to W_D in all the four series, including the presence of a minimum in the $W_\sigma(x)$ dependence in the first three cases. Note that within the region where W_σ and W_D increase, their ratio falls off gradually. Indeed, in the annealed series, the ratio W_σ/W_D decreases from 0.36 and 0.42 at $x=0.05$ to 0.21 and 0.24 at $x=0.25$ for the samples doped with lanthanum and cobalt, respectively.

The observed nonmonotonic variation in the conduction-band width correlates with the extent of disorder on the chain-oxygen subsystem and can be accounted for assuming the Anderson mechanism of localization of states to operate in the systems studied. Recall that, for low lanthanum concentrations in $Y(Ba_{1-x}La_x)_2Cu_3O_y$, the O(1) oxygen sites are believed to continue filling.[8] It may be posited that a similar process takes place in the $YBa_2Cu_{3-x}Co_xO_y$ compound as well. In this case the impurity concentration $x\approx 0.05$ corresponds to the maximum order in the oxygen subsystem, where all O(1) sites are filled, whereas the O(5) sites remain vacant. As a result, it is at this impurity content that the conduction-band width becomes minimum. Further increase of x in both systems gives rise to a statistically distributed filling of the O(5) oxygen sites throughout the crystal, thus setting in and increasing disorder on the oxygen subsystem. Accordingly, W_D increases, and the ratio W_σ/W_D decreases, i.e. one observes a relative narrowing of the interval of delocalized states at the band edges.

As for the superconducting properties of the systems under study, one observes a clear correlation between the effective band width and T_c (see Figs. 1 and 4), which finds explanation within our model. If the number of band states remains constant or varies only weakly, a decrease in W_D for low impurity concentrations results in an increase of the DOS function at the Fermi level, $D(E_F)$, which reaches a maximum at $x=0.05$, thus favoring the maximum critical temperature. Further growth in concentration of both impurities broadens the band and, hence, causes $D(E_F)$ to decrease. This decrease is still more enhanced by the increasing band filling, which shifts the Fermi level toward higher energies away from the DOS maximum. The decrease of $D(E_F)$ brings about the observed falloff of T_c. Note that the $Y(Ba_{1-x}La_x)_2Cu_3O_y$ and $YBa_2Cu_{3-x}Co_xO_y$ compounds exhibit similar trends in variation of the band structure parameters and of T_c. One observes only some quantitative differences in their dependences on doping level, and to the critical temperatures T_c, which, on the whole, are higher for the $YBa_2Cu_{3-x}Co_xO_y$ series, correspond smaller effective band widths.

The total increase in oxygen content in each of the sample series studied resulted in an increase of W_D due to the additional oxygen disordering, in agreement with the data[1,2] for $YBa_2Cu_3O_y$ obtained with different values of y (see Fig. 4). At the same time the observed correlation between the width of the conduction band and the critical temperature in the $Y(Ba_{1-x}La_x)_2Cu_3O_y$ and $YBa_2Cu_{3-x}Co_xO_y$ compounds is retained also when additional off-stoichiometry in oxygen is produced (see Figs. 1 and 4). To the minimum in the $W_D(x)$ dependence for $Y(Ba_{1-x}La_x)_2Cu_3O_y$ at $x=0.05$ corresponds the maximum value of T_c, and in the $YBa_2Cu_{3-x}Co_xO_y$ system the monotonic growth of W_D is accompanied by a continuous decrease of the critical temperature. For the $YBa_2Cu_{3-x}Co_xO_y$ series, W_D is, on the whole, larger, and T_c, accordingly, lower than those for $Y(Ba_{1-x}La_x)_2Cu_3O_y$, with the exception of the $x=0.25$ samples, where both the effective band widths and the critical temperatures are approximately the same. Thus our data support the existence for $YBa_2Cu_3O_y$ of a universal correlation between the effective conduction-band width and T_c, which was observed[19] earlier for various types of off-stoichiometry.

An analysis of results obtained on all four sample series studied permits the following conclusion. The mechanism of the effect produced by the impurities entering into chain copper or barium sites is basically the same and is determined primarily by the influence these atoms exert on the oxygen content and the pattern of oxygen distribution among lattice sites. It is the change in the properties of the oxygen subsystem induced by incorporation of nonisovalent impurities that is the principal factor governing both the band-structure parameters in normal phase and the superconducting properties of the $YBa_2Cu_3O_y$ system. The broadening of the conduction band caused by increasing disorder among the chain oxygens is the main reason for the doping-induced suppression of superconducting properties of $YBa_2Cu_3O_y$.

Based on this conclusion and on the pattern of the oxygen redistribution caused by lanthanum and cobalt, consider the possible reasons for the persistent nonmonotonic course of the $T_c(x)$ and $W_D(x)$ dependences for $Y(Ba_{1-x}La_x)_2Cu_3O_y$ and for the absence of a maximum in $T_c(x)$ and of a minimum in $W_D(x)$ for $YBa_2Cu_{3-x}Co_xO_y$ after an annealing in oxygen-deficient atmosphere.

Cobalt, which substitutes for copper directly in the Cu(1) chain sites, has a larger coordination number and tends to increase the number of oxygens in its environment by forming with them sufficiently strong bonds. For this reason it is more difficult for oxygen to leave under annealing the cells that contain cobalt atoms. Therefore, as the crystal-averaged oxygen content decreases under annealing, the oxygen subsystem undergoes additional disordering because oxygen escapes nonuniformly from different cells. Thus even in samples with low cobalt concentrations the chain-oxygen subsystem becomes more disordered than that in a $x=0$ sample. This is why the variation of band width and, accordingly, of the superconducting properties with increasing cobalt content becomes monotonic after annealing. On the other hand, substitution of lanthanum for barium affects weaker the oxygen subsystem. Because lanthanum atoms are outside the chains, their bonding with excess oxygen is weaker, and oxygen escapes from various cells under annealing more uniformly to leave the oxygen distribution in the chains, on the whole, unchanged. Thus the minimum in the $W_D(x)$ dependence and, accordingly, the minimum in $T_c(x)$ for oxygen-deficient samples remain at the same lanthanum concentrations as before the annealing.

To sum up, a comparative analysis of the effects of co-

balt and lanthanum doping on the properties of $YBa_2Cu_3O_y$ permits the following conclusions.

1. $Y(Ba_{1-x}La_x)_2Cu_3O_y$ and $YBa_2Cu_{3-x}Co_xO_y$ compounds with close to stoichiometric oxygen contents in the as-prepared sample exhibit a maximum in $T_c(x)$ dependences at the impurity concentration $x=0.05$. As the oxygen content is lowered gradually in all $Y(Ba_{1-x}La_x)_2Cu_3O_y$ samples, the maximum in $T_c(x)$ remains at the same lanthanum concentration, whereas in $YBa_2Cu_{3-x}Co_xO_y$ the dependence of the critical temperature on impurity content follows a smooth decline.

2. An analysis of the $S(T)$ dependences made in terms of the narrow-band model has yielded the main band-structure parameters for the samples studied and revealed their variation with impurity concentration. A universal correlation has been shown to exist in all cases between the effective conduction-band width and the critical temperature.

3. A comparative analysis of the variation of band-structure parameters and of the critical temperature in $YBa_2Cu_3O_y$ induced by the $Co \rightarrow Cu(1)$ and $Ba \rightarrow La$ nonisovalent substitutions shows the main reason for the variation of the properties of this compound to be the impurity-induced change in the state of the oxygen subsystem, in particular, the extent of disorder among the chain oxygens.

4. The differences in the transformation of the concentration dependences of the critical temperature and band-structure parameters in $Y(Ba_{1-x}La_x)_2Cu_3O_y$ and $YBa_2Cu_{3-x}Co_xO_y$ systems induced by annealing in an oxygen-deficient atmosphere can be accounted for by different patterns of chain-oxygen distribution caused by the impurities occupying the chain copper and barium sites.

One of the authors (V. É. G.) expresses his gratitude to the St. Petersburg Administration, Russian Academy of Sciences, and Ministry of Universal and Specialized Education for financial support (Young Scientists Grant for 1998).

[1] V. E. Gasumyants, V. I. Kaidanov, and E. V. Vladimirskaya, Physica C **248**, 255 (1995).
[2] V. É. Gasumyants, S. A. Kaz'min, V. I. Kaĭdanov, V. I. Smirnov, Yu. M. Baĭkov, and Yu. P. Stepanov, Sverkhprovodimost' (KIAE) **4**, 1280 (1991).
[3] E. V. Vladimirskaya, V. É. Gasumyants, and I. B. Patrina, Fiz. Tverd. Tela (St. Petersburg) **37**, 1990 (1995) [Phys. Solid State **37**, 1084 (1995)].
[4] J. M. Tarascon, P. Barboux, P. F. Miceli, L. H. Greene, G. W. Hall, M. Eibschutz, and S. A. Sunshine, Phys. Rev. B **37**, 7458 (1988).
[5] R. S. Howland, T. H. Geballe, S. S. Laderman, A. Fischer-Colbrie, M. Scott, J. M. Tarascon, and P. Barboux, Phys. Rev. B **39**, 9017 (1989).
[6] Y. Xu, R. Sabatini, A. R. Moodenbaugh, Yi. Zhu, S.-G. Shyu, M. Suenaga, K. W. Dennis, and R. W. McCallum, Physica C **169**, 205 (1990).
[7] A. Tokiwa, Y. Syono, M. Kikuchi, R. Suzuki, T. Kajitani, N. Kobayashi, T. Sasaki, O. Nakatsu, and Y. Muto, Jpn. J. Appl. Phys. **27**, L1009 (1988).
[8] R. Liang, M. Itoh, T. Nakamura, and R. Aoki, Physica C **157**, 83 (1989).
[9] A. Manthiram and J. B. Goodenough, Physica C **159**, 760 (1989).
[10] J. J. Neumeier, Appl. Phys. Lett. **61**, 1852 (1992).
[11] R. G. Buckley, D. M. Pooke, J. L. Tallon, M. R. Presland, N. E. Flower, M. P. Staines, H. L. Johnson, M. Meylan, G. V. M. Williams, and M. Bowden, Physica C **174**, 383 (1991).
[12] V. S. Grunin, I. B. Patrina, M. M. Pivovarov, M. V. Razumenko, N. P. Baranskaya, I. A. Drozdova, and V. L. Makarov, Sverkhprovodimost' (KIAE) **3**, No. 10, 110 (1990).
[13] B. Fisher, J. Genossar, L. Patlagan, and G. M. Reisner, Phys. Rev. B **48**, 16056 (1993).
[14] Z. He, Z. Chen, Z. Zhao, Z. Xu, Y. Qian, and Q. Zhang, Phys. Lett. A **132**, 217 (1988).
[15] R. Aoki, S. Takahashi, and H. Murakami, Physica C **156**, 405 (1988).
[16] E. V. Vladimirskaya and V. É. Gasumyants, Fiz. Tverd. Tela (St. Petersburg) **36**, 1002 (1994) [Phys. Solid State **36**, 545 (1994)].
[17] E. Vladimirskaya, V. Gasumyants, and I. Patrina, Superlattices Microstruct. **21**, Suppl. A, 71 (1997).
[18] C. Y. Yang, A. R. Moodenbaugh, Y. L. Wang, Y. Xu, S. M. Heald, D. O. Welch, M. Suenaga, D. A. Fischer, and J. E. Penner-Hahn, Phys. Rev. B **42**, 2231 (1990).
[19] V. É. Gasumyants, E. V. Vladimirskaya, and I. B. Patrina, Fiz. Tverd. Tela (St. Petersburg) **39**, 1520 (1997) [Phys. Solid State **39**, 1352 (1997)].

Translated by G. Skrebtsov

Epitaxial combination of $NdBa_2Cu_3O_{7-\delta}/SrTiO_3$: growth characteristics, structure, and parameters

Yu. A. Boĭkov and V. A. Danilov

A. F. Ioffe Physicotechnical Institute, Russian Academy of Sciences, 194021 St. Petersburg, Russia

T. Claeson

Chalmers University of Technology, S-41296 Göteborg, Sweden

D. Érts

Institute of Chemical Physics, University of Latvia, 1586 Riga, Latvia

(Submitted July 6, 1998)
Fiz. Tverd. Tela (St. Petersburg) **41**, 395–403 (March 1999)

We have studied the growth characteristics, structure, and parameters of the epitaxial heterostructures $(001)NdBa_2Cu_3O_{7-\delta}/(100)SrTiO_3/(001)NdBa_2Cu_3O_{7-\delta}$ grown by laser ablation on a $(100)LaAlO_3$ substrate with a thin ($\sim$2 nm) $YBa_2Cu_3O_{7-\delta}$ intermediate layer. The use of an $YBa_2Cu_3O_{7-\delta}$ intermediate layer promotes layered growth of the (200 nm) $NdBa_2Cu_3O_{7-\delta}$ layer, whose free-surface roughness is 4–5 nm. The resistance of the $NdBa_2Cu_3O_{7-\delta}$ layers began to fall off abruptly at $T=92$ K, and at $T\approx 87$ K it vanished completely. The critical current density in the $NdBa_2Cu_3O_{7-\delta}$ layers at $T=76$ K exceeded 10^6 cm^2 A/cm^2. The dielectric constant of the (400 nm) $SrTiO_3$ layer sandwiched between the $NdBa_2Cu_3O_{7-\delta}$ epitaxial layers grew by roughly threefold as the temperature was lowered in the interval 300–4.2 K. When a bias voltage of ± 2.5 V was applied to the $NdBa_2Cu_3O_{7-\delta}$ electrodes, the relative dielectric constant of the (400 nm) $SrTiO_3$ intermediate layer fell from 1150 to 400 ($T=32$ K, $f=100$ kHz). The conductivity of the $SrTiO_3$ intermediate layer in the direction perpendicular to the substrate plane increased with temperature and the electric field strength. © *1999 American Institute of Physics.* [S1063-7834(99)00703-0]

Epitaxial films of $RBa_2Cu_3O_{7-\delta}$ (R is a rare-earth element), grown on single-crystal substrates made from materials having a low dielectric constant ε and low dielectric losses $\tan\delta$, have been used successfully to form passive elements in the microwave range, in particular narrow-band filters with working frequencies of tens of GHz.[1,2] At present, efforts are actively underway to create tunable microwave components using the epitaxial combination superconductor/ferroelectric, such as phase converters, filters, varactor structures, etc.[3,4]

The parameters of the microwave component based on a superconductor/ferroelectric heterostructure were changed by varying the dielectric constant ε of the ferroelectric layer in a controllable way under the action of an electric field. The strong dependence of ε on the electric field strength E in bulk single crystals of ferroelectric materials is observed, as a rule, at temperatures near the phase transition temperature.[5] The main ferroelectric candidates for use in epitaxial combination with $RBa_2Cu_3O_{7-\delta}$ films are $(Ba,Sr)TiO_3$ and $KTaO_3$.[6,7]

The parameters of the thin ferroelectric layer of the multi-layer epitaxial heterostructure based on $RBa_2Cu_3O_{7-\delta}$ films differ substantially from their values for the corresponding bulk samples. The main reasons for the degradation of ε and the abrupt growth of $\tan\delta$ in the thin $(Ba,Sr)TiO_3$ and $KTaO_3$ layers in comparison to the corresponding single crystals are the high density of structural defects in them and violations of stoichiometry in the vicinity of the interphase boundaries.

$NdBa_2Cu_3O_{7-\delta}$ (NBCO) films are attractive for use in microwave components and superconducting microelectronics because 1) the highest superconducting transition temperature $T_c\approx 97$ in $RBa_2Cu_3O_{7-\delta}$ superconductors is achieved for R≡Nd (Ref. 8); 2) NBCO epitaxial films have a smooth free surface (Ref. 9); and 3) neutralization of Ba vacancies in an NBCO film by Nd ions should lead to suppression of diffusion fluxes between the layers constituting the superconductor/ferroelectric epitaxial heterostructure, since barium, in particular, is capable of actively diffusing out of the superconducting film.[10]

We did not find any data in the literature on the dielectric properties of thin $(Ba,Sr)TiO_3$ layers in combination with NBCO electrodes. According to Ref. 9, to grow distinctly **c**-oriented NBCO films it is necessary to raise the substrate temperature T_s at which the vapor phase formed by laser ablation of the starting mixture still condenses, to 840 °C.

The present work investigates the possibility of achieving layered growth of a (001)NBCO film at the T_s and oxygen pressure used to grow $SrTiO_3$ (STO) epitaxial films. The trilayer epitaxial heterostructures (001)NBCO/(100)STO/(001)NBCO were formed and studied.

1. EXPERIMENT

We used laser ablation to grow films of NBCO, $YBa_2Cu_3O_{7-\delta}$ (YBCO), and STO (KrF, $\lambda = 248$, $\tau = 30$ ns). The NBCO films and the NBCO/STO/NBCO trilayer heterostructures were grown on (100)$LaAlO_3$ substrates ($5 \times 5 \times 0.5$ mm). The STO intermediate layer in the heterostructures had thickness $d = 400$ nm, and the thickness of the superconductor films was 200 nm. As the starting targets we used polycrystalline sheets of stoichiometric NBCO, YBCO, and STO, prepared by standard ceramic technology. Ablation of the targets took place in an oxygen atmosphere with $P_O = 0.3$ mbar. T_s was equal to 780 °C during growth of the superconductor films and thin layers of strontium titanate. The density of the laser radiation on the target surface during growth of the NBCO, YBCO, and STO films was equal to 1.5 J/cm^2.

To form steps of height ~1.2 nm on the substrate, a (001)YBCO intermediate layer of thickness 2 nm was grown on the (100)$LaAlO_3$ surface immediately before onset of formation of the NBCO film.

The structure and composition of the formed NBCO films and NBCO/STO/NBCO heterostructures were monitored with the aid of a Philips PW 1710 x-ray diffractometer ($\theta/2\theta$ scanning) and a Siemens D 5000 x-ray diffractometer (ϕ scanning).

The surface morphology of the formed NBCO films (of thickness 2 − 200 nm), the STO layer grown on the surface of the (200 nm)NBCO/(2 nm)YBCO/$LaAlO_3$ heterostructure, and the upper NBCO film in the (200 nm)NBCO/(400 nm)STO/(200 nm)NBCO trilayer heterostructure was investigated with the aid of a NanoScope-IIIa atomic-force microscope.

T_c was determined for the NBCO films from the temperature dependence of the resistance R and magnetic susceptibility χ. The critical current density J_c was measured on microbridges of thickness 4 μm and length 25 μm, formed in the NBCO films by means of photolithography and ion etching (Ar, 500 V, 0.2 mA).

To measure ε, the conductivity G, and $\tan\delta$ for the STO layer sandwiched between the two NBCO epitaxial layers, plane-parallel capacitor structures were formed in which the lower NBCO film served as the common electrode.

Photolithography and ion etching were used to form the upper electrodes with area $S = 35 \times 10^3$ μm^2 in the NBCO film grown on the surface of the STO layer. The capacitance C, conductivity G, and loss factor $\tan\delta$ were measured in the temperature interval 4.2 − 300 K with a HP 4263A LCR meter ($f = 0.1 - 100$ kHz). The dielectric parameters of the STO layer were measured with a bias voltage $V_b = \pm 2.5$ V on the NBCO electrodes and without it. The bias voltage was taken to be positive when a positive voltage was imposed on the upper electrode. The effective dielectric constant of the ferroelectric layer was calculated using the relation $\varepsilon = Cd/S$.

2. RESULTS

Despite the fact that all the cuprate superconductors of the group $RBa_2Cu_3O_{7-\delta}$ are isomorphic in structure, the sur-

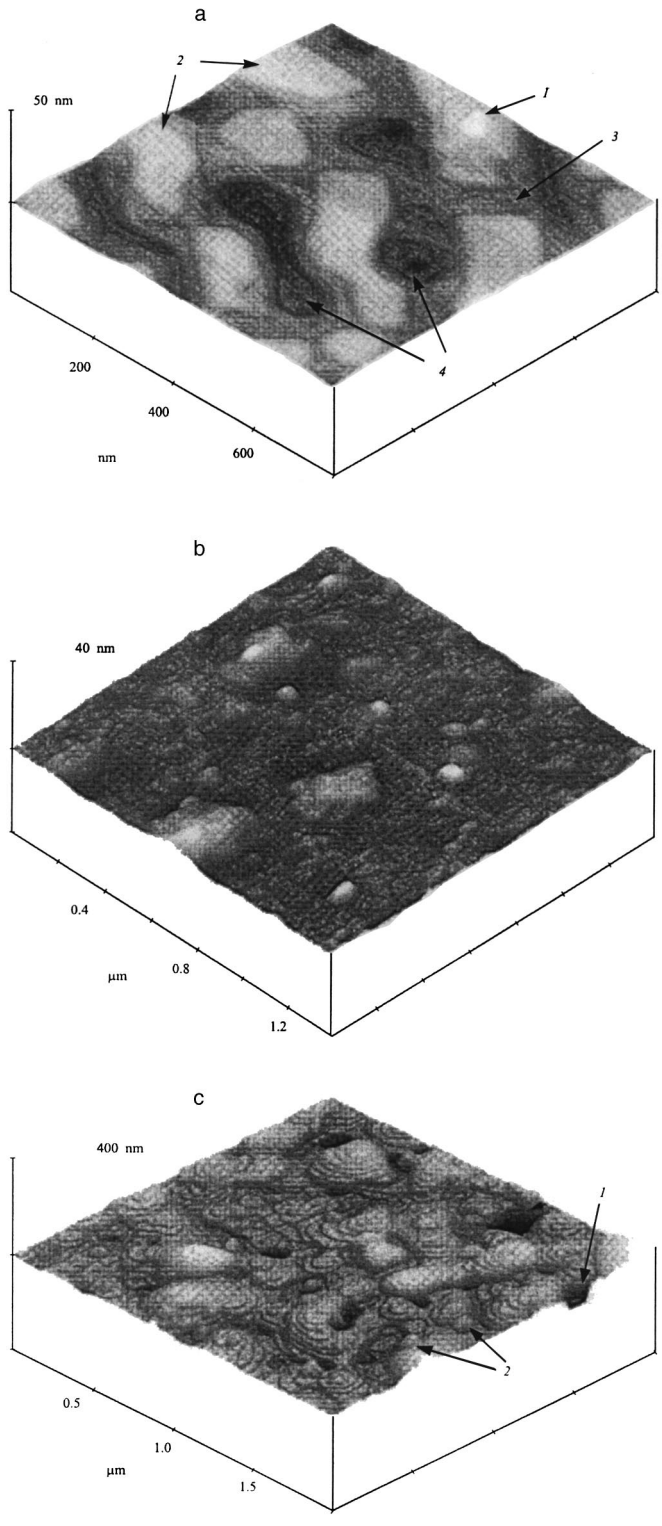

FIG. 1. a) Surface morphology of a (001)NBCO layer of thickness 200 nm, grown on (2 nm)YBCO/(100)$LaAlO_3$. Crystallites of the four upper layers of the superconductor of thickness ~1.2 nm are clearly visible: *1* — a well-formed crystallite from the upper layer, *2* — isolated crystallites of the lower-lying layer, *3* — crystallites forming a continuous network in the third layer of the superconductor, *4* — isolated ''windows'' in the fourth layer of the superconductor that have not closed up. b) Surface morphology of a (100)STO layer of thickness 400 nm, grown on (200 nm)NBCO/(2 nm)YBCO/(100)$LaAlO_3$. c) Surface morphology of an NBCO layer of thickness 200 nm, grown on (400 nm)STO/(200 nm)NBCO/(2 nm)YBCO/(100)$LaAlO_3$: *1* — micro-gaps in the superconductor layer, *2* — **a**-oriented particles.

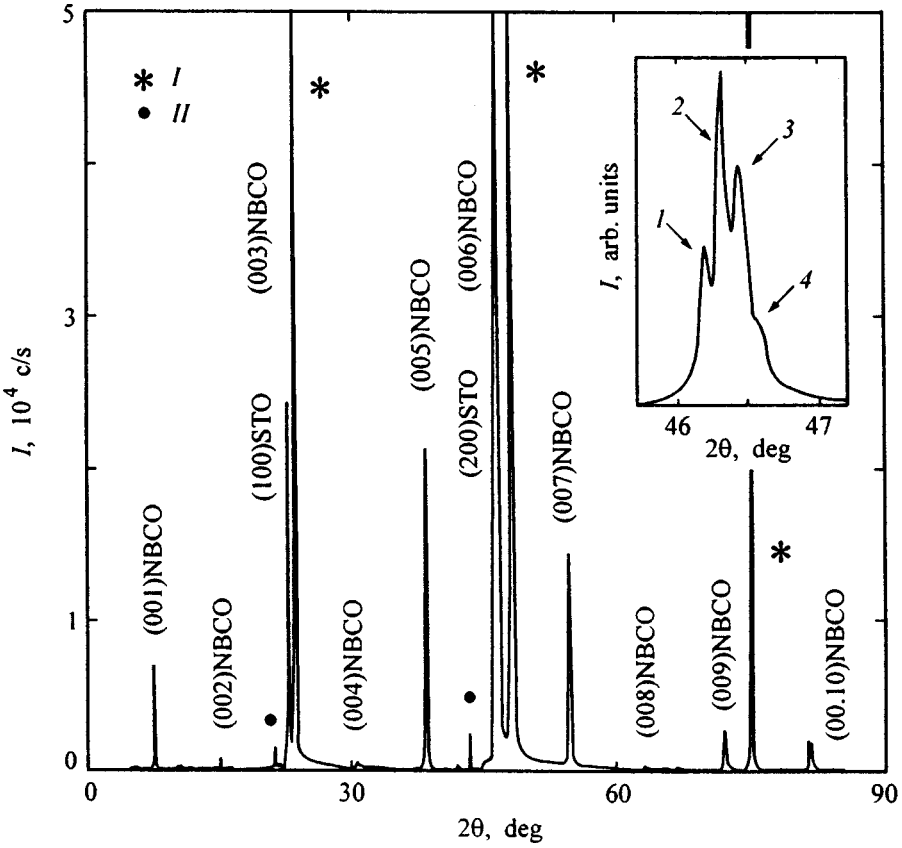

FIG. 2. Diffractogram ($\theta/2\theta$, Cu $K\alpha$) for the trilayer heterostructure (200 nm)NBCO/(400 nm)STO/(200 nm)NBCO grown on a (100)$LaAlO_3$ substrate with a (2 nm)YBCO intermediate layer. I — Cu $K\alpha$ reflections from the substrate, II — Cu $K\beta$ reflections from the substrate. The inset shows the structure of the x-ray peak at $2\theta \approx 46.5°$: *1* — (006)NBCO reflection from the lower superconducting layer, *2* — (200)STO reflection, *3* — (006)NBCO reflection from the upper superconducting layer, *4* — (200)NBCO reflection from the **a**-oriented grains in the upper superconducting layer.

face morphology of the NBCO films of thickness $2-10$ nm differed substantially from that of the YBCO thin films. The surfaces of the YBCO films of thickness $2-10$ nm, grown on (100)$LaAlO_3$ substrates, had steps of height ~ 1.2 nm, separated by flat segments, and no **a**-oriented grains (grains for which the **c** axis is parallel to the substrate plane) or micro-inclusions of secondary phases were detected in them. As a consequence of the presence of **a**-oriented grains whose density reached 10^9 cm^2 and height—5 nm, the surface of the NBCO films of thickness $d=2-10$ nm was uneven. We were able to eliminate the appearance of **a**-oriented grains in the NBCO films, both in the initial stage of its formation and during subsequent growth ($d \leqslant 200$ nm), by using (100)$LaAlO_3$ wafers as the substrate with a layer of YBCO of thickness 2 nm grown on their surface. In the images of the surface of the NBCO films ($d=200$ nm) grown on (2 nm)YBCO/$LaAlO_3$, only crystallites of the upper $3-4$ layers of the film are visible, whose thickness is equal to the lattice parameter c in the NBCO film [Fig. 1(a)]. Growth spirals and **a**-oriented grains were not detected in the surface of the (200 nm)NBCO/(2 nm)YBCO/$LaAlO_3$ films. The roughness of the free surface of the (200 nm)NBCO films grown on (2 nm)YBCO/$LaAlO_3$ was $4-5$ nm.

Examination of the surface of the (400 nm)STO films grown on (200 nm)NBCO/(2 nm)YBCO/$LaAlO_3$ films did not reveal any gaps extending down through the ferroelectric layer [Fig. 1(b)].

The surface of the upper NBCO film in the trilayer system NBCO/STO/NBCO contained pyramidal formations with characteristic growth steps of height 1.2 nm. The indicated formations were topped off with a flat segment, which unmistakably differentiated them from growth spirals, whose nucleus contains a screw dislocation. Using an atomic-force microscope we detected isolated, weakly developed **a**-oriented grains on the surface of the upper NBCO layer [see Fig. 1(b) and the inset to Fig. 2]. The superconductor film also had gaps, whose density reached 10^8 cm^{-2} [Fig. 1(c)].

An x-ray study of NBCO/STO/NBCO trilayer heterostructures grown on (2 nm)YBCO/$LaAlO_3$ revealed that the superconductor films and the intermediate ferroelectric layer were grown epitaxially, where (001)[010]NBCO$\|$(100)[010]STO (Fig. 2). Insertion of the thin (2 nm)YBCO intermediate layer between the $LaAlO_3$ substrate and the NBCO film led to an abrupt narrowing of the x-ray peaks and an increase in the lattice parameter c (see inset a to Fig. 4). The lattice parameter c for the lower and upper NBCO films in the NBCO/STO/NBCO heterostructure had the values 11.79 and 11.75 Å, respectively, while the parameter $a=3.905$ Å of the cubic unit cell of the STO intermediate layer essentially coincided with the data for bulk single crystals of strontium titanate at $T=300$ K (Ref. 11). Data on the azimuthal orientation of the layers in the heterostructure based on NBCO films and a (Ba,Sr)TiO_3 layer are given in Ref. 12.

The temperature dependence of the resistance R and of the critical current density J_c for a (001)NBCO film of thickness $d=200$ nm are plotted in Fig. 3. The variation of the effective magnetic susceptibility χ with temperature for the

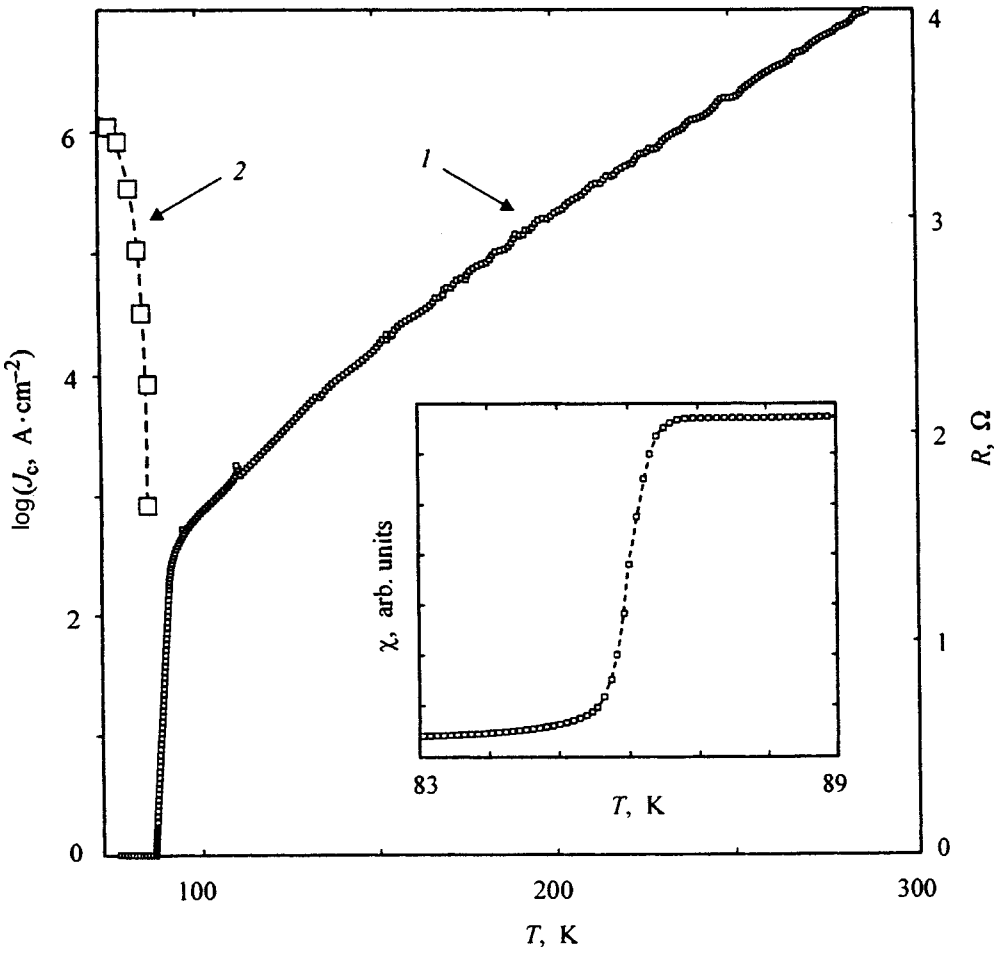

FIG. 3. Temperature dependence of the resistance R (*1*) and critical current density J_c (*2*) for a (200 nm)NBCO layer grown on a (2 nm)YBCO/(100)$LaAlO_3$ substrate. The inset plots the temperature dependence of the magnetic susceptibility χ for the trilayer heterostructure (200 nm)NBCO/(400 nm)STO/(200 nm)NBCO.

trilayer heterostructure NBCO/STO/NBCO is shown in the inset.

The ratio $\varepsilon/\varepsilon_0$ (ε_0 is the dielectric constant of vacuum) for the STO layer sandwiched between the NBCO electrodes grew from 320 to 1150 as the temperature was lowered in the interval 300−4.2 K (Fig. 4). The loss factor $\tan\delta$ for the ferroelectric layer depended weakly on the temperature in the temperature interval $4.2<T<150$ K and had values ~ 0.02 ($f=100$ kHz), whereas for $T>200$ K it grew steeply with increase of T. The value of ε for the STO layer fell by roughly a factor of three when a bias voltage $V_b=\pm 2.5$ V ($T=32$ K) was placed on the superconducting electrodes (Fig. 5). As the strength of the external electric field E was increased, the conductivity of the ferroelectric layer in the direction perpendicular to the substrate plane grew as $E^{1/2}$.

3. DISCUSSION

The results of our study of the surface morphology of YBCO and NBCO thin films and the data in the literature[13] on the formation of the crystalline phase in the initial growth stage of films of the indicated materials, obtained using high-energy electron diffraction, allow us to assert that replacing Y^{+3} ions by Nd^{+3} ions, having a roughly 11% larger radius,[14] in the cuprate superconductor $RBa_2Cu_3O_{7-\delta}$ has a substantial effect on the process of nucleus formation.

The low values of the surface free energy for the (001) planes are the motive force behind the formation of stable YBCO nuclei preferentially oriented along the **c** axis perpendicular to the plane of the substrate,[15] even when using materials with a large lattice mismatch as the substrate. It is specifically anisotropy in the free energy and the rate of growth that makes it possible to achieve layered growth of the YBCO films on substrates with a small lattice mismatch under conditions of high mobility of the adsorbed particles. The variation of the Gibbs free energy G_N for the system vapor phase–substrate during formation on the substrate surface of a nucleus of the crystalline phase with volume V and free surface area S_1 can be represented in the form[15]

$$\Delta G_N=\Delta G_V V+\gamma_1 S_1+(\gamma_3-\gamma_2+E_d)S_2, \qquad (1)$$

where $\Delta G_V=\Omega_i^{-1}[kT_s\ln(1+\zeta)+\mu_i]$, γ_1 is the specific free energy of the free surface of the nucleus, γ_2 and γ_3 are the specific free energies of the substrate surface and the substrate–nucleus interface, respectively, E_d is the elastic deformation energy in the system substrate–nucleus, S_2 is the area of the nucleus–substrate interphase boundary, Ω_i is the molecular volume of the material of the formed film, μ_i characterizes the change in the internal energy of the system during formation of a molecule of the compound of the particles adsorbed on the substrate surface, and ζ is the effective supersaturation of the vapor phase above the substrate surface.

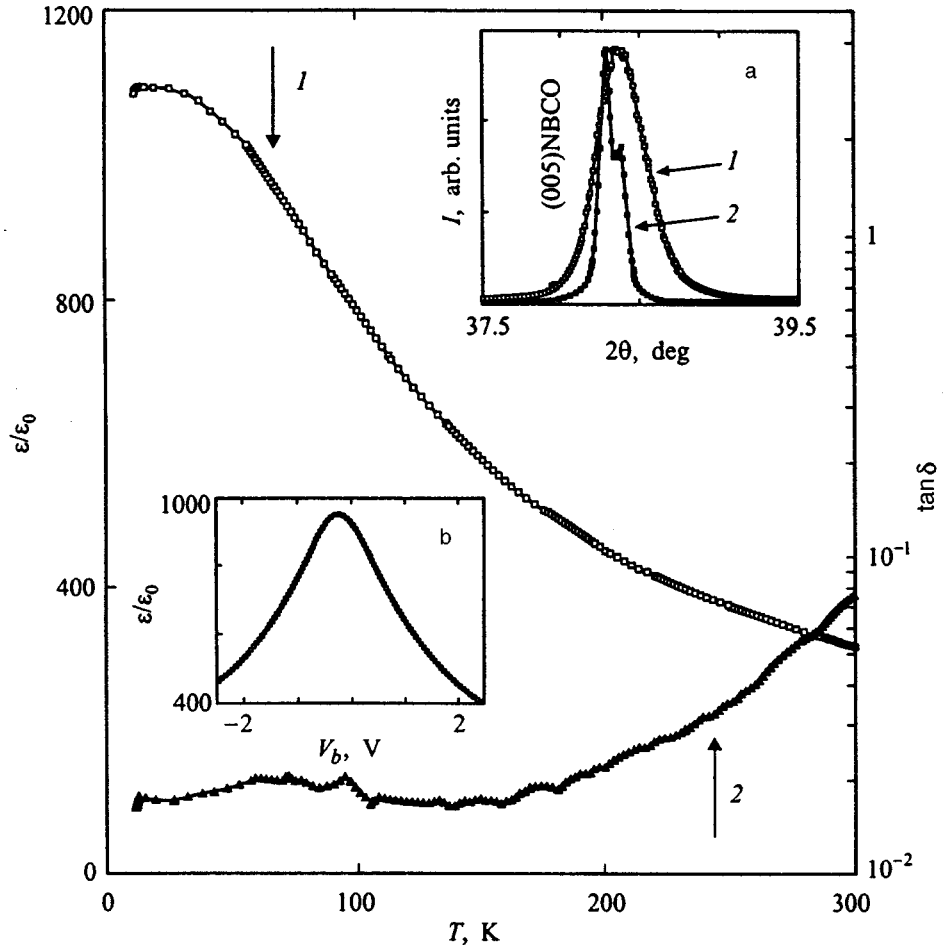

FIG. 4. Temperature dependence of $\varepsilon/\varepsilon_0$ (*1*) and $\tan\delta$ (*2*) for a STO layer of thickness 400 nm in the trilayer heterostructure (001)NBCO‖(100)STO ‖(001)NBCO ($f=100$ kHz). Inset a shows the (005) x-ray diffraction peaks ($\theta/2\theta$, Cu $K\alpha$) for (200 nm)NBCO layers grown on (100)$LaAlO_3$ (*1*) and on (2 nm)YBCO/(100)$LaAlO_3$ (*2*). Inset b shows the maximum in the dependence $\varepsilon/\varepsilon_0(V_b)$ for the (400 nm)STO layer in the heterostructure (001)NBCO‖ (100)STO‖(001)NBCO, shifted relative to the point $V_b=0$ toward negative values of the bias voltage.

There are no grounds to assume the presence of substantial differences in ζ during the growth of NBCO and YBCO films since the thickness of the films of both of the indicated superconductors grew by roughly 4 Å as a result of the action of ten laser pulses on the corresponding targets, and the size and shape of the flare formed upon ablation of the targets practically coincided. It is natural to associate the appearance of a significant number of **a**-oriented particles during the initial growth stage of the NBCO film with a smaller value of the difference in the specific free energy of the free surface for the (001) and (100)NBCO planes in comparison with the difference in γ_1 for the (001) and (100)NBCO planes or with a change in the value of the sum γ_3+E [see Eq. (1)]. According to Ref. 9, Nd can replace Ba in the unit cell of NBCO, accompanied by a change in the oxygen concentration in the Cu–O chains. Replacement of Ba^{+2} ions by Nd^{+3} ions can lead to a change in the specific free surface energy for different crystallographic planes, first of all in (001)NBCO. Whereas growth of a $RBa_2Cu_3O_{7-\delta}$ film starts from the Ba–O planes,[16] replacement of yttrium by neodymium should lead to a change in E as well as γ_3. The observed differences in the surface morphology of NBCO and YBCO thin films are apparently due to differences in the activation energy for the formation of stable nuclei of the indicated materials, for which the **c** axis is perpendicular to the substrate plane.

In the presence of steps of height 1.2 nm on the substrate surface, the NBCO nuclei, for which the **c** axis is perpendicular to the substrate surface, are the first to become stable. The absence of **a**-oriented grains in the interior and in the near-surface layer of NBCO films grown on (2 nm)YBCO/(100)$LaAlO_3$ substrates is evidence of a high mobility of the adsorbed particles on the surface of the growing film, and a low concentration of micro-inclusions of secondary phases.

Onset of decline of the resistance in NBCO films was observed at 92 K, and at $T=87$ K the resistance vanished. These T_c values are in good agreement with literature data for NBCO films grown using stoichiometric starting targets.[17] To grow NBCO films with T_c as high as 94 K, it is necessary to enrich the starting mixture with barium.[9] At $T=76$ K the critical current density for the NBCO films exceeded 10^6 A/cm^2. Temperature-dependence data on the magnetic susceptibility, obtained for NBCO films, correlate well with the T_c values obtained from the $R(T)$ curves.

For $T>150$ K the temperature dependence of ε for the STO layer sandwiched between the NBCO electrodes is in good agreement with data obtained for a strontium-titanate layer sandwiched between two YBCO epitaxial films.[18] For $T<100$ K ε for the STO layer in the NBCO/STO/NBCO heterostructure grew more steeply than in the case of the heterostructure YBCO/STO/YBCO. When using NBCO electrodes the maximum in the $\varepsilon(T)$ dependence for the STO layer became weakly expressed and shifted by

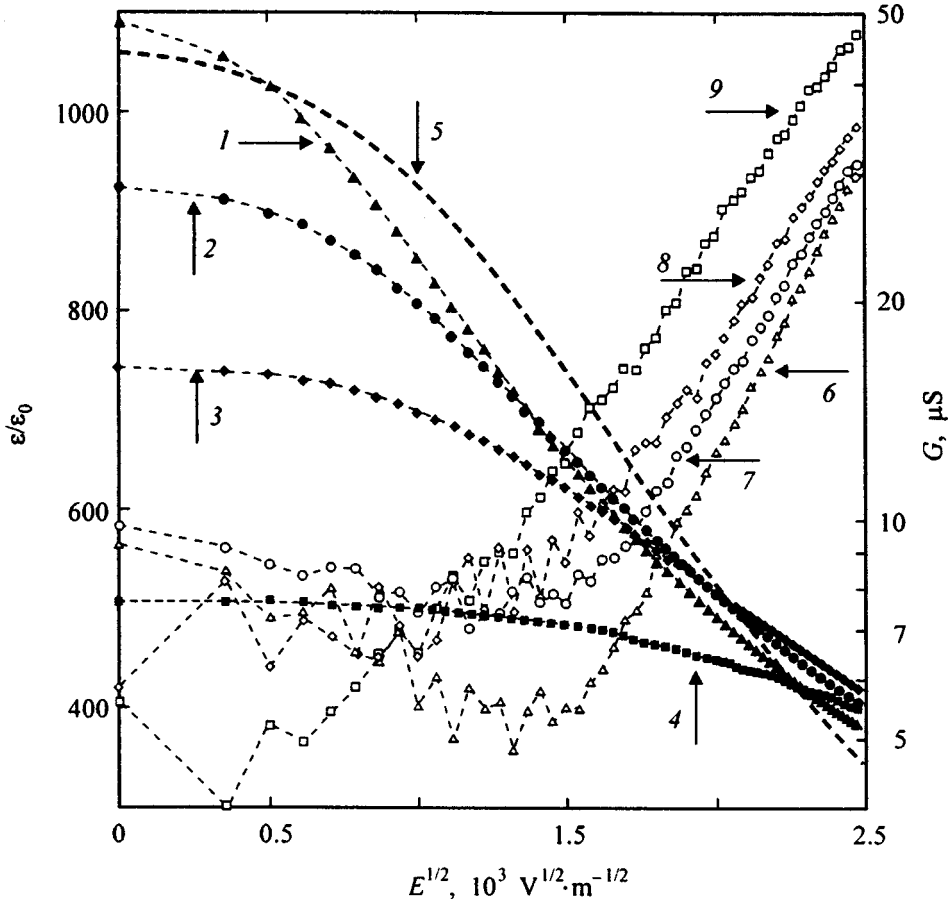

FIG. 5. The dependence of $\varepsilon/\varepsilon_0$ (*1–5*) and G (*6–9*) on the external electric field strength for an STO layer of thickness 400 nm in the trilayer heterostructure (001)NBCO‖(100)STO‖ (001)NBCO ($f = 100$ kHz) at different temperatures. T (K): *1, 6* — 32; *2, 7* — 75; *3, 8* — 112; *4, 9* — 178; *5* — the dependence of $\varepsilon/\varepsilon_0$ on E at $T = 32$ K, calculated using relation (2) for $\xi = 1.2\times10^{10}\,\mathrm{F^{-3}\cdot m^5\cdot V^{-2}}$.

$20-30$ K toward lower temperatures in comparison with its position on the corresponding curve obtained for the plane-parallel capacitor structure YBCO/STO/YBCO. At $T = 20$ K the absolute values of ε for an STO layer sandwiched between NBCO epitaxial films exceeded the values obtained using YBCO films as the electrodes by roughly 15%. The indicated differences in the temperature dependences of ε for the STO layer in the heterostructures NBCO/STO/NBCO and YBCO/STO/YBCO reflect differences in the character of the NBCO/STO and YBCO/STO interphase boundaries.

The dielectric constant of the STO layer fell by roughly a factor of three at $T = 32$ K when a bias voltage $V_b = \pm 2.5$ V was imposed on the NBCO electrodes (Fig. 5), which is substantially larger than in the case of YBCO electrodes.[18] When the temperature was raised, the dependence of ε on the external electric field weakened. The maximum in the dependence $\varepsilon(V_b)$ was shifted toward negative values of V_b, due to differences in the structure and electrophysical properties of the NBCO/STO and YBCO/STO interphase boundaries. According to the x-ray data, the lattice parameter c for the lower NBCO film in the NBCO/STO/NBCO heterostructure is equal to 11.79 Å while for the upper film it is equal to 11.75 Å. The surface of the lower NBCO layer, as follows from the images obtained using an atomic-force microscope [Fig. 1(a)], are smooth with characteristic steps ~ 1.2 nm. The upper superconductor film apparently had some **a**-oriented particles at the NBCO/STO interphase boundary. This is in fact indicated by data on the surface morphology of thin ($d = 2-10$ nm) NBCO films grown on insulating substrates, and by the x-ray data shown in the inset to Fig. 2.

$\varepsilon(E)$ dependences measured at different temperatures for the STO layer in the NBCO/STO/NBCO heterostructure are well described by a relation that has been successfully applied in the analysis of the field dependence of the dielectric constant of bulk single crystals of strontium titanate in low fields (E),[19,20]

$$\varepsilon^{-1} = \eta(T)[1 + \eta(T)^{-3}\xi E^2], \tag{2}$$

where $\eta(T)$ is an electric-field-independent parameter and ξ is the ''anharmonism constant,'' which is independent of the electric field and the temperature. Figure 5 plots the dependence $\varepsilon(E)$ for the STO layer, calculated using relation (2) and the parameter value $\xi = 1.2\times10^{10}\,\mathrm{F^{-3}\cdot m^5\cdot V^{-2}}$. The indicated value of ξ was determined from the slope of the dependence $\varepsilon^{-2}d\varepsilon/dE(E)$ in the limit $E\to 0$. For E close to zero, $\varepsilon^{-2}d\varepsilon/dE$ fell linearly with increase of the electric field. Based on the field dependence of the frequency of the soft mode in STO single crystals, the authors of Ref. 19 obtained the value $\xi = 1\times10^{10}\,\mathrm{F^{-3}\cdot m^5\cdot V^{-2}}$. On the whole, good agreement is observed between the experimental and calculated values of ε for the STO layer in the indicated interval of electric fields.

As follows from the data plotted in Fig. 4, for $T > 200$ K a steep increase in $\tan\delta$ with temperature is observed for STO films. Figure 5 plots the variation of the conductivity $G = C\omega\tan\delta$ with increase of the electric field for an STO film in the direction perpendicular to the substrate plane

($\omega = 2\pi f$). The experimentally obtained dependence of the conductivity of the STO layer on the temperature and electric field can be explained in terms of Poole–Frenkel' emission.[21] The experimentally observed dependence of the STO layer on the electric field strength (Fig. 5) follows closely the relation obtained for Poole–Frenkel' emission, $\ln G \sim E^{1/2}$. The growth of the conductivity of the ferroelectric layer with increase of the electric field is due to a lowering in an electric field of the barrier to ejection of carriers from impurity levels to the corresponding band. A detailed analysis of the temperature and field dependence of the conductivity of (Ba,Sr)TiO_3 films inserted in superconductor/ferroelectric heterostructures is given in Ref. 22.

Thus, the x-ray data and the reported study of the surface morphology of NBCO films grown on (2 nm)YBCO/(100)$LaAlO_3$ substrates allow us to assert that an important prerequisite of layered growth of a superconductor film is the presence on the substrate surface of steps ~ 1.2 nm in height. A (400 nm)STO layer free from micro-gaps can be grown epitaxially on the surface of a (200 nm)NBCO film. The use of NBCO epitaxial films instead of YBCO films as the electrodes in a plane-parallel superconductor/ferroelectric/superconductor capacitor structure makes it possible to substantially increase the dependence of the effective dielectric constant of the ferroelectric layer on the external electric field.

Financial support for the completion of this work was provided by Project 98041 ''Combination'' conducted within the scope of the scientific direction ''Superconductivity,'' by Project No. 98-02-18222 funded by the Russian Fund for Fundamental Research, and by the project TFR N 240-97-382.

[1] I. S. Gergis, J. T. Cheung, T. H. Trinh, E. A. Sovero, and P. H. Kobrin, Appl. Phys. Lett. **60**, 2026 (1992).
[2] J. P. Hong and J. S. Lee, Appl. Phys. Lett. **68**, 3034 (1996).
[3] F. W. Van Keuls, R. R. Romanofsky, D. Y. Bohman, M. D. Winters, F. A. Miranda, C. H. Mueller, R. E. Treece, T. V. Rivkin, and D. Galt, Appl. Phys. Lett. **71**, 3075 (1997).
[4] C. M. Jackson, J. H. Kobayashi, A. Lee, C. Pettiette-Hall, J. F. Burch, and R. Hu, Microwave Opt. Technol. Lett. **5**, 722 (1992).
[5] O. G. Vendik, L. T. Ter-Martirosyan, A. I. Deduk, S. F. Karmanenko, and R. A. Chakalov, Ferroelectrics **144**, 33 (1993).
[6] Yu. A. Boikov, Z. G. Ivanov, A. N. Kiselev, E. Olsson, and T. Claeson, J. Appl. Phys. **78**, 4591 (1995).
[7] Yu. A. Boikov, Z. G. Ivanov, A. L. Vasiliev, I. Pronin, E. Olsson, and T. Claeson, Appl. Phys. Lett. **67**, 2708 (1995).
[8] J. G. Lin, C. Y. Huang, Y. Y. Xue, C. W. Chu, X. W. Cao, and J. C. Ho, Phys. Rev. B **51**, 12 900 (1995).
[9] M. Badaye, J. G. Wen, K. Fukushima, N. Koshizuka, T. Morishita, T. Nishimura, and Y. Kido, Supercond. Sci. Technol. **10**, 825 (1997).
[10] L. A. Tietz, C. B. Carter, D. K. Lathrop, S. E. Russek, R. A. Buhrman, and J. R. Michael, J. Mater. Res. **4**, 1072 (1989).
[11] F. W. Lytle, J. Appl. Phys. **35**, 2212 (1964).
[12] Yu. A. Boikov, V. A. Danilov, E. Carlsson, D. Erts, and T. Claeson, Physica B in press.
[13] T. Shimizu, H. Nonaka, and K. Arai, Appl. Phys. Lett. **59**, 600 (1991).
[14] *Handbook of Chemistry and Physics*, edited by R. C. Weast, 59th ed. (CRC Press, Inc., Florida, 1979), p. E-81.
[15] Yu. A. Boĭkov, Z. G. Ivanov, E. Olson, V. A. Danilov, T. Klaeson, M. Shcheglov, and D. Érts, Fiz. Tverd. Tela (St. Petersburg) **37**, 880 (1995) [Phys. Solid State **37**, 478 (1995)].
[16] A. L. Vasiliev, G. Van Tendeloo, A. Amelincks, Yu. A. Boikov, E. Olsson, and Z. Ivanov, Physica C **244**, 373 (1991).
[17] M. Badaye, F. Wang, Y. Kanke, K. Fukushima, and T. Morishita, Appl. Phys. Lett. **66**, 2131 (1995).
[18] Yu. A. Boikov and T. Claeson, J. Appl. Phys. **81**, 3232 (1997).
[19] J. M. Worlock and P. A. Fleury, Phys. Rev. Lett. **19**, 1176 (1967).
[20] G. Rupprecht, R. O. Bell, and B. D. Silverman, Phys. Rev. **123**, 97 (1961).
[21] J. R. Yeargan and H. L. Taylor, J. Appl. Phys. **39**, 5600 (1968).
[22] Yu. A. Boikov and T. Claeson, Supercond. Sci. Technol. in press.

Translated by Paul F. Schippnick

SEMICONDUCTORS, DIELECTRICS

The electronic structure of a silicon divacancy calculated by the open shell method

S. S. Moliver

Ul'yanovsk State University, 432700 Ul'yanovsk, Russia
(Submitted April 29, 1998)
Fiz. Tverd. Tela (St. Petersburg) **41**, 404–410 (March 1999)

The restricted Hartree–Fock–Roothaan method with projection of the electron density matrices for a filled and an open electron shell and the quasimolecular large unit cell model are used to calculate the electronic structure of a silicon divacancy in the charge states 0, ± 1 in the fully-symmetric atomic configuration with relaxation and with symmetry-lowering distortions. It is shown that the Jahn–Teller effect is bimodal and that there is a vibronic coupling between the electron orbital doublet and the resonant mode and pairing mode of the distortion. © *1999 American Institute of Physics.* [S1063-7834(99)00803-5]

A silicon divacancy V_2 is formed in an ideal crystal under the action of different types of irradiation and under conditions of ion implantation, but in contrast to a simple vacancy, the primary radiation defect forming the divacancies, the divacancy is stable at room temperature and is therefore more accessible to study. According to Refs. 1–12 it is possible to follow the development of the overall picture of the properties of the divacancy as a multiply charged deep center subject to the Jahn–Teller effect, with characteristic electron bands for optical infrared absorption and photoconductivity, and characteristic electron paramagnetic resonance (EPR) spectra.

It has been established that the Fermi level (chemical potential) thresholds between the charge states, which characterize the energy of a divacancy in thermodynamic equilibrium, are equal to[1,3,5]

$$E(2-/-)=E_c-0.23\ \text{eV},$$

$$E(-/0)=E_c-(0.43-0.41)\ \text{eV},$$

$$E(0/+)=E_v+(0.23-0.25)\ \text{eV}.$$

These energies are most accurately determined from the recharging spectra of the divacancies found in the space-charge region (DLTS spectroscopy or similar methods).[5,11]

In charge states with an unpaired electron, the divacancy has EPR spectra Si–G6 (V_2^+) and Si–G7 (V_2^-) of ground states with spin $S=1/2$, spatial symmetry C_{2h}, and reorientation energies of the divacancy axis $C_2 \| [110]$ equal to 73 and 56 meV, respectively, where the wave function of the unpaired electron does not vanish in the mirror plane.[8] Thus, the unpaired electron of the singly charged divacancy V_2^+ is found in an orbital having one of two possible irreducible representations (A_g and B_u), in connection with which a discussion has arisen[8,9] regarding to the Jahn–Teller effect in the divacancy. In the fully-symmetric atomic configuration D_{3d}, four of the six electrons of the dangling bonds are located in orbitals resonant with the valence band, and the two remaining electrons are found in the open shell formed by the doubly degenerate orbitals e_g and e_u in the band gap. Simple chemical bonding arguments as well as many-electron calculations show that an open shell is formed by the e_u orbitals; consequently, for a small distortion $D_{3d} \rightarrow C_{2h}$ (corresponding to a component of the distortion E_g) the levels obtaining when the degeneracy is removed are ordered in one of two ways: $b_u<a_u<a_g<b_g$, corresponding to a pairing configuration (p), and $a_u<b_u<b_g<a_g$, corresponding to resonant-bond configuration (r).

According to the first point of view,[8] a one-dimensional distortion mode p is set up in the divacancy and, as a consequence, the distortion should be so large that the a_g and a_u levels intersect: $a_g<a_u$. In this case, the configuration V_2^- has an unpaired electron with a nonzero orbital in the mirror plane $b_u^2 a_g^1$.

According to the second point of view,[9] the distortion E_g has two modes: p and r, where the total energy minimum for V_2 corresponds to resonant bonding with electron configuration $a_u^2 b_u^1$ and nonzero density of the unpaired electron in the mirror plane. Density functional calculations for the large unit cell (LUC) model $V_2^{\pm}$ (Ref. 7) and V_2^0 (Ref. 10) showed that the equilibrium magnitude of the resonant-type distortion r is small. This point of view is in agreement with the optical properties of the divacancies.

The electron spectra for optical absorption of the charge states of the divacancy contain three bands denoted according to their central wavelength or transition energy: V_2^+: 3.9 μm and 0.32 eV, with hole photoconductivity $V_2^+ \rightarrow V_2^0 + h$ (Refs. 4 and 12); $V_2^{0,\pm}$: 1.8 μm or 0.73 eV, without photoconductivity[3]; V_2^{2-}: 3.3 μm or 0.36 eV (three bands 0.343, 0.358, and 0.375 eV), without photoconductivity.[3]

The photoconductivity spectrum of V_2^+ has small thermal broadening, which indicates a small value of the distortion. On the other hand, the experimental EPR data[8] are insufficient to permit a firm conclusion in favor of a large distortion or Jahn–Teller stabilization energy.[4]

When a V_2^0 divacancy is illuminated, it is promoted to an

excited state with spin $S=1$ and the same symmetry of the g tensor as in the $V_2^{\pm}$ states (EPR spectrum Si–PT5, Ref. 6, where the properties of the density of the triplet electron pair with respect to mirror reflection are not reported).

The goal of the present work was to study all of the charge states of the divacancy and both modes of the E_g distortion within the framework of a unified calculational scheme. The Jahn–Teller effect in the strongly correlated system of the dangling bonds of the divacancy can be described only by a self-consistent calculation of the fully-symmetric atomic configuration with an open electron shell and the atomic configurations with reduced symmetry. Three of these configurations (D_3, C_{3v}, and S_6) and the fully-symmetric configuration D_{3d} have a doubly orbitally-degenerate open shell. The present work calculates the corresponding multiplet structures in order to show that none of their terms lowers the energy of the fully-symmetric ground state, i.e., to prove by direct calculation that the E_g distortion lowering the symmetry to C_{2h} is a Jahn–Teller distortion.

The molecular orbital (MO) method was used. In comparison with other many-electron approaches, an important advantage of calculational schemes based on the MO method is the fact that they make it possible to investigate a wide range of electronic and structural properties and also, in turn, to estimate the electron correlation by adding excited configurations to the ground-state configuration—the configurational interaction method. With these advantages in mind, the author applied the restricted Hartree–Fock–Roothaan open-electron-shell method (ROHF in the customary acronym for this method in quantum chemistry)[13] and the quasimolecular large-unit-cell (QLUC) model[14] to the calculation of the electronic structure of the three charge states $V_2^{0,\pm}$.

Using a symmetric analysis, the multiplet structures of the open-shell configurations were obtained and the ROHF coefficients describing the contributions of the direct and exchange interelectron integrals formed by the open-shell MO's were found for all terms and diagonal sums.[15,16] In those cases in which the term does not admit of a self-consistent calculation, it was included in one of the diagonal Slater sums, which was then expanded in the energies of its component terms in accordance with their ROHF coefficients. Such self-consistent calculations yielded the total energies and orbital energies of the terms of the multiplet structures, and the corresponding wave functions in the MO LCAO representation—all as functions of the magnitudes of the corresponding distortions.

1. THE OPEN-SHELL MOLECULAR-ORBITAL (ROHF) METHOD

The ROHF method is based on the universal technique of projecting the density matrices of the electron shells.[13] N electrons in this model are distributed between a closed shell formed from n_a MO's and an open shell formed from n_b MO's such that the occupation number of the open shell (according to Roothaan) for the given configuration is equal to

$$f=\frac{N-2n_a}{2n_b}<1.$$

The ROHF method can be used to self-consistently calculate either the energy of a term, E', or the diagonal Slater sum[15,16] of n terms, E''

$$E''=\frac{1}{n}\sum_{i=1}^{n}\langle\Phi_i|H|\Phi_i\rangle=E_0+f^2g^{(b)}. \tag{1}$$

The first term of the sum does not depend on the electron distribution of the open shell and is written the same for all terms and diagonal sums of the given configuration. Using the notation d' for the MO's of the closed shell and b' for the MO's of the open shell, and h for the one-electron part and g for the two-electron part, we have

$$E_0=H^{(a)}+2f\sum_{b'}^{n_b}g_{b'}^{(a)}+f\sum_{b'}^{n_b}2h_{b'b'}.$$

Here we have introduced the energy of the closed shell and the interaction energy of the closed shell with one of the MO's of the open shell

$$H^{(a)}=\sum_{a'}^{n_a}2h_{a'a'}+\sum_{a'}^{n_a}\sum_{a''}^{n_a}[2\langle a'a''|g|a'a''\rangle-\langle a'a''|g|a''a'\rangle],$$

$$g_{a'}^{(a)}=\sum_{a'}^{n_a}[2\langle a'b'|g|a'b'\rangle-\langle a'b'|g|b'a'\rangle].$$

The essence of the ROHF method is that the two-electron part of the total energy (1) corresponding to the open shell should have an expression similar to the part corresponding to the closed shell, i.e., the ROHF coefficient A_I, introduced below, should be equal to zero,

$$g^{(b)}=\Sigma_{b'}^{n_b}\Sigma_{b''}^{n_b}[2A_J\langle b'b''|g|b'b''\rangle-A_K\langle b'b''|g|b''b'\rangle]+\Sigma_{b'}^{n_b}A_I\langle b'b'|g|b'b'\rangle. \tag{2}$$

In order to apply the described method, it is necessary to find expression (2) for each term, i.e., to calculate the ROHF coefficients A_I, A_J, and A_K. If $A_I=0$ for a given term, then its energy can be calculated self-consistently; in the opposite case, the term for which $A_I=0$ must be included in the Slater diagonal sum (and there may be several of them) and the energy of each term entering into it must be found using the MO's of the diagonal sum and the ROHF coefficients of the given term. The accuracy of the ROHF method can be estimated by comparing the energies of those terms obtained by self-consistent calculation and from the diagonal sum.

The variational principle in the presence of an open shell must be calculated in each cycle of the self-consistent calculation of two (of the three obtaining) density matrices constructed using the LCAO coefficients (LCAO stands for linear combinations of atomic orbitals) ψ_μ^i of the three electron shells: the closed shell a, the open shell b, and the virtual shell v,

TABLE I. Multiplet structure of the divacancy in states with double orbital degeneracy of the open shell.

V_2^0-configuration e^2 $(f=1/2)$						
e_g^2 or e_u^2 (D_{3d})	$e^2(C_{3v})$; $e^2(D_3)$	e_g^2 or e_u^2 (S_6)		A_J	A_K	A_I
$^3A_{2g}$	$^3A_2$	^3A_g	$e'e''\alpha\alpha$; $e'e''\beta\beta$; $\frac{1}{\sqrt{2}}e'e''(\alpha\beta+\beta\alpha)$	1	2	0
		^1A_g	$\frac{1}{\sqrt{2}}e'e''(\alpha\beta-\beta\alpha)$	1	-2	-4
$^1A_{1g}$	$^1A_1$		$\frac{1}{\sqrt{2}}(e'e'+e''e'')\alpha\beta$	0	-2	0
		^1E_g	$e'e'\alpha\beta$; $e''e''\alpha\beta$	0	0	2
^1E_g	^1E		$\frac{1}{\sqrt{4}}[(e'e'-e''e'')\alpha\beta \pm e'e''(\alpha\beta-\beta\alpha)]$	1/2	-2	0
		E_1''	$\frac{1}{3}(^1A_g+2\,^1E_g)$	1/3	$-2/3$	0
		E_2''	$\frac{1}{6}(^1A_g+2\,^1E_g+3\,^3A_g)$	2/3	2/3	0
V_2^+-configuration e^1 $(f=1/4)$ $^2E_u(D_{3d})$			$e'\alpha$; $e''\alpha$; $e'\beta$; $e''\beta$	0	0	0
V_2^--configuration e^3 $(f=3/4)$ $^2E_u(D_{3d})$			$e'e'e''\alpha\beta\alpha$; $e'e''e''\alpha\alpha\beta$; $e'e'e''\alpha\beta\beta$; $e'e''e''\beta\alpha\beta$	8/9	8/9	0

Note. e' and e'' in the Slater determinants denote the molecular orbitals (MO's), partners of the two-dimensional representations, indicated in the configurations. α and β are the spin basis functions.

$$P_{\mu\nu}^{(i)}=\sum_{i'=1}^{n_i}\psi_\mu^{i'}\psi_\nu^{i'},\quad i=a,b,v,$$

where i' denotes the MO's of the corresponding shell. The QLUC model imposes cyclic boundary conditions on the MO's and, consequently, on their LCAO coefficients: in contrast to the case of molecules and cluster models of crystals, μ and ν do not denote separate atomic orbitals (AO's), but rather sums of translationally invariant AO's over all the QLUC's.

At the start of the cycle of self-consistent calculations the LCAO coefficients were determined by the extended Hückel method, where the MO's were populated in such a way that the closed shell contained complete sets of partners of representations of the symmetry group and the open shell contained one complete set of a definite representation. The Fock matrix F is calculated in each cycle of the self-consistent calculation by projecting the density matrix with the ROHF coefficients that were found for the calculated term or diagonal sum,

$$\begin{aligned}
&F^{(a)}=h+2J(P^{(a)}+fP^{(b)})-K(P^{(a)}+fP^{(b)}),\\
&F^{(b)}=h+2J(P^{(a)}+fA_JP^{(b)})-K(P^{(a)}+fA_KP^{(b)}),\\
&F^{(v)}=2(F^{(a)}-fF^{(b)}),\\
&F=(1-P^{(b)})F^{(a)}(1-P^{(b)})+(1-P^{(a)})F^{(b)}(1-P^{(a)})\\
&\quad+(P^{(a)}+P^{(b)})F^{(v)}(P^{(a)}+P^{(b)}),
\end{aligned}\tag{3}$$

where the direct $[J(P)]$ and exchange $[K(P)]$ Coulomb interelectron interaction matrices were determined in the standard way[13] [see also Eq. (2)]. In each cycle of the self-consistent calculation the eigenvalue problem for the Fock matrix is solved, and when a prescribed level of convergence is reached, the total energy (1)

$$E''=\mathrm{Tr}\{(P^{(a)}+fP^{(b)})h+P^{(a)}F^{(a)}+fP^{(b)}F^{(b)}\}$$

and orbital energies of the closed and virtual shells are calculated, where the latter in the case of an open shell are not equal to the eigenvalues of the Fock matrix. Application of the Koopmans theorem[13,14] on the ionization and electron affinity gives the orbital energies for the filled and virtual shells

$$\varepsilon_{i'}=\sum_{\mu,\nu}\psi_\mu^{i'}\psi_\nu^{i'}F_{\mu\nu}^{(a)},\quad i=a,v.\tag{4}$$

Note that the fundamental difference from the case of a closed shell is not a modification of the energy (2) with the help of the ROHF coefficients, but a projection of the Fock matrix (3), thus ensuring orthogonality of the set of MO's of all the shells. The projection procedure takes up a large part of the computer time and significantly increases the calculation time in comparison with the case of a closed shell, but those calculational schemes for an open shell in which projection (3) is absent give a nonorthogonal set of MO's, which complicates the calculation of observed quantities and necessitates the development of a special approach for obtaining the multiplet structure.

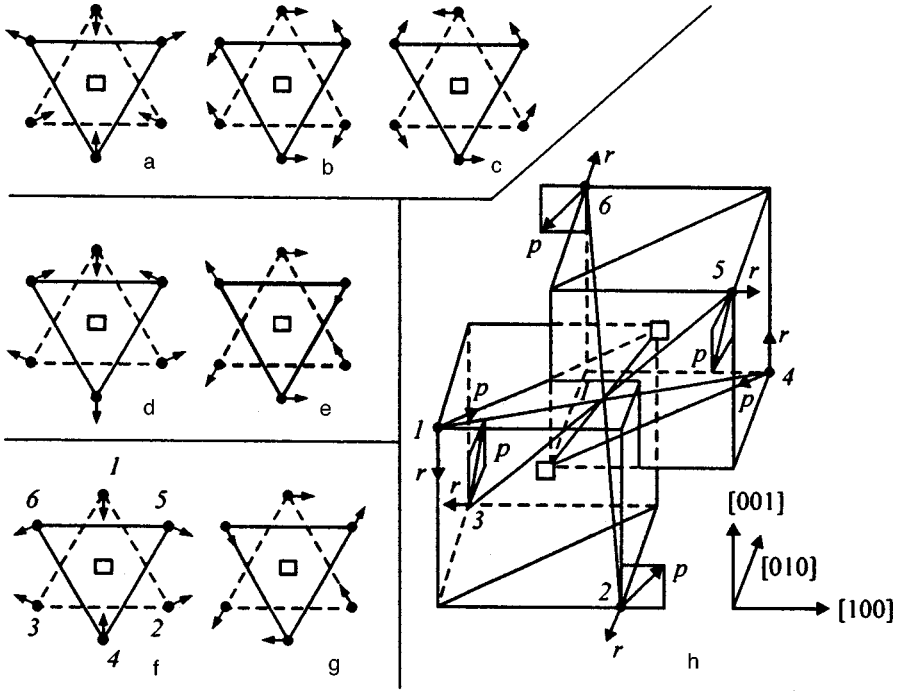

FIG. 1. Normal divacancy distortions. a — A_{2u}: $D_{3d}\rightarrow C_{3v}$; b — A_{1u}: $D_{3d}\rightarrow D_3$; c — A_{2g}: $D_{3d}\rightarrow S_6$; d — E_u, 1: $D_{3d}\rightarrow C_s$; e — E_u, 2: $D_{3d}\rightarrow C_2$; f — E_g, 1: $D_{3d}\rightarrow C_{2h}$; g — E_g, 2: $D_{3d}\rightarrow C_i$; h — $(E_g, 1)_{r,p}$: $D_{3d}\rightarrow C_{2h}$. The arrows indicate the displacements of the nearest neighbors of the vacancy. Figures a–g show the view along the [111] axis joining the vacancies. The atoms are represented by dots, the vacancies are represented by squares. The solid triangle and the dashed triangle join atoms lying in the (111) planes. *I* is the inversion center of the completely symmetric atomic configuration.

2. MULTIPLET STRUCTURES AND DIVACANCY DISTORTIONS

Depending on the atomic configuration, the open shell of a divacancy consists either of an orbital doublet or a single orbital. A group-theoretical analysis for the combinations of Slater determinants is required only in the first case, and the results of such an analysis are displayed in Table I. The distortions—displacements of the atoms leading to a lowering of the symmetry of the atomic configurations—are classified in terms of representations of the group D_{3d} and are shown in Fig. 1. The A_{1u}, A_{2u}, and A_{2g} distortions do not lead to a lowering of the dimensionality of the open shell. The last of these (the librational distortion) is a rotation of the atomic coordination sphere of the divacancy V_2 as a whole about the [111] axis on which two vacancies—the two halves of the divacancy—are located. As can be seen from the table, only for the librational distortion must the diagonal sums E'' be calculated.

Since normal coordinates should describe arbitrary displacements of the six atoms of the first coordination sphere of the divacancy, the distortions lowering the dimensionality of the open shell (all MO's become nondegenerate) have two modes—a pairing mode p and a resonant mode r, which are shown in Fig. 1 for the first component of the E_g distortion. Displacements of the atoms near a vacancy are characterized by two parameters and are equal to

$$(E_g,1)_r=[00\bar{r}]_1,[0\bar{r}0]_2,[\bar{r}00]_3,\ \ldots,$$
$$(E_g,1)_p=[pp0]_1,[p0p]_2,[0pp]_3,\ \ldots, \qquad (5)$$

where the subscripted numbers are the indices of the atoms (see Fig. 1), and the displacements of the three remaining atoms, which are not written out, are obtained by inversion. The pairing mode p corresponds to a drawing together of the pairs of atoms *2–3* and *5–6* and the formation of a weak covalent bond between atoms *1* and *4*. The resonant mode r corresponds to a 5-coordinated state of atoms *1* and *4*, whose weak bonds are in resonance.[7]

Relaxation was also taken into account for all atomic configurations—the non-symmetry-lowering normal mode with identical displacements of the atoms in the direction of the nearest vacancy A_{1g}:

$$A_{1g}=[aa\bar{a}]_1,[\bar{a}aa]_2,[a\bar{a}a]_3,\ \ldots. \qquad (6)$$

3. THE INDO PARAMETRIZATION AND THE QLUC MODEL

The ROHF method is based on a semi-empirical (INDO) quantum-chemical program for the closed shells and the QLUC model.[17–19] The parametrization of the atomic orbitals and of the interaction with the atomic cores and the convergence of the sum over the extended Bravais lattice in the case of the QLUC model of direct and exchange matrix elements are described in Ref. 20.

The Slater AO's of silicon $3s$ and $3p$ have been optimized with respect to the properties of silicon and cubic silicon carbide (lattice constant, binding energy, bulk modulus, structure of the valence band). The optimization technique and the physical meaning of the parameters are described in Ref. 19. The parameter values have since been refined somewhat, and a large number of calculations of defects and surfaces with dangling bonds have been performed for systems consisting of silicon and oxygen atoms. I list here the values of the parameters for the silicon atom (unit of length is the Bohr radius a_B).

1) The constants in the radial parts of the AO's: $\zeta_{3s}=1.28\,a_B^{-1}$, $\zeta_{3p}=1.22\,a_B^{-1}$. They determine the equilibrium lattice constant, for which we obtain the value 5.52 Å (experimental value 5.431 Å).

2) The diagonal elements of the one-electron energy of the AO's on that atomic core where the orbital is centered, $U_{3s}=-30.01$ eV, $U_{3p}=-28.93$ eV. They determine the binding energy of the crystal, for which we obtain the value 4.63 eV/atom [experimental value 4.64 eV/atom, the energy of an isolated atom was calculated for the configuration $s^2p^2(^1P)$ with an open shell].

3) The resonance integral (it gives the nondiagonal element of the one-electron energy when multiplied by the matrix element of overlap of the AO's centered on different atomic cores) $\beta_{\mathrm{Si-Si}}=-2.88$ eV. Together with other parameters, they determine the elastic (bulk) modulus, for which we obtain the value $0.63\,\mathrm{eV}\cdot\mathrm{\AA}^{-3}$ (experimental value 0.6 $\mathrm{eV}\cdot\mathrm{\AA}^{-3}$).

4) The index of nonpointlikeness of the core (inverse screening radius) for the diagonal matrix elements of the interaction with the cores $\alpha_{\mathrm{Si-Si}}=0.12\,a_{\mathrm{B}}^{-1}$.

The wave vectors of the MO's of the QLUC model form a set of *k*-points,[14] which are covered by the centers of the narrowed Brillouin zones of the model filling the crystal Brillouin zone. All of the calculations were carried out with a symmetrically extended, body-centered 32-atom QLUC having the *k*-set $\{\Gamma+12\Sigma+3X\}$ and well reproducing the structure of the valence band of the silicon crystal. The point defects in this model form a periodic structure and interact with one another through their four nearest neighbors. The interaction, however, is not large in the case of small charges on the atoms. Thus, for V^0 the calculated energy of formation is equal to 3.0 eV, which is less than the experimental value 3.6 ± 0.2 eV (Ref. 21); as the QLUC is enlarged, the agreement improves thanks to a weakening of the intervacancy bond. The formation energy of the divacancy V_2^0 was found to be equal to 5.6 eV; thus, the model and the calculational method also agree with experiment in that formation of divacancies from monovacancies is energetically favored.

If the defect is charged, then the QLUC charge translates over the entire crystal, which leads to a physically meaningless growth of the energy. In order to avoid this, when modeling a charged defect state the charge of the electrons added to or removed from the model of a neutral defect, taken with inverse sign, was distributed uniformly over all the model cores. In a 32-atom QLUC such a small change in the charges of the cores is physically equivalent to a shift of the chemical potential (Fermi level).

4. CALCULATED RESULTS

The multiplet structure of a divacancy was calculated as a function of the relaxation (6) and the corresponding distortion (Fig. 1). For all states the equilibrium relaxation was directed inward and was equal to $a=0.055-0.061$, i.e., around 0.52–0.57 Å, except for the triplet states of the neutral vacancy, for which the corresponding values were smaller: $a=0.051-0.053$. The only result that it makes sense to compare with the current level of theoretical work is the direction of relaxation (inward): it agrees with recent calculations performed on large models using the density functional method.[7,10] As for the magnitude of the relaxation itself, in the absence of experimental data, the discrepancies between the results obtained by different methods are large.

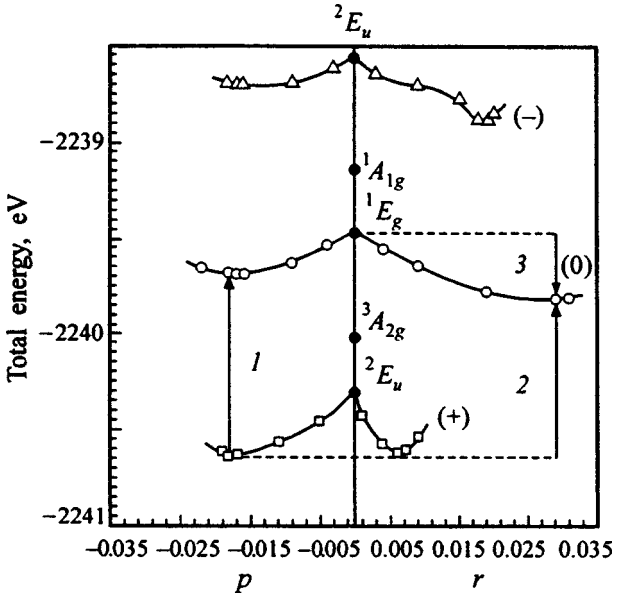

FIG. 2. Multiplet structure of the charge states of the divacancy as a function of the Jahn–Teller bimodal distortion. The filled circles are the terms of the fully symmetric atomic configuration; the empty symbols represent the ground-state energy for distortion as a function of r for a, $p=$const (right half) and as a function of p for a, $r=$const (left half). a, p, r are dimensionless values of the relaxation (6) and of the pairing and resonant distortions (5), respectively. The arrows indicate the direct (*1*) and indirect (*2*) transitions between the charge states and the Jahn–Teller stabilization energy (*3*) of the neutral state.

Calculation of the fully-symmetric atomic configuration confirmed both the relation $e_u<e_g$ for the orbital energies of the MO's in the band gap, and also that the main configuration is the e_u^2 configuration.

MO methods systematically underestimate the triplet-state energies if corrections are not introduced to the configurational interaction. In the neutral divacancy the triplet state $^3A_{2g}$ (see Table I) turned out to be lower than the singlet state ^1E_g, the ground state according to the experimental EPR data, by 0.54 eV. However, the Jahn–Teller stabilization energy (arrow *3* in Fig. 2) is of the same order of magnitude and is equal to 0.34 eV, i.e., it may be assumed that the configurational interaction lowers the energy of the singlet state below that of the triplet state. Note that the stabilization energy agrees with the value calculated using the density functional method, 0.28 eV (Ref. 10).

Direct calculation of all the multiplet structures listed in the table showed that none of the terms—neither nondegenerate nor degenerate—lowers the energy of the terms of the fully-symmetric state. Jahn–Teller stabilization is associated only with the E_g mode, which completely removes the degeneracy of the MO's: $e_g(D_{3d})\rightarrow a_g+b_g(C_{2h})$ and $e_u(D_{3d})\rightarrow a_u+b_u(C_{2h})$ (Fig. 2). The energies of the different charge states are shown as they were calculated, without correction for the different number of electrons corresponding to the same number of atoms. Thus, in Fig. 2 it is impossible to judge the values of the transition energies between charge states. In each charge state (they were first

calculated together) there are two types of local minima of the ground states which are realized at certain values a of the relaxation (6) and of the pairing mode (p) and resonant mode (r) of the distortion (5).

At the r-minimum ($r>-p>0$) the ground states are the states with the orbitally nondegenerate open shells $a_u^1(V_2^+)$ and $a_u^2 b_u^1(V_2^-)$ and the state with a closed shell $a_u^2(V_2^0)$. Their energies are plotted on the right half of Fig. 2 along with several energies of the same configurations versus the resonant distortion mode r for constant values of p and a.

At the p minimum ($-p>-r>0$) the ground states are the states with an orbitally nondegenerate open shell $b_u^1(V_2^+)$ and $b_u^2 a_u^1(V_2^-)$ and the state with a closed shell $b_u^2(V_2^0)$. Their energies are plotted on the left half of Fig. 2 along with several energies of the same configurations versus the pairing distortion mode p for constant values of r and a.

Thus, the MO method fully confirms the results of the density functional method about the two-well divacancy potential in the neutral[10] and charged states.[7] The absolute minima of the charged states are found at the distortion mode that corresponds to the symmetry of the unpaired electron according to the EPR data: in both states it occupies the MO b_u.

The calculation of the energy differences between the absolute minimum and metastable minimum of the adiabatic energies (Fig. 2) can be taken as a new result: 0.16 eV for V_2^-, the r mode of the distortion of the ground state; 0.07 eV for V_2^0, r; and 0.03 eV for V_2^+, p.

So far only the first of these differences has been calculated by the density functional method: 2.4 meV for V_2^- (Ref. 7)—too small a value in comparison with the error of the method to definitely conclude in favor of the resonant mode as the ground state. As can be seen, the MO method leads to the same directions of distortion as the density functional method, but does not give such small energy differences between the r and p minima (in any case they are comparable with the experimental values of the reorientation energies of the divacancy axis).

The two-well picture of the Jahn–Teller effect for a divacancy gives us a new perspective on the experimental photoconductivity and DLTS data. Photoexcitation of V_2^+ in the 3.9 μm band corresponds to the direct transition indicated by the arrow *1* between the p-minima in Fig. 2. Recharging, on the other hand, corresponds to an indirect transition (arrow *2* in Fig. 2) between the p-minimum V_2^+ and the r-minimum V_2^0. Thus, the difference of 0.06 eV between the transition energies measured in two different ways can be explained without resorting to the mechanism of phonon absorption[12] by the fact that the Jahn–Teller effect is bimodal, i.e., vibronic coupling of the electron doublet $^1E_g(D_{3d})$ is realized with two modes of the two distortion components: $(E_g,1)_{r,p}$ and $(E_g,2)_{r,p}$ (the corresponding vibronic problem has dimensionality 4). The discrepancy between the calculated value 0.07 eV of the energy difference between the direct and indirect transitions $V_2^+ \rightarrow V_2^0$ and the experimental value 0.06 eV lies within the limits of calculational error.

Figure 3 plots results of a calculation of the energies of intracenter excitation of the neutral divacancy by the Δ-SCF

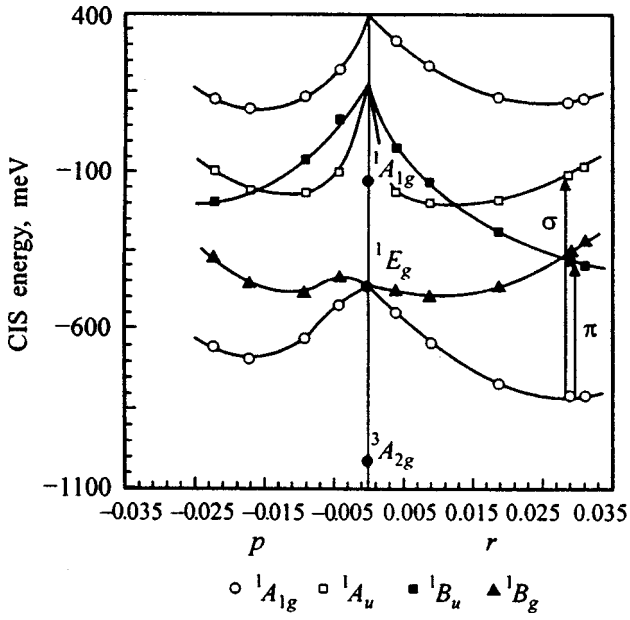

FIG. 3. One-electron excitations of a neutral divacancy as functions of the Jahn–Teller bimodal distortion. Notation indicated below the graph indicates the representation of the C_{2h} group corresponding to the ground state and excited states. Thus, the ground state, as in Fig. 2, has the representation A_g regardless of the configuration, a_u^2 on the right half and b_u^2 on the left half of the graph. The arrows point out the allowed intracenter optical transitions. Their polarizations σ and π are indicated relative to the symmetry axis of the divacancy $C_2 \| [110]$.

method.[13] One-electron excited states were constructed from the ground-state determinant, and configuration mixing (configuration interaction) of single excitations was enacted, i.e., the coefficients yielding an energy minimum of the superposition of configurations were calculated. For example, the excited state ^1B_u was obtained by mixing the configurations $a_g^1 b_u^1$ and $b_g^1 a_u^1$, where the MO's were chosen on the basis of symmetry, and one of the MO's of the indicated configurations was filled in the ground state and the other was empty. The calculated result agrees with data on the optical absorption line 1.8 μm (0.73 eV): the calculated energy of the allowed σ-polarized transition $^1A_g \rightarrow {}^1A_u$ is equal to 0.7 eV. At the same time it follows from the calculation that the unobserved π-polarized transition $^1A_g \rightarrow {}^1B_u$ with energy around 0.4 eV should be found in the spectrum of the neutral divacancy. In addition, intersection of the excited terms: ^1A_u with ^1B_u, and ^1B_u with ^1B_g, should lead to characteristic luminescence effects.

ACKNOWLEDGMENTS

I would like to express my deep gratitude to S. V. Bulyarskiĭ for support of this work.

[1] L. J. Cheng, J. C. Corelli, J. W. Corbett, and G. D. Watkins, Phys. Rev. **152**, 761 (1966).
[2] V. G. Karpov, N. V. Kolesnikov, and S. E. Mal'khanov, Fiz. Tekh. Poluprovodn. **16**, 1657 (1982) [Sov. Phys. Semicond. **16**, 1059 (1982)].
[3] F. Carton–Merlet, B. Pajot, D. T. Don, C. Porte, B. Clerjaud, and P. M. Mooney, J. Phys. C: Solid State Phys. **15**, 2239 (1982).
[4] R. G. Humphreys, S. Brand, and M. Jaros, J. Phys. C: Solid State Phys. **16**, L337 (1983).
[5] B. C. Svensson and M. Willander, J. Appl. Phys. **62**, 2758 (1987).

[6] M. P. Vlasenko and L. S. Vlasenko, Fiz. Tverd. Tela (Leningrad) **33**, 2357 (1991) [Sov. Phys. Solid State **33**, 1326 (1991)].
[7] M. Saito and A. Oshiyama, Phys. Rev. Lett. **73**, 866 (1994).
[8] G. D. Watkins, Phys. Rev. Lett. **74**, 4353 (1995).
[9] M. Saito and A. Oshiyama, Phys. Rev. Lett. **74**, 4354 (1995).
[10] H. Seong and L. J. Lewis, Phys. Rev. B **53**, 9791 (1996).
[11] B. C. Svensson, C. Jagadish, A. Hallen, and J. Lalita, Phys. Rev. B **55**, 10498 (1997).
[12] V. A. Voĭtenko and S. E. Mal'khanov, Zh. Éksp. Teor. Fiz. **112**, 707 (1997) [JETP **86**, 386 (1997)].
[13] R. McWeeny, *Methods of Molecular Quantum Mechanics* (Academic Press, Orlando, 1989).
[14] R. A. Évarestov, *Quantum-Chemical Methods in Solid State Theory* [in Russian] (Leningrad State University Press, Leningrad, 1982).
[15] J. C. Slater, Phys. Rev. **34**, 1293 (1929).
[16] D. R. Hartree, *The Calculation of Atomic Structures* (Wiley, New York, 1957).
[17] S. S. Moliver, Fiz. Tverd. Tela (Leningrad) **33**, 929 (1991) [Sov. Phys. Solid State **33**, 527 (1991)].
[18] S. S. Moliver, J. Phys.: Condens. Matter **4**, 9971 (1992).
[19] S. S. Moliver, Fiz. Tverd. Tela (St. Petersburg) **38**, 2029 (1996) [Phys. Solid State **38**, 1119 (1996)].
[20] A. Schluger, Theor. Chim. Acta **66**, 355 (1985).
[21] S. Dannefaer, P. Mascher, and D. Kerr, Phys. Rev. Lett. **56**, 2195 (1986).

Translated by Paul F. Schippnick

Kikuchi-band formation in medium-energy electron-diffraction patterns

M. V. Gomoyunova, I. I. Pronin, N. S. Faradzhev, and D. A. Valdaĭtsev

A. F. Ioffe Physicotechnical Institute, Russian Academy of Sciences, 194021 St. Petersburg, Russia
(Submitted July 24, 1998)
Fiz. Tverd. Tela (St. Petersburg) **41**, 411–417 (March 1999)

To reveal the mechanism of Kikuchi-band formation, the total Si(100) diffraction pattern produced by 2-keV quasi-elastically backscattered electrons is compared to model calculations made in the single-scattering approximation for clusters constructed with different numbers of close-packed (110) planes. The formation of the Kikuchi bands is shown to be governed by two types of electron scattering in a crystal. The dominant contribution to enhanced electron-scattering intensity within a band comes from the forward-focusing effect as the electrons move along the numerous interatomic directions in the (110) planes. The other mechanism responsible for the sharp edge regions in the Kikuchi bands involves electron scattering from the nearest planes. It is proposed to use the specific profile of the Kikuchi bands in estimating the shape and size of light-element crystallites forming during initial stages of island-film growth. [S1063-7834(99)00903-X]

Studies of surfaces and interfaces have been making increasing use of methods of atomic structure analysis based on medium-energy electron diffraction (hundreds of eV to ~ 2 keV). This relates primarily to the diffraction of x-ray generated photo- and Auger electrons,[1–3] as well as of incoherently scattered primary electrons.[3–6] The spatial distributions of all these three groups of electrons have a similar structure for close energies. As a rule, it may be considered as a superposition of maxima oriented along the close-packed directions in a crystal. This specific pattern of the diffractograms allows their fairly straightforward interpretation and provides information regarding the object under study in real space. Besides, one usually observes bands of a higher intensity oriented along the projections of the closest-packed atomic planes. For crystals made up of light elements, these bands exhibit a high contrast and have sharp boundaries.

The maxima lying along interatomic directions are usually associated with the forward electron focusing effect in crystals.[1–3] The mechanism responsible for formation of the higher-intensity bands, which in the electron backscattering patterns are traditionally called Kikuchi bands, and in photo- and Auger-electron diffraction, Kikuchi-like or Bragg features, is less clear. In the early stages of these studies, when the potential of using these patterns for structural analysis of surfaces was not yet recognized, the Kikuchi bands were considered within the dynamical theory of electron diffraction.[7] The corresponding calculations were performed, as a rule, in the simplest two-wave approximation, which permitted interpretation of the observed Kikuchi-band profile and their width equal to twice the Bragg angle.

Later studies,[8–12] where the emphasis shifted to the electron focusing effect and numerical simulation of the patterns in terms of the single-scattering cluster approximation, put forward various suggestions concerning the formation mechanism of these features. The most widely used viewpoint associates the sharp drops in intensity at the Kikuchi-band edges with electron Bragg diffraction from a system of planes, which is taken into account by introducing large clusters. For instance, the cluster used to analyze photoelectron diffraction from $CaF_2(111)$ at 1139 eV was $30\times30\times30$ Å in size.[12] Despite a good agreement of such calculations with experiment, however, the part played by the electron forward-focusing effect in Kikuchi band formation remained undisclosed. At the same time the need of understanding the mechanism which underlies generation of Kikuchi-like features has recently become particularly evident in view of the considerable progress reached recently in improving the angular resolution in photoelectron diffraction.[2,12,13]

It is the mechanism of Kikuchi band formation that forms the objective of this work. With this purpose in mind, the diffraction patterns obtained for a silicon single crystal within the takeoff angle region adjoining the projection of the (110) planes along which one observes the sharpest Kikuchi bands were compared with model calculations performed within the single-scattering approximation for clusters of different dimensions and different shape.

1. EXPERIMENTAL TECHNIQUES AND RESULTS OF MEASUREMENTS

The methods employed in obtaining diffraction patterns was described elsewhere.[14] The experiments were carried out in ultrahigh vacuum on samples with an atomically clean surface, which was monitored by LEED and Auger spectroscopy. The subjects for the study were Si(111) and Si(100) single crystals prepared for measurements as described in Refs. 11 and 15. The diffraction patterns of incoherently scattered primary electrons of interest here were obtained by measuring the dependences of the elastic-scattering peak intensity of electrons on the polar and azimuthal angles of their escape. For electron energies above approximately 1 keV such patterns were shown[14] to be dominated by the diffraction of the electrons which suffered phonon-assisted inelastic

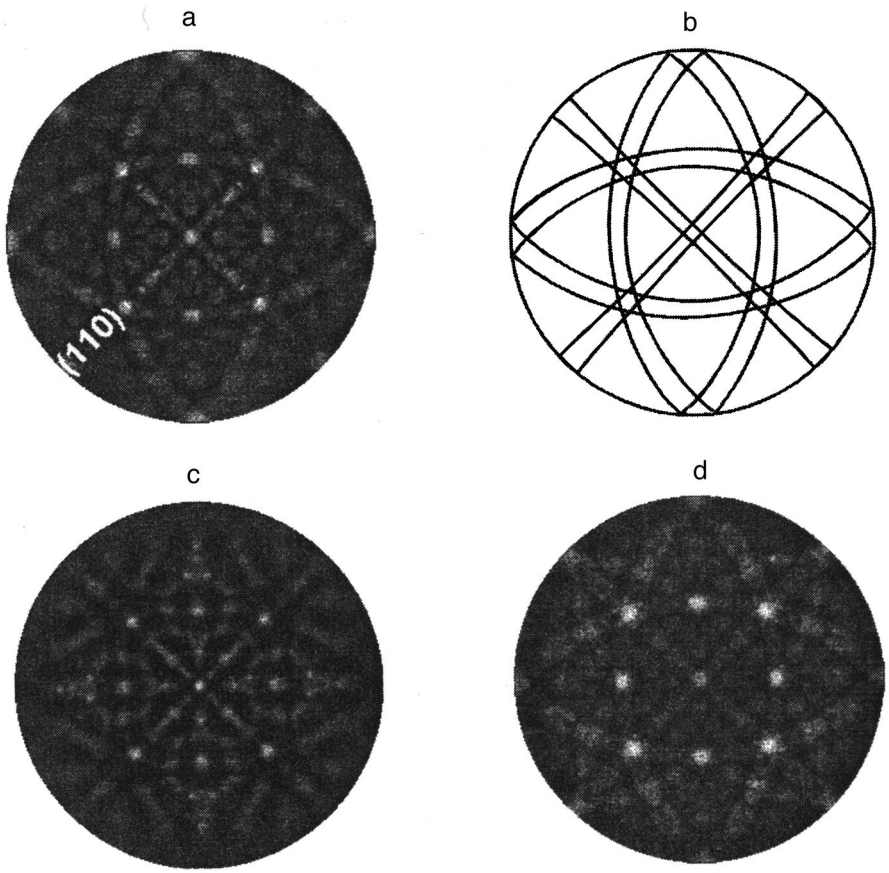

FIG. 1. (a,c) diffraction patterns of quasielastically backscattered electrons measured at 2 keV on Si(100) and Mo(100) single crystals, respectively; (b) boundaries of Kikuchi patterns in a silicon diffraction pattern; (d) silicon diffraction pattern calculated in plane-wave approximation of a single-scattering cluster model for a cluster of 8125 atoms.

scattering. It may be added that it is this peak that is most sensitive to the surface structure of the object under study, because quasielastically scattered electrons escape from the smallest depth compared to other groups of reflected electrons.

Figure 1a shows a typical diffraction pattern of quasielastically scattered electrons. It was obtained on a Si(100) single crystal with 2-keV electrons, where the features of interest are seen particularly clearly. The pattern is presented in the form of a stereographically-projected, two-dimensional scattered-electron intensity map in polar and azimuthal takeoff angles. The center of the circle corresponds to electrons escaping along the normal to the surface, and its edges, to grazing-angle electron emission. The intensity at different points of the map is given in a gray-scale contrast code, with the white and black colors referring to the maximum and minimum scattered intensities, respectively.

This pattern exhibits a clearly visible fourfold symmetry characteristic of the given face of the silicon cubic crystal. A detailed analysis of its diffraction structure can be found in Ref. 15. We note here only that it shows Kikuchi bands oriented along the closest-packed {110} atomic planes of silicon, two of which are perpendicular to the surface and pass through the center of the map. To reveal them more clearly, we have presented here for the first time the complete diffractogram of the Si(100) face obtained within the full reflection hemisphere. We have succeeded in doing this despite the fact that the rough experimental data had a small dead zone near the surface normal. Because it is this part of the pattern that is particularly important for comparing calculations with experiment, we complemented it with the data obtained in the same conditions for the other silicon plane, Si(111).

A characteristic feature of the Kikuchi bands considered here is the presence of sharp boundaries shown by lines in Fig. 1b. Their position coincides with the Bragg angle for the given plane system. It should be stressed that such sharp boundaries are typical of light-element crystals and are only weakly pronounced in crystals made of heavier elements. For illustration, Fig. 1c presents a similar diffraction pattern obtained in the same experimental conditions but on single-crystal Mo(100), whose atomic number is three times that of silicon. Indeed, the Kikuchi bands observed along the projections of the molybdenum (110) planes (which are likewise the closest packed in this crystal) reveal large drops in intensity along the bands and are conceived as a set of individual focusing maxima lying in the given plane. Note that the differences in the structure of Kikuchi bands between light and heavy elements, which are prominent in the energy range under study here, become barely visible at higher electron energies (tens of keV).[16]

2. COMPUTER SIMULATION OF KIKUCHI BANDS

Model calculations have been carried out to reveal the mechanism accounting for the formation of Kikuchi bands in

a diffraction pattern of single-crystal silicon. We present below a brief description of the single-scattering cluster model[14] used in the simulation.

2.1. Single-scattering cluster model and Si(100) diffraction pattern

The near-surface layer of the sample scattering the incident electrons was approximated by a cluster, whose atomic arrangement reflected the bulk crystal structure of silicon. Because quasielastic electron scattering at large angles occurs close to lattice sites, the cluster atoms were considered as sources of diverging electron waves. One took into account single elastic scattering of each of these waves by the other cluster atoms and interference of the incident and scattered waves. The calculation was completed by summing up the diffraction patterns due to the individual sources, which were considered incoherent.

Electron absorption in the crystal was described by a simple exponential decay characterized by an effective parameter λ. In accordance with Ref. 3, the best agreement of the calculations with experiment was reached for $\lambda \sim 0.7\lambda_0$, where λ_0 is the electron mean free path for inelastic scattering, which was calculated from the relations given in Ref. 17. For silicon and an energy of 2 keV, λ_0 is about 26 Å. Therefore for simulation of the diffraction pattern under consideration we took $\lambda = 18$ Å. For such a decay parameter, complete convergence is reached only for very large clusters, consisting of more than 10,000 atoms, which requires very time-consuming calculations (of the order of 100 h with a Pentium-166 PC). At the same time nearly all characteristic features in the observed pattern are reproduced already with clusters made up of only a few hundred atoms,[18] and further increase of their number does not affect it significantly. Therefore the optimum size of a cluster in a simulation aimed at studying the structure of near-surface layers is one to two thousand atoms. The results of such calculations made for Si(100) are given in Ref. 15. This number is not large enough, however, for a full reproduction of Kikuchi bands, because they continue to grow in contrast with further increase of cluster size. Therefore the diffraction pattern shown in Fig. 1a was simulated with a cluster consisting of 8125 atoms ($54\times54\times45$ Å).

The results thus obtained are illustrated by Fig. 1d showing the calculations in the same form as the measurements. Basically, the calculated pattern and the *R* factor, which describes quantitatively its deviation from the observed diffractogram,[11] have indeed changed little compared to the results presented in Ref. 15. At the same time the contrast of the bands improved to a certain extent, which made clearer the agreement of the calculations with experiment. A comparison of the data in Fig. 1a and d demonstrates convincingly that the single-scattering cluster approach offers an adequate description of the Kikuchi bands while providing no hint as to the mechanism of their formation. To obtain information that could shed light on this problem, clusters of different sizes and shapes were used in the band simulation. We started with a two-dimensional cluster approximating single (110) planes perpendicular to the crystal surface, along which actually the Kikuchi bands appear.

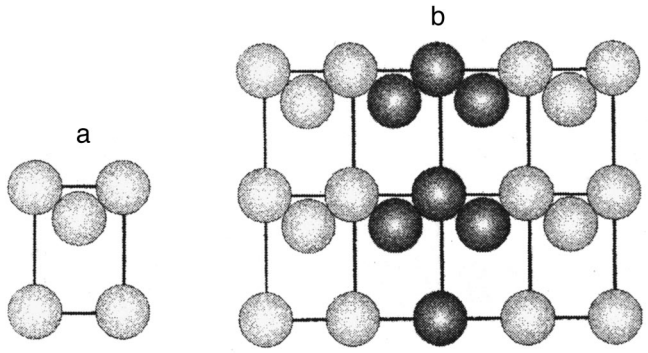

FIG. 2. (a) Unit cell of the silicon (110) lattice plane; (b) 23-atom cluster (4×2 cells), with electron-emitting atoms shaded.

2.2. Electron focusing by single planes

The atomic structure of the (110) plane is illustrated by Fig. 2a presenting its unit cell. The calculations were performed for clusters constructed of different numbers of such cells, starting with two and ending with a plane made up of 28×10 cells (599 atoms). The sources of electrons were atoms in the central chain and their nearest neighbors (Fig. 2b).

The results of the simulation are seen in Fig. 3. Because of the clusters being two-dimensional, a diffraction pattern is generated only within a limited electron-takeoff solid-angle region which adjoins the scattering plane, and it is only this angular region that is displayed in the figure. For the smallest cluster (Fig. 3a), the band under study consists of several zero-order diffraction maxima corresponding to electron focusing along the few available interatomic directions, with each of them being surrounded by higher-order annular maxima.[14] The number of interatomic directions increases with increasing linear dimensions of the plane (Fig. 3b), as does, accordingly, the number of focusing maxima within a band. A fairly complex diffraction structure forms at intersections of the corresponding rings.

As the dimensions of the plane are increased still more (to about 300 atoms), the band filling loses gradually the discrete character to make it look already as a pattern, although with a varying intensity and with local broadenings near the closest-packed directions (Fig. 3c and 3d). This is accompanied by a noticeable narrowing of the band due to the increasing contribution of focusing at scatterers distant from the emitter. Note that taking into account multiple-scattering of electrons, which should grow in significance with increasing linear dimensions of the plane because of the atomic chains becoming longer, likewise results in a decrease of the focusing maxima in angular size.

Thus it follows that the Kikuchi band observed along the (110) planes is actually produced by superposition of numerous electron focusing maxima caused by electron scattering from atoms in the given plane. A continuous band forms only if the plane consists of a large enough number of atoms.

The conclusion of the Kikuchi band formation being dominated by electron scattering from single planes finds support in the results of an earlier study,[19] where electron localization near atomic planes observed as they penetrated

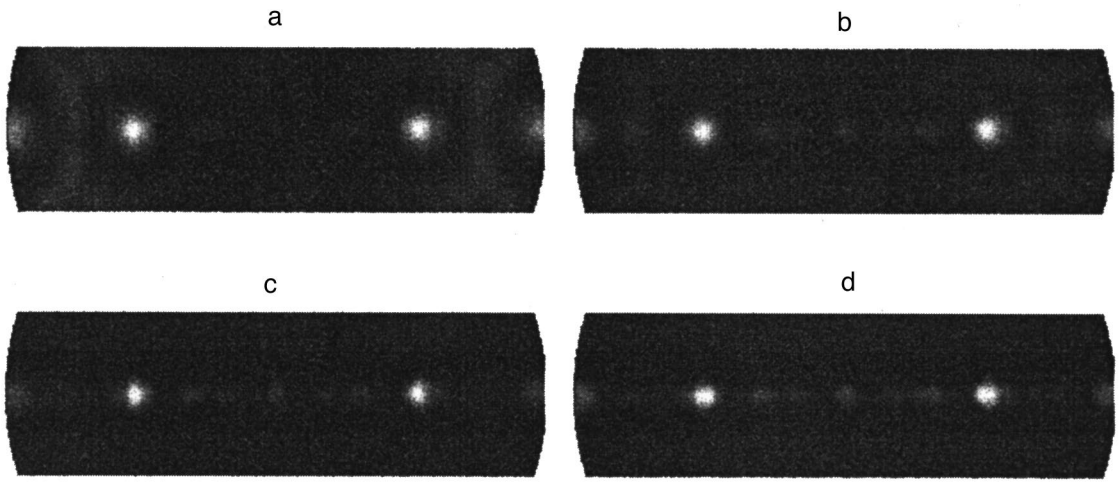

FIG. 3. Parts of the calculated silicon diffraction patterns near the (110) plane where a Kikuchi band forms. The simulation was performed for two-dimensional clusters of increasing size: (a) 2×1 cells in the (110) plane containing eight atoms; (b) 4×2 cells with 23 atoms; (c) 8×4 cells (77 atoms); and (*d*) 16×8 cells (279 atoms).

into a crystal was calculated in the Born approximation of diffraction theory with inclusion of all diffracted waves. It was shown that, similar to the present case, for electrons moving along the planes or at small angles to them electron interaction with single planes also plays a dominant part, which is due to many-wave effects.

It should be noted, however, that the results of the simulation displayed in Fig. 3 do not provide an adequate description of the transverse profile of a Kikuchi band, because they do not reproduce its sharp boundaries observed experimentally. This implies inadequacy of the above mechanism and the need of taking into account electron scattering from atoms in the adjacent planes.

2.3. Electron diffraction from a (110) plane system

To reveal the part played in Kikuchi band formation by electron scattering from planes parallel to the one containing the electron sources, calculations were carried out with wider clusters constructed of a number of (110) planes. The results obtained are illustrated by Fig. 4. We readily see that even in the case of a cluster consisting of three planes only (Fig. 4a), the lateral profile of the band under consideration has changed qualitatively compared to the data obtained using a two-dimensional cluster. Its boundaries became substantially sharper and smoother than those in Fig. 3d, so that the band on the whole has approached closer in its general pattern the experimental result.

The pattern exhibits other changes as well. In particular, new focusing maxima have appeared outside the band. They are due to the existence in the cluster of interatomic directions which, rather than lying in the (110) planes, are at a tilt to them. Further widening of the cluster (an increase in the number of planes to five in Fig. 4b) results primarily in a more pronounced diffraction structure in the periphery of the pattern. There are signs also of the formation of a new Kikuchi band, which is perpendicular to the one under study and

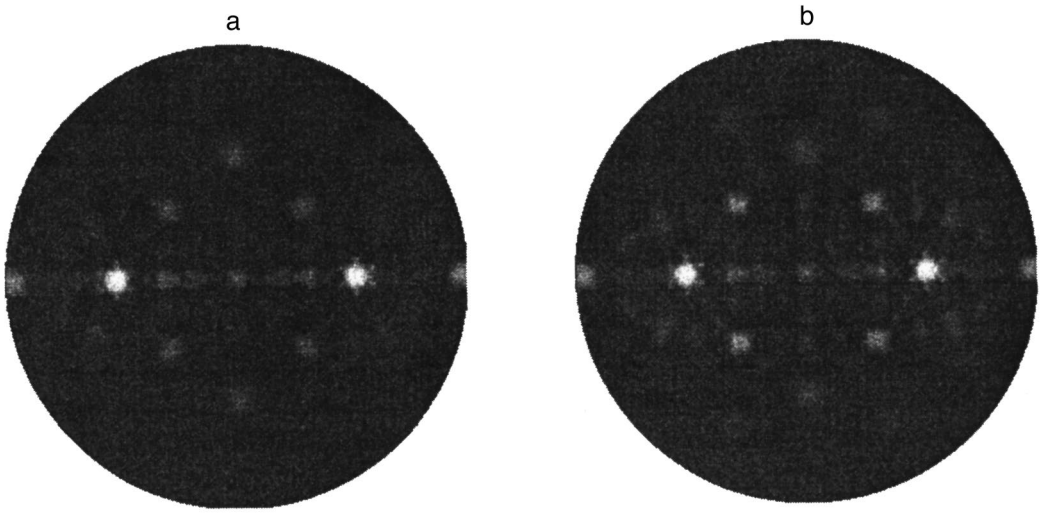

FIG. 4. Calculated diffraction patterns for clusters constructed of (a) three and (b) five (110) planes, with each containing 279 atoms.

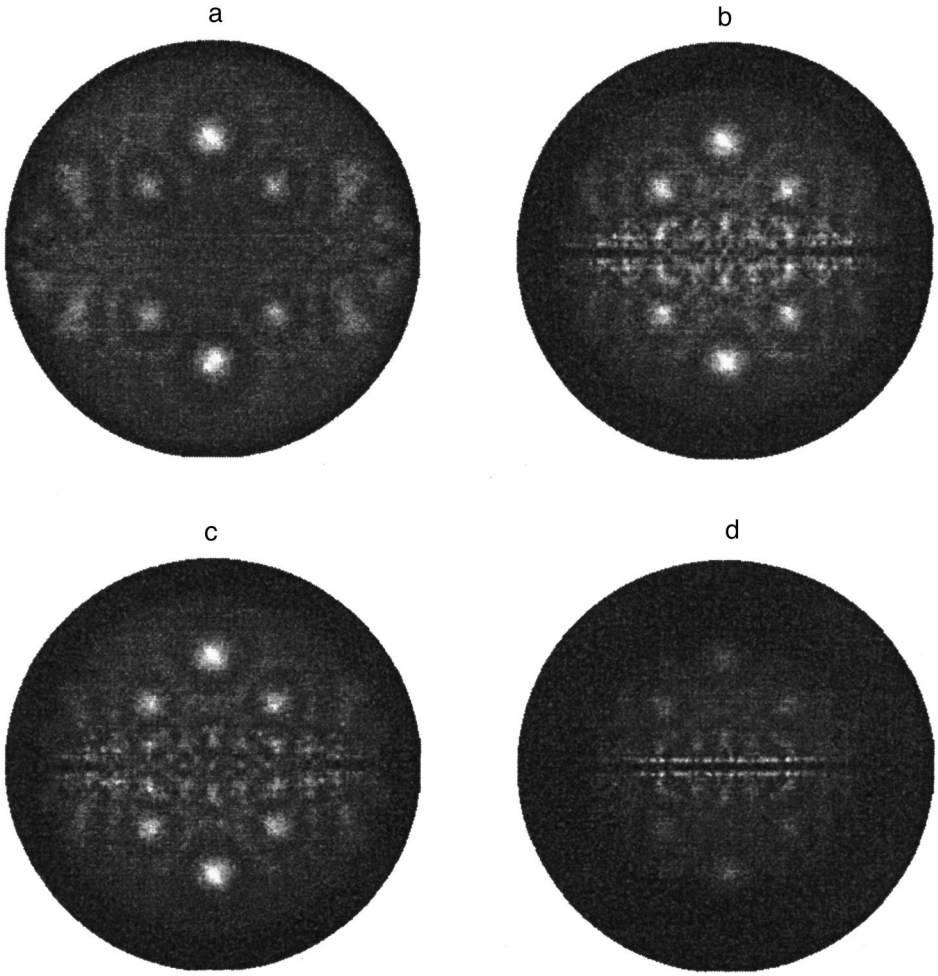

FIG. 5. Diffraction patterns from emitters located in the cluster at different depths: (a) 5.4 Å, (b) 10.9 Å, (c) 16.3 Å, and (d) 32.6 Å.

oriented vertically in the figure. As for the band itself, its pattern, strange as this might seem, has not practically changed as one crossed over from a three- to five-plane cluster. Thus in order to obtain a band similar to the one observed experimentally, it is enough to have, besides the plane containing the electron sources, at least one adjacent plane on each of its sides. Their linear dimensions, as in the above case of electron scattering from atoms in a single plane, should be large enough, however, to accommodate hundreds of atoms.

2.4. Electron diffraction from two planes of the (110) system

Special calculations were performed to understand why taking into account electron scattering from two adjacent planes improves so markedly the Kikuchi band contrast. We used a cluster of 1198 atoms distributed in two scattering (110) planes. These planes, which are perpendicular to the surface, measured 28×10 cells and were 3.84 Å distant, which is twice the interplanar separation in silicon. Single atoms considered as electron-wave sources were placed at the cluster's center at different depths (at lattice sites between these planes). Next diffraction patterns for each of these emitters were generated.

The results obtained are displayed in Fig. 5. The character of the patterns depends dramatically on the source depth. The pattern produced by emitters localized near the surface (Fig. 5a) is dominated by electron focusing maxima oriented along the $\langle 111\rangle$ and $\langle 101\rangle$ directions available in this cluster, with practically no diffraction structure in the region of the Kikuchi band under study. As the source depth increases (Fig. 5b and 5c), the intensity of these maxima falls off gradually, while that at the center grows. Note the comparatively complex structure building up in the vicinity of the band of interest. Remarkably, it starts to form in the periphery of the pattern (for large electron polar takeoff angles), where it looks as a fairly narrow, horizontal black band flanked by a series of thin light bands made up of individual lines (Fig. 5c). As the source is placed still deeper, this dark, bright-edged band grows in extent and approaches the center of the pattern to eventually fill up all of its central part (Fig. 5d). The angular position of the strongest narrow lines at its edges corresponds to the Bragg angle for the given plane system, which for the 2-keV energy is about 4°. Because the same angle determines the position of the edge of the observed Kikuchi band, one may conjecture that its sharp profile is generated by the scattering of electrons ejected by deeply lying emitters. Obviously enough, in order for this effect to become seen, the mean free path of electrons for inelastic scattering should be large enough. It is this differ-

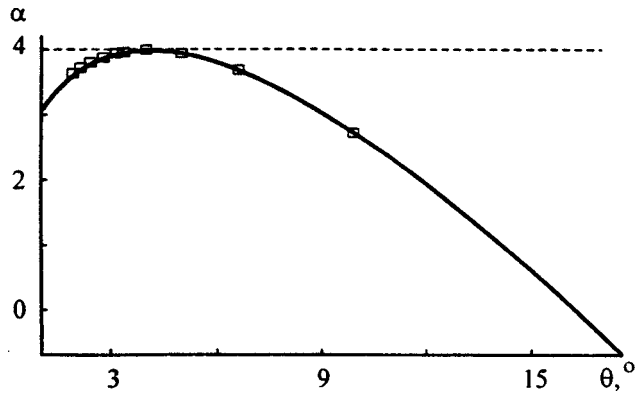

FIG. 6. Relation between the angular positions of the focusing maxima (θ) and the corresponding first-order interference maxima (α) for the case of electrons scattered from a chain of silicon atoms. The angles α and θ are reckoned from the surface normal, and the dashed line identifies the Bragg angle.

ence in mean free paths for light and heavy elements that accounts apparently for the absence of high-contrast Kikuchi bands in the case of heavy elements.

In considering Fig. 5, it should be stressed that the maxima forming at Bragg angles are usually assumed to be produced in diffraction of waves reflected specularly from a system of planes in a semi-infinite crystal. Our case is completely different, because the emitter is located only between two planes, a situation where even two waves scattered specularly in the same direction cannot be generated. Therefore the origin of the strong narrow lines at the edges of a Kikuchi band (Fig. 5d) with sources located at a large depth requires a special analysis.

The origin of these maxima becomes clear if one considers diffraction of electrons emitted by such sources from the closest atomic chain located at the center of one of the cluster scattering planes and oriented perpendicular to its surface. It was found that although the focusing maxima due to electron scattering from different atoms in a chain do indeed form along different directions, the corresponding first-order interference maxima practically coincide with them in orientation. This is illustrated by Fig. 6. We see that, as the scatterers in the chain move away from the emitter, the angular positions (θ) of the focusing maxima identified by points in the graph decrease noticeably (from 10 to 2°) and approach the surface normal. At the same time the positions (α) of the corresponding interference maxima change only insignificantly, increasing to the value equal to the Bragg angle with subsequent smooth falloff. Note that the α angles for the eight atoms in the chain differ by not more than 0.3°. This is what accounts for the bright feature at the Bragg angle, which is responsible for the sharp edge of the Kikuchi band.

We note in conclusion that the considerable differences in the sensitivity of the Kikuchi band profile to the longitudinal and lateral cluster dimensions revealed in this study evidence a strongly anisotropic nature of their formation. This factor can be used apparently to obtain information on the morphology of thin light-element films growing in an island pattern. Our data suggest that one can judge the shape of crystallites under certain conditions and even estimate their size from the Kikuchi bands of deposited material.

Thus we have carried out an experimental and theoretical study of the mechanism responsible for formation of the Kikuchi bands observed in diffraction patterns of a silicon single crystal along the projections of the (110) planes.

Two mechanisms governing the formation of these bands are shown to exist. The first is electron focusing, which takes place as particles propagate along the (110) planes and originates primarily from small-angle scattering by the atoms the electrons encounter on the way. To form continuous bands, the electron mean-free paths along these planes should be sufficiently large.

The second mechanism involves diffraction of electrons by the nearest adjacent planes, which is responsible for the sharp edge regions in the Kikuchi bands. An essential part is played here by coherent superposition of first-order interference maxima, which are related to the focusing maxima of electrons escaping from large depths.

Support of the Russian Fund for Fundamental Research (Grant 96-02-16909) and of the Russian State Program ''Surface Atomic Structures'' (Grant 95-1.21) is gratefully acknowledged.

[1] W. F. Egelhoff, Jr., Crit. Rev. Solid State Mater. Sci. **16**, 213 (1990).
[2] C. S. Fadley, in *Synchrotron Radiation Research: Advances in Surface and Interface Science*, Vol. 1: Techniques, edited by R. Z. Bachrach (Plenum Press, New York, 1992), p. 421.
[3] S. A. Chambers, Surf. Sci. Rep. **16**, 261 (1992).
[4] J.-M. Pan, B. L. Maschhoff, U. Diebold, and T. E. Madey, Surf. Sci. **291**, 381 (1993).
[5] M. Erbudak, M. Hochstrasser, and E. Wetli, Mod. Phys. Lett. B **8**, 1759 (1994).
[6] N. S. Faradzhev, M. V. Gomoyunova, and I. I. Pronin, Phys. Low-Dimens. Semicond. Struct. **3/4**, 93 (1997).
[7] R. Baudoing, R. M. Stern, and H. Taub, Surf. Sci. **11**, 255 (1968).
[8] W. F. Egelhoff, Jr., J. Vac. Sci. Technol. A **4**, 758 (1984).
[9] R. Trehan, J. Osterwalder, and C. S. Fadley, J. Electron Spectrosc. Relat. Phenom. **42**, 187 (1987).
[10] J. Osterwalder, E. A. Stewart, D. Cyr, C. S. Fadley, J. Mustre de Leon, and J. J. Rehr, Phys. Rev. B **35**, 9859 (1987).
[11] I. I. Pronin, N. S. Faradzhev, and M. V. Gomoyunova, Fiz. Tverd. Tela (St. Petersburg) **39**, 752 (1997) [Phys. Solid State **39**, 666 (1997)].
[12] U. Bardi, M. Torrini, Y. Ichinohe, S. Omori, H. Ishii, M. Owari, and Y. Nihei, Surf. Sci. **394**, L150 (1997).
[13] Y. Ichinohe, H. Ishii, M. Owari, and Y. Nihei, Jpn. J. Appl. Phys. **35**, L587 (1996).
[14] M. V. Gomoyunova, I. I. Pronin, and N. S. Faradzhev, Zh. Éksp. Teor. Fiz. **110**, 311 (1996) [JETP **83**, 168 (1996)].
[15] I. I. Pronin, N. S. Faradzhev, and M. V. Gomoyunova, Fiz. Tverd. Tela (St. Petersburg) **40**, 1364 (1998) [Phys. Solid State **40**, 1241 (1998)].
[16] D. J. Dingley, K. Z. Baba-Kishi, and V. Randle, *Atlas of Backscattering Kikuchi Diffraction Patterns* (IOP Publishing, Bristol, 1995).
[17] M. P. Seach, Surf. Interface Anal. **9**, 85 (1986).
[18] N. S. Faradzhev, M. V. Gomoyunova, and I. I. Pronin, Phys. Low-Dimens. Semicond. Struct. **9**, 11 (1994).
[19] M. V. Gomoyunova, O. V. Konstantinov, and I. A. Shmulevitch, Surf. Sci. **108**, 281 (1981).

Translated by G. Skrebtsov

Characteristics of the structural properties and the electric conductivity in $LaSrAl_{1-x}Ni_xO_4$ ceramics caused by the Jahn–Teller effect

T. A. Ivanova, Yu. V. Yablokov, N. S. Zinatullina, and R. M. Bayazitov

Kazan Physicotechnical Institute, Russian Academy of Sciences 420029 Kazan, Russia
(Submitted March 23, 1998; resubmitted September 1, 1998)
Fiz. Tverd. Tela (St. Petersburg) **41**, 418–422 (March 1999)

In studying $LaSrAl_{1-x}Ni_xO_4$ ceramics, anomalies are detected in the concentration dependences of the lattice parameter c, the electrical resistance, and the sign change of the Hall constant at $x \approx 0.6$. It is shown that the collection of observed phenomena can be interpreted as a manifestation of the Jahn–Teller nature of low-spin Ni^{3+} centers. © *1999 American Institute of Physics.* [S1063-7834(99)01003-5]

In studying the ceramics $LaSrAl_{1-x}Ni_xO_4$, $(0<x<1)$, Ref. 1 detected anomalies in the concentration dependence of the lattice constant c, as well as a change in the sign of the thermoelectromotive force, at $x \approx 0.6$, interpreted as a change in the type of majority charge carriers from holes to electrons. The assumption was expressed that these features are associated with a change of the ground state of low-spin Ni^{3+} ions from d_{z^2} to $d_{x^2y^2}$. The mechanism of such a change was not discussed.

Radio-frequency spectroscopic studies of $LaSrAl_{1-x}Ni_xO_4$ ceramics with $x<0.1$ showed that the NiO_6 components in them, with Ni^{3+} in a low-spin state, are characterized by strong electron–phonon coupling.[2–4] Two varieties (1 and 2) of static Jahn–Teller (JT) NiO_6 centers were observed, differing in the degree of tetragonal distortions and, when the tetragonal component of the crystal field of the complex was decreased by interplanar excess oxygen, NiO_6 centers (3) were observed with temperature JT dynamics. This paper presents new experimental data that confirm the unusual change in the structural parameters and the change in the character of the conductivity from hole-type to electron-type when $x \approx 0.6$ in $LaSrAl_{1-x}Ni_xO_4$ and proposes a mechanism that regards the observed features as the manifestation of the JT nature of the NiO_6 centers.

1. EXPERIMENT

Samples of $LaSrAl_{1-x}Ni_xO_4$ with $x=0-1$ were fabricated by decomposition of the nitrates, using the technique explained in Ref. 3. We measured the concentration dependence of the lattice constants and the temperature dependence of the electrical resistance earlier.[5] This paper presents measurements of the concentration dependence of the resistivity and the Hall constant. The resistivity r_0 was measured by the four-probe method, and the calculations allowed for the thickness w of the plate. The Hall constant R_x was obtained from measurements of the Hall emf by the van der Pauw method. The charge-carrier concentration n was defined as $n=1/eR_x$, where e is the charge of the electron. The techniques used here are explained in Ref. 6. The results of the measurements are shown in Figs. 1–3 and in Table I.

It can be seen from Fig. 1 that, as the nickel concentration increases, lattice constant a increases while c decreases, with a jump in the $c(x)$ dependence being observed in the region $x \approx 0.5$. The variation of resistivity $r_0(x)$ has a nonmonotonic character in the ceramic studied here: On the whole, a decrease of r_0 with increasing x is observed, but r_0 increases in the region $x \approx 0.6$ (Fig. 2). The fact that the Hall constant changes sign from plus to minus (see Table I) with increasing x is evidence that the character of the conductivity of the compounds changes, i.e., that the type of majority charge carriers changes (from holes to electrons in the region $x \approx 0.6$). The dependence of carrier concentration on x (Fig. 3) shows a decrease of n when $x \approx 0.6$, and this agrees with the character of the $r_0(x)$ dependence.

2. DISCUSSION OF RESULTS

For the low-spin ion Ni^{3+} ($3d^7$, $S=1/2$), as for Cu^{2+} ($3d^9$, $S=1/2$), the ground state in a regular octahedral neighborhood is an orbitally degenerate doublet. We shall therefore use the results obtained by Refs. 7 and 8 for Cu^{2+} to analyze the character of the distortion of the JT complex NiO_6 as a function of the distortions of the external crystal field. When the tetragonal component of the crystal field is small by comparison with the JT splitting of the doublet, $|\Delta| \ll |E_{JT}|$, and is directed along the z axis of the complex (the z axis in the test samples coincides with the crystal's c axis), the equation of the adiabatic potential has the form

$$E_{1,2}=M\omega^2\rho_0^2/2+V_3\rho_0^3\cos 3\varphi \pm V\rho_0(1+\Delta\cos\varphi/V\rho_0), \quad (1)$$

where the first term is the potential energy of the nuclei, caused by their normal vibrations; the second term allows for the anharmonicity of the vibrations; the third term allows for the electron–nucleus interaction, which is linear in deformations, and the splitting of the doublet by the tetragonal crystal field directed along the z axis; and the value of ρ_0 corresponds to the minimum energy in the linear approximation [$V_3=0$ and $\Delta=0$ in Eq. (1)]. The plus sign corresponds to the ground-state wave function $\Psi_1=|\theta\rangle\sin\alpha/2+|\varepsilon\rangle\cos\alpha/2$,

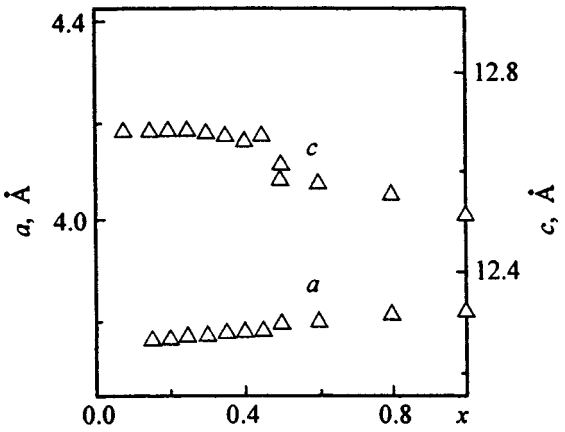

FIG. 1. Concentration dependence of lattice constants a and c of the compound $LaSrAl_{1-x}Ni_xO_4$.

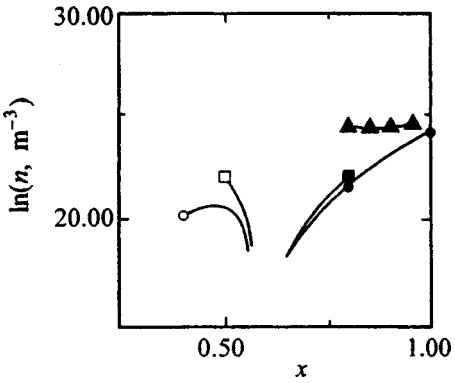

FIG. 3. Overall charge-carrier concentration vs nickel content in $LaSrAl_{1-x}Ni_xO_4$. The open symbols correspond to holes, the closed ones to conduction electrons.

the minus sign corresponds to function $\Psi_2=|\theta\rangle\cos\alpha/2 -|\varepsilon\rangle\sin\alpha/2$. Here $|\theta\rangle\equiv|d_{z^2}\rangle$, $|\varepsilon\rangle\equiv|d_{x^2y^2}\rangle$, and $\alpha\approx\varphi$ for the given approximation.

As follows from numerous experimental data, in the absence of external deformations, the JT effect for octahedral complexes of Cu^{2+} results in spontaneous equiprobable stretching of the octahedron along one of the fourth-order axes; i.e., the anharmonicity constant in Eq. (1) is $V_3<0$, and, for $\Delta=0$, energy minima occur at $\varphi=0$, $2\pi/3$, and $4\pi/3$. There are no such data for complexes of low-spin Ni^{3+}, and the question of what stabilizes the compressed or stretched configuration for a regular octahedral complex because of the JT effect has remained open. It has been established[8–10] that the linear vibronic coupling constant is $V<0$ for octahedral complexes of Cu^{2+}, where a hole is found on the orbitally degenerate doublet. It follows from Eq. (1) that, for tetragonally stretched octahedral complexes ($\Delta<0$) in an adiabatic potential, one minimum at $\varphi=0$ is lowered in this case, and the ground state is $d_{x^2-y^2}$. There are no temperature dynamics for $\Delta E\gg kT$, or restructuring of the spectrum from axial to isotropic is observed for $\Delta E\leqslant kT$. This is confirmed by numerous experimental results from studies of CuO_6 complexes in a tetragonal external field.[8,11]

For complexes of low-spin Ni^{3+}, with an electron in the orbitally degenerate doublet, V has a sign opposite to that of copper complexes. For the same reason, the tetragonal component of the crystal field in the field of a stretched octahedron also has different signs for Cu^{2+} and for low-spin Ni^{3+}. For NiO_6, as shown in Ref. 3, the tetragonal component of the stretching lowers the two equivalent minima, which correspond to rhombically distorted complexes (curve *3* in Fig. 4). As the temperature increases, the migration of the complexes between the two lower minima of the adiabatic potential causes the symmetry of the complex to be effectively axial, with a d_{z^2} ground state (centers 3). Increasing the stretching deformation suppresses the potential barrier between the minima (curve *4* in Fig. 4), and a complex of axial symmetry, with the relationship of the g factors $g_\parallel<g_\perp$ characteristic of a d_{z^2} ground state, is observed in the entire temperature interval (centers 1 and 2). As follows from Eq. (1), when $V>0$, the experimental data of Ref. 2 for low-spin Ni^{3+} will be in agreement only for $V_3>0$. This means that, for a regular octahedral complex of low-spin Ni^{3+}, energy

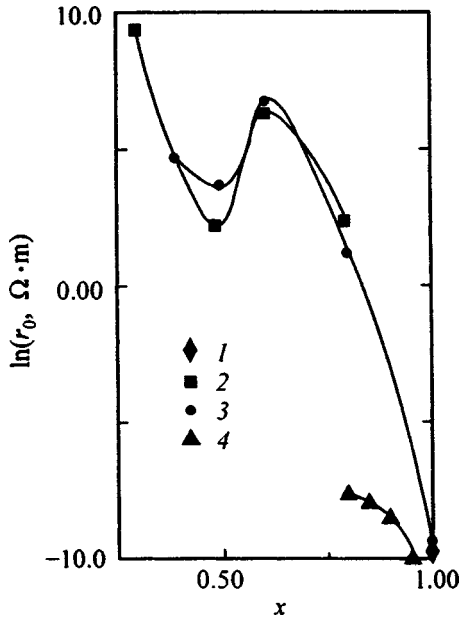

FIG. 2. Resistivity vs nickel concentration in $LaSrAl_{1-x}Ni_xO_4$. The numbers on the various points are the numbers of the series of samples.

TABLE I. Hall constant of various samples, obtained by the van der Pauw method.

Series	x	R_x, $\Omega\cdot m/T$
1	1	-2.69×10^{-6}
2	0.8	-4.5×10^{-4}
	0.6	Hall effect not observed
	0.5	0.60×10^{-3}
3	1	-3.33×10^{-6}
	0.8	-1.81×10^{-3}
	0.6	Hall effect not observed
	0.4	0.04
4	0.95	-1.33×10^{-6}
	0.9	-2.05×10^{-6}
	0.85	-2.37×10^{-6}
	0.8	-1.78×10^{-6}

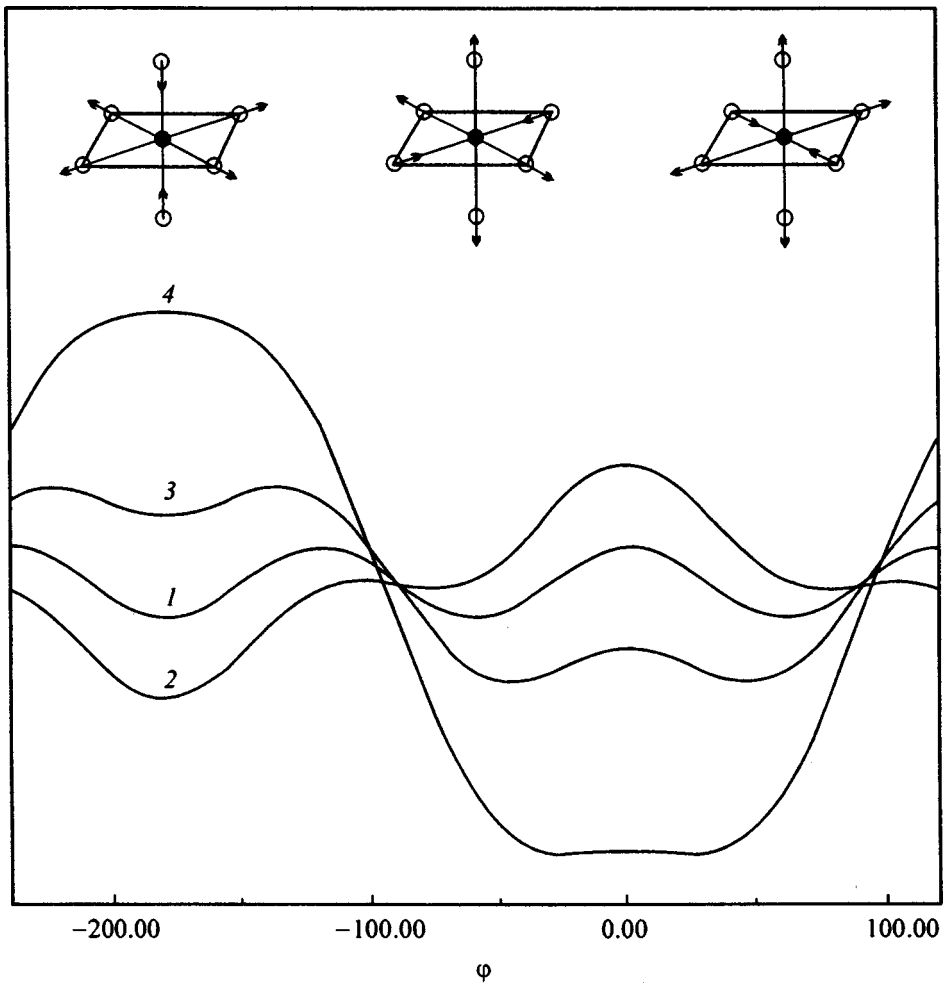

FIG. 4. Adiabatic potential of the octahedral complex MeO_6 for $V>0$, $V_3>0$, and various values of $\tau=\Delta/V_3\rho_0^3$: *1*—0, *2*—(−2.3), *3*—2.9, *4*—8.4. The upper part shows the deformation direction of the MeO_6 complex at the minima of the adiabatic potential for $\tau=0$.

minima occur for $\varphi=\pi/3$, π, and $5\pi/3$ and correspond to compression of the octahedron along one of the four-fold axes (curve *1* in Fig. 4). Otherwise, i.e., on the assumption that $V_3<0$, the temperature dynamics of the ESR spectra described above would not be observed in a stretched octahedral configuration, since only the one minimum at $\varphi=0$ would be lowered in an adiabatic potential.

Consequently, it can be concluded (1) that the JT effect results in spontaneous compression of an octahedral NiO_6 complex along a four-fold axis; and (2) that, as one goes from a tetragonally stretched to a tetragonally compressed configuration, the ground state changes from d_{z^2} to $d_{x^2-y^2}$. These conclusions make it possible to explain consistently the entire collection of experimental data that has been obtained.

We shall show that the change of the structural parameters in $LaSrAl_{1-x}Ni_xO_4$ as x increases is determined by the nature of the JT deformations of the NiO_6 centers. For rather weak stretching of the AlO_6 octahedra (the $Al-O_i$ distances in $LaSrAlO_4$ are $1.898\,\text{Å}\times 4$ and $1.997\,\text{Å}\times 2$), the decrease of parameter c in $LaSrNiO_4$ by comparison with $LaSrAlO_4$ by about 0.20 Å makes it possible to assume that the NiO_2 layers in $LaSrNiO_4$ consist of NiO_6 octahedra compressed along the c axis. For a JT complex, a decrease in the $(Ni-O)_z$ distance must be accompanied by an increase in the $(Ni-O)_{x,y}$ distances, while the mean $\langle Ni-O\rangle$ values in the complex are preserved.[12] The observed increase of a with increasing x, along with the decrease of parameter c (Fig. 1), actually reflects the fact of JT compression of the NiO_6 octahedra as one approaches the composition $LaSrNiO_4$. Allowing for the tendency of regular octahedral complexes of low-spin Ni^{3+} toward compression, it can be asserted that the cooperative interactions of the NiO_6 JT centers increase the symmetry of the local crystal field at the low-spin ion Ni^{3+} to almost cubic and stabilize the compression of the configuration with the ground state $d_{x^2-y^2}$.

The form of the $c(x)$ dependence can then be explained as follows: In solid solutions of $LaSrAl_{1-x}Ni_xO_4$, as was shown in Ref. 12, beginning with small x, microphases of composition $LaSrNiO_4$ arise. Complexes of types 1 and 2 are localized in the aluminum phase. The NiO_6 complex in them stretches tetragonally and has a d_{z^2} ground state (curve *4* in Fig. 4): $g_\parallel<g_\perp$. In the nickel microphases, as in $LaSrNiO_4$, the NiO_6 octahedra are compressed along the c axis, have a ground state $d_{x^2-y^2}$, and are not observed in ESR (curve *2* in Fig. 4). As the nickel concentration is increased, the increase in the number of complexes compressed along the c axis (corresponding to the volume of the microinclusions of the nickel phase) results in a smooth decrease in the value of c/a, averaged over the volume. The jump of the $c(x)$ dependence in the percolation region $x\approx 0.5$–0.6 is apparently associated with the spread of the nature of the distortions of the

disconnected fragments of $LaSrNiO_4$ to the entire structure and can be interpreted as a structural phase transition caused by the cooperative JT effect. The fact that, when Al^{3+} is replaced by the larger, non-Jahn–Teller ion Fe^{3+} in solid solutions of $LaSrAl_{1-x}Fe_xO_4$, according to the data of Ref. 1, a monotonic increase of both parameter a and parameter c is observed confirms that the specific features of the $c(x)$ dependence in $LaSrAl_{1-x}Ni_xO_4$ are connected with the JT effects in nickel octahedra.

We should point out that the nature of the change of c that we have established differs somewhat from that given in Ref. 1, where parameter c increases for a small (up to $x\sim0.4$) concentrations of nickel. The subsequent behavior of the $c(x)$ dependence coincides in Refs. 1 and 5. This could be associated with a difference in the microstructure of the samples. In particular, a more equiprobable distribution of Ni^{3+} ions in Ref. 1 could have the effect that there are virtually no nickel microphases when $x<0.4$, and then increasing the number of nickel octahedra stretched along the c axis in the aluminum phase would cause parameter c to increase. The fact that the discontinuous change of $c(x)$ in Ref. 1 occurs at a larger x value ($x\sim0.6$) also indicates that the Ni^{3+} ions are more uniformly distributed in the aluminum matrix. However, as pointed out above, for NiO_6 JT complexes, an increase of the $(Ni–O)_z$ distance should be accompanied by a decrease of the $(Ni–O)_{x,y}$ distances while the mean value of $\langle Ni–O\rangle$ is maintained in the complex, and it is then hard to understand the simultaneous increase of parameter a observed in Ref. 1.

As pointed out in Ref. 5, the conductivity of solid solutions of $LaSrAl_{1-x}Ni_xO_4$ has a semiconductor character: Their resistance increases with decreasing temperature. As already pointed out, the conductivity of the test samples changes from hole-type to electron-type in the region $x\approx0.6$. Compensation of the carriers of different signs apparently occurs in this critical region, which reduces the overall carrier concentration and accordingly increases the resistivity.

Hole conductivity arises in the aluminum phase in $LaSrAl_{1-x}Ni_xO_4$ with $x<0.6$, since the inclusions of the nickel microphase do not yet form a complex network. The microscopically inhomogeneous structure of the aluminum phase (for example, the statistically nonequiprobable distribution of La^{3+} and Sr^{2+} ions in a sublattice of heavy metals or the presence of defects of the type of excess interplanar oxygen) can lead to local breakdowns of the charge stoichiometry and the appearance of Ni^{2+} centers (in regions enriched in La^{3+}) and Ni^{3+} centers with a hole on an oxygen (in regions enriched in Sr^{2+} or close to excess interplanar oxygen). The appearance of this type of defects is equivalent to the appearance of holes in the hybridized valence band of the $3d_{z^2}$ orbitals of Ni^{3+} centers and of the $2p$ orbitals of oxygen. Their motion determines the type of conductivity.

At nickel concentrations that exceed the percolation limit ($x>0.6$), the nickel phase becomes responsible for the conductivity. The change of the structural and electronic properties of the nickel–oxygen octahedra caused by cooperative vibronic effects apparently changes the charge state of the NiO_2 layer by comparison with the diamagnetically dilute layer $Al_{1-x}Ni_xO_2$ in the aluminum phase. A surplus of electrons is formed in the hybridized band of the $3d_{x^2-y^2}$ orbitals of Ni^{3+} and the $2p$ orbitals of oxygen, and the conductivity becomes dependent on the correlation splitting of the band of the $3d_{x^2-y^2}$ orbitals of Ni^{3+} into two subbands—full and empty—with a small energy gap between them. The jumping of electrons from the filled $\sigma_{x^2-y^2}$ band into the free $\sigma_{x^2-y^2}$ band causes electron–hole pairs to be generated. The conductivity is electron-type in this case, because the electron conductivity is significantly larger. As x increases, the width of both bands of $d_{x^2-y^2}$ orbitals increases and the gap between them decreases, and this causes r_0 to decrease. According to the data of Ref. 5, high-temperature vacuum annealing (the removal of interplanar oxygen) causes r_0 to increase. This is associated with the decreased scatter of the local crystal fields caused by the presence of nonstoichiometric oxygen and with the corresponding narrowing of the bands of $d_{x^2-y^2}$ orbitals.

This work was carried out with the support of the Russian Fund for Fundamental Research (Project No. 96-02-18075).

[1] K. K. Singh, P. Ganguly, P. P. Edwards, and J. B. Goodenough, J. Phys.: Condens. Matter **3**, 2479 (1991).
[2] Yu. V. Yablokov, T. A. Ivanova, S. Yu. Shipunova, N. V. Chezhina, I. A. Zvereva, and N. P. Bobrysheva, Appl. Magn. Reson. **2**, 547 (1991).
[3] T. A. Ivanova, E. F. Kukovitskiĭ, A. E. Usachev, and Yu. V. Yablokov, Sverkhprovodnost' (KIAE) **5**, 860 (1992) [Sov. Phys. Superconductivity **5**, 861 (1992)].
[4] T. A. Ivanova, E. F. Kukovitskiĭ, A. E. Usachev, Yu. V. Yablokov, V. V. Zelentsov, and T. N. Fesenko, Fiz. Tverd. Tela **35**, 2829 (1993) [Phys. Solid State **35**, 1400 (1993)].
[5] A. E. Usachev, V. E. Petrashen', Yu. V. Yablokov, T. A. Ivanova, and E. F. Kukovitskiĭ, Fiz. Tverd. Tela **39**, 985 (1997) [Phys. Solid State **39**, 884 (1997)].
[6] L. P. Pavlov, *Methods of Measuring the Parameters of Semiconductor Materials* (Vysshaya Shkola, Moscow, 1987).
[7] G. S. Bir, Fiz. Tverd. Tela **18**, 1627 (1976) [Sov. Phys. Solid State **18**, 946 (1976)].
[8] Yu. V. Yablokov, A. E. Usachev, and T. A. Ivanova, in *Radio-Frequency Spectroscopy of Condensed Media* (Nauka, Moscow,1990).
[9] S. Yu. Shashkin, and A. E. Nikiforov, Fiz. Tverd. Tela **25**, 84 (1983) [Sov. Phys. Solid State **25**, 46 (1983)].
[10] D. Reinen and C. Friebel, Struct. Bonding (Berlin) **37**, No. 1, 1 (1979).
[11] D. Reinen and M. Atanasov, Magn. Reson. Rev. **15**, 167 (1991).
[12] A. Abragam and B. Bleany, *Electron Paramagnetic Resonance of Transition Ions* (Oxford Univ. Press, 1970; Mir, Moscow, 1973).

Translated by W. J. Manthey

Kinematic quasi-vacancy Frenkel biexciton in a Davydov multiplet

O. A. Dubovskiĭ

Physical Energy Institute, 249020 Obninsk, Kaluzhskaya Oblast, Russia
(Submitted June 30, 1998)
Fiz. Tverd. Tela (St. Petersburg) **41**, 423–428 (March 1999)

This paper shows that, as a consequence of paulion-type Frenkel excitons in molecular crystals such as anthracene, with several molecules per unit cell, bound biexcitons exist in the absence of dynamic exciton–exciton attraction. The coupling of excitons in ideal crystals of this type is brought about by the same kinematic effect that causes excitons in nonideal crystals to be localized close to defects such as vacancies. In the excitation spectrum, the resonance peak of the resulting biexciton is found inside a band corresponding to the sum of the energies of excitons of unlike components of a Davydov doublet, located between the bands of the total energies of excitons of the like components of the doublet. The corresponding dispersion equation is obtained, and the energy and wave function of the biexciton is determined. © *1999 American Institute of Physics.* [S1063-7834(99)01103-X]

Theoretical and experimental studies are being carried out on the spectra of coupled complexes of multiparticle elementary excitations—biexcitons, biphonons, triphonons, etc.[1–5] The coupling of excitons into biexciton complexes causes a sharp increase of two-photon absorption, the appearance of new resonance lines, and variation of the nonlinear susceptibility. Wannier–Mott biexcitons have been experimentally detected and intensively studied, but Frenkel excitons have not been experimentally detected. References 1–4 discussed the possibility of forming coupled Frenkel biexcitons in molecular crystals. The main factor that underlies the coupling of excitons into pairs was considered in this case to be the dynamic exciton–exciton interaction. In Ref. 4, this interaction was determined, as in superconductivity, to be the exciton–phonon interaction. The corresponding anharmonic interaction constants were determined in Refs. 1–3 from the matrix elements of the intermolecular and intramolecular interaction operators. The isolated biexciton term was split off from the band of two-exciton dissociated states into the high-frequency or low-frequency region according to the sign of the anharmonicity constant. It should be pointed out, however, that these matrix elements are from higher-order perturbation theory than that which determines the constants of the translational motion of the excitons which breaks up the biexciton, in particular, the width of the exciton bands. Therefore, it will be apparently hard to detect biexcitons of this type.

It is shown in this paper that, even when the dynamic exciton–exciton interaction indicated above is absent, there exist spectrally distinguished biexciton excitations inside a Davydov multiplet of two-exciton dissociated states in crystals of the type of anthracene, with a complex structure and several molecules per unit cell. In the region of one-particle states with an energy of about 3.3 eV, a band of singlet excitons in which a dipole optical transition is resolved is found in the anthracene crystal. The characteristic energy of the dipole–dipole intermolecular interaction is about 5.4 meV, the splitting of the Davydov doublet is about 100 meV, and the width of the exciton bands of the doublet, depending on the direction of the wave vector, is about 50–5 meV.

As shown below, the coupling of Frenkel excitons in ideal crystals of this type, for example, is brought about by the same kinematic effect that causes excitons in nonideal crystals to be localized close to defects such as vacancies. Reference 6 obtained the corresponding equation to determine the energy of such a local exciton and showed that the resonance term of this exciton lies between exciton bands of different types. The equation for the energy of such an exciton can be obtained from the equation for the energy of an exciton localized close to a defect—an isotopic impurity with displacement of the isotope term Δ if the formal transition $\Delta \to \infty$ is carried out, completely removing the isotope term from the region nearest to the exciton band, which corresponds dynamically to the presence of an unfilled site—a vacancy. The wave function of an exciton corresponding to this term is absolutely localized on this site. The wave function of an exciton localized close to such a vacancy is naturally equal to zero at this site.

As is well known, the two-body or two-exciton problem can be reduced to a one-particle problem with reduced mass. Frenkel excitons as elementary excitations are paulions. After the appropriate transition from the Pauli operators corresponding to a Frenkel exciton[6] to Bose operators, the contact anharmonic exciton–exciton interaction constant A determines the energy and the radius of the coupled state,[7] as Δ determines the energy and radius of a local exciton in the one-particle problem. For the limiting transition $A \to \infty$, the term of the coupled biexciton state in a crystal with one molecule per unit cell is completely removed from the region of uncoupled two-exciton states, the radius of the coupled state decreases, and two Bose particles are localized on the same site. For the other two-particle states of uncoupled but mutually scattering excitons, the wave function equals zero when the sites coincide in this case, and this corresponds to the Pauli principle for Frenkel excitons.

In crystals with two molecules per unit cell, with such a limiting transition $A\to\infty$, one of the two terms of the coupled states that split off from the bands of the Davydov doublet in the region of two-particle states is ''decelerated'' in the interband region in the same way as with a term of an exciton localized at a vacancy. The two-particle wave function of this state identically equals zero when the sites coincide in this case, and this corresponds to a paulion type of Frenkel exciton—two excitons cannot be on the same site. Note that, in the excitation spectrum, the resonance peak of this biexciton is found inside the band corresponding to the sum of the energies of excitons of unlike components of a Davydov doublet and lies between the bands of the total energies of excitons of the like components of a Davydov doublet. Below, we obtain the corresponding dispersion equation and determine the energy and wave function of a biexciton of the resulting type. We use in this case the limiting transition $A\to\infty$ in a system of interacting Bose particles, producing an adequate description of the spectrum of two-particle excitations of paulion type.

The Hamiltonian of a system of Frenkel excitons—elementary excitations of the paulion type—was obtained in Refs. 6, 8, and 9 as a quadratic form in the Pauli operators P_n (n labels the lattice sites), which obeys the corresponding commutation relations and the conditions $(P_n)^2=0$, corresponding to the forbiddenness of two excitations being found at the same site. The expansion by Agranovich and Toshich[6] of the P operators in Bose operators B causes kinematic repulsion and contact pairwise interaction to appear in a system of Bose particles, with a repulsive energy of the order of the total energy itself of the two excitations. In what follows, we do not give the details of the value and sign of the anharmonic contact interaction constant of Bose particles, since, with numerical calculations, to adequately represent the spectrum of a system of paulions, this constant will tend to the limit $A\to\infty$, which will correspond to forbiddenness of two paulions to be on the same site.

In the site representation of second quantization, the Hamiltonian of a system of Frenkel excitons as Bose particles with contact interaction has the following form:[7]

$$H=\sum_{\alpha n} E_0 B^+_{\alpha n}B_{\alpha n}+\sum_{\alpha n\beta m} V^{\alpha\beta}_{nm}B^+_{\alpha n}B_{\beta m} -A\sum_{\alpha n} B^+_{\alpha n}B^+_{\alpha n}B_{\alpha n}B_{\alpha n}. \tag{1}$$

Here $\alpha=1,2\ \ldots\sigma$ numbers the molecules in a unit cell, E_0 is the excitation energy of an isolated molecule, B^+ and B are the Bose operators for creation and annihilation of excitons, $V^{\alpha\beta}_{nm}$ are the matrix elements of the intermolecular interaction operator that determines the translational motion of the excitons, and A is the anharmonic contact interaction constant of the excitons. To specify and simplify the initial calculations, a closed, one-dimensional crystalline chain made of N cells with two molecules per unit cell ($\sigma=2$) is considered in what follows. The subsequent generalization to two-dimensional and three-dimensional crystals with $\sigma\geqslant 2$ obviously causes no fundamental difficulties. At least, the main dispersion equation obtained below, Eq. (14), has the same form except for replacing the one-dimensional wave vectors by two-dimensional and three-dimensional ones.

For one-particle exciton states with energy ε and wave function $|1\rangle$,

$$|1\rangle=\sum_{\alpha n}\Psi_{\alpha n}B^+_{\alpha n}|0\rangle, \tag{2}$$

where $|0\rangle$ is the ground state. Schrödinger's equation $H|1\rangle=\varepsilon|1\rangle$ can be solved by the standard procedure of substituting Eqs. (1) and (2) into that equation, transforming to the wave representation, and solving the corresponding system of two secular dispersion equations. As a result, for the two components of a Davydov doublet with energies $\varepsilon=E_0+\varepsilon_{\mu k}$, $(\mu=1,2)$, with wave vectors k and the corresponding wave functions $\Psi^{\alpha}_{\mu k}$, we have

$$\varepsilon_{1k}=\frac{V^{11}_k+V^{22}_k}{2}+\sqrt{\left(\frac{V^{11}_k-V^{22}_k}{2}\right)^2+|V^{12}_k|^2}, \tag{3a}$$

$$\varepsilon_{2k}=\frac{V^{11}_k+V^{22}_k}{2}-\sqrt{\left(\frac{V^{11}_k-V^{22}_k}{2}\right)^2+|V^{12}_k|^2}, \tag{3b}$$

$$V^{\alpha\beta}_k=\sum_{m(\neq n)}V^{\alpha\beta}_{nm}e^{ik(m-n)},\quad \Psi_{\alpha n}=\frac{1}{N}\sum_{\mu k}\Psi^{\alpha}_{\mu k}e^{ikn}, \tag{3c}$$

$$\Psi^1_{1k}=\sqrt{\frac{\varepsilon_{1k}-V^{22}_k}{2\varepsilon_{1k}-V^{11}_k-V^{22}_k}}e^{i\varphi_k/2},$$

$$\Psi^2_{1k}=\sqrt{\frac{\varepsilon_{1k}-V^{11}_k}{2\varepsilon_{1k}-V^{11}_k-V^{22}_k}}e^{-i\varphi_k/2}, \tag{3d}$$

$$\Psi^1_{2k}=\sqrt{\frac{\varepsilon_{2k}-V^{22}_k}{2\varepsilon_{2k}-V^{11}_k-V^{22}_k}}e^{i\varphi_k/2},$$

$$\Psi^2_{2k}=\sqrt{\frac{\varepsilon_{2k}-V^{11}_k}{2\varepsilon_{2k}-V^{11}_k-V^{22}_k}}e^{-i\varphi_k/2}, \tag{3e}$$

where wave vector k in units of a^{-1} (a is the chain constant) has the value $k=k_j=2\pi N^{-1}j$, $j=0,1,2\ \ldots N-1$ in the Brillouin zone; φ_k is the phase of the complex quantity $V^{12}_k=|V^{12}_k|\exp(i\varphi_k)=(V^{21}_k)^*$; and V^{11}_k and V^{22}_k are real quantities. The wave functions of Eqs. (3) are orthonormal,

$$\sum_{\mu}(\Psi^{\alpha}_{\mu k})^*\Psi^{\beta}_{\mu k}=\delta_{\alpha\beta},$$

$$\sum_{\alpha}(\Psi^{\alpha}_{\mu k})^*\Psi^{\alpha}_{\nu k}=\delta_{\mu\nu},\quad \mu,\nu=1,2. \tag{4}$$

A solution of Schrödinger's equation $H|2\rangle=E|2\rangle$ for two-particle states with energy E and wave function $|2\rangle$ is sought in the form

$$|2\rangle=\sum_{\alpha n,\beta m}\Psi^{\alpha n}_{\beta m}B^+_{\alpha n}B^+_{\beta m}|0\rangle. \tag{5}$$

Substituting Eq. (5) into Schrödinger's equation produces the following system of equations for $\Psi^{\alpha n}_{\beta m}$:

$$(E-2E_0)\Psi^{\alpha n}_{\beta m}=\sum_{\gamma p}(V^{\alpha\gamma}_{np}\Psi^{\gamma p}_{\beta m}+V^{\beta\gamma}_{mp}\Psi^{\gamma p}_{\alpha n})-2A\,\delta_{\alpha\beta}\delta_{nm}\Psi^{\alpha n}_{\beta m}. \quad (6)$$

Transforming to the wave representation,

$$\Psi^{\alpha n}_{\beta m}=N^{-1}\sum_{\mu k\nu p}\Phi_{\mu k,\nu p}\Psi^{\alpha}_{\mu k}\Psi^{\beta}_{\nu p}e^{i(kn+pm)}. \quad (7)$$

After some calculations, we get a system of secular equations for the wave functions $\Phi_{\mu k,\nu K-k}$ with identical fixed total wave vector $K=K_i=2\pi N^{-1}i$, $i=0,1,2\ \ldots N-1$:

$$(E-2E_0-\varepsilon_{\nu k}-\varepsilon_{\gamma K-k})\Phi_{\nu k,\gamma K-k}=-2AN^{-1}\times\sum_{\alpha}(\Psi^{\alpha}_{\nu k})^*(\Psi^{\alpha}_{\gamma K-k})^*\sum_{\mu\eta q}\Phi_{\mu q,\eta K-q}\Psi^{\alpha}_{\mu q}\Psi^{\alpha}_{\eta K-q}. \quad (8)$$

The sums on the right-hand side of Eq. (8),

$$X_{\alpha}(K)=\sum_{\mu\eta q}\Phi_{\mu q,\eta K-q}\Psi^{\alpha}_{\mu q}\Psi^{\alpha}_{\eta K-q} \quad (9)$$

depend only on K and α. For these quantities, after dividing Eq. (8) by the resonance factor $(E-2E_0-\varepsilon_{\nu k}-\varepsilon_{\gamma K-k})$, multiplying by $\Psi^{\beta}_{\nu k}\Psi^{\beta}_{\gamma K-k}$, and then summing over ν, γ, k, we get the system of two equations

$$X_{\beta}(K)=-2A\sum_{\alpha}W^{\beta\alpha}(K,E)X_{\alpha}(K), \quad (10)$$

where the functions $W^{\beta\alpha}(K,E)$ have the following form:

$$W^{\beta\alpha}(K,E)=N^{-1}\sum_{\nu\gamma k}\frac{\Psi^{\beta}_{\nu k}\Psi^{\beta}_{\gamma K-k}(\Psi^{\alpha}_{\nu k})^*(\Psi^{\alpha}_{\gamma K-k})^*}{E-2E_0-\varepsilon_{\nu k}-\varepsilon_{\gamma K-k}}. \quad (11)$$

It can be seen from Eqs. (11) and (3) that $W^{12}=(W^{21})^*$ are complex quantities and W^{11} and W^{22} are real. We get directly from Eq. (10) the dispersion equation for determining the energy of the two-particle coupled states with total wave vector K, which is conserved because of translational invariance:

$$\left[\frac{1}{2A}+W^{11}(K,E)\right]\left[\frac{1}{2A}+W^{22}(K,E)\right]=|W^{12}(K,E)|^2. \quad (12)$$

This equation has two solutions for $A=A(K,E)$:

$$\frac{1}{2A}=\frac{W^{11}(K,E)+W^{22}(K,E)}{2}\pm\sqrt{\left[\frac{W^{11}(K,E)-W^{22}(K,E)}{2}\right]^2+|W^{12}(K,E)|^2}, \quad (13)$$

which can easily be inverted into solutions for $E=E(K,A)$.

For anharmonicity constants whose modulus goes to the limit $|A|\to\infty$ and ruling out, in accordance with what was said above, two-particle states with two excitons at one site, Eq. (12) takes the form

$$F(K,E)\equiv W^{11}(K,E)W^{22}(K,E)-|W^{12}(K,E)|^2=0. \quad (14)$$

The solution $E=E_b(K)$ of this equation gives the dispersion dependence of the biexciton energy on the wave vector. It is easy to see how the one-particle problem of an isotopic impurity at site α is complete analogous to a shift of term Δ. The equation for the energy of localized excitons in this case has the form[6,10,11]

$$\frac{1}{\Delta}=N^{-1}\sum_{\mu k}\frac{|\Psi^{\alpha}_{\mu k}|^2}{\varepsilon-E_0-\varepsilon_{\mu k}}. \quad (15)$$

As $|\Delta|\to\infty$, excluding the states of an exciton fixed on a defect, i.e., when we reduce to the problem concerning a vacancy, Eq. (15) transforms to the energy equation of an exciton localized close to a vacancy,[6]

$$0=N^{-1}\sum_{\mu k}\frac{|\Psi^{\alpha}_{\mu k}|^2}{\varepsilon-E_0-\varepsilon_{\mu k}}, \quad (16)$$

and has the corresponding solution $\varepsilon=\varepsilon_{\nu}$ between the two bands $\varepsilon_2<\varepsilon_{\nu}<\varepsilon_1$. The wave function of such an exciton localized close to a vacancy is naturally equal to zero at this site.

It can be shown that the wave function of the resulting quasi-vacancy biexciton equals zero when the sites coincide in Eq. (5); i.e., the corresponding relationship for paulions is satisfied. For the wave function of a biexciton with wave vector K, we get from Eqs. (7)–(9) to within a small factor, in this case $2A$,

$$\Psi^{\alpha n}_{\beta m}=N^{-1}\sum_{\mu\nu k}\left[\sum_{\gamma}\frac{(\Psi^{\gamma}_{\mu k})^*(\Psi^{\gamma}_{\nu K-k})^*X_{\gamma}(K)}{E_b-2E_0-\varepsilon_{\mu k}-\varepsilon_{\nu K-k}}\right]\times\Psi^{\alpha}_{\mu k}\Psi^{\beta}_{\nu K-k}e^{ik(n-m)+iKm}. \quad (17)$$

As can easily be seen, when the sites coincide, $\alpha=\beta$, $n=m$, we get from Eq. (17) and the definition of W given in Eq. (11) that

$$\Psi^{\alpha n}_{\alpha n}=N^{-1}e^{iKn}\sum_{\gamma}W^{\alpha\gamma}(K,E_b)X_{\gamma}(K,E_b)=0, \quad (18)$$

as directly follows from Eq. (10) for $|A|\to\infty$ and can be obtained from the exact solution of Eqs. (10) and (12) for X_{γ}.

A general analysis of the basic Eq. (14) with the explicit dependence of $W^{\alpha\beta}(E)$ given by Eq. (11) indicates that it is possible for an interband biexciton to exist inside a Davydov multiplet in the two-particle region of the spectrum in the same way as is seen from Eq. (16) for a vacancy. An initial, orienting representation of the existence of the effect can be obtained by considering a system of two molecules with $N=2$. For a more detailed calculation, a crystal with a distinct separation in energy of the nonoverlapping components of a Davydov doublet was studied.

To limit the number of necessary parameters, it was assumed that the Coulomb dipole–dipole interaction energy of the molecules in the sublattices coincides. For example, dipole moments 1 and 2 are symmetrically tilted relative to the axis of the chain; i.e., $V^{11}_{nm}=V^{22}_{nm}=V|n-m|^{-3}$, where V is the energy approximately equal to a quarter of the width of

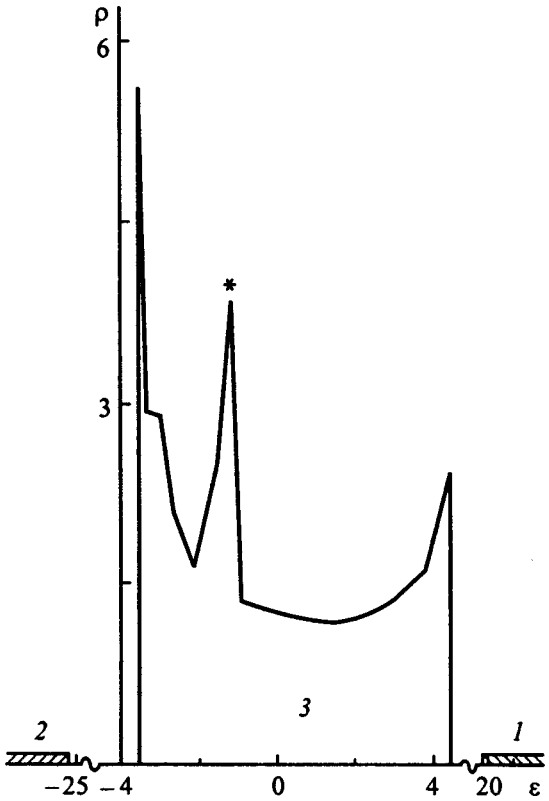

FIG. 1. The biexciton resonance in the density of states of band *3* of the Davydov biexciton multiplet is indicated by an asterisk.

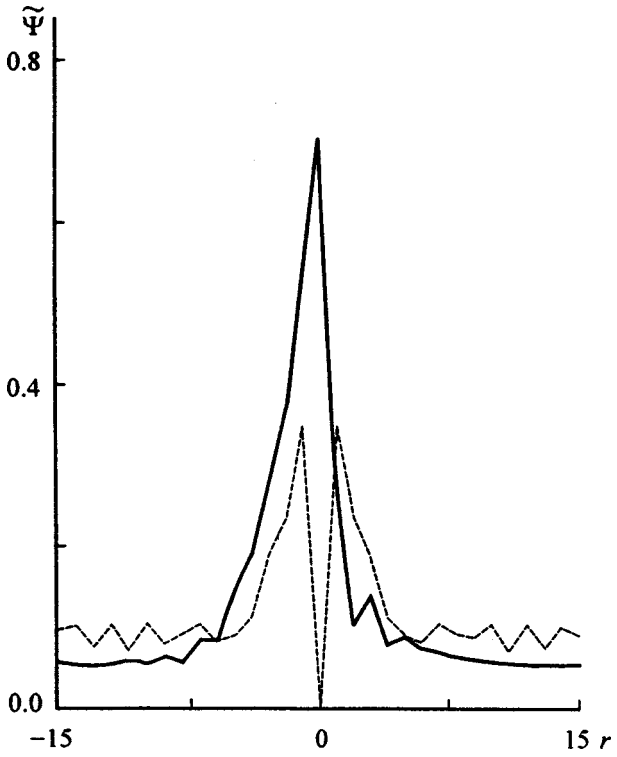

FIG. 2. Wave functions of a kinematic biexciton.

the exciton band. In what follows, all the energy quantities will be presented in units of this quantity. In order to decrease the number of parameters, it was also assumed that the molecules at sites $\alpha=2$ are displaced relative to the molecules at sites $\alpha=1$ by a distance of $a\delta$, ($\delta<1$), and the Coulomb dipole–dipole interaction energy in the different sublattices is accordingly $V_{nm}^{12}=V|n-(m+\delta)|^{-3}$. The calculations were carried out for the value $\delta=0.4$, close to the actual displacement of the molecules, for example, in anthracene. In this case, as follows from the calculations of $\varepsilon_{\mu k}$ in Eqs. (3), Davydov doublets are found in the bands $10<\varepsilon_{1k}<23$ V (band *1*) and $-19<\varepsilon_{2k}<-13$ V (band *2*). Naturally, in actual three-dimensional crystals like anthracene, the exciton bands of the two components of a Davydov doublet overlap, the dependence of the energy on the three-dimensional wave vector k is extremely complex, and the solution of Eq. (14) represents an independent, extremely complex and, at the same time, merely computational problem.

There are three distinct bands in the energy region of two-particle states (Fig. 1): Band *1* ($20<\varepsilon_{1k}+\varepsilon_{1K-k}<46$ V) corresponds to the sum of the energies of excitons of the first type, band *2* ($38<\varepsilon_{2k}+\varepsilon_{2K-k}<-26$ V) to the sum of the energies of excitons of the second type, and band *3* ($4<\varepsilon_{1k}+\varepsilon_{2K-k}<5$ V), located in the gap between the first two, corresponds to the sum of energies of excitons of the first and second types. It is this inner band *3* that contains a biexciton of the type under consideration. Since the biexciton does not have an isolated term, but lies in band *3*, the roots of Eq. (14) in this band, $E=E_i$, $i=1,2,3\ldots$ (in order of increasing energy) and in bands *1* and *2* were calculated on a Pentium computer. All the calculations were done at the given stage for the wave vector $K=0$, and it is assumed in what follows that the total dispersion dependence for the biexciton has been determined. The calculations were carried out with increasing values $N=3,5,7\ldots$. The fundamental features of the spectrum and of the wave functions already begin to show up for small N, and these features only become more detailed as N is increased further.

Figures 1–3 show the results of calculating the spectrum and the wave functions for a chain with sixty-two molecules ($N=31$), in which the density of states $\rho(E)$ and the wave functions already represent fairly smooth functions, and increasing N further only further smoothes the curves. The calculations showed that the functional dependence of $F(E)$ on the left-hand side of Eq. (14), having at the edges of inner band *3* the usual form $\Sigma_j c_j(E-e_j)^{-1}$, with discontinuities at e_j and zeroes in the gaps, has a section in the middle part of the band where it depends parabolically on E, with two zeroes of function $F(E)$. This is associated with allowing for the functional dependences of $\varepsilon_{\mu k}$ and $\Psi_{\mu k}^{\alpha}$ exactly in Eqs. (3), (11), and (14). The zeros of function $F(E)$ become locally more dense in the neighborhood of this parabolic section. Since only a primary proof of the existence of the biexciton is needed, a complete calculation of the density of states in band *3* with breakdown of the band into channels, computation of a density histogram, normalization, etc. were not carried out. The quantity $\rho(E_i)=(E_{i+1}-E_i)^{-1}$, computed from the difference of the successive roots of Eq. (14), was used as a measure of the density of states. The adequacy of a monotonic mapping of the density of states by function $\rho(E)$ is determined by the fact that, when the density of

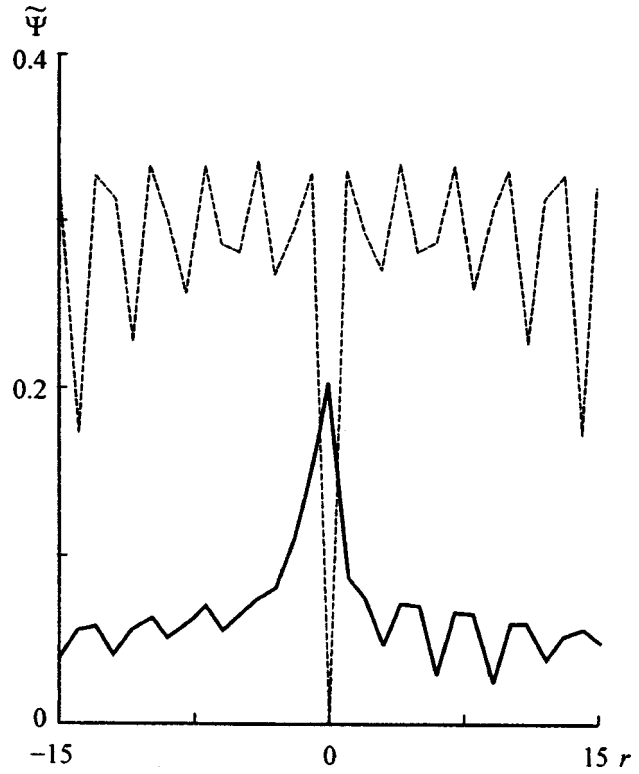

FIG. 3. The wave functions of two-exciton states in band *3* far from the biexciton resonance.

states is higher close to E_i, the distance between the successive energies E_{i+1} and E_i is less, and ρ is greater.

Figure 1 shows this dependence $\rho(\varepsilon)$, $\varepsilon \equiv (E-2E_0)/V$ in the middle band *3*. The low-frequency edge of band *1* and the high-frequency edge of band *2* are shown schematically, since the detailed behavior of the density of states in these bands does not seem necessary at this stage. It can be seen that an increase of $\rho(\varepsilon)$ typical of a one-dimensional crystal occurs at the edges of band *3*. However, an additional density-of-states peak can be seen inside this band, in the region $E=2E_0-1.2\,\mathrm{V}$; this corresponds to a bound kinematic quasi-vacancy biexciton of the type found here. That this is a bound exciton is confirmed by calculating the biexciton wave function $\Psi^{\alpha n}_{\beta m}$. Figure 2 shows the dependences $\Psi^{12}(r)=|\Psi^{1n}_{2n+r}|^2$ (solid curve) and $\Psi^{11}(r)=|\Psi^{1n}_{1n+r}|^2$ (dashed curve) for the biexciton state whose energy corresponds to the peak inside band *3* in Fig. 1. To clarify the features on the wings of the wave functions, Fig. 2 shows the dependences of $\tilde{\Psi}=|\Psi^{12}|^{1/4}$ and $\tilde{\Psi}=|\Psi^{11}|^{1/4}$. Wave function $\Psi^{22}(r)$, having the same behavior as $\Psi^{11}(r)$, is not shown in Fig. 2 in order to avoid visual confusion. It can actually be seen that the wave function of the internal motion of the biexciton decreases with increasing r, and $\Psi^{11}(0)=\Psi^{22}(0)=0$ in accordance with the paulion forbiddenness, having local maxima close to this point. Certain oscillations are noticeable on the wings, as is natural, since the resonance peak of the biexciton is immersed in complex band *3*. The displacement of the biexciton maximum of the $\Psi^{12}(r)$ curve relative to point $r=0$ and its asymmetry are determined by the circumstance that this function is naturally maximal at $r=\delta$, $n=m$, when the two excitons are at adjacent sites $\alpha=1$, $\beta=2$ in one unit cell; furthermore, the distances between the sites $\alpha=1$, $\beta=2$, n, $m=n+r$ and $\alpha=1$, $\beta=2$, n, $m=n-r$ are different, and the wave function accordingly has different values, which also produces asymmetry. We should point out that the wave function Ψ^{12} in Fig. 2 exceeds Ψ^{11} and Ψ^{22} at the center. Note also that the dependences of the separate real and imaginary parts of the wave functions, not shown for the sake of brevity, also decrease with oscillations and have some interesting features. For comparison with Fig. 2, Fig. 3 shows the wave functions $\Psi^{12}(r)$ (solid curve) and $\Psi^{11}(r)$ (dashed curve) for the energy $E=2E_0+1.4V$ in band *3* far from the biexciton resonance peak. It can be seen that strong oscillations of the wave functions already occur and, at the same time, definite localization is present, since the distant biexciton peak still has an effect. Unlike Fig. 2, the value of Ψ^{11} exceeds that of Ψ^{12} in this case because of the distance from the biexciton resonance.

It is natural that it is rather difficult to solve Eq. (14) for actual two-dimensional and three-dimensional crystals with several molecules per unit cell with complex structure of the Davydov multiplets in the one-exciton region and the still more complex structure of the bands in the two-exciton region of the spectrum, although it is a purely calculational problem. There undoubtedly is interest in theoretical studies of and experimental research in biexciton resonances which, as is now clear, are found somewhere inside the Davydov multiplets in the two-particle region of the spectrum. There is interest in studying binary states of the type discussed above as applied to lower-frequency excitation, for example optical vibrations of hydrogen atoms in metal hydrides.[12,13]

In conclusion, the author is sincerely grateful to V. M. Agranovich for useful discussions.

This work was carried out with the support of the Russian State Scientific and Technical Program ''Crucial directions in the physics of condensed media.'' The author is grateful for partial support from INTAS Grant 93-461 and from a grant of the Volkswagen Foundation I/69928.

[1] V. M. Agranovich and S. Mukamel, Phys. Lett. **147**, 155 (1990).
[2] V. M. Agranovich, The Sixth Electrical and Related Properties of Organic Solids (ERPOS-6), Capri (1992).
[3] F. C. Spano and S. Mukamel, Phys. Rev. A **40**, 5783 (1989).
[4] O. A. Dubovsky and S. Mukamel, J. Chem. Phys. **95**, 7828 (1991).
[5] V. M. Agranovich, O. A. Dubovsky, and A. V. Orlov, Phys. Lett. A **119**, 83 (1986).
[6] V. M. Agranovich, *Theory of Excitons* (Nauka, Moscow, 1968).
[7] V. M. Agranovich and O. A. Dubovsky, *Optical Properties of Mixed Crystals* (North-Holland, Amsterdam, 1988), p. 297.
[8] V. M. Agranovich, Zh. Eksp. Teor. Fiz. **37**, 307 (1960) [Sov. Phys. Solid State **10**, 216 (1960)].
[9] J. J. Hopfield, Phys. Rev. **112**, 1555 (1958).
[10] O. A. Dubovskiĭ and Yu. V. Konobeev, Fiz. Tverd. Tela **6**, 2599 (1964) [Sov. Phys. Solid State **6**, 2071 (1965)].
[11] O. A. Dubovskiĭ and Yu. V. Konobeev, Fiz. Tverd. Tela **7**, 946 (1965) [Sov. Phys. Solid State **7**, 762 (1965)].
[12] O. A. Dubovskiĭ and A. V. Orlov, Fiz. Tverd. Tela **39**, 542 (1997) [Phys. Solid State **39**, 472 (1997)].
[13] O. A. Dubovskiĭ and A. V. Orlov, Fiz. Tverd. Tela **39**, 163 (1997) [Phys. Solid State **39**, 141 (1997)].

Translated by W. J. Manthey

The effect of temperature on the pulsed conductivity of a KCl crystal excited by picosecond electron pulses

B. P. Aduev, V. M. Fomchenko, and V. N. Shvaĭko

Kemerovo State University, 650043 Kemerovo, Russia
(Submitted July 9, 1998)
Fiz. Tverd. Tela (St. Petersburg) **41**, 429–430 (March 1999)

This paper discusses the temperature dependence of the pulsed conductivity of a KCl crystal in the interval 12–300 K when it is excited by an electron beam (0.2 MeV, 50 ps, 300 A / cm^2) with a time resolution of 150 ps. It is shown that the electron lifetime is $\tau<100$ ps in the entire interval under consideration, while the conductivity increases with temperature. The experimental results make it possible to obtain the temperature dependences of the effective electron–hole recombination cross section $S\sim T^{3.5}$ and the separation probability of genetic pairs.
 [S1063-7834(99)01203-4]

Reference 1 discussed the effect of the excitation density on the radiation-induced conductivity σ of alkali-halide crystals excited by picosecond electron pulses. On the basis of analyzing the experimental data, a model was proposed according to which the conductivity is associated with the thermalized electrons at the bottom of the conduction band, while the form of the dependence is determined by the capture and recombination mechanism of the latter.[1] Additional information on the process could be obtained from the temperature dependence of the conductivity for fixed excitation densities.

This paper discusses the radiation-induced conductivity of a KCl crystal excited by an electron beam (0.2 MeV, 50 ps) in the temperature interval 12–300 K, with an electron-beam current density of $j=300$ A/cm^2. The time resolution of the measurement channel is 150 ps. Using the results of Ref. 1, we chose j so that the electron concentration in the conduction band was controlled predominantly by their bimolecular recombination with holes, i.e., in the interval of excitation density $\sigma\sim j^{0.5}$.

As shown by experiment, the pulse of conductivity current repeats with no lag the pulse characteristic of the measurement channel in the entire temperature interval. It follows from this that the conduction has a quasi-steady-state character under the experimental conditions in the entire range of electron lifetime in the conduction band $\tau<100$ ps. The temperature dependence of the conductivity amplitude σ is shown in Fig. 1. The conductivity smoothly increases with increasing temperature, whereas the Hall mobility μ_h for KCl drops by more than a factor of 10^3 in the corresponding temperature interval.[2,3]

As is well known, the equation for the conductivity, $\sigma=ne\mu_d$, contains μ_d, the drift mobility. In general, in the presence of capture and trapping centers, $\mu_h\neq\mu_d$. Therefore, at first glance, it is incorrect to use the data of Refs. 2 and 3 for μ_h when analyzing our experimental data. However, it can be shown that an experimental estimate of τ makes it possible to estimate the temperature interval where $\mu_h=\mu_d$. Actually, μ_h is associated with μ_d by the expression

$$\mu_d=\mu_h\frac{1}{1+\tau_0/\tau_t}, \tag{1}$$

where τ_0 is the mean electron lifetime in the conduction band, $\tau_t=1/\nu\exp(E/kT)$ is the electron lifetime at the center of a trap, $\nu=10^{12}-10^{13}$ sec^{-1} is a frequency factor, and E is the activation energy of electron emission from a trapping center. Starting from the experimental estimate $\tau<100$ ps and assuming that $\tau_t\leqslant 100$ ps at 12 K, we can estimate that $E\leqslant(4-7)\times10^{-3}$ eV. On the other hand, the estimate $\tau_0\approx 10$ ps can be made from measurements of the formation time of F centers in KCl with excitation by picosecond laser beams[4] and electron beams.[5] Using the estimates of E and τ_0, Eq. (1) can be used to calculate that $\mu_h\approx\mu_d$ when $T_1\geqslant 30$ K.

In connection with what is explained above, the authors used the experimental data of Refs. 2 and 3 for μ_h and obtained the temperature dependence of the electron concentration in the conduction band $n(T)=\sigma(T)/e\mu(T)$, shown in Fig. 2.

In the case of bimolecular recombination of electrons and holes, the quasi-steady-state electron concentration in the conduction band is described by

$$n=\left(\frac{G_0}{\upsilon S}\right)^{1/2}, \tag{2}$$

where G_0 is the generation rate of electron–hole pairs ($G_0=Aj$, where A is a factor),

$$\upsilon=(3kT/m)^{1/2} \tag{3}$$

is the thermal velocity of the electrons, and S is the effective recombination cross section. The $S(T)$ dependence is usually approximated by the power law

$$S=BT^{-\alpha}, \tag{4}$$

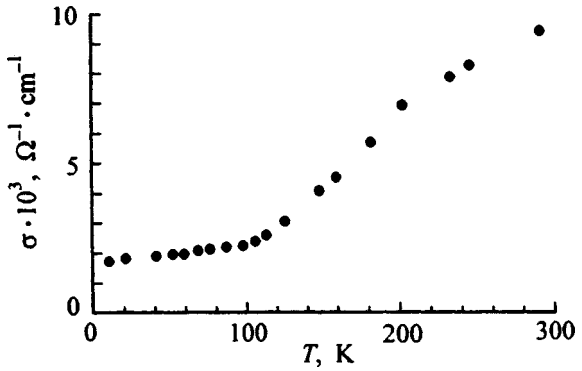

FIG. 1. Temperature dependence of the conductivity for a KCl crystal.

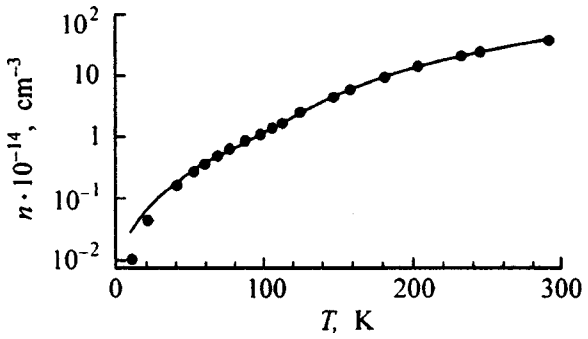

FIG. 2. Temperature dependence of the electron concentration in the conduction band for a KCl crystal.

where B is a factor. Using Eqs. (2)–(4), the experimental results of Fig. 2 cannot be satisfactorily approximated for reasonable values of α and the condition that $G=\text{const}$.

It is well known that the initial electron–hole pair distribution in alkali halide crystals after charge-carrier thermalization contains not only uncorrelated statistical electrons and holes but also genetic pairs whose fraction can be significant.[6] In this case $G(T)$ can be represented as

$$G(T)=G_s-G_g e^{-E_s/kT}, \tag{5}$$

where $G_g=(G_0-G_s)$; G_s and G_0 are the generation rates of electron–hole pairs: statistical at $T=0$ and total, respectively; and E_s is the activation energy of genetic-pair separation.

The solid curve in Fig. 2 is obtained by approximating the experimental results, using Eq. (2) and taking Eqs. (3)–(5) into account for the following values of the parameters: $G_0/G_s=1500$, $E=0.07$ eV, and $\alpha=3.5$. As can be seen from Fig. 2, the calculated curve correlates well with the experimental points for $T\geqslant 40$ K. The value $\alpha=3.5$ in Eq. (4) correlates fairly well with $\alpha=3$ for the scattering of electron energy at DA phonons and $\alpha=4$ at PA phonons in the field of a charged center.[5]

The authors express their gratitude to É. D. Aluker for useful discussions and for supporting the work.

This work was carried out with the support of a grant of the MOiPO of the Russian Federation.

[1] B. P. Aduev and V. N. Shvaĭko, Fiz. Tverd. Tela, in press (1999) [Phys. Solid State (1999)].
[2] R. K. Ahrenkiel and F. C. Brown, Phys. Rev. A **36**, 223 (1964).
[3] C. H. Seager and D. Emin, Phys. Rev. B **2**, 3421 (1970).
[4] R. T. Williams, J. N. Bradford, and W. L. Faust, Phys. Rev. B **18**, 7038 (1978).
[5] É. D. Aluker, B. Z. Gorbenko, R. G. Deĭch, G. S. Dumbadze, A. D. Tal'vinskiĭ, and V. G. Shpak, Fiz. Tverd. Tela **28**, 3154 (1986) [Sov. Phys. Solid State **28**, 1775 (1986)].
[6] É. D. Aluker, D. Yu. Lusis, and S. A. Chernov, *Electron Excitations and Radio-Luminescence of Alkali Halide Crystals* (Zinatne, Riga, 1979).

Translated by W. J. Manthey

Description of the migration of a cation vacancy in mixed alkali-halide crystals having a common cation

L. G. Gorbich and A. N. Varaksin*)

Institute of Industrial Ecology, Ural Section, Russian Academy of Sciences, 620219 Ekaterinburg, Russia
(Submitted June 17, 1998; resubmitted September 4, 1998)
Fiz. Tverd. Tela (St. Petersburg) **41**, 431–432 (March 1999)

For mixed alkali-halide crystals having a common cation (of the type KCl + KBr), a new equation is proposed for calculating the hopping diffusion coefficient of a cation vacancy. It is based on the concepts of probability theory and gives good agreement with numerical calculations by the Monte Carlo method. © *1999 American Institute of Physics.* [S1063-7834(99)01303-9]

In mixed alkali-halide crystals (AHCs) having a common cation, of the type $MeA_{1-x}B_x$ (Me is the cation, A and B are halide ions, and x is the fraction of component B in the mix), the diffusion coefficient D of the majority charge carrier (the cation vacancy V_c) is defined as

$$D = 1/6 f a^2 W_{\text{hop}} = f D_{\text{hop}}, \tag{1}$$

where f is the correlation factor, a is the hopping length, W_{hop} is the hopping probability, and D_{hop} is the hopping diffusion coefficient (the diffusion coefficient in the absence of the correlation effect). The diffusion coefficients in mixed AHCs are usually calculated by numerical methods, for example, by the Monte Carlo method.[1,2] Numerical methods make it possible to do calculations for rather complex actual systems, but do not give the analytical dependences of the diffusion coefficients and do not make it possible to predict how the properties of the crystal change as the experimental conditions change.

This paper is devoted to the development of analytical methods for describing defect migration in mixed AHCs. It proposes a new model for calculating the hopping diffusion coefficient for disordered systems of the type of mixed AHCs, based on the concepts of probability theory. In crystals having the NaCl structure, there are twelve directions for a vacancy to hop into a neighboring site. Each of the hops is made through a saddle point (a barrier), formed by two anions. For a mixed crystal having a common cation and anions of types A and B, three types of saddle points are possible: types *aa* or *bb* (both anions have type A or B) and type *ab* (the anions of the saddle point have different types).[1,2] For arbitrary x (the fraction of component B in the mix), we shall characterize state S_i of vacancy V_c by the number of barriers $J_{aa}(i)$, $J_{ab}(i)$ and $J_{bb}(i)$ of these three types that surround a vacancy at the given site (see Table I). The normalization condition $\Sigma_i W(S_i) = 1$ is satisfied for any x.

The probability equations $W(S_i)$ are obtained using probability theory and are checked by numerical calculations.

The expression for the vacancy diffusion coefficient is obtained as follows: Let there be a vacancy in some state S_i. The probability that such a state will appear for a given x is defined in Table I. When it passes to an adjacent site, the vacancy overcomes a potential barrier of height E_{aa}, E_{ab} or E_{bb}, depending on the type of barrier. The number of barriers of various types for state S_i is also given in Table I. The probabilities W_{aa}, W_{ab}, and W_{bb} of the transitions through the barrier depend on the fraction x (via the x dependence of the barrier heights) and on temperature T and can be calculated from $W_{aa}(x,T) = \exp(-E_{aa}(x)/kT)$, and the others analogously. After completing the hop, the vacancy falls into another state S_j, and the calculation of the hopping probability is repeated by the method described above. Thus,

$$D_{\text{hop}}(x,T) = 1/6\, a^2 \Sigma_i W(S_i)[W_{aa}(x,T) J_{aa}(i) + W_{ab}(x,T) J_{ab}(i) + W_{bb}(x,T) J_{bb}(i)]. \tag{2}$$

Equation (2) was used to calculate the diffusion coefficients of a cation vacancy in a mixed KCl + KBr crystal for various x and T. The barrier heights and their x dependence are taken from Refs. 1 and 2. The results of certain calculations are shown in Fig. 1. It can be seen that the diffusion coefficient given by Eq. (2) demonstrates a surprising averaging effect: The sum of the three exponentials of Eq. (2) in a rather wide temperature interval behave like one exponential. This makes it possible to introduce an effective activation energy E_M for the migration of a vacancy in a mixed crystal and to rewrite Eq. (2) in standard form:

TABLE I. Possible states S_i of a cation vacancy in an $MeA_{1-x}B_x$ crystal and probabilities $W(S_i)$ of their appearance.

Number i of the possible state	State S_i			Probability $W(S_i)$
	$J_{aa}(i)$	$J_{ab}(i)$	$J_{bb}(i)$	
1	12	0	0	$(1-x)^6$
2	8	4	0	$6x(1-x)^5$
3	4	8	0	$3x^2(1-x)^4$
4	5	6	1	$12x^2(1-x)^4$
5	3	6	3	$8x^3(1-x)^3$
6	2	8	2	$12x^3(1-x)^3$
7	1	6	5	$12x^4(1-x)^2$
8	0	8	4	$3x^4(1-x)^2$
9	0	4	8	$6x^5(1-x)$
10	0	0	12	x^6

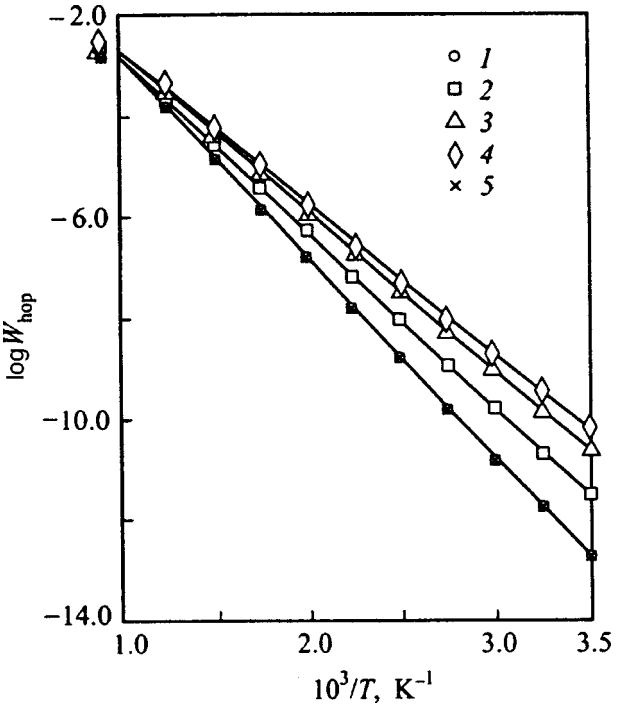

FIG. 1. Temperature dependence of the hopping probability $W_{hop}(x,T)$ for certain x values (the probabilities coincide for $x=0$ and 1). x: *1*—0, *2*—0.3, *3*—0.6, *4*—0.8, *5*—1.

$$D_{hop}(x,T)=1/6a^2\exp(-E_M(x)/kT).$$

The results of calculations of $E_M(T)$ for the KCl + KBr system are shown in Fig. 2. Figure 3 shows the dependence of the logarithm of hopping probability $W_{hop(x,T)}$ and consequently of $D_{hop}(x,T)$ on parameter x for two fixed temperatures T. It can be seen that, as temperature decreases, the maximum of D_{hop} as given by Eq. (2) is displaced toward larger x. The same figure shows the corresponding $W_{hop}(x,T)$ dependences, obtained numerically by the Monte Carlo method, using program MCARLO.[1–3] Very good agreement of the analytical and numerical calculations can be noted. The time to calculate $D_{hop}(x)$ from Eq. (2) is less than 1 min on a Pentium 100 personal computer; the same calculation by the Monte Carlo method takes 20 min for a temperature of $T=1000$ K and more than 30 min for $T=250$ K.

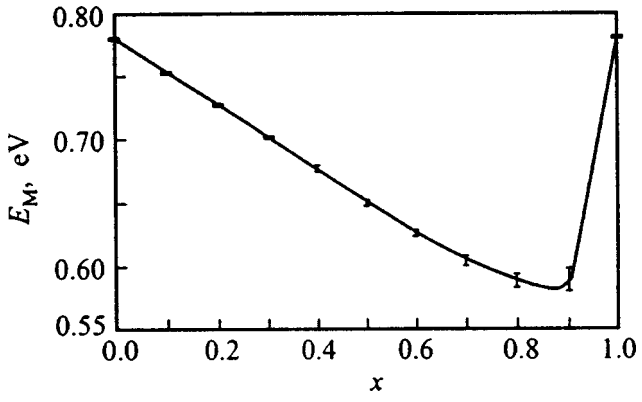

FIG. 2. Activation energy vs the composition of a mixed crystal. The error bars show the standard error of processing the data of Fig. 1 by the method of least squares.

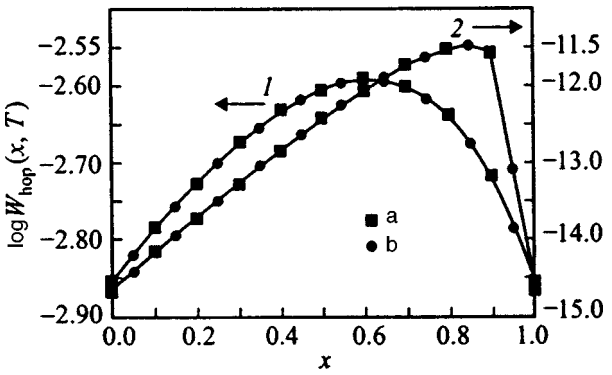

FIG. 3. Hopping probability $W_{hop}(x,T)$ vs the composition of the mix. $T=1000$ (*1*), 250 K (*2*). (a) Calculation from Eq. (2), (b) Monte Carlo calculation.

This paper has thus proposed a new equation for calculating the hopping diffusion coefficient of a vacancy in a mixed AHC having a common cation, giving good agreement with numerical calculations.

This work was carried out with the support of the Russian Fund for Fundamental Research (Grant No. 96-02-19785-a) and is part of the studies on constructing a theory of macroscopic mass (and/or charge) transfer on the basis of the characteristics of elementary events of defect interaction and migration in crystals.

*)E-mail: varaksin@ecko.uran.ru

[1] A. N. Varaksin, *Interaction and Migration of Point Structural Defects in Insulators Based on Alkali Halide Crystals. Computer Modelling* (Izd. Uralsk. Otdel. Ross. Akad. Nauk, Ekaterinburg, 1997).
[2] Yu. N. Kolmogorov, A. N. Varaksin, and L. G. Gorbich, Fiz. Tverd. Tela **32**, 3618 (1990) [Sov. Phys. Solid State **32**, 2098 (1990)].
[3] A. N. Varaksin, Fiz. Tverd. Tela **34**, 2595 (1992) [Sov. Phys. Solid State **34**, 1392 (1992)].

Translated by W. J. Manthey

Formation and stabilization of *F* centers following direct generation of self-trapped excitons in KCl crystals

I. A. Kudryavtseva, E. A. Vasil'chenko, A. Ch. Lushchik, and Ch. B. Lushchik

Institute of Physics, Tartu University, EE2400 Tartu, Estonia
(Submitted July 21, 1998; resubmitted September 4, 1998)
Fiz. Tverd. Tela (St. Petersburg) **41**, 433–441 (March 1999)

The spectrum of luminescent *F* centers generated in high-purity KCl crystals by 7–10.2-eV photons has been measured at 230 K. The pulsed annealing of these centers (250–550 K), as well as the dependence of the efficiency of stable *F*-center generation on irradiation temperature (80–500 K) has been studied. The efficiencies of F^- and Cl_3^--center generation are maximum under direct optical creation of self-trapped excitons in the region of the Urbach intrinsic-absorption tail. Besides the exciton decay with formation of *F* centers and mobile *H* centers, a high-temperature exciton decay channel which involves creation of cation defects stabilizing the *H* centers has been revealed. © *1999 American Institute of Physics.* [S1063-7834(99)01403-3]

Following the discovery by W. C. Röntgen and A. Ioffe of *F* center formation in NaCl crystals irradiated by x rays,[1] this phenomenon has been studied in considerable detail in many laboratories (see, e.g., Refs. 2 and 3). Particular attention was focused on the mechanisms by which radiation creates *F* centers (electrons localized in the field of an anion vacancy, $v_a e$) and other microdefects in wide-gap crystals. The interest in these crystals is currently increasing in connection with development of optical recording media and radiation dosimeters. The very first high-sensitivity measurements of the luminescence spectra of UV-generated *F* centers[4,5] and anion vacancies[6] (α centers) revealed that Frenkel defects form in the anion sublattice of alkali halide crystals in recombination of electrons with self-trapped holes (STH) or in radiationless decay of self-trapped excitons (STE). The electron-hole (e–h) and exciton mechanisms of generation in alkali halides of anion Frenkel defects (AFD) by radiation were extensively investigated (see Refs. 7 and 8 and references therein). At the same time the relative contributions of the e–h and exciton mechanisms of AFD formation by particles and quanta with energies $E \gg E_g$ (E_g is the energy gap width) still remain unknown.

Because the number of relaxed e–h pairs left after the fast intermediate processes in an x-ray-irradiated alkali halide crystal have ended exceeds by more than an order of magnitude that of generated anion excitons,[9,10] the attention of both experimenters and theorists has recently been increasingly focused on the e–h mechanism of creating *F* centers, both short-lived, $10^{-9}-10^{-6}$ s,[8,11,12] and stable[7,13,14] (lifetime on the scale of hours). Simultaneously with *F* centers, there form in alkali halide crystals *H* centers, i.e. interstitial halogen atoms which, in the relaxed state, have the configuration of a two-halogen molecule residing in one anion site (in KCl it is Cl_2^-). At low temperatures (in KCl, for $T<40$ K), the relaxed *H* centers are immobile. At 40 K, *H* centers can start moving by hopping. To prevent recombination in the 200–400-K region of the mobile *H* centers with the *F* centers that remain immobile up to 500 K, one has to stabilize the former by associating them with other defects on the anion and cation sublattices of the crystal.[15–18] The significance of the e–h mechanism in the creation of AFDs is beyond question, but the exciton mechanism also plays a substantial role in radiation-induced defect formation. A study was carried out of the exciton mechanism of creation at 4.2 K of stable F–H and α–I pairs (I is the interstitial halogen ion, Cl_i^- in KCl) in high-purity KCl crystals[19] and in KCl:Tl (Ref. 20). The efficiency of the exciton-assisted creation of stable F–H pairs and, particularly, of the α–I pairs at 4.2 K was found to be an order of magnitude higher than that of AFDs in electron recombination with relaxed STHs (V_k centers, which in KCl are Cl_2^- molecules at two anion sites). Particularly suitable for direct generation in KCl at 4.2 K of Γ excitons (3/2,1/2) and (1/2,1/2) with $n=1$ is the narrow spectral region of 7.8–7.9 eV with an absorption coefficient $A \approx 3\times 10^6$ cm^{-1},[21] while the Urbach intrinsic-absorption tail (UIAT) capable of directly producing self-trapped excitons[21,22] declines at 4.2 K down to 10^2 cm^{-1} already at 7.72 eV, and at 80 K, to as low as 7.60 eV (Ref. 21).

The objective of this work was to study the processes involved in formation and stabilization of *F* centers in high-purity KCl crystals under direct generation of STEs by VUV radiation in the UIAT region in the 180–480-K interval, where the intrinsic-absorption edge (at the 10^2-cm^{-1} level) shifts from 7.4 to 6.9 eV. One obtains here a possibility of investigating the exciton mechanism of defect formation far from the defected surface layer of the crystal. We studied the STE decay with creation of the F–H pairs and of other defects in KCl with a high-sensitivity technique based on measuring the IR luminescence of *F* centers (F_{IRL}), which was predicted[23] by Pekar and observed experimentally in the 1.2-eV region.[24] This technique was already employed at 80 K in detection of *F* centers in VUV-irradiated KCl:Br (Ref. 25) and KBr (Ref. 26) at 80 K. The investigation of the

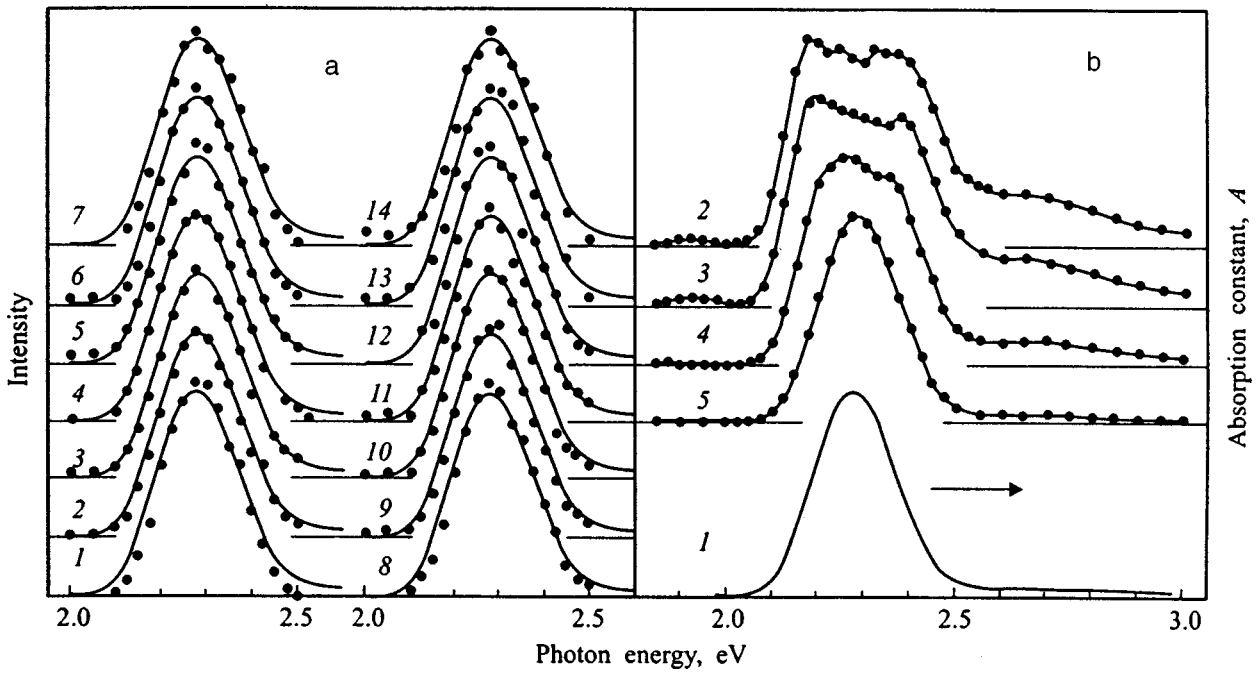

FIG. 1. (a) F_{IRL} excitation spectra (points) measured after irradiating a KCl crystal for 20 min at 230 K by photons of energy (eV): *1* — 7.2, *2* — 7.3, *3* — 7.4, *4* — 7.5, *5* — 7.6, *6* — 7.7, *7* — 7.8, *8* — 8.0, *9* — 8.15, *10* — 8.3, *11* — 8.45, *12* — 8.6, *13* — 8.8, and *14* — 10.2. The solid line is the profile of the *F* absorption band. (b) (*1*) Absorption spectrum of x-ray irradiated KCl crystal. F_{IRL} excitation spectra obtained after x-ray irradiation of a KCl crystal for 2.5 h at 295 K (*2*), and subsequent warmup to 380 K (*3*), 430 K (*4*), and 480 K (*5*). All measurements performed at 80 K.

high-temperature processes of defect formation and stabilization under selective creation of STEs has permitted us to reduce considerably the number of acceptable hypotheses concerning high-temperature stabilization of radiation defects in KCl and to demonstrate once more the active part played in these process by defects in the cation sublattice.[15,16,27]

1. OBJECTS OF STUDY. EXPERIMENTAL TECHNIQUES

The crystals traditionally studied in many laboratories are grown from a melt of commercial raw materials in an air ambient and are unsuitable for investigation of direct STE generation by VUV radiation. It is well known that such KCl crystals contain more than 100 ppm of Br^-, I^-, Na^+ ions and more than 10 ppm of Rb^+, OH^-, Ca^{2+}, and Sr^{2+}.

A special technique of purification and growth of KCl crystals developed at the Institute of Physics of the Estonian Academy of Sciences permits obtaining crystals with the content of Ca^{2+}, Sr^{2+}, and Ba^{2+} ions not in excess of 10^{-2} ppm, of OH^- radicals not over 10^{-1} ppm, and of Br^-, I^-, Rb^+, and Na^+ ions, not over 1 ppm.[28–31] This technique includes, in particular, treating the melt in a Cl_2 flow, which permits one to reduce dramatically the content of the Br^- and I^- ions accounting for most of the interference in UIAT measurements, as well as 60-fold zone melting. The techniques used to grow crystals by the Stockbarger and Kyropoulos methods in an inert atmosphere were described in Ref. 7 and 30. Crystals grown at an oriented seed had a dislocation density of 10^5 cm^{-2}. For the KCl crystals used in this work, which passed this special purification treatment, the region $A>10$ cm^{-1} was dominated by intrinsic absorption resulting in direct optical generation of STEs.

The main experiments were performed in an arrangement including a vacuum monochromator VMR-2, a high-power gas-discharge source making possible operation in the region from 4 to 10.2 eV, and a cryostat permitting temperature control from 80 to 580 K. A cooled FÉU-83 PM tube with standard associated electronics was used to measure F_{IRL}. The short-wavelength part of F_{IRL} was selected by an IKS-7 filter. After irradiation of a crystal by monochromatic VUV light at a fixed temperature it was cooled down to 80 K, where excitation in the *F* absorption band does not produce photothermal ionization of centers. The light stimulating F_{IRL} was passed from an incandescent lamp onto the crystal through a DMR-2 double-grating monochromator. The excitation spectrum of this luminescence measured in the 1.8–3.0-eV region was reduced to the equal number of exciting photons. The optical slit of the monochromator was 20–30 meV. Because the total number of the *F* centers generated in our experiments was small enough to obtain $A<1$ cm^{-1}, the F_{IRL} excitation spectrum was an exact replica of the *F* absorption band. After each measurement, the crystal was warmed up with a rate of 0.3 K/s to 550 K, thus ensuring complete deexcitation. In some experiments, uniform heating was interrupted abruptly once every 30 K by cooling down to 80 K, where the F_{IRL} excitation spectrum was measured. Such a pulsed heating regime permitted one to study the annealing of the VUV-produced *F* centers by the luminescence technique.

Figure 1a presents F_{IRL} excitation spectra measured at 80 K following KCl irradiation at 230 K by photons of various energies (7.2–10.2 eV). The excitation spectra coincide in profile with the *F* absorption band of the same crystal measured by us at 80 K after its irradiation by x rays (45

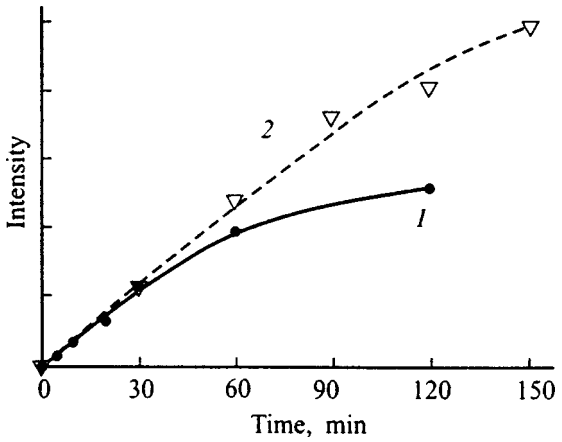

FIG. 2. Dependences of the number of luminescent F centers at 80 K (*1*) and of that of luminescent α centers at 4.2 K (*2*) on irradiation time of a KCl crystal at 230 K (*1*) and 4.2 K (*2*) by photons of energy 7.4 eV (*1*) and 7.77 eV (*2*).

keV, 18 mA) at a level providing a 10^3 times stronger F absorption. The F center generation spectra were taken with equal doses of VUV radiation incident on the crystal at 45° to the (100) surface. The doses were equalized by properly varying the monochromator slit width. The slit optical width was varied in the 7–10.2-eV region from 25 to 100 meV. The excitation time was 20 min, and further irradiation resulted in a sublinear growth of the number of F centers. We estimate the absolute dose as $\approx 10^{14}$ photons/cm^2. The exciting radiation reflected from the crystal was neglected. Within the temperature range of 180–480 K, it rose to 25–35% only in the region of the 7.6–7.9-eV exciton fundamental absorption band. Parallel experiments with x-ray treated crystals were carried out on a standard Specord 40M spectrophotometer with a cryostat, which permitted measurement of absorption spectra within the 1.4–6.2-eV region and thermal annealing of F centers and hole (V) centers under continuous heating with a rate of ~ 0.3 K/s, or in a pulsed mode in the 80–550 K region. It should be stressed that our technique of F_{IRL} measurement increased the sensitivity of a standard spectrophotometer by 10^3-10^4 times. Besides the use of high-purity crystals, this offered a possibility of studying physical processes occurring in KCl crystals in the 140–440 K region under direct optical generation of STEs with different initial energies.

We studied as-cleaved $10\times10\times1$-mm^3 samples. As seen from Fig. 1b, the F_{IRL} excitation spectrum taken at 80 K repeats the absorption band profile only in the case where the optical density of F absorption does not exceed 0.3. For higher densities, the exciting radiation is completely absorbed in the central part of the F band, so that the excitation spectrum reflects the quantum yield of the luminescence rather than the absorption spectrum. In the F-center K absorption band (2.7 eV), which in KCl at 80 K is 20 times weaker than the F band, the luminescence intensity still continues to be proportional to the number of centers.

2. EXPERIMENTAL RESULTS

Figure 2 demonstrates the increase in the number of luminescent F centers of a KCl crystal with increasing irradiation dose at 230 K with photons of energy $h\nu_e=7.40\pm0.04$ eV, for which $A=3\times10^2-6\times10^3$ cm^{-1}. This plot can be compared with the growth of the number of luminescent α centers (2.7 eV), when excited in the α-absorption band (6.95 eV) by photons with 7.77 ± 0.05 eV at 4.2 K. Both curves in Fig. 2 exhibit an initial linear portion becoming eventually sublinear. At 4.2 K, the α–I pairs are stable, because relaxed I centers are immobile. At 230 K, the F centers produced by direct STE generation by excitation within the UIAT are immobile, but the H centers move with large velocities. Therefore the F centers survive if the H crowdions become localized at traps stable at 230 K, which may be other pre-radiation or radiation-induced defects.

We measured the F-center excitation spectrum under KCl irradiation by equal 7–10.2-eV photon doses at 230 K (Fig. 3). The F-center luminescence intensity when excited at the maximum of the F absorption band at 80 K (2.275 eV) was taken as a measure of the number of F centers. As follows from Fig. 1a, for all $h\nu_e$ the excitation spectra are the same and coincide with the F-center absorption spectrum. The efficiency of F-center generation by VUV radiation at 230 K is maximum for $h\nu_e=7.3-7.4$ eV, where $A=10^2-3\times10^3$ cm^{-1}, i.e. it is considerably higher than the possible extrinsic or dislocation-induced absorption. Figure 3 displays also an absorption spectrum of a thin deposited KCl layer measured at 295 K, which practically coincides with the one presented in Ref. 32. The left-hand part of the figure shows fragments[21] of the log dependence of the KCl intrinsic-absorption coefficient on $h\nu_e$ measured at 183, 295, and 373 K.

In the region of fundamental exciton absorption at 230 K (7.65–8.0 eV), where photons produce $n=1$ excitons, and the values of A are particularly high ($2\times10^6-5\times10^5$ cm^{-1}), the efficiency of F-center generation decreases four times compared to that for $h\nu_e=7.4$ eV. While this decrease is partially due to the increasing fraction of radiation reflected from the crystal, it is predominantly caused by the small depth of VUV penetration into the crystal ($10^{-6}-3\times10^{-6}$ cm). This results in a buildup in a very thin layer of the crystal of high F-center concentrations (in excess of 10^{18} cm^{-3}). Such concentrations may give rise to concentration quenching of the F-center luminescence.[24] Within the 8.1–8.6-eV region, radiation produces in KCl at 230 K both $n=2$ excitons and separated electrons and holes (in the region of the Urbach tail of interband absorption). Here $A\approx10^5-7\times10^4$ cm^{-1}, which makes concentration quenching of F_{IRL} practically absent. The efficiency of F-center production is particularly low in the 8.6–10.2-eV interval, where interband transitions involving creation of free electrons and holes take place.

Figure 3 displays an F-center creation spectrum in KCl:Tl crystals obtained at 295 K by another method. In this case we took for the measure of the number of F centers the intensity of Tl^+ luminescence with F centers excited at 295 K by 2.2-eV photons. In the 8–10.2-eV interval, this spectrum agrees quite well with the one derived from F_{IRL}. At the same time in the region of $n=1$ exciton creation (7.2–8.0 eV) considerable differences are observed. Mea-

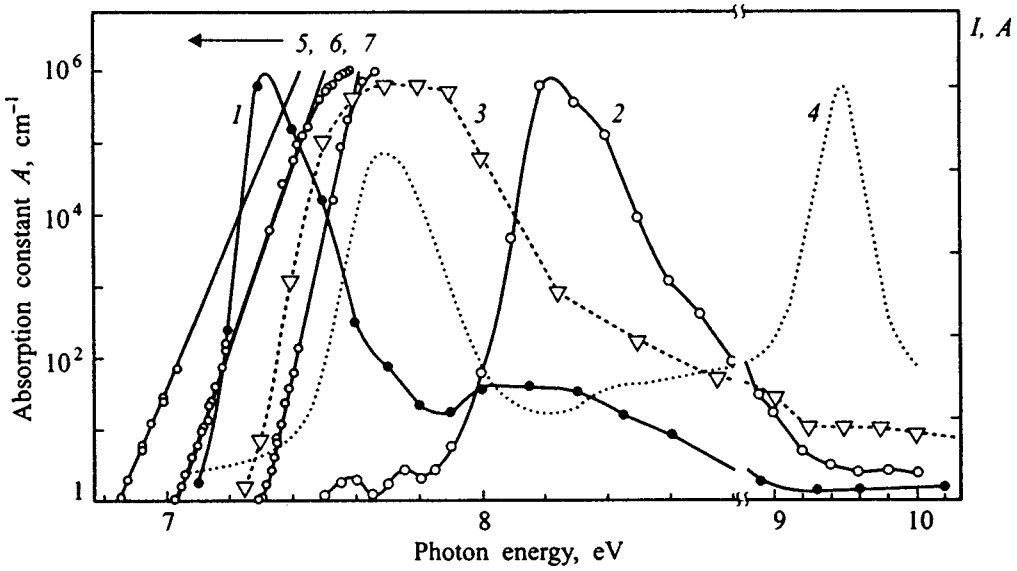

FIG. 3. *F*-center generation spectra: from F_{IRL} under excitation by 2.275-eV photons at 80 K in a KCl crystal irradiated at 230 K (*1*); from Tl^+-center luminescence under *F*-center excitation by 2.2-eV photons in a KCl:Tl crystal at 295 K (*2*); from photostimulated electron emission of *F* centers in a KCl crystal (*3*). (*4*) Absorption spectrum of a thin KCl film at 295 K; fragments of the Urbach intrinsic-absorption tail at (*5*) 373 K, (*6*) 295 K, and (*7*) 183 K (from Ref. 21).

surements of *F*-stimulated recombination luminescence of Tl^+ centers require preliminary ionization of the Tl^+ centers by mobile holes or excitons. The efficiency of Tl^{2+} creation under optical STE generation by photons is low and increases only for $h\nu_e > 8$ eV, where V_k centers, which are mobile at 295 K, are produced. Figure 3 presents also an *F*-center generation spectrum measured in KCl at 295 K in our laboratory[33] from photostimulated electron emission of *F* centers. The optimum conditions for the spectral measurements in these experiments were 3.0-eV photon excitation at 410 K, which ensured effective escape of electrons from the crystal. The generation efficiency of *F* centers appropriate for photostimulated electron emission is maximum in the region $A > 3\times10^5$ cm^{-1}, where the *F* centers were created in a thin near-surface layer of the crystal.

Note that, as seen from the *F*-center generation spectra measured by different techniques, stable *F* centers can be effectively created at 230–295 K by combined creation by photons of both excitons and *e*–*h* pairs (the 8.0–8.6-eV region). This process is less efficient when spatially separated electrons and holes are optically produced ($h\nu_e \geqslant 9$ eV). Accurate detection of *F* centers under direct optical STE production by 7.2–7.4-eV photons can be reached only by the F_{IRL} measurement method used in this work.

Figure 4 shows pulsed annealing of the *F*-center IR luminescence in KCl following its irradiation by 7.35-eV photons at 295 K and by 7.6-eV photons at 180 and 230 K. The measurements were performed at 80 K after each warmup stage. The F_{IRL} excitation spectra were identical and reproduced the profile of the *F* absorption band. Most of the *F* centers are annealed in two stages within the 380–500-K interval. Also shown in Fig. 4 are thermostimulated luminescence (TSL) curves obtained after irradiation at 230 K by 7.4- and 8.3-eV photons. In this temperature range, TSL in pure KCl is weaker by several orders of magnitude than that in KCl:Tl crystals. When 8.3-eV photons produce both excitons and *e*–*h* pairs, the main TSL peak lies at 410 K. In the case of direct STE creation by 7.4-eV photons, the TSL peak at 410 K is very weak, and the main peak was observed to lie at 360 K. Figure 4 demonstrates also pulsed annealing of F_{IRL} following irradiation by 7.4-eV photons at 295 K of KCl:Sr (30 ppm) containing $Sr^{2+}+v_c$ impurity dipoles in amounts hundreds of times larger than that in KCl. The profiles of the *F*-center excitation spectra in KCl and KCl:Sr are practically identical. When excited in the intrinsic absorption region, the impurity dipoles capture one or two *H* centers.[6,7,26,34] Most of the *F* centers in KCl:Sr are pulse-annealed within the 340–380-K interval, i.e. at substantially lower temperatures than is the case with pure KCl. Follow-

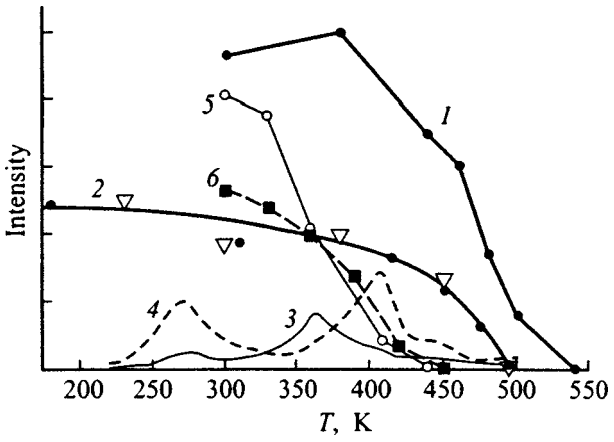

FIG. 4. Pulsed annealing of *F* centers (F_{IRL}) (*1*,*2*) and thermally stimulated luminescence (*3*,*4*) of a KCl crystal irradiated for 20 min by photons of energy 7.35 eV at 295 K (*1*), 7.6 eV (*2*) at 180 K (points) and 230 K (triangles), 7.4 eV (*3*) and 8.3 eV (*4*) at 230 K for 60 min. Pulsed annealing of F_{IRL} (*5*,*6*) in a KCl:Sr crystal irradiated for 60 min at 295 K by photons of energy 7.4 eV (*5*) and 8.8 eV (*6*).

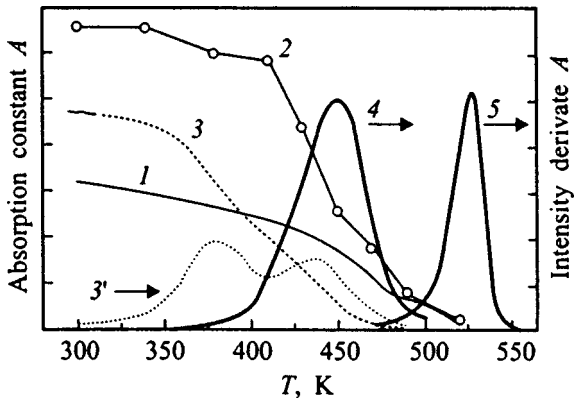

FIG. 5. Annealing of *F*-center absorption in KCl (*1*,*2*) and KCl:Sr (*3*) crystals, which were x-ray irradiated at 295 K, measured under continuous (*1*,*3*) and pulsed (*2*) heating. Integrated TSL of a KCl crystal (*4*) measured 20 h after x-ray irradiation at 295 K, as well as after a preliminary warmup to 520 K (*5*). Curve *5* is shown amplified 100 times. The values of the differential *F*-center annealing curve for a KCl:Sr crystal (*3′*) are multiplied by -1.

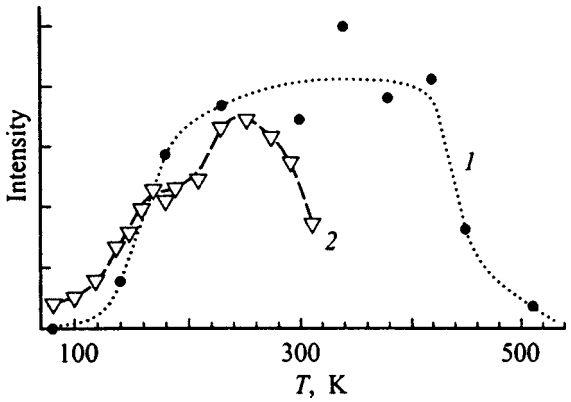

FIG. 6. (*1*) Dependence of the number of *F* centers (F_{IRL}) on the temperature of irradiation of a KCl crystal for 20 min by photons capable of directly creating STEs at approximately equal $A \approx 10^4$ cm^{-1} (80 K — 7.65 eV, 140 K — 7.60 eV, 180 K — 7.50 eV, 230 K — 7.45 eV, 295 K — 7.40 eV, 340 K — 7.30 eV, 380 K — 7.25 eV, 420 K — 7.20 eV, 450 and 510 K — 7.1 eV). (*2*) The light sum of the TSL peak at 390–440 K plotted against x-ray irradiation temperature for a KCl crystal.

ing irradiation of KCl:Sr at 295 K by 8.8-eV photons producing both excitons and separated e–h pairs, the 390–430-K stage rises in intensity.

Figure 5 shows thermal annealing of *F*-center absorption in KCl and KCl:Sr crystals x-ray irradiated at 295 K, which was measured under continuous uniform and pulsed heating (the measurements relate to 2.2 eV). Also presented are TSL curves for total luminescence. In pure KCl, most of the *F* centers are annealed at 400–500 K in two stages, with maximum annealing rates at ~430 and 485 K. For KCl:Sr, an additional strong *F*-center annealing stage was observed at 340–390 K, with the maximum rate at 380 K. Heating at 400–460 K an x-ray irradiated KCl sample removes primarily the broad absorption band with a halfwidth of ~0.8 eV and a maximum at 5.40 eV, which is due to linear, $\langle 100 \rangle$-oriented $(Cl_3^-)_{aca}$ molecules residing at two anion and one cation lattice sites.[15,16,35] Annealing up to 460 K, which destroys nearly all $(Cl_3^-)_{aca}$ centers, leaves unchanged the absorption band peaking at 5.85 eV, which was tentatively assigned[16,18] to a pair association of three-halogen molecules. Most of this absorption is annealed at 460–510 K with the maximum rate at 475 K. After a preliminary heating of x-ray irradiated KCl to 520 K, the last stage of *F*-center annealing was observed, which is accompanied by TSL with a maximum at ~530 K and a halfwidth of ~23 K (see Fig. 5). The activation energy of this process (2.37 eV), which is actually a first-order reaction, is higher than the energy of the maximum in *F* absorption and can possibly be identified with thermal ionization of the *F* centers. In x-ray irradiated KCl:Sr crystals, interaction of two *H* centers with impurity dipoles produces, besides *F* centers, also complex $Sr_c^{2+}(Cl_3^-)_{aca}Cl_i^-$ centers characterized by two simultaneously annealed absorption bands at 5.6 and 6.4 eV.[34] The latter band is associated with interstitial chlorine ions Cl_i^-. Destruction of these complex centers releases two *H* centers in the 340–400-K interval and is practically not accompanied by TSL.

Because after direct optical STE generation most of the *F* centers in high-purity KCl are annealed only for $T > 400$ K, we were able to obtain for the first time the temperature dependence of the efficiency of the excitonic mechanism of *F*-center generation from F_{IRL} measurements. The results of these measurements are plotted in Fig. 6. The crystals were irradiated with equal numbers of photons (10^{14} cm^{-2}). The UIAT varies with temperature,[21] and therefore we varied slightly the incident photon energy at different temperatures. The photons were absorbed in a layer approximately 10^{-4} cm thick. The sensitivity of our measuring system was not sufficient to permit detection of the creation of luminescent *F* centers in high-purity KCl crystals at 80 K. At 140 K, these centers were detected after irradiation with 7.6-eV photons. Most of these centers are annealed at 200–380 K. *F* centers that are thermally stable at 400 K are efficiently produced at 180–230 K. As the irradiation temperature is increased, the efficiency of *F*-center production remains high until 415 K (see also Ref. 36), to decline strongly thereafter, which is associated with the increase in this region of the annealing temperatures of the *F*, $(Cl_3^-)_{aca}$, and still more complex molecular aggregates.

Figure 6 presents also the dependence of the efficiency of TSL peak excitation at 390–440 K on the temperature of x-ray irradiation, which was measured on high-purity KCl crystals.[28] The optimum temperature for creation of the $(Cl_3^-)_{aca}$ centers lies at 230–270 K. The temperature dependence of the efficiency of *F*-center generation, q_F, under x-ray irradiation of nominally pure KCl crystals was measured by the direct absorption technique.[37] The falloff of q_F is observed to occur at $T = 310$ K. Within the 4.2–200-K range, q_F does not depend on intensity and is determined by the irradiation dose It. For $T > 230$ K and low irradiation levels, of the order of 10^{15} eV/(cm$^3 \cdot$s), q_F is observed to decrease strongly with the temperature increasing to 300 K. This decline becomes progressively weaker as the dose rate increases to 10^{17} and 10^{18} eV/(cm$^3 \cdot$s), to stop finally at 10^{19} eV/(cm$^3 \cdot$s). The explanation of this phenomenon consists in that *F* centers are not only created at high temperatures but destroyed as well.[3] In particular, V_k centers recombine effi-

ciently with F centers.[7] Only at high dose rates the double and triple association of H and V_k centers with one another and with other defects proceeds with rates higher than that of V_k-center recombination with F centers. In the case of x-ray irradiation at high temperatures, the equivalence of the duration and intensity of irradiation in KCl is no longer valid. Our data suggest that the deviations from this equivalence relation under direct STE creation by VUV light are small. When KCl was irradiated by 7.3-eV photons at 380 K by equal doses $D=I_1t_1=I_2t_2$, the variation of intensity from I_1 to $I_2=0.25I_1$ and of $t_2=4t_1$ changed the number of created F centers by not more than 15%.

3. DISCUSSION OF RESULTS

The above results permit a conclusion that direct optical generation of STEs in high-purity KCl crystals at 180–480 K gives rise to efficient creation of F centers, most of which persist under heating to 400 K. More than half of the F centers anneal at 400–450 K. In this temperature region, V centers, whose absorption band has a maximum at 5.4 eV and a halfwidth of 0.8 eV, anneal too. Earlier studies showed this absorption to be due to ⟨100⟩-oriented three-halogen linear molecules produced under irradiation.[7,15,18,35] This molecule occupies two anion and one cation lattice site. Thermal dissociation of $(Cl_3^-)_{aca}$ centers produces H centers $[(Cl_2^-)_a]$ and V_F centers $[(Cl_2^-)_{aa}v_c]$.[35,38,39] The latter recombine with F centers to form divacancies v_av_c. 390→440 K heating of irradiated KCl resulted in an increase of dipole dielectric losses.[39] The growth in the number of divacancies in the same region was supported by electron microscopy, which revealed an increasing number of gold microcrystallites on the vacuum-cleaved surface of KCl irradiated with a XeCl laser. Divacancies and vacancy quartets served as traps for the deposited gold layer and decorated the radiation defects.[38]

The $(Cl_3^-)_{aca}$ centers produced by irradiation of KCl at 230–380 K in the UIAT region undoubtedly contain radiation-induced cation vacancies. Irradiation of pure KCl at 350 K gives also rise to formation of interstitial dislocation loops.[40,41] A study of the loops under x-ray irradiation showed that the interstitial anions Cl_i^- and interstitial cations K_i^+ likewise take part in their creation.[41]

Several main mechanisms of generation of cation Frenkel defects (CFD) in alkali halide crystals were discussed in the literature (see review Ref. 16). Our results bearing on the formation of $(Cl_3^-)_{aca}$ centers under direct optical STE generation in the UIAT region reduce the number of mechanisms of radiation-induced CFD formation which can operate in the conditions of our experiments. There is no need of invoking impact processes involving high-energy electrons, as well as double ionization of anions (for this mechanism to operate in KCl, photons with $E>200$ eV would be required). It was earlier conjectured that CFDs are created in the decay of cation excitons, but in KCl and KBr the decay of cation excitons produced by photons with energies of 20–21 eV involves creation of two e–h pairs,[13,18] and cannot be an efficient source of CFDs.

Irradiation of KCl in the 7.3–7.7-eV interval produces anion STEs, and formation of CFDs should be a direct or indirect consequence of their decay. The hypothesis of a possibility of direct anion STE decay involving creation of CFDs ($v_c+K_i^-$ or $v_ch+K_i^0$) was put forward as far back as 1968.[42] This was followed by consideration of the possibility of CFD formation through association of two H centers,[43] or of H and V_k centers (Refs. 16 and 17). Theoretical calculations showed[44] that pair association of H centers in regular parts of a crystal with formation of the $(Cl_3^-)_{aca}$ center by the reaction

$$(Cl_2^-)_a+(Cl_2^-)_a\rightarrow(Cl_3^-)_{aca}+Cl_i^-K_i^+ \quad (1)$$

is not exothermal and requires additional energy. At 80 or 140 K, it cannot proceed in KCl at all. At 140 K, direct creation of STEs entails formation, besides F centers, of low-stability associations of H centers with defects that were present before the irradiation. In this case the majority of F centers are annealed already when heated to 300 K, the process coming to an end when the temperature is raised to 380 K. At the same time at still higher temperatures, 230–400 K, one cannot exclude the possibility of reaction (1) contributing to CFD creation.[16] When H and V_k centers are associated by the reaction

$$(Cl_2^-)_a+(Cl_2^-)_{aa}\rightarrow(Cl_3^-)_{aca}K_i^++Cl_a^-, \quad (2)$$

the energy expended in transferring the cation to an interstitial site can already be compensated in transformation of two halogen-pair molecules into one three-halogen molecule.[16] This reaction requires participation of a large number of self-trapped holes.

Attempts at detecting the direct decay of anion STEs with creation of CFDs proposed in Ref. 42 have been carried out for a long time. At 4.2 and 80 K, they failed.[7] In the low-temperature domain, the predominant process is the decay of anion STEs involving creation of anion rather than cation defects. In the 300–350-K interval, direct manifestation of radiation-induced CFD creation in KCl was observed.[7,27] In this work, we detected CFD formation at 230–470 K through direct creation of anion STEs as well.

The process particularly well studied in KCl is the creation of short-lived (1–100 ps) F–H pairs in low-temperature recombination of electrons with V_k centers.[8,11,12] Besides the radiative STE annihilation channel with a relaxed hole component (the 2.3-eV luminescence), two F–H pair formation channels were detected. It was shown also that about one half of the recombination-produced STEs generate neither emission nor F–H pairs. It was assumed that this ''thermal'' channel originates from STE states with a high vibrational energy and corresponds to nonradiative creation of a phonon packet.[11] This channel can be suppressed by initiating tunneling recombination at 200 K of mobile V_k centers with electrons localized at deep (2–3 eV below the conduction-band bottom) traps (for instance, at Ag^+ ions in RbCl).[45] Experiments involving direct STE generation by 7.3–7.5-eV photons, whose energy at 230–380 K is less by about 1 eV than E_g, still do not exclude the thermal channel of nonradiative STE decay (without F–H pair production). Estimates show[36] that only 40% of e–h pairs undergoing

nonradiative recombination in KCl at 380 K transform to short-lived (46 ps) F–H pairs, and that the number of long-lived ($\tau > 10$ s) F–H pairs created at 350 K constitutes only 0.8% of that of recombining e–h pairs.

It was suggested[13,17] that the thermal channel of STE annihilation in KCl and KBr is not necessarily accompanied by formation of a phonon packet, and can instead (particularly at high temperatures) cause CFD creation. Particularly favorable for the CFD creation in the decay of anion STEs is the instant at which the optically-produced one-halogen self-trapped excitons (OSTE) transform to the conventional two-halogen self-trapped excitons (TSTE). In the OSTE configuration, it is the two cations, and in the TSTE, the two anions that are brought close to one another. An OSTE $\rightarrow$ TSTE transition may result in concentration of the vibrational energy on cations with subsequent formation of CFDs. A study of high-purity KCl at 10–80 K revealed a weak luminescence at 7.0 eV, which was tentatively identified with the luminescence of metastable OSTEs.[7,46] Taking into account the Stokes losses associated with OSTE radiation, one may expect the OSTE $\rightarrow$ TSTE transition region in KCl to lie ≈ 0.4 eV below the maximum of exciton absorption, i.e. in the UIAT region (7.3–7.5 eV). With a due allowance for a pure coincidence, we note nevertheless that it is in this region that we observed at 230–300 K a maximum efficiency of F- and $(Cl_3^-)_{aca}$-center formation.

There are presently no strong grounds for choosing between the associative mechanism of $(Cl_3^-)_{aca}$ formation in the interaction of two H centers and the nonradiative decay of a part of STEs with creation of CFDs. It is possible that both processes contribute to radiative CFD creation at high temperatures, which are necessary not only for the formation of short-lived CFDs but for efficient CFD dissociation into a vacancy and an interstitial as well.

If the decay of anion STEs gives rise to creation not only of F centers that remain immobile up to 500 K but of the mobile H centers and vacancies in the anion and cation sublattices, one can conceive the following reaction

$$\nu_a + \nu_c + (Cl_2^-)_a + (Cl_2^-)_a \rightarrow (Cl_3^-)_{aca} + Cl_a^- . \qquad (3)$$

Because relaxed H centers in KCl are mobile already at 40 K, the low-temperature threshold for the onset of reaction (3) is determined by the mobility of v_a and v_c. At 230 K, all components of reaction (3) in KCl are already mobile, while at 140 K v_a and v_c cannot move. As follows from our studies, efficient formation of F and $(Cl_3^-)_{aca}$ centers stable at 400 K takes place at 230–430 K. At 140 K, the F-center generation efficiency is an order of magnitude lower than that at 350 K, while $(Cl_3^-)_{aca}$ formation under direct STE generation at 140 K has not been observed by us at all. As seen in Fig. 6, the pure exciton mechanism of F-center formation in KCl differs from the complex process of F-center formation under x-ray irradiation, which produces, besides excitons, a considerably larger number of e–h pairs as well. The onset of efficient hopping diffusion of V_k centers at $T > 230$ K brings about their recombination with F centers, which reduces substantially the probability of F-center survival. In the pure exciton mechanism of defect formation, these effects become manifest to a much lesser extent than in the conditions where the exciton and e–h mechanisms are both operative. Combined operation of the two mechanisms becomes possible at 230 K when KCl is irradiated by 8.3–8.5-eV photons, and is most clearly pronounced when one 17-eV photon produces both an e–h pair and an exciton.[18]

We are not discussing here the processes of stabilizing and annealing at 450–500 K F centers generated by irradiation. It should be stressed only that the mechanisms involved in high-temperature radiation-induced formation and annealing of cation defects in alkali halide crystals remain an important problem awaiting its solution.

Partial support of the Estonian Scientific Foundation (Grant 1931) is gratefully acknowledged.

[1] W. C. Röntgen and A. F. Ioffe, Ann. Phys. (Leipzig) **62**, 1 (1921).
[2] F. Seitz, Rev. Mod. Phys. **26**, 7 (1954).
[3] Ch. B. Lushchik, I. K. Vitol, and M. A. Élango, Usp. Fiz. Nauk **122**, 223 (1977) [Sov. Phys. Usp. **20** 489 (1977)].
[4] Ch. B. Lushchik, G. G. Liidja, and I. V. Jaek, in *Proc. Intern. Conf. Semicond. Physics* (Prague, 1961), p. 717.
[5] Ch. B. Lushchik, G. G. Liidja, and M. A. Élango, Fiz. Tverd. Tela (Leningrad) **6**, 2256 (1964) [Sov. Phys. Solid State **6**, 1789 (1964)].
[6] E. A. Vasil'chenko, A. Ch. Lushchik, N. E. Lushchik, Ch. B. Lushchik, H. A. Soovik, and M. M. Taĭirov, Fiz. Tverd. Tela (Leningrad) **23**, 481 (1981) [Sov. Phys. Solid State **23**, 271 (1981)].
[7] Ch. B. Lushchik and A. Ch. Lushchik, *Decay of Electronic Excitations with Formation of Defects in Solids* (Nauka, Moscow, 1989).
[8] K. S. Song and R. T. Williams, *Self-Trapped Excitons* (Springer Series in Solid-State Sciences, Vol. 105 (Springer, Berlin, 1993).
[9] E. A. Vasil'chenko, Ch. B. Lushchik, and K. Osmonaliev, Fiz. Tverd. Tela (Leningrad) **28**, 1991 (1986) [Sov. Phys. Solid State **28**, 1113 (1986)].
[10] A. Lushchik, E. Feldbach, R. Kink, Ch. Lushchik, M. Kirm, and I. Martinson, Phys. Rev. B **53**, 5379 (1996).
[11] H. Fujiwara, T. Suzuki, and K. Tanimura, J. Phys.: Condens. Matter **9**, 923 (1997).
[12] V. M. Lisitsyn, V. I. Korepanov, and V. Yu. Yakovlev, Izv. Vyssh. Uchebn. Zaved. Radiofiz. **11**, 5 (1996).
[13] A. Lushchik, I. Kudryavtseva, Ch. Lushchik, E. Vasil'chenko, M. Kirm, and I. Martinson, Phys. Rev. B **52**, 10069 (1995).
[14] M. Kirm, A. Lushchik, Ch. Lushchik, I. Martinson, V. Nagirnyi, and E. Vasil'chenko, J. Phys.: Condens. Matter **10**, 3509 (1998).
[15] Ch. B. Lushchik, R. I. Gindina, A. A. Maaroos, L. A. Ploom, A. Ch. Lushchik, L. A. Pung, Yu. V. Põllusaar, and H. A. Soovik, Fiz. Tverd. Tela (Leningrad) **19**, 3625 (1977) [Sov. Phys. Solid State **19**, 2117 (1977)].
[16] Ch. Lushchik, A. Elango, R. Gindina, L. Pung, A. Lushchik, A. Maaroos, T. Nurakhmetov, and L. Ploom, Semicond. Insul. **5**, No. 2, 133 (1986).
[17] I. A. Kudryavtseva, E. A. Vasil'chenko, A. Ch. Lushchik, Ch. B. Lushchik, and L. A. Pung, Fiz. Tverd. Tela (St. Petersburg) **38**, 527 (1996) [Phys. Solid State **38**, 289 (1996)].
[18] A. Lushchik, M. Kirm, I. Kudryavtseva, E. Vasil'chenko, and Ch. Lushchik, Mater. Sci. Forum **239–241**, 581 (1997).
[19] Ch. Lushchik, J. Kolk, A. Lushchik, N. Lushchik, M. Taiirov, and E. Vasil'chenko, Phys. Status Solidi B **114**, 103 (1982).
[20] Ch. Lushchik, Y. Kolk, A. Lushchik, and N. Lushchik, Phys. Status Solidi A **86**, 219 (1984).
[21] T. Tomiki, J. Phys. Soc. Jpn. **22**, 463 (1967); *Ibid.* **23**, 1280 (1967).
[22] H. Sumi and Y. Toyozawa, J. Phys. Soc. Jpn. **31**, 342 (1971).
[23] S. I. Pekar, Zh. Éksp. Teor. Fiz. **22**, 641 (1952).
[24] H. Pick, in *Optical Properties of Solids*, edited by F. Abeles, Vol. 5, 655 (1974).
[25] M. Maki, N. Nagasawa, and M. Hirai, Solid State Commun. **17**, 1409 (1975).
[26] F. C. Brown, J. Stott, and B. R. Sever, Phys. Rev. Lett. **57**, 2279 (1986).
[27] A. Lushchik, Ch. Lushchik, N. Lushchik, A. Frorip, and O. Nikiforova, Phys. Status Solidi B **168**, 413 (1991).
[28] R. I. Gindina, L. A. Ploom, A. A. Maaroos, and Yu. V. Põllusaar, Zh. Éksp. Teor. Fiz. **27**, 520 (1977) [*sic*].
[29] R. I. Gindina, A. A. Maaroos, L. A. Ploom, and N. A. Jaanson, Tr. IF AN ÉSSR **49**, 45 (1979).

[30] O. A. Nikiforova, A. A. Maaroos, and N. A. Jaanson, Tr. IF AN ÉSSR **57**, 157 (1985).
[31] N. E. Lushchik, A. A. Maaroos, O. A. Nikiforova, A. G. Frorip, and N. A. Jaanson, Tr. IF AN ÉSSR **61**, 7 (1987).
[32] J. E. Eby, K. J. Teegarden, and D. B. Dutton, Phys. Rev. **116**, 1099 (1959).
[33] V. Bichevin, H. Käämbre, and Ch. Lushchik, Phys. Status Solidi A **5**, 525 (1971).
[34] K. M. Shunkeev and R. I. Gindina, Tr. IF AN ÉSSR **54**, 122 (1983).
[35] A. Ch. Lushchik, Tr. IF AN ÉSSR **49**, 25 (1979).
[36] R. T. Williams, J. N. Bradford, and W. L. Faust, Phys. Rev. B **18**, 7038 (1978).
[37] E. Sonder and W. A. Sibley, in *Point Defects in Solids*, edited by J. H. Crawford, Jr., and L. M. Slifkin (Plenum Press, New York), Vol. 1, 201 (1972).
[38] A. Baĭmakhanov, H. R.-V. Jõgi, and Ch. B. Lushchik, Fiz. Tverd. Tela (Leningrad) **28**, 684 (1986) [Sov. Phys. Solid State **28**, 381 (1986)].
[39] R. I. Gindina, F. I. Zaitov, Sh. I. Ismailov, Ch. B. Lushchik, and L. A. Ploom, Tr. IF AN ÉSSR **51**, 125 (1980).
[40] A. Baĭmakhanov, H. R.-V. Jõgi, and A. Ch. Lushchik, Fiz. Tverd. Tela (Leningrad) **29**, 1356 (1987) [Sov. Phys. Solid State **29**, 776 (1987)].
[41] A. B. Gektin, G. B. Ptitsyn, G. H. Rozenberg, and N. V. Shiran, Ukr. Fiz. Zh. **29**, 1208 (1984).
[42] Ch. B. Lushchik, I. K. Vitol, and M. A. Élango, Fiz. Tverd. Tela (Leningrad) **10**, 2753 (1968) [Sov. Phys. Solid State **10**, 2031 (1968)].
[43] C. R. A. Catlow, K. M. Diller, and N. J. Norgett, J. Phys. C **8**, L34 (1975).
[44] C. R. A. Catlow, K. M. Diller, and L. W. Hobbs, Philos. Mag. A **42**, 123 (1980).
[45] E. A. Vasil'chenko, I. A. Kudryavtseva, A. Ch. Lushchik, Ch. B. Lushchik, and A. A. Maaroos, Fiz. Tverd. Tela (St. Petersburg) **40**, 1238 (1998) [Phys. Solid State **40**, 1128 (1998)].
[46] Ch. B. Lushchik, A. Ch. Lushchik, E. A. Vasil'chenko, and F. A. Savikhin, Fiz. Tverd. Tela (St. Petersburg) **37**, 525 (1995) [Phys. Solid State **37**, 284 (1995)].

Translated by G. Skrebtsov

DEFECTS. DISLOCATIONS. PHYSICS OF STRENGTH

Creating primary defects in calcium fluoride crystals with various prehistories, using pulsed electron irradiation

E. P. Chinkov and V. F. Shtan'ko

Tomsk Polytechnic University, 634034 Tomsk, Russia
(Submitted May 6, 1998; resubmitted August 31, 1998)
Fiz. Tverd. Tela (St. Petersburg) **41**, 442–450 (March 1999)

Optical spectroscopy with nanosecond resolution has been used to study how the prehistory (the presence of impurities, heat treatment) of CaF_2 crystals affects the processes of creating autolocalized excitons (AEs) under the influence of a pulse of accelerated electrons. The breakdown of the dispersivity condition for the creation of AEs is detected in a nominally pure, nonheat-treated crystal. It is shown that the initial structural defects play a defining role in creating the initial defect density. A model of the radiation disordering of an actual fluorite crystal is constructed. An analogy is traced to the processes of impurity and thermal disordering.
 [S1063-7834(99)01503-8]

Anion Frenkel defects (AFDs) dominate in crystals having the fluorite structure.[1] Their concentration in a nominally pure crystal usually does not exceed $\sim 10^{15}\ cm^{-3}$, but sharply increases in the presence of impurities or external influences (radiation, temperature). Let us consider the most thoroughly studied types of disorder.

Radiation disordering. The primary products of radiolysis are autolocalized excitons (AEs), which are identical to closely-spaced $F-H$ pairs.[2,3] Several configurations can be differentiated, depending on the distance between the components;[4] a geometrical factor is introduced to describe the structure.[5] As temperature increases, the creation efficiency (CE) of closely-spaced pairs decreases, while that of spatially separated pairs increases.[6] It is assumed that they are created by nonradiative decay of anion excitons in an ideal sublattice. However, the density dependences have a sublinear character[6] at concentrations of the resulting defects significantly lower than those corresponding to the Mott transition condition.

Thermal disordering. Anomalies in the behavior of the specific heat and the conductivity are also associated with anion disordering in the premelting temperature region.[1,7] The presence of anion vacancies is regarded as a criterion of high mobility.[1] The transition to the superionic phase is ascribed to the clustering of defects, although it indicates that impurities[8] and external influences are present.

Impurity disordering. In crystals having an anion excess, defect-aggregation processes are accompanied by the formation of clusters[9,10] that are similar in structure to those observed with thermal disordering.[1] In this respect, they can be regarded as a more complex analog of crystals having an excess of anion vacancies, although the latter have been insufficiently studied from the viewpoint of clustering.[11] However, the qualitative similarity of the processes of the creation and evolution of the primary defect content in crystals both with an excess and with a deficit of anions[12,13] makes it possible to draw an analogous conclusion about the type and level of their initial defect content.[14]

The types of disordering considered above mainly assume the breakdown of the anion sublattice of an ideal crystal and can be described qualitatively from consistent viewpoints. Nevertheless, it is possible to distinguish one more type of disordering in actual crystals.

Intrinsic disordering. Several identical stages of structural disordering that do not show up in x-ray analysis are detected in natural and synthetic CaF_2 having different histories (growth technology, heat-treatment regime).[15] Thermal depolarization[14] and dipole relaxation[16] processes are qualitatively similar in pure and doped crystals. The possibility of forming clusters in a pure crystal is theoretically predicted in Ref. 17.

The goal of this paper is to check experimentally the initial defect level of nominally pure fluorites. It will be shown below that the introduction of mesoscopic structure makes it possible to explain consistently the collection of accumulated data concerning disordering.

1. EXPERIMENTAL METHOD AND THE CHOICE OF SAMPLES FOR THE STUDIES

The pulsed measurement method is similar to that of Ref. 18 and was used earlier in Refs. 19 and 20. The maximum electron energy is 0.28 MeV, the pulsewidth at half-maximum is 12 ns, the time resolution is 7 ns, the repetition rate is about 10^{-3} Hz, and the energy density is $0.1-0.2\ J\cdot cm^{-2}$.

The objects of study consisted of crystals grown by the Stockbarger method: nominally pure (three batches) and doped (0.0023 mol % NaF according to the data of neutron-activation analysis; 0.03 and 1 mol % YF_3 in the mix) GOI samples (State Optical Institute, St. Petersburg) and nominally pure Harshaw Chemical Co. samples. The undoped

TABLE I. Prehistory of the CaF_2 crystals.

Samples	Exposure dose, Gy ($T=295$ K)	Color of the samples after irradiation	CE of the AEs, $\log I_0/I$ ($h\nu=2.75$ eV)
CaF_2-1 } nominally pure	1.5×10^4	Colorless	0.215
CaF_2-2 } nominally pure	1.5×10^4	Colorless	0.165
CaF_2-3 } nominally pure	1.5×10^3	Gray	0.240
CaF_2 (Harshaw)	1.5×10^4	Colorless	0.170
CaF_2–0.0023 mol % NaF	1.5×10^3	Bright blue	0.022
CaF_2–0.03 mol % YF_3	1.5×10^3	Gray	0.150
CaF_2–1.0 mol % YF_3	1.5×10^3	Dark	0.075

samples were transparent to 125 nm and had no absorption bands caused by the presence of oxygen or lead impurities; the introduction of sodium and yttrium shifts the transmission limits into the visible region.[21]

The initial purity of the crystals was monitored as follows: First, from the absence of stable coloration when electron-irradiated at room temperature with a dose of $\sim10^5$ Gy.[22] The results are shown in Table I. Second, from the CE of the AEs, which is a function of temperature[3,6,23] and impurity content.[24] Quantitative estimates are made from the amplitudes of the optical density, measured at the time the pulse ends, at the maximum of one of the AE absorption bands.[19] The stable absorption was not taken into account; the samples were thermostatically controlled during irradiation. The results are shown in Table I. Radiation-stable GOI samples, distinguished by the CE of the AEs, are designated as CaF_2-1 and CaF_2-2. The CE of the AEs is approximately identical in the CaF_2-2 and Harshaw crystals. Since the data on the prehistory of the latter are ambiguous,[25] the radiation-stable GOI samples of various batches were chosen as the main objects in studying the influence of the prehistory (quenching).

The samples were cleaved from one block. One of the parallel cleaved pieces was quenched, while the other served as a standard. The thickness of the quenched samples was determined by the total range of the electrons ($\sim300\ \mu$m). The samples were quenched in room-temperature water or in liquid nitrogen to eliminate the hydrolysis reaction[26] after heating (about 7 min) at fixed temperatures (T_q), chosen according to Refs. 14 and 16. The quenched samples had no milky coloration, and no impurity-perturbed electron color centers accumulated in them upon subsequent irradiation.[26] This is evidence that the adsorption and diffusion of oxygen from the ambient atmosphere has low efficiency. The samples were prepared for the measurements as follows: The standard and quenched samples were mounted on a copper holder at room temperature and were cooled to 80 K in a vacuum of 0.13 Pa for 15 min.

The usual measurement systems were used,[18] and the electrons were normally incident on the sample. In the latter case, the absorption spectra were measured with spatial resolution ($\sim10\times20\ \mu$m). Measurements in polarized light were made by means of a Glan–Thompson prism. The luminescence spectra were not corrected.

2. EXPERIMENTAL RESULTS

2.1. Luminescence

Figure 1a shows the luminescence spectra of standard CaF_2-1 at 80 K, measured 10 ns (curve *1*) and 300 ns (curve *2*) after the end of a pulse. The spectral-kinetic characteristics [the quenching time ($\tau_1=10$ ns, $\tau_2\approx430\ \mu$s) and the spectral position of the maxima ($\lambda_1\approx360$ nm, $\lambda_2\approx280$ nm) of the dominant bands] only qualitatively agree with the known luminescence parameters of AEs in

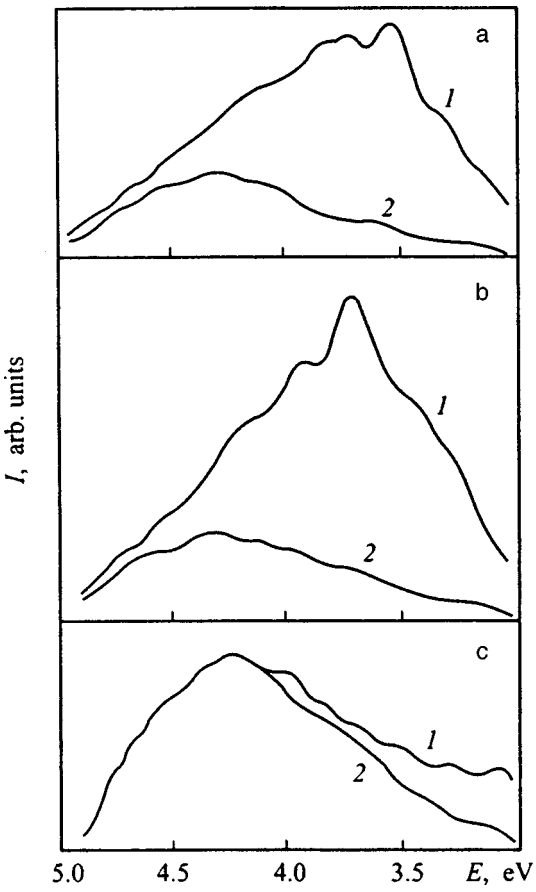

FIG. 1. Luminescence spectra of CaF_2-1 crystals of various prehistories at 80 K, measured 10 (*1*) and 300 ns (*2*) after the end of the electron pulse. (a) is the initial sample, (b) and (c) are those quenched in liquid nitrogen from 295 K (the spectrum was measured without preliminary heating) and 723 K, respectively.

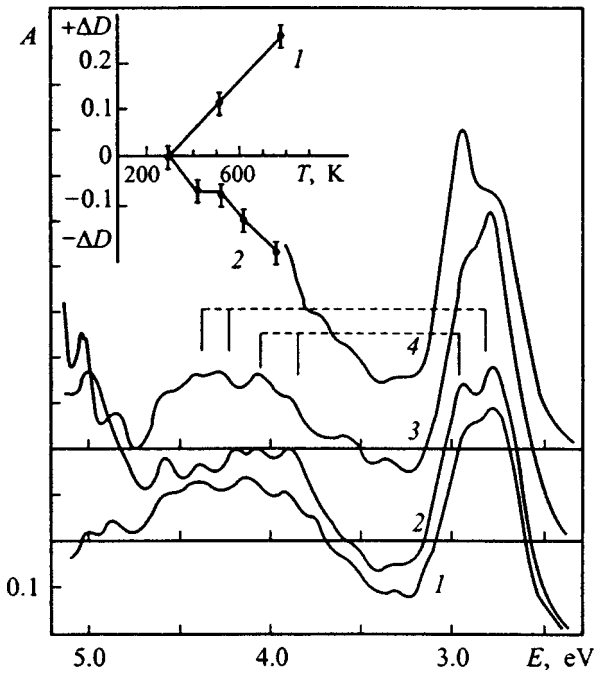

FIG. 2. Transient absorption spectra of CaF_2-1 samples of various prehistories at 80 K, measured 10 ns after the end of the electron pulse. *1*—initial sample, *2–4*—quenched in liquid nitrogen from 523, 773 and 1023 K, respectively. The inset shows the variation of the CE of AEs in CaF_2-1 (*1*) and CaF_2-2 (*2*) crystals as a function of the increase of T_q. Measured at 2.75 eV and 80 K.

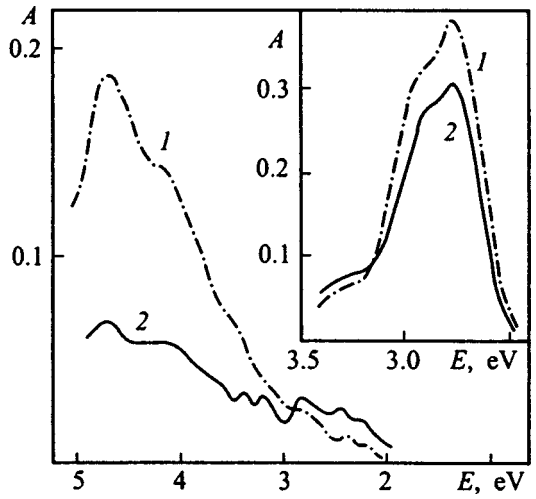

FIG. 3. Steady-state optical absorption spectra of CaF_2-1 (*1*) and CaF_2-2 (*2*) standard samples, measured at 80 K after isodose irradiation with a total dose of $\sim 2\times10^3$ Gy. The inset shows segments of the total absorption spectra of CaF_2-1 (*1*) and CaF_2-2 (*2*) in the region of the electronic components of the AEs at 80 K, measured 10 ns after the end of the electron pulse.

CaF_2.[3,23] It follows from the data of Fig. 1a (curve *1*) that the spectrum of the fast component has a complex structure. A complex structure has recently been detected in the spectrum of the slow component of the luminescence of AEs in CaF_2.[19] The luminescence spectra of the CaF_2-1 samples quenched in liquid nitrogen from 295 and 723 K are shown in Figs. 1b and 1c. An analysis of the results makes it possible to establish the following regularities: (1) Quenching from 295 K increases the intensity of the rapidly quenched luminescence selectively over the spectrum (see curves *1* in Figs. 1a and 1b), whereas the intensity of the inertial component remains unchanged (see curves *2* in Figs. 1a and 1b). (2) Quenching from high temperature changes the ratio of the intensities of the fast and slow components (curves *1* and *2* in Fig. 1c).

The resulting data serve as additional arguments in favor of the different nature of the luminescence centers.[23]

2.2. Optical absorption

Figure 2 shows the transient absorption spectra at 80 K, measured 10 ns after the end of the pulse in CaF_2-1 having various prehistories. The relaxation of the optical density in the dominant bands in the standard and quenched samples is described by an exponential dependence with a time constant of $\tau \approx 40\ \mu$s, which agrees with the estimates of the AE lifetime in Ref. 27. The absorption in the UV region (~ 5 eV) relaxes according to an exponential law with a time constant of $\tau \leqslant 100$ ns at 295 K. (A similar absorption is observed in nonheat-treated SrF_2 and BaF_2.[20]) As T_q is increased in the CaF_2-1 samples, the intensity of the short-lived absorption increases (see curves *1–3* in Fig. 2). The increase of the total absorption and the change of the intensity ratio of the selective bands in quenched CaF_2-1 (see curves *1–4* in Fig. 2) are evidence both of an increase of the CE of the AEs and of a change in the AE distribution over configurations as a function of the distance between the components of a primary pair. The spectral position of the maxima of the selective bands is shown in Fig. 2 in accordance with Ref. 19.

The variation of the CE of the AEs in CaF_2-1 and CaF_2-2 with increasing T_q is shown in the inset to Fig. 2. The contribution of the long-lived component ($\tau \gg 40\ \mu$s) to the total absorption at 2.75 eV increases, for example, from 2% in the standard CaF_2-1 to 10–15% in the CaF_2-1 quenched from $T_q = 1023$ K, with the CE of the AEs not being taken into account when making the estimate. It can be seen by comparing the data that the quenching of crystals of different batches has opposite effects: it can either increase or decrease the CE of the AEs. The prehistory has a substantial influence on the creation not only of short-lived (see the inset to Fig. 3) but also of long-lived defects (curves *1* and *2* in Fig. 3). We shall discuss the possible causes of this below.

Curves *2* and *3* in Fig. 4 show the transient absorption spectra of the CaF_2-2 crystal, measured in perpendicular geometry with two microscopic zones that are identical in area ($\sim 10\times 20\ \mu$m) and separated by about 225 μm (Fig. 4a). Regions of the crystal were chosen in this case in which no optical microinhomogeneities were clearly observed: They are easily visible from birefringence effects at local stress fields in crossed polarizers and are usually interpreted[28] as the result of the clustering of dislocations in the cleavage planes. Curve *1* represents the transient absorption spectrum, measured from an area of about 3.75 mm^2 in the same geometry. All the spectra were recorded from the entire depth of the electron range in the sample (about 300 μm). The variation of the CE of the AEs along an arbitrary coordinate is shown in Fig. 4a; the probing zone crossed the boundary

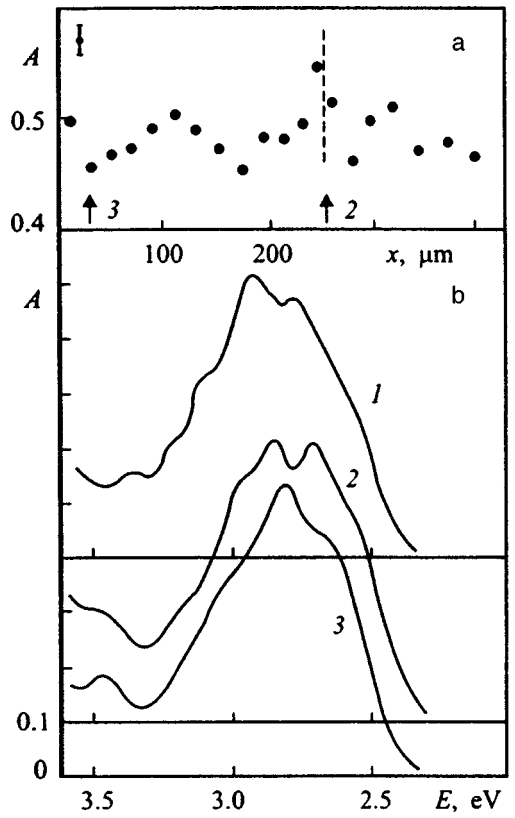

FIG. 4. (b) Transient absorption spectra of a CaF_2-2 crystal at 295 K, measured in perpendicular geometry 10 ns after the end of the electron pulse *1*—from a surface of 3.75 mm^2; *2, 3*—from 10×20-μm microscopic zones identical in area, separated from each other by about 225 μm (a). The dashed line schematically shows the position of the boundary of the blocks.

of the blocks, whose position is schematically shown by a dashed line. The spatially inhomogeneous variation of the intensities of the selective bands assumes that the original structure of the CaF_2 significantly affects the AE distribution over configurations.

The transient absorption in fluorites is partially polarized.[20] Figure 5 shows the characteristic form of the angular dependences of the optical densities, measured in CaF_2-2 at 295 K at fixed wavelengths 10 ns after the end of the pulse. The electric field vector of the light wave was rotated in the (110) and (100) planes, parallel to which the samples were cut. Even though the angular dependences are distorted by spectral overlap of the bands, the data of Fig. 5 are direct evidence that a high but different degree of polarization is present in the region of the electron component of the AE absorption.

3. DISCUSSION OF THE RESULTS

3.1. Basis for choosing the defect-formation model

It has so far been assumed[29] that the creation of AEs in fluorites occurs in the intact lattice. Before beginning to construct a model of defect formation in the disturbed lattice, it is necessary to establish the main criteria that it must satisfy.

3.1.1. Intrinsic defects

The concentration of residual impurities in radiation-stable CaF_2 does not exceed $\sim10^{-4}$ mol %.[3] The AE concentration can be calculated from Smakula's equation; according to the estimates of Ref. 6, it reaches $\sim10^{17}-10^{18}$ cm^{-3} for the densities used in this work. Therefore, residual impurities cannot be responsible for the changes in the CE of the AEs that take place with isodose irradiation of the standard (see Table I) and quenched samples (Fig. 2). The AE-creation process is insensitive to the impurity-disordering level (see Table I and also Ref. 24).

3.1.2. The absence of free and associated vacancies

Thermal disordering of the anion sublattice can be neglected at the temperatures at which the CE of AEs was estimated for CaF_2 with various prehistories (see Table I and Fig. 3): An appreciable increase of the conductivity[1,7] and of the CE of F centers[6] in nominally pure CaF_2 is observed above the Debye temperature ($T_D\approx510$ K, Ref. 22). The associated defects should be excluded from consideration: The mobility of the AFDs at $T<T_D$ exceeds by orders of magnitude the mobility of the base cations or of the impurity ions;[1,11] delocalization of the AFDs occurs when $T<T_D$,[1,11,22] while their diffusion mechanisms are qualitatively similar in nominally pure and doped fluorites;[14,16] ''cold quenching'' of CaF_2 ($T_q\leqslant T_D$) does not result in a sharp increase of the CE of F color centers (see curves *1–3* in Fig. 2).

3.1.3. Stoichiometric excess

An excess of anions in fluorites results in relaxation of the anion sublattice.[9] Interstitial aggregation is caused by covalent interaction between interstitials.[10] The transition to a superionic phase is associated with clustering processes. However, clusters can also form even at low temperatures because of relaxation processes close to thermodynamically nonequilibrium defects.

Thus, a model of radiation disordering in a nominally pure (in terms of impurity content) crystal must be constructed on the assumption that it initially contains defects and must include the most important features that characterize the thermal and impurity disordering of fluorites; the interstitials occupy positions that are not strictly at cube centers; their presence is accompanied by disordering of the anion sublattice; and there is a tendency toward clustering.

3.2. Defect-formation model

3.2.1. Clusters of the V:I:R type

Figure 6a schematically shows a cluster that can include one or two interstitials (I) in the cavities of the anion cubes. If the interstitials are located in adjoining cubes, they occupy positions that are not strictly central and are oriented along a $\langle110\rangle$ direction. Their presence causes the appearance of relaxed anions (R) that are displaced from their site positions into empty anion cubes along $\langle111\rangle$ directions. Figure 6a

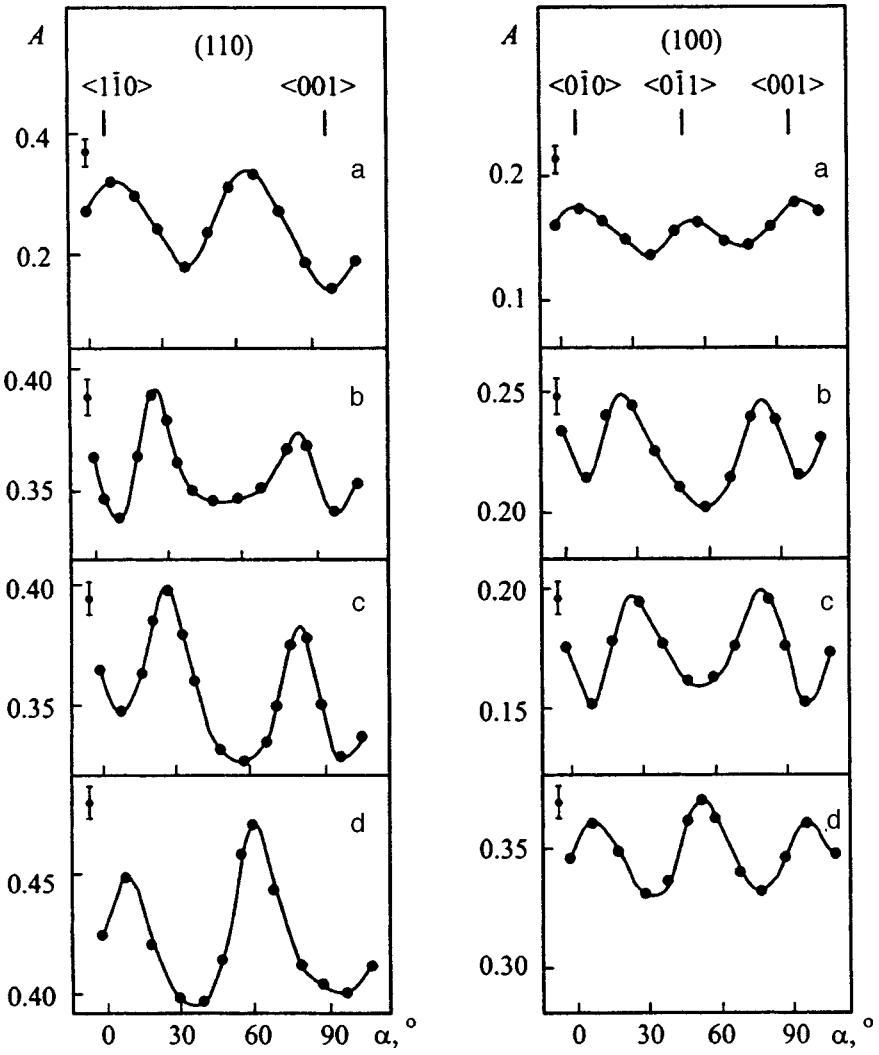

FIG. 5. Angular dependences of the optical density, measured in polarized light at fixed wavelengths 10 ns after the end of an electron pulse of perpendicular geometry: a—2.55 eV, b—2.65 eV, c—2.95 eV, d—2.82 eV. The electric field vector of the light wave was rotated in the (110) and (100) planes parallel to which the CaF_2-2 samples were cut.

also shows two incipient vacancies (V). We assume that the interstitial cation (C) lies beyond the boundaries of the cluster.

The breaking of the bond in a $V-R$ pair during irradiation by ionizing radiation can be represented as follows: Since, in a defect cluster, there is a barrier for recombination of the interstitial with the vacancy,[17] we can assume that the fluorine atom formed during ionization of an R anion does not occupy the position of the vacancy, but makes a jump in the opposite direction, with subsequent formation of a bond with one of the nearest lattice anions. The localization of an electron at an anion vacancy causes the formation of an F center, in the nearest neighborhood of which is located an H center lying along a $\langle 111 \rangle$ direction. This mechanism of forming an AE does not require preliminary autolocalization of a hole in the form of an X_2^- molecular ion with purely covalent bonding. It is characteristic that the hole is distributed nonuniformly on the core of the AE.[2] The process of creating an AE occurs quickly, since the hole core does not complete complex combined motion during its formation. (In SrF_2, this time does not exceed 500 fs at 295 K.[29]) It is easy to note that the process of forming neutral AFDs stimulated by local charge transfer is, in essence, a modification of one of the best-known mechanisms for creating AEs.[2] In the case of nonlocal charge transport, the model gives a good description of the formation of charged AFDs ($\alpha-I$ pairs).

The $V{:}I{:}R$ model does not exclude the formation of adjacent pairs of neutral or charged AFDs, nor their combination. A discussion of fast electron capture mechanisms with the formation of $F-I$ pairs in fluorites[29,30] and low-temperature formation of correlated pairs and triplets of defects in AHCs[31] can serve as examples. An important consequence that follows from the breakdown of the additivity condition should be emphasized. The low-energy transitions in AE absorption in fluorites and AHCs qualitatively recall the Rydberg series at P_2 centers,[3] although the multiplicity of the states should be taken into account.[32] The model makes it possible to use the Pauli exclusion principle[33] to explain why the energies of the triplet transitions in AEs and F_2 centers coincide.[32] Finally, the breakdown of the additivity condition determines in the fluorites the predominant photoinduced conversion of some AE configurations into others,[4] the sublinear dependence on the excitation density,[6] and the irreversible breakdown of all the configurations with selective optical pre-excitation.[20]

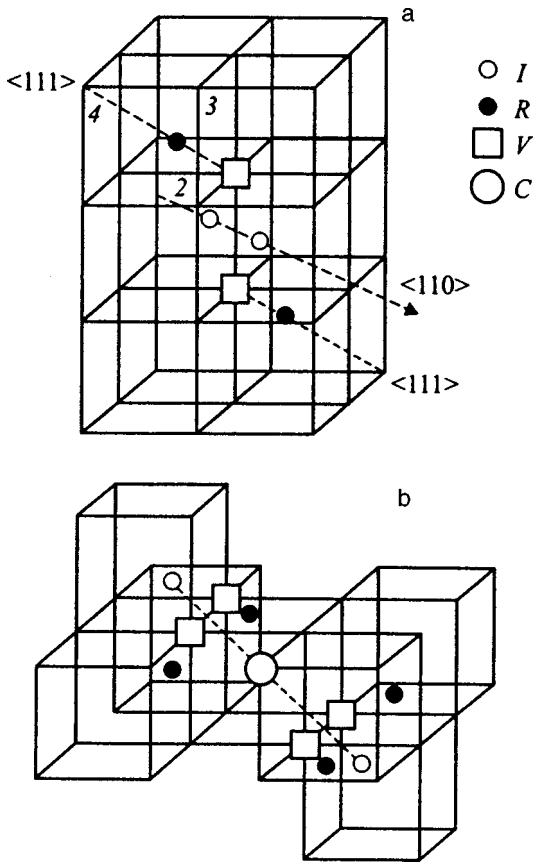

FIG. 6. Schematic representation of $V{:}I{:}R$ (a) and $V{:}I{:}R{:}C$ (b) clusters in a fluorite lattice. Interstitials (I) are represented by small open circles and relaxed anions (R) by small closed circles. The large open circle shows an interstitial cation (C), and the squares indicate anode vacancies (V). The lattice ions are not shown. The numbers denote the lattice positions of anions that can be occupied by a molecular ion X_2^- with the formation of the corresponding AE configuration (the numbering corresponds to Ref. 5).

3.2.2. The V:I:R:C cluster

The $V{:}I{:}R$ model (Fig. 6a) does not assume that the AE distribution function varies over configurations (Fig. 4). On the other hand, F centers but not F_2 centers accumulate during low-temperature ($T<77$ K) irradiation in fluorites,[22] and it is necessary to take into account the tendency to clustering, in the same way that this is done, for example, with impurity disordering.[1,9,10]

Let us assume that the $V{:}I{:}R$ clusters contain interstitial cations, which, even with long irradiation with low-intensity fluxes of ionizing radiation, as a consequence of Coulomb repulsion forces, will prevent spatial separation of the $V-R$ pairs, i.e., the formation of stable defects. However, their presence does not exclude the creation of short-lived defects of the AE type, and this is observed with pulsed high-intensity irradiation. Moreover, cations can stimulate both inverse annealing reactions (this apparently sharply alters the kinetic characteristics of the AE absorption[19,27]), and change the type of configurations that are created; i.e., they can prevent the hole core of the AE from forming along the body diagonal of the anion cube. The latter must be reflected in the variation of the spectral and polarization characteristics of the AE absorption (see Fig. 5, as well as the data of Ref. 20).

We assume that AEs are created in an ideal sublattice and in a sublattice that has been disturbed on the basis of the proposed $V{:}I{:}R$ cluster model (Fig. 6a). If geometrical factors[5] are taken for the basis of the separation of an AE into an electron and a hole [in the makeup of a hole core, an $F^{0.7-}$ ion occupies a normal anion site, and an $F^{0.3-}$ ion is displaced along the $\langle 111\rangle$ axis by about 3.6 a.u. (1 a.u. $=0.0529$ nm)], then, except for the configuration oriented along the body diagonal of the anion cube, the direction of the *sp* transitions for other configurations must not coincide with the principal crystallographic directions.

The tightest configuration (an H center is formed at the position of the site anion noted by number *2* in Fig. 6a) is regarded as the regular geometry of the AE:[29] The difference between the configurations is not noted in papers on the optical detection of electron paramagnetic resonance (OD EPR), and it only introduces a positive contribution into the value of parameter D,[2,5] which is used in the spin Hamiltonian to describe the deviation of the neighborhood of the AE from cubic symmetry. It is assumed in Ref. 19 that the lifetime of a specific AE configuration depends on the spatial orientation of the hole core relative to the position of the vacancy. Modified AE configurations created close to interstitial cations can provide a positive contribution to parameter D while maintaining agreement of the results of optical and magnetic measurements concerning only the structures and symmetries of the hole core of the AE, since the possibilities of the OD EPR method are limited.[19]

3.2.3. Cluster complexes

Local stresses, clearly visible in polarized light, are evidence that a certain ordering in the distribution of the initial defect content is present in the crystal. The high degree of polarization of the transient AE absorption (Fig. 5) indicates an ordered distribution of the primary defects in the crystal. Moreover, a direct connection is detected between the prehistory and the process of creating the primary defects: The CE of AEs increases close to the boundary of the blocks, i.e., in the zone of increased mechanical stresses (Fig. 4). An analogous effect is observed in other crystals.[20] Therefore, in describing below the intrinsic disordering of fluorites, we shall start from the qualitative analogy inherent in their thermal and impurity disordering: There is a tendency at low temperatures to form cluster structures, whereas there is a tendency at high temperatures to form clusters of large extent.[1,7–10,34] Simultaneous thermal disordering of impurity and intrinsic cluster complexes promotes the reduction of the temperature for the transition into the superionic state.[8] Cluster complexes in doped crystals[34] and extended clusters in nominally pure crystals[7] are oriented along definite directions.

When the $V{:}I{:}R$ cluster was constructed, the well-known[10,17] cluster of type 2:2:2 was used as a prototype. The $V{:}I{:}R{:}C$ cluster is constructed arbitrarily: An interstitial cation is added to one of the empty anion cubes. Different versions of the construction of both the clusters and of the complexes based on them are possible in principle. For example, a linear (crowd-ion) cluster can be formed with the

interstitial ions placed along any definite direction. (Qualitatively similar structures were proposed in Ref. 7 as one version in describing thermal disordering in the superionic phase.) However, a stability problem arises in such structures.

Let us assume that the principle of local charge compensation of the interstitial ions should be used during their construction. This principle is closely obeyed in doped fluorite crystals.[9,10]

Figure 6b shows a modified $V{:}I{:}R{:}C$-cluster model. It should be pointed out that all those considerations that related to questions of radiation disordering on the basis of an arbitrarily constructed model (Fig. 6a) are valid for this. Versions of the construction of oriented cluster complexes in the fluorite lattice are shown in Fig. 7. Unlike clusters used to describe thermal disordering,[1,7] our models do not contain free anion vacancies. This makes it possible to explain the low conductivity of fluorites at room temperature and to assume a mechanism for thermally activating it: for example, bond breaking in a $V-R$ pair. This mechanism requires significant energy expenditure and must be implemented at a rather high temperature (i.e., in thermally disordered samples). Actually, the irradiation of samples quenched from $T_q \geqslant 1000$ K causes stable coloration that is qualitatively similar to what appears with additive coloration of nominally pure CaF_2.

Additional disordering of the anion sublattice similar to what occurs in doped samples[1,9] will be observed in the near-boundary regions (between clusters and complexes). It can be understood from this why low-temperature ($T<T_D$) diffusion is described from a single viewpoint in nominally pure and doped crystals: reorientation hopping of ''locally coupled'' anions.[16] Moreover, a change in the symmetry of the surroundings of an impurity can be observed at temperatures (about 50 K, Ref. 35) at which not only diffusional but also reorientational processes would seem to be frozen. It is logical to assume that the local configuration instability of the impurity is also the consequence of defect-clustering processes of intrinsic and impurity nature.

We assume that it is the reorientational hopping of the anions in the near-boundary regions between the clusters and their complexes that causes the output of the fast ($\tau_1 = 10$ ns, $T = 80$ K) component in the luminescence damping to change as a function of either the temperature during irradiation of the standard CaF_2,[3,23] or T_q at fixed irradiation temperature of the quenched samples (see Figs. 1a–1c). It is assumed[3,23] that the fast component in the CaF_2 luminescence appears when electrons recombine with isolated V_k centers. However, the complex spectral content of this luminescence and its variation as a function of T_q (Figs. 1a–1c) indicate that the clusters have a perturbing effect on the V_k centers. It is no accident that not only the CE of the V_k centers[13] but also their thermal stability[12] changes in the doped fluorites as the irradiation temperature increases.

References 3, 23, and 27 associate the slow component ($\tau_2 \approx 40$ μs, $T = 80$ K) in the luminescence quenching of CaF_2 with the radiative annihilation of AEs. The lifetime of an AE is determined by the time an electron can spend on an anion vacancy; the radiative transition is allowed.[19] An AE

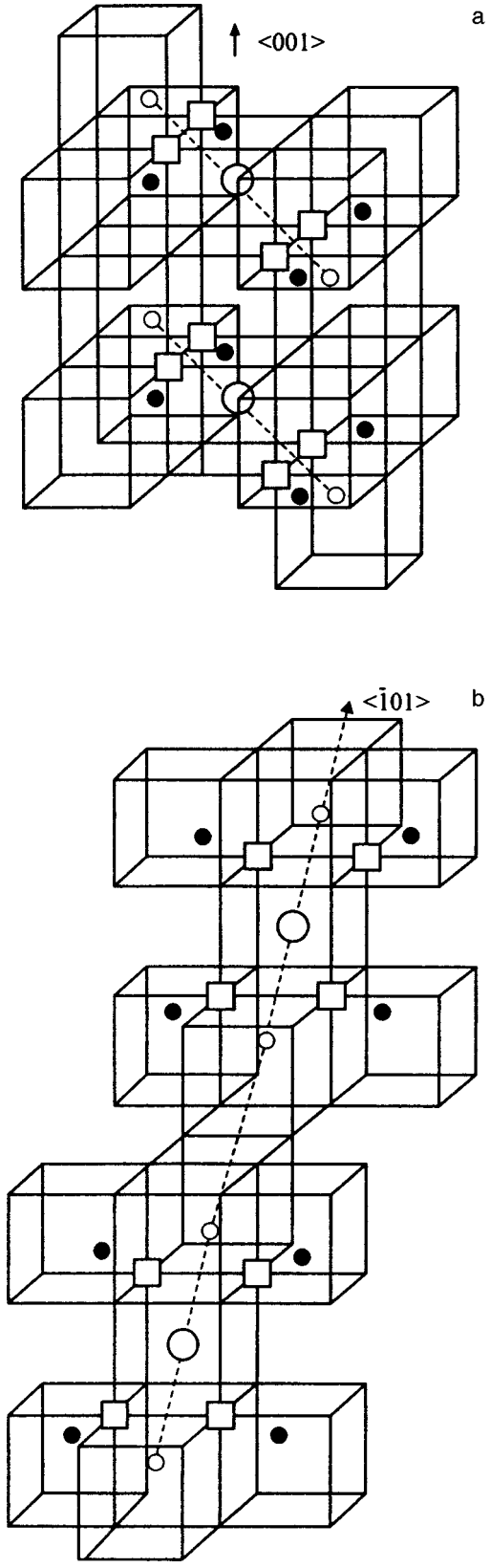

FIG. 7. Schematic representation of cluster complexes in a fluorite lattice oriented along the $\langle 001 \rangle$ (a) and $\langle -101 \rangle$ directions (b). The notation corresponds to that used in Fig. 6.

can be created in a damaged lattice as a result of the direct radiative separation of a $V-R$ pair. Higher energy expenditures are necessary to thermally separate a $V-R$ pair than for reorientation hoppings of locally coupled anions. Therefore, by comparison with the fast component, the output of the slow luminescence component in CaF_2 changes insignificantly with increasing irradiation temperature of the standard samples[3,23] or increasing T_q at fixed irradiation temperature of the quenched samples (see Figs. 1a and 1b).

Finally, we should dwell on the mechanism of post-radiation AE formation with optical or thermal stimulation of recombination of the type (V_k+e^-).[3,22] It is assumed that prolonged irradiation of fluorites at low temperature (<77 K) promotes the accumulation of correlated defects, since the Coulomb field of a hole next to a captured electron is partially screened.[3] However, no correlated stable defects are formed in crystals with pre-radiation AFDs, since, when a vacancy and an interstitial are close to each other, there is no barrier against recombination.[17]

If the pre-radiation defects form clusters, the formation of correlated defects can be represented as follows: With radiation separation of $V-R$ pairs, the localization of an electron on the resulting vacancy results in the formation of an F center, in the neighborhood of which a V_k center stabilized by an interstitial is formed. The presence of an interstitial prevents not only spontaneous transfer of the bond of the V_k center and AE formation directly during irradiation but also the recombination of free electrons with them; i.e., it is possible to form correlated pairs and triplets (type V_k,I,F) of defects both in AHCs[31] and in fluorites. The transfer of a bond with AE formation is possible in an excited state of the V_k center, i.e., during recombination with optically or thermally liberated F electrons. The formation of AEs during activation of the motion of V_k centers occurs in a qualitatively similar way in the case of uncorrelated pairs.

Depending on the growth conditions of nominally pure crystals, various clusters and complexes based on them can be formed. It is evident that, when crystals with different prehistories are cold-quenched, reorientational and diffusional hopping of anions can produce different effects when the crystals are irradiated (Figs. 1–3). The presence of oriented cluster complexes makes it possible to qualitatively explain the origin of local stresses and of spatial modulation of the CE of various AE configurations (Fig. 4), as well as the high degree of polarization of the absorption (Fig. 5) in the untreated samples.

In this paper, the authors have mainly adhered to commonly used terminology, although it is quite obvious why the classical theory of point defects is inapplicable for describing not only impurity and thermal disordering of fluorites[36] but also radiation disordering. The mesoscopic (cluster) approach to describing the intrinsic disordering of actual crystals does not require the presence of a high concentration of thermodynamically nonequilibrium defects and makes it possible to unambiguously explain the cause of the appearance of ferroelectric properties[37] and superionic conductivity in fluorites.

[1] *Inorganic Solid Fluorides: Chemistry and Physics*, edited by P. Hagenmuller (Academic Press, Orlando, Florida, 1985).
[2] P. J. Call, W. Hayes, and M. N. Kabler, J. Phys. C **8**, 160 (1975); N. G. Romanov, V. A. Vetrov, and P. G. Baranov, JETP Lett. **37**, 386 (1983).
[3] R. T. Williams, M. N. Kabler, W. Hayes, and J. P. H. Stott, Phys. Rev. B **14**, 725 (1976).
[4] T. Eshita, K. Tanimura, and N. Itoh, Phys. Status Solidi B **122**, 489 (1984).
[5] C. H. Leung, C. G. Zhang, and K. S. Song, J. Phys.: Condens. Matter. **4**, 1489 (1992).
[6] L. A. Lisitsyna, V. M. Lisitsyn, and E. P. Chinkov, Izv. Vyssh. Uchebn. Zaved. Fiz. No. 1, 13 (1995).
[7] A. R. Allnatt, A. V. Chadwick, and P. W. M. Jacobs, Proc. R. Soc. London, Ser. A **410**, No. 1839, 385 (1987).
[8] E. Vlieg, H. M. den Hartog, and M. Winnink, Phys. Chem. Solids **47**, 521 (1986); A. V. Chadwick, Solid State Ionics **8**, 209 (1983).
[9] A. K. Cheetham, B. E. F. Fender, and M. J. Cooper, J. Phys. C **4**, 3107 (1971).
[10] C. R. A. Catlow, J. Phys. C **9**, 1845 (1975).
[11] A. Amara, G. Cremer, F. Martin-Brunetiere, and M. Thuau, J. Phys.: Condens. Matter **1**, 10 281 (1989).
[12] E. P. Chinkov, *Abstracts of the Sixth International Conference on Radiative Heterodyne Processes*, Kemerovo (1995), p. 124.
[13] R. G. Deĭch and V. I. Flerov, Izv. Akad. Nauk LatvSSR No. 6, 42 (1977).
[14] I. Parakash and A. K. Nishad Rahul, Jpn. J. Appl. Phys., Part 1 **25**, (Pt 1), 701 (1985).
[15] J. Berak and W. Szuszkiewicz, Rocz. Chem. **57**, 2463 (1977).
[16] S. H. N. Wei and D. C. Ailion, Phys. Rev. B **19**, 4470 (1979).
[17] C. R. A. Catlow and W. Hayes, J. Phys. C **15**, No. 3, L9 (1982).
[18] É. D. Aluker, V. V. Gavrilov, R. G. Deĭch, and S. A. Chernov, *Fast Radiatively Stimulated Processes in Alkali Halide Crystals* (Zinatne, Riga, 1987).
[19] E. P. Chinkov and V. F. Shtan'ko, Fiz. Tverd. Tela **39**, 1197 (1997) [Phys. Solid State **39**, 1060 (1997)]; Fiz. Tverd. Tela **40**, 1226 (1998) [Phys. Solid State **40**, 1117 (1998)].
[20] V. F. Shtan'ko and E. P. Chinkov, Pis'ma Zh. Tekh. Fiz. **23**, No. 21, 45 (1997) [Tech. Phys. Lett. **23**, 837 (1997)]; Fiz. Tverd. Tela **40**, 1228 (1998) [Phys. Solid State **40**, 1119 (1998)]; Fiz. Tverd. Tela **40**, 1460 (1998) [Phys. Solid State **40**, 1326 (1998)].
[21] V. A. Arkhangel'skaya, V. M. Reĭterov, and L. M. Trofimova, Zh. Prikl. Spektrosk. **32**, 103 (1980).
[22] *Crystals with the Fluorite Structure: Electronic, Vibrational and Defect Properties*, edited by W. Hayes (Clarendon Press, Oxford, 1974).
[23] N. N. Ershov, N. G. Zakharov, and P. A. Rodnyĭ, Opt. Spektrosk. **53**, 89 (1982) [Opt. Spectrosc. **53**, 51 (1982)]; N. N. Ershov, N. G. Zakharov, V. M. Reĭterov, and P. A. Rodnyĭ, Opt. Spektrosk. **52**, 372 (1982) [Opt. Spectrosc. **52**, 222 (1982)].
[24] L. A. Lisitsyna, V. M. Reĭterov, V. M. Lisitsyn, E. P. Chinkov, and L. M. Trofimova, Opt. Spektrosk. **55**, 875 (1983) [Opt. Spectrosc. **55**, 526 (1983)].
[25] R. Birsoy, Phys. Status Solidi A **62**, 169 (1980).
[26] R. Rauch and G. Schwotzer, Phys. Status Solidi A **74**, 123 (1982).
[27] K. Tanimura, T. Katoh, and N. Itoh, Phys. Rev. B **40**, 1282 (1989).
[28] L. Dressler, Cryst. Res. Technol. **21**, No. 4, K53 (1986).
[29] E. D. Thoma, H. M. Yochum, and R. T. Williams, Phys. Rev. B **56**, 8001 (1997).
[30] C. R. A. Catlow, J. Phys. C **12**, 969 (1979).
[31] Ch. B. Lushchik and A. Ch. Lushchik, *Decay of Electronic Excitations with the Formation of Defects in Solids* (Nauka, Moscow, 1989).
[32] L. A. Lisitsyna, Izv. Vyssh. Uchebn. Zaved. Fiz. No. 8, 115 (1995); Izv. Vyssh. Uchebn. Zaved. Fiz. No. 11, 57 (1996).
[33] M. C. Day, Jr. and D. Selbin, *Theoretical Inorganic Chemistry* (Reinhold, New York, 1962; Khimiya, Moscow, 1975).
[34] N. H. Andersen, R. N. Clausen, J. K. Kjems, and J. Schoonmam, J. Phys. C **19**, 2377 (1986).
[35] V. S. Vikhnin, Pis'ma Zh. Tekh. Fiz. **12**, 586 (1986) [Sov. Tech. Phys. Lett. **12**, 240 (1986)].
[36] V. I. Arkharov, Fiz. Tverd. Tela (Karkhov) **20**, 4 (1990); V. A. Mezrin, Phys. Status Solidi A **114**, 145 (1989).
[37] S. Sawada, S. Hirotsu, M. Takashige, Y. Shiroishi, and H. Iwamura, J. Phys. Soc. Jpn. **36**, 1211 (1974).

Translated by W. J. Manthey

The effect of hydrogen atoms on the mobility of edge dislocations

N. M. Vlasov and V. A. Zaznoba

Luch State Scientific Research Institute Scientific Manufacturing Organization, 142100 Podol'sk, Moscow Region, Russia

(Submitted June 4, 1998; resubmitted September 1, 1998)
Fiz. Tverd. Tela (St. Petersburg) **41**, 451–453 (March 1999)

This paper discusses the process by which a thermodynamically unstable impurity atmosphere consisting of hydrogen atoms displaces an edge dislocation. Relationships are obtained for the displacement force in the approximation of dilute solid solutions. The results of theoretical analysis are used to explain the hydrogen embrittlement of nonhydride-forming metals.
 [S1063-7834(99)01603-2]

The results of numerous studies show that the hydrogen embrittlement of metals is closely related to defects in the crystal structure.[1–5] For hydride-forming metals, embrittlement in a hydrogen medium is associated with the formation of hydride phases close to structural imperfections. If the metals do not form hydride phases, their embrittlement on a macroscopic scale shows up as the coalescence of dislocation microcracks with a major crack. In this case, an increase of the mobility of the edge dislocations is experimentally observed in the presence of hydrogen.[6,7] However, the physical mechanism of this phenomenon is not quite clear. This paper attempts to describe quantitatively how hydrogen atoms affect the mobility increase of edge dislocations. The results of a theoretical analysis have been used to explain hydrogen embrittlement of nonhydride-forming metals.

The physical mechanism of the mobility increase of edge dislocations is based on the assumption that a thermodynamically unstable impurity atmosphere forms because hydrogen electrostatically interacts with the compression region of an edge dislocation. Such an interaction occurs because hydrogen can occur in metals in an anion state (a proton and two bound electrons).[8] The positive charge of the compression region of an edge dislocation results from the transition of electrons from the compression region to a tensile region in accordance with the dilatation field of the edge dislocation. Since the electrostatic interaction of the impurity atom with the edge dislocation in a number of cases exceeds the elastic interaction due to the size effect by a factor of 2 or 3,[2] impurity atmospheres made up of hydrogen atoms will form predominantly on the extra plane of the edge dislocation. After the crystal attains electrical neutrality, the hydrogen in octahedral or tetrahedral voids in the compression region of the edge dislocation is in the atomic state. Its behavior is now determined purely by elastic interaction with the edge dislocation. Since the solubility of hydrogen atoms in the compression region of an edge dislocation is lower than that in a tensile region, the existence of a thermodynamically unstable impurity atmosphere is energetically unfavorable. The energy of the system can be reduced by two methods: (1) diffusional migration of hydrogen atoms from the compression region to the tensile region of the edge dislocation, (2) displacement of the edge dislocation by the unstable impurity atmosphere. The former usually occurs when the hydrogen atoms have high diffusional mobility. The latter characterizes lower temperatures and low mobility of the hydrogen atoms. It is interesting to point out that hydrogen embrittlement occurs right away at temperatures from -100 to 100 °C.

Let us consider the physical essence of the mobility increase of edge dislocations in a hydrogen medium, using the elastic interaction of a dislocation with an unstable series of hydrogen atoms along a dislocation line over an extra plane as an example (Fig. 1a). Such an unstable system is formed by the electrostatic interaction of hydrogen in the form of an anion with the positively charged compression region of the edge dislocation. When the dislocation moves a distance x without changing the position of the hydrogen atom, the energy decrease of the dislocation–hydrogen-atom system (calculated per atomic plane) is written

$$\Delta W = \frac{\beta (x/r_0)^2}{r_0[1+(x/r_0)^2]},$$

where $\beta = \dfrac{\mu b}{3\pi}\dfrac{(1+\nu)}{(1-\nu)}\delta v$, μ is the shear modulus, ν is the Poisson ratio, b is the modulus of Brewster's vector of the edge dislocation, r_0 is the radius of the dislocation core, and δv is the volume change of the crystal when a hydrogen atom is introduced. Thus, for example, for transition metals, hydrogen atoms are located predominantly in tetrahedral sites. The corresponding size of the cavity for metals with a bcc lattice is $r_1 = 0.29R$, where R is the ionic radius of a solvent atom. For $R = 1.56$ Å (tungsten), $r_1 = 0.45$ Å, while the ionic radius of a hydrogen atom is $r_2 = 0.50$ Å. This means that, when a hydrogen atom is inserted, since the size difference of voids and hydrogen atom, the volume of the crystal changes by δv, and there is consequently an elastic interaction energy with the stress field of the edge dislocation. We should point out that δv can be expressed in terms of the partial volume $\bar{v}$ of the hydrogen impurities, i.e. $\delta v = \bar{v}/N_A$, where N_A is Avogadro's number. Thus, for example, for hydrogen atoms in iron, v is 2 cm^3/mol. The corresponding displacement force of the edge dislocation by an

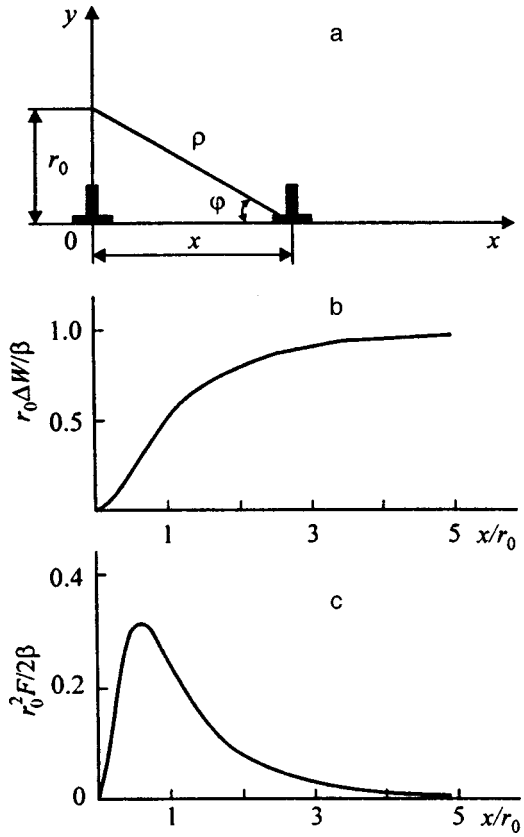

FIG. 1. Interaction of an edge dislocation with a hydrogen atom. (a) Relative location of the hydrogen atom and the dislocation, (b) energy decrease of the system as the dislocation moves, (c) displacement force of the edge dislocation by hydrogen atoms.

unstable series of hydrogen atoms (on an atomic plane) is determined as the derivative of the energy decrease of the system with respect to displacement x

$$F=-\frac{\partial(\Delta W)}{\partial x}=\frac{2\beta(x/r_0)}{r_0^2[1+(x/r_0)^2]^2}.$$

The graphical dependences of ΔW and F are shown in Figs. 1b and 1c. The maximum displacement force for $x=r_0/\sqrt{3}$ equals $F_{\max}=(3\sqrt{3}\beta)/(8r_0^2)$. Without applying an external load, the system is found in a state of unstable equilibrium, i.e., $F=0$ at $x=0$. A slight displacement of the dislocation from this position is accompanied by the appearance of a displacement force. Thus, the presence of hydrogen atoms over the extra plane of an edge dislocation decreases the activation energy of the formation of a double bend.[9]

The electrostatic interaction of hydrogen in the form of an anion with the positively charged compression region of an edge dislocation also causes a thermodynamically unstable impurity atmosphere to form in the neighborhood of the latter. Because of the electrical neutrality of the crystal, the hydrogen in the impurity atmosphere is present in the atomic state. Since the radius of the octahedral and tetrahedral voids into which the hydrogen atoms are inserted (especially in the compression region above the dislocation) is less than the radius of the hydrogen atom, the energy of the dislocation–impurity-atmosphere system is increased. As the dislocation slips, the energy of the system decreases; i.e., the unstable impurity atmosphere displaces the edge dislocation.

To quantitatively describe the effect under consideration, we write the concentration distribution of hydrogen atoms in the neighborhood of the dislocation line in the form

$$C=C_0\exp\left(\frac{\beta\sin\theta}{kTr}\right)$$

$$=C_0+\frac{C_0\beta\sin\theta}{kTr}+\frac{C_0}{2}\left(\frac{\beta}{kT}\right)^2\frac{\sin^2\theta}{r^2},$$

and, for $\beta/(kTr_0)<1$, we restrict ourselves to the term of the expansion that is linear in β

$$C-C_0=\frac{C_0\beta\sin\theta}{kTr},$$

where r and θ are polar coordinates, C_0 is the mean concentration of hydrogen atoms, k is Boltzmann's constant, and T is the absolute temperature. Below we write the energy decrease of the system when the dislocation moves by distance x with no change of the position of the cloud of hydrogen atoms (per unit length of the dislocation line)

$$\frac{\Delta W(x)}{L}=\int_{r_0}^{\infty}\int_0^{2\pi}\beta(C-C_0)\left(\frac{\sin\theta}{r}-\frac{\sin\varphi}{\rho}\right)r\,dr\,d\theta,$$

$$\rho^2=r^2+x^2-2rx\cos\varphi,\quad \rho\sin\varphi=r\sin\theta.$$

It is assumed that the velocity of the dislocation is much larger than the diffusional redistribution rate of hydrogen atoms close to the dislocation line. After some simple transformations, we get

$$\frac{\Delta W(x)}{L}=\frac{\pi C_0\beta^2}{kT}\left[\frac{1-(x/r_0)^2}{2(x/r_0)^2}+\ln\left(\frac{x}{r_0}\right)\right]\quad\text{for}\quad x>r_0,$$

$$\frac{\Delta W(x)}{L}=0\quad\text{for}\quad x\leqslant r_0.$$

Because of the logarithmic divergence of the expression $\Delta W(x)/L$, the displacement x must not exceed the mean distance between dislocations.

The displacement force of the edge dislocation by a thermodynamically unstable impurity atmosphere made up of hydrogen atoms is determined by the derivative of the energy decrease of the system with respect to displacement x (per unit length of the dislocation line)

$$\frac{F(x)}{L}=\frac{\pi C_0\beta^2}{r_0kT}-\left[\frac{r_0}{x}-\left(\frac{r_0}{x}\right)^3\right]\quad\text{for}\quad x>r_0,$$

$$\frac{F(x)}{L}=0\quad\text{for}\quad x\leqslant r_0.$$

The corresponding graphic dependences according to the equations for $\Delta W(x)/L$ and $F(x)/L$ are shown in Figs. 2a and 2b. In the region $(0\leqslant r\leqslant r_0)$, there is no displacement of the edge dislocation by the impurity atmosphere composed of hydrogen atoms. This is because, for a continuum description of the distribution in the hydrogen atom concentration, the region $(r_0<r<\infty)$ does not contribute to the displace-

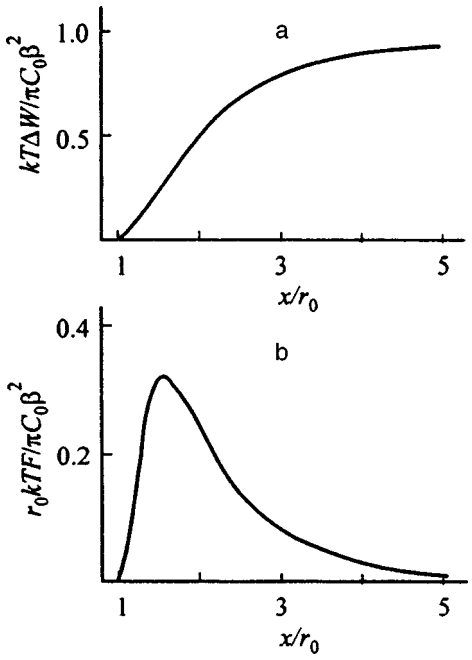

FIG. 2. Interaction of an edge dislocation with an unstable hydrogen atmosphere. (a) Energy change of the system as the dislocation moves, (b) displacement force of the edge dislocation by an impurity atmosphere composed of hydrogen atoms.

ment force when the dislocation line moves inside the zone $(0 \leqslant r \leqslant r_0)$. This result is physically general and characteristic of interactions that depend quadratically on the coordinates. The maximum $F(x)/L$ in the model used here is reached at $x = \sqrt{3}\, r_0$:

$$\left(\frac{F(x)}{L}\right)_{\max} = \frac{2\pi C_0 \beta^2}{3\sqrt{3}\, r_0 kT}.$$

For the Fe–H system ($\mu = 8.3\times 10^{10}$ N/m^2, $b = 2.48\times 10^{-10}$ m, $\nu = 0.28$, $kT = 10^{-20}$ J, $r_0 = 2b$, $C_0 = 10^{27}$ m^{-3}, and $\delta v = 3\times 10^{-30}$ m^3), $(F/L)_{\max} = 9\times 10^{-9}$ N/m, while the corresponding displacement stress is $\tau = (F/Lb) \simeq 0.37\times 10^8$ N/m^2 (37 MPa). This result physically means that an additional stress acts at an edge dislocation. On a macroscopic scale, this shows up as plasticizing of the material in a hydrogen medium. Naturally, such processes occur most intensely in the neighborhood of a crack vertex. This is because a crack vertex strongly concentrates external stresses. Moreover, the pressure of molecular hydrogen substantially contributes to the stressed state in a crack-shaped cavity. All this increases the mobility of edge dislocations. Dislocation microcracks are formed in front of the accumulation of such dislocations at an obstacle (for example, dislocation stoppers). The latter coalesce with the main crack, and this manifests itself as hydrogen embrittlement of nonhydride-forming materials.

In conclusion, we should point out that the process of displacing an edge dislocation by a thermodynamically unstable impurity atmosphere has the same nature as the process of pinning structural imperfections by impurity atoms.[10,11] It should also be mentioned that dislocation mobility is observed to increase in semiconductor crystals when they are doped with donor or acceptor impurities.[12] Thermodynamically unstable impurity atmospheres can be formed in this case because of the electrostatic interaction of the doping elements with various types of dislocations. These atmospheres displace the dislocations, and this shows up as a decrease of the activation energy of dislocation slip.

This work was carried out with the partial support of the International Scientific and Technical Center (Project No. 0.58-95).

[1] L. S. Moroz and B. B. Chechulin, *Hydrogen Embrittlement of Metals* (Metallurgiya, Moscow, 1967).
[2] P. V. Gel'd, R. A. Ryabov, and E. S. Kodes, *Hydrogen and Imperfections of Metal Structure* (Metallurgiya, Moscow, 1979).
[3] P. V. Gel'd, R. A. Ryabov, and L. P. Mokhracheva, *Hydrogen and the Physical Properties of Metals and Alloys* (Nauka, Moscow, 1985).
[4] N. M. Vlasov and B. Ya. Lyubov, Fiz. Khim. Obrab. Mater. **4**, 89 (1970).
[5] V. V. Kolesnikov, Fiz. Tverd. Tela **36**, 2648 (1994) [Phys. Solid State **36**, 1443 (1994)].
[6] D. S. Shin, I. M. Robertson, and H. K. Dirnbaum, Acta Metall. **36**, 111 (1988).
[7] L. V. Spivak, M. Ya. Kats, and N. E. Skryabina, Fiz. Met. Metalloved. No. 6, 142 (1991).
[8] G. S. Solov'ev, Zh. Éksp. Teor. Fiz. **68**, 1324 (1975) [Sov. Phys. JETP **41**, 658 (1975)].
[9] B. V. Petukhov, Fiz. Met. Metalloved. **56**, 1177 (1983).
[10] N. M. Vlasov and B. Ya. Lyubov, Dok. Akad. Nauk SSSR **259**, 348 (1981) [Sov. Phys. Dokl. **26**, 693 (1981)].
[11] N. M. Vlasov, Fiz. Met. Metalloved. **56**, 583 (1983).
[12] S. A. Erofeeva and Yu. A. Osip'yan, *The Dynamics of Dislocations: A Collection* (Naukova Dumka, Kiev, 1975), p. 26.

Translated by W. J. Manthey

Accumulation of dislocations and thermal strengthening of alloys having an $L1_2$ superstructure

V. A. Starenchenko, Yu. V. Solov'eva, and Yu. A. Abzaev

Tomsk State Architectural–Construction Academy, 634003 Tomsk, Russia
(Submitted July 20, 1998)
Fiz. Tverd. Tela (St. Petersburg) **41**, 454–460 (March 1999)

This paper discusses the dislocation-accumulation mechanism in alloys having an $L1_2$ superstructure, which is associated with the formation of Kira–Wilsdorf barriers and the retardation of superdislocations during plastic deformation. A model of the dislocation-accumulation kinetics during plastic deformation is constructed, on the basis of which a mathematical model is formulated for the thermal and deformation strengthening of single crystals of alloys having the $L1_2$ superstructure. The results of numerical calculations based on the model are compared with the experimentally observed regularities of the deformation and thermal strengthening of single crystals of Ni_3Ge. © *1999 American Institute of Physics.* [S1063-7834(99)01703-7]

As a result of experimental studies of the mechanical properties and the dislocation structure of single crystals of the intermetallic compound Ni_3Ge, we have established the following characteristics of the temperature dependence of the yield point, the strengthening curves, and the evolution of the dislocation structure of this alloy:[1–3]

(1) The temperature dependence of the yield point is multistage, and the upward branch of this dependence, formed under conditions of octahedral slip, can be described as two-stage, with two activation energies.

(2) As the temperature increases, the strengthening curves change shape from curves close to the strengthening curves of the pure metals in the low-temperature region to parabolic curves convex upward in the high-temperature region. The rates of change of the strengthening curves, like the intensity of the increase of the yield point, increase with temperature as one goes from multiple to single slip.

(3) The accumulation intensity of the dislocation density increases with temperature to a greater extent for single slip than for multiple slip.

(4) Kira–Wilsdorf (KW) barriers are intensely accumulated in the region of moderate temperatures (near room temperature). At higher temperatures, a process of displacement of the KW barriers by dislocations blocked in arbitrary nonrectilinear configurations is observed, and the intensity of the accumulation of KW barriers decreases.

(5) The length of the KW barriers is proportional to the distance between the dislocations of the ''forest.''

(6) In orientations close to the [111] angle of a stereographic triangle, a maximum in the temperature dependence of the yield point is observed in the high-temperature region under conditions in which the deformation occurs by cubic slip. The dislocation structure is formed in this case by edge-oriented blocked dislocations.

This collection of experimental data suggests that the processes of thermal hardening in alloys having an $L1_2$ superstructure involve not only the mechanisms of blocking screw dislocations caused by the formation of KW barriers, but also mechanisms associated with the climbing of edge dislocations when they interact with point defects.

This paper proposes a mathematical model of thermal hardening that takes into account the features of the formation of KW barriers in the presence of forest dislocations, as well as the interaction with point defects and its influence on the process of forming KW barriers. This model also describes certain regularities in the formation of the dislocation structure of yield and the strengthening curves in intermetallic compounds having an $L1_2$ superstructure.

1. THE LENGTH OF KIRA–WILSDORF BARRIERS

A superdislocation that crosses the dislocations of other slip systems, as it moves under the action of deforming stresses, acquires a complex configuration consisting of a set of dislocation segments pinned by interdislocation reactions. Let us consider a dislocation segment of screw orientation located in the (111) plane and pinned at the ends at points A and B in the field of shear stresses τ (Fig. 1).

Under the action of stress τ, a free dislocation segment takes on the shape of an arc with a radius of curvature $R=2Gb/\tau$,[4] where $2b$ is the modulus of Brewster's vector of the superdislocation, and G is the shear modulus. Let the dislocation segment change its configuration because of thermal fluctuation: The guiding superparticle dislocation passes into the (100) plane; i.e., it begins to form a KW barrier (the initial stage of the thermal-fluctuation formation of KW barriers is discussed in detail in Refs. 5 and 6; here we present calculations of the activation energy of KW-barrier formation). As a result, a new configuration appears, consisting of a straight segment of a superdislocation (length x), which is the KW barrier, and of two arcs of radius R, which are superdislocations that remain in the (111) plane (Fig. 1).

Let us determine the length x of the resulting barrier from a consideration of the energy of the resulting disloca-

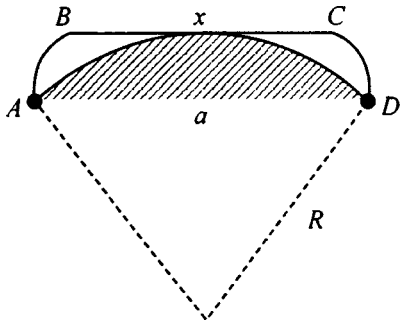

FIG. 1. Diagram of the variation of the configuration of a dislocation segment when a Kira–Wilsdorf barrier is formed.

tion configuration, which can be written approximately as a sum of the energies of the KW barriers and of the segments lying in the plane of the octahedron,

$$U = xU_k + U_s(AB + CD), \tag{1}$$

where U_k is the energy per unit length of the KW barrier, and U_s is the dislocation energy in the plane of the octahedron. The meaning of the other quantities is clear from Fig. 1. We recall that a configuration with a KW barrier has appeared in a stress field, as a consequence of which part of the energy is acquired by the barrier at the expense of the work done by the stress. Then the function whose minimum will determine the linear size x of the KW barrier takes the form

$$\phi(x) = U_k x + U_s(AB + CD) + 4\tau_{(111)} bS(x) - \tau_{(100)} bx\delta, \tag{2}$$

where $S(x)$ is the area covered by segments AB and CD; $\tau_{(111)}$ and $\tau_{(100)}$ are the stresses in the planes of the octahedron and the cube, respectively; and δ is the width of the superdislocation in the plane of the cube.

Neglecting the splitting of the superparticle dislocations, we represent the energies U_k and U_s as a sum of the energies of the antiphase boundaries included between the superdislocations ($U^{(1)}$), the elastic interaction energies of the superparticle dislocations ($U^{(2)}$), and the intrinsic energies of the superdislocations ($U^{(3)}$):

$$U_k = U_k^{(1)} + U_k^{(2)} + U_k^{(3)}, \quad U_s = U_s^{(1)} + U_s^{(2)} + U_s^{(3)}. \tag{3}$$

In the calculation per unit dislocation length, it can be assumed that

$$U_k = \zeta_{(100)} r_1 - \frac{Gb^2}{2\pi} \ln \frac{r_1}{R_0} + 2Gb^2,$$

$$U_s = \zeta_{(111)} r_2 - \frac{Gb^2}{2\pi} \ln \frac{r_2}{R_0} + 2Gb^2. \tag{4}$$

Here $\zeta_{(100)}$ and $\zeta_{(111)}$ are the energies of the antiphase boundaries (APBs) in planes (100) and (111), r_1 and r_2 are the widths of the superdislocation, and R_0 is the screening radius of the elastic field of the dislocation. The width of the superdislocation in the plane of the octahedron is determined from the equilibrium condition of the tensile forces of the APBs and the elastic repulsion forces of the superparticle dislocations[7]

$$r_2 = Gb^2/2\pi\zeta^{(111)}. \tag{5}$$

In the case of a KW barrier, when determining its width, it is also necessary to allow for the stress that acts in this plane, since one of the superparticle dislocations is pinned in the process of forming the barrier. Taking this circumstance into account leads to the expression

$$r_2 = Gb^2/2\pi(\zeta_{(100)} - \tau_{(100)} b). \tag{6}$$

Using the explicit form of $S(x)$, Eq. (2) can be reduced to

$$\phi(x) = 4U_s R \sin Y + U_k x - \tau_{(100)} b\delta x - 2\tau b\Big\{[R - \sqrt{R^2 - a^2/4}]\frac{x}{4} - \frac{R^2}{2}(2\arcsin Y + 2\sin Y - \sin(\arcsin Y) + 2\sin Z - \sin(2\arcsin Z))\Big\}, \tag{7}$$

where

$$Y = \frac{\sqrt{(a-x)^2/4 + (R + \sqrt{R^2 - a^2/4})^2}}{2R},$$

$$Z = \frac{\sqrt{a^2/4 + (R + \sqrt{R^2 - a^2/4})^2}}{2R}.$$

Function $\phi(x)$ has a minimum on the interval $x \in [0,a]$, whose position depends on the value of $\gamma = \zeta_{(100)}/\zeta_{(111)}$ and is determined by

$$\frac{d\phi(x)}{dx} = 0, \tag{8}$$

which determines the equilibrium length of the KW barrier as a function of the parameters included in $\phi(x)$.

Without presenting the results of calculations using Eq. (8) for the parameters that characterize Ni_3Ge ($G = 70$ GPa, $\rho = 10^{14}$ m^{-2}, $b = 2.5 \times 10^{-10}$ m, $\tau = 175$ MPa, $\zeta = 0.25$ J/m^2, $R = 2Gb/\tau$, $a = 1/\sqrt{\rho}$),[8] let us consider their qualitative analysis.

Increasing the dislocation density increases the deforming stresses (it is assumed here that $\tau = \alpha Gb\rho^{1/2}$, $\alpha = 1$), which in turn increases the relative length of the barrier. This change is not very great and does not exceed 10% as the dislocation density increases by an order of magnitude.

The variation of the stresses in the plane of the cube (it was assumed that $\tau_{(100)} = \beta\tau_{(111)}$) does not significantly change the barrier length. Changing the value of β from 0 to 1.5 changes the barrier length by a factor of 1.1. It should be pointed out, however, that, for large stresses $\tau_{(100)}$, it is possible to form short KW barriers ($x/a \approx 0.1$) even with identical APB energies in the planes of the octahedron and the cube, and this is evidence that it is possible for barriers to appear with resplitting in the stress field of superdislocations in the planes of the octahedron.

The leading parameter that determines the barrier length is the relative change of the APB energy during a transition of the superdislocation into the plane of the cube (parameter $\gamma = \zeta_{(100)}/\zeta_{(111)}$), whose variation can produce extremely significant changes of the barrier lengths, to the point where they disappear. For the parameters that characterize Ni_3Ge

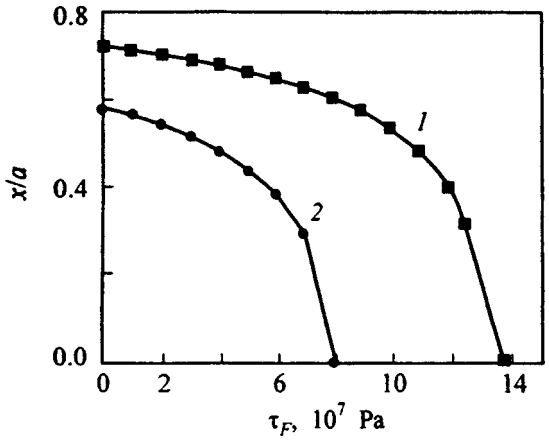

FIG. 2. Relative length of a Kira–Wilsdorf barrier vs friction stress $\gamma=0.2$ (*1*) and 0.5 (*2*).

($\gamma\approx 0.2$), the barrier length is $\approx 0.7a$, where a is the distance between the points where the superdislocation segment is pinned.

To further analyze the KW barriers, it is necessary to allow for at least two factors. The former is associated with the fact that segments *AB* and *CD* during the formation of the barrier acquire an orientation that approximates an edge orientation and consequently experience additional retardation τ_F when these segments interact with point defects. The equilibrium length in this case must be determined by function $\phi^*(x)=\phi(x)+\tau_F S(x)$. The second factor is that, when a barrier is formed, the angle of attack changes at the stopper that pins the dislocation segment. If the angle exceeds a critical value, this breaks through the stopper and increases the length of the KW barrier.

Let us consider the first factor. Calculations (it was assumed that $\rho=10^{12}$ m^{-2}, $\tau=60$ MPa, $\beta=1$) of the dependence of the relative length of the KW barrier on the frictional stress of the edge component of the dislocation segment for various values of the APB energy showed that there is a significant dependence of the KW barrier length on the friction experienced by the edge component of the loop (Fig. 2). As soon as the friction exceeds the acting stress by 25%, the formation of KW barriers becomes energetically unfavorable for moderate APB energies ($\zeta\approx 0.5$ J/m^2). At high APB energies, higher frictional stresses are required in order to halt the barrier-formation process.

The dependence of the KW barrier length on the value of the friction experienced by the edge dislocations can have the result that, as the temperature increases, despite the increase of the probability of forming these barriers, their overall length will decrease as a consequence of the ''displacement'' of the edge components of the dislocation loop.

Let us consider the possibility that the inter-dislocation reactions that pin the free segments of the dislocations will break down, taking into account the frictional forces of the edge dislocation. We shall assume that the length of the dislocation barrier (for $\zeta=0.2$ J/m^2) will take equilibrium values corresponding to the minimum of function $\phi^*(x)$. On this assumption, estimates of the variation of the angle of attack at the stoppers that pin a dislocation segment show

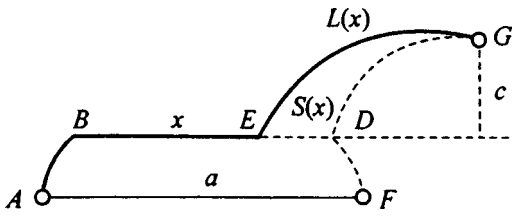

FIG. 3. Diagram of the breakdown of a Kira–Wilsdorf barrier. *ABDF* is the initial configuration of the Kira–Wilsdorf barrier (*A* and *F* are dislocation reactions); *ABEG* is the configuration that results from the breakdown of reaction *F* [*G* is a new stopper that prevents segment $L(x)$ from moving].

that the rupture stresses of a stopper vary in different ways when a KW barrier appears, depending on the critical angle of attack (i.e., the strength of the stopper). In this case, little sensitivity to the presence of a barrier is shown by the rupture stresses of weak stoppers (whose critical angle of attack is 2.8–3 rad) or very strong stoppers, which are overcome by the Orovan mechanism (and whose critical angles are close to zero). The stress of overcoming stoppers of moderate strength can vary by 20–25%. In the presence of friction (τ_F), the strength of the stoppers varies less, the larger the frictional stress.

The variation of the strength of the stoppers will have the effect that the KW barriers, when they appear, will not be held back by the nearest-neighbor stoppers; on the contrary, by rupturing stoppers of moderate strength, they will increase their length until they reach a high-strength stopper.

It is possible, therefore, to assume that the mean length of a KW barrier is proportional to the distance between strong stoppers, which in the given case are high-strength interdislocation reactions. Without loss of generality, we can set $L=\omega\rho^{-1/2}$, where L is the length of a KW barrier, ρ is the dislocation density of the forest, and ω is a constant of proportionality. This assumption allows us to calculate the intensity of the accumulation of dislocations, which is connected with the formation of KW barriers.

2. THE STRENGTH OF KIRA–WILSDORF BARRIERS. THEIR CONTRIBUTION TO THE RESISTANCE TO THE MOTION OF DISLOCATIONS

It is traditional to assume that KW barriers make a large contribution to the resistance to the motion of dislocations, which reaches a limiting value of $\tau\approx\zeta/b$, where ζ is the APB energy. Such an opinion is associated, first of all, with the fact that the dislocations are treated as point objects; in this connection, the stress needed to break down a KW barrier equals ζ/b, since dislocation motion requires that an APB sweep through a (111) plane.[9]

In reality, a dislocation is not a point object and, therefore, may the mechanism of breaking down a KW barrier can be different. Several versions are possible: (1) the KW barrier is pinned at the ends by interdislocation reactions, which break down at a certain critical angle; (2) the KW barrier is overcome by the Orovan mechanism. In the former case, the configuration shown in Fig. 3 appears. In this configuration, x is the KW barrier length, and $L(x)$ is the length of the moveable dislocation segment. The question of the strength

of the KW barrier in this case reduces to the question of the equilibrium of the dislocation configuration shown in Fig. 3 in a field of shear stresses τ. The problem reduces to finding the minimum of the function

$$\Phi(x)=xU_k+L(x)U_s-\tau bS(x), \tag{9}$$

where $S(x)$ is the area covered by segment L. The solution of the problem shows that the KW barriers are broken down by a stress whose value is close to the values of $\tau\approx\alpha Gb\rho^{1/2}$ determined by the resistance of the dislocation forest. Only barriers for which the parameter $c\cong 0$ can be maintained at higher stresses. Barriers pinned by strong interdislocation reactions whose critical angle is close to zero are stable against the action of external stress. The KW barrier in this case can be overcome by the Orovan mechanism, and the corresponding barrier strength will be determined by this stress.

Let us estimate the contribution that the barriers thus formed will make to the resistance to the motion of dislocations. In the first case, the contribution will be determined by the area of the barriers in the shear zone and by the energy difference $\Delta U=U_k-U_s$.

As a result of thermal fluctuations, let N barriers per unit area appear in the shear zone, which are then broken down as the dislocation loop moves farther. The mean length of such virtual barriers can be taken as approximately equal to $\rho^{-1/2}$, i.e., equal to the length of a free segment of a dislocation.

The work of deformation performed by the external stress $(\tau\Delta a)$ equals the work put into broadening the dislocation loops. Then

$$\tau=\frac{\delta A}{b\Delta S}, \tag{10}$$

where S is the mean area covered by a dislocation loop during the formation of a shear zone, and

$$\delta A=\delta A_s+\delta A_\rho+\delta A_F. \tag{11}$$

Here A_s is the work put into breaking down the KW barriers, A_ρ is the work to overcome the dislocation forest, and A_F is the work of the frictional forces. The work put into breaking down the KW barriers equals

$$\delta A_s=NS\rho^{-1/2}\Delta U, \quad N=\frac{\nu b}{v}\frac{w_s}{l_{cs}^2}\exp\left(-\frac{U}{kT}\right), \tag{12}$$

where ν is the Debye frequency, w_s is the fraction of screw dislocations, l_{cs} is the length of the section of the dislocation that experiences thermally activated recombination, U is the activation energy for forming a KW barrier, and v is the mean velocity of the dislocation. Then

$$\frac{dA_s}{dS}=\tau_s\cong\frac{\nu b}{v}\frac{w_s}{l_{cs}^2}\Delta U\exp\left(-\frac{U}{kT}\right).$$

In the limiting case $(T\to\infty)$,

$$\exp\left(-\frac{U}{kT}\right)=1; \quad \tau_s^{(\max)}\cong\frac{\nu b}{v}\frac{w_s}{l_{cs}^2}\Delta U\rho^{-1/2}.$$

Let us estimate τ_s from the following considerations: $w_s\approx 0.5$, $v\approx 100$ m/sec, $\nu=10^{13}$ sec^{-1}, $l_{cs}=10^{-6}$ m.[9] At the yield point ($\rho^{-1/2}\approx 10^{-6}$ m^{-1}, $\Delta U\approx 7\times 10^9$ eV$\cdot$m^{-1}, $\tau_s^{(\max)}\approx 13.4$ MPa), we get a value that is small even by comparison with the contribution to the resistance to motion from the forest dislocations.

When a KW barrier is overcome by the Orovan mechanism, the value of ΔU is determined by the energy needed to form the dislocation that completes a dislocation dipole configuration. This energy can be assumed to be approximately equal to $U_s\approx 1.3\times 10^{11}$ eV$\cdot$m^{-1}, which, when τ_s is computed, gives $\tau\approx 200$ MPa. This overestimated result makes it possible to obtain the maximum value $\tau_s^{(\max)}$. It is smaller by more than a factor of 2 than the quantity ζ/b and accordingly significantly less than the experimentally observed value of the yield point in the temperature region of the anomaly peak.

3. INTENSITY OF THE ACCUMULATION OF DISLOCATIONS DETERMINED BY THE KIRA–WILSDORF MECHANISM

Let us consider the process of accumulating dislocations during plastic deformation. We shall assume that plastic deformation is a consequence of the formation of shear zones—regions of retarded shear. Let n dislocation shear-forming loops be emitted during the operation of the dislocation source, as a result of the broadening of which a shear zone was formed. A certain structure is formed from the dislocations when they stop moving. All the dislocations that result from the appearance of a shear zone can be separated into two categories in this case: intrazone dislocations, which are always dipole structures (because of the conservation of Brewster's vector) so that, on the scale of the shear zone, they do not carry excess dislocation charge, and peripheral dislocation clusters, which are retarded shear-forming dislocations and, on the scale of the shear zone, do carry excess charge. The density accumulations of these two types of dislocation obey different laws, since the density of the intrazone dislocations is proportional to the area of the shear zone, while the density of the peripheral dislocations is proportional to the length of its perimeter. Let a shear zone be formed as a result of the broadening of one dislocation loop emitted by the source. A dislocation-density increment $\Delta\rho_i$ then results from the increase in the number of both the peripheral and the internal dislocations. Calculated per unit volume, this is

$$\Delta\rho_i=\frac{\Gamma_1 D+L_s\Gamma_2 D^2}{V_i}, \tag{13}$$

where D is the mean diameter of the shear zone, Γ_1 and Γ_2 are factors that connect the perimeter and area of a shear zone of a given geometry, L_s is the mean length of the intrazone dislocations arriving at unit area of the zone, and V_i is the volume of the crystal belonging to one shear zone.

The value of the shear that results from the generation of one loop equals $\Delta a_i=b\Delta S$, where ΔS is the area covered by a dislocation loop when a shear zone is formed ($\Delta S\cong\Gamma_2 D^2-\chi d^2$, χd^2 is the area limited by the intrazone loops, d is the mean size of the loops that remain inside the

zone, and χ is a geometrical factor). Then, neglecting the area of the intrazone loops ($\chi d^2 \ll \Gamma_2 D^2$), we get

$$a_i = b\Gamma_2 D^2 / V_i . \tag{14}$$

If $\langle D \rangle$ represents the mean size of the shear-forming loops, the overall shear that appears during the broadening of n loops will equal

$$\Delta a = n\Delta a_i = n\Gamma_2 \langle D \rangle^2, \tag{15}$$

and the change in dislocation density is

$$\Delta \rho = n\Delta \rho_i . \tag{16}$$

Taking this into account, we get the dislocation-accumulation rate when a shear zone is formed:

$$\frac{\Delta \rho}{\Delta a} = \frac{\Gamma_1 \langle D \rangle}{B\Gamma_2 \langle D \rangle^2} + \frac{L}{b}\frac{\langle D \rangle^2}{\langle D \rangle^2} \rightarrow \frac{d\rho}{da} = \frac{\Gamma_1}{\Gamma_2 B \langle D \rangle} + \frac{L_s}{b}. \tag{17}$$

It is shown in Ref. 10 that $\langle D \rangle = \frac{B}{Gb}\frac{\tau}{\rho}$, where B is a constant of the material ($B = 180-1000$). Let us compute the term that determines the accumulation of intrazone dislocations when the KW mechanism is active. To do this, let us take into account, first of all, the fact that, as we have shown, the KW barrier length is proportional to the distance between the forest dislocations. The activation frequency of elementary recombination events of the screw sections of dislocations of length l_{cs}, by analogy with Ref. 9, can be written as $\gamma_s = \nu (b/l_{cs}) \exp(-U_s/kT)$, where l_{cs} is the length of the dislocation section that is undergoing thermally activated recombination, and U_s is the activation energy.

The number of dislocations formed per unit length in the time that a dislocation moves in a shear zone ($\Delta t = D/\upsilon$) of thermally activated recombined sections equals

$$K = \Delta t \gamma_s = \frac{D\nu b}{2\upsilon l_{cs}} \exp(-U_s/kT), \tag{18}$$

where υ is the mean velocity of the dislocation in the shear zone, and D is the mean size of the shear zone.

The thermally activated recombination of a screw section l_{cs}, as shown above, is accompanied by the formation of a KW barrier of length $\sim \rho^{-1/2}$. Then, assuming that the length of the dislocation remaining at the KW barrier is equal to $2\rho^{-1/2}$, we get that dislocations whose overall length equals

$$L_s = \frac{\nu b}{\upsilon}\frac{w_s \Gamma_1 D^2}{l_{cs}^2}\rho^{-1/2} \exp(-U_s/kT) \tag{19}$$

will be generated inside the shear zone because of the action of the KW mechanism.

Using Eq. (18), we get

$$\frac{\Delta \rho}{\Delta a} = \frac{\Gamma_1}{\Gamma_2 Db} + \frac{\nu w_s \Gamma_1}{l_{cs}^2 \upsilon \Gamma_2}\rho^{-1/2} \exp(-U_s/kT). \tag{20}$$

Recalling that $D = B\tau/ZGb\rho$ (Z is the number of acting slip systems),[10] while $\tau = \tau_F + \alpha Gb\rho^{1/2}$, we get that

$$\frac{d\rho}{da} = C_1 \frac{\rho}{\tau} + C_2 \alpha \frac{e^{-U_s/kT}}{\tau - \tau_F}, \tag{21}$$

where

$$C_1 = \frac{\Gamma_1 ZGb}{\Gamma_2 B}, \text{ and } C_2 = \frac{\nu w_s \Gamma_1}{l_{cs}^2 \upsilon \Gamma_2} Gb$$

can be taken as approximately temperature-independent constants. Then Eq. (21) will describe the dislocation-accumulation intensity at various temperatures.

Equation (21) is obtained on the assumption of multiple slip, i.e., on the assumption that the length of the free segment of a dislocation and the corresponding length of the KW barrier are proportional to the distance between dislocations, which varies during deformation.

In the case of single slip, it can be assumed in the idealized case that the density of forest dislocations does not change with deformation, but remains equal to the initial dislocation density ρ_0. Then, after obvious transformations, we get that

$$\frac{d\rho}{da} = C_1 \frac{\rho}{\tau} + C_2^* \exp(-U_s/kT), \tag{22}$$

where $C_2^* = C_2/Gb\rho_0$.

4. STRENGTHENING CURVES OF SINGLE CRYSTALS OF ALLOYS HAVING AN $L1_2$ SUPERSTRUCTURE

We recall that the resistance to the motion of the dislocations due to the dislocation forest is described in uniform dislocation structures by

$$\tau = \tau_F + \alpha Gb\rho^{1/2}. \tag{23}$$

For alloys having an $L1_2$ superstructure, the values of τ_F and α can be written as[1]

$$\tau_F = \tau_0^{(1)} \exp(-U_1/kT) + \tau_0^{(2)} \exp(-U_2/kT),$$
$$\alpha = \alpha_0 - \beta T, \tag{24}$$

where $\tau_0^{(1)}$, $\tau_0^{(2)}$, α_0, and β are constants that are independent of temperature, and U_1 and U_2 are the activation energies of the self-blocking of the screw and edge components of superdislocation loops. It follows from Eq. (23) that $d\tau/da = (\alpha Gb/2\sqrt{\rho})\, d\rho/da$. We obtained the value of $\frac{d\rho}{da}$ for multiple and single slip on the assumption that the only dislocation-accumulation mechanism is the KW mechanism. However, as mentioned above, a substantial role in the stabilization of the KW barriers that appear when dislocations move through the dislocation forest is played by the mobility of the edge components of the dislocations: Reducing the mobility of the edge components increases the number of such segments containing KW barriers that are surmounted by the Orovan mechanism and consequently increases the density of dislocations remaining inside the zone. The relative fraction of straight configurations then decreases. We take this circumstance into account in the relationship that describes the dislocation accumulation by supplementing the accumulation intensity by analogy with the KW mechanism

considered above, recalling that the activation energy in this case is determined by diffusion mechanisms. Allowing for this, we get the systems of differential equations

$$\begin{cases} \dfrac{d\rho}{da} = C_1 \dfrac{\rho}{\tau} + \dfrac{C_2 e^{-U_1/kT} + C_3 e^{-U_2/kT}}{Gb\rho_z^{1/2}}, \\ \dfrac{d\tau}{da} = \dfrac{\alpha Gb}{2\sqrt{\rho}} \left(C_1 \dfrac{\rho}{\tau} + \dfrac{C_2 e^{-U_1/kT} + C_3 e^{-U_2/kT}}{Gb\rho_z^{1/2}} \right), \end{cases} \tag{25}$$

where $\rho_z = \rho$ is the current dislocation density in the case of multiple slip, and $\rho_z = \rho_0$ is the initial dislocation density in the case of single slip.

Given the initial conditions $a_0 = 0$ and $\tau_0 = \tau_F + \alpha Gb\rho_0^{1/2}$ [τ_F and α are determined from Eqs. (24)] and having numerically solved the system of Eqs. (24) and (25), we get the $\tau(a)$ and $\rho(a)$ dependences, which can be compared with the experimentally observed dependences for Ni_3Ge.[1] The values of parameters C_1, C_2, are C_3 are needed to solve these systems of equations, and we determine them from the following considerations: We set C_1 equal to the value characteristic of pure metals ($C_1 = 6\times10^4$ Pa,[9] $\alpha = 1.8$–1.8×10^{-3} T, Ref. 8), and we choose C_2 and C_3 so that they best describe the deformation dependence of the dislocation-accumulation rate obtained experimentally for Ni_3Ge in the [100] orientation at 523 K ($C_2 = 5\times10^{16}\,\mathrm{Pa\cdot m^{-2}}$, $C_3 = 10^{23}\,\mathrm{Pa\cdot m^{-2}}$).[8] We assume $G = 80$ GPa, $b = 2.5\times10^{-10}$ m, and $\rho_0 = 10^{10}\ \mathrm{m^{-2}}$.

The activation energies U_1 and U_2 and the preexponential factors $\tau_0^{(1)}$ and $\tau_0^{(2)}$ in Eqs. (24) we assume to be equal to the values experimentally determined from the temperature dependences of the yield point for single crystals of Ni_3Ge in the [100] orientation: $U_1 = 0.01$ eV, $U_2 = 0.07$ eV, $\tau_0^{(1)} = 300$ MPa, and $\tau_0^{(2)} = 700$ MPa.[1] In order to trace the effect of the orientation of the crystals, which is associated with the number of slip systems that are deforming the single crystals, we leave the parameters identical here for both multiple and single slip. Let us compare the results of the calculations with the experimentally observed regularities of the thermal and deformation strengthening of single crystals of Ni_3Ge.

The results of numerically integrating the system of Eqs. (25) are shown in Fig. 4b. Figure 4a shows for comparison the experimental $\tau(\varepsilon)$ curves. As follows from Fig. 4, the system of Eqs. (25) reliably describes the experimentally observed features of the variation of the deformation curves.[1–3]

However, by attentively comparing the experimental and calculated curves, a quantitative discrepancy is detected in their features in the high-temperature region. Let us indicate possible ways to improve the agreement between the model calculations and experiment.

The intensity of the dislocation accumulation is large in the high-temperature region, so that a density of about $10^{15}\ \mathrm{m^{-2}}$ is already achieved at low deformations. With such dislocation densities, it is obvious that dislocation annihilation must be allowed for even when the dislocations in $L1_2$ superstructures have low mobility. Another factor that must be considered is that the activation energies depend on the stresses and the orientation of the deformation axis, as repeatedly indicated by a number of authors.[11]

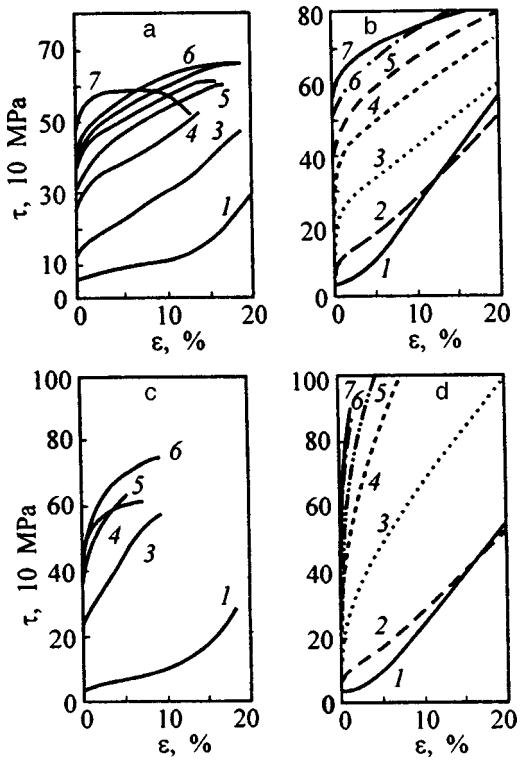

FIG. 4. Strengthening curves of single crystals of Ni_3Ge, oriented for multiple and single slip. (a) and (b) compression axis [100], (c) and (d) compression axis [139], (a) and (c) experimental data, (b) and (d) model calculations. The experimental temperatures (K) are *1*—77, *2*—100, *3*—293, *4*—423, *5*—523, *6*—673, *7*—893.

Despite the indicated difficulties of the phenomenological model represented by the system of Eqs. (25), it can be assumed that the analyses presented above reflect the main features of the formation of the dislocation structure and the thermal strengthening in alloys having an $L1_2$ superstructure.

[1] V. A. Starenchenko, Yu. V. Solov'eva, Yu. A. Abzaev, V. I. Nikolaev, V. V. Shpeĭzman, and B. I. Smirnov, Fiz. Tverd. Tela **38**, 3050 (1996) [Phys. Solid State **38**, 1668 (1996)].
[2] Yu. A. Abzaev, V. A. Starenchenko, and N. A. Koneva, Izv. Vyssh. Uchebn. Zaved. Fiz. No. 3, 65 (1987).
[3] V. A. Starenchenko, Yu. V. Solov'eva, Yu. A. Abzaev, É. V. Kozlov, V. V. Shpeĭzman, V. I. Nikolaev, and B. I. Smirnov, Fiz. Tverd. Tela **40**, 672 (1998) [Phys. Solid State **40**, 618 (1998)].
[4] J. P. Hirth and J. Lothe, *Theory of Dislocations* (McGraw-Hill, New York, 1967; Atomizdat, Moscow, 1972).
[5] B. A. Grinberg, M. A. Ivanov, and Yu. N. Gornostyrev, Fiz. Met. Metalloved. **46**, No. 4, 812 (1978).
[6] B. A. Grinberg and V. I. Syutkina, *New Methods of Strengthening Ordered Alloys* (Metallurgiya, Moscow, 1985).
[7] J. Friedel, *Dislocations* (Pergamon Press, Oxford, 1964; Mir, Moscow, 1967).
[8] V. A. Starenchenko, Yu. A. Abzaev, and L. G. Chernov, Metallofizika (Kiev) **2**, No. 12, 22 (1987).
[9] L. E. Popov, V. S. Kobytev, and T. A. Kovalevskaya, *Plastic Deformation of Alloys* (Metallurgiya, Moscow, 1984).
[10] S. N. Kolupaeva, V. A. Starenchenko, and L. E. Popov, *Instabilities of the Plastic Deformation of Crystals* (Izd. Tomsk. Univ., Tomsk, 1994).
[11] F. E. Heredia and D. P. Pope, Acta Mater. **39**, 2027 (1991).

Translated by W. J. Manthey

MAGNETISM, FERROELECTRICITY

Field-induced spin-reorientation transitions in magnetic superlattices with uniaxial anisotropy and biquadratic exchange

A. K. Zvezdin

Institute of General Physics, Russian Academy of Sciences, 117942 Moscow, Russia

V. V. Kostyuchenko

Institute of Microelectronics, Russian Academy of Sciences, 150007 Yaroslavl', Russia
(Submitted July 17, 1998)
Fiz. Tverd. Tela (St. Petersburg) **41**, 461–463 (March 1999)

Phase transitions induced by an external field are investigated in magnetic multilayer systems with uniaxial anisotropy and biquadratic exchange. A magnetic field directed perpendicular to the plane of the layers changes the effective anisotropy and exchange constants, determining the orientation of the magnetization in the plane of the layers, and can give rise to spin-reorientation transitions. All possible types of such transitions are investigated for the case of uniaxial anisotropy, which differs substantially from the case of cubic anisotropy by the different renormalization of the effective anisotropy constants. © *1999 American Institute of Physics.* [S1063-7834(99)01803-1]

The change produced in the magnetization distribution in magnetic multilayer structures by an external magnetic field is now the object of intense investigation. This problem is of interest not only because these materials have unusual physical properties but also because of the promising practical applications of these materials in memory devices.

Let us consider a system of thin magnetic layers alternating with layers of a nonmagnetic spacer. The magnetization distribution in such a system is determined by the combined effect of the exchange interaction between layers through the nonmagnetic spacer, the anisotropy, and the Zeeman interaction of the magnetic layers with the external field. In addition, these quantities generally have the same order of magnitude, which complicates the phase diagram. The leading term of the exchange interaction between layers has the form of the Heisenberg interaction $J_1\mathbf{n}_i\cdot\mathbf{n}_{i+1}$, where $\mathbf{n}_i$ is a unit vector determining the magnetization orientation in the i-the magnetic layer. The quantity J_1 depends on the thickness of the spacer and the magnetic layer and can change sign as the spacer thickness increases.[1–3] In the absence of an external field the Heisenberg exchange interaction between layers strives to orient the magnetization vectors in neighboring layers parallel (for $J_1<0$) or antiparallel (for $J_1>0$). Thus, the Heisenberg interaction cannot explain the experimentally observed noncollinear orientation of the magnetization in neighboring layers.[4–7] To explain the noncollinearity of the magnetization in neighboring layers, several mechanisms have been proposed for the non-Heisenberg exchange between magnetic layers, but quantitative agreement between the theory and experimental data has, for the present, not been attained.[8,9] Ordinarily, the non-Heisenberg exchange interaction between layers is represented in the form of a biquadratic exchange interaction $J_2(\mathbf{n}_i\cdot\mathbf{n}_{i+1})^2$,[4,10–12] but other expressions have also been used to describe the non-Heisenberg exchange interaction (see, for example, Ref. 13).

Field-induced phase transitions under the action of an external magnetic field oriented perpendicular to the plane of the magnetic layers have been investigated previously in Refs. 14–16. However, in Ref. 14 anisotropy was completely neglected, and in Refs. 15 and 16 only cubic anisotropy was considered. Taking account of anisotropy is very important, since in magnetic multilayers of the type Fe/Cr/Fe or Co/Cu/Co the anisotropy energy is of the same order of magnitude as the exchange interaction energy between the layers. Cubic anisotropy is a fourth-order anisotropy, while uniaxial anisotropy is a second-order anisotropy. For this reason, the case of uniaxial anisotropy differs substantially from the case of cubic anisotropy and requires a separate analysis (for a more detailed analysis, see below and the results presented in Ref. 16 for cubic anisotropy).

In the present paper external-field-induced phase transitions in magnetic superlattices with uniaxial anisotropy are investigated theoretically. This case is similar to a magnetic multilayer system of the type Fe/Cr/Fe (110). In a zero external field the demagnetization energy prevents the magnetization vector from tilting out of the plane of the layers. The orientation of the magnetization vectors in the plane of the layers is determined by the combined effect of the anisotropy and exchange fields. A magnetic field applied perpendicular to the plane of the layers causes the magnetization vectors to tilt out of the plane of the layers and leads to renormalization of the effective anisotropy and exchange constants, which determine the orientation of the magnetization in the plane of the layers. Thus a magnetic field applied perpendicular to the

plane of the layers changes the magnetization in the plane of the layers. The case of uniaxial anisotropy differs from the case of cubic anisotropy by a different renormalization of the effective anisotropy constants.

1. PHASE DIAGRAM FOR ZERO EXTERNAL FIELD

Let us consider a multilayer system consisting of N magnetic layers, alternating with $N-1$ spacer layers, with antiferromagnetic interaction between the layers. For an infinite number of layers $N \gg 1$ or a spin-valve structure $N=2$ the energy functional for the superlattice has the form of the functional for a two-sublattice magnet. It differs from a classical antiferromagnet only by a term describing the biquadratic interaction between layers. For definiteness, we assume that the z axis is directed perpendicular to the plane of the layers, the x axis is directed along the easy axis in the plane of the magnetic layers, and the y axis completes the system so as to form a right-handed triplet.

The energy functional for such a system can be represented by

$$F=\sum_{i=1}^{2}\left[-\frac{1}{2}k(n_i^x)^2+\frac{1}{2}m(n_i^z)^2-hn_i^z\right] + \frac{1}{2}J_1(\mathbf{n}_1\cdot\mathbf{n}_2)+\frac{1}{2}J_2(\mathbf{n}_1\cdot\mathbf{n}_2)^2, \quad (1)$$

where J_1 is the Heisenberg exchange energy between layers, J_2 is the biquadratic exchange energy between layers, k is the uniaxial anisotropy energy, and h is the Zeeman energy. It is preferable to measure all of these quantities in units of the magnetic field.

It is convenient to switch from Cartesian coordinates $\mathbf{n}_i$ to polar coordinates θ_i and φ_i, where the polar angle θ_i is the angle between the z axis and the vector $\mathbf{n}_i$ and the azimuthal angle φ_i is the angle between the projection of $\mathbf{n}_i$ on the xy plane and the easy axis x.

In a zero external field the high demagnetization energy prevents the magnetization from tilting out of the planes of the layers. In this case $\theta_1=\theta_2=$ const $=\pi/2$ and the expression for the energy functional (1) has the form

$$F=\frac{1}{2}k\sum_{i=1}^{2}\sin^2\varphi_i+\frac{1}{2}J_1\cos(\varphi_1-\varphi_2) + \frac{1}{2}J_2\cos^2(\varphi_1-\varphi_2). \quad (2)$$

Minimizing this potential shows that only four phases can satisfy the condition for a global minimum of the potential (2). Two of these phases are collinear (ferromagnetic phase I and antiferromagnetic phase II), and the two others are noncollinear canted phases, symmetrically oriented with respect to the easy (phase III) or hard (phase IV) axis. The stability conditions and the energy for each phase are presented in Table I.

The phase diagram displayed in Fig. 1 can be constructed on the basis of the data presented in Table I.

TABLE I. Phases minimizing the energy functional (2).

	Phase	Stability condition	Energy
I	$\varphi_1=\varphi_2=0$	$k>J_1+2J_2$	$(J_1+J_2)/2$
II	$\varphi_1=0,\ \varphi_2=\pi$	$k+J_1>2J_2$	$(J_2-J_1)/2$
III	$\varphi_1=-\varphi_2=\frac{1}{2}\arccos\frac{k-J_1}{2J_2}$	$J_1<0,\ k<J_1+2J_2$	$\frac{4kJ_2-(k-J_1)^2}{8J_2}$
IV	$\varphi_1=\pi-\varphi_2=\frac{1}{2}\arccos\frac{k+J_1}{2J_2}$	$J_1>0,\ k+J_1<2J_2$	$\frac{4kJ_2-(k+J_1)^2}{8J_2}$

2. FIELD-INDUCED SPIN-REORIENTATION TRANSITIONS

An external magnetic field applied perpendicular to the plane of the magnetic layers causes the magnetization to tilt out of the plane of the layers. In this case the problem of minimizing the functional (1) becomes much more complicated and in the general case it has no exact analytic solution. However, in magnetic multilayers of the type Fe/Cr/Fe or Co/Cu/Co the demagnetization energy is an order of magnitude larger than the anisotropy energy and the exchange interaction between the layers ($m \gg J_1, J_2, k$). Then the equations $\partial F/\partial\theta=0$ and $\partial F/\partial\theta_2=0$ have the approximate solution

$$\theta_1=\theta_2=\cos^{-1}(h/m). \quad (3)$$

Substituting the relations obtained into Eq. (1), we obtain an energy functional thatis similar to the functional (2):

$$F=\frac{1}{2}k(h)\sum_{i=1}^{2}\sin^2\varphi_i+\frac{1}{2}J_1(h)\cos(\varphi_1-\varphi_2) + \frac{1}{2}J_2(h)\cos^2(\varphi_1-\varphi_2), \quad (4)$$

where $k(h), J_1(h)$, and $J_2(h)$ are now functions of the external magnetic field and are determined by the expressions

$$J_1(h)=\left(1-\frac{h^2}{m^2}\right)\left(J_1+2J_2\frac{h^2}{m^2}\right),$$

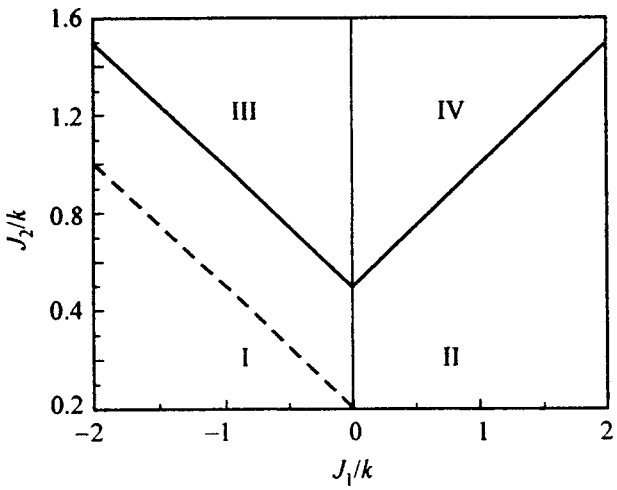

FIG. 1. Phase diagram in the variables J_2/k and J_1/k. The enumeration of the phases corresponds to the notations used in Table I. The dashed line separates the region of possible spin-reorientation transitions.

TABLE II. Field-induced spin-reorientation transitions in magnetic multilayers with uniaxial anisotropy.

Region	Phase transitions
$J_1+2J_2<0$	No transitions
$k>J_1+2J_2>0$	First-order at $h=h_1$
$J_1+2J_2>k$, $J_1<0$	First-order at $h=h_1$ and second-order at $h=h_2$
$k+J_4>2J_2$, $J_1>0$	Second-order at $h=h_2$
$k+J_1<2J_2$, $J_1>0$	No transitions

Note. h_1 and h_2 denote the following expressions for the critical fields: $h_1=m\sqrt{|J_1|/2J_2}$ and $h_2=m\sqrt{(2J_2-J_1-k)/4J_2}$.

$$J_2(h)=\left(1-\frac{h^2}{m^2}\right)^2, \quad k(h)=k\left(1-\frac{h^2}{m^2}\right), \tag{5}$$

Therefore the equilibrium values for $\varphi_1(h)$ and $\varphi_2(h)$ can be determined on the basis of the data presented in Table I, provided that the renormalized constants (5) are used instead of k, J_1, and J_2. It follows from Eqs. (5) that $J_2(h)/2J_1(h)\to 0$ as $h\to m$ and $|\varphi_1(h)-\varphi_2(h)|=0$, π at $h=m$. If the equilibrium values $\varphi_1(m)$ and $\varphi_2(m)$ are different from $\varphi_1(0)$ and $\varphi_2(0)$, then the applied external magnetic field gives rise to spin-reorientation transitions as h varies from 0 to m.

To investigate possible types of field-induced phase transitions it is convenient to employ the phase diagram displayed in Fig. 1. The state of the system is determined completely by the two quantities $J_1=J_1(h)/k(h)$ and $J_2=J_2(h)/k(h)$. It is easy to see from the expressions (5) that the trajectory $J_2(J_1)$ is a straight line

$$2J_2+J_1=(J_1(0)+2J_2(0))/k(0).$$

The intersection of this straight line with the lines of phase transitions in the phase diagram (see Fig. 1) shows the possibility of phase transitions induced by an external field. The list of possible types of field-induced phase transitions and the dependences on the initial values of k, J_1, and J_2 are presented in Table II.

For a first-order phase transition, which occurs at the critical field $h=h_1$ (Table II), the magnetization orientation in the even-numbered (or odd-numbered) layers changes by π, while in all other layers it does not change. The change in the angle between the magnetization vectors in neighboring layers is maximum if this transition is a transition from ferromagnetic to antiferromagnetic ordering in the plane of the magnetic layers. This happens when the initial values of the parameters satisfy the relations $k>J_1+2J_2>0$ and $J_1<0$. It is easy to see that in this case the angle between the magnetization vectors in neighboring layers changes abruptly from 0 to $\cos^{-1}(|J_1|/J_2-1)$. For small values of $|J_1|/J_2$ this angle is close to π. This case could be of great interest for practical applications.

In summary, external-field-induced spin-reorientation phase transitions in magnetic multilayers with uniaxial anisotropy with the field directed perpendicular to the plane of the layers was investigated theoretically. It was shown that the orientation of the magnetization vectors in the plane of the layers is determined by the effective anisotropy and exchange constants, whose value is determined by the external field. Therefore an external field applied perpendicular to the plane of the layers changes the orientation of the magnetization in the plane of the magnetic layers.

[1] S. S. P. Parkin, N. More, and K. P. Roche, Phys. Rev. Lett. **64**, 2304 (1990).
[2] S. S. P. Parkin, Phys. Rev. Lett. **67**, 3598 (1991).
[3] P. Bruno, Phys. Rev. B **52**, 411 (1995).
[4] M. Rührig, R. Schäfer, A. Hubert, R. Mosler, J. A. Wolf, S. Demokritov, and P. Grünberg, Phys. Status Solidi A **125**, 635 (1991).
[5] V. I. Nikitenko, L. M. Dedukh, V. S. Gornakov, Yu. P. Kabanov, L. H. Bennett, M. J. Donahue, L. J. Swartzendruber, A. J. Shapiro, and H. J. Brown, IEEE Trans. Magn. **33**, 3661 (1997).
[6] A. Schreyer, J. F. Ankner, Th. Zeidler, H. Zabel, M. Schäfer, J. A. Wolf, P. Grünberg, and C. F. Majkrzak, Phys. Rev. B **52**, 16 066 (1995).
[7] C. D. Potter, R. Schad, P. Beliën, G. Verbanck, V. V. Moshchalkov, and Y. Bruynseraede, Phys. Rev. B **49**, 16 055 (1994).
[8] J. C. Slonczewski, J. Magn. Magn. Mater. **126**, 374 (1993).
[9] D. M. Edwards, J. M. Ward, and J. Mathon, J. Magn. Magn. Mater. **126**, 380 (1995).
[10] J. C. Slonczewski, Phys. Rev. Lett. **67**, 3172 (1991).
[11] J. Slonczewski, J. Appl. Phys. **73**, 5957 (1993).
[12] R. P. Ericson, K. B. Hathaway, and J. R. Cullen, Phys. Rev. B **47**, 2626 (1993).
[13] J. C. Slonczewski, J. Magn. Magn. Mater. **150**, 13 (1995).
[14] V. V. Ustinov, M. M. Kirillova, I. D. Lobov, V. M. Maevskiĭ, A. A. Makhnev, V. I. Minin, L. N. Romashev, A. R. Del', A. V. Semerikov, and E. I. Shreder, Zh. Éksp. Teor. Fiz. **109**, 477 (1996) [JETP **82**, 253 (1996)].
[15] V. V. Kostyuchenko and A. K. Zvezdin, J. Magn. Magn. Mater. **176**, 155 (1997).
[16] V. V. Kostyuchenko and A. K. Zvezdin, Phys. Rev. B **57**, 5951 (1998).

Translated by M. E. Alferieff

Width of the ferromagnetic resonance line in highly dispersed powders of crystalline and amorphous Co–P alloys

R. S. Iskhakov,*) L. A. Chekanova, and E. A. Denisova

L. V. Kirenskiĭ Institute of Physics, Siberian Branch of the Russian Academy of Sciences, 660036 Krasnoyarsk, Russia

(Submitted August 19, 1998)
Fiz. Tverd. Tela (St. Petersburg) **41**, 464–467 (March 1999)

The resonance characteristics (inhomogeneous FMR linewidth ΔH) in highly dispersed ($d=0.1-3\ \mu$m) powders of crystalline and amorphous Co–P alloys are investigated as a function of the composition, particle size, and atomic structure. It is established that ΔH for powders of amorphous Co–P alloys is two to three times larger than ΔH for crystalline Co–P powders. According to the investigations performed, this is caused by thermodynamically stimulated segregation of nonmagnetic Co_2P inclusions, apparently an effective relaxation channel, in the amorphous state of Co–P powders. © *1999 American Institute of Physics.* [S1063-7834(99)01903-6]

Ferromagnetic resonance (FMR) is widely used to investigate amorphous ferromagnetic alloys obtained by various methods in the form of thin films, foils, and coatings.[1–4] The magnetic properties of these materials (static, quasistatic, and microwave characteristics) are largely determined by their composition and structure.

In the last few years amorphous alloys have been obtained by different methods (see, for example, Ref. 5) in the form of small particles: ultradispersed ($d=10-100\ \mu$m), highly dispersed ($d=0.1-4\ \mu$m), and dispersed ($d>5\ \mu$m).

Investigations have established that the magnetic properties of small amorphous particles differ substantially from the analogous properties characterizing amorphous films, foils, and coatings having the same composition.[6]

The present paper reports the results of an investigation of the resonance characteristics (inhomogeneous width ΔH of the FMR line) in highly dispersed Co–P powders having different compositions, particle sizes, and structure. The objective is to determine the differences and similarities of the dependences of ΔH in Co–P alloys obtained by the same technological method in different morphological modifications (powders, films). Of special interest in this investigation is to check the assumption advanced in Ref. 2 that the inhomogeneous FMR linewidth ΔH in amorphous alloys is completely determined by the magnitudes H_a of the local anisotropy field in these alloys on microscopic scales.

1. EXPERIMENT

Highly dispersed powders of the alloys Co–P were obtained by chemical deposition from water solutions ($T=80\,^{\circ}$C) of Co salts ($CoSO_4$) using sodium hypophosphite (NaH_2PO_2) as the reducing agent. Next, they were washed in distilled water and acetone to passivate the surface of the particles. The phosphorus concentration was determined by chemical analysis (to within ± 0.5 at. % P). The particle sizes were found by analyzing electron micrographs obtained in a JEM-100C electron microscope. Prewashed powder was sorted by a sedimentation method into six fractions differing by the average particle diameter (0.1, 0.3, 0.7, 1, 2, and 3 μm). The electron micrographs for each fraction contained of the order of 200 particles, which made it possible to construct a histogram of the particle size distribution, determine the average particle diameter, and the standard deviation.

Diffraction investigations (DRON-3 diffractometer) with Cu $K\alpha$ radiation was used to determine the atomic structure of the powders of the Co–P alloys. The FMR linewidth ΔH was measured on a standard EPA-2M spectrometer (frequency 9.2 GHz). The method developed in Ref. 7 was used to calculate the local anisotropy field in the region where the magnetization approached saturation. The magnetization curve $M(H)$ was measured with a vibrating magnetometer in the range of fields from 0 to 14 kOe.

2. RESULTS

Chemical analysis showed that the phosphorus concentration in the powders of Co–P alloys ranged from 4 to 27 at. %, depending on the technological conditions of the chemical deposition process (hypophosphate concentration, Ph of the solution). The phosphorus concentration (x) in a Co–P solid solution influenced the shape of the particles formed. Morphological analysis of the electron micrographs shows that $Co_{100-x}P_x$ particles with $x\leqslant 9$ at. % are predominantly hexahedral prisms and that for $x\geqslant 12$ at. % the ideal shape of the $Co_{100-x}P_x$ particles is spherical. The results of x-ray diffraction analysis agree with the morphological data. The typical x-ray diffraction patterns of powders with different phosphorus content are presented in Fig. 1. Powders of Co–P alloys with phosphorus content less than 9 at. % P were characterized by x-ray diffraction patterns with a set of reflections attesting to a hexagonal close-packing (hcp) structure of the powder particles. The x-ray diffraction patterns of the powders $Co_{100-x}P_x$ ($x\geqslant 12$ at. %) contained one diffuse

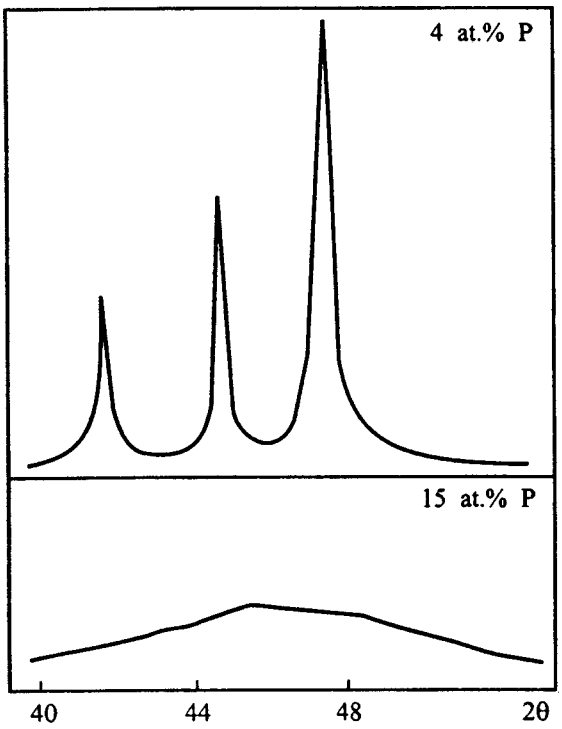

FIG. 1. Diffraction curves for powders of crystalline and amorphous alloys Co–P with phosphorus concentrations of 4 at. % and 15 at. %.

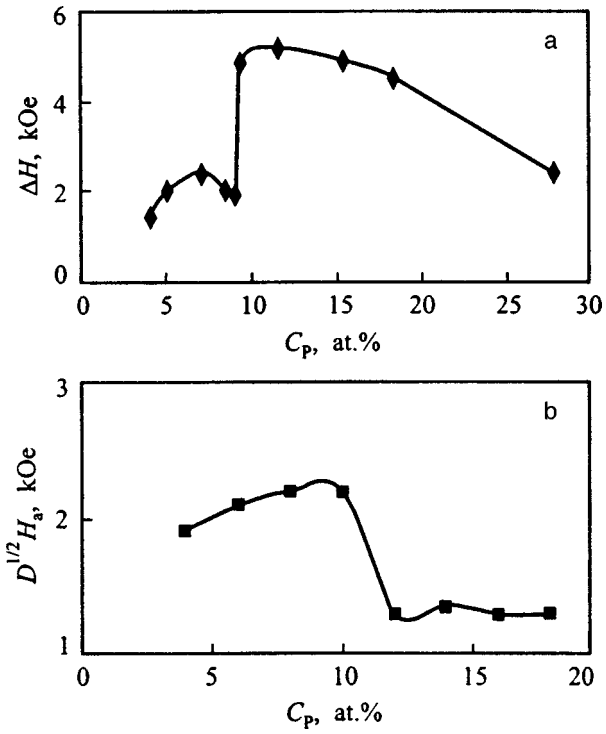

FIG. 2. a — Concentration dependence of the linewidth ΔH for powders of Co–P alloys, b — concentration dependence of the local anisotropy field H_a for powders of the alloys Co–P.

peak, centered near $d_{hkl}=2.01$ Å with width $\sim 10^0$ (2θ). Such diffraction curves attest to an amorphous structure of the particles of these powders. (According to the x-ray diffraction analysis, powders of Co–P alloys in the range from 9 to 11 at. % P consisted of a mixture of crystalline (hcp) and amorphous phases.) Co–P powders obtained with phosphorus concentration $x>20$ at. % (eutectic region of the melting diagram of Co–P) were also characterized by a crystalline impurity. The x-ray diffraction data attest to the formation, in this case, of the crystalline phosphide Co_2P — for 27 at. % P the diffraction curve is mainly formed by reflections of this chemical compound.

The measurements of the FMR linewidth for the initial Co–P powders (not separated into size fractions) with different phosphorus concentration are presented in Fig. 2a. The characteristic linewidth ΔH is 1.5–2 kOe for crystalline powders and 4–5 kOe for amorphous powders. We note that the FMR linewidth of amorphous ferromagnetic alloys prepared in the form of films, foils, and coatings, as a rule, does not exceed several hundreds of oersteds (see, for example, Refs. 2 and 3). Another difference of the concentration dependence $\Delta H(x)$ in Co–P powders from the analogous concentration dependences $\Delta H(x)$ in Co–P films is the following. The concentration phase transition ''crystalline solid solution — amorphous state of the alloy'' detected by x-ray diffraction analysis does not appear in the curve ΔH(at. % P) in Co–P films;[2] this transition does appear in the concentration dependence ΔH(at. % P) in Co–P powders in the form of an abrupt increase in ΔH by a factor of two or three near the critical concentration $x_c=10$ at. % P.

Measurements of the magnetization curve $M(H)$ for Co–P powders showed that in the region where the magnetization approaches saturation the high-field part of this curve is described by the function $M(H)=M_0(1-DH_a^2/H^2)$. This latter property made it possible to determine the concentration dependence $M_0(x)$ of the saturation magnetization and to calculate the local anisotropy field H_a characterizing the powder particles. (According to Ref. 7, here $D=2/105$ for cubic symmetry and 1/15 for hexagonal symmetry; for the crystalline phase $H_a=2K/M_0$, where K is the magnetocrystallographic anisotropy constant.) It was found that the values of M_0 decrease monotonically with increasing phosphorus concentration in Co–P powders. However, here, in contrast to the linear functions $M_0(x)$ found in Refs. 7–9 for films and coatings of Co–P alloys, a change in the gradient $\partial M_0/\partial x$ from ≈ 37 G/at. % P to 45 G/at. % P is observed near $x=x_c$. The concentration dependence of the computed values of the local anisotropy field H_a for powders is presented in Fig. 2b. The local anisotropy field H_a obviously is sensitive to the concentration phase transition of the crystalline solid solution Co–P into an amorphous state: A jump-like decrease of H_a by a factor of two is recorded near $x=x_c$. This latter behavior distinguishes the concentration variation of $H_a(x)$ in Co–P powders from the analogous dependence measured previously for Co–P coatings.[7]

Measurement of the static and resonance characteristics of Co–P powder fractions sorted according to the average particle size d made it possible to study the effect of the sizes of the particles on their magnetic characteristics. It was found that the functional dependence of the measured characteristics on d depends on the type of atomic structure of the particles — crystalline or amorphous. Thus, the saturation

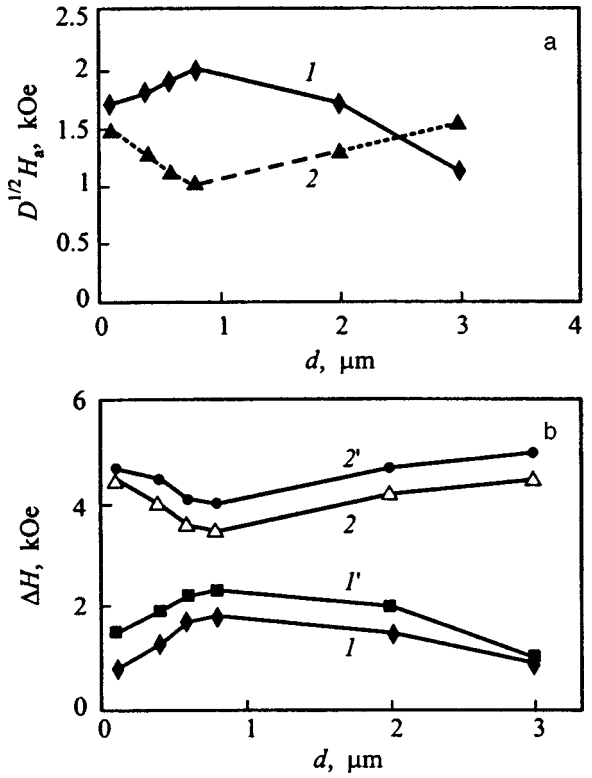

FIG. 3. a — Dependence of the local anisotropy field H_a on the average diameter of particles of Co–P powder: 1 — 4 at. % P, *1′* — 6 at. % P, 2 — 15 at. % P, *2′* — 18 at. % P. b — Linewidth ΔH versus the average diameter of particles of Co–P powder: 1 — 4 at. % P, 2 — 15 at. % P.

magnetization M_0 of amorphous powders (11 at. % P $< x \leqslant$ 20 at. % P) as a function of the particle size d in Co–P powder remains constant within the experimental accuracy of the measurements. For crystalline Co–P powders, however, M_0 decreases by 15% as d increases from 0.1 to 3 μm. The local anisotropy field H_a (Fig. 3a) increases linearly up to $d=1\,\mu$m (H_a changes by 35%) with increasing average particle size in Co–P powder for crystalline particles and then decreases by 40% as d increases to 3 μm. For Co–P powder particles with amorphous structure, the dependence $H_a(d)$ (Fig. 3a) is as follows: As the average particle size increases to $d=0.7\,\mu$m, H_a decreases linearly (by 30–20% depending on the P content in the powders) and as d increases further, H_a increases (by 15–25%).

The measurements of the FMR linewidths $\Delta H(d)$ for amorphous and crystalline Co–P powders are displayed in Fig. 3b. One can see that the particle-size dependence of ΔH is determined mainly by the structural state of the particles: For crystalline powders $\Delta H(d)$ is a convex curve with a maximum at $d=1\,\mu$m, while for amorphous powders $\Delta H(d)$ is a concave curve with a minimum also at $d=1\,\mu$m. We note that the relative deviation of ΔH on the curves $\Delta H(d)$ for crystalline particles is more pronounced than for amorphous particles.

3. DISCUSSION

The experimental curves $\Delta H(x)$, $H_a(x)$, and $\Delta H(d)$, $H_a(d)$ presented in Figs. 2 and 3 are of interest for two reasons. One is the qualitative similarity of the dependences $\Delta H(d)$ and $H_a(d)$ in both crystalline and amorphous states and the other is the substantially different — by the direction of the jump in ΔH and H_a near $x \approx x_c$ — concentration dependences $\Delta H(x)$ and $H_a(x)$. The correlation of the curves $\Delta H(d)$ and $H_a(d)$ agrees with the supposition advanced in Ref. 2 on the basis of the results of an experimental study of the dependences $\Delta H(x)$ and $H_a(x)$ in films and coatings of Co–P alloys. Therefore, in powders of Co–P alloys the FMR linewidth can be represented as a sum of two contributions: $\Delta H(x,d)=\Delta H_u(x,d)+\Delta H_{1,a}(x,d)$, where $\Delta H_{1,a}$ is the contribution of the local anisotropy to the linewidth and ΔH_u is the contribution of some source that creates ''relaxation'' channels, which is reflected in the increase of the FMR linewidth and which predominates in the amorphous state of the powders. (See, for example, Ref. 10 for a detailed analysis of the possible sources of relaxation.) The origin of this source is to be determined by analyzing the experimental results presented. First, we shall study the phase diagram of Co–P powders and compare it with the phase diagram of films and coatings of Co–P alloys, which, apparently, are characterized by the inequality $\Delta H_u \ll \Delta H_{1,a}$.

Films and coatings of Co–P alloys, obtained by chemical deposition, in the concentration range from 1 to 20 at. % P are metastable solid solutions (substitution type), as is indicated by the linearity of $M_0(x)$ observed in Refs. 7–9. The gradient of $M_0(x)$ in this case is due to electronic mechanisms of transport of the p electrons of P into the d band of Co and does not depend on the type of structural ordering of the solid solution.[11] Indeed, films and coatings of Co–P alloys are characterized by a hexagonal close-packed structure (hcp) in the concentration range 1–4 at. % P, face-centered cubic structure (fcc) in the range 5–8 at. % P, and an amorphous structure in the range 9–20 at. % P, but the critical concentrations $x_{i,c}$ of these concentration phase transitions were not manifested in the linear dependence $M_0(x)$. We note also the results obtained in Ref. 12, where the NMR method was used to show that short-range order in films of amorphous Co–P alloys is characterized by fcc symmetry. The latter fact served as a reason (as shown in Refs. 2 and 7) why the transition fcc Co–P $\rightarrow$ amorphous state in films, in contrast to the transition hcp Co–P $\rightarrow$ fcc Co–P, was not manifested in the curves $\Delta H(x)$ and $H_a(x)$.

The form of the phase diagram of powders of Co–P alloys is qualitatively different — here there is no region of fcc crystalline states. The powders of Co–P alloys have hcp structure in the region 1–8 at. % P and amorphous structure in the region 10–20 at. % P. Comparing the curve $H_a(x)$ with the analogous curve for films,[7] due to the jump-like decrease of H_a near concentrations $x \approx x_c$, suggests that short-range order in powders of amorphous Co–P alloys (just as in films) is characterized by fcc symmetry. This supposition corresponds to the form of the diffraction curve of amorphous powders (Fig. 1), which can be obtained by broadening of the [111] line of the fcc lattice according to the Debye–Scherrer equation. We note that according to this equation the broadening of the reflections of an hcp lattice will lead to an asymmetric diffraction curve, which is at variance with the experimental curve presented in Fig. 1.

Therefore the concentration transition ''hcp Co–P $\rightarrow$ amorphous state'' is accompanied by a decrease of the contribution $\Delta H_{1,a}$ to the total FMR linewidth near x_c. The latter signifies that the relaxation source due to which the contribution of ΔH_u to $\Delta H(x)$ predominates is activated near the concentration transition x_c.

The indication of the origin of this relaxation source contains the above-discussed dependence $M_0(x)$ for Co–P powders, which is characterized by a change in the gradient of $M_0(x)$ near x_c. Since the electron transport mechanism does not depend on the type of structural ordering of the solid solution,[11] the increase at $x \approx x_c$ of the rate of decrease of M_0 with increasing x is initiated by an additional factor which is realized in amorphous powders. Such a factor is the thermodynamically stimulated stratification of the supersaturated solid solution Co–P into a less concentrated Co–P solution and Co_2P inclusions (precipitates). This supposition does not contradict the x-ray diffraction data which show that the Co_2P inclusions first appear in the diffraction curves (for $x > 20$ at.% P) only if the inclusions are sufficiently large. Just like nonmagnetic pores, Co_2P inclusions strongly influence the formation of the linewidth ΔH_u from the moment of formation, while nonmagnetic pores have a negligible effect on the local anisotropy H_a. We note that in the Ref. 2, where a radical difference was observed between the temperature dependences $\Delta H(T)$ and $H_a(T)$ for films of the amorphous alloy $Co_{87}P_{13}$ in the temperature range $T > 300$ °C was observed, stratification of Co–P into Co and Co_2P was also invoked to explain the shape of these curves. In amorphous powders of Co–P alloys with an anomalously high vacancy density (which is indicated indirectly by a change in the morphology of the particles at x_c, indicating a change in the growth mechanism of the particles), stratification effects in the solid solution Co–P can occur at lower temperatures (preparation temperature 80 °C) and P concentrations ($x \approx 10$ at. %).

In summary, our investigations established the following. The resonance characteristics (inhomogeneous FMR linewidth ΔH) of Co–P powders obtained by chemical deposition are more than an order of magnitude larger than the analogous characteristics of films and coatings of Co–P alloys (prepared by the same method). The linewidth ΔH of powders of the alloys Co–P with amorphous particles is two to three times larger than ΔH for Co–P powders of crystalline particles. This is a result of stratification processes with the precipitation of nonmagnetic Co_2P formations in the amorphous powders. For a constant concentration of nonmagetic precipitates in the powder particles, the dependence of the linewidth ΔH on the average particle size correlates with the analogous dependence of the local anisotropy field H_a.

*)E-mail: rauf@iph.krasnoyarsk.su

[1] L. Kraus, Z. Frait, and J. Shneider Phys. Status Solidi A **63**, 596 (1981).
[2] R. S. Iskhakov, L. A. Chekanova, V. I. Ivanov, and G. V. Popov, Fiz. Tverd. Tela (Leningrad) **27**(9), 2593 (1985) [Sov. Phys. Solid State **27**, 1556 (1985)].
[3] G. Balasubramanian, A. N. Tiwari, and C. M. Srivastava, J. Mater. Sci. **25**, 1636 (1990).
[4] R. S. Iskhakov, M. M. Burshtunov, A. G. Narmonev, I. A. Turpanov, and L. A. Chekanova, Fiz. Met. Metalloved. **79**, 122 (1995).
[5] K. V. Chuistov and A. E. Perekos, Metallofiz. Noveĭshie Tekhnol. **19**, 68 (1997).
[6] W. Wernsdorfer, K. Hasselbach, and A. Sulpice, Phys. Rev. B **53**, 3341 (1996).
[7] V. A. Ignatchenko, R. S. Iskhakov, and G. V. Popov, Zh. Éksp. Teor. Fiz. **82**, 1518 (1982) [Sov. Phys. JETP **55**, 878 (1982)].
[8] R. S. Iskhakov, G. P. Popov, and M. M. Karpenko, Fiz. Met. Metalloved. **56**, 95 (1983).
[9] K. Huller and G. Dietz, J. Magn. Magn. Mater. **50**, 250 (1985).
[10] A. G. Gurevich, *Magnetic Resonance in Ferrites and Antoferromagnetics* (Nauka, Moscow, 1973).
[11] R. C. O'Handley, J. Appl. Phys. **62**, R15 (1987).
[12] R. S. Iskhakov, G. I. Fish, V. K. Mal'tsev, and R. G. Khlebopros, Fiz. Met. Metalloved. **58**, 1214 (1984).

Translated by M. E. Alferieff

Studies of the surface magnetic state of the Sr–M hexagonal ferrites near the phase transition at the Curie temperature

A. S. Kamzin and V. L. Rozenbaum

A. F. Ioffe Physicotechnical Institute, Russian Academy of Sciences, 194021 St. Petersburg, Russia
(Submitted July 21, 1998; resubmitted August 20, 1998)
Fiz. Tverd. Tela (St. Petersburg) **41**, 468–474 (March 1999)

A study is reported of the temperature dependences of the hyperfine (HF) interaction parameters in a ~200-nm thick surface layer and in the bulk of macroscopic hexagonal ferrite crystals of the Sr–M type ($SrFe_{12}O_{19}$ and $SrFe_{10.2}Al_{1.8}O_{19}$). The method used for the measurements is Mössbauer spectroscopy with simultaneous detection of gamma quanta, characteristic x-ray emission, and electrons, which permits direct comparison of the HF parameters in the bulk and the near-surface layers of a sample. As follows from the experimentally determined temperature dependences of the effective magnetic fields, the fields at the nuclei of the iron ions located in a ~200-nm thick near-surface layer decrease with increasing temperature faster than those of the ions in the bulk. The transition to paramagnetic state in a ~200-nm thick surface layer was found to occur 3° below the bulk Curie temperature. This offers the first experimental evidence for the transition to paramagnetic state in a surface layer of macroscopic ferromagnets to take place below the Curie temperature T_c for the bulk of the crystal. It has been established that the transition temperature $T_c(L)$ of a thin layer at a depth L from the surface of a crystal increases as one moves away from the surface to reach T_c at the inner boundary of the surface layer called critical. In the vicinity of T_c one observes a nonuniform state, with the crystal being magnetically ordered in the bulk but disordered on the surface. The experimental data obtained were used to construct a phase diagram of surface and bulk states for macroscopic magnets near the Curie (or Néel) temperature. © *1999 American Institute of Physics.* [S1063-7834(99)02003-1]

The need of studying surface properties and the influence of such a ''defect'' as the surface on the magnetic characteristics of the surface and near-surface crystal layers has been attracting an ever increasing interest of researchers starting in the 70's. Such studies could be of significance for applications as well, because a surface exerts considerable effect on the properties of nanosized powders and films, and understanding the nature of these materials could, for instance, pave the way toward tailoring their characteristics to our needs during the synthesis.

Of particular interest are surface processes accompanying such fundamental phenomena in the bulk of a crystal as phase transitions. The first theoretical descriptions of the surface properties of semi-infinite crystals introduced the concept of surface magnetic energy[1] and showed that if this energy is negative, the crystal surface can be magnetized at temperatures above the Curie point in the bulk, with the magnetization damping exponentially away from the surface. Theoretical studies of the surface of antiferromagnetic crystals also predicted the existence of surface magnetism above the Néel point.[2] These publications[1,2] were followed by attempts to describe surface characteristics by practically all methods developed to investigate the properties of bulk crystals.[3–5] Such theoretical studies culminated in construction of a phase diagram for states on the surface and in the bulk of a semi-infinite magnet in the vicinity of the Curie point (see, e.g., Ref. 5). Figure 1 presents the phase diagram of a magnet with respect to a phenomenological order parameter q, which governs the surface energy and was first introduced[1] when describing the specific features of the behavior of a system on the surface. The notation of the phase transition lines, namely, 1 — surface, 2 — ordinary, and 3 — extraordinary, were first proposed in Ref. 6. As follows from a theoretical consideration, in an ordinary transition the transformations in the bulk of the crystal and on its surface take place simultaneously. When the q parameter has the opposite sign, the surface shows a tendency to magnetic ordering before magnetization sets in in the bulk.

Experimental studies of surface properties until recently have been carried out either on fine-grained powder samples (where the number of ions on the surface is enhanced substantially compared to that in the bulk of crystallites), or on ultrathin films. Investigation of such objects provided support for the theoretical conclusions of the existence of magnetization on the surface of magnets at temperatures above the phase-transition point in the bulk of the sample. For instance, magnetization was experimentally observed to exist on the surface of Cr, Co, Ni, Tb, and Gd above the temperature of bulk magnetic ordering of these substances (see Refs. 3–5,7 and references therein). At the same time experimental studies of the surface of macrocrystals in the vicinity of the Curie (Néel) point have been certainly lagging behind theory. The reason for this lies in the lack of experimental techniques which would permit one to probe a thin surface

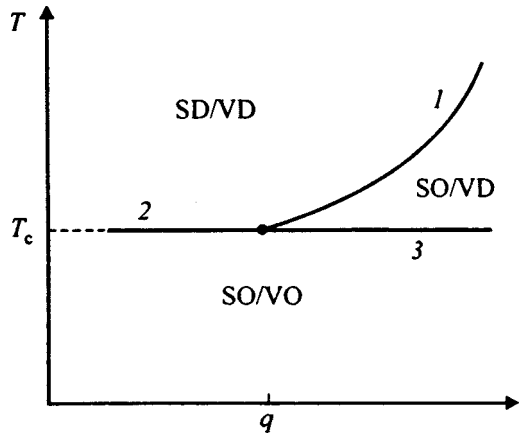

FIG. 1. Theoretical surface and bulk phase diagram for a ferromagnet near the Curie temperature.[5] *1* — surface phase transition line, *2* — ordinary phase transition line, *3* — extraordinary phase transition line, VO — magnetically-ordered bulk, SO — magnetically ordered surface, VD — magnetically disordered bulk, SD — magnetically disordered surface.

layer and the bulk of a massive crystal and compare their properties. In order to understand surface phenomena and to find how the effects on the surface are related to those in the bulk, one has to develop methods capable of probing the surface of a macrocrystal and the profile of variation of the properties in a near-surface layer and of comparing them directly with those for the bulk.

A unique approach meeting the above requirements is the method of simultaneous Mössbauer spectroscopy with detection of gamma quanta, x rays, and electrons (SGXEMS) proposed in Ref. 8 and described in Ref. 9. This method was used to establish experimentally that the surface of antiferromagnet macrocrystals with weak ferromagnetism transfers to paramagnetic state below the Néel temperature.[10–12] The order-disorder transition temperature decreases smoothly within the surface layer of a ''critical'' thickness.[10–12]

Thus experimental evidence for the existence of surface magnetism above the Curie point is in agreement with theoretical predictions.[1–5] At the same time observations[10–12] of a thin layer in paramagnetic state on the surface of macroscopic antiferromagnetic crystals below the Néel temperature is at odds with theoretical descriptions[1–5] of surface magnetism. Indeed, the phase diagram in Fig. 1 shows that below the Curie point the surface of a magnet can reside only in an ordered state. The reason for the disagreement between theory and our experiments consists possibly in that the former considered ferromagnets, whereas the experiments were carried out on antiferromagnets possessing a weak ferromagnetism.

This work reports an experimental study of the behavior of the magnetic system of a thin surface layer and of the bulk of macroscopic ferromagnetic crystals with temperature, as well as of the magnetic state of the surface in the vicinity of the phase transition at the Curie point.

We chose for the study single crystals of the hexagonal ferrites $SrFe_{12}O_{19}$ (the Sr–M type), as well as ferrites of the same structure with the Al diamagnetic ions substituted for part of the iron ions (the chemical formula $SrFe_{10.2}Al_{1.8}O_{19}$). The Sr–M–type ferrites have the hexagonal structure of magnetoplumbite.[13] Below the Curie point, $T_c = 730$ K, the magnetic structure of $SrFe_{12}O_{19}$ is a collinear ferrimagnet with a large anisotropy field, whose easy-magnetization axis coincides with the hexagonal or crystallographic *c* axis (see, e.g., Ref. 14 and references therein).

The plates used for the measurements, 70 to 100 μm thick, were cut from single crystals synthesized from a melt

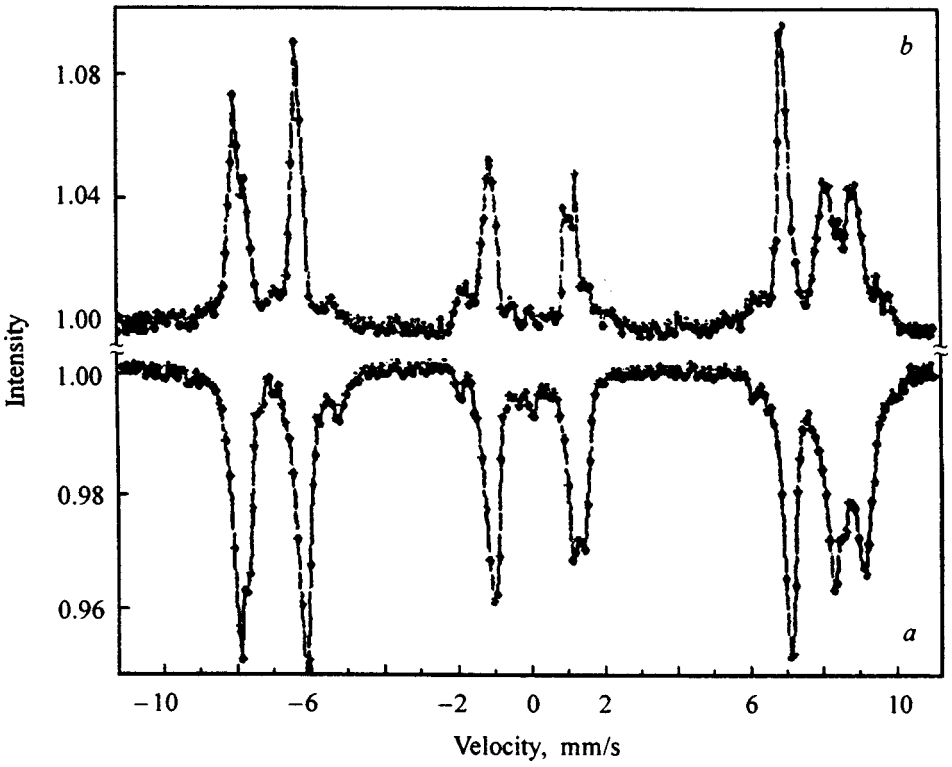

FIG. 2. Mössbauer spectra of $SrFe_{12}O_{19}$ obtained at $T = 300$ K with detection of (a) gamma rays and of (b) conversion and Auger electrons.

TABLE I. Room-temperature effective magnetic fields H_{eff}, isomer shifts δ, and quadrupole splittings ΔE for $SrFe_{12}O_{19}$ (the isomer shift δ determined relative to α Fe).

	H_{eff}, kOe		δ, mm/s		ΔE, mm/s	
Sublattice	$[\gamma]$	$[e]$	$[\gamma]$	$[e]$	$[\gamma]$	$[e]$
$12k$	413±1	415±1	0.36±0.01	0.35±0.01	0.40±0.02	0.40±0.02
$4f_1$	498±1	497±3	0.32±0.01	0.31±0.02	0.18±0.02	0.20±0.04
$4f_2$	519±2	529±3	0.44±0.01	0.42±0.03	0.44±0.02	0.43±0.06
$2a$	510±2	516±7	0.31±0.01	0.30±0.06	0.18±0.02	0.18±0.12
$2b$	405±4	400±20	0.37±0.02	0.34±0.07	2.37±0.04	2.25±0.14

solution. The crystallographic axis c was perpendicular to the plate plane. The crystals intended for surface studies were etched in orthophosphoric acid at $\sim 90\,^{\circ}\text{C}$ for one min. Previous experiments[15,16] showed that this crystal treatment results in a high quality surface while not creating any distortions in its structure.

The magnetic state of the surface and in the bulk of a crystal was studied by the SGXEMS method first proposed in Refs. 8,9. The SGXEMS method involves simultaneous measurement of Mössbauer spectra with radiations having different mean free paths in the material, namely, gamma rays, characteristic x-ray emission, and secondary (conversion and Auger) electrons, which carry information on the properties of the bulk, surface layers a few μm thick, and a 300-nm thick massive crystal, respectively. The energy of an electron escaping from a sample is the lower the deeper is the atom which has produced this electron, and therefore in order to study the properties of surface layers less than 300 nm thick by this method, the secondary electrons are energy selected.[17] This approach was realized in the form of a Mössbauer system.[18] The motion of the source followed a triangular function in time. The linearity of motion was controlled both by a conventional negative-feedback circuit and by a computer.[18]

The SGXEMS method was used to obtain experimental spectra within a temperature range of 300 to 750 K. The temperature was maintained to within ± 0.1 K. Figure 2 presents a room-temperature gamma-ray and secondary electron spectrum of $SrFe_{12}O_{19}$ measured with the gamma-photon wave vector parallel to the c axis. Because Mössbauer spectra obtained with detection of x-ray radiation provide information on a layer a few μm thick and are similar to gamma-resonance spectra, they are not demonstrated to make the figure more revealing.

Iron ions in type-M hexagonal ferrites occupy five inequivalent sites, and therefore the Mössbauer spectrum of this compound taken below the Curie point consists of five Zeeman sextuplets. Such a large number of spectral lines degrades substantially their resolution and, hence, the accuracy of HF parameter determination. To improve the line resolution, the crystal cut was chosen so that the Mössbauer gamma-ray wave vector is oriented parallel to the magnetic-moment orientation in the crystal. This reduces the number of lines in the experimental spectrum, because the longitudinal Zeeman effect suppresses the second and fifth Zeeman-sextuplet lines. As evident from Fig. 2, the spectral lines are now well resolved. This permitted one to determine the HF interaction parameters with a high enough accuracy.

The experimental spectra were used to compute the HF parameters, and the intensities and widths of the Zeeman sextuplet lines. The improved accuracy of mathematical treatment of the spectra was favored (besides the above-mentioned absence in the spectra of the second and fifth Zeeman-sextuplet lines) by the following factors: the different numbers of magnetic bonds between iron ions occupying inequivalent sites results in different effective magnetic fields at the iron-ion nuclei, and quadrupole splitting shifts the sextuplet lines considerably from one another.

The HF interaction parameters calculated from experimental room-temperature Mössbauer spectra of $SrFe_{12}O_{19}$ and $SrFe_{10.2}Al_{1.8}O_{19}$ are presented in Tables I and II, respectively. These data are in a good agreement with published results[19–22].

Figure 3a,b presents, respectively, temperature dependences of the effective magnetic fields at the nuclei of the iron ions occupying sites $12k$ and $4f$ in $SrFe_{12}O_{19}$ and $SrFe_{10.2}Al_{1.8}O_{19}$. To make the plots more revealing, the de-

TABLE II. Room-temperature effective magnetic fields H_{eff}, isomer shifts δ, and quadrupole splittings ΔE for $SrFe_{10.2}Al_{1.8}O_{19}$ (the isomer shift δ determined relative to α Fe).

	H_{eff}, kOe		δ, mm/s		ΔE, mm/s	
Sublattice	$[\gamma]$	$[e]$	$[\gamma]$	$[e]$	$[\gamma]$	$[e]$
$12k$	415±1	415±1	0.36±0.01	0.36±0.01	0.42±0.02	0.40±0.02
$4f_1$	482±2	482±2	0.29±0.02	0.26±0.04	0.18±0.04	0.10±0.08
$4f_2$	518±2	513±2	0.44±0.02	0.38±0.02	0.40±0.04	0.20±0.04
$2a$	510±2	–	0.31±0.02	–	0.10±0.04	–
$2b$	405±4	–	0.29±0.02	–	2.22±0.04	–

pendences of the fields at the iron nuclei in the inequivalent $2a$ and $2b$ sublattices are not shown.

The temperature of the transition to paramagnetic state was determined by all methods used in Mössbauer spectroscopy, namely (1) The experimental spectra obtained near the phase transition were used to derive a spectrum with no Zeeman splitting, where one observes only the quadrupole lines of the paramagnetic phase. The temperature at which the Zeeman lines disappeared was taken for the Curie point; (2) By temperature scanning, where the transition point is determined from the temperature dependence of the number of quanta detected with the gamma source moving with a constant velocity (or fixed). In the latter case, as one approaches the transition point from low temperatures, the number of detected quanta, as seen from Fig. 3, increases. At the transition, the curve reaches saturation, and the number of detected quanta does not change with further increase of temperature. The temperatures of transition to paramagnetic state determined by the above methods were found to coincide.

As seen from Fig. 3, the effective fields at the iron-ion nuclei in the ~200-nm thick surface layer of the crystal under study decrease with increasing temperature faster than those in the bulk of this crystal. In $SrFe_{12}O_{19}$ (Fig. 3a), the effective magnetic fields at the nuclei of the bulk iron ions vanish at the Curie temperature of 731 K. It should be noted that the temperature dependences of the fields derived from gamma-resonance spectra are in a good agreement with the data quoted by other authors (see, e.g., Ref. 23). The effective magnetic fields obtained from the spectra of conversion and Auger electrons, i.e. the fields at the iron nuclei in the ~200-nm thick surface layer, vanish at 728 K, i.e. three degrees below the Curie temperature.

In the case of $SrFe_{10.2}Al_{1.8}O_{19}$ (Fig. 3b), the effective magnetic fields at the bulk iron nuclei vanish at the Curie temperature of 646 K. Hence a $\Delta x = 1.8$ substitution of iron ions in the compound reduces the Curie temperature by ~100 K. This is in accord with Refs. 23,24 presenting the Curie temperature as a function of Al content in the compound. The effective magnetic fields at the iron ion nuclei in the ~200-nm thick surface layer vanish at 641 K. Hence in $SrFe_{10.2}Al_{1.8}O_{19}$ the surface layer with a thickness of ~200 nm becomes paramagnetic at a temperature lower by 5 K than that in the bulk of the crystal.

A direct support for the transition of a surface layer to paramagnetic state occurring below the Curie point for the bulk comes from experimental Mössbauer spectra obtained with $SrFe_{12}O_{19}$ at 723 K and $SrFe_{10.2}Al_{1.8}O_{19}$ at 639 K, which are shown in Figs. 4 and 5, respectively. It should be pointed out that the spectra measured with gamma quanta (Figs. 4a and 5a) are similar to the gamma-resonance spectra obtained near the Curie point by other authors (see Ref. 14 and references therein). A comparison of the spectra taken near the Curie temperature shows that the splitting of the Zeeman lines in the gamma-resonance spectra (Figs. 4a and 5a) is substantially larger than that in the spectra obtained by measuring conversion and Auger electrons (Figs. 4b and 5b). Hence the effective magnetic fields at the iron nuclei in the bulk of a sample are stronger than those in the surface layer.

An analysis of the experimental spectra shows that the

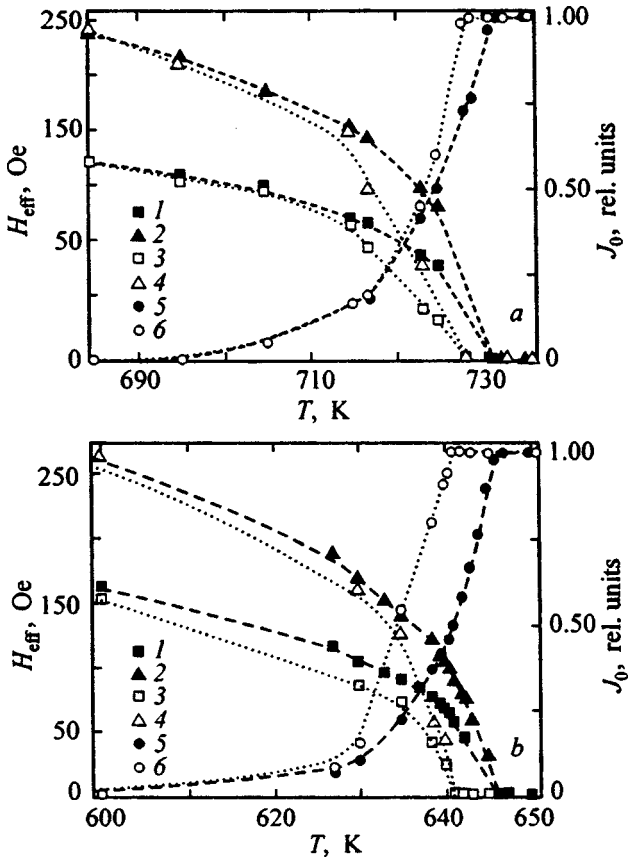

FIG. 3. Temperature dependences of effective magnetic fields in (a) $SrFe_{12}O_{19}$ and (b) $SrFe_{10.2}Al_{1.8}O_{19}$ at iron ion nuclei occupying inequivalent $12k$ and $4f$ sites (*1,2*) in the bulk and (*3,4*) in a 200-nm thick surface layer of the crystal, as well as the paramagnetic-line intensity of iron ions (*5*) in the bulk and (*6*) in the surface layer.

transition of a massive ferromagnet to paramagnetic state takes place in the following way. When the crystal is heated, the paramagnetic phase appears on its surface at temperatures below the Curie point. The transition temperature of a thin layer at a depth L from the surface, $T_c(L)$, increases with distance from the surface to reach the bulk value R_c for $L \gtrsim 300$ nm. As the temperature is raised still more, progressively deeper layers transfer apparently to the paramagnetic phase. At the Curie point, thermal energy destroys magnetic ordering throughout the remainder of the crystal.

As already mentioned, there is experimental evidence (see Refs. 3–5,7 and references therein) indicating possible existence of magnetization on the surface of a crystal without magnetic ordering in the bulk of the sample. These results correspond to the case of positive values of the phenomenological order parameter q in the phase diagram of Fig. 1, which was derived from theoretical studies.

The experimental studies of antiferromagnets with weak ferromagnetism,[10–12] as well as the experimental data obtained in this work indicate that a surface can transfer to paramagnetic state at temperatures below the Néel or Curie points as well. These data are at odds with the phase diagram based on theoretical considerations. Summing up the experimental results, one arrives at the phase diagram for the sur-

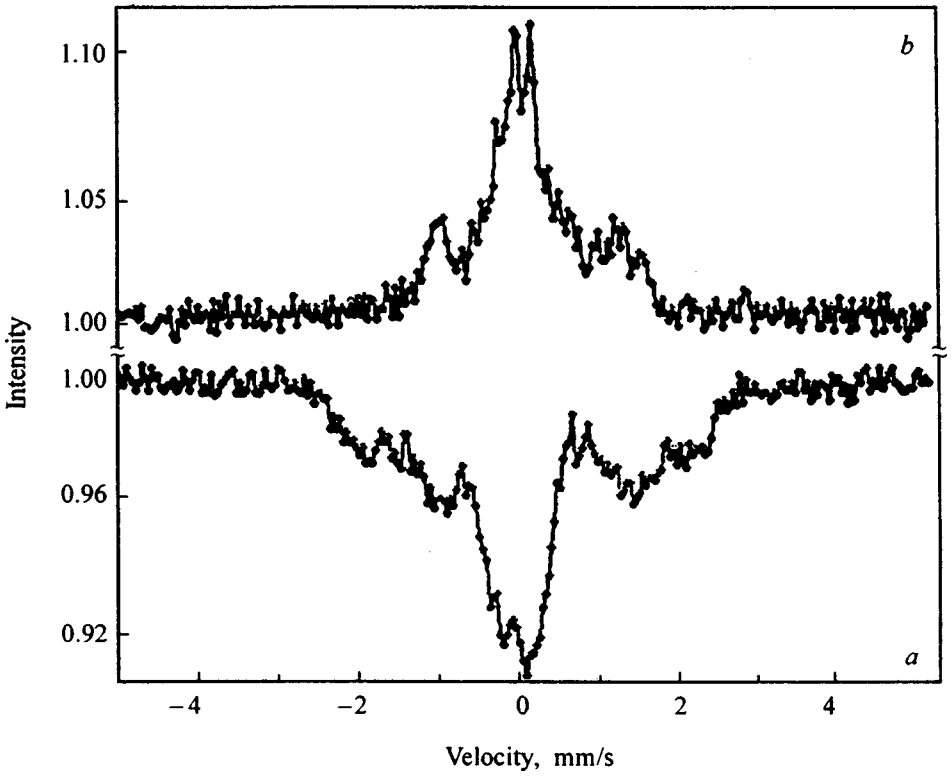

FIG. 4. Mössbauer spectra of $SrFe_{12}O_{19}$ obtained at $T=723$ K with detection of (a) gamma quanta from the bulk of the crystal and of (b) conversion and Auger electrons from a ~200-nm thick surface layer.

face and bulk of a crystal near the Curie (Néel) temperature displayed in Fig. 6.

Thus we have presented the first direct experimental evidence showing that a thin surface layer of a macroscopic ferrimagnetic crystal becomes paramagnetic at a temperature below the Curie point for the bulk of the crystal. In a temperature region below the Curie point, one observes on the surface a nonuniform state, namely, a magnetically disordered surface layer, with the bulk of the crystal remaining ordered. A phase diagram based on the experimental data is proposed, which describes the state of the surface and of the bulk of the crystal in the vicinity of the Curie (or Néel) point.

Support of the Russian Fund for Fundamental Research (Grant 98-02-18279) is gratefully acknowledged.

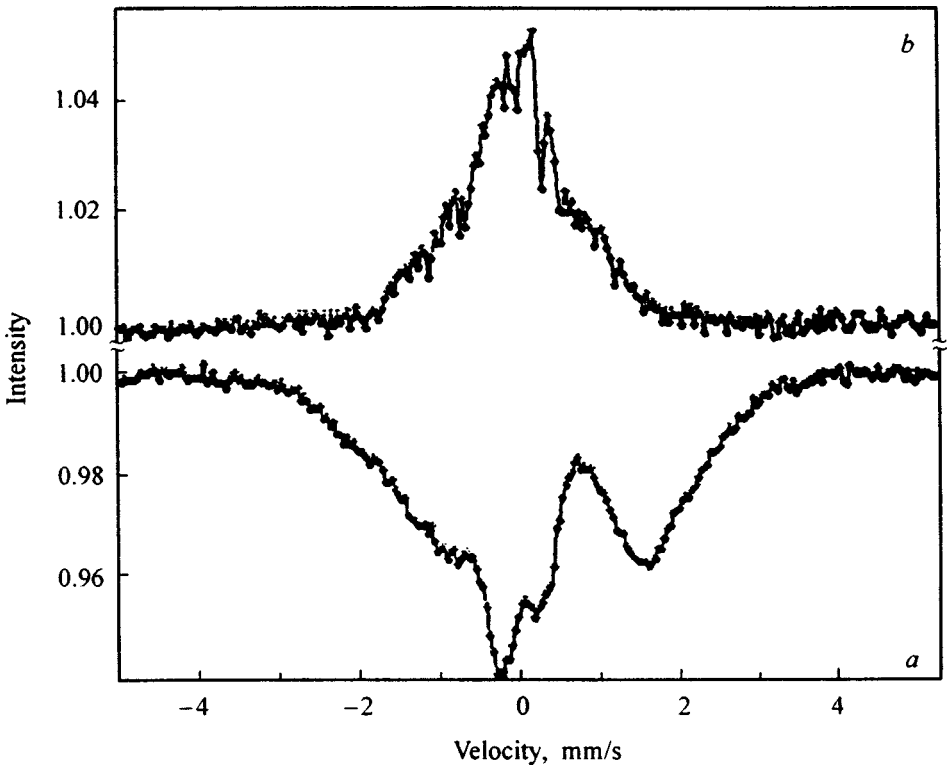

FIG. 5. Mössbauer spectra of $SrFe_{10.2}Al_{1.8}O_{19}$ obtained at $T=639$ K with detection of (a) gamma quanta from the bulk of the crystal and of (b) conversion and Auger electrons from a ~200-nm thick surface layer.

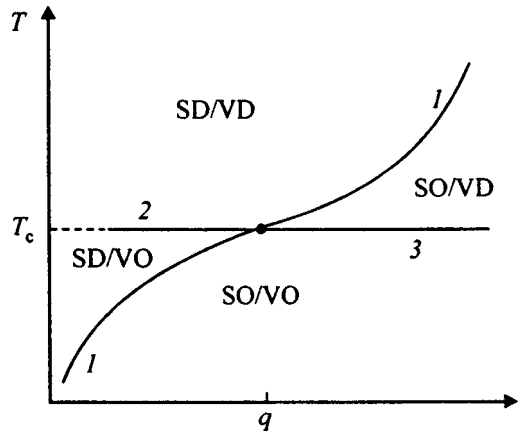

FIG. 6. Phase diagram of the surface and bulk states of a magnet near the Curie temperature, which is proposed by the present authors based on the experimental data obtained. *1* — surface transition, *2* — ordinary transition, *3* — extraordinary transition, VO — magnetically ordered bulk, SO — magnetically ordered surface, VD — magnetically disordered bulk, SD — magnetically disordered surface.

[1] M. I. Kaganov and A. M. Omel'yanchuk, Zh. Éksp. Teor. Fiz. **61**, 1679 (1971) [Sov. Phys. JETP **34**, 895 (1971)].
[2] D. L. Mills, Phys. Rev. B **3**, 3887 (1971).
[3] K. Binder, in *Phase Transitions and Critical Phenomena* (Academic, New York, 1983), Vol. 3, p. 325.
[4] M. P. Kaganov and A. V. Chubukov, in *Magnetic Properties of Crystalline and Amorphous Media* [in Russian] (Nauka, Novosibirsk, 1989), p. 148.
[5] H. W. Diehl, J. Mod. Phys. B **11**, 3503 (1997).
[6] T. C. Lubensky and H. Rubin, Phys. Rev. B **12**, 3885 (1975).
[7] T. Kaneyoshi, J. Phys.: Condens. Matter **3**, 4497 (1991).
[8] A. S. Kamzin, V. P. Rusakov, and L. A. Grigor'ev, in *Proc. Intern. Conf. Physics of Transition Metals* (Kiev, 1988), Pt. 2, p. 271.
[9] A. S. Kamzin and L. A. Grigor'ev, Pis'ma Zh. Tekh. Phys. **16**, No. 16, 38 (1990) [Tech. Phys. Lett. **16**, 616 (1990)].
[10] A. S. Kamzin and L. A. Grigor'ev, JETP Lett. **57**, 552 (1993); Zh. Éksp. Teor. Fiz. **105**, 377 (1994) [JETP **78**, 200 (1994)].
[11] A. S. Kamzin and L. A. Grigor'ev, Fiz. Tverd. Tela (St. Petersburg) **36**, 1399 (1994) [Phys. Solid State **36**, 765 (1994)].
[12] A. S. Kamzin, L. A. Grigor'ev, and S. A. Kamzin, Fiz. Tverd. Tela (St. Petersburg) **37**, 67 (1995) [Phys. Solid State **37**, 33 (1995)].
[13] G. Amonoff, Geof. Foren. Stockholm Forhandl. **47**, 283 (1925).
[14] Sh. Sh. Bashkirov, A. B. Liberman, and V. I. Sinyavskiĭ, *Magnetic Microstructure of Ferrites* [in Russian] (Kazan Univ., 1978), 181 pp.
[15] A. S. Kamzin, L. P. Ol'khovik, and V. L. Rozenbaum, JETP Lett. **61**, 936 (1995); J. Magn. Magn. Mater. **161**, 139 (1996); Zh. Éksp. Teor. Fiz. **111**, 1426 (1997) [JETP **84**, 788 (1997)]; JETP Lett. **67**, 991 (1998).
[16] B. Stahl, R. Gellert, A. Kamzin, G. Klingelhöfer, and E. Kankeleit, J. Phys. IV France, Vol. 7, Coll. C1, Suppl. JP-III, C1-219 (1997).
[17] A. S. Kamzin and L. A. Grigor'ev, Pis'ma ZTF **19**, No. 8, 50 (1993) [Tech. Phys. Lett. **19**, 245 (1993).
[18] A. S. Kamzin, L. A. Grigor'ev, and Yu. N. Mal'tsev, Pis'ma ZTF **19**, No. 21, 32 (1993) [Tech. Phys. Lett. **19**, 680 (1993); A. S. Kamzin, S. M. Irkaev, Yu. N. Mal'tsev, and L. A. Grigor'ev, Prib. Tekh. Éksp. No. 1, 80 (1993).
[19] J. M. D. Coey, D. C. Price, and A. H. Morrish, Rev. Sci. Instrum. **43**, 54 (1972).
[20] V. Florescu, D. Barb, M. Moranin, and D. Tarina, Rev. Roum. Phys. **19**, 249 (1974).
[21] R. H. Fogel and B. J. Evans, J. Appl. Phys. **49**, 1570 (1978).
[22] B. J. Evans, F. Granjean, A. P. Lilot, R. H. Vogel, and A. Gerard, J. Magn. Magn. Mater. **67**, 123 (1987).
[23] G. Albanese, M. Carbucicchio, and A. Deriu, Phys. Status Solidi A **23**, 351 (1974).
[24] D. R. Taft, J. Appl. Phys. **35**, 776 (1964).

Translated by G. Skrebtsov

Contribution of carriers to optical conductivity spectra of lanthanum manganites

N. N. Loshkareva, Yu. P. Sukhorukov, V. E. Arkhipov, S. V. Okatov, S. V. Naumov, and I. B. Smolyak

Institute of Metal Physics, Ural Branch of the Russian Academy of Sciences, 620219 Ekaterinburg, Russia

Ya. M. Mukovskiĭ and A. V. Shmatok

Institute of Steel and Alloys, 117936 Moscow, Russia
(Submitted August 27, 1998)
Fiz. Tverd. Tela (St. Petersburg) **41**, 475–482 (March 1999)

To study the band structure and carriers in lanthanum manganites, measurements have been made of the reflectance spectra of single crystals and polycrystals in the 0.04–1.6-eV range and of the optical conductivity σ_{opt} calculated by the Kramers-Kronig method as functions of the concentration and species of divalent ions in the paramagnetic (PM) and ferromagnetic (FM) regions. The optical gap for single-crystal $La_{0.9}Sr_{0.1}MnO_3$ is ~ 0.17 eV, and the polaron-band energy is 0.12 eV. In the PM region, σ_{opt} spectra do not indicate a band-carrier contribution, and conduction is dominated by polaron hopping and activation to the mobility edge. In the FM region, the variation in the σ_{opt} and absorption spectra of $La_{0.7}Sr_{0.3}MnO_3$ epitaxial films indicate the appearance of band carriers and a red shift of the absorption edge. The two band-carrier contributions, with weak and strong dependences on photon energy, are related to conduction in the antiferromagnetic matrix and the ferromagnetic regions. © *1999 American Institute of Physics.* [S1063-7834(99)02103-6]

The interest in lanthanum manganites having perovskite structure stems from the giant magnetoresistance observed in these compounds and from its possible application potential.[1,2] From among the large number of papers dealing with their investigation, however, only a few were devoted to the optical properties, although optical methods are a powerful tool to probe the band structure and the conduction mechanisms in a material.

Our earlier study of the reflectance spectra of polycrystalline $La_{0.67}Ba_{0.33}MnO_3$ (Ref. 3) and single-crystal $La_{1-x}Sr_xMnO_3$ ($x=0.1$, 0.2, 0.3) (Ref. 4) has led to the conclusion of the presence in these compounds of carriers of two types. For temperatures above the Curie point (T_c), conduction occurs by low-mobility carriers, and for $T<T_c$ an additional conduction mechanism involving mobile band-type carriers sets in.

The transition from paramagnetic (PM) to ferromagnetic (FM) state in weakly strontium-doped $La_{0.9}Sr_{0.1}MnO_3$ single crystals is accompanied by a red shift of the optical-absorption edge,[4] which is typical of ferromagnetic semiconductors and is associated with the conduction-band splitting caused by exchange interaction of band electrons with localized spins. Within the $95<T<165$ K interval, the shift was found to be 0.16 eV, and application of an external magnetic field increased the shift. When the temperature was decreased below T_c, the spectrum of optical conductivity, σ_{opt}, was observed to undergo rearrangement in $La_{0.6}Sr_{0.4}MnO_3$ (Ref. 5) and $Nd_{0.7}Sr_{0.3}MnO_3$ (Ref. 6) films. These compositions exhibit an increase of the absorption coefficient and, hence, of σ_{opt} for energies below 1.2 eV. A peak was observed at ~ 1.2 eV, which shifts to lower energies (the ''red shift'') as the system transfers to ferromagnetic state. The spectral behavior of a $La_{0.825}Sr_{0.175}MnO_3$ single crystal with a lower strontium concentration observed for $T<T_c$ is somewhat different,[7] namely, the increase of optical conductivity in the low-energy domain is accompanied by a decrease of absorption in the region of the 1.5-eV band with a slight shift of the band maximum toward higher energies (the ''blue shift''). A variety of different interpretations were proposed for the observed spectral rearrangement.[5–7] It is essential that all optical experiments evidence a strong effect of magnetic ordering on optical properties, and that the discrepancies among the data quoted by different authors may be due to the concentrations of divalent ions being different.

The objective of this work was to study the variation of the energy spectrum and nature of carriers in lanthanum manganites with concentration of divalent ions (Sr^{2+}) and with variation of the species of the divalent ion (Ca^{2+}, Ba^{2+}, Sr^{2+}) for their fixed concentration ($x\sim 0.3$). The objects were single-crystal and polycrystalline samples, as well as epitaxial films, which would permit studying the effect of the technique used to prepare a lanthanum manganite on its optical property.

1. SAMPLES AND EXPERIMENTAL CONDITIONS

The optical properties of strongly absorbing materials, a class to which lanthanum manganites belong, are usually inferred from studies of reflectance spectra treated by the Kramers-Kronig method. This permits determining the optical conductivity and detailed information on the band structure. We studied in this work the reflectance of single-crystal and polycrystalline lanthanum manganites and calculated the

TABLE I. Composition, electrical resistivity ρ at 293 K, Curie temperature T_c, and method of lanthanum-manganite preparation.

Composition	ρ at 293 K, $\Omega\cdot$cm	T_c, K	Method
Single crystals			Floating zone with radiation heating,[4]
$La_{0.9}Sr_{0.1}MnO_3$	2	150	
$La_{0.8}Sr_{0.2}MnO_3$	4.5×10^{-3}	321	
$La_{0.7}Sr_{0.3}MnO_3$	8×10^{-4}	350	
Polycrystals			Solid-phase synthesis
$LaMnO_3$	8×10^{-1}	190	
$La_{0.67}Ca_{0.33}MnO_3$	8×10^{-2}	220	
$La_{0.7}Sr_{0.3}MnO_3$	6×10^{-3}	352	
Polycrystal $La_{0.67}Ba_{0.33}MnO_3$	5.3×10^{-2}	327	Coprecipitation from solution,[3]
Films			Epitaxial growth on $SrTiO_3$ substrate.
No. 1 $La_{0.7}Sr_{0.3}MnO_3$	3×10^{-1}	196	
No. 2 $La_{0.7}Sr_{0.3}MnO_3$	1×10^{-1}	227	

optical conductivity from a Kramers-Kronig analysis. The data for the samples used are listed in Table I. The calculated optical-conductivity and absorption spectra are compared with absorption measurements on the epitaxial films prepared in this work and with an absorption spectrum of single-crystal $La_{0.9}Sr_{0.1}MnO_3$ obtained earlier[4].

The reflectance spectra R of the single crystals and polycrystals were measured within the 0.035–1.6-eV range, and the absorption spectra of the films, in the 0.09–2.2-eV interval on an IKS-21 computerized spectrometer and a KSVU-12 setup.

The two films with a nominal composition $La_{0.7}Sr_{0.3}MnO_3$ studied by us differ in the substrate temperature during the deposition, namely, 500 °C for film 1 and 600 °C for film 2. Following the deposition, the films were annealed in an $Ar-O_2$ plasma at 500 °C and 600 °C, respectively. X-ray diffraction analysis showed crystallization in film 1, unlike film 2, not to have been completed, making it a partially amorphized film. The film thickness was 90 nm. The electrical resistivity of film 1 ($T_c=196$ K) within the temperature region of 77–293 K follows a semiconducting pattern (with the resistivity decreasing by a factor twenty with increasing temperature), while film 2 exhibits a metallic behavior below the Curie temperature ($T_c=227$ K) and a semiconducting one, above T_c. The Curie temperatures of the films are substantially lower than those of the single crystals and polycrystals of the same composition, while ρ is larger, which may be due to the films having been heavily defected.

2. RESULTS OF MEASUREMENTS

Figure 1 plots the reflectance *vs* wavelength for some polycrystals and a $La_{0.7}Sr_{0.3}MnO_3$ single crystal, whose parameters are given in Table I. Reflection for wavelengths longer than 14 μm (0.09 eV) is due to the light coupling to lattice vibrations. Light with wavelengths below 14 μm interacts with carriers, and interband transitions are initiated close to the short-wavelength edge of the range studied ($\sim$1.5 eV).

The absorption spectra of the $La_{0.9}Sr_{0.1}MnO_3$ single crystal derived by Kramers-Kronig analysis from reflectance spectra coincide with the measurements[4] made directly on this single crystal, which supports the validity of our treatment of the reflectance data.

The optical conductivity spectra of $La_{1-x}Sr_xMnO_3$ single crystals ($x=0.1$, 0.2, 0.3) exhibit below 0.09 eV phonon bands (see inset to Fig. 2), which coincide in position with the ones reported[7] for a $La_{0.825}Sr_{0.175}MnO_3$ single crystal. The band at 0.12 eV is well resolved for the $x=0.1$ composition with semiconducting behavior (inset in Fig. 2). The 0.12-eV band associated with localized carriers was observed earlier in the absorption spectra of this sample.[4] At $E\sim0.17$ eV, the $x=0.1$ sample passes through a minimum of conductivity, after which σ_{opt} rises up to the band maximum at $\sim$1.5 eV. Note that the position of the band maximum was accurately determined only for $La_{0.7}Sr_{0.3}MnO_3$ films dealt with below (Fig. 4), whereas in other samples this position

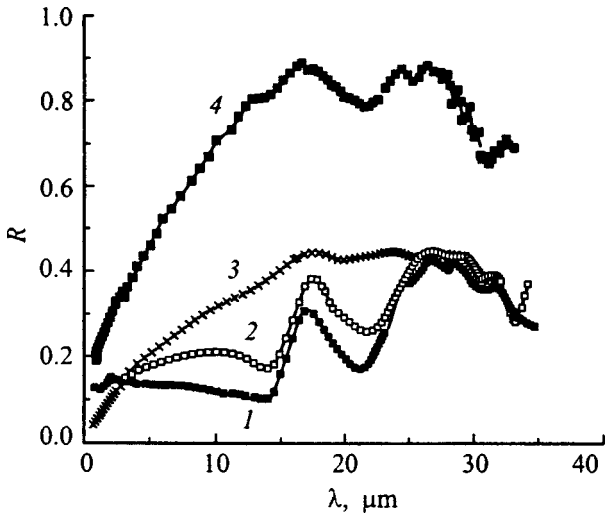

FIG. 1. Reflectance spectra of lanthanum-manganite single crystals (SC) and polycrystals (PC): *1* — $LaMnO_3$ (PC), *2* — $La_{0.67}Ca_{0.33}MnO_3$ (PC), *3* — $La_{0.67}Ba_{0.33}MnO_3$ (PC), *4* — $La_{0.7}Sr_{0.3}MnO_3$ (SC).

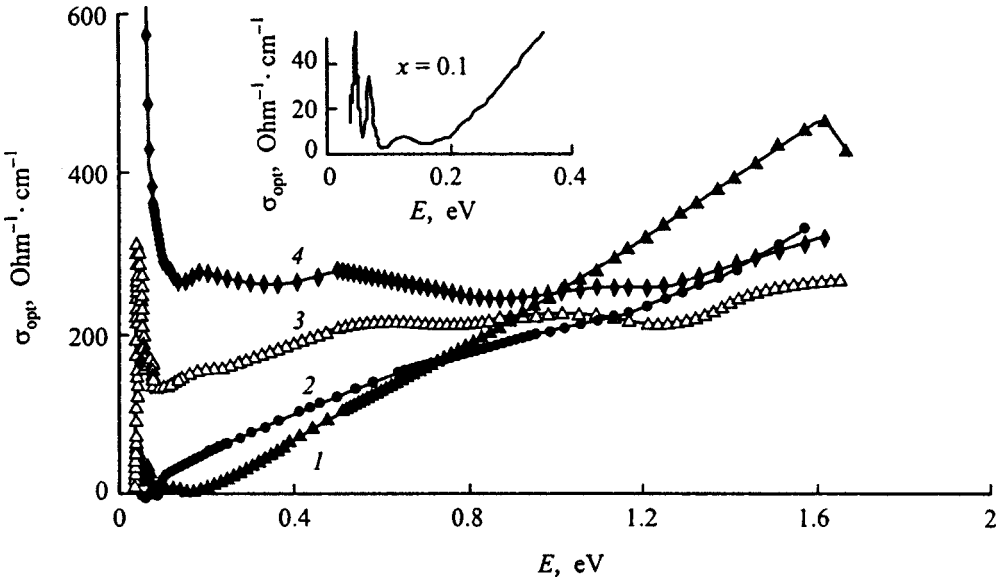

FIG. 2. Optical conductivity spectra of $La_{1-x}Sr_xMnO_3$ single crystals: *1* — $x=0.1$, $T=293$ K; *2* — $x=0.2$, $T=340$ K; *3* — $x=0.2$, $T=293$ K; *4* — $x=0.3$, $T=293$ K. The inset shows a fragment of the optical conductivity spectrum of a $x=0.1$ single crystal in the low-energy region.

can vary within ± 0.2 eV because of the error in σ_{opt} determination at the high-energy boundary of the measurement range. The shape of the spectrum warrants a conclusion that the minimum optical gap for the $x=0.1$ sample is ~ 0.17 eV. Increasing the Sr ion concentration to $x=0.2$ results in disappearance of the gap in the PM temperature region and in a weakening of the ~ 1.5-eV band. In the FM region, the optical gap in the $x=0.2$ and 0.3 samples undergoes filling. As the $x=0.2$ single crystal crosses over from the PM to FM region, σ_{opt} near the ~ 1.5-eV band decreases (curves 2 and 3).

Figure 3 illustrates the effect of La ion substitution by various divalent ions (Ca^{2+}, Ba^{2+}, Sr^{2+}) for the same nominal concentration ($x \cong 0.3$) on optical conductivity spectra of lanthanum manganites obtained at 293 K. One readily sees the optical conductivity spectra of single-crystal $La_{0.7}Sr_{0.3}MnO_3$ (Fig. 2) and polycrystalline $La_{0.67}Ba_{0.33}MnO_3$ and $La_{0.7}Sr_{0.3}MnO_3$, which are ferromagnetic at 293 K, to be similar. The low values of σ_{opt} for polycrystalline samples are the consequence of the comparatively small reflectance (Fig. 1). The optical conductivity spectrum of polycrystalline $LaMnO_3$ with the smallest optical gap ~ 0.13 eV resembles that of single-crystal $La_{0.9}Sr_{0.1}MnO_3$ (Fig. 1), while the spectrum of polycrystal-

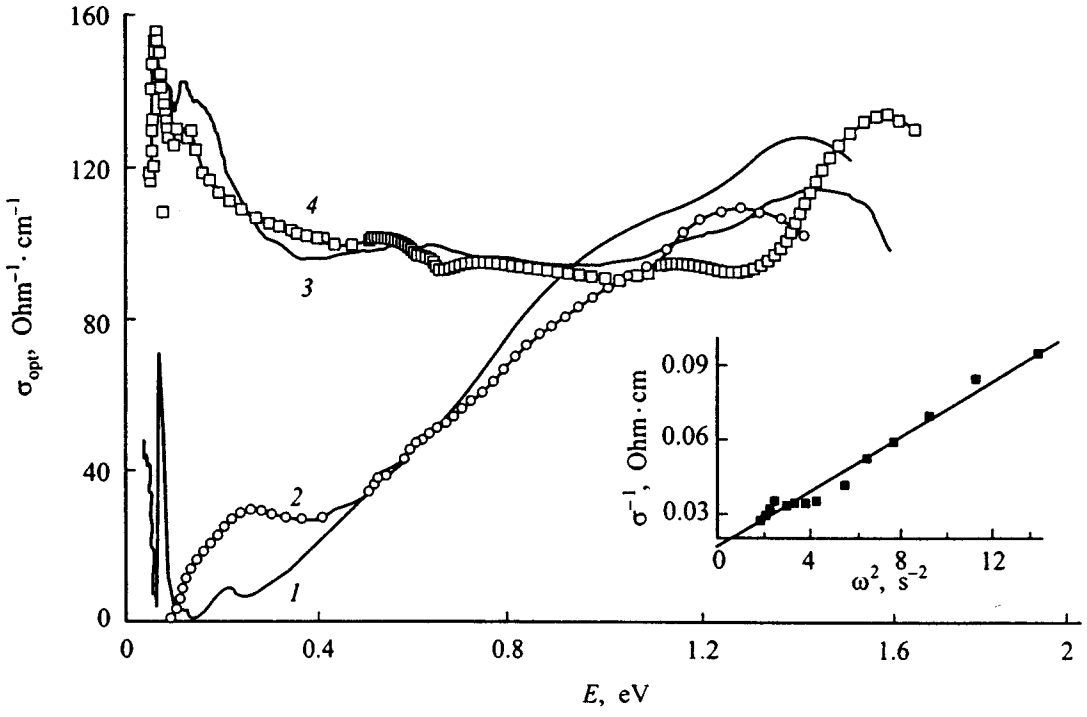

FIG. 3. Optical conductivity spectra of polycrystals: *1* — $LaMnO_3$, *2* — $La_{0.67}Ca_{0.33}MnO_3$, *3* — $La_{0.7}Sr_{0.3}MnO_3$, *4* — $La_{0.67}Ba_{0.33}MnO_3$. The inset shows inverse optical conductivity plotted vs squared light frequency for $La_{0.67}Ba_{0.33}MnO_3$.

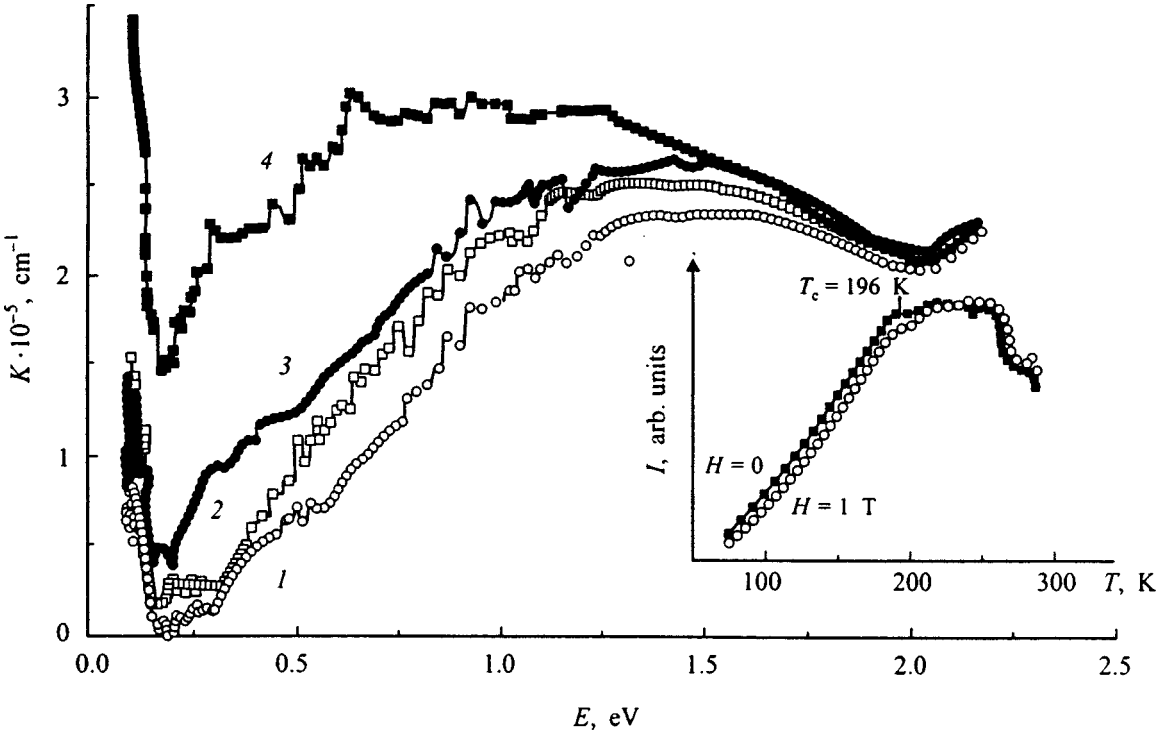

FIG. 4. Absorption spectra of $La_{0.7}Sr_{0.3}MnO_3$ films 1 (curves *1,2*) and 2 (curves *3,4*) obtained at two temperatures: *1,3* — 293 K, and *2,4* — 80 K. The inset shows the temperature dependence of light intensity transmitted through film 1 for photon energy of 0.5 eV in a magnetic field of 1 T and without field.

line $La_{0.67}Ca_{0.33}MnO_3$ is similar to that of single-crystal $La_{0.8}Sr_{0.2}MnO_3$ in the PM region. Stoichiometric $LaMnO_3$ is known to be an antiferromagnet with a Néel temperature of 141 K.[8] That the $LaMnO_3$ sample studied is a ferromagnet indicates a deviation from stoichiometry (the presence of Mn^{4+} ions).

As can be seen from $\sigma_{opt}(E)$ spectra, single-crystal $La_{0.7}Sr_{0.3}MnO_3$, and particularly polycrystalline $La_{0.67}Ba_{0.33}MnO_3$ and $La_{0.7}Sr_{0.3}MnO_3$, exhibit a strong rise in conductivity characteristic of free carriers in the region of ferromagnetic ordering near the phonon spectrum. The real part of dielectric permittivity ε_1 calculated from the Kramers-Kronig relation for $La_{1-x}Sr_xMnO_3$ single crystals in the FM region vanishes at an energy of 0.173 eV for the $x=0.3$ composition, and at 0.135 eV for $x=0.2$. For lower energies the free-carrier contribution becomes dominant. The absence in the σ_{opt} spectrum when $x=0.2$ of a noticeable contribution from free carriers is due to its being in the region of the phonon spectrum.

The absorption spectra of films 1 and 2 measured at 80 and 293 K are displayed in Fig. 4. They are in agreement with the spectral response of σ_{opt} for single crystals (Fig. 1). The spectrum of film 1 (a partly amorphized one), which exhibits a temperature dependence of electrical resistivity characteristic of semiconductors throughout the temperature range studied, resembles that of the $La_{0.9}Sr_{0.1}MnO_3$ single crystal. The minimum optical gap for film 1 is $\sim$0.2 eV. When cooled below T_c (curve 2), the fundamental absorption edge of this film shifts toward lower energies, i.e. exhibits the so-called red shift of the absorption edge characteristic of magnetic semiconductors[9]. It is such a behavior of the spectrum that we observed for a weakly doped $La_{0.9}Sr_{0.1}MnO_3$ single crystal, whose resistivity followed the semiconducting pattern throughout the temperature region covered, except for a narrow interval near T_c where an anomaly was seen in the temperature dependence of the resistivity.[4] As evident from the absorption spectra of film 2 (curves 3 and 4) which exhibits a metallic behavior of resistivity in the FM region, the absorption at the low-energy band edge and near the phonon spectrum increases strongly as one crosses over into the FM region. As a result of this rise in absorption, the band maximum at 1.5 eV is found shifted toward lower energies.

The inset to Fig. 4 shows the effect of a magnetic field on absorption in film 1. As the temperature decreases, the transmitted light intensity measured at a photon energy of 0.5 eV first starts to increase, which reflects the conventional blue shift of the band, only to fall off slightly above the Curie temperature ($T_c=196$ K), thus indicating a red shift. Magnetic field enhances this decrease, i.e. amplifies the red shift. While in the $La_{0.9}Sr_{0.1}MnO_3$ single crystal the increase in absorption observed in a magnetic field of 1 T and at a photon energy of 0.5 eV and temperature of 80 K was found to be 30%, for film 1 it was 12%. For film 2, the magnetic-field-induced change in absorption turned out to be one half that for film 1.

3. DISCUSSION OF RESULTS

Within the 0.04–1.60-eV spectral region, the optical conductivity of the lanthanum manganites studied exhibits the following common features: a phonon spectrum below 0.09 eV, an absorption band at $\sim$1.5 eV with a tailing low-energy edge, a minimum optical gap $<$0.2 eV for undoped

and weakly doped $LaMnO_3$, and the filling of this gap for heavily doped lanthanum manganites in the FM region.

The width of the optical gap observed by us in nonstoichiometric polycrystalline $LaMnO_3$ (~ 0.13 eV) and in a weakly doped single crystal (~ 0.17 eV) is in accord with the calculated electronic structure of $LaMnO_3$,[10] which yields ~ 0.2 eV for the minimum width of the gap. Most of the available band-structure calculations,[10,11] as well as the experimental optical spectra of $LaMnO_3$ and $CaMnO_3$,[12] suggest that the lowest-in-energy charge-transfer transition in $LaMnO_3$ is the indirect transition from a filled $e_{g\uparrow}^1$ to an empty $e_{g\uparrow}^2$ state, where the e_g^1 and e_g^2 states belong to the Jahn-Teller-split e_g band of Mn^{3+} ions. While such an electric-dipole *d-d* transition is made possible by the hybridization of the e_g states of Mn with $2p$ states of oxygen, its intensity, however, is considerably lower than that of the *p-d* transitions observed to occur at higher energies. The position of the maximum in the absorption band (optical conductivity) corresponds to the distance between the centers of gravity of the e_g^1 and e_g^2 states and for $LaMnO_3$ was calculated[12] to be 1.5 eV. The experimental data on the band maximum position and on the minimum optical gap for $LaMnO_3$ exhibit a considerable scatter,[12,13] apparently because of different deviations from stoichiometry. It appears difficult to identify the optical gap observed in undoped and weakly doped $LaMnO_3$ with a transition between states corresponding to particular points in the Brillouin zone. In this sense the gap in the σ_{opt} spectrum is actually the difference in energies between two levels, e_g^1 and e_g^2, of a finite width and can be identified with the transport gap.

No optical gap is observed in compositions with $x \geqslant 0.2$, and σ_{opt} was found to vary noticeably near the 1.5-eV band. This behavior of σ_{opt} can be attributed to the following reasons:

(i) A broadening of the localized-state region at the band edges;

(ii) A rearrangement of the optical transition system caused by the doping-induced rearrangement of the band structure. A comparison of the spectra obtained[12] for $LaMnO_3$ and $CaMnO_3$ suggests that the formation of a σ_{opt} spectrum in solid solutions should be affected by the strong transition from $O2p$ to the empty e_g band of Mn^{4+} ions. This conjecture derives from the observation that the intense σ_{opt} band at 3.07 eV corresponding to this transition in $CaMnO_3$ (nearly all manganese ions in this transition are quadrivalent) produces in the spectral range under study optical conductivity tails which practically do not differ in intensity from the $LaMnO_3$ spectrum;

(iii) Band carriers contribute to intensity rearrangement in the spectrum.

On the whole, it may be considered established that the 1.5-eV absorption band and its low-energy edge derive from transitions involving the states of the Mn^{3+} and Mn^{4+} ions and from a carrier contribution.

The optical conductivity band at 0.12 eV in $La_{0.9}Sr_{0.1}MnO_3$ (see inset in Fig. 2) was observed by us directly in the absorption spectra of this crystal[4] and of other lanthanum manganites.[14] Similar medium-infrared bands are observed in the spectra of various $3d$ oxides, including those with perovskite structure, for instance, of HTSC compounds,[15] where they are assigned to polarons, i.e. localized carriers. In some oxides, for example, CuO, the low-mobility conduction is totally determined by polarons, which is evidenced, in particular, by the fact that the activation energy of resistance, E_a, is equal to the sum of that of mobility, E_u, and of the polaron binding energy E_p derived from σ_{opt} spectra: $E_a = E_u + E_p$ (Ref. 16).

Conduction in the PM region of lanthanum manganites is apparently not dominated by the polaron mechanism. The energy position of the band, $E_{\max} = 0.12$ eV, determines the activation energy of the polaron mobility, $E_{\max} = 4E_u$, $E_u = 0.03$ eV. The polaron binding energy $E_p = 2E_u = 0.06$ eV. The sum $E_u + E_p = 0.09$ eV differs considerably from the activation energy of static conduction for this sample (0.2 eV). For high temperatures (in the PM region), the mechanism associated with carrier excitation to the mobility edge could be a more likely activated process.[17] Note that the concept of mobility edge motion with temperature which causes variation of the number of carriers in delocalized states is capable of interpreting satisfactorily such phenomena as the metal-insulator (MI) transition below T_c and specific features of the Hall effect and magnetoresistance in lanthanum manganites.[14,18]

As follows from σ_{opt} spectra, band carriers do not provide a noticeable contribution in the PM temperature region in single-crystal and polycrystalline lanthanum manganites even in low-resistivity samples ($\rho \sim 6 \times 10^{-3}\ \Omega \cdot \text{cm}$), provided the activated variation of $\rho(T)$ is weak enough, i.e. in $La_{0.8}Sr_{0.2}MnO_3$ and $La_{0.67}Ca_{0.33}MnO_3$ (Figs. 2 and 3). One may conclude that in the PM temperature region conduction occurs by localized carriers, apparently both by polaron hopping and by activation to the mobility edge, with the relative significance of each process being dependent on the divalent-ion concentration. As the temperature is decreased below the Curie point, where the mobility edge crosses the Fermi level, the MI transition sets in, and the optical conductivity spectra exhibit a strong rise of the band-carrier contribution (Figs. 2–4). That the change of the conduction mechanisms at the MI transition occurs abruptly is evidenced also by the temperature dependence of the reflectance, which is presented for single-crystal $La_{0.8}Sr_{0.2}MnO_3$ in Ref. 4. Estimates of the relaxation time τ made for single-crystal $La_{0.8}Sr_{0.2}MnO_3$ by fitting the experimental reflectance spectrum in the FM region to calculations performed for a simple one-carrier band yield 3×10^{-16} s. Assuming $m^*/m_0 = 1$, we obtain for the carrier mobility 0.5 $\text{cm}^2\text{V}^{-1}\text{s}^{-1}$. These parameters argue for a narrow valence band of lanthanum manganites.

To reveal the nature of the band carrier spectrum in single-crystal $La_{0.8}Sr_{0.2}MnO_3$, the σ_{opt} spectrum taken at 340 K (PM region) was subtracted from that measured at 293 K (FM region). The difference thus obtained, $\Delta\sigma_{\text{opt}}$, indicates that the carrier contribution depends only weakly on energy (Fig. 5).

A similar spectrum subtraction procedure was performed for film 2 ($La_{0.7}Sr_{0.3}MnO_3$). The difference between absorption spectra 4 and 3 obtained at 80 K (FM) and 239 K (PM), accordingly, is likewise only weakly dependent on energy

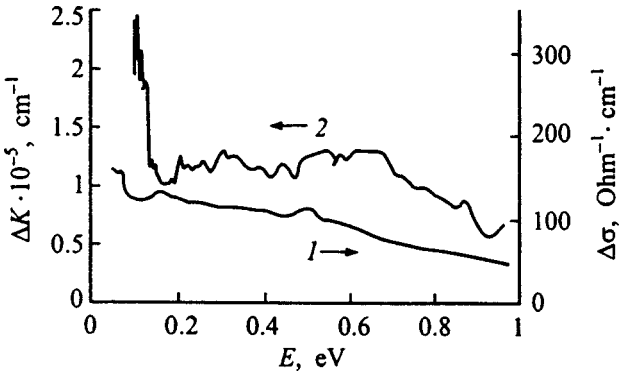

FIG. 5. Difference between optical-conductivity and absorption spectra measured in the ferromagnetic and paramagnetic regions. *1* — $La_{0.8}Sr_{0.2}MnO_3$ single crystal, *2* — $La_{0.7}Sr_{0.3}MnO_3$ film 1.

within a broad energy range. For energies less than ~ 0.3 eV, however, a strong increase of ΔK was found, which is similar to the one observed in σ_{opt} spectra of heavily doped lanthanum manganites with $x=0.3$ (Figs. 2 and 3) and is apparently due to free carriers.

One can thus conclude that σ_{opt} spectra obtained in the FM region exhibit two band-carrier contributions differing in the $\sigma_{\text{opt}}(E)$ dependence. Consider the contribution which depends weakly on energy and is probably associated with low-mobility band carriers. For small τ, one should take into account both terms in the denominator of the expression for high-frequency conductivity $\sigma_{\text{opt}}=\sigma_0/(1+\omega^2\tau^2)$, where σ_0 is the static conductivity. For $\omega^2\tau^2<1$, a condition which is met in our case for $\tau=3\times10^{-16}$ s (from reflectance data), σ_{opt} does indeed depend only weakly on energy, because within the 0.2–0.5-eV interval the value of $1/(1+\omega^2\tau^2)$ decreases by only 5%.

The second contribution, which depends strongly on energy, originates probably from mobile (free) band carriers. The plasma frequency for $La_{1-x}Sr_xMnO_3$ single crystals with $x=0.2$ and 0.3 in the FM region can be estimated from the energies at which the equality $\varepsilon_1=0$ is upheld. This approach yields 2.1×10^{14} s^{-1} for $x=0.2$ and 2.6×10^{14} s^{-1} for $x=0.3$. Assuming the hole effective mass $m^*/m_0=1$, the plasma frequency can be used to estimate the free carrier concentration. Such estimates yield a concentration of 0.5×10^{20} cm^{-3} for the $x=0.2$ composition and 0.9×10^{20} cm^{-3} for $x=0.3$. Note that the free carrier concentration is lower by 1.5 orders of magnitude than the concentration extracted[18] from Hall effect data for polycrystalline $La_{0.67}Ba_{0.33}MnO_3$. Estimates of the relaxation time τ made for the region of strong conductivity growth near the phonon spectrum for $La_{0.67}Ba_{0.33}MnO_3$ and $La_{0.7}Sr_{0.3}MnO_3$ polycrystals yield $\sim5\times10^{-15}$ s, a value higher by an order of magnitude than the one derived from reflectance data. The method of τ determination is based on assuming a linear dependence $\sigma^{-1}(\omega^2)$, which is illustrated by the inset in Fig. 3. Making a similar estimate of τ for single-crystal $La_{0.7}Sr_{0.3}MnO_3$ is difficult because of the free-carrier region being close to the phonon spectrum.

The nature of the two carrier types becomes clear if one assumes that lanthanum manganites belong to materials exhibiting phase separation.[19] In this case the low-mobility carriers belong to the antiferromagnetic matrix, and the high-mobility ones, to the metallic FM regions. The conductivity of the crystal as a whole is a sum of two conductivities, namely, due to free carriers with a low concentration but high mobility and to carriers having a lower mobility but present in a higher concentration.

The above subtraction of the spectra was performed under the assumption that a crossover from the PM to FM region in a sample with a given composition results in the appearance of a band-carrier contribution without any change in the band structure. If, however, changes in the band structure are to be taken into account, one should first determine the part played by the red shift of the absorption edge in the spectral changes associated with a magnetic phase transition.

The absorption spectra of the $La_{0.7}Sr_{0.3}MnO_3$ film (film 1) exhibiting semiconducting behavior of $\rho(T)$ at all temperatures (Fig. 4) demonstrate clearly a red shift of the absorption edge experienced by the film as it crosses over from the PM to FM temperature region, and support our results obtained[4] on a $La_{0.9}Sr_{0.1}MnO_3$ single crystal. The red shift of the absorption edge is similar to the one observed in magnetic semiconductors, for instance, in EuO and $HgCr_2Se_4$, where it was related to the exchange interaction of carriers with localized magnetic-ion spins.[9] The red shift detected in lanthanum manganites may be caused by spin splitting of the e_g state. This presupposes, however, that the Hund exchange energy is not too high compared to the conduction-band width. Indeed, band structure calculations made for $LaMnO_3$ yield 2 eV for the width of the e_g^2 band, and about 3 eV for the exchange splitting,[11] a not too dramatic discrepancy.

The red shift of film 1 is smaller by a factor 2.5 than that in single-crystal $La_{0.9}Sr_{0.1}MnO_3$, which can be explained as due to the smaller volume of FM regions in a film compared to that in a crystal. The strong change in the spectrum of film 2 exhibiting metallic conduction, which is observed to occur at a magnetic phase transition, cannot, however, be a result only of the red shift in the ferromagnetic regions occupying a larger volume than those in film 1. It can be associated with the following factors. First, it is known that the band edges are most sensitive to a red shift, and therefore the displacements of curve 4 (absorption at 293 K) relative to curve 3 (absorption at 80 K) for a fixed absorption coefficient K should be larger for smaller K. In experiment, however, the reverse is observed, namely, the maximum displacement of curve 4 with respect to curve 3 in film 2 is observed to occur at maximum absorption and is ~1.0 eV. Such a shift of the band is in no way reasonable, because it exceeds the largest red shift measured thus far, viz. that for $HgCr_2Se_4$ (0.84 eV), which is a magnetic semiconductor with a wide conduction band. Second, it is also known that the red shift decreases with increasing carrier concentration. This was observed to occur in Gd-doped EuO with increasing Gd^{3+} concentration,[20] and was attributed[9] to a Fermi level shift. Therefore the red shift for film 2 could be expected to be smaller than that for film 1.

It can be maintained that, in heavily doped lanthanum manganites, the fraction of the red-shift-induced changes in

the total variation of the spectra accompanying a magnetic phase transition should be insignificant, and that the observed changes should be determined to a larger extent by band carriers.

Thus lanthanum manganites prepared by different techniques exhibit common spectral features. The fundamental absorption edge in lanthanum manganites derives from transitions involving Mn^{3+} and Mn^{4+} states. In the PM region, band carriers do not contribute noticeably even in low-resistivity samples ($6\times10^{-3}\,\Omega\cdot$cm), and the conduction is dominated by polaron hopping and activation to the mobility edge. In the FM region, the changes observed in the optical conductivity spectra of lanthanum manganites are primarily due to the appearance of band carriers and, to a lesser degree, to the red shift of the absorption edge. The two band-carrier contributions with different dependences on photon energy may be connected with conduction in the matrix and in FM regions.

The authors owe sincere thanks to N. G. Bebenin, B. A. Gizhevskiĭ, V. E. Naĭsh, and G. A. Bolotin for fruitful discussions.

Partial support of the Russian Fund for Fundamental Research (Grant 97-02-16008) is gratefully acknowledged.

[1] É. L. Nagaev, Usp. Fiz. Nauk **166**, 833 (1996).
[2] A. P. Ramirez, J. Phys.: Condens. Matter **9**, 8171 (1997).
[3] N. N. Loshkareva, Yu. P. Sukhorukov, A. P. Nosov, V. G. Vasil'ev, B. V. Slobodin, K. M. Demchuk, and N. G. Bebenin, Fiz. Tverd. Tela (St. Petersburg) **39**, 1616 (1997) [Phys. Solid State **39**, 1440 (1997)].
[4] N. N. Loshkareva, Yu. P. Sukhorukov, B. A. Gizhevskii, A. A. Samokhvalov, V. E. Arkhipov, B. E. Naish, S. P. Karabashev, and Ya. M. Mukovskii, Phys. Status Solidi A **164**, 863 (1997).
[5] Y. Moritomo, A. Machida, R. Matsuda, M. Ichida, and A. Nakamura, Phys. Rev. B **56**, 5088 (1997).
[6] S. G. Kaplan, M. Quijada, H. D. Drew, D. B. Tanner, G. C. Xiong, R. Ramesh, C. Kwon, and T. Venkatesan, Phys. Rev. Lett. **77**, 2081 (1996).
[7] Y. Okimoto, T. Katsufuji, T. Ishikawa, A. Urushibara, T. Arima, and Y. Tokura, Phys. Rev. Lett. **75**, 109 (1995).
[8] G. Matsumoto, J. Phys. Soc. Jpn. **29**, 615 (1970).
[9] É. L. Nagaev, *Physics of Magnetic Semiconductors* [in Russian] (Nauka, Moscow, 1979).
[10] I. Solovyev, N. Hamada, and K. Terakura, Phys. Rev. B **53**, 7158 (1996).
[11] S. Satpathy, Z. S. Popović, and F. R. Vukajlović, J. Appl. Phys. **79**, 4555 (1996).
[12] J. H. Jung, K. H. Kim, D. J. Eom, T. W. Noh, E. J. Choi, Jaejun Yu, Y. S. Kwon, and Y. Chung, Phys. Rev. B **55**, 15489 (1997).
[13] T. Arima, Y. Tokura, and J. B. Torrance, Phys. Rev. B **48**, 17006 (1993).
[14] N. G. Bebenin, N. N. Loshkareva, and Yu. P. Sukhorukov, Solid State Commun. **106**, 357 (1998).
[15] J. P. Falck, A. Levy, M. A. Kastner, and R. J. Birgeneau, Phys. Rev. B **48**, 4043 (1993).
[16] A. A. Samokhvalov, N. A. Viglin, B. A. Gizhevskiĭ, N. N. Loshkareva, V. V. Osipov, N. I. Solin, and Yu. P. Sukhorukov, Zh. Éksp. Teor. Fiz. **103**, 951 (1993) [JETP **76**, 463 (1993)].
[17] N. F. Mott and E. A. Davis, *Electronic Processes in Non-Crystalline Materials* (Clarendon Press, Oxford, 1979) [Russ. transl. Mir, Moscow, 1982].
[18] N. G. Bebenin, R. I. Zaĭnullina, V. V. Mashkautsan, A. M. Burkhanov, V. V. Ustinov, V. V. Vasil'ev, and V. V. Slobodin, Zh. Éksp. Teor. Fiz. **113**, 981 (1998) [JETP **68**, 534 (1998)].
[19] É. L. Nagaev, Usp. Fiz. Nauk **165**, 529 (1995).
[20] J. Schoenes and P. Wachter, Phys. Rev. B **9**, 3097 (1974).

Translated by G. Skrebtsov

Mössbauer studies of the surface and bulk magnetic structure of scandium-substituted Ba–M-type hexaferrites

A. S. Kamzin and V. L. Rozenbaum*)

A. F. Ioffe Physicotechnical Institute, Russian Academy of Sciences, 194021 St. Petersburg, Russia

L. P. Ol'khovik

Kharkov State University, 310077 Kharkov, Ukraine

(Submitted July 17, 1998; resubmitted September 10, 1998)
Fiz. Tverd. Tela (St. Petersburg) **41**, 483–490 (March 1999)

A direct comparison of the magnetic structures of a surface layer and of the bulk of Ba–M-type hexagonal ferrites with iron ions partially replaced by Sc diamagnetic ions ($BaFe_{12-x}Sc_xO_{19}$) has been made by simultaneous Mössbauer spectroscopy with detection of gamma rays, characteristic x-ray emission, and electrons. It has been found that, if the magnetic lattice of a Ba–M-type hexagonal ferrite is weakly diluted by Sc diamagnetic ions, a ~300-nm thick macroscopic layer forms on the surface of a $BaFe_{11.4}Sc_{0.6}O_{19}$ crystal, in which the iron-ion magnetic moments are noncollinear with the moments in the bulk. The noncollinear magnetic structure forms in the near-surface layer of $BaFe_{12-x}Sc_xO_{19}$ crystals because the exchange interaction energy is additionally reduced by the presence of such a ''defect'' as the surface. This is the first observation in ferromagnetic crystals of an anisotropic surface layer whose magnetic properties, as predicted by Néel, differ from those of the bulk. © *1999 American Institute of Physics.* [S1063-7834(99)02203-0]

Starting with late '70s, there has been an increasing interest in the magnetic properties of crystal surfaces. The reason for this lies in the need to understand the influence of such a ''defect'' as the surface on the magnetic structure and characteristics of the surface layer and the contribution of the surface to the properties of materials. The significance of the processes involved in such fundamental phenomena as phase transitions in the surface layer, their differences from and relations to those in the bulk is also presently recognized. These studies are acquiring considerable application potential as well, because the properties of finely dispersed, nanosized powders, for instance, depend essentially on those of the crystallite surface. Hence proper understanding of the mechanisms responsible for the formation of the magnetic properties of nanosized crystallites can eventually pave the way to developing magnetic information carriers with superhigh recording densities.

1. STATE OF CRYSTAL-SURFACE MAGNETIC-STRUCTURE RESEARCH

The surface anisotropic layer in ferromagnets was described theoretically by L. Néel in 1954.[1] The concept of the effect of the surface on the properties of a material was applied to interpretation of experimental data, however, much later. Indeed, Ref. 2 suggested the existence on the surface of Fe, Co, and Ni of thin films of a nonmagnetic (dead) layer ~6 Å thick.

Subsequent investigation of surface properties was done on fine powders and thin films. This can be attributed to the fact that the specific weight of the surface of a crystallite increases with its decreasing volume, as well as to the lack of experimental techniques capable of discriminating between signals produced by a thin surface layer and the bulk of a macroscopic crystal. The wide use of Mössbauer spectroscopy in studies of the surface properties of thin films or finely dispersed powders finds explanation in the possibility of amplifying (or attenuating) the signal due to the surface layer by enriching this layer in the iron-57 (or iron-56) isotope. Recall the unusual experimental finding first reported in Ref. 3, namely, that the saturation magnetization of a fine powder is less than that of the macroscopic crystal of which the powder was prepared. Mössbauer studies led to a conclusion that it is a change in the magnetic structure of the crystallite surface that accounts for the decrease in the saturation magnetization of a finely dispersed powder.[4] To explain the experimental data obtained on fine powders of α-Fe_2O_3,[5] γ-Fe_2O_3,[6,7] $CrFe_2O_4$,[8] CrO_2,[9] $NiFe_2O_4$, $Y_3Fe_5O_{12}$, $Dy_2BiFe_5O_{12}$,[10] and $BaFe_{12}O_{19}$,[11] a ''shell'' model was proposed,[11,12] by which the magnetic structure of the inner part of a crystallite is similar to or, possibly, totally identical to that of a bulk crystal, whereas in a thin surface layer (i.e. in the shell) the magnetic moments are arranged noncollinearly.

The shell model is, however, far from being universally accepted to explain experimental data, with other approaches being available as well. For instance, the spins on the surface of $NiFe_2O_4$, assumed to be angularly ordered with many stable configurations possible, can transfer to a spin-glass phase with decreasing temperature.[13] $CoFe_2O_4$ and Fe_3O_4 were suggested to have a disordered shell (Refs. 14 and 15, respectively). It is believed that the spins in γ-Fe_2O_3 particles are arranged noncollinearly not only on the surface.[16] It

was suggested[17] that in order to overcome the bulk anisotropy and reach complete ordering of magnetic moments along the external magnetic field, one has to apply substantially higher fields than those used to prove the shell model. On the other hand, the results obtained on textured γ-Fe_2O_3 samples in strong magnetic fields were assigned[18] to noncollinear spin ordering, and it was shown that the incomplete magnetic-moment ordering cannot be due to a large magnetic anisotropy, as was suggested in Ref. 17.

Using thin films to study surface properties paved the way to a considerable progress toward understanding the importance of the problem of ''surface'' magnetism. It should be pointed out, however, that the nonuniformity in size of an ensemble of particles, the superparamagnetic phenomena, the strong dependence on the method of preparation employed, etc., make investigation of surface properties of fine powders still more difficult. All these problems are, however, removed if one uses macroscopic crystals.

The first experimental observation of surface anisotropy predicted in Ref. 1 was made in 1972 by Krinchik with coworkers on weakly ferromagnetic antiferromagnets.[19] It was proposed[19] that a macroscopic anisotropic surface layer can exist in such magnets when the energy of demagnetizing field is small compared to ferromagnets and there is no magnetic anisotropy in the basal plane, which increases the role of surface anisotropy. It is in exactly these conditions that one succeeded in observing surface anisotropy for the first time in hematite, a weakly ferromagnetic antiferromagnet.[19] The experimental data thus obtained permitted a conjecture that within this surface anisotropic layer, called[19] a transition layer, magnetic moments change smoothly their orientation from that in the bulk to the direction at the surface.[19] Anisotropic surface layers were subsequently observed to exist in macroscopic crystals of $FeBO_3$,[20,21] $ErFeO_3$ and $TbFeO_3$,[22] which are likewise weak ferromagnets. The thickness of the transition layer in $FeBO_3$ was experimentally found to be $\sim$500 nm.[20,21]

The method involving simultaneous measurement of gamma-, x-ray, and electron Mössbauer spectra (SGXEMS), first proposed by the present authors and described in Ref. 23, offers unique possibilities for probing the surface properties of macroscopic crystals. Its uniqueness consists in that the information on the state of the surface layer and of the bulk of a crystal is obtained simultaneously, and the fact that it is based on a single technique (the Mössbauer effect) permits one to compare directly the experimental data relating to the surface and to the bulk.

The SGXEMS produced the first direct experimental evidence for the existence of a $\sim$400-nm thick transition layer in macroscopic Fe_3BO_6 crystals (which, like the hematite, is a weakly ferromagnetic antiferromagnet).[23] Layer-by-layer measurements made by the SGXEMS showed that as one approaches the crystal surface the deflection of the iron-ion magnetic moments from their orientation in the bulk increases gradually within the transition layer.[24] A SGXEMS study of the surface of $Fe_{2.75}Ga_{0.25}BO_6$ crystals revealed that substitution of 9% Ga diamagnetic ions for iron in Fe_3BO_6 increases by an order of magnitude the thickness of the transition layer.[25]

No transition surface layer with a magnetic structure differing from that of the bulk was found by SGXEMS in M-type hexagonal ferrites ($BaFe_{12}O_{19}$, $SrFe_{12}O_{19}$, $PbFe_{12}O_{19}$).[26] An analysis of model Mössbauer spectra showed that if the M-type hexaferrites in question do have a transition layer, its thickness cannot exceed a few nm, which in order of magnitude coincides with theoretical estimates[1] and is substantially beyond the experimental accuracy of $\sim$10 nm.

Thus the existence in weakly ferromagnetic antiferromagnets of a macroscopic surface layer with a magnetic structure different from that of the bulk of the crystal (called[21,22] transition layer) was convincingly established. No such layer was found on the surface of type M hexagonal ferrites.

2. EXPERIMENTAL TECHNIQUES AND RESULTS OF MEASUREMENTS

The objective of this work was to study the magnetic structure of the surface layer and compare it directly to that of the bulk of the $BaFe_{12}O_{19}$ hexagonal ferrites (Ba–M type), with part of the iron ions replaced by Sc diamagnetic ions. Experimental observation of a transition surface layer in substituted hexaferrites was assumed to be possible due to the following factors. First, substitution in type-M hexaferrites of diamagnetic ions of In, Sc, Ga, or Al for a large fraction of iron ions gives rise to formation in the bulk of a crystal of a noncollinear magnetic structure.[27–29] Second, the present authors showed[25] that substitution in Fe_3BO_6 of diamagnetic Ga ions for 9% of iron ions increases by an order of magnitude the thickness of the transition layer as a result of a weakening of the intersublattice exchange bonding due not only to the incorporated diamagnetic ions but to the presence of the surface as well. This led the authors to assume that substitution of diamagnetic ions for a small part of the iron ions (i.e. where a collinear magnetic structure still persists in the bulk) could initiate formation on the surface of hexagonal ferrite macrocrystals of a macroscopic surface layer, in which magnetic moments would be ordered noncollinearly. These conditions can be upheld in a Ba–M-type hexagonal ferrite, in which part of the iron ions are replaced by Sc diamagnetic ions, $BaFe_{12-x}Sc_xO_{19}$. It was shown that for substitutions $x>1.2$ a noncollinear magnetic structure forms in the bulk of the crystal.[27–29] Thus for $x<1.2$ the collinear structure persists in the crystal. We chose a composition with $x=0.6$, i.e. $BaFe_{11.4}Sc_{0.6}O_{19}$, in order to be confident that the noncollinear structure would not appear with such an amount of scandium ions in the crystal.

Single crystals of the $BaFe_{11.4}Sc_{0.6}O_{19}$ hexaferrite were synthesized by spontaneous crystallization from a solution in the $NaFeO_2$ melt. The chemical formula and the type-M hexagonal structure of the ferrite crystals prepared were confirmed by x-ray diffraction, chemical analysis, and the structure of the Mössbauer spectra. The extent of iron ion substitution was derived also from the dependence of the Curie temperature on Sc concentration. The Curie temperature was deduced both from the temperature dependences of

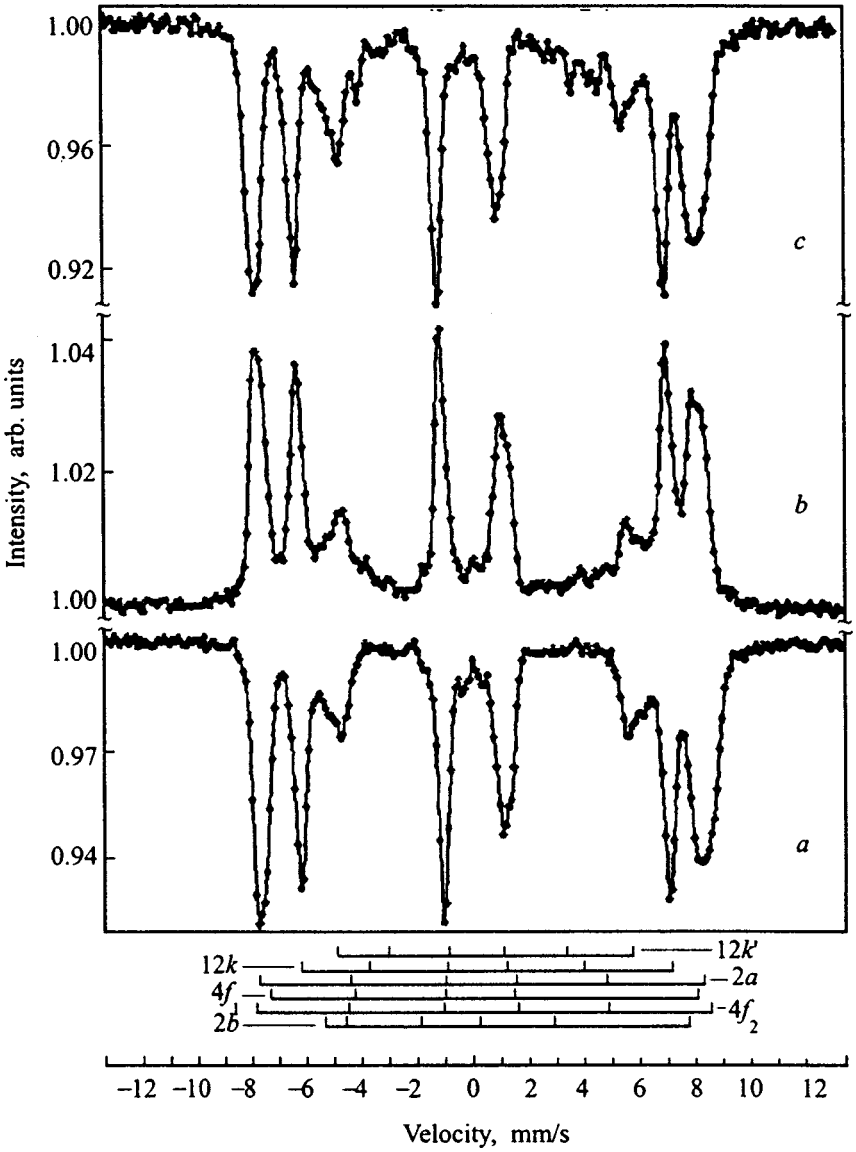

FIG. 1. Room-temperature Mössbauer spectra of the single-crystal $BaFe_{11.4}Sc_{0.6}O_{19}$ hexaferrite; (a,c) with measurement of gamma quanta carrying information on the bulk of the crystal, (b) with measurement of secondary electrons from a surface layer with thickness from zero to 200 nm. For (a) and (b), the gamma-ray wave vector is parallel to the *c* axis, and for (c) it is at an angle of 28° to the *c* axis.

the effective magnetic fields and by temperature scanning at a constant gamma-ray source velocity.

The samples for the Mössbauer studies were ~80-μm thick disk-shaped plates ~8 nm in diameter cut from single crystals. The crystallographic *c* axis was perpendicular to the plate plane. Particular attention was paid to the quality of crystal surface. The faces of the $BaFe_{11.4}Sc_{0.6}O_{19}$ single crystals selected for the surface studies were naturally specular or chemically etched for one minute in orthophosphoric acid at 90 °C. Unsubstituted $BaFe_{12}O_{19}$ ferrite plates, similarly surface treated, were used as references.

The magnetic structure of the surface layer and of the bulk was probed by the SGXEMS method. It involves simultaneous measurement of Mössbauer spectra of radiations having different mean free path lengths in the material, namely, gamma quanta, characteristic x-ray radiation, and secondary (conversion and Auger) electrons carrying information on the properties of the bulk and of the surface layers a few microns and 300 nm thick, respectively. The energy of the electron escaping from the sample is the lower the deeper the atom from which this electron was ejected so that SGXEMS studies of surface layers less than 300 nm thick are based on energy selection of the secondary electrons.[30]

The experimental spectra obtained by SGXEMS covered a temperature range from 300 to 750 K. Figure 1 illustrates room-temperature spectra obtained with gamma rays and secondary electrons, with the gamma-radiation wave vector oriented parallel to the crystallographic axis *c*. X-ray Mössbauer spectra carry information on the layer a few μm thick and are similar to those measured with gamma rays. Therefore to make the corresponding plots more revealing, the x-ray Mössbauer spectra obtained in this work are not shown. As seen from Fig. 1, the spectral lines are well resolved. This permits high-precision determination of both the hyperfine-interaction parameters and of the orientation of magnetic moments in the crystal.

3. DISCUSSION OF RESULTS

The ratio of the first to second, as well as of the fifth to sixth, Zeeman sextuplet lines in a Mössbauer spectrum permits one to determine from the relation (see, e.g., Ref. 31)

$$A_{1.6}/A_{2.5}=3(1+\cos^2\theta)/(4\sin^2\theta) \quad (1)$$

the angle θ characterizing magnetic-moment orientation in the crystal with respect to the wave vector of the gamma radiation.

As seen from Fig. 1a, the gamma-ray Mössbauer spectrum of $BaFe_{11.4}Sc_{0.6}O_{19}$ is similar to that of the unsubstituted Ba–M ferrite, with the addition of the well resolved lines corresponding to the $12k'$ sublattice. An analysis of the gamma-resonance spectra in Fig. 1a showed that the intensities of the second and fifth lines in the Zeeman sextuplets of each inequivalent site, which correspond to $\Delta m=0$ transitions, are zero. This means that the angle θ is zero and, hence, the magnetic moments of iron ions in the bulk of the crystal are collinear with the gamma-ray wave vector and parallel to the *c* axis. This pattern is observed throughout the temperature range covered and is in a good agreement with available data on the bulk properties of these crystals (see Ref. 31 and references therein).

As evident from the secondary-electron spectra (Fig. 1b), their portions corresponding to the velocities of ± 4 and $+5$ mm/s contain weak lines not observed in the gamma-ray spectra (Fig. 1a). An analysis of the secondary-electron spectra revealed these additional lines to be actually the second and fifth components of the Zeeman sextuplets. This means that the magnetic moments of the iron ions occupying sites in the $\sim$200-nm thick surface layer are canted at an angle θ to the gamma-ray wave vector and, accordingly, to the crystallographic axis *c*. This pattern persists up to a temperature of $\sim$600 K, above which the degraded line resolution complicates spectral analysis. The canting angle θ of the magnetic moments from the gamma-ray wave vector calculated using Eq. (1) was found to be $(17\pm 2)°$. Thus the magnetic moments of iron ions in the surface layer $\sim$200 nm thick are noncollinear both with the *c* axis along which the gamma-ray wave vector is aligned and with magnetic moments in the bulk of the crystal.

The above analysis of Mössbauer spectra was checked by obtaining spectra on single crystals tilted in such a way that the crystallographic *c* axis made an angle α with the wave vector of gamma rays. Figure 1c shows for illustration a gamma-ray spectrum obtained with $\alpha=(28\pm 2)°$. We readily see that canting of the magnetic moments away from the gamma-ray propagation direction gives rise to the appearance in the spectrum of the Zeeman sextuplet lines corresponding to transitions with $\Delta m=0$. The angle θ derived from the gamma-ray spectrum in Fig. 1c with the use of Eq. (1) is $(27\pm 2)°$. Taking into account the error involved in crystal alignment and in calculations, a good agreement obtains with the angle α set experimentally. It should be pointed out that a comparison of the experimental spectra in Fig. 1 shows a good agreement in velocity positions of the second and fifth gamma-resonance lines obtained with a tilted crystal (Fig. 1c) with those in the spectra measured with secondary electrons (Fig. 1b).

These results prove convincingly that the magnetic moments of the iron ions contained within a $\sim$200-nm thick surface layer are canted away both from the *c* axis and from the spins of the iron ions in the bulk of the crystal.

It may be conjectured that the observed magnetic-moment canting is actually the result of the magnetic ions having been etched out of the surface layer in the course of chemical polishing, which would entail additional decrease of the exchange interaction energy in this layer. To test this suggestion, Mössbauer spectra were measured of $BaFe_{12}O_{19}$ single crystals prepared simultaneously with the $BaFe_{11.4}Sc_{0.6}O_{19}$ samples under study by the same chemical-polishing technology. The experimental Mössbauer spectra obtained on these $BaFe_{12}O_{19}$ crystals are displayed in Fig. 2. We readily see that both the electron (Fig. 2b) and gamma-ray (Fig. 2a) spectra do not have the second and fifth Zeeman sextuplet lines when the crystallographic axis *c* is parallel to the gamma-ray wave vector. We measured also for comparison gamma-ray Mössbauer spectra on the same $BaFe_{12}O_{19}$ single-crystal plates tilted so that the *c* axis was at an angle α to the gamma-ray beam. Figure 1c shows such a Mössbauer spectrum obtained with gamma rays at $\alpha=(28\pm 2)°$. One readily sees that canting the magnetic moments away from the gamma-ray propagation direction results in the appearance in the spectrum of Zeeman sextuplet lines corresponding to the $\Delta m=0$ transitions. Thus these experiments show convincingly that the sample-surface preparation used here does not affect in any way the magnetic structure of the surface layer.

Consider the reasons responsible for the canting of magnetic moments in the surface layer from those in the bulk. The orientation of magnetic moments in a sublattice is dominated by exchange interactions in the hexagonal block *R* between $Fe(2b)-O-Fe(4f_2)$ and $Fe(4f_2)-O-Fe(12k)$. The corresponding bond angles are fairly large, $\sim$140 and 130°, and the Fe–O distance is $\sim$1.8 and 1.95 Å, respectively. These interactions account for the largest exchange integrals. Because the $Fe(2b)-O-Fe(4f_2)$-O-$Fe(12k)$ interaction is somewhat stronger, and the chain consists of two exchange bonds, the spins of the $Fe(2b)$ and $Fe(12k)$ ions are oriented antiparallel to that of the $Fe(4f_2)$ ion despite the strong counteracting interaction between the $Fe(2b)$ and $Fe(12k)$ ions, for which the interaction angle $\sim$125°, and the Fe-O distance is 2.3 and 1.87 Å, respectively. The interaction in the spinel block is conventional, which results in the mutual magnetic-moment orientation specified in Table I. The formation of this axial structure, as well as of the magnetocrystalline anisotropy, is governed to a considerable extent by iron ions in the $2b$ site, which generates a strong trigonal crystal field with the symmetry axis coinciding with the crystallographic axis. The significance of the contribution to the magnetic anisotropy due to the $12k$ irons in the low-symmetry octahedron (Table I) was pointed out in Ref. 32.

As follows from neutron-diffraction and Mössbauer studies of type-M hexagonal ferrites,[27–29] substitution of Sc diamagnetic ions for iron in such ferrites affects considerably the exchange interaction even in compounds with a relatively small amount of Sc ions. For Sc contents $x>1.2$, a noncollinear magnetic structure sets in.[28] In a Sc-substituted ferrite $(x=1.8)$, the magnetic moments of individual blocks make up a conical block spiral, with the magnetic moments of iron ions in each block being arranged collinearly.

The areas under the peaks in the experimental Möss-

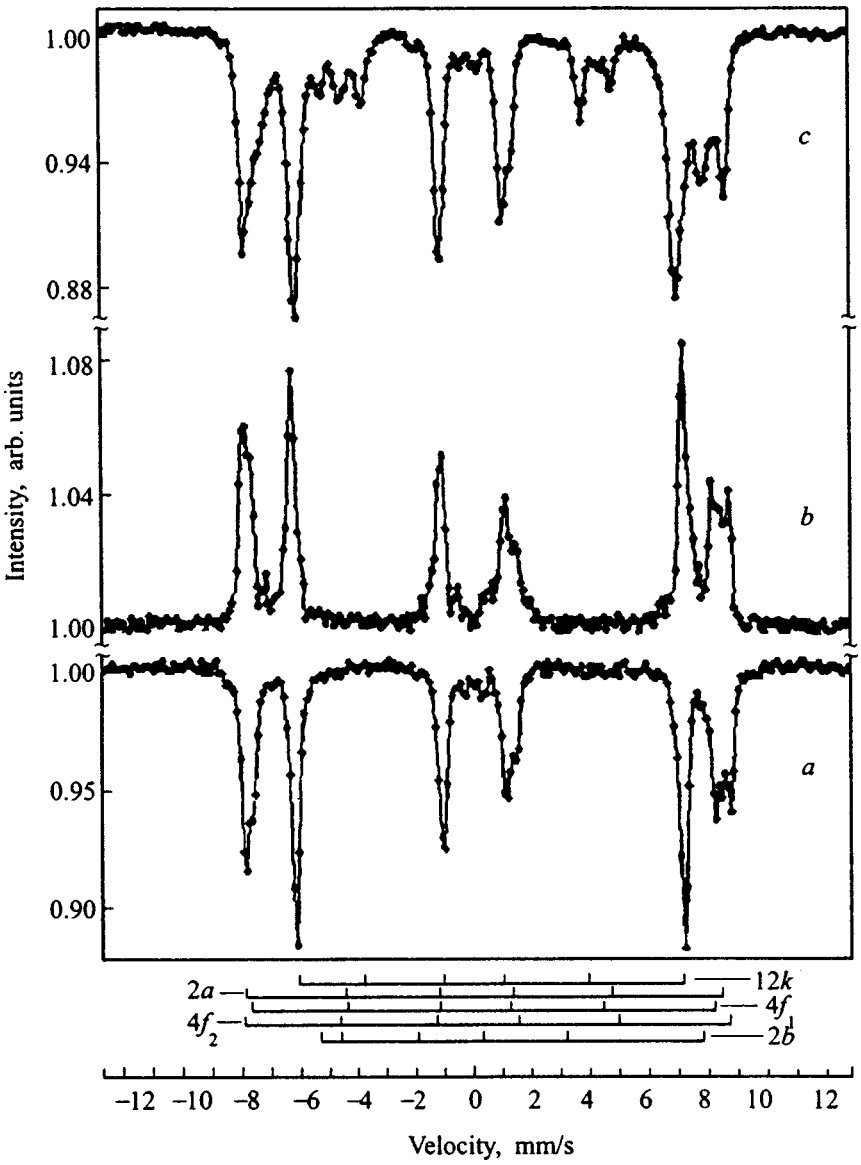

FIG. 2. Room-temperature Mössbauer spectra of single-crystal $BaFe_{12}O_{19}$. (a,c) Gamma rays, the bulk of the crystal; (b) secondary electrons, surface layer zero to 200 nm thick. For (a) and (b), the gamma-ray wave vector is parallel to the *c* axis, and for (c) it is at an angle of 28° to the *c* axis.

bauer spectra were used to calculate the resonant-absorption probabilities (Mössbauer effect) given in Table I. One readily sees that the probabilities of resonant absorption in $BaFe_{12}O_{19}$ agree well within experimental error with the amount of ions on the corresponding sublattices in the crystal unit cell. The HF interaction parameters derived from experimental Mössbauer spectra of $BaFe_{12}O_{19}$ and $BaFe_{11.4}Sc_{0.6}O_{19}$ are presented in Tables II and III, respectively. The figures listed in Tables II and III are in a good agreement with published data (see Ref. 31 and references therein, as well as

TABLE I. Distribution of Fe^{3+} ions over unit cell sites, their spin orientation, and the magnitude of the Mössbauer effect (the areas bounded by the corresponding spectral lines) for the $BaFe_{12}O_{19}$ and $BaFe_{11.4}Sc_{0.6}$ O_{19} hexaferrites.

	Distribution of Fe^{3+} ions over unit cell sites and their spin orientation			Mössbauer effect	
				$BaFe_{12}O_{19}$	$BaFe_{11.4}Sc_{0.6}O_{19}$
Sublattice	Number of ions	Environment	Spin direction	Area, % (normalized to 24)	Area, % (normalized to 22.8)
12*k*	12	Octa	up	12.4±0.2	7.3±0.3
12*k*′				–	4.4±0.4
$4f_1$	4	Tetra	down	4.9±0.4	5.4±0.4
$4f_2$	4	Octa	down	3.9±0.2	3.6±0.4
2*a*	2	Octa	up	1.4±0.6	1.1±0.5
2*b*	2	Trigonal dipyramid	up	1.4±0.2	0.9±0.2

TABLE II. Effective magnetic fields H_{eff}, isomer shifts δ, and quadrupole splittings ΔE for $BaFe_{12}O_{19}$ measured at room temperature (the isomer shift δ determined relative to α Fe).

	H_{eff} (kOe)		δ (mm/s)		ΔE (mm/s)	
Sublattice	$[\gamma]$	$[e]$	$[\gamma]$	$[e]$	$[\gamma]$	$[e]$
$12k$	416±1	422±1	0.34±0.01	0.35±0.01	0.42±0.01	0.42±0.02
$4f_1$	493±1	495±1	0.27±0.01	0.29±0.02	0.19±0.02	0.09±0.04
$4f_2$	520±3	523±1	0.38±0.01	0.35±0.02	0.27±0.01	0.20±0.04
$2a$	508±3	508±3	0.33±0.01	0.31±0.02	0.16±0.02	0.11±0.04
$2b$	403±5	401±5	0.30±0.02	0.25±0.10	2.07±0.04	1.84±0.20

Refs. 33,34). A comparison of the HF parameters obtained for $BaFe_{12}O_{19}$ and $BaFe_{11.4}Sc_{0.6}O_{19}$ reveals a pronounced change in these parameters induced by such a seemingly insignificant ($x=0.6$) substitution of Sc for iron ions, which implies a selective pattern of Sc ion arrangement.

As seen from the experimental spectra and the tables, Sc doping brings about the formation of the $12k'$ sublattice and a weakening of the lines corresponding to the irons sitting at the $2b$ and $12k$ sites. The formation of the $12k'$ sublattice can be explained by the Sc ions occupying the $2b$ sites. The $12k$ iron ions are involved in six exchange bonds, namely, three bonds with the irons in the $4f_1$ sites, two - with $4f_2$ Fe ions, and one, with the Fe in the trigonal dipyramid. As a result of Sc ions entering the $2b$ sites, part of Fe ions in the $12k$ sites will no longer take part in the Fe($2b$)–O–Fe($12k$) bond, whereas the other part of the Fe($12k$) ions will retain this bond, thus creating an inequivalent situation. The ratio of the numbers of ions in the $12k$ and $12k'$ sites will be proportional to that of the magnetic and nonmagnetic $2b$ ions.

As seen from Table I, the numbers of iron ions at the $12k$ and $12k'$ sites in $BaFe_{11.4}Sc_{0.6}O_{19}$ are related approximately as 2:1. At the same time if Sc ions occupy only $2b$ sites, the ratio of the magnetic to nonmagnetic ions on the $2b$ sublattice in a ferrite with this composition, $x=0.6$, should be, as follows from the above discussion, 2:3, which is at odds with the observations (see Table I). Hence iron ions are replaced by Sc not only in $2b$ but in other sites as well. As evident from Table I, for this value of x iron ions with oppositely oriented magnetic moments are replaced approximately in the same amounts, i.e. substitution takes place for both the $2b$ irons with spins up and the spin-down iron ions occupying the $4f_2$ sites.

These data agree with neutron diffraction measurements which imply that, when present in low concentrations, Sc ions occupy $2b$ sites, while for substitutions below 30% they enter also $4f_2$ sites.[27–29] The strengthening of the lines corresponding to the $4f_1$ irons (Table I) should be assigned to the large calculational error with which the poorly resolved sextuplets for the $4f_1$ and $2a$ iron ions were treated. Localization of Sc ions at $2b$ sites weakens exchange bonds connecting the S and R blocks, and therefore the Curie temperature per substituting Sc diamagnetic ion decreases by 160–170 K, whereas incorporation of Al or Ga ions reduces the Curie temperature T_c by 50–60 K for $\Delta x=1$. The present authors derived the Curie temperatures from the experimental data. For the $x=0.6$ ferrite, we obtained $T_c=647$ K, which is in a good agreement with available data[34].

Summing up, it can be argued that Sc diamagnetic ions substitute for iron ions in the $BaFe_{11.4}Sc_{0.6}O_{19}$ crystals chosen by us at the $2b$ and $4f_2$ sites and favor formation of a noncollinear magnetic structure by breaking the magnetic bonds. A Sc content of 0.6 is, however, far from being sufficient to disrupt collinearity in the bulk.[27–29] The exchange interaction energy in the surface layer of the crystals under study decreases not only because of the presence of the diamagnetic ions but as a result of an additional surface-induced decrease of the exchange interaction energy. Indeed, it was shown[25] that substitution of Ga diamagnetic ions for 9% only of iron ions in Fe_3BO_6 increases by an order of magnitude the thickness of the transition surface layer. This gives us grounds to assume that the reason for the formation of a noncollinear magnetic structure in a surface layer of the $BaFe_{11.4}Sc_{0.6}O_{19}$ crystals is the additional decrease in the exchange energy caused by such a ''defect'' as the surface.

Thus we have presented the first experimental evidence

TABLE III. Effective magnetic fields H_{eff}, isomer shifts δ, and quadrupole splittings ΔE for $BaFe_{11.4}Sc_{0.6}O_{19}$ measured at room temperature (the isomer shift δ determined relative to α Fe).

	H_{eff} (kOe)		δ (mm/s)		ΔE (mm/s)	
Sublattice	$[\gamma]$	$[e]$	$[\gamma]$	$[e]$	$[\gamma]$	$[e]$
$12k$	413±1	414±1	0.37±0.01	0.38±0.01	0.41±0.02	0.39±0.03
$12k'$	325±1	327±2	0.38±0.01	0.35±0.03	0.41±0.03	0.36±0.06
$4f_1$	486±1	486±1	0.31±0.01	0.30±0.02	0.24±0.02	0.24±0.04
$4f_2$	512±1	514±1	0.43±0.01	0.33±0.02	0.32±0.02	0.41±0.04
$2a$	505±2	–	0.33±0.01	–	0.12±0.02	–
$2b$	406±3	–	0.43±0.02	–	2.03±0.05	–

for the existence in Ba-M-type diamagnetically substituted hexagonal ferrites of a ~200-nm thick surface layer with the iron-ion magnetic moments canted away from the *c* axis, while the magnetic moments of the bulk ions are oriented parallel to the crystallographic axis *c*. This is the first observation in ferrites of a surface layer whose magnetic structure differs from that of the bulk and whose existence was predicted theoretically by L. Néel (Ref. 1).

Support of the Russian Fund for Fundamental Research (Grant 98-02-18279) is gratefully acknowledged.

*)E-mail: Kamzin@kas.ioffe.rssi.ru

[1] L. Néel, J. Phys. Radium **15**, 225 (1954).
[2] L. Liebermann, D. R. Fridkin, and H. B. Shore, Phys. Rev. Lett. **22**, 539 (1969); L. Liebermann, J. Clinton, D. M. Edwards, and J. Mathon, *ibid.* **25**, 232 (1970).
[3] A. E. Berkowitz, W. J. Schuele, and P. J. Flanders, J. Appl. Phys. **39**, 1261 (1968).
[4] J. M. D. Coey, Phys. Rev. Lett. **27**, 1140 (1971); Can. J. Phys. **65**, 1210 (1987).
[5] A. M. van der Kraan, Phys. Status Solidi A **18**, 215 (1973).
[6] A. H. Morrish, K. Haneda, and P. J. Schurer, J. Phys. (Paris) **37**, C6-301 (1976).
[7] P. M. de Bakker, E. DeGrave, R. E. Vandenberghe, and L. H. Bowen, Hyperfine Interact. **54**, 493 (1990).
[8] A. E. Berkowitz, J. A. Lahut, and C. E. van Buren, IEEE Trans. Magn. **MAG-16**, 184 (1980).
[9] K. Haneda, H. Kojima, A. H. Morrish, P. J. Picone, and K. Wakai, J. Appl. Phys. **53**, 2686 (1982).
[10] A. H. Morrish and K. Haneda, IEEE Trans. Magn. **MAG-25**, 2597 (1989); J. Appl. Phys. **52**, 2496 (1981).
[11] K. Haneda and A. H. Morrish, Nucl. Instrum. Meth. B **76**, 132 (1993).
[12] K. Haneda, Can. J. Phys. **65**, 1233 (1987).
[13] R. H. Kodama, A. E. Berkowitz, E. J. McNiff, Jr., and S. Foner (In print).
[14] D. Lin, A. C. Nunes, C. F. Majkrzak, and A. E. Berkowitz, J. Magn. Magn. Mater. **145**, 343 (1995).
[15] S. S. Parkin, R. Sigsbee, R. Felici, and G. P. Felsher, J. Appl. Phys. **57**, 1371 (1985).
[16] F. T. Parker, M. W. Foster, D. Margulis, and A. E. Berkowitz, Phys. Rev. B **47**, 7885 (1993).
[17] Q. A. Pankhurst and R. J. Pollard, Phys. Rev. Lett. **67**, 325 (1991).
[18] P. V. Hendriksen, S. Linderoth, C. A. Oxborrow, and S. Mǿrup, J. Phys.: Condens. Matter **6**, 3091 (1994).
[19] G. S. Krinchik, A. P. Khrebtov, A. A. Askochenskiĭ, and V. E. Zubov, JETP Lett. **17**, 335 (1973); G. S. Krinchik and V. E. Zubov, Zh. Éksp. Teor. Fiz. **69**, 707 (1975) [Sov. Phys. JETP **42**, 359 (1975)].
[20] V. G. Labushkin, V. V. Rudenko, É. R. Sarkisov, V. A. Sarkisyan, and V. N. Seleznev, JETP Lett. **34**, 544 (1981).
[21] V. E. Zubov, G. S. Krinchik, V. N. Seleznev, and M. B. Strugatskiĭ, Zh. Éksp. Teor. Fiz. **94**, No. 10, 290 (1988) [Sov. Phys. JETP **67**, 2122 (1988)]; V. E. Zubov, G. S. Krinchik, V. N. Seleznyov, and M. B. Strugatsky, J. Magn. Magn. Mater. **86**, 105 (1990).
[22] E. A. Balykina, E. A. Gan'shina, and G. S. Krinchik, Zh. Éksp. Teor. Fiz. **93**, 1879 (1987) [Sov. Phys. JETP **66**, 1073 (1987)]; Fiz. Tverd. Tela (Leningrad) **30**, 570 (1988) [Sov. Phys. Solid State **30**, 326 (1988)].
[23] A. S. Kamzin, V. P. Rusakov, and L. A. Grigor'ev, *Proc. Intern. Conf. Phys. Transition Metals* (Kiev, 1988), Pt. II, p. 271; A. S. Kamzin and L. A. Grigor'ev, Pisma Zh. Tekh. Fiz. **16**, No. 16, 38 (1990) [Tech. Phys. Lett. **16**, 616 (1990)].
[24] A. S. Kamzin and L. A. Grigor'ev, JETP Lett. **57**, 557 (1993); Zh. Éksp. Teor. Fiz. **104**, 3489 (1993) [JETP **77**, 658 (1993)].
[25] A. S. Kamzin, L. A. Grigor'ev, and S. A. Kamzin, Fiz. Tverd. Tela (St. Petersburg) **36**, 1399 (1994) [Phys. Solid State **36**, 765 (1994)]; *ibid.* **37**, 67 (1995) [Phys. Solid State **37**, 33 (1995)].
[26] A. S. Kamzin, L. P. Ol'khovik, and V. L. Rozenbaum, JETP Lett. **61**, 936 (1995); J. Magn. Magn. Mater. **161**, 139 (1996); Zh. Éksp. Teor. Fiz. **111**, 1426 (1997) [JETP **84**, 788 (1997)].
[27] M. I. Namtalishvili, O. P. Aleshko-Ozhevskiĭ, and I. I. Yamzin, Fiz. Tverd. Tela (Leningrad) **13**, 2543 (1971) [Sov. Phys. Solid State **13**, 2137 (1971)].
[28] O. P. Aleshko-Ozhevskiĭ, R. A. Sizov, I. I. Yamzin, and V. A. Lyubimtsev, Zh. Éksp. Teor. Fiz. **55**, 820 (1968) [Sov. Phys. JETP **28**, 425 (1968)].
[29] O. P. Aleshko-Ozhevskiĭ, Ya. Litsievich, A. Murasik, and I. I. Yamzin, Kristallografiya **19**, 391 (1974) [Sov. Phys. Crystallogr. **19**, 201 (1974)].
[30] A. S. Kamzin and L. A. Grigor'ev, Pisma Zh. Tekh. Fiz. **19**, No. 8, 50 (1993) [Tech. Phys. Lett. **19**, 245 (1993)].
[31] Sh. Sh. Bashkirov, A. B. Liberman, and V. I. Sinyavskiĭ, *The Magnetic Microstructure of Ferrites* [in Russian] (Kazan. Univ., 1978).
[32] Yu. A. Mamaluĭ, L. P. Ol'khovik, and L. F. Checherskaya, Fiz. Tekhn. Vys. Davl. **12**, 17 (1983).
[33] B. J. Evans, F. Granjean, A. P. Lilot, R. H. Vogel, and A. Gerard, J. Magn. Magn. Mater. **67**, 123 (1987).
[34] G. Albanese, A. Deriu, L. Lucchini, and G. Slokar, Appl. Phys. A **26**, 45 (1981); IEEE Trans. Magn. **MAG-17**, 2639 (1981).

Translated by G. Skrebtsov

Characteristic features of the magnetic ordering of Dy^{3+} ions in a monoclinic $RbDy(WO_4)_2$ single crystal

V. P. D'yakonov, V. I. Markovich, V. L. Kovarskiĭ, and A. V. Markovich*)

Donetsk Physicotechnical Institute, Ukrainian Academy of Sciences, 340114 Donetsk, Ukraine

M. Borowiec, A. Jendrzejczak, and H. Szymczak

Institute of Physics, Polish Academy of Sciences, 02-668 Warsaw, Poland
(Submitted June 9, 1998; resubmitted September 14, 1998)
Fiz. Tverd. Tela (St. Petersburg) **41**, 491–496 (March 1999)

The investigation of the specific heat of a $RbDy(WO_4)_2$ single crystal at temperatures 0.2–2.5 K and in magnetic fields up to 2 T are reported. The temperature dependence of the specific heat near $T_N=0.818$ K is compared with the predictions for different models. The $2D$ Ising model describes satisfactorily $C(T)$ below T_N, while for $T>T_N$ none of the theoretical models agree with the behavior of $C(T)$ of $RbDy(WO_4)_2$. The $H-T$ phase diagram for $\mathbf{H}\|\mathbf{c}$ is complicated and possesses a triple point, where regions of existence of three magnetic phases converge. The magnetic ordering is analyzed from the standpoint of the Jahn–Teller nature of the structural phase transitions occurring in $RbDy(WO_4)_2$ at higher temperatures. It is shown that the form of the phase diagram depends on the direction of the vector **H**, for the general case of an arbitrary direction of **H**, two phase transitions can occur with increasing field.
 [S1063-7834(99)02303-5]

Investigations of alkali-halide ditungstates $MRe(WO_4)_2$ (M — alkali ion, Re — rare-earth element) are of special interest because of the possibility of magnetic and structural phase transitions (MPT and SPT) in these materials. These low-symmetry compounds contain Re ions with close-lying energy levels, which results in an SPT associated with the Jahn–Teller effect (JT). Indeed, such a transition has been recorded in a monoclinic $KDy(WO_4)_2$ ($T_c=6.38$ K) single crystal.[1] In $KDy(WO_4)_2$ a transition has also been observed into the antiferromagnetic (AFM) state at $T_N=0.6$ K.[2] However, in $KDy(WO_4)_2$ the character and characteristic features of the magnetic ordering (MO) of the Dy^{3+} sublattice could not be investigated in detail because of the low value of T_N. We have reported the observation of an MPT to an AFM state with $T_N=0.818$ K in the compound $RbDy(WO_4)_2$.[3] The results reported are a continuation of investigations of MO of the Dy^{3+} sublattice in $RbDy(WO_4)_2$. The existence and relative influence of the JT effect and magnetic interactions could lead to interesting features of MO in crystals with JT ions.[4] In the present paper we report the results of measurements of the specific heat of an $RbDy(WO_4)_2$ single crystal near T_N for two orientations of the magnetic field relative to the crystallographic axes: $\mathbf{H}\|\mathbf{c}$ and $\mathbf{H}\|\mathbf{a}$.

1. SAMPLES AND EXPERIMENTAL PROCEDURE

Rubidium-dysprosium ditungstate has a monoclinic α-$KY(WO_4)_2$ structure (C_{2h}^6-C2/c), characteristic for a number of rare-earth ditungstates at room temperature. The lattice parameters are $a=10.66$ Å, $b=10.45$ Å, and $c=7.569$ Å.[5,6] The samples and a number of methodological features of the specific-heat measurements are described in preceeding publications.[2,3,7,8]

The use of a He^3 cryostat made it possible to obtain, in the standard manner, a minimum temperature of the calorimeter together with the sample of about 0.5 K. In the present measurements adiabatic demagnetization was used for further cooling. For this, the $RbDy(WO_4)_2$ sample was cooled in a 1.5–2.0 T magnetic field to temperature 0.55–1.0 K as a paramagnetic salt. Then the intensity H was decreased slowly. In the process, cooling of the sample and the addendum occurred. In this manner, we were able to achieve a minimum temperature of the calorimeter together with the $RbDy(WO_4)_2$ sample of 0.2 K for $\mathbf{H}\|\mathbf{a}$ and about 0.3 K for $\mathbf{H}\|\mathbf{c}$. The lowest temperature in each experiment performed using adiabatic demagnetization (with a definite value of H) corresponded to an MPT to MO, after which a further decrease of H resulted in a rapid increase of the sample temperature. Fixing the temperature and the magnetic field intensity at the commencement of heating gave the value of the point on the phase line of the $H-T$ magnetic phase diagram.

2. EXPERIMENTAL RESULTS AND DISCUSSION

The temperature dependence of the specific heat of the $RbDy(WO_4)_2$ crystal near T_N is presented in Fig. 1. One can see that $C(T)$ has a peak at $T_N=0.818$ K, associated with the MO of the rare-earth sublattice. The asymmetric shape of the peak in the specific heat attests to the different nature of the change in $C(T)$ as T_N is approached from the high- and low-temperature sides.

We note that the temperature dependence $C(T)$ for $T<2.5$ K actually characterizes the magnetic contribution to the total specific heat, since $RbDy(WO_4)_2$ is an insulator and conduction electrons do not contribute to the specific heat, while the lattice specific heat at these temperatures is negli-

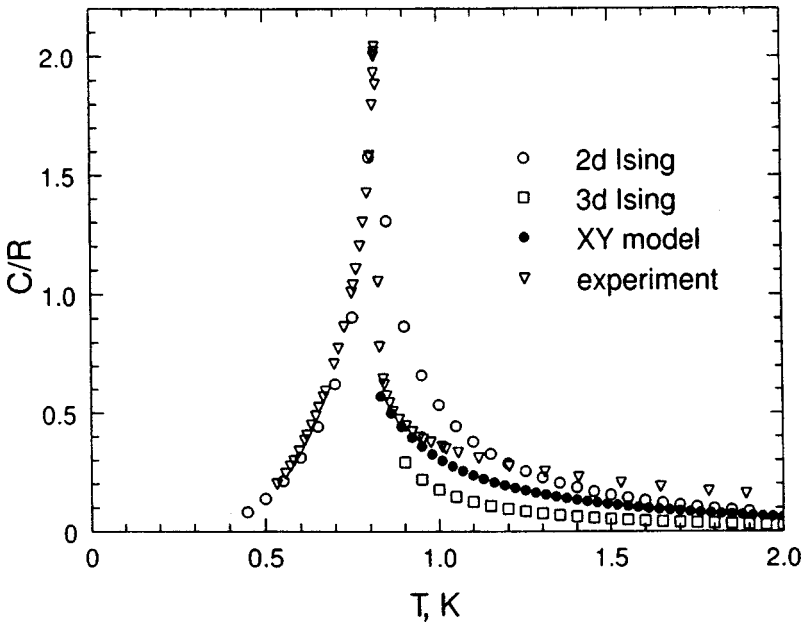

FIG. 1. Temperature dependence of the specific heat of an $RbDy(WO_4)_2$ single crystal near a magnetic transition.

gibly small. This is confirmed by measurements of $C(T)$ for the compound $KDy(WO_4)_2$, which is close in composition and structure and also has a monoclinic structure.[1,7] Indeed, the Debye temperature in $KDy(WO_4)_2$ is about 280 K,[7] and the phonon contribution to the specific heat at temperatures $T<2.5$ K is very small. It is known that the existence of an arbitrarily small anisotropy has the effect that, based on its Heisenberg type, the system near the critical point manifests Ising behavior.[9] The existence of anisotropy in the $RbDy(WO_4)_2$ crystal is confirmed by measurements of the magnetization in the paramagnetic (PM) phase. This gives a basis for comparing the behavior of the specific heat $C(T)$ near the Néel temperature with the dependences for the $2D$ and $3D$ Ising models (Fig. 1). Figure 1 also shows the theoretical dependence for the XY model. It is well known that the behavior of $C(T)$ for the XY model near T_N is virtually identical to that of the Heisenberg model in the same temperature range.[10] As one can see from Fig. 1, the behavior of the specific heat near T_N agrees well with the theoretical behavior for the $2D$ Ising model at temperatures $T<T_N$, while for $T>T_N$ none of the models presented describes the experimental dependence of the specific heat.

Figure 2 shows in double logarithmic coordinates a plot of the reduced specific heat C/R (R is the gas constant) as a function of the reduced temperature T^* ($T^*=1-T_N/T$ for $T>T_N$ and $T^*=1-T/T_N$ for $T<T_N$). As is well known, the critical behavior of the specific heat in the limit $T\to T_N$ above and below T_N is characterized by the critical exponents α and α' in the following equations:

$$C/R \propto A'(1-T/T_N)^{-\alpha'} \quad \text{for} \quad T<T_N, \tag{1}$$

$$C/R \propto A(1-T_N/T)^{\alpha} \quad \text{for} \quad T>T_N. \tag{2}$$

The slopes of the curves $\log(C/R)$ versus $\log T^*$ as T_N is approached from the high and low temperature sides (Fig. 2) give directly the values of the critical exponents α and α'. It is well known that for the $3D$ Ising model $\alpha=\alpha'=1/8$, while for the $2D$ Ising model the critical exponents are close to zero. As one can see from Fig. 2, the critical exponents for $RbDy(WO_4)_2$ are close to the values for the $2D$ Ising model.

The temperature dependence of the magnetic entropy of $RbDy(WO_4)_2$ near T_N is shown in Fig. 3. The plot was obtained by integrating the specific heat

$$\Delta S(T)=\int_0^T \frac{c(T)dT}{T}. \tag{3}$$

Above T_N the entropy should approach the value $R\ln 2$ in accordance with the molar entropy of the electronic doublet of the ground state of the Dy^{3+} ion. As one can see from Fig. 3, this does not happen. Indeed, at T_N the entropy is only 40% of $R\ln 2$ and is much less than this value even at $T\sim 2.5$ K. We note that for $T>2$ K contributions from the lattice and the SPT appear in $C(T)$ and correspondingly $S(T)$. Indeed, measurements of $C(T)$ show that two SPTs with $T_{C1}=4.9$ K and $T_{C2}=9.0$ K occur in $RbDy(WO_4)_2$.[8] However, the contributions of the lattice and SPT to $S(T)$

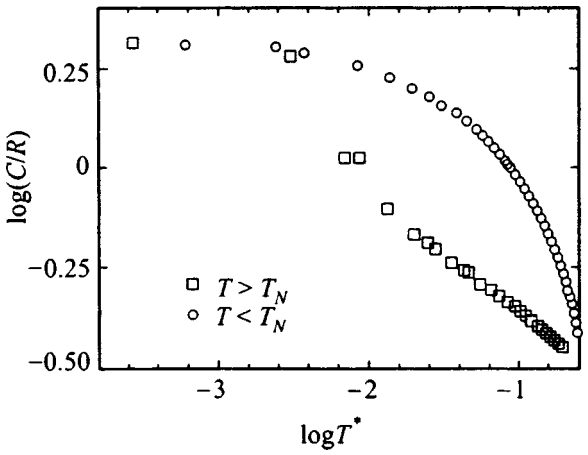

FIG. 2. Log–log plot of the specific heat of an $RbDy(WO_4)_2$ single crystal as a function of the reduced temperature T^* ($T^*=1-T_N/T$ for $T>T_N$ and $T^*=1-T/T_N$ for $T<T_N$).

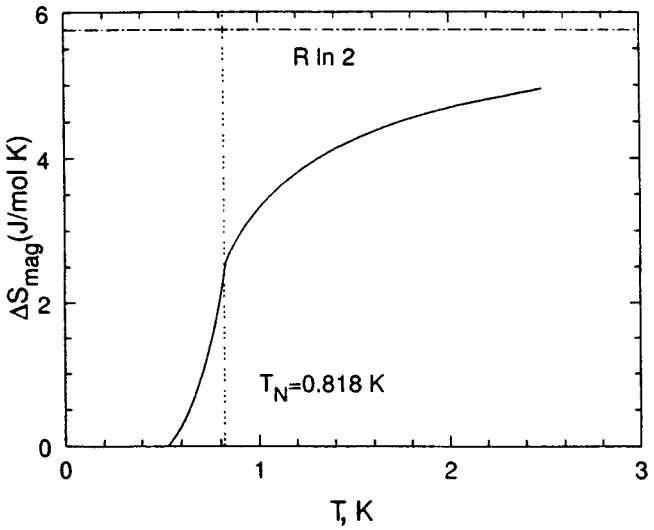

FIG. 3. Entropy increase due to magnetic ordering of Dy^{3+} ions in an $RbDy(WO_4)_2$ single crystal.

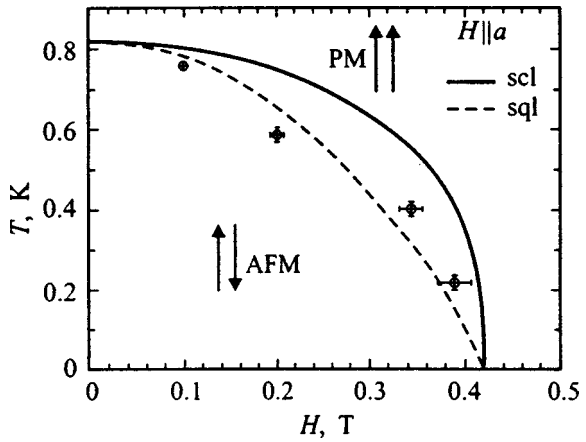

FIG. 4. $H-T$ magnetic phase diagram of $RbDy(WO_4)_2$ for $\mathbf{H}\|\mathbf{a}$. The solid line shows the theoretical curve for a simple cubic lattice (*scl*) — it corresponds to a $3D$ Ising model; the dashed line shows the theoretical curve for a simple square lattice (*sql*) and corresponds to the $2D$ Ising model.

can only decrease ΔS_{mag}. The observed behavior of ΔS_{mag} could be due to the characteristic features of the MO of Dy^{3+} ions. For an SPT into an antiferrodistortional phase (just as in low-symmetry dysprosium compounds $KDy(MoO_4)_2$ (Ref. 4) and $KDy(WO_4)_2$ (Ref. 11), it apparently also occurs in $RbDy(WO_4)_2$ (Ref. 8)) the crystal separates into two or more crystallographic sublattices. For AFM ordering below the Néel temperature additional separation of the crystal into two or more magnetic sublattices occurs in each of the crystallographic sublattices. In reality, for example, in the case of $KDy(MoO_4)_2$, a complicated magnetic configuration with AFM interactions along the crystallographic *c* axis and FM interactions along the *a* axis arises. In this case, the $KDy(MoO_4)_2$ crystal below the Néel temperature indeed separates into four magnetic sublattices.[4,12] In an $RbDy(WO_4)_2$ single crystal the magnetic structure can be even more complicated than in the case of $KDy(MoO_4)_2$, considering the fact that the crystal symmetry is lower than in molybdates. Ultimately, the crystal can separate into a large number of sublattices, actually into clusters. In the case of clusters, especially with a small number of magnetic ions, the value of ΔS_{mag} should not reach $R\ln 2$.[13] Thus, it is quite difficult to determine unambiguously the reason for such behavior of ΔS_{mag}, and it could be due to diverse factors, primarily, the complicated magnetic structure realized at temperatures $T<T_N$.

Measurements of the specific heat of an $RbDy(WO_4)_2$ single crystal in magnetic fields applied in the direction of the crystallographic *a* axis have been reported previously.[3] As the field increases, the specific-heat peak corresponding to a transition into the AFM phase shifts in the direction of the low temperatures, and its amplitude decreases.[3] This means that the interaction along the *a* axis is of an AFM nature. The field-dependence $T_N(H)$ constructed according to the positions of the peaks in the specific heat in a magnetic field is the line of a metamagnetic transition between AFM and PM phases (Fig. 4).

The experimental phase line was compared with the theoretical lines calculated for an Ising AFM by constructing a high-temperature expansion in terms of the shift of the anomaly of the magnetic susceptibility in a magnetic field[14]

$$T_N(H)=T_N(\mathrm{O})\{1-(H/H_{cr})^2\}^{\xi}, \tag{4}$$

where $\xi=0.87$ and $\xi=0.35$ for square and simple cubic lattices, respectively, and H_{cr} is the field of the metamagnetic transition at $T=0$. For an $RbDy(WO_4)_2$ crystal the experimental curve $H(T)$ in a field $\mathbf{H}\|\mathbf{a}$ agrees satisfactorily with the curve calculated according to the expression (4) with $\xi=0.87$ and $H_{cr}=0.45$ T. This indicates that ordering of the Dy^{3+} sublattice is two-dimensional.

The temperature dependence of the specific heat of $RbDy(WO_4)_2$ in a magnetic field applied along the *c* axis is displayed in Fig. 5. The behavior of $C(T)$ for $\mathbf{H}\|\mathbf{c}$ was found to be more complicated than for $\mathbf{H}\|\mathbf{a}$. Thus, as the magnetic field increases to 1.4 T, the specific-heat peak shifts in the direction of low temperatures, and the amplitude of the peak decreases. As the field increases further to 2T, the position of the maximum of the specific heat remains virtually unchanged.

We constructed the $H-T$ magnetic phase diagram for a magnetic field $\mathbf{H}\|\mathbf{c}$ according to the positions of the peaks of $C(T)$ in a magnetic field and points obtained by the method of adiabatic demagnetization (Fig. 6). The points connected by the dashed line were obtained from the specific-heat curves, and the solid line was obtained by adiabatic demagnetization. A characteristic feature of the $H-T$ diagram for the case $\mathbf{H}\|\mathbf{c}$ is the existence of a triple point with the coordinates $H_{cr}\approx 1.9$ T and $T_{cr}\approx 0.6$ K. One can see that three different phases coexist at this point. Unfortunately, the maximum magnetic field was only 2 T. This is due to the fact that in contrast to the case $\mathbf{H}\|\mathbf{a}$ the application of a magnetic field $H>2$ T gives rise to strong stresses in the crystal and causes the sample to become detached from the sapphire substrate.[8]

In the case of an $RbDy(WO_4)_2$ single crystal the effect of the interaction of JT distortions on the characteristic features of the MO cannot be neglected. Indeed, in this case the

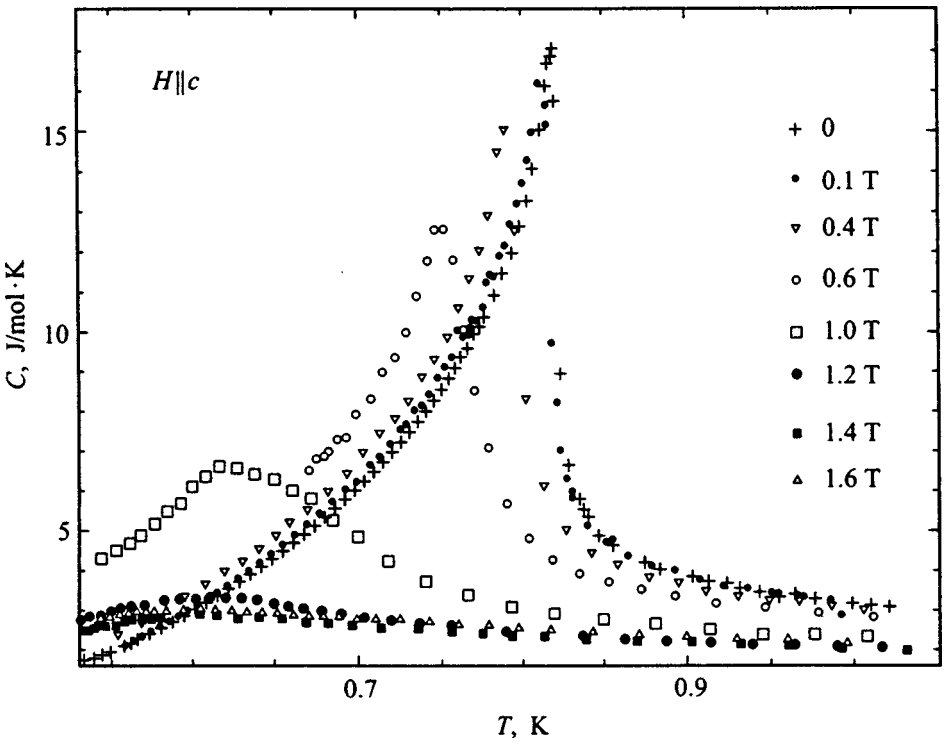

FIG. 5. Temperature dependences of the specific heat of an $RbDy(WO_4)_2$ single crystal in a magnetic field $\mathbf{H} \| \mathbf{c}$.

interactions of the JT distortions B is larger than J (J denotes the magnetic interactions), and the SPT occurs at a higher temperature[11] than the MPT. As is well known, correlations of JT distortions strongly influence the MPT temperature.[4] Moreover, the JT interactions can play a decisive role in the formation of the magnetic structure at temperatures $T<T_N$. In this case, the molecular JT field acts as part of the magnetic anisotropy, determining the orientation of the magnetic moments.[4] This anisotropy of a JT nature can give rise to separation of the ''easy'' magnetic axes in each of the sublattices into which the crystal separates. All this should lead to a complicated magnetic structure and, correspondingly, a complicated phase diagram.

The magnetic phase diagram can be explained using a four-component pseudospin model.[15] In this model the two lowest Kramers doublets of the electronic shell of the Dy^{3+} ion are studied. One contains the wave functions $|\pm J_x\rangle$ and exhibits magnetic properties along the $0x$ axis, while the other contains the states $|\pm J_y\rangle$ and manifests magnetic properties in the direction of $0y$ axis (x,y,z are the axes of the ''magnetic'' coordinate system). Tunneling splitting results in a superposition of the states on different doublets, but this does not greatly affect the qualitative picture, so that in what follows we shall assume that tunneling splitting does not occur: $\Delta=0$.

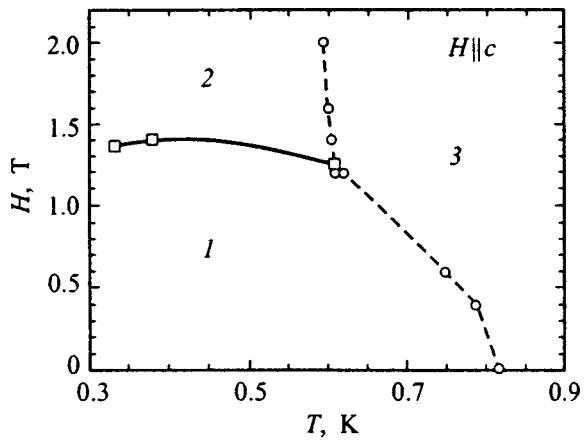

FIG. 6. $H-T$ magnetic phase diagram of $RbDy(WO_4)_2$ for $\mathbf{H} \| \mathbf{c}$: *1* — region of the AFM phase; *2* — region of the ''intermediate'' phase; *3* — region of the paramagnetic phase.

As is well known,[16] a magnetic field which is not directed along the bisector of the coordinate angle $x0y$ destroys the equilibrium between the lowest Kramers doublets and produces a difference in the populations of these doublets. This signifies the appearance of JT distortions.[15,16] In other words, a magnetic field gives rise to induced JT distortions. Therefore a magnetic field should destroy the SPT, if the low-temperature phase is ferrodistortional. Experiments show that an SPT exists in $RbDy(WO_4)_2$ samples in a wide range of magnitudes and directions of the magnetic field,[8] so that the low-temperature structurally ordered phase should not be ferrodistortional. Let us assume that the low-temperature structure is antiferrodistortional. This means that it consists of two sublattices, in each of which the magnetic properties predominate along the x and y directions, respectively.

At the MPT temperature the population of the excited Kramers doublet is exponentially small, i.e. only the $|\pm J_x\rangle$ doublet in one sublattice and the $|\pm J_y\rangle$ doublet in the other sublattice can be considered. In the magnetically ordered state each structural sublattice separates into two (or, possibly, more) magnetic sublattices with antiferromagnetism vectors directed along the $0x$ and $0y$ axes. An external mag-

netic field creates favorable conditions for a homogeneous paramagnetic phase, so that the MPT temperature decreases with increasing H. There exists a critical value H_{cr} above which the AFM phase is destroyed even at zero temperature.

If the magnetic field is directed along the bisector of the coordinate angle $x0y$, then it has the same effect on the magnetic properties of both structural sublattices, so that AFM ordering breaks down simultaneously in these sublattices, i.e. in this case we have one MPT. If the magnetic field is parallel to the $0x$ or $0y$ axis, then it acts only on the magnetic moments of one of the structural sublattices, and once again we have one MPT. In the intermediate case, the vector **H** has nonzero and unequal components $H_x \neq H_y$, which destroy antiferromagnetism in the structural sublattices at different temperatures. In this case we have two MPTs in different fields. It should be noted that these results do not agree with the corresponding results for anisotropic metamagnets, since in our model the anisotropy is inhomogeneous and has a different nature in different structural sublattices.

Tunneling splitting $\Delta \neq 0$ can change the picture somewhat. In this case the ground state of the electronic shells of Dy^{3+} in the structural sublattices is a superposition of the states $|\pm J_x\rangle$ and $|\pm J_y\rangle$, specifically, $C(|\pm J_x\rangle + \alpha|\pm J_y\rangle)$ in one sublattice and $C(|\pm J_y\rangle + \alpha|\pm J_x\rangle)$ in the other sublattice; $|\alpha| < 1$ and C is a normalization constant. Then the magnetically active directions in the structural sublattices will not be mutually perpendicular, as a result of which the magnetic moments in these sublattices will interact. This situation corresponds to the case of interacting order parameters and can lead to a phase diagram with a triple point — a phase diagram of the type shown in Fig. 6.

Apparently, for $\mathbf{H} \| \mathbf{c}$ a situation with two MPTs is indeed realized (Fig. 6), phase 1 being the AFM phase and phase 2 an ''intermediate'' phase, which consists of PM and AFM phases in different structural sublattices. The phase 3 is obviously a PM phase. This is confirmed by the fact that the adiabatic demagnetization method can be used in the phases 2 and 3. The realization of only one phase transition in a magnetic field $\mathbf{H} \| \mathbf{a}$ most likely indicates that the direction of the crystallographic a axis is close to or coincides with the x or y ''magnetic'' axes. The a axis is less likely to lie in the same direction as the bisector of the angle $x0y$ because of the low value of the critical field H_{cr} for $\mathbf{H} \| \mathbf{a}$.

In summary, features characterizing the complicated behavior of the MO of Dy^{3+} ions in $RbDy(WO_4)_2$ were observed. It was shown that below T_N the temperature dependence of the specific heat is described satisfactorily by a $2D$ Ising model, while for $T > T_N$ the critical behavior cannot be described by any known model. The phase diagram for $\mathbf{H} \| \mathbf{c}$ possesses a triple point, where three different magnetic phases merge, while for $\mathbf{H} \| \mathbf{a}$ there is only one phase line. The topology of the $H-T$ phase diagram was analyzed on the basis of a four-component pseudospin model taking account of the JT nature of the SPT. It was shown that the form of the magnetic phase diagram depends on the direction of the vector **H**, and in the case of an arbitrary orientation of **H** two MPTs are possible.

*)E-mail: markov@host.dipt.donetsk.ua

[1] M. T. Borowiec, V. P. Dyakonov, A. Jedrzejczak, V. I. Markovich, A. Nabialek, S. Piechota, A. Prokhorov, and H. Szymczak, Solid State Commun. **102**, 627 (1997).
[2] M. T. Borowiec, V. P. Dyakonov, A. Jedrzejczak, V. I. Markovich, H. Szymczak, E. E. Zubov, M. Zaleski, Phys. Lett. A **243**, 85 (1998).
[3] M. Borowiec, V. P. Dyakonov, A. Jedrzejczak, V. I. Markovich, and H. Szymczak, J. Low Temp. Phys. **110**, 1103 (1998).
[4] M. D. Kaplan and B. G. Vekhter, *Cooperative Phenomena in Jahn-Teller Crystals* (Plenum Press, N. Y., 1995)
[5] S. V. Borisov and R. F. Klevtsov, Kristallografiya **13**, 517 (1968) [Sov. Phys. Crystallogr. **13**, 420 (1968)].
[6] P. V. Klevtsov and L. P. Kozeeva, Dokl. Akad. Nauk SSSR **185**(3), 571 (1969) [Sov. Phys. Dokl. **14**, 185 (1969)].
[7] M. Borowiec, V. P. D'yakonov, A. Jedrzejczak, V. I. Markovich, and H. Szymczak, Fiz. Tverd. Tela (St. Petersburg) **38**(7), 2232 (1996) [Phys. Solid State **38**, 1229 (1996)].
[8] V. P. D'yakonov, V. I. Markovich, V. L. Kovarskiĭ, A. V. Markovich, M. Borowiec, A. Jendrzejczak, and H. Szymczak, Fiz. Tverd. Tela (St. Petersburg) **40**(12), 2221 (1998) [Phys. Solid State **40**, 2017 (1998)].
[9] K. Hirikawa and H. Ikeda, in *Magnetic Properties of Layered Transition Metal Compounds* edited by L. J. de Jongh (Kluwer Academic Publishers, Netherlands, 1990).
[10] J. Bartolome, H. A. Algra, L. J. de Jongh, and R. L. Carlin, Physica B **94**, 60 (1978).
[11] V. P. D'yakonov, V. I. Markovich, V. L. Kovarskiĭ, A. V. Markovich, M. Borowiec, A. Jendrzejczak, and H. Szymczak, Fiz. Tverd. Tela (St. Petersburg) **40**(4), 750 (1998) [Phys. Solid State **40**, 691 (1998)].
[12] A. H. Cooke, M. M. Davidson, N. J. England, M. J. M. Leask, J. B. Lewry, A. C. Tropper, and M. R. Wells, J. Phys. C: Sol. Stat. Phys. **9**, 573 (1976).
[13] P. Allenspach, M. B. Maple, and A. Furrer, J. Alloys Compd. **207/208**, 213 (1994).
[14] A. Bienenstock, J. Appl. Phys. **37**, 1459 (1966).
[15] C. J. Elliot, Proc. Roy. Soc. A **328**, 217 (1972).
[16] E. Pytte, Phys. Rev. **9**, 932 (1974).

Translated by M. E. Alferieff

Specific heat of $KTiOPO_4$ within the 80–300 K range

A. U. Sheleg, T. I. Dekola, N. P. Tekhanovich, and A. M. Luginets

Institute of Solid-State and Semiconductor Physics, National Academy of Sciences of Belarus, 220072 Minsk, Belarus

(Submitted June 22, 1998)
Fiz. Tverd. Tela (St. Petersburg) **41**, 497–498 (March 1999)

The specific heat of the $KTiOPO_4$ crystal has been measured with a vacuum adiabatic calorimeter within the 80–300 K range. A peak-shaped anomaly in the specific heat indicating a phase transition has been revealed in the $C_p(T)$ curve at $T \cong 279$ K. Numerical integration of smoothened experimental $C_p(T)$ curves yielded the thermodynamic functions of $KTiOPO_4$, namely, the entropy, enthalpy, and reduced Gibbs energy. The entropy and enthalpy of the observed transition have been determined. © *1999 American Institute of Physics.* [S1063-7834(99)02403-X]

The potassium titanyl phosphate $KTiOPO_4$ (KTP) belongs to the class of highly promising nonlinear optical materials enjoying wide use in laser technology and micro- and opto-electronics. These crystals possess also a unique combination of interesting physical properties. Besides the nonlinearity in optical characteristics, they exhibit ferro- and pyroelectric properties, a high optical strength, and ionic conduction.[1–5] Because the KTP crystal is known as a nonlinear optical material, the relevant published data relate primarily to its optical properties. At the same time its thermal and thermodynamic characteristics, which are undoubtedly both of pure scientific and applied interest remain very poorly investigated. This work reports a study of the specific heat of KTP crystals in the 80–300 K range.

1. EXPERIMENTAL TECHNIQUES AND RESULTS

The KTP single crystals were grown from a $TiO–K_2HPO_4–KH_2PO_4$ melt solution. The seed was (100)-oriented to within 5'. The seed was totally immersed into the melt solution and was rotated during the growth with a rate of 80 to 120 min^{-1} in different stages of the process, depending on the size of the growing crystals and the actual temperature gradients in the crystallization zone. The temperature at the beginning of synthesis was varied from 1320 to 1360 K. The grown crystals were $\sim 50 \times 40 \times 12$ mm in size.

The specific heat was measured in a vacuum adiabatic calorimeter with discrete heat injection in steps of 0.9–2.1 K.

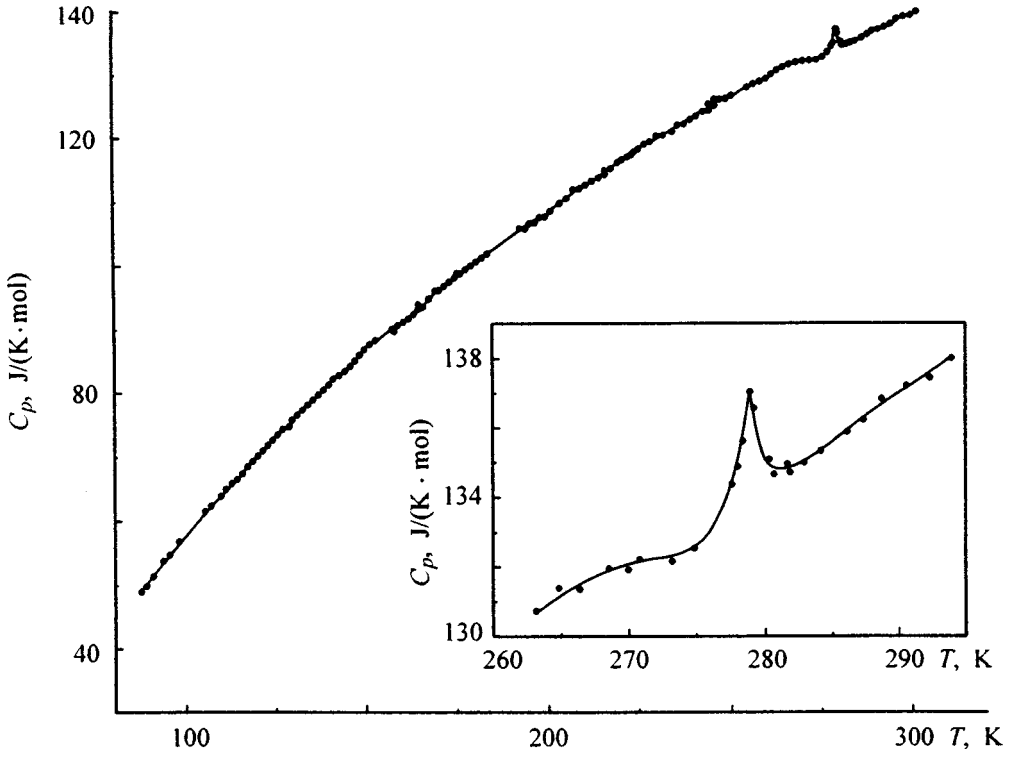

FIG. 1. Temperature dependence of the specific heat of $KTiOPO_4$.

TABLE I. Smoothened values of the specific heat and the changes of the thermodynamic functions of $KTiOPO_4$.

T, K	$C_p(T)$	$S(T)-S(80\ \mathrm{K})$	$\Phi(T)-\Phi(80\ \mathrm{K})$	$H(T)-H(80\ \mathrm{K})$, J/mol
	J/(K·mol)			
80	44.42	0.000	0.000	0.0
100	57.95	11.35	2.623	1 024
120	70.26	22.99	6.530	2 306
140	81.44	34.67	11.14	3 823
160	91.57	46.21	16.14	5 553
180	100.7	57.53	21.37	7 476
200	109.0	68.57	26.71	9 573
220	116.5	79.32	32.11	11 828
240	123.2	89.74	37.52	14 224
260	129.2	99.85	42.91	16 748
280	134.7	109.63	48.25	19 388
300	139.8	119.10	53.53	22 133

The sample, 9.76 g in mass, was heated during the measurements with a rate of 0.04–0.10 K/min. The error in specific heat measurement, estimated against Class 1 KV-quartz reference did not exceed 0.3% within the temperature range covered. The experimental data on the specific heat were least-squares fitted to a $C_i=\Sigma_{i=0}^{3}A_iT^i$ polynomial.

Figure 1 plots experimental values of the specific heat of KTP against temperature. The specific heat C_p of the KTP crystal is seen to grow monotonically with temperature, but at $T\cong 279$ K one observes a clearly pronounced peak-shaped anomaly in the $C_p(T)$ curve (see the inset). The presence of an anomaly in specific heat implies a structural transformation in the KTP crystal at this temperature. It should be pointed out that a dielectric study of KTP revealed breaks in the temperature dependences of ε and $\tan\delta$ at $T\cong 280$ K.[2] It was concluded[2] that the crystal undergoes at this temperature a structural rearrangement associated with disorder in the potassium sublattice at $T\geqslant 280$ K. In order to establish the nature and mechanism of the structural transformation occurring in KTP at $T\cong 280$ K, however, comprehensive x-ray diffraction measurements have to be carried out. Numerical integration of the smoothened experimental $C_p(T)$ curve yielded the changes in the thermodynamic functions of KTP, namely, the entropy, enthalpy, and reduced Gibbs energy. The smoothened values of the specific heat and the changes in thermodynamic functions derived from them are given in Table I. The changes in the entropy and enthalpy of the observed transition are, respectively, 0.014 J/(K·mole) and 3.8 J/mole.

[1] F. C. Zumsteg, J. D. Bierlin, and T. E. Gier, J. Appl. Phys. **47**, 4980 (1976).
[2] V. A. Kalesnikas, N. I. Pavlova, I. S. Rez, and I. P. Grigas, Litov. Fiz. Sb. **22**, No. 5, 87 (1982).
[3] V. K. Yanovskiĭ, V. I. Voronkova, A. P. Leonov, and S. Yu. Stefanovich, Fiz. Tverd. Tela (Leningrad) **27**, 2516 (1985) [Sov. Phys. Solid State **27**, 1508 (1985)].
[4] A. P. Leonov, V. I. Voronkova, S. Yu. Stefanovich, and V. K. Yanovskiĭ, Pis'ma Zh. Tekh. Fiz. **11**, No. 2, 85 (1985) [Sov. Tech. Phys. Lett. **11**, 209 (1985)].
[5] A. A. Bogomolov, R. M. Grechishkin, O. N. Sergeeva, V. A. Maslov, and V. V. Shcherbakov, Kristallografiya **42**, 478 (1997) [Crystallogr. Rep. **42**, 432 (1997)].

Translated by G. Skrebtsov

Two forms of polarization relaxation in polydomain ferroelectrics in an electric field

V. V. Gladkiĭ, V. A. Kirikov, E. S. Ivanova, and S. V. Nekhlyudov

A. V. Shubnikov Institute of Crystallography, Russian Academy of Sciences, 117333 Moscow, Russia
(Submitted July 20, 1998)
Fiz. Tverd. Tela (St. Petersburg) **41,** 499–504 (March 1999)

The characteristic features of the polarization and depolarization kinetics of polydomain ferroelectrics with square and narrow ''extended'' dielectric hysteresis loops are investigated for the model of TGS and Rb_2ZnCl_4 crystals. It is shown that for the second crystal, in contrast to the first crystal, the local free energy is asymmetric relative to the direction of polarization, the coercive field does not have a definite value, and only part of the crystal volume participates in the slow thermoactivational relaxation. The slow relaxation follows a universal empirical power law in all cases. The distribution functions of the relaxation times in crystals are constructed on the basis of experimental data, and comparative estimates are made of the relaxation parameters and the parameters of the energy barriers for domain walls.
 [S1063-7834(99)02503-4]

Investigations, performed over many years, of relaxation processes in dielectrics have yielded extensive information about the characteristic features of the polarization kinetics of diverse poly- and single-crystal materials.[1] In the last few years, inhomogeneous systems (mixed or defective crystals, spatially modulated structures,[2,3] glasses, and so on) for which many long-lived metastable states and, in consequence, extremely slow relaxation to thermodynamic equilibrium are characteristic have been attracting most interest mainly because of their potential technical applications.

Polydomain ferroelectrics are an example of such inhomogeneous systems. These materials apparently can serve as a model for experimental investigations of the general features of slow kinetics of structural and physical properties because it is possible to use highly sensitive electrical measurement methods. Slow relaxation of the polarization of a triglycine sulfate (TGS) crystal in weak electric fields was investigated in Ref. 4, where it was shown that the spectra of the energy distribution of the potential barriers for domain walls can be reconstructed from the experimental data and it was found that they transform when the state of the domain structure, surface and magnitude of the field change. The experimental data were analyzed assuming that the process is thermoactivational and that the relaxation centers (nuclei) are independent and their contribution to the total polarization is additive. For a TGS crystal these assumptions are natural since, during measurements in weak fields (much weaker than the coercive field), no fast process leading to switching of the polarization above the barriers was present. In the present paper we report the results of the detection and analysis of a different form of slow relaxation of domain structure in an Rb_2ZnCl_4 crystal (RZC), for which there is no definite value of the coercive field and an entire interval of such fields exists, while the equilibrium value of the polarization depends on the strength of the field. The results of these investigations are compared to data for a TGS crystal.

1. EXPERIMENTAL PROCEDURE

The polarization of the crystal was measured with an equal-arm electrometric bridge. A standard capacitor with capacitance C_0 was connected to the first arm and the experimental crystal was connected to the second arm and sources of a constant voltage V polarizing the crystal and compensating voltage v were connected to the two other arms. A B7-29 electrometer served as a null indicator in the diagonal of the bridge. When the bridge was balanced by adjusting v, the voltage on the crystal was equal to V and the electric charge on the electrodes was $Q=C_0v$. The required sensitivity of the circuit $\Delta Q=C_0\Delta v$ can be fixed by choosing a definite value of C_0. The maximum sensitivity (for $C_0=10$ pF, $\Delta v=1$ mV) was $\Delta Q=10^{-8}\mu$C. Voltage compensation in the bridge diagonal and measurement recording were automated using a system that permits constructing on the monitor screen of an IBM PC the time-dependence of the compensating voltage v and therefore the charge Q or polarization $P=Q/S$ (S is the area of the electrodes). A detailed description of the apparatus and the operation of the system is given in Ref. 4. The crystal sample consisted of $4\times5\times1$ mm rectangular wafers cut from a single crystal perpendicular to the Y polar axis. The large faces of the wafers were ground and coated with an electrically conducting silver paste. The samples were placed in a cryostat. The temperature stabilization error did not exceed 0.01 K.

The measurements were performed in the polar phase of the crystals at fixed temperatures for the following three regimes of variation of the external electric field: The polarization was recorded with a slow stepped cyclic variation of the field with period ~1.5 h (quasistatic dielectric hysteresis loops), a constant field with relatively small amplitude was switched on virtually instantaneously, and the constant field was switched off after short-time (~5 min) prepolarization (depolarization).

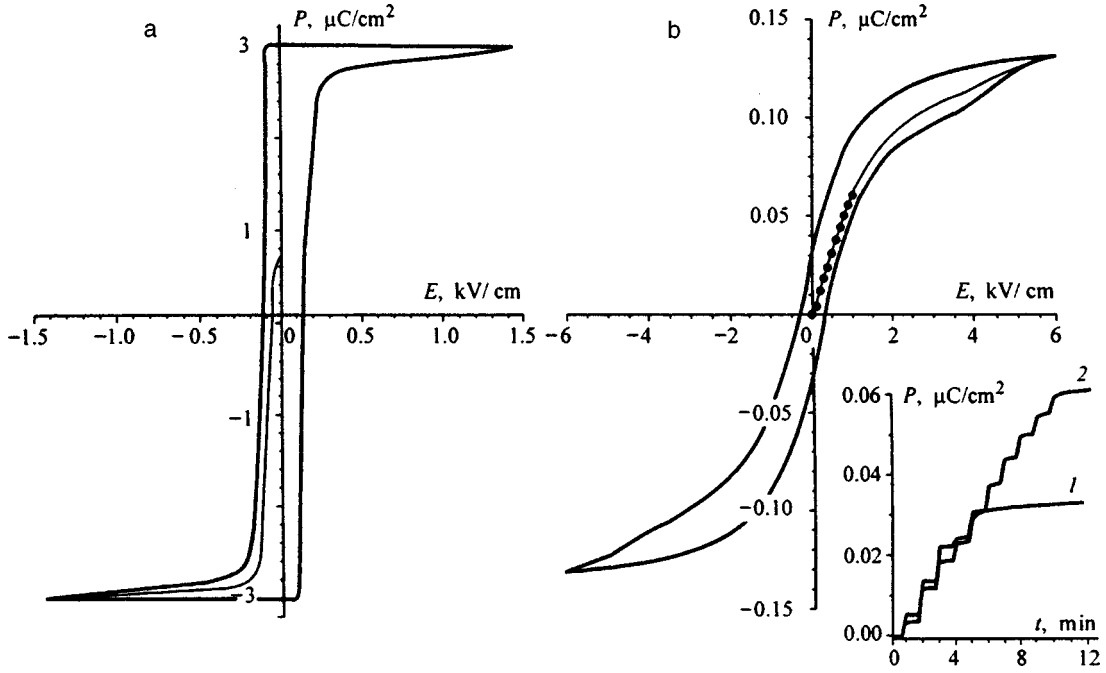

FIG. 1. Quasistatic dielectric hysteresis loops of the polarization P in an electric field E for TGS and Rb_2ZnCl_4 crystals. a — TGS, $T=293$ K, $T_c=323$ K; b — Rb_2ZnCl_4, $T=175$ K, $T_c=194.9$ K. Inset: P versus time with a step change in E.

2. RESULTS AND DISCUSSION

The difference between polarization processes in TGS and RZC crystals is clearly seen in the dielectric hysteresis loop in a periodic electric field (Fig. 1). For the crystal the loop has a pronounced square shape and the values of the coercive field E_c, which equals the half-width of the loop, and the spontaneous polarization P_s are determined reliably. After the field E has decreased to zero, the residual polarization is almost half of P_s and remains virtually unchanged for a long time (the depolarization time is long). For the second crystal the loop has an extended shape, it is doubtful that P_s can be determined reliably from the shape of the loop, and the residual polarization P vanishes comparatively rapidly as E decreases to zero (the depolarization time is short). The hysteresis loops in Fig. 1 pass through the experimental values of P, obtained with a sharp step change of the field E by 20–100 V/cm with an interval of 1 min. The fast stage of the relaxation of P terminates over this time and a slow process of further change in P commences. The fast stages for the crystals also differ substantially. For TGS in fields $E<E_c$ the polarization changes gradually, following a definite temporal law. For RZC in a wide interval of fields (both less and more than the half-width of the loop in Fig. 1b), P changes abruptly at first, then gradually, and a kink, indicating a sharp change in the relaxation mechanism of the domain structure, exists in the curve of the time-dependence of P. A fragment of this dependence from $P=0$ to the value at $E=0.5$ (curve *1*) and 1 kV/cm (curve *2*) is displayed in the inset in Fig. 1b. The duration of the fast stage of the relaxation of P with a sharp change in E does not exceed 15 s. The values of P corresponding to the moments when the jumps are completed lie on the curve of the first one-fourth period of the loop, presented in Fig. 1b (shown by the dots).

A characteristic feature of the initial stages of the polarization P for the two crystals is also manifested on the relaxation curves in a comparatively long time interval (Figs. 2a, b). After the field E is switched on instantaneously, at the initial moment ($t=0$) of the slow relaxation the values of P_0 for different values of $E<E_c$ are the same for TGS (no jumps in P) and different for RZC. The jump in P for RZC is all the larger, the larger E. Thus, for TGS rapid changes (jumps) in P are observed only in fields $E\geqslant E_c$, whereas for RZC they are observed in a wide range of values of E. It is natural to attribute this feature of the RZC crystal to the existence of a wide spectrum of the distribution of the coercive field E_c over the volume of the sample. As a result, in a field of virtually any strength part of the crystal is polarized rapidly (above-barrier process) and a part is polarized slowly (thermally-active process). If necessary, the spectrum of the distribution of E_c can be constructed from the experimental data presented.

In principle, the processes leading to the depolarization of the crystals should contain information about the spectra of the distribution of the energy barriers for domain walls in the absence of an electric field. The results of an investigation of the slow depolarization for TGS are contained in Ref. 5, and the results for RZC are displayed in Fig. 2c. Just as for the polarization of a crystal, after the field is switched off the polarization P at first decreases abruptly and then it slowly relaxes to the zero equilibrium value (inset in Fig. 2c). The preliminary polarization time of the crystal in fields of different magnitude E before they are switched off was 5 min.

We shall make a phenomenological analysis of the slow stages of polarization and depolarization, which are shown in Fig. 2, making the assumption, just as in Ref. 4, that after the jump in P the process proceeds in a thermal activation man-

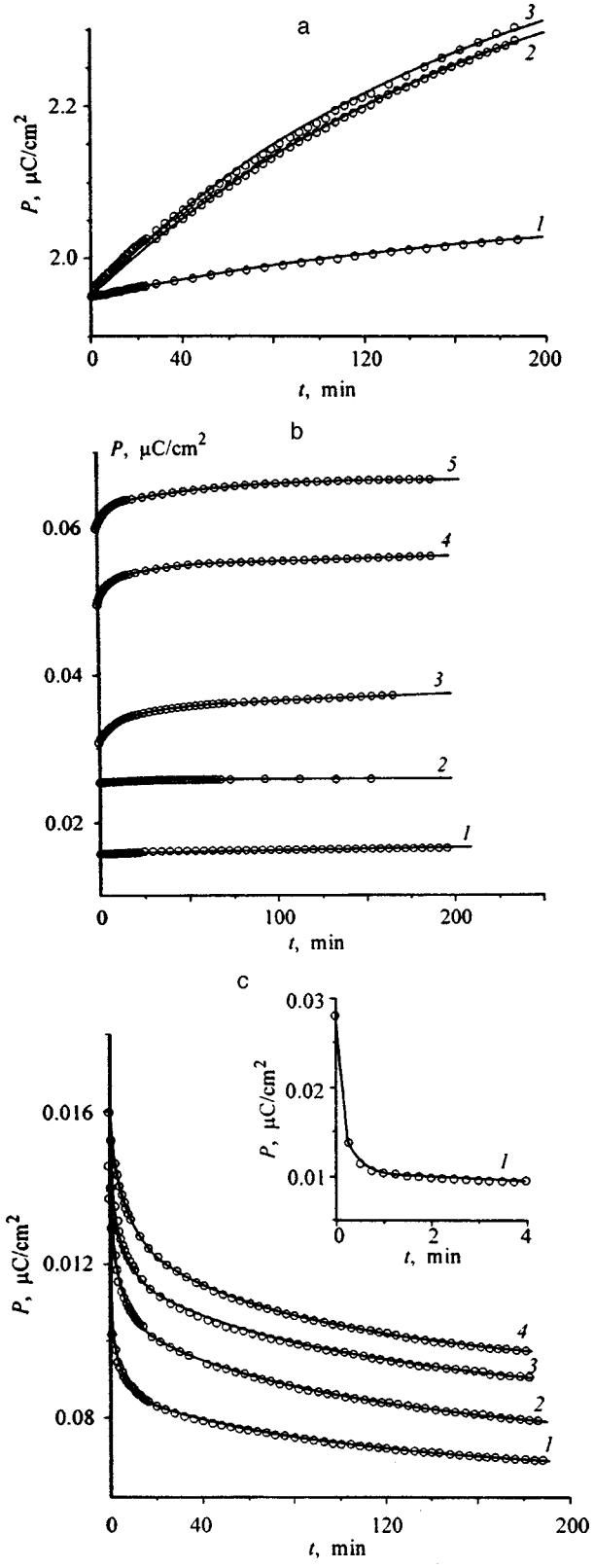

FIG. 2. Slow polarization of TGS and Rb_2ZnCl_4 in various electric fields E. a — TGS, $E=5.6$ (*1*), 15 (*2*), 25 V/cm (*3*); b — Rb_2ZnCl_4, polarization process in the field $E=200$ (*1*), 300 (*2*), 500 (*3*), 800 (*4*), 1000 V/cm (*5*); c — Rb_2ZnCl_4, depolarization process after the field $E=400$ (*1*), 600 (*2*), 800 (*3*), 1000 V/cm (*4*) is switched off. Inset: Initial section of the process, $t_0=1$ min.

ner and for a small change in P the relaxation centers (nuclei) are independent and make an additive contribution to the total value of P. Then

$$y(t)=(P_e-P(t))/(P_e-P_0)=\int_0^\infty f(\tau)\exp(-t/\tau)d\tau, \tag{1}$$

where P_e is the equilibrium polarization, $P(t)$ is the polarization at time t, P_0 is the polarization at $t=0$, $f(\tau)$ is the distribution function of the relaxation times τ, and $\int_0^\infty f(\tau)d\tau=1$. If the form of the function $y(t)$ can be determined from the experimental data, then Eq. (1) makes it possible to reconstruct easily the distribution function $f(\tau)$, since $\tau^2 f(\tau)$ and $y(t)$ are related by a Laplace transform, where the first function is the original function and the second function is its transform.

In Ref. 4, the spontaneous polarization P_s was taken as the equilibrium value P_e for TGS. In the case of a crystal with a definite value of the coercive field E_c, this appears to be fully justified and in Landau's phase transition theory it coincides with general ideas about polarization switching of ferroelectrics.[6] However, if an entire spectrum of values of E_c is present, then the equilibrium value P_e will depend on the magnitude of the field E. The simplest examples of this evidently are real ferroelectrics, where, on account of impurities or defects, which also apper as a result of ionizing radiation,[7] internal bias fields E_b exist. These fields lead to local asymmetry of the polarization-dependent double-minimum free energy and, in consequence, to forced local polarization. As a result, if the external field $E<E_b$ in some sections of the crystal, then these sections do not participate in the relaxation process. On this basis, P_e was assumed to be an unknown parameter, and an analytic expression describing the experimental data for both crystals was sought for the directly measured polarization

$$\Delta P(t)=P(t)-P_0=(P_e-P_0)(1-y), \tag{2}$$

where y is the function (1). Just as in Ref. 4, all the data obtained agree satisfactorily with the power-law dependence

$$y=1/(1+t/a)^n, \tag{3}$$

where the parameters a and n are also unknown.

The computed curves of $P(t)$ in Fig. 2 are shown by solid lines, while the experimental points fall on the lines with adequate accuracy. The least-squares method, employing a standard program, was used to fit the function (3) to the measurements $P(t)$. The deviation δP of the experimental values of P from the computed curves did not exceed $\delta P/P=0.005$. The parameters P_e, a, and n are given in Table I for all cases.

The empirical law (3) is possibly universal for inhomogeneous systems of various types. For example, the slow relaxation of the permittivity of mixed crystals $K_{(1-x)}Li_xTaO_3$ in the glass state follows the same law.[8] For $n\ll 1$ the law (3) becomes logarithmic $y\simeq 1-n\ln(1+t/a)$, and for $t\gg a$ it becomes a power law $y\simeq 1/t^n$, which are particular cases of Eq. (3) and were recorded earlier in many observations.[1] The law (3) describes better than the well-known Kohlrausch law $y\sim\exp(-t/\tau^\beta)(\beta<1)$ the experimen-

TABLE I. Parameters of the spectra of the relaxation times τ for TGS and RZC crystals.

Crystal	Process	E, V/cm	P_e, μC/cm^2	a, min	n	τ_m, min	τ_1, min	τ_2, min	ΔU, eV
TGS	Polarization	5.6	3.17±0.17	150±30	0.070±0.011	140±30	29±7	3038±3	0.1173
		15	3.02±0.05	210±10	0.55±0.02	135±9	35.0±2.5	1473±1	0.0944
		25	2.84±0.04	200±10	0.76±0.03	116±8	32±2	1046±2	0.0879
RZC	Polarization	200	0.0176±0.0002	36±10	0.29±0.04	30±9	6.7±2.2	428±1	0.0628
		500	0.0410±0.0003	4.5±0.8	0.26±0.01	3.5±0.7	0.8±0.2	58.3±0.1	0.0643
		800	0.0603±0.0005	1.7±0.6	0.19±0.01	1.4±0.5	0.3±0.1	25.00±0.05	0.0658
	Depolarization	400	0	0.024±0.002	0.0730±0.0005	0.022±0.003	0.005±0.003	0.4860±0.0003	0.07

tal data for short times t, since at $t=0$ the derivative dy/dt is infinite for the Kohlrausch law and finite for the second law (Fig. 2). Moreover, the law (3) corresponds to the simple distribution function[9]

$$f(\tau)=(1/a\Gamma(n))(a/\tau)^{n+1}\exp(-a/\tau), \tag{4}$$

where $\Gamma(n)$ is the gamma function. The maximum of $f(\tau)$ occurs at $\tau_m=a/(1+n)$. The errors δP_e, δa, and δn in determining the parameters of $P(t)$ from the experimental data are not difficult to estimate, using Eqs. (2) and (3), as

$$\left|\frac{\delta P_e}{(P_e-P_0)}\right|=\left|\frac{\delta P(t)}{P(t)-P_0}\right|=\frac{|\delta P(t)|}{(P_e-P_0)[1-1/(1+t/a)^n]},$$

$$\left|\frac{\delta a}{a}\right|=\frac{(1+t/a)}{n(t/a)}\left|\frac{\delta P(t)}{P_e-P(t)}\right|=\frac{(1+t/a)^{n+1}|\delta P(t)|}{n(P_e-P_0)(t/a)},$$

$$\left|\frac{\delta n}{n}\right|=\frac{1}{n\ln(1+t/a)}\left|\frac{\delta P(t)}{P_e-P(t)}\right|=\frac{(1+t/a)^n|\delta P(t)|}{n\ln(1+t/a)(P_e-P_0)},$$

$$\left|\frac{\delta f(\tau)}{f(\tau)}\right|=|n-a/\tau|\left|\frac{\delta a}{a}\right|+n|\ln(a/\tau)-\varphi(n)|\left|\frac{\delta n}{n}\right|, \tag{5}$$

where $\delta P(t)$ is the error in measuring P and $\varphi(n)=\Gamma'(n)/\Gamma(n)$ is the logarithmic derivative of $\Gamma(n)$. Significantly, the errors depend on the time interval during which the relaxation is recorded. For short times ($t\ll a$) they are extremely large and decrease with increasing t. As $t\to\infty|\delta P_e|\to|\delta P(t)|$, δa and δn at first decrease, and then increase: The minimum $|\delta a/a|_{\min}$ occurs at $t=a/n$, $|\delta a/a|_{\min}=[(n+1)/n]^{n+1}|\delta P(t)/(P_e-P_0)|$, and the minimum $|\delta n/n|_{\min}$ occurs at a value of t^* determined from the equation $n\ln(1+t^*/a)=1+t^*/a$.

The spectra $f(\tau)$ of the times τ of the slow relaxation stages, calculated using Eq. (4), for polarization processes in TGS and RZC and depolarization processes in RZC are presented in Fig. 3. The nature of the evolution of the spectra for the polarization accompanying a change in the magnitude of the field E is the same for both crystals: As E increases, the maximum of $f(\tau)$ shifts in the direction of smaller values of τ. The most detailed data on the influence of the field on the spectrum of τ for TGS are contained in Ref. 4. The spectrum $f(\tau)$ for depolarization of RZC, within the limits of the measurement error $\delta f(\tau)/f(\tau)\simeq 50-100\%$, is virtually independent of the field strength (200–1000 V/cm) of the preliminary polarization of the crystal and lies in the range of small values of τ with a maximum at $\tau_m\approx 1.2$ s, and its width is smaller than for the polarization process (Fig. 3). A similar estimate $\tau_m'\approx 100$ min can be obtained, from the data of Ref. 5, for the depolarization of TGS, whose rate is much lower than in RZC.

Table I gives, besides the parameters a, n, and P_e, the characteristics of the spectra: the minimum τ_1 and maximum τ_2 values of τ and the width ΔU of the spectra determined at the level $f(\tau)=0.1f(\tau_m)$, where $f(\tau_m)$ is the maximum value of $f(\tau)$. According to the Arrhenius law $\tau=\tau_0\exp(U/kT)$ (τ_0 is the kinetic factor), i.e. $\Delta U=kT\ln(\tau_2/\tau_1)$. The absolute error in determining ΔU does not exceed 0.001 eV. The errors for other quantities are indicated in Table I. In accordance with Eq. (5), the measurement accuracy should increase appreciably, if the recording time of the relaxation is increased. We note once again that, in contrast to Ref. 4, in fitting a power-law dependence (3) with the free parameters a and n to the experimental data for both crystals, the quantity P_e was also assumed to be arbitrary (a third free parameter). For TGS this additional assumption actually does not give anything new compared with Ref. 4, since in this case P_e once again is virtually identical to the spontaneous polarization P_s for all values of $E<E_c$ (see Table I). For RZC, however, P_e depends on E, approximately repeating the dependence of P on E in the first one-fourth of the period of the variation of the field (Fig. 1b).

The results of recording P, which are presented above, enable us to make the following remarks about the characteristic features of the P-dependent local free energy F for both crystals (Fig. 4). For TGS $F(P)$ (Fig. 4a) is the standard symmetric function with two minima (curve *1*).[10] When an arbitrarily weak polarizing field E_p is switched on, the function $F(P)$ changes (curve *2*), and a slow thermoactivational relaxation from the state A into the state B commences. When E_p is switched off, the reverse process of relaxation from the state C into the state D (curve *3*) occurs under the action of the depolarizing field E_d. Both processes are indicated by arrows in Fig. 4a. If $E_p\simeq E_d$ is small, then the states A, B, C, and D are close to the states corresponding to the minima of the function $F(P)$ which is not perturbed by the field (curve *1*), and the potential barriers $U_p=F_A$ in the presence of polarization and $U_d=F_C$ in the presence of depolarization are virtually identical, $U_p\simeq U_d$ (the index of F is the point on the curve $F(P)$ where the value of F is taken). Indeed, for barrier energies corresponding to the times τ_m and τ_m' of the maxima of the distribution $f(\tau)$ for polariza-

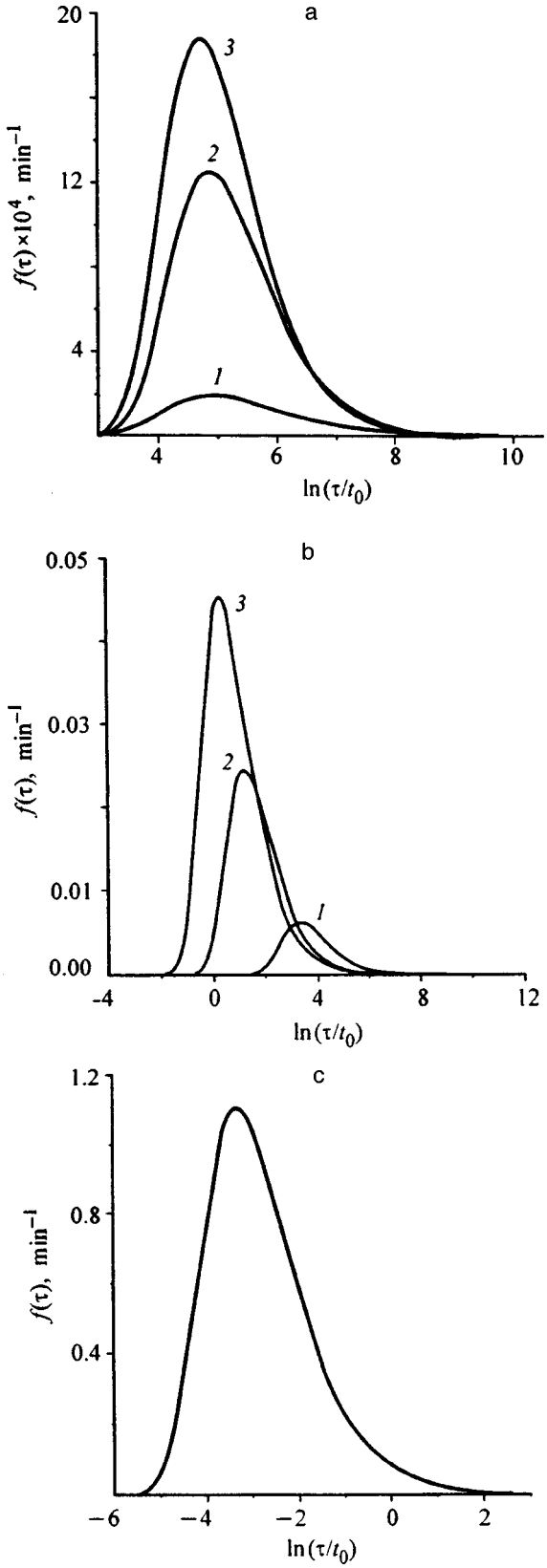

FIG. 3. Distribution $f(\tau)$ of the relaxation time τ for polarization of TGS (a) and Rb_2ZnCl_4 (b) and depolarization of Rb_2ZnCl_4 (c) in various electric fields E. a — $E=5.6$ (*1*), 15 (*2*), 25 V/cm (*3*); b — $E=200$ (*1*), 500 (*2*), 800 V/cm (*3*); c — $E=400$ V/cm, $t_0=1$ min.

tion and depolarization, respectively, we have $U_p-U_d=kT\ln(\tau_m/\tau_m')$. The values $\tau_m\sim100$ (see Table I) and $\tau_m'\sim100$ (rough estimate based on the experimental data of Ref. 5), i.e. $U_p-U_d\sim0$. The coercive field $E_c(F_A=0)$ has a definite value for the entire crystal, since the width of the distribution function decreases sharply as $E\to E_c$.[4]

The energy F for RZC is an asymmetric double-minimum function. Figure 4b shows a schematic diagram of the local F for the half of the sample with a zero total polarization (curve *1*) (for the other half F has a similar form but its deeper minimum lies to the right for $P>0$). The polarizing field E_p changes the form of F (curve *2*), and for a definite threshold value of the field, for which $F_A\geqslant F_B$, thermoactivational relaxation from the state A into the state B commences. When E_p is switched off, depolarization from the state C into the state D (curve *3*) occurs. One can see that in contrast to TGS both processes differ substantially: polarization is slow, while depolarization is relatively rapid, the barrier $U_p=F_A>U_d=F_C$. For the barrier energies U_p and U_d corresponding to the times τ_m and τ_m' of the maxima of the distribution $f(\tau)$ for polarization and depolarization respectively (see Table I and Fig. 3), we have $U_p-U_d=kT\ln(\tau_m/\tau_m')\simeq0.11$ eV. Since in accordance with the experimental data the parameters of the curve $F(P)$ should have a certain distribution in the volume, the values of the coercive fields E_c at local points of the crystal are different, and only the part of the volume where $F_A\geqslant0$ always participates in the above-barrier polarization process. The asymmetry of $F(P)$ for RZC could be due to the appearance of internal bias fields E_b on account of inhomogeneities of the crystal, for example, as in TGS crystals containing impurities or irradiated with ionizing radiation.[7] The reason why E_b with opposite signs appears in ''pure'' RZC remains unclear. It could be due to the accumulation of defects in antiphase boundaries and in planes occupied by solitons in an incommensurate phase at temperatures $T>T_c$.[2]

A large number of various ferroelectric materials in which the electric-field dependence of the polarization (dielectric hysteresis loop) is either square or ''extended'' are now known. The latter is characteristic mainly for inhomogeneous systems with different kinds of macroscopic inhomogeneities, for example, so-called relaxation oscillators, glasses, or ceramics. The relaxation data presented in the present work for polarization and depolarization processes for the example of two crystals make it possible to relate the characteristic features of the shape of the loop, the spectra of the distribution of energy barriers for domain walls, and the local free energy. For a square loop the free energy at any point in the crystal is a standard symmetric double-minimum function, whose parameters have a certain distribution in the volume, the coercive field has a definite value, and a slow thermoactivation relaxation commences in arbitrarily weak fields and encompasses the entire crystal. In the case of an ''extended'' loop the free energy is asymmetric relative to the polarization of the double-minimum function, whose parameters are distributed in the volume in a manner such that the average spontaneous polarization is zero, the coercive field is different in different sections of the crystal, and a

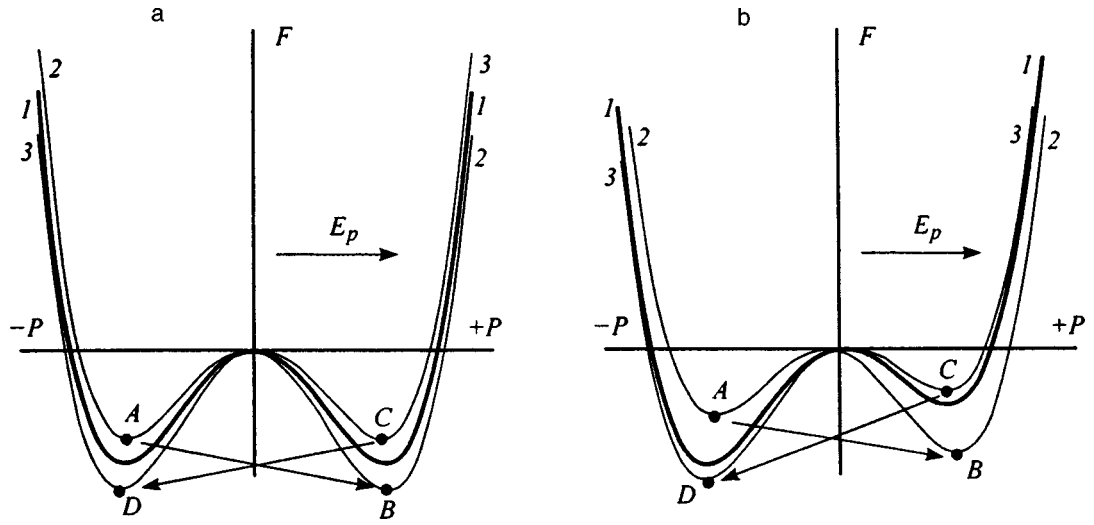

FIG. 4. Schematic diagram of local free energy functions $F(P)$ for TGS (a) and Rb_2ZnCl_4 (b).

limited part of the sample, whose volume increases with increasing field, participates in the relaxation of the polarization. However, it is important that in both cases the thermoactivation relaxation processes obey a single empirical power law, which apparently is universal for all inhomogeneous systems.

This work was supported by the Russian Fund for Fundamental Research (Project No. 96-02-18456).

[1] A. K. Jonscher, *Dielectric Relaxation in Solids* (Chelsea Dielectric Press Ltd, London, 1983, p. 380).
[2] H. Z. Cummins, Phys. Rep. **185**, 211 (1990).
[3] L. E. Cross, Ferroelectrics **151**, 305 (1994).
[4] V. V. Gladkiĭ, V. A. Kirikov, S. V. Nekhlyudov, and E. S. Ivanova, Fiz. Tverd. Tela (St. Petersburg) **39**(11), 2046 (1997) [Phys. Solid State **39**, 1829 (1997)].
[5] W. Osak and K. Tkacz-Smiech, Appl. Phys. A **65**, 439 (1997).
[6] L. D. Landau and E. M. Lifshitz, *Electrodynamics of Continuous Media* (Pergamon Press, N. Y.) [Russian original, Nauka, Moscow, 1982, p. 620].
[7] M. Lines and A. Glass, *Principles and Applications of Ferroelectrics and Related Materials* (Clarendon Press, Oxford, 1977) [Russian translation, Mir, Moscow, 1981, p. 736].
[8] F. Alberici, P. Doussineau, and A. Levelut, J. Phys. I France **7**, 329 (1997).
[9] V. I. Ditkin and A. P. Prudnikov, *Integral Transforms and Operational Calculus* (Pergamon Press, Oxford, 1966) [Russian original, Vyssh. shkola, Moscow, 1965, p. 467].
[10] B. A. Strukov and A. P. Levanyuk, *The Physical Principles of Ferroelectric Phenomena in Crystals* (Nauka, Moscow, 1995, p. 301).

Translated by M. E. Alferieff

Fractal-cluster kinetics in phase transformations in the relaxor ceramic PLZT

V. Ya. Shur, G. G. Lomakin, V. P. Kuminov, D. V. Pelegov, S. S. Beloglazov, S. V. Slovikovskiĭ, and I. L. Sorkin

Institute of Physics and Applied Mathematics, Ural State University, 620083 Ekaterinburg, Russia
(Submitted July 27, 1998)
Fiz. Tverd. Tela (St. Petersburg) **41**, 505–509 (March 1999)

Fractal formalism has been used to study the evolution of a heterophase state (consisting of polar nanoregions in a nonpolar matrix) subjected to polarization in an electric field within the diffuse phase transition in the transparent relaxor ferroelectric ceramic PLZT 8/65/35. The time dependences of the fractal dimensions of polar clusters under polarization switching and spontaneous backswitching at different temperatures have been derived from measurements of the elastic scattering of transmitted light. Various scenarios for the evolution of the heterophase and nanodomain states in relaxors with variation of the temperature and electric field are proposed. © *1999 American Institute of Physics.* [S1063-7834(99)02603-9]

The relaxor state in ferroelectrics has become recently a subject of intensive studies. The interest in this class of substances is stimulated by the existence in these materials within a broad temperature range of susceptibility anomalies, which in conventional ferroelectrics are observed only near the phase-transition point. The record-high susceptibilities open up a wide potential in applications.[1]

The heterophase state existing over a broad temperature range in ferroelectrics having a diffuse phase transition is known to consist of nanosized ferroelectric (polar) regions embedded in a paraelectric (nonpolar) matrix. Individual polar nanoregions can be seen only with a high-resolution electron microscope.[1,2] Cooling increases the fraction of the polar phase, which gives rise to coalescence of the nanoregions to form eventually polydomain clusters of a complex shape. The spontaneous polarization ($\mathbf{P}_s$) of individual polar nanoregions and nanodomains in clusters is oriented in a random manner, thus resulting in no bulk-averaged polarization $\mathbf{P}_s$. Only an external electric field can align the $\mathbf{P}_s$ orientation in the nanoregions.

The extremely small size of the nanoregions precludes the use of optical visualization techniques to study the kinetics of their rearrangement in the course of polarization switching. At the same time application of an electric field to a relaxor ceramic enhances strongly the intensity of scattered light.[3] The high sensitivity of light scattering to local magnitude of spontaneous polarization permits one to derive information on polarization kinetics from *in situ* measurements. The fractal approach to an analysis of experimental data on light scattering from polar-phase clusters in relaxors can provide quantitative information on the kinetics of growth and orientation of otherwise invisible objects in an electric field.[4–8]

Variation of the fractal dimension of a system can be judged from both indirect (integrated) and direct measurements. Direct measurements involve recording sequences of instantaneous images of a system in different stages of its evolution. Their use entails considerable experimental difficulties and time-consuming mathematical processing of huge arrays of information. By contrast, integral methods, particularly the small-angle scattering technique, which is widely employed in determination of the fractal dimensions of static structures,[9–12] has considerable advantages. *In situ* measurements of the angular dependence of scattered light intensity is most appropriate for studying fast kinetic processes.[13] Among its obvious merits are its universality (measurements in both transmitted and reflected light), fast response (measurement frequencies of up to 200 Hz), high locality (probe diameters of down to 100 μm), and a high sensitivity and spatial resolution (down to 100 nm).[6,7,13]

This work applies fractal formalism to angular dependences of scattered light intensity to derive the spatial distribution of scattering centers in a relaxor.

1. EXPERIMENT

As the object for the study was chosen the hot-pressed, coarse-grained (grain size $4-7\ \mu$m) lanthanum-doped PLZT 8/65/35 ceramic (lead zirconate-titanate), which exhibits a classic relaxor behavior within a broad temperature range. We analyzed the variation in longitudinal scattering of monochromatic light under application of rectangular field

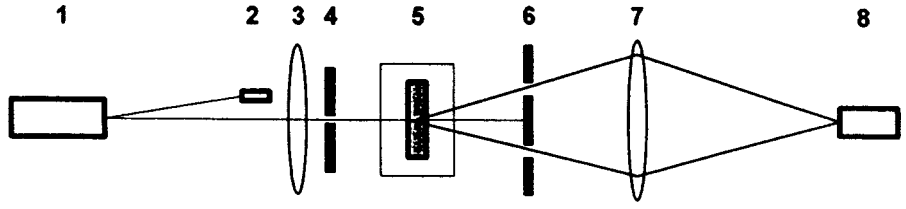

FIG. 1. Optical arrangement: *1* — laser, *2* — photodiode, *3, 7* — lenses, *4* — diaphragm, *5* — sample in a cryostat, *6* — interchangeable annular diaphragm, *8* — PM tube.

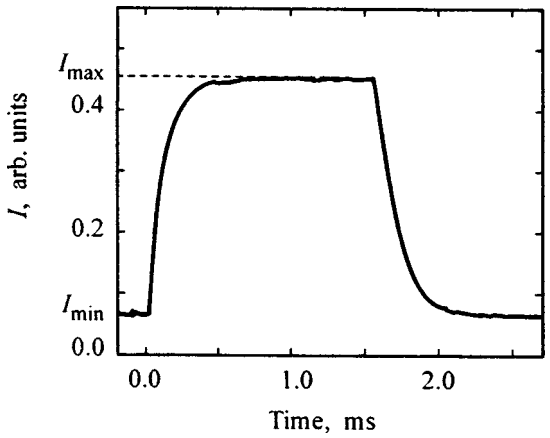

FIG. 2. Typical variation of integrated scattered light intensity under application of rectangular voltage pulses ($E=10$ kV/cm, pulse length 1.5 ms, $T=60\,^{\circ}$C).

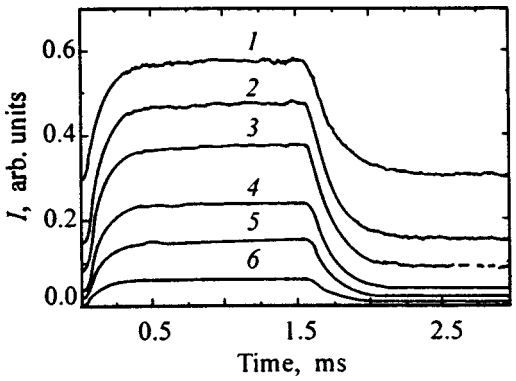

FIG. 4. Variation of scattered light intensity for different angles φ(deg): *1* — 0.72, *2* — 1.03, *3* — 1.82, *4* — 2.29, *5* — 2.33, *6* — 2.93) under application of rectangular voltage pulses ($T=60°$C).

pulses. Continuous transparent electrodes based on indium and tin oxides were deposited on the surfaces of plane-parallel ceramic plates less than 100 μm in thickness. The polarization was generated by 0.001–1-s long unipolar field pulses with a repetition frequency of 0.1–0.5 Hz and amplitude of up to 400 V.

The behavior of the light intensity scattered at an angle α in time, $I(t)_\alpha$, reproduced itself under cyclic repetition of the field pulses. This feature permitted determination of the instantaneous scattering indicatrix $I(\alpha)_t$ (for an instant of time t) from a series of consecutive measurements of $I(t)_\alpha$ for light scattered through various angles α (selected with a set of annular diaphragms).

The optical arrangement used to measure the angular dependences of scattered light is presented in Fig. 1. The source of light is a He–Ne laser (*1*) operating at a wavelength of 0.63 μm with a power of 3 mW. The radiation intensity is monitored with a photodiode (*2*). A parallel fundamental-mode beam collected by lens (*3*) and cut out by diaphragm (*4*) passes through sample (*5*) mounted in an optical thermostat. Interchangeable annular diaphragms (*6*) make possible light-intensity measurements at scattering angles from 20′ to 10° with a resolution of about 20′. Lens (*7*) focuses the scattered light onto the photocathode of a PM tube (*8*). A computer-controlled system permits measurement of the laser beam and scattered light intensity with a time resolution of less than 1 μs.

2. RESULTS OF MEASUREMENTS

The variation of integrated scattered intensity under application of a rectangular field pulse can be separated into two parts, namely, switching, during which the intensity increases to reach a maximum level I_{max}, and spontaneous backswitching, a process recovering the original transparent state with a background scattering I_{min} (Fig. 2). As seen from the temperature dependence of scattered-light amplitudes (Fig. 3), the field-induced variation in the scattered intensity is observed within a temperature region from 45 to 120 °C, where $T_{max}=120°$C is the temperature of the maximum in dielectric permittivity, and $T_{ph}=45°$C is the temperature of the phase transition from the relaxor to ferroelectric state.

The set of the time dependences of the intensity scattered at fixed angles, $I(t)_\alpha$ (Fig. 4), was used to determine the angular dependences of the scattered intensity $I(\alpha)_t$ for

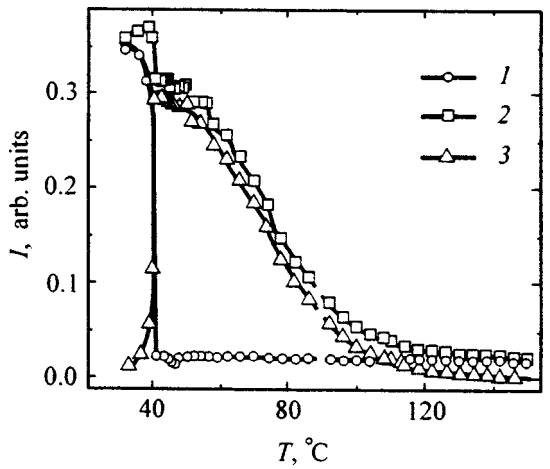

FIG. 3. Temperature dependence of the scattered intensity parameters (*1* — I_{min}, *2* — I_{max}, *3* — ΔI) obtained under cooling ($E=10$ kV/cm, pulse length 1.5 ms).

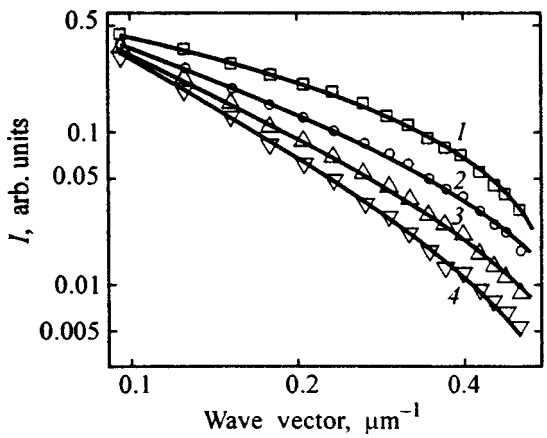

FIG. 5. Instantaneous angular dependences of scattered light intensity t(ms): *1* — 1.59, *2* — 1.72, *3* — 1.85, *4* — 2.17. The experimental data are fitted to Eq. (2).

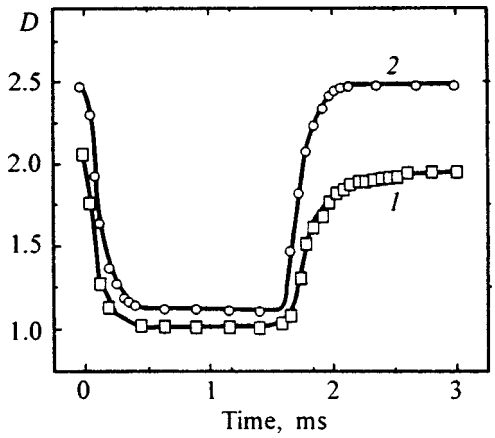

FIG. 6. Variation of instantaneous values of fractal dimension under application of a rectangular field pulse T(°C): *1* — 47, *2* — 60.

different instants of time (i.e. switching phases) (Fig. 5). The experimental data were treated under the assumption that the scattering centers are fractal clusters.

It is known that polar-phase clusters in relaxors are objects with a complex structure presenting difficulties for analysis of angular dependences of elastically scattered light, and fractal formalism is used successfully here.[14–16] Besides, as demonstrated for the classical relaxors PST and PMN, field-induced polar clusters are also fractal objects,[14,15] for which the classical dependence of the scattered intensity I_{sc} on wave vector q holds[12]

$$I_{sc}(q) \sim q^{-D}, \tag{1}$$

where $q=(4\pi/\lambda)\sin(\varphi/2)$, φ is the scattering angle, λ is the wavelength, and D is the fractal dimension.

Obviously enough, relation (1) is not satisfied in our case throughout the range of angles (sizes) covered (Fig. 5). Therefore in our treatment of experimental data an upper length-scale cutoff on clusters was introduced using a modified dependence[9–11]

$$I_{sc}(q) \sim \Gamma(D-1)\xi^{D}(1+q^2\xi^2)^{-(D-1)/2} \times (q\xi)^{-1/2}\sin[(D-1)\arctan(q\xi)], \tag{2}$$

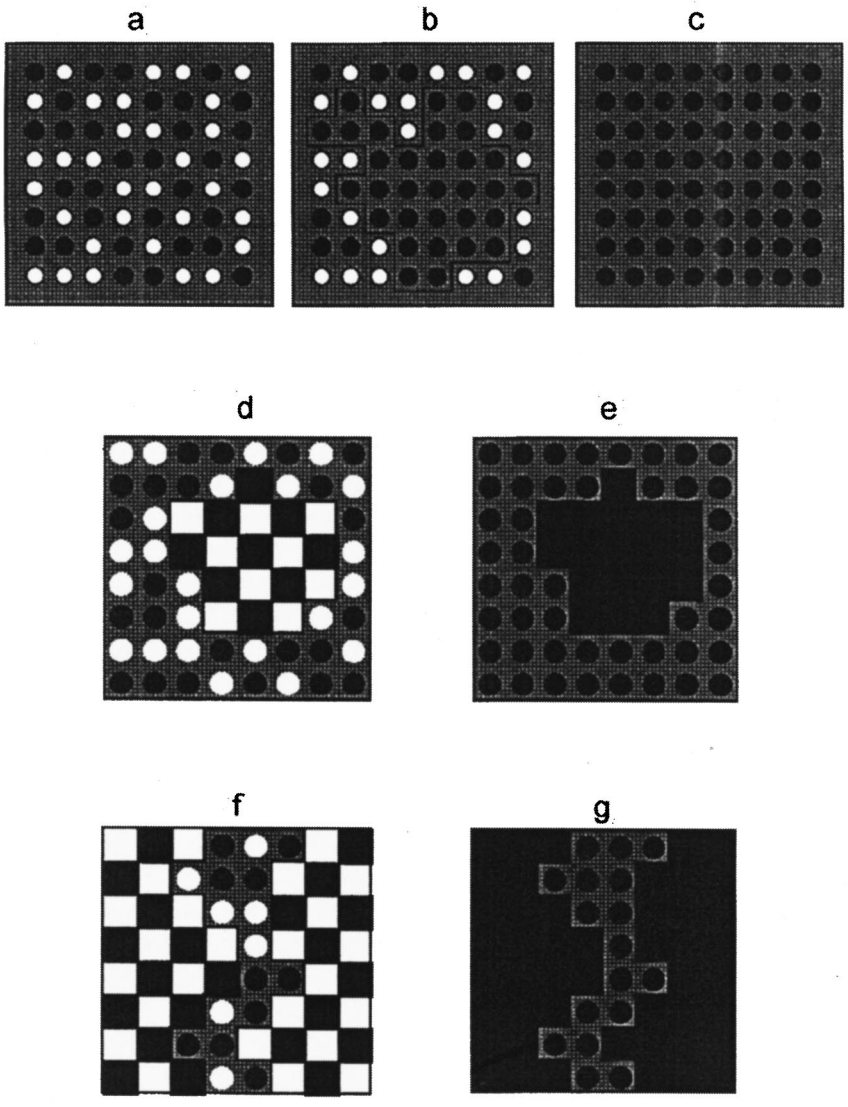

FIG. 7. Schematic evolution of a heterophase structure existing in a relaxor phase at various temperatures and driven by an electric field: (a–c) substantially above T_{ph}; (d,e) near T_{ph}; (f,g) at T_{ph}; (a,d,f) without field; (c,e,g) with applied field; (b) in the course of polarization switching. Filled and open circles — polar nanoregions with differently oriented polarization, filled and open squares — differently oriented nanodomains, gray region — nonpolar matrix. A dynamic cluster is outlined in (b).

where $\Gamma(x)$ is the gamma function, and ξ is the fractal correlation length.

The experimental points were approximated within the total angular range by relation (2) with a fixed ξ, which permitted reliable determination of the fractal dimension.

3. DISCUSSION OF RESULTS

Figure 6 demonstrates the variation of fractal dimension induced by switching and backswitching for two temperatures. We readily see that the kinetics of heterophase state driven by a field pulse may be considered as evolution of a fractal object. The noticeable decrease of fractal dimension under the action of an external field resembles the trend observed as the temperature is decreased. An analysis of $D(t)$ permits one to follow the kinetics of the process; indeed, the initial decrease evidences a change in the structure of the scattering centers when the relaxor is being polarized, the value of D within the linear portion characterizes the structure of the polarized state, and the subsequent increase of the fractal dimension describes the kinetics of system recovery to the initial state.

The scatterers change their nature under cooling as the transition to the ferroelectric phase is approached. Far from T_{ph}, only single disordered polar nanoregions exist in the nonpolar matrix (Fig. 7a). After the field has been turned on, they gradually orient in one direction to form ''dynamic polar clusters,'' which consist of adjacent nanoregions with the same direction of polarization (Fig. 7b). The fairly large dynamic clusters act as scattering centers. In a completely polarized sample, scattering takes place only from grain boundaries (Fig. 7c).

In the vicinity of T_{ph}, polar nanoregions coalesce to form polydomain clusters with nanosized domains (Fig. 7d). In this case, however, there is also no macropolarization in the absence of a field, and the medium is optically homogeneous, because spontaneous polarization in adjacent nanodomains is randomly oriented. The linear dimensions of polydomains are large enough for scattering to set in after the field-induced transfer to the single-domain state (Fig. 7e).

In the immediate vicinity of the complete transition to the ferroelectric phase (Fig. 7f), percolation transition gives rise to formation of ''infinite'' polydomain clusters with dimensions equal to those of the grains. In this case scattering after the polarization switching occurs from grain boundaries and nonpolar ''windows'' (Fig. 7g).

Thus we have studied the statics and kinetics of the heterophase state, which contains nanosized regions of a polar phase with randomly oriented spontaneous polarization and exists in the region of the diffuse ferroelectric phase transition. Based on the assumption that the scattering centers (field-induced clusters of nanoregions of the polar phase and nanodomains) may be considered as fractal objects, the time evolution of their fractal dimensions under a pulsed field and at different temperatures has been studied. It has been demonstrated that fractal formalism permits determination of the scenarios of evolution of the heterophase and nanodomain state in relaxors under variation of temperature and application of an electric field.

Partial support of the Russian Fund for Fundamental Research (Grant 98-02-17562) is gratefully acknowledged.

*)E-mail: Vladimir.Shur@usu.ru

[1] L. E. Cross, Ferroelectrics **151**, 305 (1994).
[2] X. Dai, Z. Xu, and D. Viehland, Philos. Mag. B **70**, 33 (1994).
[3] M. D. Ivey and V. W. Bolie, IEEE Trans. Ultrason. Ferroelectr. Freq. Control **38**, 579 (1991).
[4] V. Ya. Shur, V. P. Kuminov, G. G. Lomakin, S. S. Beloglazov, A. Sternberg, and A. Krumins, *Abstr. Intern. Symp. Ferroic Domains and Mesoscopic Structures* (Vienna, 1996), p. 110.
[5] V. Ya. Shur, V. P. Kuminov, G. G. Lomakin, S. S. Beloglazov, S. V. Slovikovski, A. Krumins, and A. Sternberg, J. Korean Phys. Soc. **32**, S985 (1998).
[6] V. Ya. Shur, *Proc. IEEE Intern. Symp. Applications of Ferroelectrics* (1996), p. 233.
[7] V. Ya. Shur, E. L. Rumyantsev, V. P. Kuminov, G. G. Lomakin, S. S. Beloglazov, A. Sternberg, and A. Krumins, Ferroelectrics **199**, 159 (1997).
[8] V. Ya. Shur, Phase Transit. **65**, 49 (1998).
[9] S. K. Sinha, Physica D **38**, 310 (1989).
[10] A. Hasmy, M. Foret, J. Pelous, and R. Jullien, Phys. Rev. B **48**, 9345 (1993).
[11] R. Vacher, T. Woignier, J. Pelous, and E. Courtens, Phys. Rev. B **37**, 6500 (1988).
[12] J. Feder, *Fractals* (Plenum Press, New York, 1988) [Russ. transl. Mir, Moscow, 1991, 254 pp.].
[13] A. L. Korzhenevskiĭ, Fiz. Tverd. Tela (Leningrad) **26**, 1223 (1984) [Sov. Phys. Solid State **26**, 744 (1984)].
[14] V. Ya. Shur, S. A. Negashev, E. L. Rumyantsev, A. L. Subbotin, and S. D. Makarov, Ferroelectrics **169**, 63 (1995).
[15] A. L. Korzhenevskiĭ, L. S. Kamzina, and O. Yu. Korshunov, JETP Lett. **61**, 219 (1995).
[16] L. S. Kamzina, N. N. Kraĭnik, and O. Yu. Korshunov, Fiz. Tverd. Tela (St. Petersburg) **37**, 2765 (1995) [Phys. Solid State **37**, 1523 (1995)].

Translated by G. Skrebtsov

Local charge formation in $LiNbO_3$ using a mobile needle-shaped electrode

S. O. Fregatov and A. B. Sherman*)

A. F. Ioffe Physicotechnical Institute, Russian Academy of Sciences, 194021 St. Petersburg, Russia
(Submitted July 30, 1998)
Fiz. Tverd. Tela (St. Petersburg) **41**, 510–512 (March 1999)

It is shown that local formation of electric charge in a region near the surface of lithium niobate crystals can take place both by local polarization switching of the sample and by local injection of electric charge from a needle-shaped electrode. A local change, due to the electrooptic effect, in the birefringence of the sample near the charged region is used to investigate the nature and the formation mechanism of the charge relief. © *1999 American Institute of Physics.* [S1063-7834(99)02703-3]

Dielectrics, having a low electric conductivity, can maintain for a long period of time a nonequilibrium spatial distribution of electric charge that is produced in them. The formation of such a distribution can be accomplished by different methods. For example, charged regions can be produced in photosensitive dielectrics by laser radiation. The radiation generates in the sample free charge carriers which are then redistributed in the internal electric fields of the crystal lattice.[1] A charge relief can be produced in a ferroelectric dielectric by forming a domain structure in the crystal having a prescribed arrangement of charged domain walls. Finally, the injection of charge carriers[2] into a dielectric from an external electrode can be used to produce such a relief.

The uniaxial ferroelectric lithium niobate, which possesses high resistivity, spontaneous polarization, and electrooptic constants, is one of the most convenient materials for studying phenomena associated with the formation of a nonequilibrium space charge distribution. Specifically, the strong electrooptic effect makes visualization of charge regions in it possible.

In the present work local penetration of electric charge into lithium niobate whose surface is scanned by a needle-shaped electrode is investigated experimentally. Such an electrode acts like an electric-field concentrator in the region where the electrode touches the surface of the crystal and at the same time a mobile (moving along the surface) source of injected charge. The local change produced in the birefringence in the crystal along the trajectory of the electrode tip is used to study the mechanism leading to the formation of a charge relief and to determine the geometric characteristics and lifetime of the charge relief.

A diagram of the experiment is shown in Fig. 1. A single-crystal sample 1 is placed on the surface of the first electrode — a half-transmitting conducting film of chromium 2 deposited on the bottom of the cell 3. A tungsten tip 4, secured to a micromanipulator, is brought up to the surface of the crystal (just as in previous experiments,[3,4] the radius of curvature of the tip was $\approx 1\,\mu$m). The tip serves as a second electrode and can move in the horizontal and vertical directions. To prevent electrical breakdown the cell holding the sample is filled with transformer oil. A polarized-light microscope 5 is used to observe in the transmitted light the motion of the tip and the local change in the birefringence in the sample. Both ''direct'' observation of the spatial relief — on the side of the surface touched by the mobile electrode (Fig. 1a) — and observation ''from the side'' — through the side face of the crystal (Fig. 1b) — are possible. To investigate the local changes in the birefringence the microscope analyzer is placed in a position close to the crossed position with respect to the polarizer and the sample is oriented so that its characteristic birefringence would not produce obstacles to observation.

Let us consider first the possibility of producing a charged relief by means of local polarization switching of the sample.[4]

Figure 2 shows a fragment of the surface of a *Z*-cut monodomain sample of lithium niobate (''direct'' observation) on which parallel lines with different values of the voltage (U) were drawn with a needle-shaped electrode. The photograph attests to the change in the birefringence in the crystal along these lines. This effect is recorded with the electric field near the tip oriented in a direction opposite to the spontaneous polarization in the crystal and with the voltage on the electrodes exceeding the threshold value (in our case 500 V).

The image obtained at room temperature remains for quite a long time: The decrease in the contrast of the image becomes noticeable two days after the polarization switching is completed, but the pattern can be distinguished even after one month. Heating the sample to 100 °C causes the imgae to vanish almost completely within 2–3 min.

In previous work[3] it was established by chemical etching that under the conditions presented above local switching of the polarization occurs in the sample (domain formation).

In uniaxial ferroelectric crystals domains with oppositely directed polarization are optically indistinguishable because their optical scattering functions are identical. The optical contrast arising with polarization switching should be associated with the state of the regions of the crystal near domain walls. Indeed, observation ''from the side''[4] established that the observed optical contrast (Fig. 2) is due to the optical

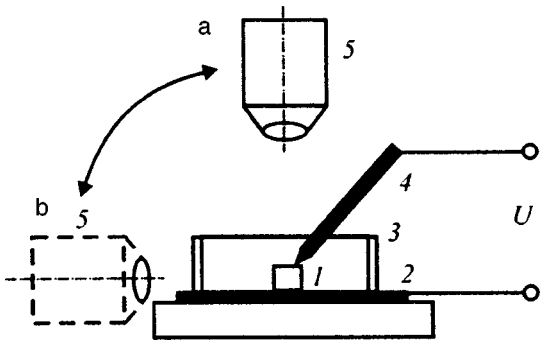

FIG. 1. Diagram of the experiments. a — ''Direct'' observation, b — observation ''from the side.''

inhomogeneity near the walls of the needle-shaped domains formed. These domains, which are arranged quasiperiodically (period $\approx 2\mu$m) along the lines drawn, extend in the direction of the Z axis. With a voltage $U=2.5$ kV they are 55 μm long and $\approx 1\mu$m across.

For domains localized near the surface of the crystal (not through domains) the domain walls cannot be parallel to the Z axis everywhere. There exist sections of the walls where P_n (the component of the spontaneous polarization that is orthogonal to the surface of the wall) is different from zero. An electric charge with density $q \simeq 2P_n$, whose electric field influences the local birefringence, forms on such sections.

Assuming the optical inhomogeneity under study is caused by the electric field produced by charges localized in the domain walls, it is easy to explain the observed decrease in the image contrast with time. After a local charge is formed, the intrinsic free carriers in the crystal start to compensate it, which decreases the local electric field with time.

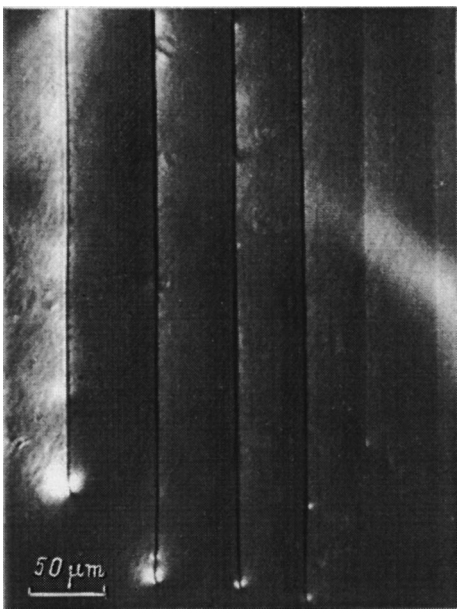

FIG. 2. Section of the surface of a Z-cut lithium niobate crystal in polarized light after drawing parallel lines with a needle-shaped electrode. The potential difference decreases (from 2.7 kV) from line to line with a ≈ 0.4 kV step. The tip velocity ≈ 1 mm/s.

Local polarization switching using a needle-shaped electrode can also be produced in Y-cut samples.[3] The threshold voltage in this case is 900 V. The needle-shaped domains formed, which are revealed by chemical etching, extend along the surface of the crystal in the direction of the Z axis. For $U=2.5$ kV the domains are 15 μm long and $\approx 1\mu$m across. However, it is not possible to record the change in the optical birefringence near the domain walls.

In Ref. 3 it is shown that under local polarization switching domains in Y-cut samples grow in a thin surface layer ($\sim 0.15\mu$m). The polarization and electric properties in this layer can differ appreciably from those in the interior volume. This could be due both to the closeness of the boundary of the sample and the corresponding boundary phenomena and to the effect of a real surface, whose properties are largely determined by the physicochemical treatment. A high conductivity and, in consequence, more rapid compensation of electric charges localized in the domain walls can be observed in this layer. Apparently, the short compensation time of these charges did not make it possible to observe the associated rapid change in the local birefringence in Y-cut samples.

Together with the long-time change in the local birefringence observed in Z-cut samples accompanying polarization switching, one other optical effect is observed in the experiments. It consists in the appearance of a stripe of optical contrast with a short lifetime ($t \leqslant 20$ s) trailing behind the tip along the trajectory of the tip along the surface of the crystal in both Z- and Y-cut samples. The phenomenon is observed for both signs of the polarity of the tip. The minimum voltage at which it could be observed was much lower than the threshold voltage for polarization switching. The image contrast increases with the voltage. As a rule, an increase in the velocity of the tip also leads to this.

In Y-cut samples this stripe is first recorded at $U=200$ V and it is 1–2 μm wide right up to $U=3$ kV. Its appearance does not depend on the direction of motion of the tip relative to the Z axis. In Z-cut samples a similar effect in the form of a diffuse trail extending behind the tip can be distinguished in the absence of higher-contrast changes in the birefringence which are due to polarization switching.

The possibility of observing the short-time effect under study depends strongly on the physicochemical treatment of the surface of the crystal (etching, chemical-mechanical polishing). A short-time change in the birefringence was recorded in Y-cut samples only after they were etched for a long time in a mixture of nitric and hydrofluoric acids at temperature ≈ 100 °C (in the process the thickness of the samples decreased to $\approx 20\mu$m). In subsequent experiments etching took place at different temperatures from 60 to 100 °C. These investigations showed that the lifetime of the changes in the birefringence can change irreversibly in the range $0 < t < 20$ s. Decreasing the etching temperature, as a rule, increases t. The short-time change in the birefringence also becomes more noticeable with prolonged chemical-mechanical polishing of the Z-cut samples. In this case, however, t did not exceed 5 s.

We shall now discuss the short-time change in the birefringence. As indicated above, it is observed for both polari-

ties of the tip, irrespective of whether or not polarization switching occurs in the process. It is natural to attribute this effect to injection of free charge carriers into the dielectric. Then it should also be observed in other dielectric (nonferroelectric) materials with quite low conductivity and a strong electrooptic effect. Indeed, we recorded a short-time change in the birefringence along the trajectory of a needle-shaped electrode in $SrTiO_3$ crystals, which are well-known not to possess spontaneous polarization.

The following experiment serves as important proof of the role of injection in the observed phenomena. It turned out that the long-time changes produced in the birefringence in a *Z*-cut $LiNbO_3$ crystal by local polarization switching can be eliminated by using the same needle-shaped electrode. For this, it is sufficient to touch this electrode once again to the surface under study after first reversing the polarity of the electrode. Thus, for $U=2$ kV ''erasing of the image'' occurs inside a region with radius $\approx 30\mu$m near the electrode in a time ≈ 5 s. This effect is evidently due to the compensation of bound charges in domain walls by charges with the opposite sign injected from the electrode.

This experiment with ''erasure'' also confirms the correctness of the assumption that in our investigations the electrooptic effect is responsible for the main changes in the birefringence near domain walls.

As mentioned above, the dependence of the experimental results on the procedure used to treat the surface of the sample is evidently due to the influence of this treatment on the structure and chemical composition of the near-surface layer of the crystal and, specifically, on its conductivity.

In summary, the investigations performed demonstrate the possibility of producing a charge relief in a region near the surface of lithium niobate crystals by using a mobile needle-shaped electrode. Local implantation of charge into lithium niobate can be accomplished by injection of charge carriers as well as by the displacement of charged domain walls. In the first case only free charge carriers are introduced into the sample, while in the second case a structural rearrangement (polarization switching) of the crystal lattice also occurs in the sample.

It follows from the results obtained that due to the large electrooptic constants it is possible to visualize in lithium niobate not only ferroelectric domain formation but also injection of charge carriers into the dielectric.

The investigations performed demonstrate that charge writing of information with quite high density in a dielectric is possible in principle. The method developed for forming charge structures can be used to produce local inhomogeneities in dielectric crystals and films when studying the propagation of electromagnetic and acoustic waves in these media.

*)E-mail: sherman@asher,ioffe.rssi.ru

[1] M. P. Petrov, S. I. Stepanov, and A. V. Khomenko, *Photosensitive Electrooptic Media in Holography and Optical Processing* (Nauka, Leningrad, 1983).
[2] M. A. Lampert and P. Mark, *Current Injection in Solids* (Academic Press, N. Y. 1970) [Russian translation, Mir, Moscow, 1973]
[3] S. O. Fregatov and A. B. Sherman, Pis'ma Zh. Tekh. Fiz. **23**(11), 54 (1997) [Tech. Phys. Lett. **23**, 758 (1997)].
[4] S. O. Fregatov and A. B. Sherman, Pis'ma Zh. Tekh. Fiz. **24**(6), 52 (1998) [IEEE Photonics Technol. Lett. **24**, 229 (1998)].

Translated by M. E. Alferieff

Relaxation processes in the incommensurate phase of a crystal with defects

S. N. Kallaev and I. K. Kamilov

Institute of Physics, Dagestan Science Center of the Russian Academy of Sciences, 367003 Makhachkala, Russia

(Submitted June 30, 1998; resubmitted September 4, 1998)
Fiz. Tverd. Tela (St. Petersburg) **41**, 513–515 (March 1999)

The nature of the relaxation of the incommensurate superstructure of a ferroelectric to the equilibrium state is investigated experimentally. It is shown that near a phase transition the temperature dependence of the relaxation time of the incommensurate phase of the defective crystal is exponential. This law agrees qualitatively with the notion of domain wall motion in an inhomogeneous medium containing ''random local phase-transition temperature'' type defects. © *1999 American Institute of Physics.* [S1063-7834(99)02803-8]

In the last few years a great deal of attention has been devoted to investigating the critical dynamics of disordered systems which can exist in a nonequilibrium state for a long time. The incommensurate phase of a ferroelectric is a striking example of such a system. A characteristic feature of the incommensurate phase is the presence of very slow relaxation to the equilibrium state. This process is determined by the motion of quasidomain boundaries (solitons) in a random medium by overcoming barriers.[1,2] According to Ref. 3, near a ferroelectric phase transition T_c the relaxation time τ varies with the temperature of a crystal according to an exponential law

$$\tau \approx \gamma^{-1} \exp[(\text{const}/T_c)|T-T_c|^{-p}], \tag{1}$$

where γ is a kinetic coefficient and p is a parameter determined by the type of defects. Thus, for a three-dimensional incommensurate ferroelectric containing defects of the type ''random local field'' (RLF) this parameter is 3/2, while for defects of the type ''random local phase-transition temperature'' (RLT) $0.78 \leqslant p \leqslant 1.0$.[4] In Ref. 5 an attempt is made to check experimentally the dependence (1) with $p=3/2$ on the basis of dielectric measurements.

In the present work a situation close to that analyzed theoretically in Ref. 2 is realized experimentally to determine the character of the relaxation of the incommensurate phase to the equilibrium state. The relaxation phenomena in the incommensurate phase of a crystal near a ferroelectric phase transition was investigated on the basis of measurements of the permittivity ε, to which the oscillations of quasidomain walls make the main contribution.

The object of investigation is an Rb_2ZnCl_4 crystal, undergoing a phase transition at $T_c=195.2$ K to the ferroelectric phase $D_{2h} \Rightarrow C_{2v}$ $(Pmcn \Rightarrow Pn2_1a)$ with spontaneous polarization along the $\mathbf{b}(Y)$ axis. The phase existing at a temperature between $T_i=303$ K and T_c is incommensurate with the polarization component P_y modulated along the $\mathbf{c}(Z)$ axis. The crystal samples consisted of 4×4.5 mm plates oriented perpendicular to the $\mathbf{b}(Y)$ axis. The measurements of ε were performed with a capacitance bridge at 1 mHz and recorded with an X–Y plotter. The accuracy of the ε measurements is not less than 0.01% and the temperature stabilization is no worse than 0.005 K.

One of the main questions in experiments of this kind is the temperature of the structural phase transition to a polar state in a real crystal. This transition ordinarily always exhibits temperature hysteresis. Taking account of the fact that the equilibrium state of an incommensurate phase of the crystal corresponds to a state in which the physical properties do not depend on the direction of temperature change, i.e. there is no temperature hysteresis, the phase transition temperature T_c can be taken as $T_c=(T_c^c+T_c^h)/2$, where T_c^c and T_c^h are the temperatures of phase transitions on cooling and heating of the crystal sample. Then expression (1) can be rewritten as

$$\eta \approx \gamma^{-1} \exp[(\text{const}/T_c)|\Delta T|^{-p}], \tag{2}$$

where $\Delta T=|T-T_c^c|+|T-T_c^h|$ is the magnitude of the temperature hysteresis. Thus, Eq. (2) makes it possible to estimate experimentally the temperature dependence of the relaxation time of a soliton lattice.

The results of investigating of the temperature dependence of the permittivity on cooling and heating of an Rb_2ZnCl_4 crystal in a quasistatic regime are presented in Fig. 1 for three different measurement time intervals. The measurement procedure was as follows. The initial nonequilibrium state was produced by cooling to a fixed temperature near T_c after holding the crystal sample at a temperature above T_i for one hour and by heating after the crystal was first cooled below 150 K. In this manner, both low and high soliton density relative to the equilibrium state can be produced at any temperature point of the incommensurate phase. On the basis of the measurements of the time dependence of the permittivity for different temperatures $T=$ const (inset in Fig. 1) the temperature dependence $\varepsilon(T)$ was determined in the process of cooling (or heating) a sample of the Rb_2ZnCl_4 crystal. The complete cycle, which includes measurement of the dependence $\varepsilon(T)$ on heating and cooling, was investigated in the following eight time intervals: 600, 1200, 2400, 4800, 7200, 12000, 21000, and 42000 s. The value $T_c=(T_c^c+T_c^h)/2$ remained constant for all measurement regimes. The complete measurement cycle for determining temperature hysteresis in each individual case was conducted after the crystal sample was annealed at room temperature for at least 24 h. The temperatures T_c^c and T_c^h correspond to

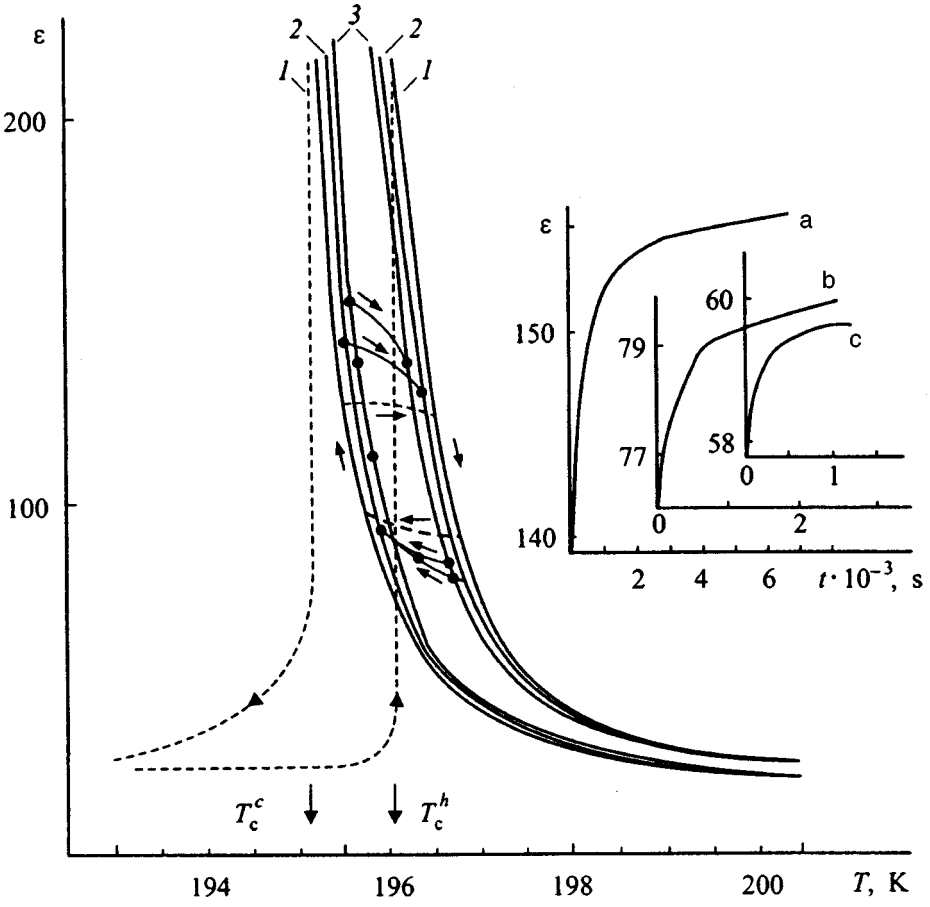

FIG. 1. Temperature dependence of the permittivity on cooling and heating of an Rb_2ZnCl_4 crystal in a quasistatic regime for the following three measurement time intervals: $t=600$ (*1*), 4800 (*2*), and 21000 s (*3*). Inset: Time-dependence of ε at three temperatures: $T-T_c^c=0.27$ (a), 0.74 (b), and 1.20 K (c).

the temperature maxima of ε on the cooling and heating curves. The results of establishing the law governing temperature variation of the relaxation time in the incommensurate superstructure (soliton system) are presented in Fig. 2, where the curves $\ln(\ln\tau)$ versus $\ln\Delta T$ are constructed from the data in Fig. 1. As one can see from Fig. 2, the temperature variation of τ follows the exponential law (2). The exponent p determined from the slope of the straight line with respect to the abscissa from Fig. 2 is 0.75 ± 0.05. According to Ref. 4, this value of the parameter corresponds, to within the error limits of the measurements, to the incommensurate phase of the ferroelectric containing RLT-type defects, which in contrast to RLF-type defects directly interact with domain walls. It should be noted that for RLT-type defects long-range translational order exists in the incommensurate phase of the crystal if the intersoliton distance exceeds a critical value.[3]

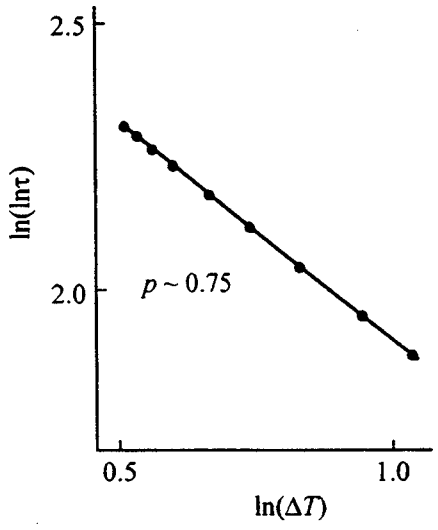

FIG. 2. Double logarithm of the relaxation time τ versus $\ln(\Delta T)$ for an Rb_2ZnCl_4 crystal.

In summary, the experimental results attest to the fact that the relaxation time of the soliton lattice of a crystal with defects to the equilibrium state varies exponentially with temperature. It was shown that this law of slow relaxation is characteristic for an incommensurate phase with RLT-type defects. This conclusion agrees with the theoretical investigations performed in Ref. 3 on the basis of the idea of the motion of a domain wall in a random medium by overcoming of barriers.

This work was supported by the Russian Fund for Fundamental Research (No. 97-02-16762).

[1] T. Nattermann and J. Villain, Phase Transit. **11**, 5 (1988).
[2] E. B. Kolomeisky, Ferroelectrics **105**, 131 (1990).
[3] E. B. Kolomeĭskiĭ, A. P. Levanyuk, and A. S. Sigov, Izv. Akad. Nauk SSSR, Ser. Fiz. **54**, 618 (1990).
[4] S. V. Maleev, Zh. Eksp. Teor. Fiz. **70**, 2375 (1976) [Sov. Phys. JETP **43**, 1240 (1976)].
[5] S. A. Gridnev, V. V. Gorbatenko, and B. N. Prasolov, Kristallografiya **39**, 106 (1994) [Crystallogr. Rep. **39**, 94 (1994)].

Translated by M. E. Alferieff

LATTICE DYNAMICS. PHASE TRANSITIONS

Anomalies in the elastic properties of silicious iron single crystals at pressures of up to 9 GPa and the $\alpha-\varepsilon$ phase transformation

F. F. Voronov and E. V. Chernysheva

L. F. Vereshchagin Institute of High-Pressure Physics, 142092 Troitsk, Moscow Region, Russia
(Submitted September 4, 1998)
Fiz. Tverd. Tela (St. Petersburg) **41**, 516–522 (March 1999)

A Fe+5.07 at. % Si single crystal has been studied by ultrasonic-pulse technique. Its density and elastic constants were determined for $p=0$ and $T=293$ K. The dependence of the elastic properties of silicious iron on Si concentration was constructed. The compression, the effective elastic constants, and the Grüneisen parameters were measured at hydrostatic pressures of up to 9 GPa. It was found that for $p=0$, $\partial c_{11}/\partial p=6.54$, $\partial c_{44}/\partial p=2.92$, $\partial c'/\partial p=1.02$, and $\partial K_s/\partial p=5.17$. The elastic constants c_{44} and c' increase linearly with pressure by 19.3 and 18.2% by $p=9$ GPa. The elastic anisotropy does not vary with pressure. For $p>4$ GPa, c_{11}, c_{12}, and K_S were observed to increase nonlinearly with decreasing pressure derivative. The Grüneisen parameter γ_{LA} decreases with pressure down to 0.70 at 9 GPa to become negative when extrapolated to the region of the $\alpha-\varepsilon$ phase transformation. The anomalies in c_{11} and the negative values of γ_{LA} for $p>11$ GPa indicate that the phase transformation in silicious iron at 13.5 GPa can take place by the crystallographic mechanism of the $\alpha-\varepsilon$ transformation in pure iron, i.e. by lattice compression in the [001] direction and shearing of the (110) planes along $[1\bar{1}0]$ or $[\bar{1}10]$. An assumption is put forward that pressure gives rise in silicious iron to $sp-d$ hybridization, which results in increased screening of the ion-ion interaction and in anomalies in elastic properties. Similar phenomena are expected to occur in pure bcc Fe as well. [S1063-7834(99)02903-2]

High-pressure studies of iron and of its alloys are of considerable interest for the physics of solid state and geophysics, which is due to a considerable extent to the fact that Fe and some of its alloys undergo under pressure a first-order phase transformation first discovered[1] at $p=13$ GPa in shock experiments. This transformation was studied comprehensively by optical techniques[2] and x-ray diffraction with synchrotron radiation[3] using diamond anvils. It was shown that bcc α Fe transfers to hcp ε Fe, and that the transformation has a martensitic nature and exhibits a large hysteresis and an extended region of coexistence of the α and ε phases. Under static pressure and room temperature, the $\alpha-\varepsilon$ transformation in pure α Fe was observed to begin at 10.3–11.3 GPa, and the reverse transformation, at 16.3–15.4 GPa.[3] Additions of small amounts of Si or Co increase slightly the transformation pressure. For instance, in shock experiments the transition in Fe containing 6 at. % Si was observed to occur at 13.5 GPa.[4]

A large number of publications deal with the properties of Fe and of its alloys at high pressures. We shall mention here only a few of them. The magnetic moment[5] and the energy of exchange splitting[6] between the majority and minority spin subbands in ferromagnetic bcc Fe were shown to decrease with pressure. The pressure coefficients for a number of Fermi-surface cross sections were determined using the de Haas-van Alfven effect.[7] A Mössbauer study showed the hcp ε Fe existing above 13 GPa to be nonmagnetic.[8] The theoretical band-structure and Fermi-surface calculations made for α Fe under pressure by the pseudopotential method within the Stoner model[6,9–12] and by the total-energy method[13] agree well with experiments. It was pointed out that Fe can be nonmagnetic and stable in a closely packed fcc structure for $p>14.5$ GPa.[10] Calculations[11] suggest the possibility for ferromagnetic bcc Fe to transfer to a paramagnetic hcp phase with the atomic radius reducing by 4% ($p=27$ GPa).

The elastic properties of pure α Fe were studied as functions of temperature[14,15] and pressure[16,17] up to 1 GPa. It was shown that the elastic constants increase linearly with pressure, their pressure derivatives were determined, and the equation of state derived. The elastic properties of Fe with small additions of Si were established only at atmospheric pressure as functions of composition and temperature.[18–21]

It appeared of interest to investigate the elastic properties of silicious iron over a broad pressure range in order to establish the variation of its elastic properties under compression and to look for anomalies in the low-frequency part of the phonon spectrum as one approaches the $\alpha-\varepsilon$ phase transformation. Determination of the pressure derivatives of the elastic characteristics of silicious iron at $p=0$ was of particular significance because this material is widely used in

TABLE I. Elastic properties of (Fe+5.07 at. % Si) single crystal. $T=293$ K, $p=0$, $\rho_0=7.7035+0.0043$ g/cm^3.

Ultrasonic wave velocity				Elastic constants	
Mode	Direction of propagation	Particle displacement	v_i, km/s	c_{ij}	c_{ij}, GPa
v_1	[110]	[1$\underline{1}$0]	6.234±0.050	c'_{11}	299.4±5.4
v_2	[110]	[0$\underline{0}$1]	3.931±0.024	c_{44}	119.0±1.6
v_3	[110]	[110]	2.033±0.006	c'	41.82±0.24
v_4	[100]	[100]	5.407±0.022	c'_{11}	225.2±2.0
v_5	[100]	[001]	3.940±0.017	c_{44}	119.6±1.1

Note. $c'=(c_{11}-c_{12})/2$, $c'_{11}=(c_{11}+c_{12}2c_{44})/2$.

studies of the dislocation structure of deformed bcc metals as a model compound.

We have studied the elastic properties of a single crystal of iron containing 5.07 at. % Si at pressures up to 9 GPa by the ultrasonic method. The samples, shaped as cylinders (diameter 14 mm, $h\cong 5-10$ mm) and truncated cones (average diameter 12 mm, $h\cong 2-4$ mm) with the axes parallel to the [110] and [100] directions, were cut from a single-crystal ingot of silicious iron grown by electron-beam melting at the IFTT RAS. The face ends of the samples were ground and lapped to be parallel within 1–2 μm at the 14-mm diameter. The orientation and degree of perfection of the samples were determined by x-ray diffraction. The end face planes coincided with the (110) and (100) planes to within 1–2°. The sample density ρ_0, measured at 293 K by hydrostatic weighing in distilled water, was found to be 7.7035–0.0043 g/cm^3. To determine the Si content in the samples, we constructed the dependence of the density ρ of disordered solid solutions of Si in Fe on composition using the x-ray data presented in Refs. 18 and 22 for 293 K:

$$\rho(\text{g/cm}^3)=7.8744-0.0337k,$$

where k is the Si content in at. %. By this relation, the Si content in our samples was 5.07 ∓ 0.12 at. %, or 2.62 ∓ 0.06 wt. %, which is in good agreement with spectroscopic measurements yielding 3.0 ∓ 0.5 wt. % Si.

We measured the propagation times of longitudinal and transverse elastic waves in the [110] and [100] directions in cylindrical samples at atmospheric pressure and at 293 K by the pulse-echo overlap technique[23] at 5 MHz. The propagation time was determined as the difference between the signal delay times in the ultrasonic channel consisting of two acoustic lines with and without the sample between them. The data obtained were averaged and used to derive the velocities of ultrasonic-wave propagation, after which, knowing ρ_0, one could find the elastic constants of silicious iron (Table I). As seen from the Table, the errors in determination of ultrasonic-wave velocities are 0.4–0.8%, and of the elastic constants, 0.9–1.5%. The difference between measurements made on differently oriented samples, $\delta=(c'_{11}+c'_{44})-(c_{11}+c_{44})$, was 1%.

The elastic constants c_{11}, c_{44}, c', and the adiabatic bulk modulus $K_S=(c_{11}+2c_{12})/3$ obtained by us are displayed in Fig. 1 together with the results of other studies[15–21] vs silicious iron composition in the region of disordered solid solutions with Si concentrations of up to 11 at. %.

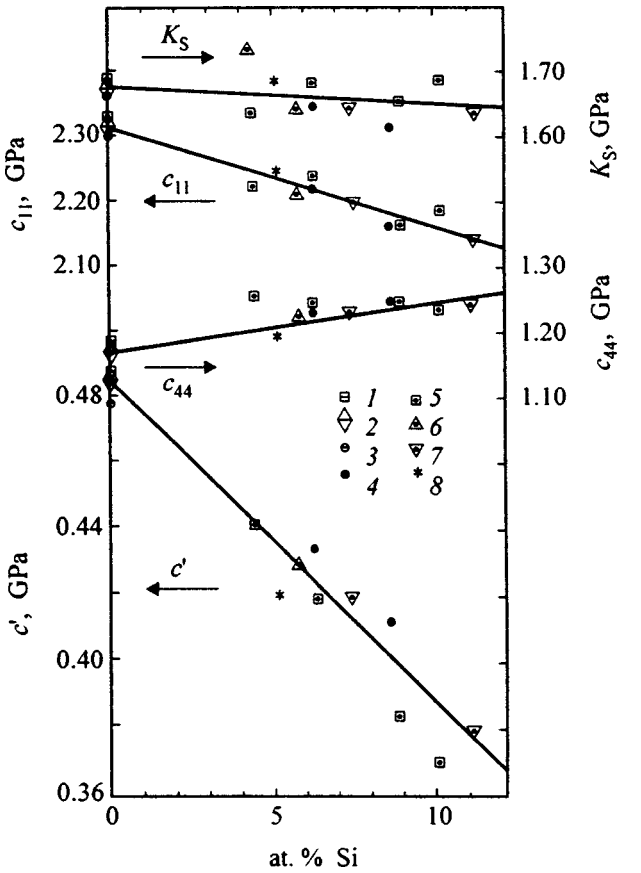

FIG. 1. Elastic constants of single-crystal silicious iron vs composition in the region of disordered solid solutions. *1* — Ref. 15, *2* — Ref. 16, *3* — Ref. 17, *4* — Ref. 18, *5* — Ref. 19, *6* — Ref. 21, *7* — data of F. X. Kayser and E. D. Gibson quoted in Ref. 21, *8* — our data.

A least-squares treatment of the data revealed that an addition of 10 at. % Si to Fe results in an increase of the elastic constants c' and c_{11} by 19.6 and 6.0%, an increase of c_{44} by 6.8%, and a weak decrease of the bulk modulus K_S (by 1.4%). The concentration dependence of the elastic constants of silicious iron is well described for $T=0$ in terms of the noncentral interaction model,[24] which does not consider, unfortunately, the nature for the interactions involved. We are not aware of any first-principles calculations of the elastic constants and electronic spectra for silicious iron.

The spontaneous magnetization of Fe decreases weakly and essentially nonlinearly with increasing Si content, namely, by 6.3% for 5 at. % Si and by 9% for 10 at. % Si.[22] This nonlinearity does not, however, manifest itself in the concentration dependence of the elastic constants of Fe $+k$Si (Fig. 1), and apparently the variation of spontaneous magnetization is not a dominant factor in this relation. The elastic properties of silicious iron were treated in terms of a simple semiempirical transition-metal model.[19] When melted with iron, silicon donates its $3s^23p^2$ outer electrons to the conduction band of Fe, which increases the contribution of electrostatic interaction to the elastic constants. These contributions to c_{44} and c' are estimated[19] as 23 and 7%, respectively. At the same time the contribution due to the ion-ion

TABLE II. Pressure derivatives of the elastic constants of single-crystal (Fe+5.07 at. % Si) and α–Fe for $p=0$ and $T=293$ K. $\partial c_{ij}/\partial p = c_{ij}/3K_T - (2c_{ij}/t)(\partial t/\partial p)$.

	Fe+5.07 at. % Si This work		α Fe	
			Ref. 16	Ref. 17
c_{ij}	$\partial t_i/\partial p$, μs/GPa	$\partial c_{ij}/\partial p$	$\partial c_{ij}/\partial p$	$\partial c_{ij}/\partial p$
c_{11}	–	(6.54)	(7.52)	(6.72)
c'_{11}	0.0208	8.43	9.01	(8.24)
c'	0.0478	1.02	1.16	1.07
c_{44}	0.0286	2.92	2.66	2.59
K_S	–	(5.17)	(5.97)	(5.29)

Note. The derivatives in parentheses were calculated from $\partial c_{ij}/\partial p$ combinations.

interaction, which includes effectively the magnetic interaction as well, decreases because of the increasing number of Fe–Fe neighbors and increasing screening by the conduction electrons. As a result, an increase in Si concentration gives rise to a weak growth of c_{44} and a decrease of c', c_{11}, and R_S.

This model offers also an explanation for the Si-induced variation of the pressure derivatives of the α–Fe elastic constants. Table II compares $\partial c_{ij}/\partial p$ for $p=0$ of silicious iron found by us with the corresponding values obtained[16,17] for pure α Fe. One readily sees that an increase of the electrostatic contribution to the elastic constants causes not only an increase of c_{44} but an increase of the stiffness of this constant, i.e. an increase of $\partial c_{44}/\partial p$. The weakening of ion-ion interaction induced by adding Si to Fe softens the elastic constants c', c_{11}, and K_S, i.e. decreases their pressure derivatives. This effect is apparently associated with the larger increase in screening of the ion-ion interaction under compression of silicious iron because of the larger number of the conduction electrons in the alloy compared to pure iron.

In order to determine $\partial c_{ij}/\partial p$ for silicious iron, measurements of $\partial t_i/\partial p$ were made on a hydrostatic-pressure setup[25] within the 0–0.8-GPa range, where these quantities could be measured with a good accuracy. The setup consisted of a booster and a thermostatted high-pressure vessel, into which [110]-oriented samples to be studied were placed. The pressure was measured with a manganin manometer calibrated against a reference piston manometer. The propagation times of the transverse and longitudinal ultrasound waves $t_i(p)$ in the silicious-iron samples at pressures of up to 0.8 GPa and within a broader range of up to 9 GPa were determined from pulse phase measurements[26] at frequencies of 7.5–10 MHz.

The studies at pressures of up to 9 GPa were carried out in a modified lentil-shaped, flat-bottom chamber[27] with a torus[28]. The larger base of the truncated-cone sample was brought in acoustic contact with the plunger that served as acoustic line. Benzene in an indium cup transmitted the pressure to the sample. The pressure was derived from a calibration graph based on the electrical resistance jumps of the reference metals Bi, Tl, and Ba, which were placed in each experiment between layers of silver chloride into a catlinite container (the lentil) in direct contact with the bottom of the indium cup. The chosen onset pressures for the phase transformations Bi I–II, Bi II–III, Tl II–III, Ba I–II, and Bi V–VI were[29] 2.57 (2.50), 2.75 (2.74), 3.94 (3.60), 5.68 (5.49), and 8.16 (7.50) GPa for measurements under increasing and decreasing pressure, respectively.

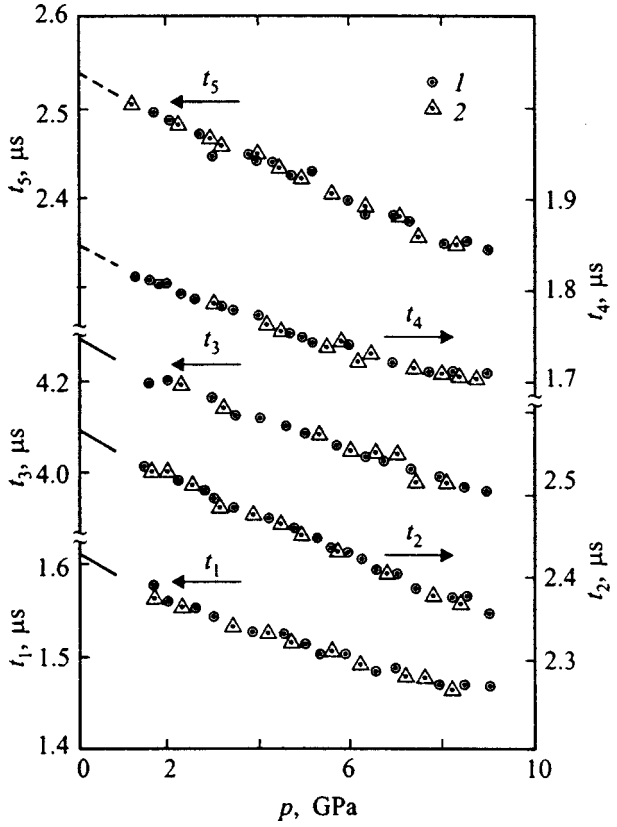

FIG. 2. Experimental pressure dependences of ultrasonic-wave propagation times in single-crystal silicious iron (Fe+5.07 at. % Si). Below 0.8 GPa: solid lines — [110] direction, dashed lines — along [100] (reduced data); up to 9 GPa: *1* — increasing pressure, *2* — decreasing pressure. Only part of the data obtained are displayed.

The absence of any disruptions in single-crystal samples which might have resulted from application of high pressure was checked by x-ray diffraction and verified by the coincidence of ultrasound propagation times measured under increasing and decreasing pressure (Fig. 2). Repeated measurements performed on the same sample produced practically identical results. Measurements made on different, but identically oriented samples exhibited a scatter of experimental points within 0.5%.

Measurements carried out on each of the five wave types yielded the initial time $t_i(0)$, the derivative $\partial t_i/\partial p$ for $p=0$, and the times $t_i(p)$ for pressures of up to 9 GPa. These data were fitted to monotonic curves (Fig. 2). Next the experimental data were reduced to unit length (1 cm for $p=0$), the optimum values of elastic-wave propagation times were chosen by Lagrange's method of undetermined multipliers with a step of 0.5 GPa, and the effective high-pressure elastic constants of single-crystal silicious iron were calculated. The variation of density with pressure, or the compression $x=\rho_0/\rho=v/v_0=l^3/l_0^3$ was calculated from the expression

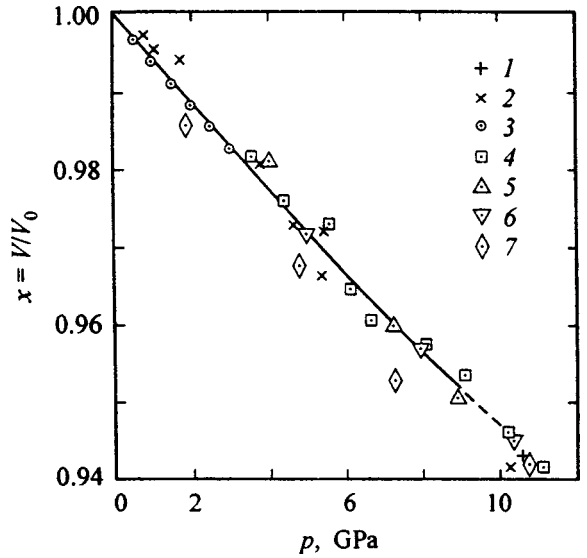

FIG. 3. Compression of silicious iron, Fe+5.07 at. % Si, our data (solid line). Compression of pure iron: shock wave experiment: *1* — Ref. 1, *2* — Ref. 30; linear compressibility method: *3* — Ref. 31; x-ray diffraction: *4* — Ref. 32, *5* — Ref. 33, *6* — Ref. 34, *7* — Ref. 35.

$$x^{-1/3} = 1 + \frac{1+\Delta}{3l_0^2\rho_0}\int_0^p \frac{dp}{1/t_1^2 - 1/3t_2^2 - 1/t_3^2},$$

which can be derived by integrating the well-known relation $K_T(p) = K_S(p)/(I+\Delta)$, where $\Delta = \alpha^2 T K_S/(\rho_0 C_p)$ is the adiabatic-isothermal correction, and l_0 is the path length of an ultrasonic wave in a sample at $p=0$, in our case $l_0 = 1$ cm. The adiabatic-isothermal correction was calculated using the values of the specific heat C_p and of the bulk thermal expansion coefficient a for pure Fe, which were pointed out[19] to differ little from those for silicious iron. The correction Δ was assumed to be pressure independent. These assumptions do not introduce significant errors, because the correction itself is small ($\sim 10^{-2}$) and varies only weakly with pressure. The calculated dependence of compression ($x = \rho_0/\rho$) on pressure for silicious iron was found to practically coincide with the experimental data obtained for pure iron (Fig. 3), which is a direct consequence of the weak concentration dependence of K_S (Fig. 1).

The effective elastic constants c_{11}, c_{12}, c_{44}, c', and K_S calculated for a (Fe+5.07 at . % Si) single crystal are listed in Table III. The decrease of the volume by 4.76%, or of the interatomic distances by 1.68% at 9 GPa brings about an increase of the effective elastic constants by 18–20%. The anisotropy in the elastic properties $A = 2c_{44}/(c_{11} - c_{12})$ remains constant within the error limits, namely, $A = 1.83$ at $p = 0$ vs 1.86 at 9 GPa.

The maximum pressure used in our experiments (9 GPa) is much less than the bulk modulus of silicious iron ($K_S = 168$ GPa), and therefore one could expect c_{ij} to vary linearly in this pressure range. As evident from Fig. 4, however, only $c_{44}(p)$ and $c'(p)$ can be fitted by linear functions. Above 4 GPa, c_{11}, c_{12}, and K_S exhibit a nonlinear variation with pressure accompanied by a decrease of their pressure derivatives. The deviations from linearity observed at 9 GPa

TABLE III. High-pressure elastic properties of (Fe+5.07 at. % Si) single crystal.

	M					
P, GPa	x	c_{11}, GPa	c_{12},GPA	c_{44}, GPa	c', GPa	K_S, GPa
0	1.0000	224.0	139.9	119.0	42.05	168.0
1.0	0.9941	230.1	144.1	121.9	43.01	172.8
2.0	0.9884	236.3	148.5	124.6	43.90	177.8
3.0	0.9828	242.2	152.7	127.1	44.75	182.5
4.0	0.9775	247.7	156.7	129.7	45.54	187.0
5.0	0.9722	253.0	160.3	132.2	46.34	191.2
6.0	0.9671	257.6	163.4	134.6	47.13	194.8
7.0	0.9621	261.7	165.8	137.1	47.96	197.7
8.0	0.9572	265.1	167.4	139.6	48.84	200.0
9.0	0.9524	267.8	168.4	142.0	49.20	201.5
$(M_{9.0}/M_0 - 1)$,%	−4.76	19.6	20.4	19.3	18.2	19.9

Note. M — measured characteristic, M_0 and $M_{9.0}$ are the values of M for $p = 0$ and 9.0 GPa, respectively.

for c_{11}, c_{12}, and K_S were found to be 20, 26, and 23%, respectively, of their change at 9 GPa.

A similar nonlinearity was observed not only for $c_{11}(p)$,

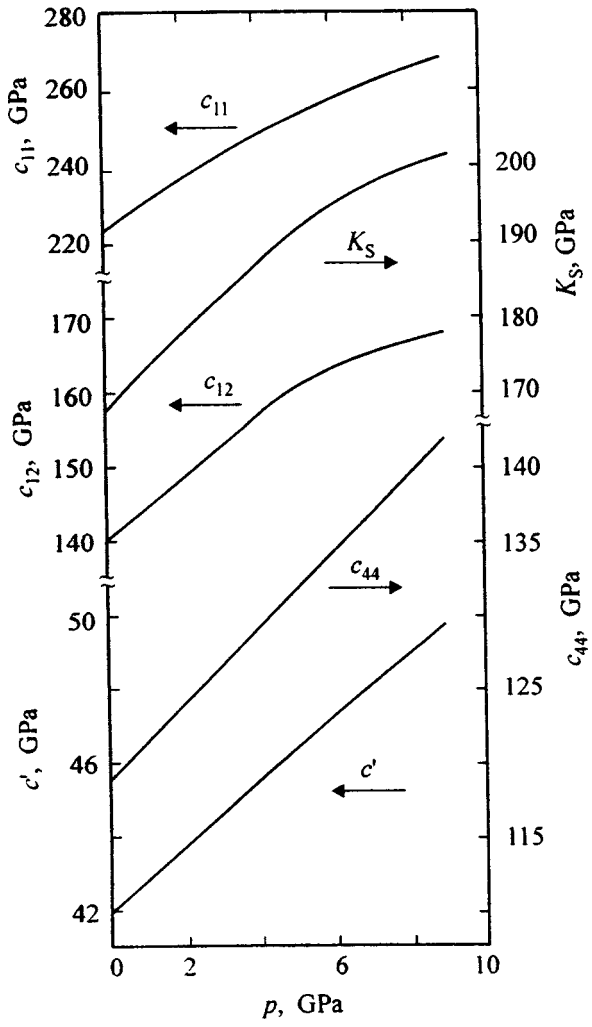

FIG. 4. Effective elastic constants of the (Fe+5.07 at. % Si) single crystal vs pressure plot.

the longitudinal elastic constant in the [100] direction, but for those along [110] and [111] as well:

$$c'_{11}(p)=(c_{11}+c_{12}+2c_{44})/2,$$

$$c''_{11}(p)=(c_{11}+2c_{12}+4c_{44})/3.$$

The deviations from linearity are smaller for c'_{11} and c''_{11} than those for $c_{11}(p)$, 17 and 16%, respectively. This is apparently because [100] is the easy-magnetization direction in silicious iron, which, due to the magnetoelastic effect, results in different elastic contributions to c_{11}, c'_{11}, and c''_{11}.

The anomalies in the $c_{11}(p)$, $c_{12}(p)$, and $K_S(p)$ observed by us, namely, the decreasing pressure derivatives, originate apparently from changes in the electronic structure of silicious iron induced by high pressures. These changes could be similar to those in the electronic structure of pure bcc Fe. At the same time the available experimental[5–8] and theoretical[6,9–13] studies of the electronic structure of Fe do not reveal possible reasons for the pressure-induced anomalies in the elastic constants of Fe. Compression of Fe causes electron transfer from the spin-up majority to the spin-down minority subband and a decrease of the exchange splitting and of the magnetic moment.[6] The decrease of the magnetic moment, however, is small, 3% at 10 GPa,[5,11] and thus cannot account for the decreasing pressure derivative K_S, because, by Ref. 10, the magnetic contribution to K_S is negative (~ -100 GPa), and its decrease should give rise to an increase of $\partial K_S/\partial p$. Calculations[13] made by the total-energy method showed that the magnetic moment of Fe vanishes at compressions of 0.87 ($p=220$ GPa), and bcc Fe transfers to nonmagnetic state. At the same time the density functional method and the Stoner model suggest that ferromagnetic bcc Fe can become paramagnetic hcp if the atomic radius decreases by only 4% at 27 GPa,[11,12] and by LMTO calculations within the Stoner model with one fitting parameter, bcc Fe can become fcc nonmagnetic at 14.5 GPa.[10] These calculations did not, however, reveal any features in the energy spectra of bcc Fe in the pre-transition regions, which could give rise to anomalies in the elastic properties.

A certain indication that compression can produce anomalous changes in the band energy of bcc Fe and, accordingly, in the band contribution to the elastic constants may be[36] the closeness to the Fermi level of the spin-up electron DOS peak[9,12] and the dip in the DOS for spin-down electrons[9]. At the same time the pressure-induced shift of these features with respect to the Fermi level has not been studied.

The decrease of the pressure derivatives of c_{11}, c_{12}, and K_S of silicious iron with pressure observed by us implies a decrease in the stiffness of the overlapping Fe ion cores, which suggests delocalization of *d* electrons, i.e. pressure-induced sp–d hybridization. This results in increased screening of the ion-ion interaction and in a decrease of c_{11}, c_{12}, and K_S and of their pressure derivatives. The assumption of *d*-electron delocalization and of increasing number of electrons in the conduction band is argued for by a noticeable decrease in electrical resistivity of bcc Fe under pressure, namely, by 20% at 10 GPa at a compression of only 5%.[37]

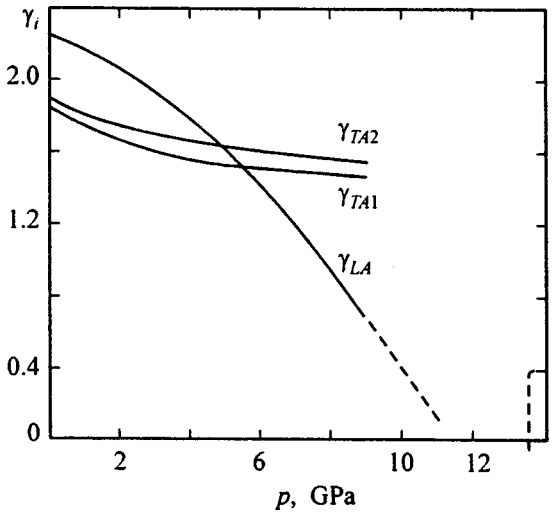

FIG. 5. Grüneisen parameters of the (Fe+5.07 at. % Si) single crystal vs pressure plot. The vertical dashed line identifies the pressure of the bcc-hcp α–ε phase transformation for Fe+6 at. % Si.[4]

An increase in sp–d hybridization changes the band contributions to the effective elastic constants and results in a deviation of $c_{11}(p)$, $c_{12}(p)$, and $K_S(p)$ from linearity. These contributions to c_{11} and c_{12} are apparently close in magnitude and vary in a similar manner under compression, because c' is a linear function of pressure (Fig. 4).

The energy differences among the structures of the $3d$, $4d$, and $5d$ transition metals calculated by the LMTO method and using the Andersen theorem showed that the hcp-bcc-hcp-fcc lattice sequence is determined at $p=0$ and $T=0$ by the *d*-band filling in these metals.[38] The compression-induced onset of sp–d hybridization in bcc Fe assumed by us results in a decrease of the number of *d* electrons and in an energetically preferable hcp structure. The possibility of a bcc-hcp transformation in Fe under pressure was demonstrated in Ref. 11. The bcc lattice of Fe should become unstable with increasing pressure, and soft modes should be expected to appear in the phonon spectrum of Fe as one approaches the bcc-hcp transformation at 13.5 GPa. A softening of the phonon spectrum in the long-wavelength domain is indicated by the onset of anomalies in the elastic properties and by an analysis of the pressure-induced changes in the Grüneisen parameters

$$\gamma_i=-\partial\ln\omega_i/\partial\ln v=(K_T/2c_{ij})(\partial c_{ij}/\partial p)-1/6.$$

The Grüneisen parameters determined by us for the long-wavelength shear modes γ_{TA1} and γ_{TA2}, which are associated with the c_{44} and c' elastic constants, decrease weakly with increasing pressure while remaining positive (Fig. 5), whereas the Grüneisen parameter for the long-wavelength longitudinal mode γ_{LA}, which is connected with c_{11}, decreases considerably under compression from 2.24 at $p=0$ to 0.70 at 9 GPa. Extrapolation to still higher pressures yields negative values of γ_{LA} for $p>11$ GPa.

Hence in the pre-transition region a soft longitudinal acoustic mode appears ($\gamma_{\mathrm{LA}}<0$), and the lattice of silicious iron loses stability with respect to longitudinal oscillations. This behavior is in accordance with the crystallographic

mechanism of the bcc-hcp lattice rearrangement of pure Fe in a pressure-induced $\alpha-\varepsilon$ phase transformation,[3] which, considered in the rigid-sphere approximation, consists in compression of the bcc lattice along [001] and slip of the [110] planes in the $[1\bar{1}0]$ or $[\bar{1}10]$ direction.

The appearance of the soft LA mode in the phonon spectrum of silicious iron at high pressures sets it apart from the other bcc metals studied. For instance, in Li and Cs (Refs. 39 and 40) and other metals the bcc-hcp transformation is preceded by the onset of a soft TA1 mode, and in Ba, of the TA1 and TA2 modes[41]. This feature of silicious iron imposes a substantial limit on its application as a model bcc metal in studies of dislocation structures, whose formation involves active participation of specific soft phonon modes.

One may thus conclude that the bcc-hcp phase transformation in silicious iron at 13.5 GPa is caused by a change in its band structure and proceeds by the mechanism proposed for the bcc-hcp transformation in pure iron.

A common crystallographic mechanism of the bcc-hcp transformation in pure and silicious iron suggests that compression of α Fe may also be accompanied by the onset of similar anomalies in the energy spectra and elastic constants.

The authors owe sincere gratitude to V. N. Semenov and V. G. Glebovskiĭ for providing silicious-iron single crystals, to V. K. Luĭkh for assistance in experiments, and to A. V. Gulyutin for the spectral analysis of the samples.

[1] D. Bancroft, E. L. Peterson, and S. Minshall, J. Appl. Phys. **27**, 291 (1956).
[2] P. M. Giles, M. H. Longenbach, and A. P. Marder, J. Appl. Phys. **42**, 4290 (1971).
[3] W. A. Bassett and E. Huang, Science **238**, 780 (1987).
[4] T. R. Loree, C. M. Fowler, E. G. Zukas, and F. S. Minshall, J. Appl. Phys. **37**, 1918 (1966).
[5] E. I. Kondorskiĭ and V. L. Sedov, Zh. Éksp. Teor. Fiz. **38**, 773 (1960) [Sov. Phys. JETP **11**, 561 (1960)].
[6] L. I. Vinokurova, A. G. Gapotchenko, E. S. Itskevich, É. T. Kulatov, and N. I. Kulikov, Zh. Éksp. Teor. Fiz. **76**, 1644 (1979) [Sov. Phys. JETP **49**, 834 (1979)].
[7] L. I. Vinokurova, A. G. Gapotchenko, and E. S. Itskevich, JETP Lett. **28**, 256 (1978).
[8] D. L. Williamson, S. Bukshpan, and R. Ingalls, Phys. Rev. B **6**, 4194 (1972).
[9] W. B. Johnson, J. R. Anderson, and D. A. Papaconstantopoulas, Phys. Rev. B **29**, 5337 (1984).
[10] G. L. Krasko and G. B. Olson, Phys. Rev. B **40**, 11536 (1989).
[11] J. Madsen, O. K. Andersen, U. K. Poulsen, and O. Jepsen, *Proc. Conf. Magn. Magn. Mater.* (AIP, New York, 1975), p. 327.
[12] O. K. Andersen, J. Madsen, U. K. Poulsen, O. Jepsen, and J. Kollar, Physica B & C **86-88B**, 249 (1977).
[13] V. L. Moruzzi, P. M. Marcus, and P. C. Pattnaik, Phys. Rev. B **37**, 8003 (1988).
[14] J. Leese and A. E. Lord, J. Appl. Phys. **39**, 3986 (1968).
[15] J. A. Rayne and B. S. Chandrasekhar, Phys. Rev. **122**, 1714 (1961).
[16] C. A. Rotter and C. S. Smith, J. Phys. Chem. Solids **27**, 267 (1966).
[17] M. W. Guinan and D. W. Beshers, J. Phys. Chem. Solids **29**, 541 (1968).
[18] A. Machová and S. Kadečková, Czech. J. Phys. B **27**, 555 (1977).
[19] H. L. Alberts and P. T. Wedepohl, Physica **53**, 571 (1971).
[20] A. Machová, Czech. J. Phys., Sect. B **27**, 904 (1977).
[21] I. L. Routbort, C. N. Reid, E. S. Fisher, and D. I. Dever, Acta Metall. **19**, 1307 (1971).
[22] S. Arajs, Phys. Status Solidi **33**, 683 (1969).
[23] E. P. Papadakis, Rev. Sci. Instrum. **47**, 806 (1976).
[24] A. Machová, V. Paidar, and F. Kroupa, Phys. Status Solidi A **42**, 713 (1977).
[25] F. F. Voronov and L. F. Vereshchagin, Prib. Tekh. Éksp. No. 6, 104 (1960).
[26] H. J. McSkimin, J. Acoust. Soc. Am. **72**, No. 4, 113 (1950).
[27] F. F. Voronov and S. B. Grigor'ev, Inventor's Certificate No. 324575 (27.10.1969).
[28] L. G. Khvostantsev, L. F. Vereshchagin, and A. P. Novikov, High Temp.-High Press. **9**, 637 (1977).
[29] F. F. Voronov, E. V. Chernysheva, and G. S. Vorotnikov, High Temp.-High Press. **5**, 621 (1973).
[30] D. S. Hughes, L. E. Gourley, and M. F. Gourley, J. Appl. Phys. **32**, 624 (1961).
[31] P. W. Bridgman, Proc. Am. Acad. Arts Sci. **74**, 11 (1940).
[32] E. Huang, W. A. Bassett, and P. Tao, J. Geophys. Res. B **92**, 8129 (1987).
[33] H. K. Mao, W. A. Bassett, and T. Takahashi, J. Appl. Phys. **38**, 272 (1967).
[34] A. P. Jephcoat, H. K. Mao, and P. M. Bell, J. Geophys. Res. B **91**, 4677 (1986).
[35] T. Takahashi and W. A. Bassett, Science **145**, 483 (1964).
[36] V. P. Antropov, V. G. Vaks, M. I. Katsnel'son, V. G. Koreshkov, A. I. Likhtenshteĭn, and A. V. Trefilov, Usp. Fiz. Nauk **154**, 525 (1988) [Sov. Phys. Usp. **31**, 278 (1988)].
[37] A. S. Balchan and H. G. Drickamer, Rev. Sci. Instrum. **32**, 308 (1961).
[38] H. L. Skriver, Phys. Rev. B **31**, 1909 (1985).
[39] F. F. Voronov, E. L. Gromnitskaya, and O. V. Stal'gorova, Fiz. Met. Metalloved. **64**, 1084 (1987).
[40] F. F. Voronov, O. V. Stal'gorova, and E. L. Gromnitskaya, Zh. Éksp. Teor. Fiz. **105**, 1456 (1994) [JETP **78**, 785 (1994)].
[41] F. F. Voronov and O. V. Stal'gorova, Fiz. Tverd. Tela (Leningrad) **20**, 452 (1978) [Sov. Phys. Solid State **20**, 261 (1978)].

Translated by G. Skrebtsov

Calorimetric investigations of phase transitions in the cryolites $(NH_4)_3Ga_{1-x}Sc_xF_6$ ($x=1.0, 0.1, 0$)

I. N. Flerov,[a] M. V. Gorev, and T. V. Ushakova

L. V. Kirenskiĭ Institute of Physics, Siberian Branch of the Russian Academy of Sciences, 660036 Krasnoyarsk, Russia

(Submitted July 14, 1998)
Fiz. Tverd. Tela (St. Petersburg) **41**, 523–528 (March 1998)

The specific heat of the cryolites $(NH_4)_3Ga_{1-x}Sc_xF_6$ with $x=1.0, 0.1$, and 0 was measured. The thermodynamic parameters of the phase transitions were determined. A previously unknown phase transition was found in the scandium compound at $T=243$ K. © *1999 American Institute of Physics.* [S1063-7834(99)03003-8]

$A_3M^{3+}X_6$ crystals having the cryolite structure (space group $Fm3m$, $z=4$) are one of the related families in a series of perovskite-like compounds having a three-dimensional crystal framework formed by AX_6 and $M^{3+}X_6$ octahedra joined to one another at the vertices. In this framework the interoctahedral polyhedra are occupied by a A^+ cation. Fluoride crystals with A^+ atomic cations, as a rule, undergo structural phase transitions (PTs) at quite high temperatures, which makes it somewhat difficult to study them in detail. In this respect, the ammonium compounds in which PTs have been discovered comparatively recently[1,2] are more attractive objects of investigation. In many cases, the presence of ammonium in the structure greatly decreases the temperature at which the cubic phase of the cryolites is stable.[1–6]

Quite extensive experimental data have now been accumulated on the ammonium cryolites $(NH_4)_3M^{3+}F_6$. Specifically, it has been found that in the series of compounds with trivalent ions M^{3+}=Al, Ga, Cr, V, Fe, Sc, and In the temperature at which the cubic phase becomes unstable increases with the unit cell parameter a_0.[6] The size of the ion M^{3+} likewise influences the sequence of PTs in the crystals. In compounds with the M^{3+} ionic radius $R_M^{3+} \leqslant R_{Fe}^{3+}$ one PT occurs and the symmetry of the distorted phase is assumed to be triclinic with space group $P\bar{1}$.[6,7] Further increase of the size of the M^{3+} ion leads to two successive structural transformations in compounds with scandium and indium. These transformations were discovered by calorimetric investigations.[6] At the same time, large differences in the x-ray diffraction patterns of the intermediate and low-temperature phases obtained from powder samples were not observed in structural investigations of these cryolites: neither according to the appearance of new lines nor according to a change in the intensities of the reflections.[6] The symmetry of the low-temperature phase at room temperature has been determined for both compounds, first as tetragonal $P4/mnc$, $z=2$[4] and then as monoclinic $P2_1/n$, $z=2$.[6,8]

The entropy changes ΔS associated with structural transformations have been determined from specific-heat measurements of all ammonium cryolites named above.[2,5,6,9] For componds with $R_M^{3+} \leqslant R_{Fe}^{3+}$, ΔS ranges from 19.4 to 24.9 $J\cdot mol^{-1}\cdot K^{-1}$ and is almost two times larger than the total entropy change $\Delta S \approx 12.8$ $J\cdot mol^{-1}\cdot K^{-1}$ due to two successive PTs in cryolites with the ions M^{3+}=Sc, In.[6] Thus it has turned out that ammonium cryolites $(NH_4)_3M^{3+}F_6$ can be divided into two groups differing both in the symmetry of the distorted phases and the thermodynamic parameters. It should be noted, however, that both groups of compounds were investigated by different calorimetric methods: the first group using an adiabatic calorimeter and the second group by the differential scanning calorimetry (DSC). The latter method makes it possible to determine reliably the integrated characteristics (enthalpy and entropy) only for sharp first-order PTs and can lead to a large error in investigations of transformations close to a tricritical point.[10]

A similar dependence of the crystallographic and thermodynamic characteristics on the size of the M^{3+} ion has been observed in the series of crystals $Rb_2KM^{3+}F_6$ having the related elpasolite structure ($Fm3m$, $z=4$).[11,12] Compounds with M^{3+} ions from Ga to Fe undergo one PT with $\Delta S \approx 15.6$ $J\cdot mol^{-1}\cdot K^{-1}$ to a phase whose symmetry has still not been determined unequivocally, but among others including the triclinic symmetry $P\bar{1}$. For crystals with the ions M^{3+}=Sc, In, Lu a sequence of PTs $Fm3m-I4/m-P2_1/n$ with a much smaller total entropy $\Delta S \approx 6$ $J\cdot mol^{-1}\cdot K^{-1}$ is characteristic. The part of the phase diagram for intermediate ionic radius $R_{Fe}^{3+} \leqslant R_M^{3+} \leqslant R_{Sc}^{3+}$ has been found to be quite complicated.[13] In the solid solutions $Rb_2KGa_{1-x}Sc_xF_6$ a sharp decrease of temperature and entropy of the PT has been observed with a low degree of substitution of scandium for gallium ($x=0.05-0.1$).

To determine more accurately the thermodynamic parameters of PTs in ammonium cryolites undergoing successive structural transformations and to determine the details (hysteresis of the PT temperature, latent heat of the transformation, the degree of closeness to the tricritical point) of the structural transformation $Fm3m-P\bar{1}$, which were not reported in Refs. 2, 5, 6, and 9, as well as the effect on them of a partial substitution of the M^{3+} ion, we investigated the compounds $(NH_4)_3Ga_{1-x}Sc_xF_6$ with $x=1.0$, 0.1, and 0 using an adiabatic calorimeter.

Samples in the form of powders were prepared by solid-

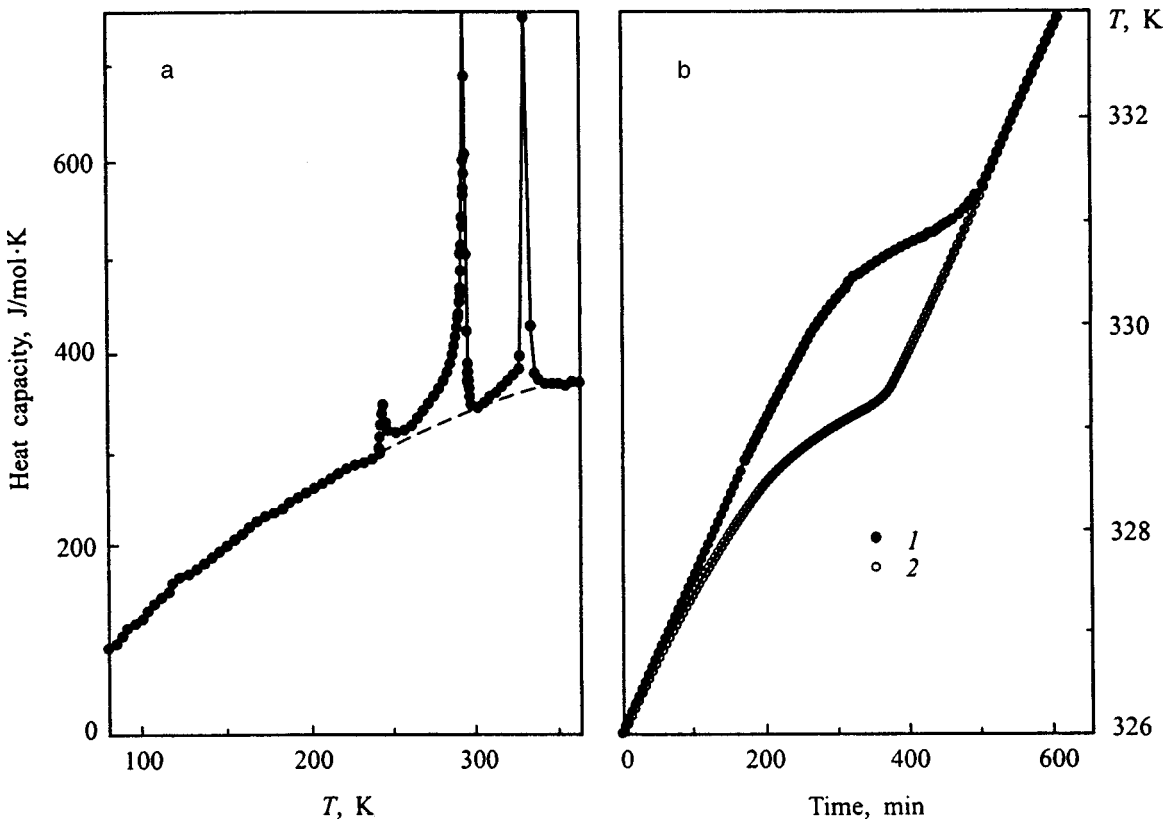

FIG. 1. Temperature dependence of the specific heat of $(NH_4)_3ScF_6$ (a) and thermograms (b) measured in heating (*1*) and cooling (*2*) regimes near the phase transition at T_1. Dashed line — lattice specific heat.

state synthesis at the Institute of the Chemistry of Condensed Materials (Bordeaux, France).

The methods of discrete and continuous heatings were used to measure the specific heat in the temperature interval from 80 to 370 K. Regions close to the PT temperatures were investigated by the method of quasistatic thermograms in the heating and cooling regimes with rates of temperature variation $|dT/dt| \approx (0.9-1.5) \times 10^{-2}$ K/min.

Figure 1a shows the results of measuring the specific heat $C_p(T)$ of cryolite $(NH_4)_3ScF_6$. Three anomalies of the specific heat were found. Two high-temperature peaks have maxima at temperatures 330 and 293 K, differing little from the PT temperatures reported in Ref. 7. The third specific-heat anomaly was recorded at 243 K. Repeated measurements showed that this PT is reproducible.

In all specific-heat measurements a large increase in the time required to establish thermal equilibrium in the sample was observed near the temperatures of all PTs: from 5–10 to 60–90 min. This is a characteristic indication of a first-order PT, as is confirmed by the results of thermographic investigations.

The more accurate value of the temperature of the phase transition from the cubic phase $T_1 = 330.8 \pm 0.2$ K is characterized by a comparatively large hysteresis $\delta T_1 = 1.8 \pm 0.2$ K (Fig. 1b). The latent heat of this transformation was $\delta H_1 = 3820 \pm 370$ J·mol^{-1}.

The enthalpies corresponding to the latent heat for the two other PTs were significantly smaller, and for greater clarity the results of the investigations near the transformation temperatures $T_2 = 293.4$ K and $T_3 = 243.1$ K are presented in Figs. 2a and b in the form of the temperature dependences of the specific heat which were calculated from thermograms measured in heating and cooling regimes. The corresponding values of the hysteresis and latent heat for these transitions are $\delta T_2 = 0.52 \pm 0.15$ K, $\delta H_2 = 160 \pm 20$ J·mol^{-1} and $\delta T_3 = 7.1 \pm 0.3$ K, $\delta H_3 = 170 \pm 25$ J·mol^{-1}.

To determine the total changes in the enthalpy and entropy which are associated with PTs, the lattice specific heat was separated out by interpolating the low- and high-temperature specific heats far from T_i into the anomalous region. The corresponding values of ΔH_i and ΔS_i were obtained by integrating the functions $\Delta C_p(T)$ and $(\Delta C_p/T) \times (T)$:

$$\Delta H_1 = 4420 \pm 310 \text{ J} \cdot \text{mol}^{-1},$$

$$\Delta S_1 = 13.36 \pm 0.95 \text{ J} \cdot \text{mol}^{-1} \cdot \text{K}^{-1},$$

$$\Delta H_2 = 1970 \pm 140 \text{ J} \cdot \text{mol}^{-1},$$

$$\Delta S_2 = 6.73 \pm 0.48 \text{ J} \cdot \text{mol}^{-1} \cdot \text{K}^{-1},$$

$$\Delta H_3 = 170 \pm 25 \text{ J} \cdot \text{mol}^{-1},$$

$$\Delta S_3 = 0.70 \pm 0.10 \text{ J} \cdot \text{mol}^{-1} \cdot \text{K}^{-1}.$$

The temperature dependences of the specific heats of the gallium compound and the solid solution $(NH_4)_3Ga_{0.9}Sc_{0.1}F_6$, which are presented in Figs. 3a and 3b,

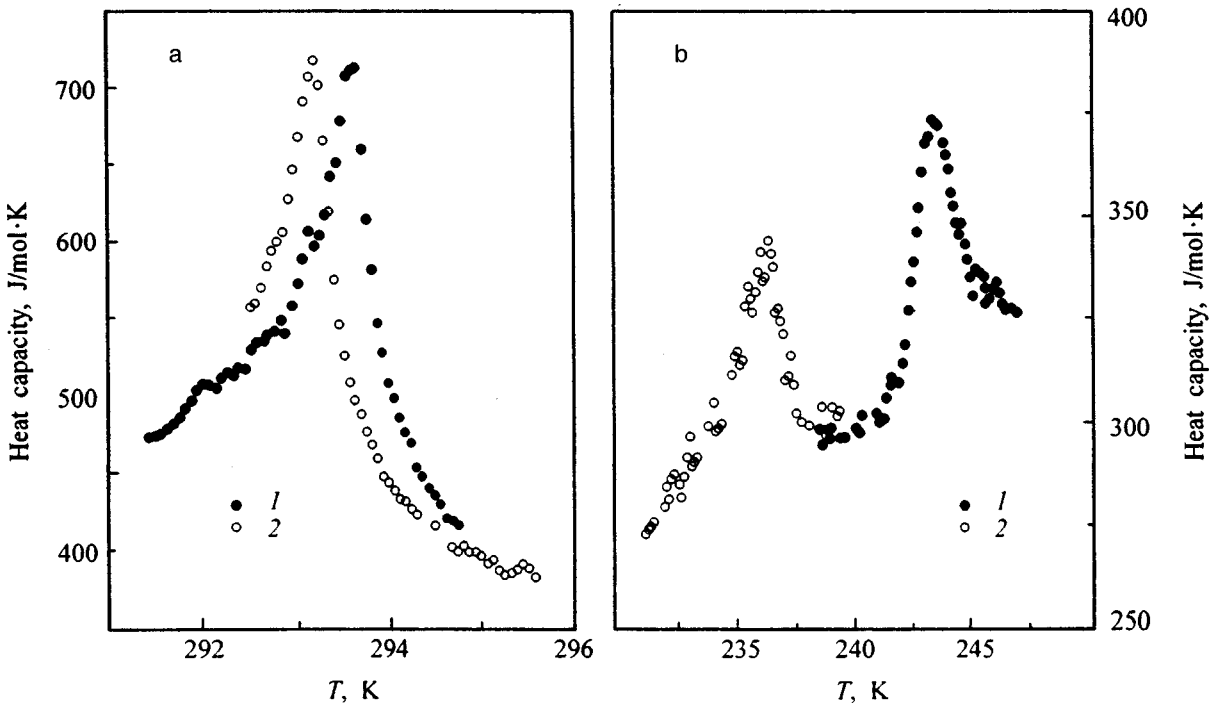

FIG. 2. Temperature dependences of the specific heat near phase transitions at T_2 (a) and T_3 (b) in the compounds $(NH_4)_3ScF_6$. *1* — Heating regime, *2* — cooling regime.

are essentially identical. The PT temperature in gallium cryolite $T_0 = 249.8 \pm 0.2$ K was found to be ~ 3.5 K higher than the temperature reported in Ref. 6. A 10% substitution of scandium for gallium did not change the temperature of the PT $Fm3m - P\bar{1}$ within the limits of its uncertainty (for the solid solution $T_0 = 249.7 \pm 0.2$ K), but it did result in a broadening of the temperature interval of the latent heat, as is clearly demonstrated in Figs. 4a and b. The hysteresis of the PT temperature and the latent heat were, respectively, $\delta T_0 = 0.84 \pm 0.20$ K and $\delta H_0 = 2690 \pm 190$ J·mol^{-1} for gal-

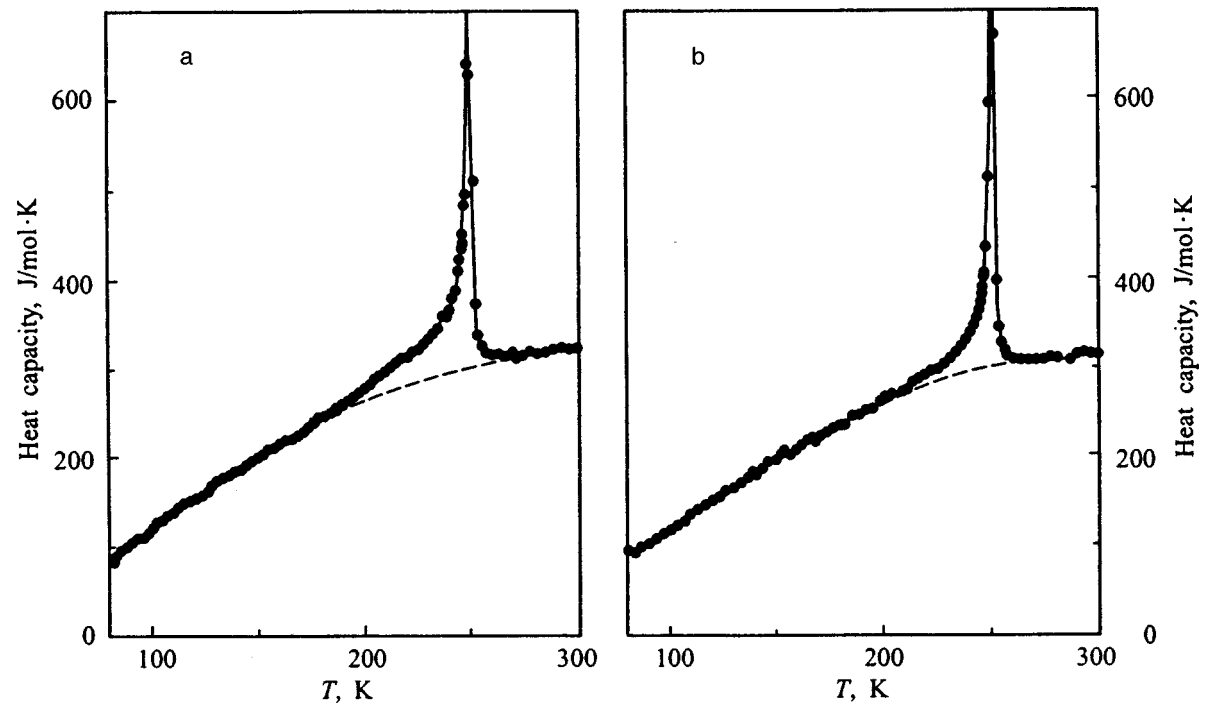

FIG. 3. Temperature dependences of the specific heat of the compounds $(NH_4)_3GaF_6$ (a) and $(NH_4)_3Ga_{0.9}Sc_{0.1}F_6$ (b). Dashed line — lattice specific heat.

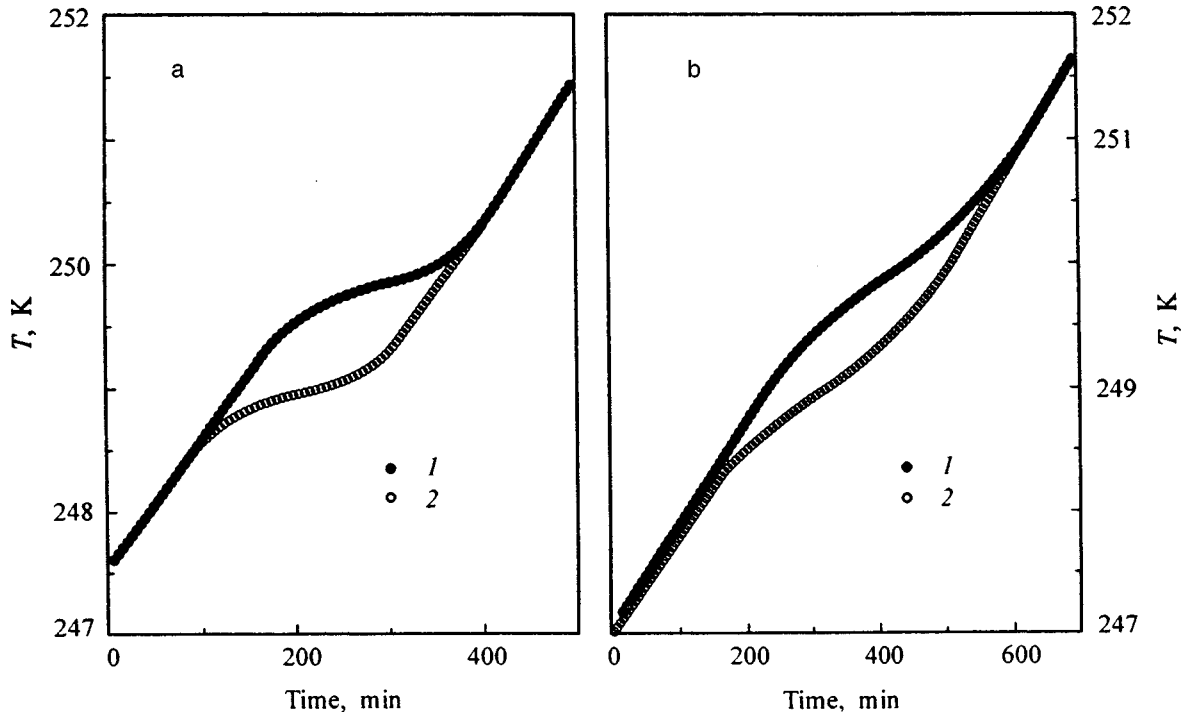

FIG. 4. Thermograms measured in heating (*1*) and cooling (*2*) regimes near phase transitions in $(NH_4)_3GaF_6$ (a) and $(NH_4)_3Ga_{0.9}Sc_{0.1}F_6$ (b).

lium cryolite and $\delta T_0 = 0.80 \pm 0.20$ K and $\delta H_0 = 2550 \pm 200$ $J \cdot mol^{-1}$ for the solid solution. The integrated characteristics of the two samples likewise differ little:

$(NH_4)_3GaF_6$: $\Delta H_0 = 5600 \pm 390\ J \cdot mol^{-1}$,

$\Delta S_0 = 23.0 \pm 1.6\ J \cdot mol^{-1} \cdot K^{-1}$,

$(NH_4)_3Ga_{0.9}Sc_{0.1}F_6$: $\Delta H_0 = 5040 \pm 350\ J \cdot mol^{-1}$,

$\Delta S_0 = 21.3 \pm 1.5\ J \cdot mol^{-1} \cdot K^{-1}$.

The absence of appreciable changes in the thermodynamic parameters of the PT in the solid solution with $x = 0.1$ as compared with the gallium compound indicates that it would be useful to continue studying the mixed compounds with composition close to scandium cryolite.

It can be concluded on the basis of the results of our work and of Ref. 6 that scandium ammonium cryolite undergoes three structural transformations with the following sequence of phases: $Fm3m - ? - P2_1/n - ?$. It should be noted that the observation of a specific-heat anomaly in the compound $(NH_4)_3InF_6$ at temperature ~ 230 K has been reported in a previous work.[14] Together with the data of Ref. 6, this suggests that there exists a third PT in this cryolite also.

The total change in entropy for the indicated sequence of PTs in $(NH_4)_3ScF_6$, $\Sigma \Delta S_i = 20.83 \pm 1.45\ J \cdot mol^{-1} \cdot K^{-1}$, is much larger than the value $\Sigma \Delta S_i = 12.8\ J \cdot mol^{-1} \cdot K^{-1}$ determined by DSC,[6] and it falls in the range of values $\Delta S_0 = 19.4 - 24.9\ J \cdot mol^{-1} \cdot K^{-1}$ which are characteristic for ammonium cryolites undergoing the PT $Fm3m - P\bar{1}$ (Fig. 5).

The closeness of the PT to the tricritical point can be estimated from the ratio $\delta S / \Delta S$ of the entropy jump at the transition point and the total entropy change. The PT from the cubic phase in the gallium compound is much closer to the tricritical point ($\delta S_0 / \Delta S_0 = 0.46$) than in the scandium compound ($\delta S_1 / \Delta S_1 = 0.86$). For the other two PTs, in the latter compound $\delta S_2 / \Delta S_2 = 0.08$ and $\delta S_3 / \Delta S_3 \approx 1$. Thus the PT at T_2 into the monoclinic phase $(NH_4)_3ScF_6$ is very close to the tricritical point, and this is why the total entropy change ΔS_2 determined in the present work using an adiabatic calorimeter is three times larger than the values found by DSC.[6]

Thus, the quantities characterizing the total entropy change in crystals which have undergone single and successive PTs are close. How do the PT mechanisms in ammonium cryolites of both types differ? The possibility of attributing the PT $Fm3m - P\bar{1}$ to ordering of ionic groups was considered in Refs. 2, 5, and 6. The ammonium group located at the center of the $(NH_4)F_6$ octahedra and in the interoctahedral polyhedra are structurally nonequivalent. Only tetrahedra of the first type participate in the PT, since the cubic symmetry of their location in the initial phase permits two possible orientations. Thus, as the symmetry is lowered, the contribution of ordering of the ammonium tetrahedra to the entropy of the PT is $\Delta S = R \ln 2$. However, to substantiate the large value found experimentally for ΔS, it must be conjectured that the $M^{3+}F_6$ octahedra are also disordered in the cubic phase. If the fluorine atoms occupy 192*l* or 96*k* positions, the contributions of their ordering (one position in the monoclinic phase) to the entropy of the PT are $R \ln 8$ and $R \ln 4$, respectively. The interval of possible entropy changes, determined in this manner, for the PT $Fm3m - P\bar{1}$ corresponds to the experimentally found values of ΔS for the compounds $(NH_4)_3M^{3+}F_6$ with the ions M^{3+} = Al, Ga, Cr, V, Fe. The correctness of the choice of model for describing this PT is confirmed by NMR investigations of compounds

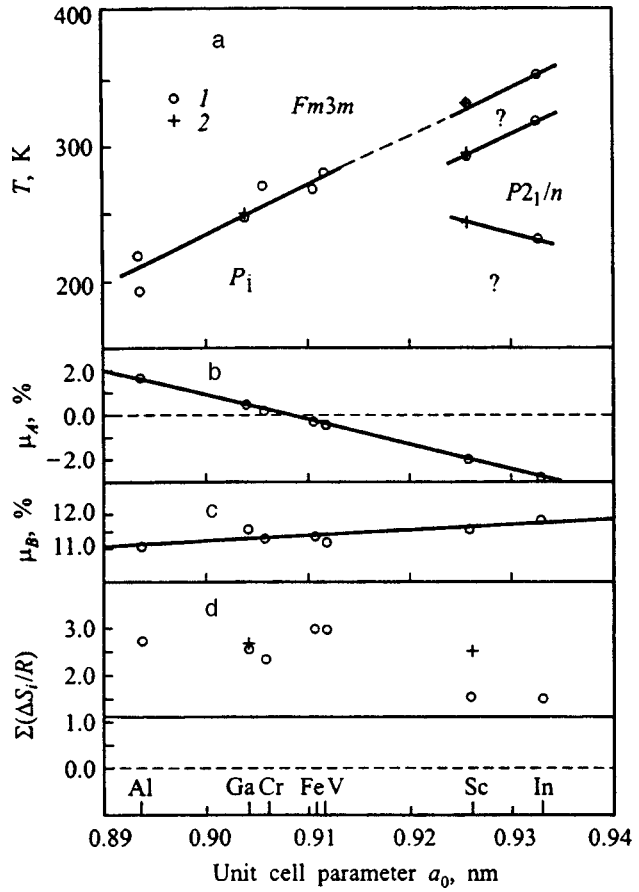

FIG. 5. Effect of the cubic lattice parameter a_0 of ammonium cryolites $(NH_4)_3M^{3+}F_6$ on the phase-transition temperatures (a), bond strains μ_A (b) and μ_B (c), and the total excess entropy (d). *1* — Data of Refs. 2, 5, 6, 9, and 14; *2* — data of the present work.

with gallium and aluminum.[5,15] Substantial jumps in the quantities characterizing the spin-lattice relaxation time of hydrogen and fluorine nuclei have been found at temperatures corresponding to the PT temperatures. This attests to a change in the nature of the motion of both the NH_4 tetrahedral and $M^{3+}F_6$ octahedral ionic groups.

In $(NH_4)_3InF_6$ undergoing successive structural transformations the behavior of the relaxation times of fluorine and oxygen is the same only in the intermediate phase: In both cases this quantity increases rapidly on heating from T_2 to T_1.[15] At the point of the transition to the cubic phase, the spin-lattice relaxation time of fluorine undergoes a substantial jump-like increase, just as in crystals with one PT. For protons, however, this quantity, after reaching a maximum at T_1, decreases with further heating. Therefore it can be inferred that in ammonium cryolites, which have undergone successive structural transformations $Fm3m-?-P2_1/n-?$, at least the PT from the cubic phase is related with ordering of the octahedral ionic groups $M^{3+}F_6$. The experimentally determined value $\Delta S_1=1.61R$ for the scandium compound also attests to an order–disorder PT, though it is less than ΔS_0 for the transformation $Fm3m-P\bar{1}$. The PT into the monoclinic phase at T_2 is characterized by an entropy change close to $R\ln 2$. It is tempting to infer that it is related with the ordering of the tetrahedra. However, such conclusion, which is based on the temperature dependence of the proton relaxation time, is premature.

According to Ref. 5, the presence of ammonium in the position (1/4, 1/4, 1/4) energetically stabilizes the cubic structure of cryolite. On the other hand, the question of the stability of the cubic phase can be studied from the standpoint of the hypothesis of the strains of the interatomic bonds.[16] It has been shown in previous work that this hypothesis makes it possible to describe satisfactorily displacement-type PTs associated with small rotations of the octahedral ionic groups,[17,18] and it is not applicable in the case when distortions in the perovskite-like structures cannot be interpreted in terms of the rotations of octahedra.[19] Ordering of octahedral ionic groups accompanying an order–disorder type PT can also be regarded as a rotation of octahedra, but by a larger angle. In this case there is nothing to prevent the applicability of the above-mentioned hypothesis to the PT under study. The stability of the initial cubic phase is determined by the ratio of the sizes of individual ions and the lattice parameter a_0, i.e. the strains of the bonds of the ions in the chains $(NH_4)^+-F^-$ and $M^{3+}-F^--(NH_4)^+-F^--M^{3+}$. The following quantities can serve as a quantitative measure of these strengths:

$$\mu_A=(a_p'-a_0)/a_p', \quad \mu_B=(a_p-a_0)/a_p,$$

where $a_p=2(R_{NH_4}+2R_F+R_{M_{3+}})$ and $a_p'=2\sqrt{2}(R_{NH_4}+R_F)$. An increase of μ_B is equivalent to an increase in the repulsion energy in the crystal potential and intensifies the anisotropy of the motion of F ions and therefore decreases the stability of the initial phase. An increase in μ_A prevents rotation of the octahedra and tends to stabilize the undistorted lattice.

In ammonium cryolites an increase in the size of the unit cell is accompanied by a substantial decrease in μ_A and an increase in μ_B, which increases the PT temperature (Fig. 5). Therefore the bond strain hypothesis is also applicable to order–disorder type PTs. On the other hand, the present results show that in ammonium cryolites undergoing successive transformations the PT from the cubic phase is associated mainly with the ordering of octahedral ionic groups.

To further clarify the characteristic features of the PT mechanisms in ammonium cryolites, it is certainly of interest to investigate the effect of hydrostatic pressure. This will be done in the near future.

We are deeply grateful to Professor A. Tresso and Professor J. Grannec (Institute of the Chemistry of Condensed Materials, Bordeaux, France) for providing the experimental samples.

This work was supported by the Krasnoyarsk Kraĭ Science Fund (grant No. 7F0021) and the Russian Fund for Fundamental Research (grant No. 96-02-16542).

[a]E-mail: flerov@iph.krasnoyarsk.su

[1] S. Mørup and N. Thrane, Solid State Commun. **11**, 1319 (1972).
[2] K. Moriya, T. Matsuo, H. Suga, and S. Seki, Bull. Chem. Soc. Jpn. **50**, 1920 (1977).
[3] E. G. Steward and H. P. Rocksby, Acta Crystallogr. **6**, 49 (1953).
[4] H. Bode and E. Voss, Z. Anorg. Allgem. Chem. **290**, 1 (1957).

[5] K. Moriya, T. Matsuo, H. Suga, and S. Seki, Bull. Chem. Soc. Jpn. **52**, 3152 (1979).
[6] A. Tressaud, S. Khairoun, L. Rabardel, T. Kobayashi, T. Matsuo, and H. Suga, Phys. Status Solidi A **98**, 407 (1986).
[7] M. Epple, Thesis, University of Tubingen (1978).
[8] S. Schwarzmann, Fortschritt Mineral **42**, 231 (1965).
[9] K. Kobayashi, T. Matsuo, H. Suga, S. Khairoun, and A. Tressaud, Solid State Commun. **53**, 719 (1985).
[10] M. V. Gorev, I. N. Flerov, V. N. Voronov, A. Tresso, J. Grannec, and J.-P. Chaminade, Fiz. Tverd. Tela (St. Petersburg) **36**(4), 1121 (1994) [Phys. Solid State **36**, 609 (1994)].
[11] I. N. Flerov, A. Tressaud, K. S. Aleksandrov, M. Couzi, M. V. Gorev, J. Grannec, S. V. Melnikova, J. P. Chaminade, S. V. Misyul, and V. N. Voronov, Ferroelectrics **124**, 309 (1991).
[12] I. N. Flerov, M. V. Gorev, and V. N. Voronov, Fiz. Tverd. Tela (St. Petersburg) **38**(3), 717 (1996) [Phys. Solid State **38**, 396 (1996)].
[13] M. V. Gorev, I. N. Flerov, A. Tressaud, J. Grannec, H. Faget, R. Sonntag, and J. Linhart, Ferroelectrics **22**, 127 (1997).
[14] R. A. Vecher, L. M. Volodkovich, G. S. Petrov, and A. A. Vecher, Thermochim. Acta **87**, 377 (1985).
[15] A. Sasaki, Y. Furukawa, and D. Nakamura, Ber. Bunsenges. Phys. Chem. **93**, 1142 (1989).
[16] K. S. Aleksandrov, A. T. Anistratov, B. V. Beznosikov, and N. V. Fedoseeva, *Phase Transitions in Crystals of the Halide Componds* ABX_3 (Nauka, Novosibirsk, 1981).
[17] I. N. Flerov, M. V. Gover, and K. S. Aleksandrov, Fiz. Tverd. Tela (St. Petersburg) **35**(6), 1657 (1993) [Phys. Solid State **35**, 834 (1993)].
[18] I. Flerov, M. Gorev, W. Bührer, P. Böni, A. Tressaud, and J. Grannec, Physica B **234–236**, 144 (1997).
[19] I. N. Flerov, M. V. Gorev, V. N. Voronov, and A. F. Bovina, Fiz. Tverd. Tela (St. Petersburg) **38**(7), 2203 (1996) [Phys. Solid State **38**, 1213 (1996)].

Translated by M. E. Alferieff

Order-disorder phase transformations and specific heat of nonstoichiometric vanadium carbide

V. N. Lipatnikov and A. I. Gusev

Institute of Solid-State Chemistry, Ural Branch of the Russian Academy of Sciences, 620219 Ekaterinburg, Russia

P. Ettmeier and W. Lengauer

Institut für Chemische Technologie Anorganischer Stoffe, Technische Universität Wien, A-1060 Wien, Österreich

(Submitted May 19, 1998; resubmitted September 30, 1998)
Fiz. Tverd. Tela (St. Petersburg) **41**, 529–536 (March 1999)

A study has been made of the order-disorder phase transformations in the homogeneity region of the VC_y nonstoichiometric cubic vanadium carbide ($0.66<y<0.88$). It has been established that an ordered V_6C_5 phase with monoclinic (space group $C2/m$) or trigonal ($P3_1$) symmetry, and a cubic (space group $P4_332$) ordered V_8C_7 phase can form in the VC_y carbide below 1450 K, depending on the actual composition. The effect of off-stoichiometry and structural vacancy ordering on the specific heat of the VC_y carbide has been investigated. The temperatures and heats of the reversible order-disorder equilibrium transitions have been determined. The ordering in the VC_y carbide is shown to be a first-order phase transition. An equilibrium diagram of the V-C system taking into account ordering in the nonstoichiometric vanadium carbide has been constructed. © *1999 American Institute of Physics.* [S1063-7834(99)03103-2]

The disordered cubic vanadium carbide has a $B1$ (NaCl) structure and a homogeneity region $VC_{0.65}-VC_{0.88}$. Within the $VC_{0.86}-VC_{0.88}$ interval, one observes in the VC_y carbide a V_8C_7-type cubic disordered phase.[1–3] This superstructure has a doubled lattice period compared to that of the disordered carbide. The unit cell of the ordered cubic phase V_8C_7 belongs to space group $P4_332$ (or $P4_132$). The other ordered phase, V_6C_5, can have trigonal (space group $P3_1$, Ref. 4) or monoclinic [$C2$ (Ref. 5) or $C2/m$ (Ref. 6)] symmetry, and was observed in the vanadium carbide VC_y within the interval $0.76\leqslant y\leqslant 0.86$.

Thermodynamic characteristics of nonstoichiometric vanadium carbide above 300 K were a subject of several studies.[7–10] All of them, however, were done without taking into account possible formation in VC_y of some ordered structures, and the measurements were carried out with too large steps in temperature. Besides, poor chemical characterization and, most essentially, the absence of reliable structural characterization of samples in the above studies do not inspire confidence in the results obtained.

The scatter in experimental data on specific heat and enthalpy of nonstoichiometric vanadium carbides is fairly large, and there is no calorimetric study with even a single mention of the structural state of the carbides investigated. At the same time studies of the carbides of niobium, tantalum, and titanium showed that a disordered and an ordered carbide of the same composition may differ in specific heat by 2–5% (see, e.g., Refs. 11–14).

It should be pointed out that the question of whether the order-disorder phase transitions in the vanadium carbide are first or second order remains a point of controversy. There is still no direct experimental evidence for either of these viewpoints.

Thus the literature on the vanadium carbide VC_y contains, on the one hand, fairly good structural studies of ordering, and on the other, thermodynamic studies performed without taking into account possible order-disorder transformations and using such a large step in temperature that such phase transitions just could not have been detected.

This has stimulated the present work with the same samples used for structural studies of ordering in vanadium carbide and for calorimetric measurements within the 300–1600 K range, where phase transformations associated with ordering of the nonstoichiometric vanadium carbide VC_y having the basic $B1$ structure (NaCl) take place.

1. SAMPLES AND EXPERIMENTAL TECHNIQUES

The samples of nonstoichiometric vanadium carbide VC_y with different carbon contents ($y=0.66$, 0.79, 0.83, and 0.87) were prepared by hot pressing. All the samples had a porosity less than 3%, were homogeneous, and contained only one phase, VC_y, with a $B1$-type structure.

To obtain VC_y carbides in ordered state, the samples were annealed with the temperature decreased from 1200 to 300 K. The disordered carbide $VC_{0.87}$ was prepared by water quenching the sample sealed in a quartz ampoule and annealed preliminarily at 1450 K.

The x-ray diffraction analysis was carried out with Cu $K\alpha$ radiation. The measurements were done in the scanning mode with a step of $\Delta 2\theta=0.02°$ within the angular range $2\theta=14-120°$. The exposure time at each point was 10 s.

The metallographical studies were done in reflection on

TABLE I. Chemical composition and lattice periods of annealed ordered (a_{ord}) and quenched disordered (a_{disord}) vanadium carbides.

	Chemical composition							Period a, nm	
	wt.%			at.%					
Carbide VC_y	C	N	O	V	C	N	O	a_{ord}	a_{disord}
$VC_{0.87}$	16.94	0.09	0.31	53.1	46.1	0.21	0.64	0.41660	0.41638
$VC_{0.83}$	16.33	0.07	0.13	54.4	45.2	0.16	0.27	0.41651	0.41596
$VC_{0.79}$	15.70	0.04	0.24	55.5	43.9	0.11	0.50	0.41607	0.41548
$VC_{0.66}$	13.38	0.04	not determined	60.2	39.7	0.12	not determined	0.41305	0.41305

polished samples of sintered and annealed carbides, with the surface of the sections etched in a water solution of 10% KOH + 10% K_3 [$Fe(CN)_6$].

The samples were analyzed chemically for the presence of carbon and nitrogen on a Carlo Erba CHN 1108 gas chromatograph. No free carbon was detected in the samples. The content of oxygen in VC_y samples was checked by hot vacuum extraction on a EAO-201 exalograph (Balzers). The chemical composition and lattice period of the vanadium carbide samples are listed in Table I.

The thermodynamic properties of the carbides were studied on a Netzsch DSC 404 (Germany) differential scanning calorimeter within a temperature range of 300 to 1600 K in an extra high-purity argon ambient. The measurements were carried out with heating and cooling rates of 20 K/min in 5-K steps. For precise determination of the heats of transitions in the vanadium carbide, calibration was performed preliminarily in the same conditions. High-purity aluminum and gold were employed for calibration. Sapphire was used as a reference in the calorimetric experiments.

2. EXPERIMENTAL RESULTS AND THEIR DISCUSSION

After annealing of the samples of nonstoichiometric vanadium carbide by the technique described in the preceding Section, the diffraction patterns of the $VC_{0.79}$, $VC_{0.83}$, and $VC_{0.87}$ samples were found to contain, besides the strong structure reflections, additional peaks with an intensity not over 5% of that of the structure lines. The appearance of additional low-intensity reflections evidences formation of ordered phases in thermally treated samples. No extra reflections were observed in the diffractogram of the $VC_{0.66}$ sample after annealing.

A. Crystal structure

Figure 1 shows parts of diffraction patterns obtained on annealed $VC_{0.79}$, $VC_{0.83}$, and $VC_{0.87}$ samples. The strong lines observed in the angular interval $2\theta = 37.4°$ and 43.4° are the $(111)_{B1}$ and $(200)_{B1}$ structure reflections. The diffractograms of annealed carbides contain in the intervals $2\theta \approx 21.2-22.0°$ and $\sim 30.0-31.0°$ diffuse maxima which are not seen in those of the disordered carbides. These maxima are parasitic reflections of the $\lambda/2$ radiation and correspond to the $(200)_{B1}$ and $(220)_{B1}$ structure reflections. They appear because of the long exposure of the corresponding diffractograms. Besides, all diffractograms exhibit within the $2\theta \approx 44.5-45.0°$ interval an impurity line left unidentified.

The first superstructure reflection with the diffraction vector $|\mathbf{q}| = (2a_{B1}\sin\theta)/\lambda \approx 0.710$ in the diffraction pattern of the annealed $VC_{0.87}$ carbide was observed at an angle $2\theta = 15.14°$ (Fig. 1). This reflection corresponds to a superstructure vector {1/2,1/2,0} of length $|\mathbf{q}| \approx 0.707$, which belongs to the $\{\mathbf{k}_4\}$ star with a running index $\mu_4 = 1/4$ (here and subsequently, the notation of the $\{\mathbf{k}_s\}$ stars of the wave vectors in the first Brillouin zone of an fcc crystal, as well as of their arms $\mathbf{k}_s^{(j)}$, is given in accordance with Ref. 11). The next reflection with $|\mathbf{q}| \approx 0.871$ is observed at $2\theta = 18.55°$ and corresponds to the {1/2,1/2,1/2} vector of the $\{\mathbf{k}_9\}$ star. The third reflection (at $2\theta = 24.04°$) is the strongest of all the superstructure peaks. This peak corresponds to the {1,1/2,0} vector of the $\{\mathbf{k}_8\}$ star. The next three superstructure reflections present in the diffractogram of the annealed $VC_{0.87}$ sample (Fig. 1) and observed at the angles $2\theta = 26.34°$, 39.14°, and 46.34° correspond to the {1,1/2,1/2} vector of the $\{\mathbf{k}_4\}$ star, {3/2,1,0} vector of the $\{\mathbf{k}_8\}$ star, and {3/2,3/2,0} vector of the $\{\mathbf{k}_4\}$ star. Altogether, the diffraction spectrum of the annealed $VC_{0.87}$ carbide sample exhibits within the $2\theta = 14-110°$ interval 19 superstructure reflections corresponding to three stars: $\{\mathbf{k}_9\}$, $\{\mathbf{k}_8\}$, and $\{\mathbf{k}_4\}$.

An analysis of the positions and intensity of the superstructure reflections attests to the formation in the course of the thermal treatment of the $VC_{0.87}$ carbide of the ordered cubic phase V_8C_7 (space group $P4_332$). The unit cell of the V_8C_7 phase has a doubled period compared to that of the fundamental structure of the disordered phase. All arms of the Lifshits stars $\{\mathbf{k}_9\}$ and $\{\mathbf{k}_8\}$ and of the non-Lifshits star $\{\mathbf{k}_4\}$ (for $\mu_4 = 1/4$) enter the channel of the order-disorder phase transition $VC_{0.87} \rightarrow V_8C_7$. As follows from symmetry considerations, the ordered V_8C_7 phase can form only in a first-order transition. This is in accord with theoretical conclusions[15].

A metallographic analysis of the annealed carbide $VC_{0.87}$ confirmed the presence in it of an ordered phase of cubic symmetry. On the etched sections one sees domains of an ordered phase which have isometric shape. When viewed in reflected polarized white light, the ordered domains do not produce interference, which argues that the V_8C_7 ordered phase is isotropic. A study of the microstructure showed that the order-disorder transformation in the $VC_{0.87}$ carbide starts

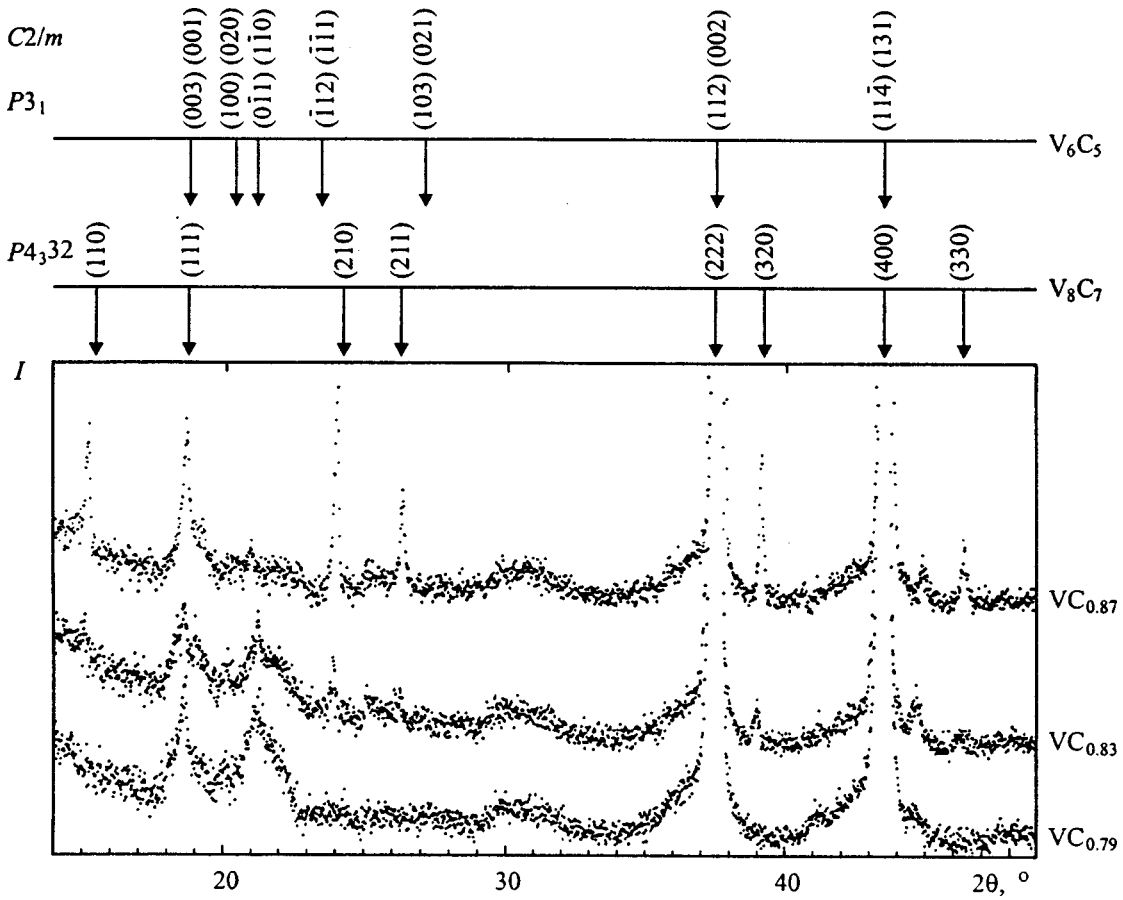

FIG. 1. Parts of x-ray diffractograms of annealed nonstoichiometric vanadium carbides $VC_{0.87}$, $VC_{0.83}$, and $VC_{0.79}$. The arrows identify the position of superstructure reflections for the V_6C_5 and V_8C_7 ordered phases; all reflections are assigned by Miller indices identifying the space group of the ordered phase.

at the grain boundaries of disordered carbide to propagate subsequently into the bulk of the crystallites.

As follows from an x-ray diffraction pattern of the annealed $VC_{0.83}$ carbide (Fig. 1), this sample contains two ordered phases. Besides the superstructure reflections belonging to the V_8C_7 ordered phase, one can see also lines due to the V_6C_5 ordered phase with trigonal (space group $P3_1$) or monoclinic (space group $C2/m$) symmetry. In the diffractogram of the annealed $VC_{0.83}$ carbide, the V_6C_5 ordered phase corresponds to the $\{1/2,1/2,1/2\}$ superstructure reflection ($2\theta=18.54°$) of the $\{\mathbf{k}_9\}$ star, which coincides in position with a similar reflection for the V_8C_7 cubic ordered phase, as well as the reflections $\{2/3,2/3,0\}$ ($2\theta=20.11°$), $\{1/6,-5/6,-1/2\}$ ($2\theta=21.14°$), $\{-1/3,-1/3,1\}$ ($2\theta=23.74°$), and $\{7/6,1/6,1/2\}$ ($2\theta=27.34°$) corresponding to the $\{\mathbf{k}_4\}$ ($\mu_4=1/3$) and $\{\mathbf{k}_3\}$ ($\mu_3=1/6$) stars. Thus the order-disorder phase-transition channel associated with the formation of the V_6C_5 superstructure contains the arms of the Lifshits star $\{\mathbf{k}_9\}$ and of the non-Lifshits stars $\{\mathbf{k}_4\}$ and $\{\mathbf{k}_3\}$. As follows from symmetry considerations, the V_6C_5 ordered phase should form as a first-order transition.

The totality of the observed superstructure wave vectors making up the $VC_{0.83}\rightarrow V_6C_5$ transition channel can be identified with either trigonal (space group $P3_1$) or monoclinic (space group $C2/m$) superstructures of the M_6C_5 type.

The annealed $VC_{0.83}$ carbide contains domains of two ordered phases. One of them has predominantly isometrically shaped grains and does not produce interference, which gives us grounds to believe that it is the V_8C_7 cubic ordered phase present in the sample to 15–20%. The content of the second phase in the sample is 80–85%. Its domains have a tabular and prismatic shape characteristic of monoclinic and trigonal symmetries and exhibit interference coloring, i.e. they are anisotropic. This suggests that the second phase is V_6C_5.

The diffraction pattern of the annealed $VC_{0.79}$ carbide contains superstructure reflections due only to the V_6C_5 phase (Fig. 1), and its microstructure exhibits domains only of an anisotropic ordered phase. This means that annealing resulted in the formation in the $VC_{0.79}$ carbide solely of a V_6C_5-type ordered phase.

No additional reflections appeared in the diffractogram of the $VC_{0.66}$ carbide after annealing, although one could expect formation in it of the ζV_4C_{3-x} phase. The ζV_4C_{3-x} carbide is not an ordered phase of the cubic carbide VC_y, because it has a rhombic rather than the fcc metal sublattice.[16] It forms and remains stable below 1593 K.[17] The ζV_4C_{3-x} phase is absent in the annealed carbide $VC_{0.66}$ apparently due to the annealing having started from a lower temperature, 1200 K.

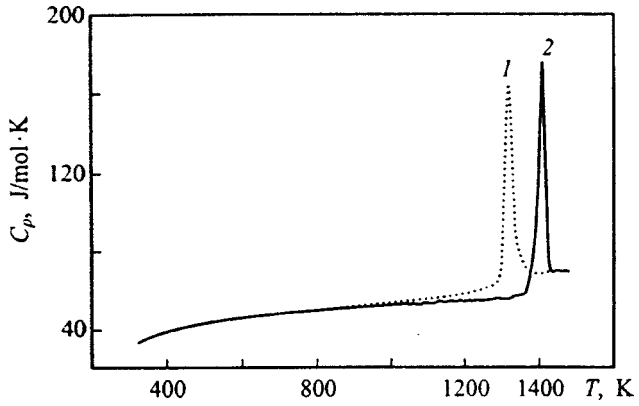

FIG. 2. Variation of the specific heat C_p of the $VC_{0.87}$ carbide measured under (*1*) heating and (*2*) cooling.

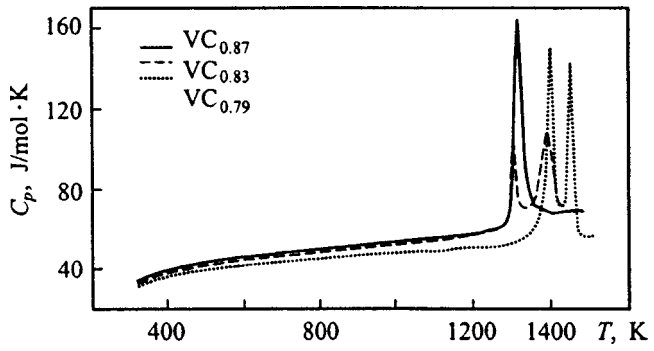

FIG. 3. Comparison of the phase-transformation manifestations in the temperature dependences of the specific heat $C_p(T)$ of the carbides $VC_{0.87}$, $VC_{0.83}$, and $VC_{0.79}$ measured under cooling from 1500 K.

B. Specific heat

The specific heat of annealed VC_y samples was measured under heating from 300 to 1500–1600 K and subsequent cooling down to 300 K.

The measurements of the specific heat C_p of the annealed $VC_{0.87}$ carbide showed it to increase smoothly with the temperature increased from 300 to 1350 K as a result of excitation of the phonon subsystem. At ~1380 K, one observes a sharp jump (discontinuity) in the specific heat (Fig. 2) associated with the equilibrium order-disorder transformation $V_8C_7 \rightarrow VC_y$ and characteristic of first-order phase transitions. The pattern observed when cooled from 1500 is similar, the only difference being that the peak in the specific heat due to the equilibrium order-disorder phase transition is shifted toward lower temperatures (Fig. 2). The temperature interval between the peaks seen in the heating and cooling runs is a region of metastability, whose existence likewise indicates that the reversible order-disorder phase transition connected with the formation of the V_8C_7 ordered phase is first order. Note that in the vicinity of the transition temperature T_{trans} the specific heat of disordered carbide is markedly higher than that of the ordered one. The temperature dependences $C_p(T)$ for the $VC_{0.87}$ carbide exhibit only one peak, which implies the formation of only one ordered phase, V_8C_7, in the $VC_{0.87}$ carbide within the temperature range studied.

The temperature dependences of the specific heat of the vanadium carbides $VC_{0.83}$, $VC_{0.79}$, and $VC_{0.87}$ measured under cooling from 1500 K are presented in Fig. 3. In contrast to $VC_{0.87}$, the $C_p(T)$ dependences of the $VC_{0.79}$ and $VC_{0.83}$ carbides are seen to have two peaks each.

Consider first the specific heat of the $VC_{0.83}$ carbide. When the disordered carbide $VC_{0.83}$ is cooled from 1500 K, one observes in the 1440–1400-K interval the first jump in the specific heat, to be followed under further cooling by a second peak in $C_p(T)$ in the 1330–1300-K interval (Fig. 3). The carbon content in the $VC_{0.83}$ carbide corresponds to the stoichiometric composition of the ordered phase V_6C_5, and therefore one may assume the first jump in the specific heat at 1400–1440 K to be associated with the $VC_{0.83} \rightarrow V_6C_5$ transition. The next transformation occurring at 1330 K could be the V_6C_5 $(VC_{0.83}) \rightarrow V_8C_7$ order-order transition. This assumption is corroborated by the presence in the diffractogram of the annealed carbide $VC_{0.83}$ of superstructure lines due not only to the V_6C_5 phase but to the cubic ordered phase V_8C_7 as well (Fig. 1). This means that the region of existence of the ordered phase V_8C_7 in the vanadium carbide VC_y extends at least to the $VC_{0.83}$ composition.

The $C_p(T)$ dependence obtained for the annealed carbide $VC_{0.79}$ in a heating run also exhibits two peaks, at ~1440 and ~1475 K. When cooled from 1500 K, both peaks persist, but the intensity of the high-temperature one increases slightly (Fig. 3). The low-temperature peak in the $C_p(T)$ dependence of the $VC_{0.79}$ carbide nearly coincides in position with the high-temperature one in the $C_p(T)$ dependence obtained for $VC_{0.83}$, and one feels justified to assign it to the reversible $V_6C_5 \leftrightarrow VC_y$ order-disorder transition. This is in accord with the structural data; indeed, the diffractogram of the annealed carbide $VC_{0.79}$ reveals superstructure

TABLE II. Temperatures and heats of phase transformations in the nonstoichiometric vanadium carbide VC_y.

	Phase transformation											
	$V_6C_5 \leftrightarrow VC_y$				$V_8C_7 \leftrightarrow VC_y$				ζ-$V_4C_{3-x} \leftrightarrow VC_y$			
	$T_{trans} \pm 5$, K		ΔH_{trans}, kJ/mol		$T_{trans} \pm 5$, K		ΔH_{trans}, kJ/mol		$T_{trans} \pm 5$, K		ΔH_{trans}, kJ/mol	
Carbide VC_y	heating	cooling	heating	cooling	heating	cooling	heating	cooling	heating	cooling	heating	cooling
$VC_{0.79}$	1433	1428	2.11	−2.22	–	–	–	–	1473	1473	1.56	−1.64
$VC_{0.83}$	1445	1438	1.16	−1.37	1336	1331	0.64	−0.75	–	–	–	–
$VC_{0.87}$	–	–	–	–	1358	1353	2.23	−2.35	–	–	–	–

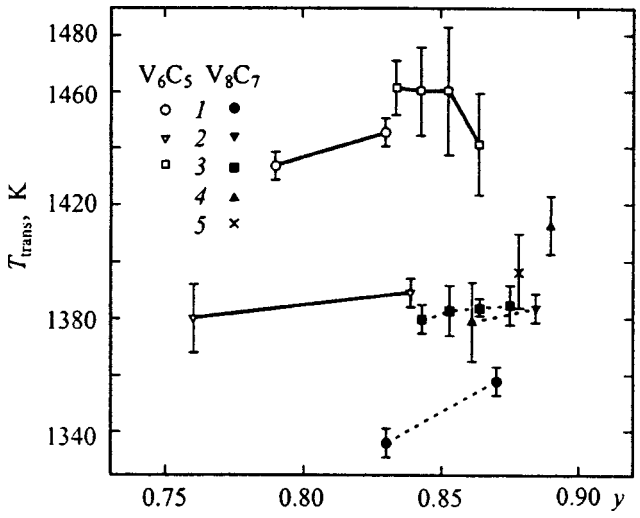

FIG. 4. Temperatures of the $V_6C_5 \leftrightarrow VC_y$ and $V_8C_7 \leftrightarrow VC_y$ phase transitions for the VC_y vanadium carbide with different carbon content: *1* — This work, *2* — Ref. 8, *3* — Ref. 18, *4* — Ref. 19, *5* — Ref. 20.

reflections only from the ordered phase V_6C_5 (Fig. 1).

The high-temperature peak in the $C_p(T)$ curve of the $VC_{0.79}$ carbide originates apparently from the ζV_4C_{3-x} rhombic phase of the vanadium carbide. The ζV_4C_{3-x} carbide is observed only in the presence of other phases in amounts not over 15–20%, and forms, according to Ref. 17, for $T<1593$ K. By its carbon content, the $VC_{0.79}$ carbide corresponds to the upper limit of the ζV_4C_{3-x} phase homogeneity region, and therefore it can have a small amount (less than 3–5%) of the ζ-phase.

The $VC_{0.83}$ and $VC_{0.87}$ carbides corresponding to the stoichiometric compositions of the ordered phases exhibit the maximum temperatures T_{trans} of the $V_6C_5 \leftrightarrow VC_y$ and $V_8C_7 \leftrightarrow VC_y$ transitions (Table II). The T_{trans} temperatures of the former transitions are $\sim$90 K higher than those of the latter.

Figure 4 presents data on T_{trans} for the $V_6C_5 \leftrightarrow VC_y$ and $V_8C_7 \leftrightarrow VC_y$ transitions obtained in this work and by other authors.[8,18–20] The values of T_{trans} measured by us are about 20–25 K lower than those quoted in Ref. 18; taking into account the errors in T_{trans} measurement, which are ± 5 K in this work and ± 15 K in Ref. 18, the agreement may be considered quite good. The data on T_{trans} for the $V_6C_5 \leftrightarrow VC_y$ transition presented in Ref. 8 are obviously underestimates, and the value $T_{trans}=1548\pm 8$ K quoted[20] for the same transition is too high. The highest value $T_{trans}=1413$ K (apparently an overestimate) for the $V_8C_7 \leftrightarrow VC_{0.89}$ transition is quoted in Ref. 19; our data and the measurements reported in Refs. 8, 18 and 20 suggest that T_{trans} for the $V_8C_7 \leftrightarrow VC_{0.87-0.88}$ transition lies in the 1358–1397-K interval (Fig. 4).

The heats of the order-disorder phase transformations in the VC_y carbide (Table II) measured by us are fairly close to the literature data; indeed, by Ref. 18, the heats ΔH_{trans} of the $V_6C_5 \leftrightarrow VC_{0.833}$ and $V_8C_7 \leftrightarrow VC_{0.875}$ transitions are 1.45 ± 0.71 and 1.54 ± 0.62 kJ/mol, respectively, while Ref. 8 gives 2.38 and 2.06 kJ/mol for the heats of phase transformations in the $VC_{0.842}$ and $VC_{0.884}$ carbides.

On the whole, both calorimetric and structural studies show that the formation of the V_6C_5 and V_8C_7 ordered phases in nonstoichiometric vanadium carbide occurs as a first-order phase transition.

The experimental data on the temperature dependences of the specific heat of vanadium carbides with different carbon contents can be approximated within the 300–1300-K range by the following relation

$$C_p(T)=f_1+f_2T+f_5T^2+f_0T^{-1}. \quad (1)$$

The coefficients in Eq. (1) for the $VC_{0.79}$, $VC_{0.83}$, and $VC_{0.87}$ carbides, which for $T<1300$ K are in a thermodynamically equilibrium ordered state, are listed in Table III.

C. Phase diagram

A reliable phase diagram for the V-C system, which would take into account the formation of ordered phases, is still lacking. The first approach to constructing the part of the V–C diagram where the V_6C_5 and V_8C_7 phases coexist was undertaken in Ref. 5. Later, an attempt was made to include phase equilibria in VC_y within narrow regions of composition, $0.84\leqslant y\leqslant 0.93$, and temperatures, $1273<T<1473$ K.[19]

TABLE III. Coefficients of polynomials, Eq. (1) and Eq. (3), describing the specific heat, parameters $F_0(T)$, $F_1(T)$, and $F_2(T)$ of the free energy $F(y,0,T)$ of disordered nonstoichiometric vanadium carbide VC_y, and free energy $F(T)$ of the hexagonal disordered carbide V_2C_y (β-V_2C) and ordered carbide V_8C_7 ($VC_{0.875}$).

		Coefficients					
Phase	Parameter	f_0 kJ/mol	$f_1\times 10^3$, kJ(mol·K)	$f_2\times 10^6$, kJ(mol·K^2)	f_3 kJ·K/mol	$f_4\times 10^3$ kJ/(mol·K)	$f_5\times 10^9$, kJ(mol·K^3)
$VC_{0.79}$	C_p (298–1300 K)	−8.437	61.26	−13.6	–	–	8.479
$VC_{0.83}$	C_p (298–1300 K)	−9.687	68.66	−21.2	–	–	1.295
$VC_{0.87}$	C_p (298–1300 K)	−9.041	65.31	−11.8	–	–	7.562
VC_y	F_0 (298–2000 K)	97.09	145.0	−11.84	−208	−26.95	–
	F_1 (298–2000 K)	−437.49	−86.23	11.75	932	18.29	–
	F_2 (298–2000 K)	211.36	267.21	0	0	−42.27	–
V_2C_y (βV_2C)	F (298–1600 K)	−180.96	513.67	−1.70	1290	−83.12	–
V_8C_7 ($VC_{0.875}$)	F (298–1400 K)	−123.89	274.13	−1.56	608	−43.46	–

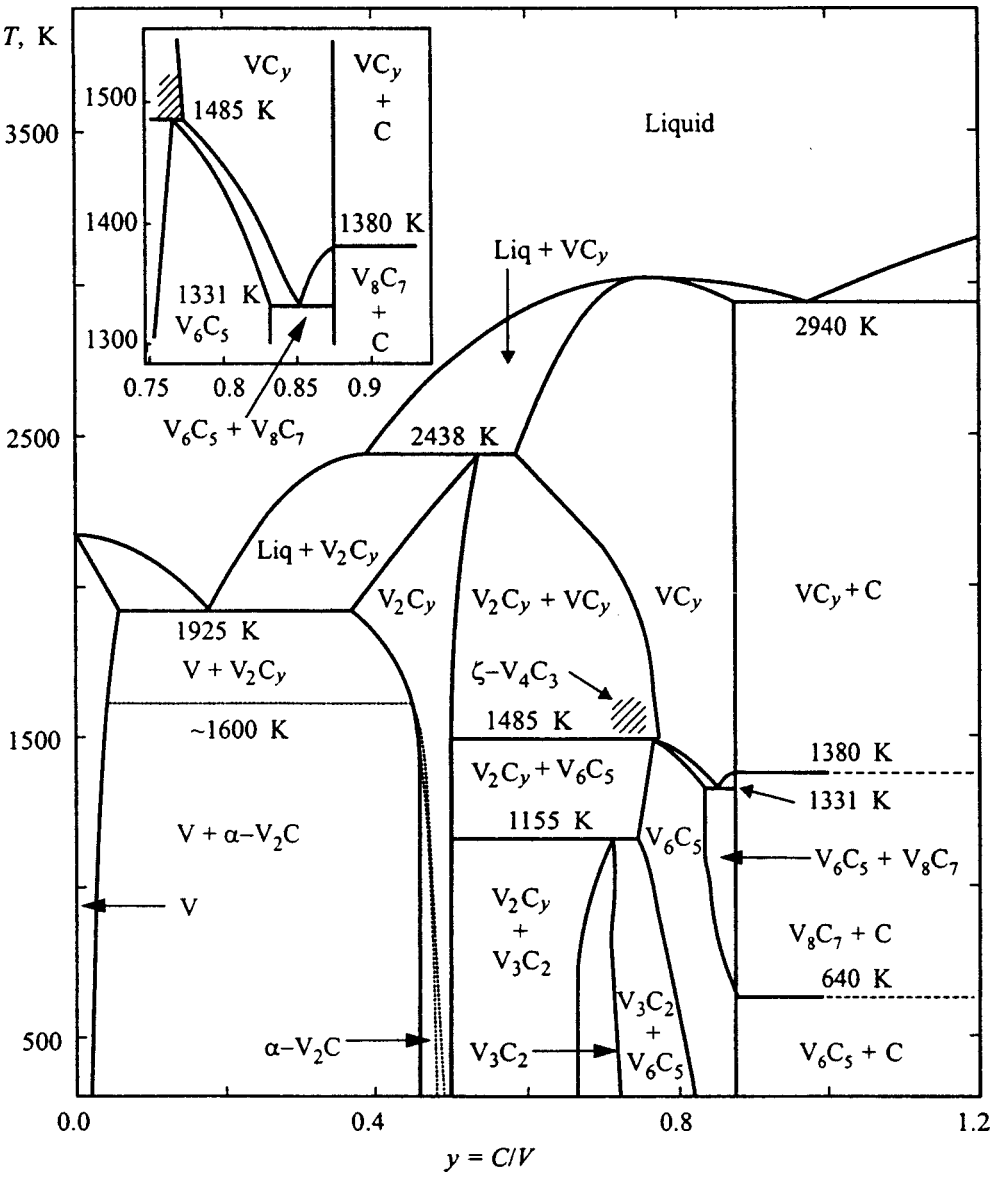

FIG. 5. Equilibrium diagram of the V-C system constructed taking into account atomic ordering of the nonstoichiometric cubic vanadium carbide VC_y: V_8C_7, V_6C_5, and V_3C_2 are ordered phases of the VC_y cubic carbide, αV_2C is an ordered phase of the lowest hexagonal carbide V_2C_y (βV_2C); the inset shows an amplified part of the ordering region near the homogeneity region of the VC_y carbide; the phase boundaries beyond the ordering regions are shown in accordance with Ref. 21.

In the phase diagram of the V-C system proposed in Ref. 21 the ordering region is shown tentatively, and it essentially repeats the one given in Ref. 5.

The main difficulty on the way to constructing a phase diagram for the V-C system lies in that the upper boundary of the homogeneity region for the disordered cubic vanadium carbide VC_y is $VC_{0.88}$ rather than the stoichiometric carbide $MC_{1.0}$, as is the case with carbides of other transition metals. The unusual position of the upper boundary of the VC_y homogeneity region gives rise to an edge effect, which manifests itself in the formation in VC_y of an M_8C_7-type ordered phase not present in other carbides.

The experimental data obtained in this work on the temperatures and heats of the $V_6C_5 \leftrightarrow VC_y$ and $V_8C_7 \leftrightarrow VC_y$ transformations permit one to take into account the ordering of the VC_y carbide in the phase diagram of the V-C system.

The phase equilibria in the region of ordering of the nonstoichiometric cubic carbide VC_y were calculated by the order-parameter functional method[11–13,22,23] using the technique described in detail in Ref. 24. The free energy $F(y,0,T)=F_0(T)+yF_1(T)+y^2F_2(T)-TS_c(y,0)$ of the disordered cubic carbide VC_y and the free energy $F(T)$ of the hexagonal carbide V_2C_y (β–V_2C) were found using tabulated thermodynamic data and published results.[8–10] The calculations were performed assuming the V_8C_7 ordered phase not to have a homogeneity region. The free energy of the V_8C_7 ($VC_{0.875}$) phase was presented in the form

$$F_{V_8C_7(VC_{0.875})}(T)=F(T)-TS_c+(\Delta H_{\text{trans}}/T_{\text{trans}})(T-T_{\text{trans}}), \tag{2}$$

where $F(T)=F_0(T)+xF_1(T)+x^2F_2(T)$ for $x=0.875$ [the $F_0(T)$, $F_1(T)$, and $F_2(T)$ parameters are the same as for the disordered carbide VC_y], S_c is the configurational entropy of the $VC_{0.875}$ carbide, and $\Delta H_{\text{trans}}=3$ kJ/mol and $T_{\text{trans}}=1380$ K are the heat and temperature of the $V_8C_7 \leftrightarrow VC_{0.875}$ transition estimated from experimental data. The energy parameters $F(T)$ of the free energies were presented by polynomials

$$F(T)=f_0+f_1T+f_2T^2+f_3T^{-1}+f_4T\ln T. \tag{3}$$

The magnitudes of the coefficients f_i are given in Table III.

Figure 5 displays the phase diagram of the V-C system constructed in this way. The main ordered phase of vanadium carbide is the V_6C_5 phase, which forms below 1485 K and has a homogeneity region at 1100 K extending from $VC_{0.745}$ to $VC_{0.831}$. This phase can be observed also in two-phase regions, so that the domain of its existence covers nearly the whole homogeneity region of the VC_y carbide (Fig. 5). The V_8C_7 ordered phase forms at a lower temperature of 1380 K, and at 1330 K it can coexist with V_6C_5 within the two-phase region extending from $VC_{0.83}$ to $VC_{0.875}$, which is in accord with the experimental data of Refs. 18 and 19. The width of the $V_6C_5+V_8C_7$ two-phase region where the V_8C_7 ordered phase exists narrows with decreasing temperature. The V_6C_5 and V_8C_7 phases form a eutectic with $T_e=1331$ K and $y_e=0.852$, which is very close to the estimate[19] by which $T_e\approx1300$ K and $y_e\approx0.852$. As follows also from these calculations, in equilibrium conditions an ordered phase V_3C_2 with a fairly narrow homogeneity region can appear in the vanadium carbide at 1155 K and lower in the peritectoid reaction $V_2C_y+V_6C_5\rightarrow V_3C_2$, but it has not been observed experimentally up to date.

In the homogeneity region of the lowest hexagonal carbide V_2C_y (βV_2C), an ordered rhombic phase αV_2C. forms. The ordering temperature is not known accurately, and according to Ref. 21 it is below 1870 K. An attempt at detecting the structural phase transition $\alpha V_2C\rightarrow V_2C_y$ (βV_2C) from magnetic susceptibility measurements performed on the αV_2C ordered carbide within the 300–1300 K range did not meet with success up to 1300 K.[25] Taking into account the results presented in Refs. 21 and 25, the temperature of the order-disorder transition $\alpha V_2C\rightarrow V_2C_y$ (βV_2C) in the V-C phase diagram of Fig. 5 is tentatively set at ~1600 K.

As evident from the phase diagram of the V-C system (Fig. 5), all order-disorder transformations in the vanadium carbide VC_y are first-order transitions. Calculations have yielded for the temperature T_{trans} and heat ΔH_{trans} of the $V_6C_5\rightarrow VC_{0.79}$ transition 1450 K and 2.84 kJ/mol, respectively; the experimental value of ΔH_{trans} (Table II) is slightly smaller, because calorimetric measurements indicate formation in $VC_{0.79}$ of a certain amount of the ζV_4C_{3-x} phase.

On the whole, our study of the crystalline structure and specific heat of the nonstoichiometric vanadium carbide VC_y ($0.66\leqslant y\leqslant0.88$) has shown that ordering in the vanadium carbide gives rise to formation of the V_6C_5 and V_8C_7 ordered phases. The presence in the $C_p(T)$ dependences of the studied carbides of discontinuities in the interval of reversible equilibrium order-disorder transitions argues for the $V_6C_5\leftrightarrow VC_y$ and $V_8C_7\leftrightarrow VC_{0.875}$ transformations being first order. The temperatures of the above transitions are 1400–1450 and 1360–1380 K, respectively.

Support of the Russian Fund for Fundamental Research (Grant 98-03-32890a) is gratefully acknowledged.

[1] C.-H. de Novion, R. Lorenzelli, and P. Costa, C. R. Acad. Sci. B **263**, 775 (1966).
[2] D. Froidevaux and D. Rossier, J. Phys. Chem. Solids **28**, 1197 (1967).
[3] S. I. Alyamovskiĭ, P. V. Gel'd, G. P. Shveĭkin, and E. N. Shchetnikov, Zh. Neorg. Khim. **13**, 895 (1968).
[4] J. D. Venables, D. Kahn, and R. G. Lye, Philos. Mag. **18**, 177 (1968).
[5] J. Billingham, P. S. Bell, and M. H. Lewis, Philos. Mag. **25**, 661 (1972).
[6] R. Kesri and S. Hamar-Thibault, Acta Metall. **36**, 149 (1988).
[7] E. G. King, J. Am. Chem. Soc. **71**, 316 (1949).
[8] N. M. Volkova and P. V. Gel'd, in Trudy Inst. Khimii UFAN SSSR (Sverdlovsk) **14**, 41 (1967).
[9] N. M. Volkova, P. V. Gel'd, and S. I. Alyamovskiĭ, Zh. Neorg. Khim. **10**, 1758 (1965).
[10] L. A. Korolev, I. I. Spivak, and M. L. Taubin, Izv. Akad. Nauk SSSR, Neorg. Mater. **18**, 54 (1982).
[11] A. I. Gusev and A. A. Rempel', *Structural Phase Transitions in Nonstoichiometric Compounds* [in Russian] (Nauka, Moscow, 1988) 308 pp.
[12] A. I. Gusev, *Physical Chemistry of Nonstoichiometric Refractory Compounds* [in Russian] (Nauka, Moscow, 1991) 286 pp.
[13] A. A. Rempel', *Ordering Effects in Nonstoichiometric Interstitial Compounds* [in Russian] (Nauka, Ekaterinburg, 1992) 232 pp.
[14] A. A. Rempel', Usp. Fiz. Nauk **166**, No. 1, 33 (1996).
[15] A. I. Gusev and A. A. Rempel, Phys. Status Solidi A **135**, 15 (1993).
[16] K. Yvon and E. Parthé, Acta Crystallogr., Sect. B: Struct. Crystallogr. Cryst. Chem. **26**, 149 (1970).
[17] A. H. Chaneya and O. N. Carlson, J. Less-Common Met. **109**, 57 (1985).
[18] G. H. Emmons and W. S. Williams, J. Mater. Sci. **18**, 2589 (1983).
[19] T. Athanassiadis, N. Lorenzelli, and C.-H. de Novion, Ann. Chim. (Paris) **12**, 129 (1987).
[20] L. W. Shacklette and W. S. Williams, Phys. Rev. B **7**, 5041 (1973).
[21] O. N. Carlson, A. N. Chaneya, and J. F. Smith, Bull. Alloy Phase Diagrams **6**, 115 (1985).
[22] A. I. Gusev, Philos. Mag. B **60**, 307 (1989).
[23] A. I. Gusev, Fiz. Tverd. Tela (Leningrad) **32**, 2752 (1990) [Sov. Phys. Solid State **32**, 1595 (1990)].
[24] A. I. Gusev and A. A. Rempel, Phys. Status Solidi A **163**, 273 (1997).
[25] V. N. Lipatnikov and A. I. Gusev, in *Proc. 5th All-Union Meeting on the Chemistry, Technology, and Application of Vanadium Compounds*, Ural Scientific Research Center, AN SSSR (Sverdlovsk, 1987), Pt. I, p. 166.

Translated by G. Skrebtsov

LOW DIMENSIONAL SYSTEMS, SURFACE PHYSICS

Specific features in the magnetoresistance oscillation spectrum from the two-dimensional accumulation layer on Te$(10\bar{1}0)$ surface

V. A. Berezovets and I. I. Farbshteĭn

A. F. Ioffe Physicotechnical Institute, Russian Academy of Sciences, 194021 St. Petersburg, Russia

D. Schneider

Institut für Technische Physik und Hochmagnetfeldanlage, Technische Universität Braunschweig, D-38106 Braunschweig, Germany

(Submitted July 14; resubmitted September 3, 1998)
Fiz. Tverd. Tela (St. Petersburg) **41**, 537–539 (March 1999)

Additional magnetoresistance and Hall effect oscillations have been revealed in the 2D hole system of an accumulation layer on the Te$(10\bar{1}0)$ surface. The oscillation frequency was found to be equal to a linear combination of the frequencies of Shubnikov–de Haas 2D-hole conductivity oscillations in the two 2D subbands formed in a near-surface potential. The mechanism responsible for these oscillations is related to the oscillating probability of intersubband scattering in transitions between Landau levels of two size- and magnetic-field-quantized subbands, as they pass near the Fermi level. © *1999 American Institute of Physics.* [S1063-7834(99)03203-7]

As follows from studies of the Shubnikov–de Haas (S–dH) effect (see, e.g., Refs. 1–3), size quantization in the accumulation layer (AL) on the Te$(10\bar{1}0)$ surface (cleavage plane) creates two quantum-confined subbands with strongly anisotropic 2D-hole Fermi surfaces, namely, for the shallow subband with a low Fermi energy they are two contacting ellipses extended along the C_3 crystal axis, and for the deep subband with a high Fermi energy it is a dumbbell-shaped figure. The waist between the ellipses (or in the dumbbell at higher Fermi energies) was observed to undergo a magnetic breakdown giving rise to coexistence of S–dH oscillations having two periods, one corresponds to Landau quantization of the area of one ellipse while the other, about twice the former, to that of the joint dumbbell-shaped figure.[4] The concentrations and mobilities of the 2D holes in both subbands were determined.[2]

A computer analysis of the oscillating components in the experimentally measured magnetic-field dependences of the resistance and Hall voltage revealed, besides the S–dH oscillations due to the Landau quantization of the two 2D subbands, additional small-amplitude extrema, which likewise showed a periodicity on the inverse-magnetic-field scale (Fig. 1). The effect was reproducible from one sample to another and was only weakly temperature dependent.

The method of sample preparation and measurement were described elsewhere.[2,4] We only note here that the measurements were carried out in a quasi-steady-state regime on a superconducting solenoid at the Ioffe Physicotechnical Institute (up to 12 T) and on a Bitter-type solenoid at the Strong Magnetic Fields Laboratory, Technische Universität Braunschweig, Germany. The signal was fed into a computer for subsequent mathematical processing.

Fourier transforms were used for a detailed analysis of the oscillation spectra. Figure 2 presents the results of such a transform having a rectangular window, which was performed for the functions displayed in Fig. 1. Application of various filters in the Fourier transform[5] did not affect the pattern in a radical manner. We readily see that, besides the sharp peak near zero with a frequency Ω_1, which corresponds to long-period oscillations due to the shallow subband (Fig. 1), the Ω_0 peak near 80 T, which originates from the deep-subband quantization, and a weakly pronounced feature at the $2\Omega_1$ frequency resulting from the magnetic breakdown, there are also a number of peaks (identified by arrows in Fig. 2), with the most prominent of them located at a frequency near $\Omega_{com} \cong 20$ T. To exclude the possibility of an error stemming from the use of a discrete Fourier transform, we subtracted computer-simulated curves from the spectra in Fig. 1 corresponding to the lowest of the frequencies (Fig. 2). The amplitudes and frequencies of the peaks denoted by arrows in Fig. 2 were not affected by this operation. It may be added that the additional oscillations become noticeable when the Landau levels in the shallow subband have small numbers, that the oscillation amplitude changes very little with increasing magnetic field, and that the oscillations are better resolved and have a larger amplitude in the field dependence of the Hall voltage.

A quantitative analysis showed that the period of the observed oscillations does not match the principal harmonics of the S–dH oscillations at the $(\Omega_0 \pm \Omega_1)/2$ frequencies, which could arise in linear superposition of oscillations with

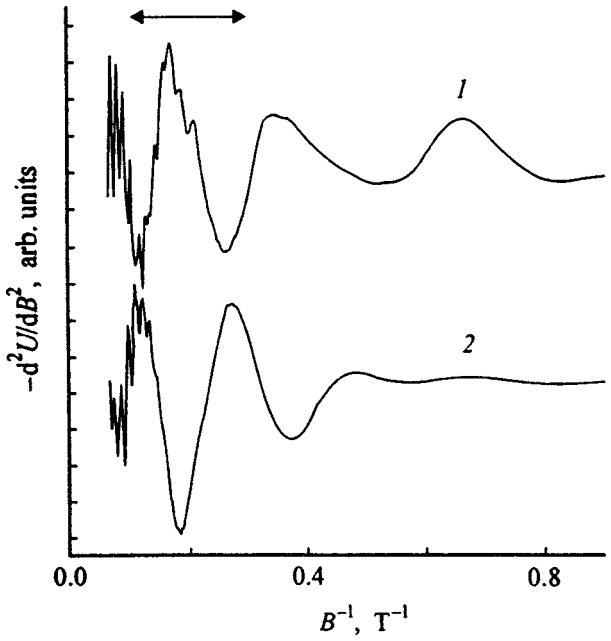

FIG. 1. Oscillating part of the Hall voltage (*1*) and magnetoresistance (*2*) of a tellurium sample with a 2D accumulation layer on the Te($10\bar{1}0$) surface. The arrow specifies the region of the most clearly pronounced extra oscillations. $T=1.9$ K.

different periods corresponding to the two 2D subbands.

A similar phenomenon, observed earlier in a study of Bi and Bi–Sb alloys doped with the Te donor impurity, suggested a strong nonlinearity of the S–dH effect, which makes a single crystal in a magnetic field act as a frequency mixer[6]. The most consistent explanation of this effect relates[7] the appearance of the extra frequencies in the S–dH effect to the presence in the semiconductor of several carrier groups with different Fermi-surface cross sections (in Bi and Bi–Sb alloys they are electronic valleys differently oriented in k space). The effect of intervalley scattering on the S–dH oscillation spectrum arising in transitions between the quantized levels of different valleys lying near the Fermi level was also considered in detail.[7] It was shown that besides the ''traditional'' renormalization of the effective relaxation time at the Landau level (the ''Dingle temperature''), the inclusion of intervalley scattering in transitions between quantized levels results in the appearance in the expression derived in quasiclassical approximation for the conductivity tensor components off-diagonal in the valley index, σ_{ij}, of additional terms $\delta\sigma_{ij}$

$$\delta\sigma_{ij}\sim\cos 2\pi[n(\varepsilon_F^{\alpha}/\hbar\Omega^{\alpha})\pm m(\varepsilon_F^{\beta}/\hbar\Omega^{\beta})]\,, \tag{1}$$

where $\Omega^{\alpha,\beta}$ are the cyclotron frequencies for the α and β valleys, respectively, n and m are integers, $\varepsilon_F^{\alpha,\beta}$ are the Fermi energies for the corresponding valleys, and $\hbar$ is the Planck constant. Equation (1) shows that the S–dH effect should include, besides its fundamental frequencies (Ω^{α} and Ω^{β}), combination frequencies as well

$$\Omega_{\text{com}}=n\Omega^{\alpha}\pm m\Omega^{\beta}\,. \tag{2}$$

Because two 2D subbands with different 2D-hole mobilities and concentrations exist on the Te($10\bar{1}0$) surface, and the experimental spectrum of S–dH oscillations is similar to that predicted in Ref. 7, it appeared reasonable to attempt to relate the observed extra S–dH oscillation frequencies to a mechanism of intersubband scattering in the spectrum of both magnetic-field-quantized 2D subbands. We applied the conclusions drawn in Ref. 7 to our case. It was found that the largest extra peak in the Fourier spectrum denoted by an arrow in Fig. 2 fits to the relation

$$\Omega_{\text{S-dH}}=\Omega_0-13\Omega_1\,. \tag{3}$$

An analysis of the S–dH spectra of all samples showed that this peak was observed for all 2D-hole concentrations in the AL, with the coefficient of Ω_1 in Eq. (3) varying within a narrow interval $11\leqslant m\leqslant 14$. Such a large magnitude of the m coefficient can be accounted for within the proposed explanation by the quantized Fermi-surface cross sections in the two subbands under study differing strongly from one another.

The origin of all the other extra peaks in the Fourier spectrum in Fig. 2 requires a separate consideration.

Thus precision measurements of the magnetic-field dependence of the resistance and Hall effect in the two-dimensional accumulation layer on the Te($10\bar{1}0$) surface at helium temperatures have revealed oscillations of these quantities with frequency multiples of those of the S–dH oscillations for 2D-hole Fermi surfaces in the size-quantized subbands created in the near-surface potential. The onset of these oscillations is associated with the probability of intersubband scattering in a quantizing magnetic field.

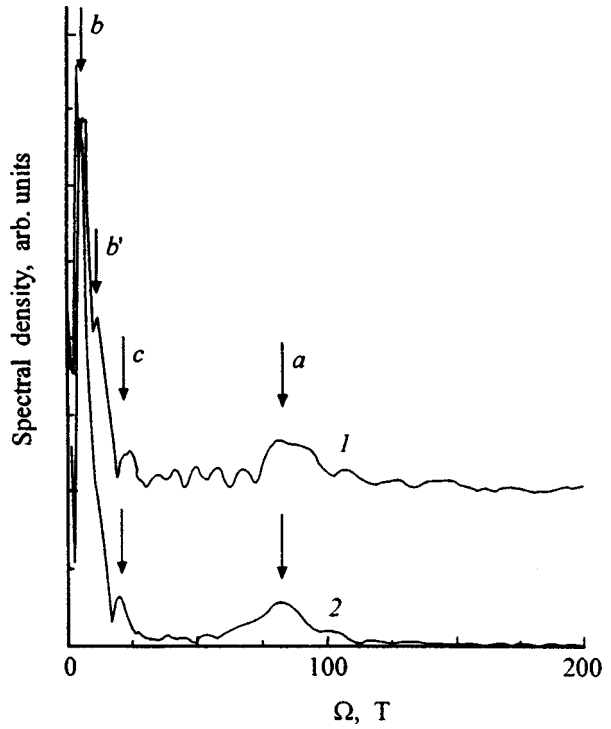

FIG. 2. The Fourier-analyzed dependences of Fig. 1. *1* — Hall voltage, *2* — magnetoresistance. a — frequency Ω_0 corresponding to deep-subband quantization, b and b′ — frequencies Ω_1 and $2\Omega_1$ corresponding to quantization of the shallow subband in magnetic breakdown conditions, c — extra-oscillation frequency Ω_{com}.

Support of the Russian Fund for Fundamental Research (Grant 96-02-16959) and DAAD (Germany) is gratefully acknowledged.

[1] V. A. Berezovets and I. I. Farbshteĭn, Fiz. Tekh. Poluprovodn. **29**, 965 (1995) [Semiconductors **29**, 500 (1995)].
[2] V. A. Berezovets, D. V. Mashovets, A. O. Smirnov, D. V. Smirnov, and I. I. Farbshteĭn, Fiz. Tverd. Tela (Leningrad) **33**, 3502 (1991) [Sov. Phys. Solid State **33**, 1966 (1991)].
[3] V. A. Berezovets, A. O. Smirnov, I. I. Farbshtein, and D. Schneider, Solid State Commun. **96**, 349 (1995).
[4] V. A. Berezovets, A. O. Smirnov, and I. I. Farbshteĭn, Fiz. Tverd. Tela (Leningrad) **30**, 2218 (1988) [Sov. Phys. Solid State **30**, 1279 (1988)].
[5] F. J. Harris, Proc. IEEE **66**, 51 (1978).
[6] N. B. Brandt and S. M. Chudinov, Usp. Fiz. Nauk **137**, 479 (1982) [Sov. Phys. Usp. **25**, 518 (1982)].
[7] V. A. Kozlov, E. E. Narimanov, and K. A. Sakharov, Fiz. Tverd. Tela (St. Petersburg) **36**, 309 (1994) [Phys. Solid State **36**, 168 (1994)].

Translated by G. Skrebtsov

Erbium-induced interdiffusion of gallium and aluminum in GaAs/AlGaAs quantum-well structures

O. B. Gusev, B. Ya. Ber, M. S. Bresler, B. P. Zakharchenya, I. N. Yassievich

A. F. Ioffe Physicotechnical Institute, Russian Academy of Sciences, 194021 St. Petersburg, Russia

G. Khitrova, H. M. Gibbs, D. P. Prineas, and E. K. Lindmark

Optical Research Center, Arizona University, Tucson AZ 85721, USA

V. F. Masterov

St. Petersburg State Technical University, 195251 St. Petersburg, Russia
(Submitted September 14, 1998)
Fiz. Tverd. Tela (St. Petersburg) **41**, 540–544 (March 1999)

Incorporation of erbium into GaAs/AlGaAs quantum-well structures in the course of their MBE growth has been shown experimentally to initiate effective Ga and Al interdiffusion and Er diffusion due to the erbium-induced enhanced vacancy formation. A mechanism for the formation of cation vacancies is proposed, which is based on the generation of local strains by the incorporating erbium. It is shown that erbium interacts with aluminum to produce in AlGaAs aluminum-enriched, erbium-containing clusters. © *1999 American Institute of Physics.* [S1063-7834(99)03303-1]

Recent years have witnessed increasing interest in the luminescent properties of erbium-doped semiconductors.[1,2] The reason for this lies in that the absorption of optical quartz fibers used in communications passes through a minimum exactly at the wavelength of 1.54 μm corresponding to the intra-$4f$ radiative transition $^4I_{13/2}\rightarrow{}^4I_{15/2}$ in the Er^{3+} ion, and that doping a semiconductor matrix with erbium permits one to fabricate electrically pumped sources of this radiation. At the same time development of such sources could benefit considerably from erbium doping of GaAs/AlGaAs quantum-well structures providing spatial current and light confinement, which may result in a higher efficiency of the corresponding light-emitting diodes.

We are reporting here on a study of MBE-grown, erbium-doped GaAs/AlGaAs structures and bulk AlGaAs. The study made use of secondary-ion mass spectrometry (SIMS) and erbium absorption and photoluminescence spectra.

The study showed that incorporation of erbium into GaAs/AlGaAs quantum wells during growth stimulates effective Er diffusion and interdiffusion of Ga and Al. In the limit of high erbium concentrations introduced during the MBE growth the quantum-well structures break down, and one observes practically uniform distribution of erbium, gallium, and aluminum in the region of the quantum wells and of the barriers. Besides, at lower erbium concentrations, it is observed also to interact with aluminum, which gives rise to nucleation in AlGaAs of aluminum-enriched erbium-containing clusters.

1. EXPERIMENTAL RESULTS

Erbium-doped GaAs/AlGaAs structures were MBE grown on a 625-μm thick GaAs substrate at 600 °C. The first layer of the structures, labeled Er21 through Er23 and 0.6 μm thick, was made of $Al_xGa_{1-x}As$ ($x=0.3$). Next 50 GaAs:Er quantum wells, 10 nm thick, with erbium-free AlGaAs barriers 21-nm thick were grown. One could control the erbium concentration by properly adjusting the erbium-source temperature (900, 870, and 930 °C for the Er21, Er22, and Er23 structures, respectively). The barriers separating GaAs:Er from AlGaAs were terminated at each end by 0.9-nm thick spikes. A second AlGaAs layer with a thickness of 0.6 μm was grown atop the 50 quantum wells to make the voltage symmetric. AlGaAs was protected from oxidation by a 7-nm thick GaAs cap layer. The structure thus obtained is shown schematically in Fig. 1.

In addition an Er26 structure, which consisted of 50 8-nm thick GaAs:Er layers separated by 22-nm thick layers of undoped GaAs, was fabricated (with the erbium source maintained at 900 °C). We also fabricated for reference an undoped GaAs/AlGaAs structure (Er20) and an AlGaAs sample with $x=0.3$ doped uniformly with erbium (Er29). The erbium concentration in the structures was measured by SIMS. The results of the measurements are listed in Table I.

Figure 2 shows the dependence of erbium concentration, as derived from SIMS data, on the erbium source temperature. This dependence can be fitted by a relation

$$N_{\mathrm{Er}}=N\exp(-E_b/kT)\,, \tag{1}$$

where $N=2.85\times10^{34}$ cm^{-3} and $E_b=3.6$ eV. The activation energy derived from the data in Fig. 2 is very close to the well-known energy of erbium evaporation from a metal source, $E_b=3.3$ eV (see, e.g., Ref. 3).

Photoluminescence (PL) spectra of the structures were obtained at $T=1.8$ K. The PL was analyzed by a two-grating

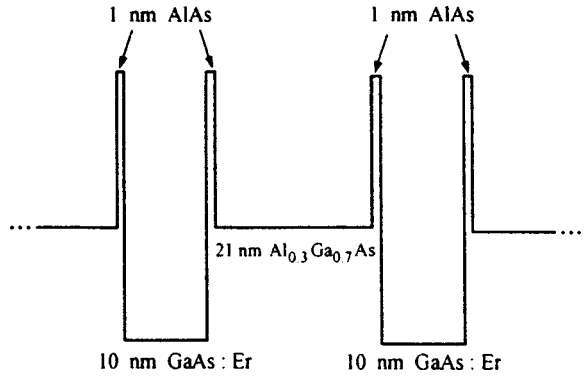

FIG. 1. Schematic view of erbium-doped GaAs/AlGaAs structures (shown is the conduction-band edge profile).

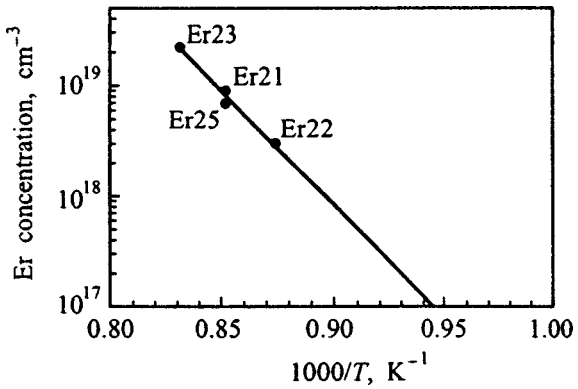

FIG. 2. Erbium concentration in GaAs/AlGaAs structures vs erbium-source temperature (from SIMS data).

monochromator with a focal length of 822 mm and detected with a cooled germanium photodiode. Photoluminescence was excited by a cw argon laser at 488 nm.

The absorption spectra were measured at 4 K with a spectrometer with a focal length of 1/8 m, with the GaAs substrate etched off preliminarily.

Figure 3 displays a SIMS profile for the Er26 sample (GaAs:Er) obtained with 50-Å resolution. The SIMS data show the erbium concentration to become averaged out at a 4×10^{18} cm^{-3} level, irrespective of whether the shutter before the erbium source was open or closed in the course of GaAs growth. Thus no erbium layers exist in GaAs. This implies a high erbium diffusion coefficient in the bulk of the MBE-grown GaAs, as distinct from the case of erbium introduced by diffusion.

Figure 4 shows SIMS profiles for three samples in the order of increasing concentration of erbium doped only into the quantum-well region. In the Er20 structure with no erbium introduced into the quantum wells, the latter are seen clearly. In the Er21 structure ($N_{Er}=9\times10^{18}$ cm^{-3}), their outlines are diffuse, and in Er23 ($N_{Er}=2.2\times10^{19}$ cm^{-3}) the quantum wells are washed out completely, and the concentrations of erbium, aluminum, and gallium are constant throughout the structure. Thus the rate of gallium and aluminum interdiffusion and of erbium diffusion directly depend on the concentration of the doped erbium.

Because SIMS provides a limited spatial resolution, it could be expected not to reveal any modulation of the average concentration while the quantum wells would still persist to some extent. The absorption spectra presented in Fig. 5 support, however, the SIMS data of the quantum wells being strongly washed out. The absorption spectrum of Er20 shows clearly two-dimensional stepped density of states for the quantum levels with $n=1,2$. As the erbium concentration in the Er22, Er21, and Er23 structures increases, the stepped structure diffuses to make the absorption spectrum similar to that of bulk GaAs.

Figure 6a displays a PL spectrum of the Er26 sample obtained at 1.8 K in the region of erbium luminescence (1.5–1.6 μm). This is a layer of bulk GaAs doped by erbium during its growth. The positions of the erbium PL lines corresponding to the intra-$4f$ $^4I_{13/2}\rightarrow{}^4I_{15/2}$ transition in the Er^{3+} ion are in good agreement with the available literature data[4] for GaAs:Er.

Shown in Fig. 6b is a PL spectrum of the Er21 sample. Erbium was introduced in this case only into the GaAs quantum-well region. We readily see that it differs strongly from the spectrum of GaAs:Er while practically coinciding with that of the Er29 sample (Fig. 6c), where erbium was doped into bulk AlGaAs (the photoluminescence of MBE-grown, erbium-doped bulk AlGaAs was studied in Ref. 5). This supports the preliminary SIMS data on interdiffusion of

TABLE I. Parameters of GaAs/AlGaAs structures.

Sample No.	Erbium source temperature, °C	Erbium concentration from SIMS data	Note
Er20			without erbium
Er21	900	9×10^{18}	
Er22	870	3×10^{18}	
Er23	930	2.2×10^{19}	
Er24	800	$<10^{17}$	
Er25	900	7×10^{18}	
Er26	900	4×10^{18}	GaAs:Er
Er29	900	9×10^{18}	AlGaAs:Er

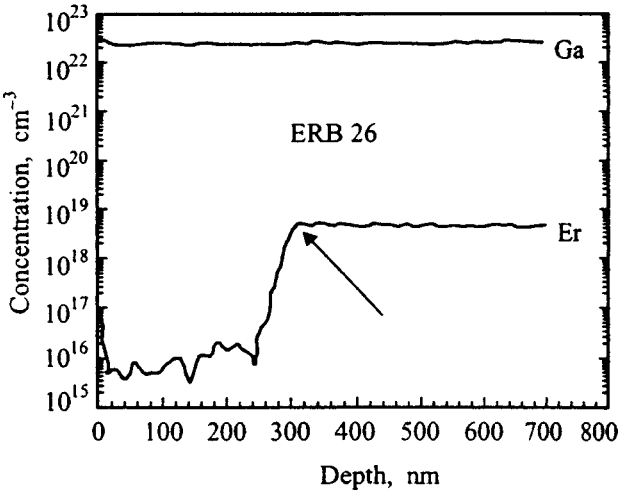

FIG. 3. SIMS profile of sample Er26. The arrow identifies the thickness at which the erbium-source shutter was opened.

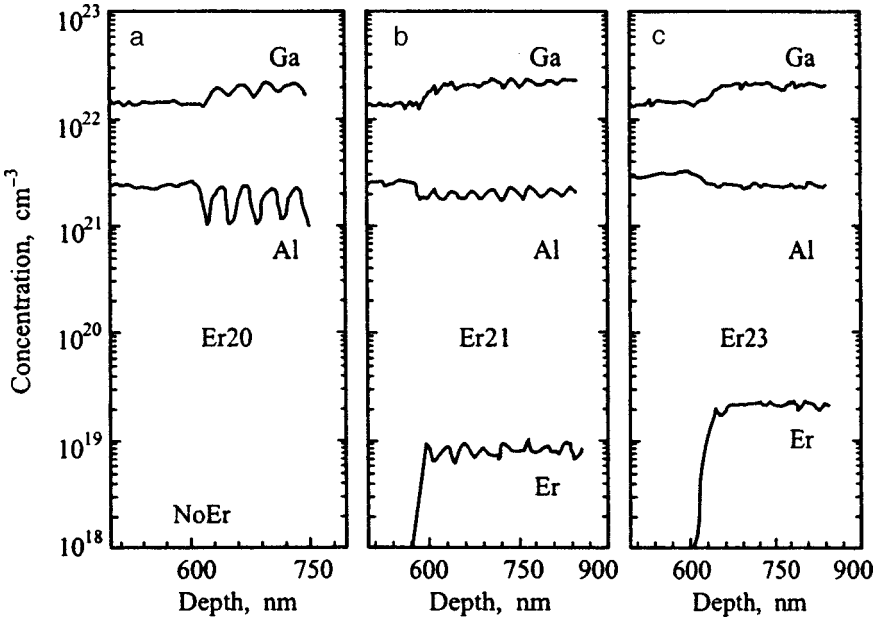

FIG. 4. SIMS profiles for Er20, Er21, and Er23 structures.

gallium and aluminum when erbium is introduced into GaAs quantum wells during growth.

Experiment shows also the existence of interaction between erbium and aluminum, which stimulates diffusion of erbium into the aluminum-enriched regions, and that of aluminum, into the erbium-doped regions of the structure. Figure 6 provides evidence for erbium preferring to have aluminum in its nearest environment. Even in the case where erbium was introduced during the growth of the Er21 and Er23 structures only into the GaAs layers, the PL spectrum near 1.5 μm is characteristic of AlGaAs (it is more complex than the Er spectrum in GaAs). It should be pointed out that all lines in the AlGaAs:Er photoluminescence spectrum (Fig. 6c) were observed also in GaAs/AlGaAs structures with a low concentration of erbium ($\approx 10^{17}$ cm^{-3}) introduced into the GaAs quantum wells, while SIMS data attested to the quantum-well structures still remaining in good condition. The absorption spectra presented in Fig. 5 also argue for the formation of Er-Al clusters. Thus our results evidence strong interaction between aluminum and erbium.

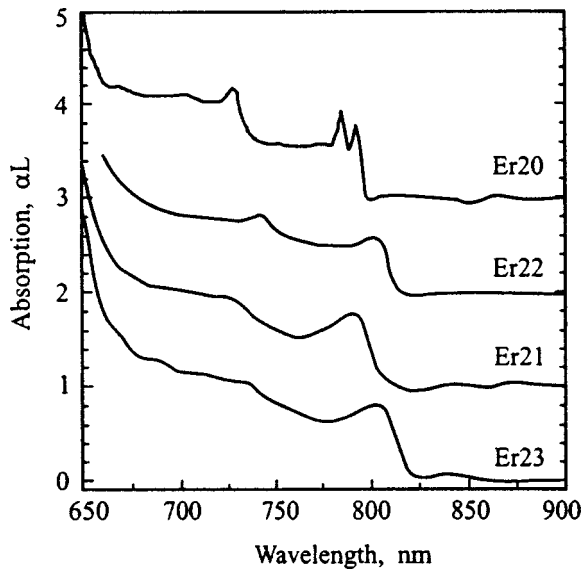

FIG. 5. Absorption spectra of Er20 through Er23 structures in the order of increasing erbium concentration obtained at $T=4$ K. Spectral resolution 2 nm.

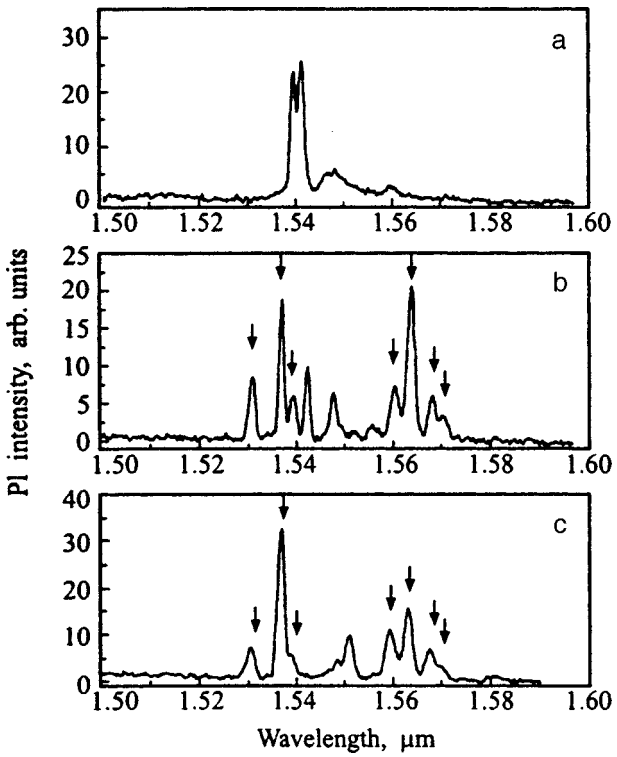

FIG. 6. Photoluminescence spectra of (a) Er26, (b) Er21, and (c) Er29. $T=1.8$ K. Er26 is bulk GaAs, into which erbium was doped to a thickness of 8 nm with an open erbium-source shutter with 30-nm intervals. Er21 is a structure obtained with erbium doped during the growth only into the quantum-well region with the GaAs/AlGaAs barriers remaining undoped. Er29 is erbium-doped bulk GaAs/AlGaAs.

2. DISCUSSION OF RESULTS

The phenomenon of Ga and Al interdiffusion, which results in washout of GaAs/AlGaAs quantum wells in the presence of high concentrations of electrically active impurities (donors or acceptors), is well known in growth technology of GaAs/AlGaAs quantum-well structures and has been a subject of intensive studies.[6,7] It was shown that incorporation of electrically active impurities raises the Fermi level in the system, which favors formation of additional cation vacancies increasing the diffusion coefficient.[7]

At the same time the Er^{3+} ions occupy substitutional, i.e. cation sites in the III-IV lattice and behave as an isovalent impurity, i.e. without donating additional charge. The observation of strong erbium diffusion and of Ga and Al interdiffusion in our case can be explained if one takes into account the internal strains generated in the lattice as an erbium ions enters the site of a Group III cation. Because the radius of the erbium ion is considerably larger than those of gallium and aluminum, incorporation of erbium creates local strains around it and, in this way, contributes to the elastic energy of an erbium-doped semiconductor. This local strain may initiate formation of additional vacancies (compared to the equilibrium state), and their concentration can be estimated from energy conservation considerations.[8,9]

Let us estimate the number of vacancies which may appear with erbium entering a substitutional site. Although we do not know the covalent radius of erbium, its ionic (and atomic) radius exceeds by about 10% the radii of Group III cations, which permits a conclusion that the deformation of the erbium environment could be of the order of $3\Delta R/R_0 \approx 0.3$, where ΔR is the change in the cation radius, and R_0 is the cation radius itself. The corresponding elastic energy per cc can be estimated from[9]

$$U=\frac{2\pi}{3}c\left(\frac{3\Delta R}{R_0}\right)^2(R_0^3N_{\mathrm{Er}}), \tag{2}$$

where c is the elastic constant, R_0 is the host-cation (Ga, Al) radius, $\Delta R=R_1-R_0$, R_1 is the erbium ion radius, and N_{Er} is the doped erbium concentration. The energy of internal strain is energetically preferable to be spent in vacancy formation. If we assume the accumulated elastic energy to be spent completely in vacancy formation, the concentration of the vacancies thus produced can be estimated from

$$[V_{III}]=U/E_V, \tag{3}$$

where E_v is the vacancy-creation energy determined by the GaAs bond energy. Taking $c=10^{12}$ erg/cm^3, $\Delta R/R_0\approx 0.1$, $R_0\approx 10^{-8}$ cm, $N_{\mathrm{Er}}=10^{18}$ cm^{-3}, and $E_v=1.6$ eV,[8] we obtain $[V_{III}]=7.3\times 10^{16}$ cm^{-3}. It is well known that cation vacancies are effectively generated in GaAs and AlGaAs in an arsenic-enriched atmosphere.[7] Because MBE growth of structures takes place only under these conditions, it may be assumed that erbium doping stimulates formation of cation vacancies whose concentration was estimated above.

We have to compare now the concentration thus obtained with the equilibrium cation-vacancy concentration at $\sim$900 K

$$[V_{III}]=N_0\exp(-E_v/kT), \tag{4}$$

where $N_0=1.1\times 10^{22}$ cm^{-3} is the total number of cation states per cc, and the equilibrium vacancy concentration $[V_{III}]=1.2\times 10^{13}$ cm^{-3}. Thus doping with erbium can increase considerably the concentration of cation vacancies.

It should be pointed out that the diffusion coefficient is small if erbium is doped into GaAs by diffusion, because the radius of erbium is larger than that of gallium. The impurity diffusion coefficient depends also on the concentration of cation and anion vacancies, but because the vacancy concentration in equilibrium conditions is constant at a fixed temperature, the rate of diffusion is determined by the radius of the impurity atom. The situation is different if vacancies are created during the growth, and this is exactly what happens when erbium is doped into MBE-grown GaAs/AlGaAs structures in the course of growth. In MBE-grown $Al_{0.5}Ga_{0.5}As$ with erbium concentration $\sim 10^{18}$ cm^{-3}, 88% of erbium atoms occupy substitutional sites (cation states).[10] For higher erbium concentrations, part of the erbium ions fill interstitial sites, and for $N_{\mathrm{Er}}=5\times 10^{19}$ cm^{-3} only 30% Er sit at substitutional sites. (Besides, the strain created by an interstitial erbium ion can be expected to be even larger.)

The cation diffusion coefficient in GaAs (or in AlGaAs) can be written[7]

$$D_{III}=fD_{III}^0[V_{III}], \tag{5}$$

where f is a factor accounting for the crystalline structure and the probability of encountering a vacancy at the neighboring lattice site, and D_{III}^0 is the cation diffusion coefficient describing jumping into a neghboring cation site, which in order of magnitude is $\omega a^2\exp(-E_b/kT)/2$ (ω is the ion vibrational frequency, a is the lattice constant, and E_b is the energy barrier separating two adjacent cation states). Because $[V_{III}]$ is proportional to N_{Er}, the diffusion coefficient increases strongly in the presence of erbium ions. This result relates to diffusion of both gallium and aluminum and of erbium ions. Our estimates of the erbium diffusion coefficient derived from the characteristic length of the erbium profile (Fig. 4) and from the time required to grow the corresponding layer yield $D_{\mathrm{Er}}\sim 10^{-15}$ cm^2/s, which is a very large value for the temperature of 900 K.

As for the tendency of erbium to surround itself by aluminum atoms, it can probably be traced to their chemical interaction; indeed, erbium is known[11] to form several intermetallic compounds with aluminum. One could therefore expect formation of erbium-aluminum complexes in our samples.

Thus we have shown that doping GaAs/AlGaAs quantum-well structures with erbium results in a very efficient Ga and Al interdiffusion and Er diffusion because of the formation of cation vacancies. A mechanism is proposed for the cation vacancy formation, which is based on the local strains created by incorporation of erbium due to its radius differing strongly from that of the host ions.

Erbium has been shown to interact with aluminum. This interaction is responsible for the formation in AlGaAs of aluminum-enriched, erbium-containing clusters.

Support of the Russian Fund for Fundamental Research (Grant 98-02-18246), Ministry of Science of the RF (Grant

97-1036), and AFOSR (Grant F49620-94-1-0390), ARPA, and NSF Lightwave Technology is gratefully acknowledged.

[1] *Rare-Earth Doped Semiconductors*, edited by G. S. Pomrenke, P. B. Klein, and D. W. Langer (Materials Research Society, Pittsburgh, 1993).
[2] *Rare-Earth Doped Semiconductors II*, edited by S. Coffa, A. Polman, and R. N. Schwartz (Materials Research Society, Pittsburgh, 1996).
[3] C. Kittel, *Introduction to Solid-State Physics* (Wiley, New York, 1956; Nauka, Moscow, 1978), Table 3.1.
[4] J. E. Colon, D. W. Elsaesser, Y. K. Yeo, R. L. Hengehold, and G. S. Pomrenke, in Ref. 1, p. 251.
[5] T. Zhang, J. Sun, N. V. Edwards, D. E. Moxey, R. M. Kolbas, and P. J. Caldwell, in Ref. 1, p. 257.
[6] W. D. Laidig, N. Holonyak, Jr., M. D. Camras, K. Hess, J. J. Coleman, P. D. Dapkus, and J. Bardeen, Appl. Phys. Lett. **38**, 776 (1981).
[7] D. G. Deppe and N. Holonyak, Jr., J. Appl. Phys. **64**, R93 (1988).
[8] Ya. I. Frenkel, *Collection of Works*, Vol. III, *Kinetic Theory of Liquids* [In Russian] (AN SSSR, Moscow, 1959), p. 18.
[9] B. I. Boltaks, *Diffusion and Point Defects in Semiconductors* [In Russian] (Nauka, Leningrad, 1972).
[10] E. Alves, M. F. Da Silva, A. A. Melo, J. C. Soares, G. N. van den Hoven, A. Polman, K. R. Evans, and C. R. Jones, in Ref. 1, p. 175.
[11] W. E. Wallace, *Rare-Earth Intermetallics* (Academic, New York, 1973), pp. 34 and 58.

Translated by G. Skrebtsov

SAW spectral characteristics of the YZ–$LiNbO_3$–thin-lead-film layered structure

L. A. Kulakova, K. V. D'yakonov, and É. Z. Yakhkind

A. F. Ioffe Physicotechnical Institute, Russian Academy of Sciences, 194021 St. Petersburg, Russia
(Submitted July 31, 1998)
Fiz. Tverd. Tela (St. Petersburg) **41**, 545–549 (March 1999)

An acousto-optical study of the effect of a lead film on propagation of high-power surface acoustic waves (SAW) along the *Z* direction on the *Y* cut of $LiNbO_3$ is reported. The presence of the metal film has been found to stimulate spatial oscillations of SAW components and suppress the onset of nonlinearity. If the film is more narrow than the SAW aperture, one observes considerable inflow of acoustic energy from the free surface to the film region. A study of the film-induced sound-velocity dispersion revealed it to have a linear pattern. An analysis of the results within the present theoretical models of soliton development showed that a soliton-like monopulse can form only if a very thin ($\sim$150 Å) lead film is present. © *1999 American Institute of Physics.* [S1063-7834(99)03403-6]

Science and technology are witnessing presently an increasing interest in nonlinear dispersion systems. This interest is stimulated, on the one hand, by their application potential, and on the other, by present progress in applied mathematics which has made possible analytical solution of the various nonlinear wave-dispersion equations.

One of the most popular nonlinear dispersion systems is the layered structure made up of a metal film and a substrate supporting propagation of a Rayleigh-type surface acoustic wave, with the film thickness *h* substantially smaller than the sound wavelength λ.

The effect of metal films on SAW propagation on a piezoelectric substrate is dealt with in a number of publications.[1,2] Most of the works used aluminum films. The published results permit the following two basic conclusions: (i) The electric loading by the film shorts the piezoelectric fields and reduces the SAW velocity by an amount proportional to one half the squared electromechanical coupling constant of the substrate; and (ii) The mechanical loading by the film mass results in a linear dispersion of the sound velocity.

Our earlier studies[3] of the nonlinear acousto-electronic interaction in superconducting lead films posed a number of problems associated with the influence of the lead film itself on the SAW spectral response, namely, how the film affects the amplitude and shape of the SAW signal and whether it generates a series of soliton-like monopulses with the periodicity of the original signal.

To find an answer to these questions, we have performed acousto-optical studies of the effect of a lead film on SAW propagation along the *Z* direction on the *Y* cut of $LiNbO_3$.

The measurements were carried out at $T=300$ K by the acousto-optical technique in reflection. The radiation source was a gas (He–Ne) laser ($\lambda=0.63\,\mu$m), and the photoreceiver, a FÉU-62 PM tube. The laser beam spot focused on the sample measured $\sim 0.3\times 0.7$ mm. The sonic signal was excited by an interdigital transducer with a resonance frequency of 87 MHz fabricated on a $3.2\times 1.0\times 0.15$-cm YZ–$LiNbO_3$ substrate. The SAW intensity could be varied by an attenuator from zero to 10^4 W/cm^2. The lead film was $h=1100$ Å thick. The configurations studied were (a) a film with a width *d* larger than the SAW aperture *a* ($d\geqslant a$), and (b) a narrow film, $d<a$ (Fig. 1).

The intensity of various SAW harmonics was determined as the ratio of light intensity in the corresponding diffracted order (I_k) to that in zero order (I_0).

Figure 2 shows the evolution of the SAW spectrum as the wave propagated over the free surface of the substrate for various input sound intensities. We readily see that the propagation conditions are essentially nonlinear.

The effect of a metal film on SAW propagation was investigated both in the conditions of a well developed nonlinearity, i.e. at a certain distance from the transducer, where one observes saturation of the higher harmonics created in the course of SAW propagation over the substrate free sur-

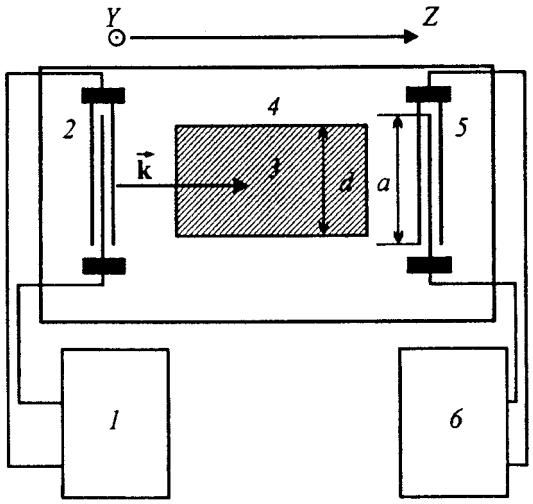

FIG. 1. Schematic representation of SAW excitation in the layered structure *YZ*-$LiNbO_3$–lead film. *1* — microwave generator, *2* — input interdigital transducer, *3* — lead film, *4* — YZ–$LiNbO_3$ substrate, *5* — output interdigital transducer, *6* — microwave receiver; *a* is the sound beam aperture, and *d* is the film width.

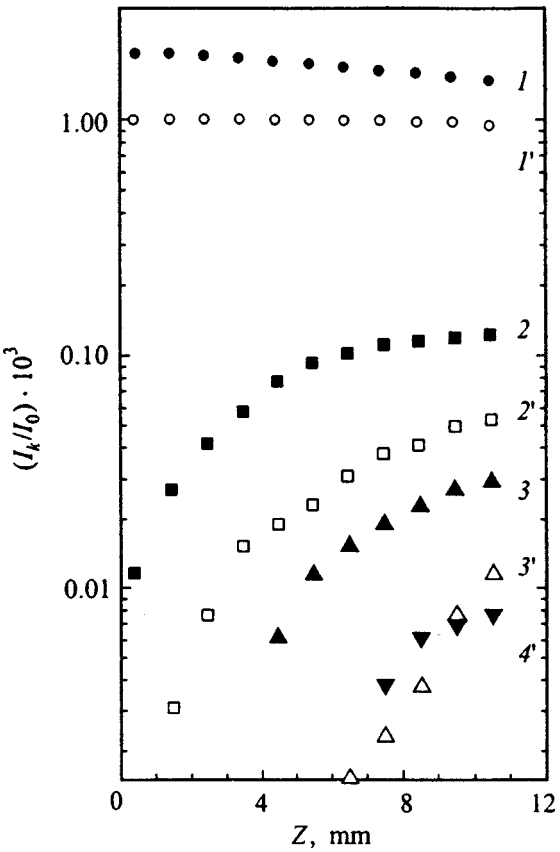

FIG. 2. Spatial distribution of SAW harmonic intensity on the free surface for $P_{ac}=2.5$ and 5 W (filled and open symbols, respectively). *1*, *1′* — fundamental frequency, *2*, *2′* — second harmonic, *3* — third harmonic, *4′* — fourth harmonic.

face, and in the initial (linear) conditions, i.e. near the interdigital transducer, where the acoustic response consisted only of the fundamental-frequency component.

The effect of the metal film located where the higher harmonics reach saturation ($x\sim 6$ mm) appears in the onset of oscillations in the intensity of all SAW components (Fig. 3a). If the film is located in the starting region (Fig. 3b), its presence substantially suppresses the onset of nonlinearity to leave only a weak oscillating second harmonic.

The effect of a narrow film ($d<a$) on SAW propagation was studied in detail on the first two harmonics, viz. with the fundamental and double frequency. We were interested here in the variation of the intensity both in the direction of propagation and over the flow cross section at different distances from the input.

As seen from Fig. 4, in the region covered by the film one observes a substantial growth in intensity of the fundamental component with distance, whereas on the free surface its intensity decreases.

The observed pattern is a result of inflow of the acoustic energy from the free surface into the region occupied by the film, which is due to a difference between the SAW velocities caused by the shorting of the substrate piezofield by the metal film. The pattern of spatial variation of the second-harmonic intensity implies a substantial suppression of the nonlinearity. While on the free surface one sees an active growth of the second harmonic in intensity (despite the at-

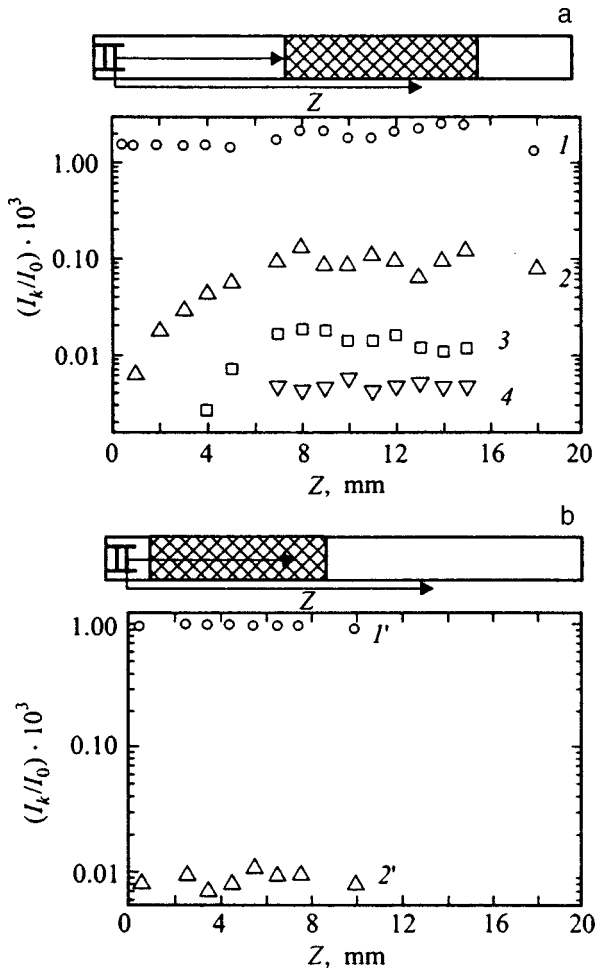

FIG. 3. Spatial distribution of SAW harmonic intensity on the metallized surface. *1*, *1′* — fundamental frequency, *2*, *2′* — second harmonic, *3* — third harmonic, *4* — fourth harmonic.

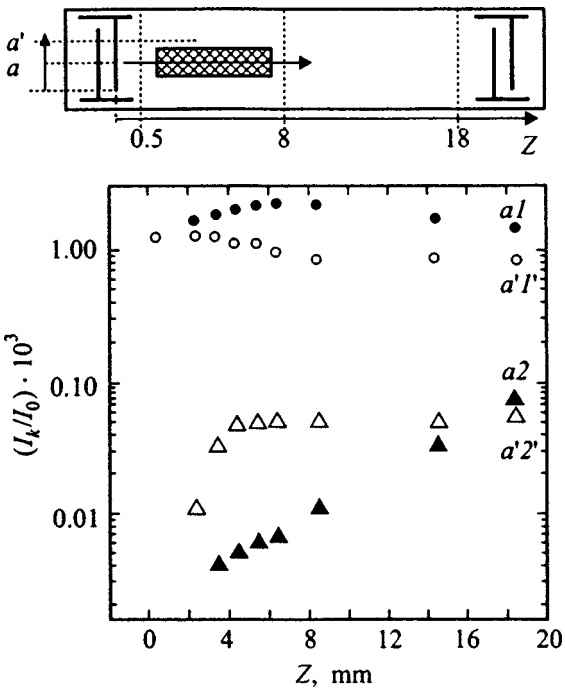

FIG. 4. Variation of SAW intensity along the film for $a=1.6$ mm and $a'=2.4$ mm. *1*, *1′* — fundamental frequency, *2*, *2′* — second harmonic.

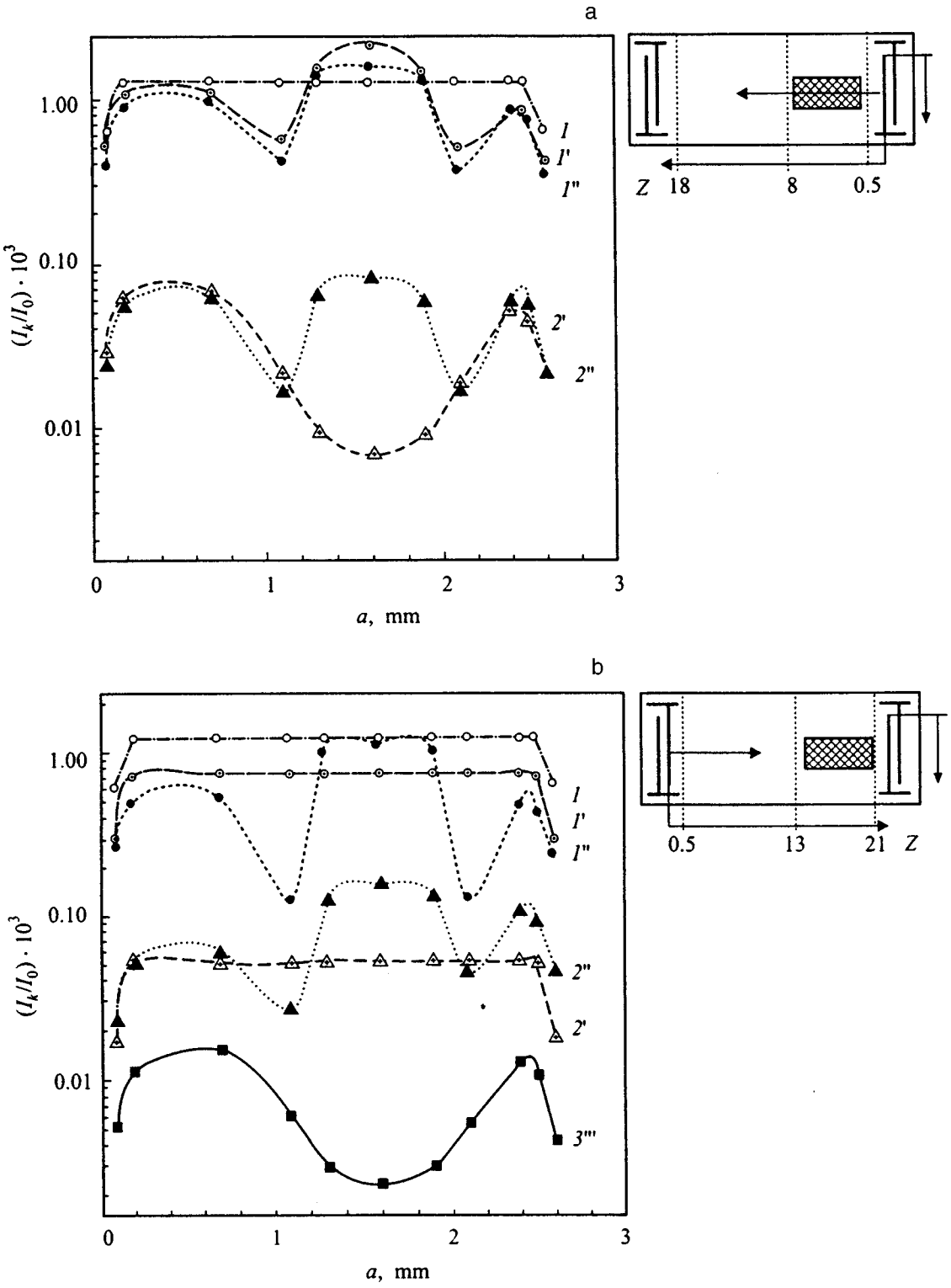

FIG. 5. Transverse distribution of SAW harmonic intensity at different distances from the input interdigital transducer. (a) *1*, *1′*, *1″* — fundamental frequency, $Z=0.5$, 8.5, and 18.5 mm, respectively; *2′*, *2″* — second harmonic, $Z=8.5$ and 18.5 mm, respectively; (b) *1*, *1′*, *1″* — fundamental frequency, $Z=0.5$, 13, and 21 mm, respectively; *2′*, *2″* — second harmonic, $Z=13$ and 21 mm, respectively; *3″* — third harmonic, $Z=21$ mm.

tenuation of the SAW intensity at the fundamental frequency), within the film the second harmonic grows insignificantly despite the noticeable increase of the fundamental harmonic in the same region.

These effects are particularly clearly pronounced in Fig. 5 showing the transverse intensity distribution of both SAW components at different distances from the interdigital transducer for two cases, namely, of the film located (a) near the transducer and (b) at a certain distance from it, where the second harmonic reaches saturation.

As seen from the figure, ahead of the film, the SAW intensity is distributed uniformly over the acoustic-beam

cross section and is determined only by one component of the fundamental-frequency. The film changes the transverse SAW-intensity distribution. Behind the film we observe in both cases [(a) $Z=8$ mm and (b) $Z=21$ mm] a growth of the fundamental component (by a factor ~ 1.5), which results in the appearance of a maximum in the film region and of a dip on the free-surface region adjoining the film.

In case (a), the pattern of the transverse second-harmonic intensity distribution behind the film ($Z=8$ mm) evidences substantial suppression of the nonlinearity compared to the free surface. As a result, the intensity distribution at the frequency of the second harmonic exhibits a deep minimum in the film region. Further growth of the second harmonic is dominated by the nonlinear properties of the free surface of the substrate and the transverse intensity distribution at the fundamental frequency. Therefore at a certain distance from the film ($Z=18$ mm) the patterns of both components are qualitatively similar.

In case (b), the effects are similar, the only difference being that here suppression of the nonlinearity becomes most pronounced in the behavior of the third harmonic whose level was insignificant at the input to the film.

Thus the above experiments showed that the lead film initiates, on the one hand, suppression of nonlinearity due to the sound velocity dispersion, similar to the case of an aluminum film,[1] and on the other, effective inflow of acoustic energy from the free surface supporting sound propagation to the film region.

It should be stressed that while this energy inflow is in no way a radically new phenomenon, we are unaware of experiments on its direct observation. The quantitative results derived by us from acousto-optical measurements and demonstrating an intense (of about 50%) energy inflow are rather unexpected, because theoretical estimates[3] predict weak localization of acoustic energy due to the small ($\sim 2\%$) difference between the SAW velocities on the free and metal-coated surfaces.

Let us discuss whether conditions favoring SAW energy transformation, say, into a train of quasimonopulses are realizable.

The soliton is known to form in interaction of the elastic nonlinearity of a medium (which accounts for the shock front formation) with velocity dispersion (which destroys this shock). It was shown[4] that in the case of linear sound-velocity dispersion the possibility for an originally sine-shaped signal to evolve into a soliton is characterized by two important parameters, namely, the distance Z_B at which the shock forms in the absence of dispersion and the dispersion to nonlinearity ratio R_{DN}.

The solution of the nonlinear equation becomes many valued at a distance

$$Z_B=(kS_0^1\Gamma_{\mathrm{nl}})^{-1}, \tag{1}$$

where k is the acoustic wave number, S_0^1 is the amplitude of fundamental-frequency deformation, $\Gamma_{\mathrm{nl}}=4(S_0^2/S_0^1)/(S_0^1kZ)$ is a nonlinear coefficient, S_0^2 is the second-harmonic deformation amplitude, and Z is the distance from the input interdigital transducer. For the R_{DN} parameter one can write

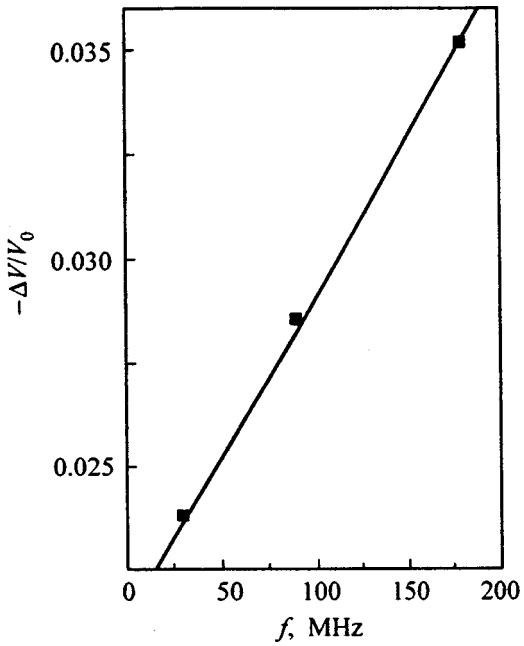

FIG. 6. Frequency dependence of SAW velocity on the metallized surface.

$$R_{\mathrm{DN}}=\frac{\gamma_k}{S_0^1\Gamma_{\mathrm{nl}}}, \tag{2}$$

where $\gamma k=\Delta V/V_0$ is the sonic velocity dispersion.

In order for nonlinear effects to become pronounced, the system dimensions should be about a few Z_B, and for the dispersion to be compensated by nonlinearity, the R_{DN} parameter should be of the order of unity.

The frequency dispersion of the sound velocity induced by the lead film was derived both from the spatial oscillations of the second SAW harmonic (Fig. 3a) using the well-known relation[1] $\Delta V/V_0=\pi/Z_0k$ (Z_0 is the oscillation period), and from our direct measurements of the variation of the surface wave velocity at different frequencies with the film etched off the substrate.

The results thus obtained (Fig. 6) agree fairly well with one another and with theoretical predictions[5]. The dispersion is linear, $\Delta V/V_0=C-\gamma k$, and the magnitude of the frequency-independent contribution $C=0.22$ is in accord with one half the squared electromechanical coupling constant.[6]

We used our data on nonlinearity (Fig. 2) and dispersion (Fig. 6) to estimate the parameters Z_B and R_{DN} from Eqs. (1) and (2). For an acoustic power of 3.5 W (the displacement along the surface normal ~ 40 Å) we obtained $Z_B\approx 0.5$ cm and $R_{\mathrm{DN}}\approx 9$. This means that a soliton-like monopulse cannot be produced just by increasing acoustic power. One has to reduce strongly the dispersion, i.e. the film thickness to about 150 Å.

As for the soliton-like solution for the envelope of SAW microwave pulse, our analysis of the criteria derived in Ref. 4 suggests that, in order for such a solution to exist, the system should meet the following most essential requirement, namely, the SAW group and phase velocities must have opposite signs. Because the dispersions of the SAW

group and phase velocities, which are caused by surface metallization, are, as a rule, of the same sign,[2] additional conditions have to be satisfied in such systems in order for the SAW microwave pulse envelope to have a soliton solution.

Thus our study showed that the presence of a 1100-Å thick metal film suppresses the onset of nonlinearity. If the film is more narrow than the interdigital transducer width, one observes a substantial ($\sim 50\%$) inflow of SAW energy from the free surface supporting the sound propagation to the film region. An investigation of the metallization-induced sound-velocity dispersion has demonstrated it to be linear. An analysis of the results in terms of the present theoretical models of the creation and development of the soliton showed that a soliton-like monopulse can form only in the presence of a very thin (~ 150 Å) lead film.

We owe sincere thanks to Yu. V. Ilisavskiĭ for initiating this work and criticisms and to A. V. Gol'tsev for fruitful comments.

Partial support of the International Science Foundation and of the Russian Fund for Fundamental Research (Grant 95-02-04093a) is gratefully acknowledged.

[1] A. P. Mayer, Phys. Rep. **256**, 238 (1996).
[2] *Acoustic Surface Waves*, edited by A. A. Oliner (Springer, Berlin, 1978) [Russ. transl. Mir, Moscow, 1981].
[3] K. V. D'yakonov, Yu. V. Ilisavskiĭ, and É. Z. Yakhkind, Pisma Zh. Tekh. Fiz. **14**, 2249 (1988) [Sov. Tech. Phys. Lett. **14**, 976 (1988)].
[4] J. F. Ewen, R. L. Gunshor, and V. H. Weston, J. Appl. Phys. **53**, 5682 (1982).
[5] H. Skeie, J. Acoust. Soc. Am. **48**, 1098 (1970).
[6] J. Melngailis, J. Vetelino, A. Jhunjhunwala, T. B. Reed, R. E. Fahey, and E. Stern, Appl. Phys. Lett. **32**, 203 (1978).

Translated by G. Skrebtsov

FULLERENES, ATOMIC CLUSTERS

Effect of low-temperature compression on the parameters of the phase transition at 250–260 K in C_{60} single crystals

V. M. Egorov, V. I. Nikolaev, B. I. Smirnov, and V. V. Shpeĭzman

A. F. Ioffe Physicotechnical Institute, Russian Academy of Sciences, 194021 St. Petersburg, Russia

R. K. Nikolaev

Institute of Solid-State Physics, Russian Academy of Sciences, 142432 Chernogolovka, Moscow District, Russia

(Submitted July 15, 1998)
Fiz. Tverd. Tela (St. Petersburg) **41**, 550–553 (March 1999)

A thermodynamic transition in C_{60} crystals, subjected beforehand to uniaxial compression at various temperatures and to thermal action, was investigated by differential scanning calorimetry. It was established that compression of the crystal at temperatures below the phase transition has a much smaller effect on the transition itself than a similar or even much weaker action at a temperature above the phase transition. A ''quenching'' effect was also found. This effect is probably due to the orientational order of individual fullerene molecules. A correlation was established between the magnitude of the effect and the preliminary deformation of C_{60} crystals. © *1999 American Institute of Physics.* [S1063-7834(99)03503-0]

The phase transition in C_{60} fullerene near the temperature 260 K has been studied quite completely by various physical methods that made it possible to obtain a more or less clear picture at a molecular level of the intertransition of the face-centered (fcc) and the primitive cubic (pc) phases. It has been established that, at temperatures $T>260$ K, to each site in the fcc C_{60} lattice there corresponds one C_{60} molecule which undergoes almost free rotation.[1] The lattice constant of fullerene remains virtually unchanged as the temperature drops below the phase transition point ($T\approx 260$ K),[2] but the symmetry of the crystal jumps from fcc to pc. In the process, the fcc structure of the positions of the C_{60} molecules remains, and the additional orientational order is due to the fact that to each site of the pc lattice there corresponds a tetrahedron formed by four molecules with fixed orientations along four different directions.[3,4] C_{60} molecules can become fixed in tetrahedra in two different equilibrium positions with close interaction energies, the so-called pentagonal (p) and hexagonal (h) configurations. In a quite wide temperature range 85 K $<T<260$ K the C_{60} molecules are in a state of jump-like rotation with the ratio of the populations of the pentagonal (n_p) and hexagonal (n_h) configurations $n_p/n_h \approx 4$. With deeper cooling ($T<85$ K) the jump-like rotation of the C_{60} molecules becomes ''frozen'' and the fullerene crystal passes into a nonequilibrium state called an ''orientational glass.''[5]

Recent investigations have shown that orientational transformations in fullerene strongly influence its mechanical properties.[6,7] In Ref. 8 a dependence of the phase-transition enthalpy ΔH on the compressive strain at 293 K, i.e. above the transition temperature, where the additional orientational order is completely absent and the C_{60} molecules in the fcc lattice execute free rotational motion, was found by differential scanning calorimetry (DSC). The objective of the present work is to investigate the parameters of the pc–fcc phase transition as a function of the compressive strain at 77 K, corresponding to the nonequilibrium state of fullerene crystals with completely ''frozen'' rotational motion of the C_{60} molecules.

1. EXPERIMENTAL PROCEDURE

The C_{60} single crystals were obtained from the vapor phase. Small C_{60} crystals, prepurified by repeated vacuum sublimation, were chosen as the starting material. The procedure for preparing this material was as follows. Chromatographically purified 99.95% pure C_{60} fullerene powder was placed in a quartz ampul, which was evacuated to pressure 10^{-6} torr and heated to 573 K. The powder underwent a purification process in which organic solvents and volatile impurities were removed in a dynamic vacuum in 8–10 h. Next, it was subjected three times to vacuum sublimation. The yield of purified crystals was 70% of the weight of the initial load. Next, the crystals were once again transferred into a smaller quartz ampul, which was evacuated to pressure 10^{-6} Torr and sealed. The ampul was placed into a horizontal two-zone furnace. The single crystals were grown under the following conditions: sublimation temperature 873 K, crystallization temperature 813 K, and growth time of the crystals 8–12 h. The well-faceted C_{60} crystals up to 30 mg obtained by this method up to several millimeters in size. The structural investigations revealed growth twins and microtwin formations in the crystals.

The calorimetric measurements were performed on a Perkin–Elmer DSC-2 differential scanning calorimeter by the method of Refs. 9 and 10, and the mechanical action consisted of compressing the C_{60} crystals at 77 and 293 K in an Instron 1342 universal testing machine by the method described in Ref. 8.

The fullerene sample compressed at 77 K was transferred in a capsule with liquid nitrogen into the calorimeter chamber, which was precooled to 220 K. Next, the sample was heated from 220 K up to 300 K at a constant rate of 5 K/min and the thermal processes occurring in the sample in the course of the pc–fcc phase transition were recorded on the DSC curve. The C_{60} crystals placed into the calorimeter chamber were subjected three times to the same preliminary mechanical action with an increasing load at 77 K. Next, the sample was loaded additionally at 293 K and cooled in the calorimeter chamber to 220 K. In this manner a series of four calorimetric tests of C_{60} single crystals subjected to compression was obtained.

The fullerene samples were rapidly cooled (''quenched'') from room temperature in liquid nitrogen, after which the samples were transferred in a capsule with liquid nitrogen into the calorimeter chamber precooled to 220 K and heated in the chamber up to 300 K with the heat effects recorded on the DSC curve.

2. EXPERIMENTAL RESULTS AND DISCUSSION

Figure 1 displays the DSC curves in the interval 220–300 K for C_{60} samples with different mechanical history. One can see that the endothermal peak corresponding to a thermodynamic transition in the initial C_{60} (curve *1*) decreases negligibly, as the mechanical load increases at 77 K (curves *2–4*), in amplitude and washes out in the direction of low temperatures. Aside from this, a temperature-broadened endothermal effect in the form of a wide peak with a maximum in the range 245–250 K can be seen in the curves *2–4* against the background of the low-temperature shoulder of the amplitude-diminished peak of the pc–fcc phase transition. The wide peak vanishes on the DSC curves with repeated heating from 220 K, and the first heating only to temperatures falling between the two peaks is sufficient. This shows that the process leading to the appearance of this peak is a nonequilibrium one and that there is no relation between the appearance of the peak and the phase transition. At the same time the endothermal peak of the equilibrium thermodynamic transition repeats with repeated heating. The transition enthalpy of the deformed samples, determined from the area of the endothermal peak with repeated heating, decreases with respect to the enthalpy of the initial sample ($\Delta H = 8.8$ J/g) and is 8.6, 8.5, and 7.9 J/g, respectively, for the samples subjected to low-temperature loading (curves *2–4* in Fig. 1).

The curve *5* for the sample deformed at room temperature is sharply different from preceding curves. Just as in Ref. 8, it demonstrates a sharp drop in intensity and broadening of the low-temperature shoulder of the phase-transition peak. The transition enthalpy decreases appreciably and is $\Delta H = 6.2$ J/g. Moreover, there is no low-temperature endothermal effect on the curve. We note that the temperature scanning range indicated in Fig. 1 for the predeformed samples was extended to 500 K in order to observe heat effects associated with the release of the latent energy that could be stored in deformed solids. As a result, it turned out that in all cases with repeated scanning of the deformed samples in the region 255–500 K the DSC curves were identical to the initial curves, indicating that there are no irreversible heat effects in this range.

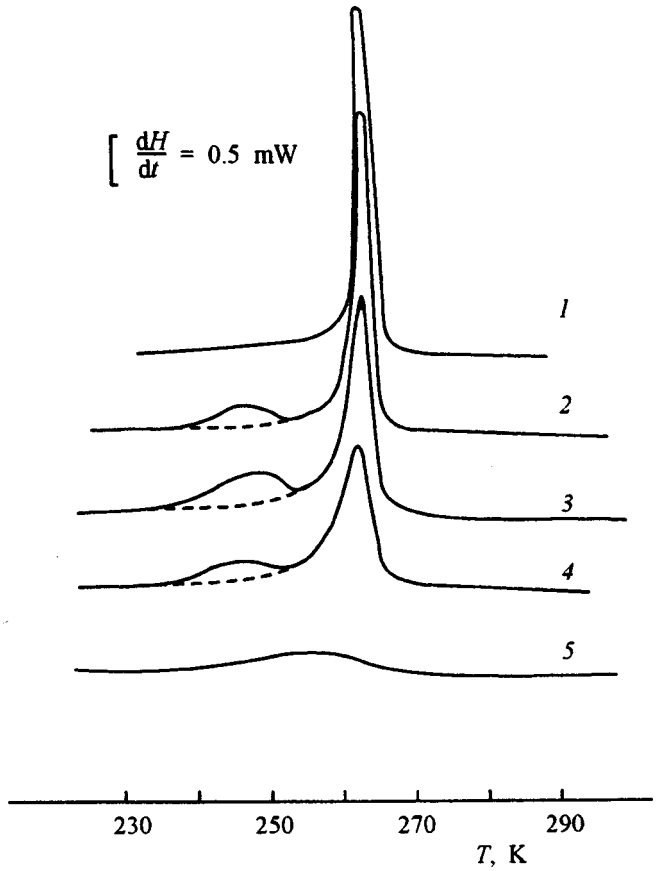

FIG. 1. DSC curves of the initial (*1*) and precompressed at $T = 77$ K (*2–4*) and $T = 293$ K (*5*) C_{60} samples. Specific compressive strain σ, MPa: 180 (*2*, *5*), 320 (*3*), and 460 (*4*). Dashed line — repeated heating after cooling to 220 K. The heating rate is 5 K/min. The samples (*1*) and (*5*) were cooled in the calorimeter to 220 K.

We note that the maximum load applied at low temperature is approximately 2.5 times larger than in experiments at room temperature (Fig. 1) and nonetheless the distortion of the peak corresponding to the phase transition was found to be much smaller. Such a different influence of the load is evidently due to the different magnitude of the lattice distortions produced by the load. In the pc lattice the formation energy of crystallographic defects (dislocations and dislocation pile-ups) is high, and the main effect of a load is to fracture the sample, i.e. to convert it into powder in which the particles decrease in size with increasing load but retain a regular, undistorted strcuture. Pulverization also occurs under a load above the transition, but aside from that, distortions arise in the fcc lattice, specifically, formation of C_{60} dimers,[11] which are responsible for the decrease in the amplitude and broadening of the peak.

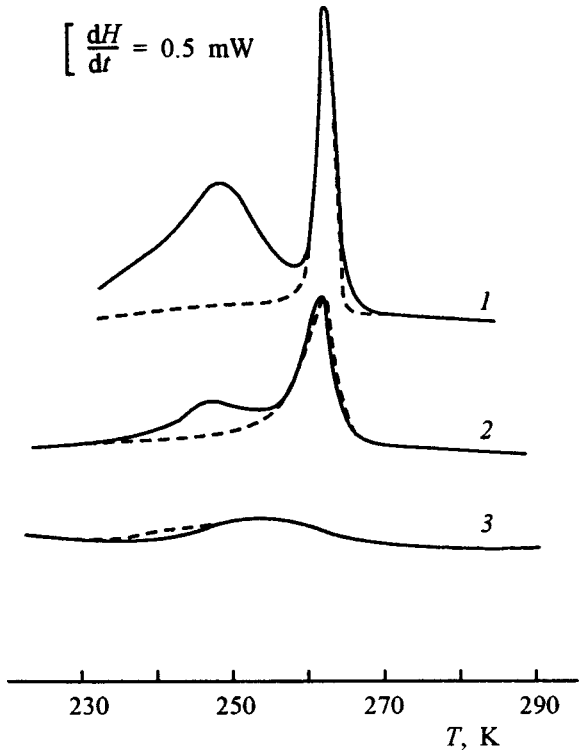

FIG. 2. DSC curves of the initial C_{60} sample (*1*) and C_{60} samples prequenched in liquid nitrogen and deformed at $T=77$ K, $\sigma=460$ MPa (*2*) and $T=293$ K, $\sigma=180$ MPa (*3*). Dashed line — repeated heating after cooling to 220 K. The heating rate is 5 K/min.

The appearance of an additional endothermal effect on the DSC curves of the sample subjected to deformation at low temperatures is most likely not due directly to the deformation, but rather it is determined mainly by the cooling dynamics or the persistence at low temperature. This conjecture follows, for example, from the fact that there is no additional peak in the DSC curves of the sample deformed at room temperature and the initial sample, which were not cooled below 220 K. Therefore there are grounds for believing that the nonequilibrium in the experimental C_{60} samples is due to thermal and not mechanical actions.

To check this assertion we performed a series of additional experiments on C_{60} samples which were prequenched in liquid nitrogen. The data from these experiments are presented in Fig. 2. One can see that an additional endothermal peak, comparable in enthalpy with the peak of the pc–fcc phase transition, appears in the curve *1* obtained when the prequenched initial, i.e. undeformed, C_{60} sample is heated. This peak is due to a metastable effect, since it does not occur with repeated heating. The same kind of metastable effect but with a lower intensity is also observed in the quenched C_{60} sample deformed at 77 K prior to quenching and heated in a calorimeter from 220 K to room temperature (curve *2*). Comparing the curves *4* and *2* in Figs. 1 and 2, respectively, shows that they are similar. Evidently, this is due to the fact that the cooling rates on quenching and prior to the mechanical loading are comparable (the cooling time differed by not more than one order of magnitude). However, if the rate of cooling from room temperature to 77 K is decreased to 5 K/min, then the ''quenching'' effect is not observed. It is also virtually absent in the DSC curve of the C_{60} sample which is deformed in advance at room temperature and then quenched in nitrogen (curve *3*). Only a very small exothermal effect at 240 K is observed. Just as in the preceding case, the curves *5* and *3* in Figs. 1 and 2, respectively, are observed to be similar.

The comparative experiment performed shows clearly that the metastable effect appears as a result of a thermal action so that this effect can be termed a ''quenching'' effect. As one can see by comparing the curves in Fig. 2, the magnitude of the effect depends on the mechanical history of the C_{60} sample.

The nature of the ''quenching'' effect is probably due to the presence of the nonequilibrium orientational order in quenched fullerene crystals. The orientational order is determined by the population ratio n_p/n_h, whose equilibrium value depends on the temperature. Thus, at room temperature, where the C_{60} molecules rotate almost freely, it can be assumed that $n_p/n_h \approx 1$. In the temperature range $85<T<260$ K this ratio, as indicated above, is $n_p/n_h \approx 4$ and at $T<85$ K, i.e. in the ''orientational glass'' state, $n_p/n_h \approx 5$.[5] Rapid cooling (quenching) fixes at low temperature a nonequilibrium state corresponding to a higher temperature in which the ratio n_p/n_h changes in favor of the higher-energy hexagonal (h) configuration. Therefore quenching defects exist in the pc lattice of fullerene and anneal even before the pc–fcc transition temperature. This distinguishes these defects from deformation defects, which arise mainly in the fcc lattice and lead to a gradual washing out of the transition.

This work was performed as part of the scientific program ''Fullerenes and Atomic Clusters'' (project No. 98065).

[1] M. P. Gelfard and J. P. Lu, Phys. Rev. Lett. **68**, 1050 (1992).
[2] X. D. Shi, A. R. Kortan, J. M. Williams, A. M. Kini, B. M. Savall, and P. M. Chaikin, Phys. Rev. Lett. **68**, 827 (1992).
[3] P. A. Heiney, J. A. Fischer, A. R. McChie, W. J. Romanov, A. M. Denenstein, J. P. McCauley, A. B. Smith, and D. E. Cox, Phys. Rev. Lett. **66**, 2911 (1991).
[4] O. Gunnarsson, S. Satpathy, O. Jepsen, and O. K. Andersen, Phys. Rev. Lett. **67**, 3002 (1992).
[5] M. I. F. David, R. M. Ibberson, T. J. S. Dennis, J. P. Hare, and K. Prassides, Europhys. Lett. **18**, 219 (1992).
[6] M. Tachibana, M. Michiyama, K. Kikuchi, Y. Achiba, and K. Kojima, Phys. Rev. B **49**, 14945 (1994).
[7] L. S. Fomenko, V. D. Hatsik, S. V. Lubenets, V. G. Lirtsman, N. A. Aksenova, A. P. Isakina, A. I. Prokhvatilov, M. A. Strzhemechnyĭ, and R. Ruoff, Fiz. Nizk. Temp. **21**, 465 (1995) [Low Temp. Phys. **21**, 364 (1995)].
[8] V. M. Egorov, B. I. Smirnov, V. V. Shpeĭzman, and R. K. Nikolaev, Fiz. Tverd. Tela (St. Petersburg) **38**(7), 2214 (1996) [Phys. Solid State **38**, 1219 (1996)].
[9] V. M. Egorov, V. V. Shpeĭzman, and I. N. Kremenskaya, Pis'ma Zh. Tekh. Fiz. **19**(19), 49 (1993) [Tech. Phys. Lett. **19**, 621 (1993)].
[10] V. M. Egorov, I. N. Kremenskaya, B. I. Smirnov, and V. V. Shpeĭzman, Fiz. Tverd. Tela (St. Petersburg) **37**(11), 3493 (1995) [Phys. Solid State **37**, 1919 (1995)].
[11] A. L. Kolesnikova and A. E. Romanov, Fiz. Tverd. Tela (St. Petersburg) **40**(6), 1178 (1998) [Phys. Solid State **40**, 1075 (1998)].

Translated by M. E. Alferieff

Light-induced transformation of C_{60} films in the presence and absence of oxygen

T. L. Makarova, V. I. Sakharov, I. T. Serenkov, and A. Ya. Vul'

A. F. Ioffe Physicotechnical Institute, Russian Academy of Sciences, 194021 St. Petersburg, Russia
(Submitted July 23, 1998; resubmitted September 4, 1998)
Fiz. Tverd. Tela (St. Petersburg) **41**, 554–558 (March 1999)

The composition and structure of C_{60} fullerite films prepared by discrete evaporation in quasi-closed volume, as well as their changes induced by laser irradiation, have been studied by ellipsometry and Rutherford backscattering. The starting film has a 150-Å thick stable top layer and a carbon to oxygen ratio of 10:1. Exposure of a film both to vacuum and to air results in formation of an insoluble photo-transformed phase, but in the second case the change in the refractive index implies the appearance of compounds with oxygen. The material does not undergo complete polymerization, although all structural changes cease at an irradiation dose of 10^4 photons per fullerene molecule. Treatment of the polymerized phase with organic solvents produces a porous structure, with the voids totaling 48% in the case of exposure in vacuum, and 30% when exposed in air.
[S1063-7834(99)03603-5]

Fullerites, the spheroidal carbon compounds called equally correctly molecules or nanoclusters, become coupled by van der Waals forces when condensing to form a solid. An interesting property of the C_{60} fullerenes is their ability to form covalent bonds among individual molecules, i.e. to polymerize. Covalent bonding appears under pressure at high temperatures[1] and under irradiation within a certain spectral interval,[2] including the action of an electron or ion beam.[3] Depending on the actual conditions, the polymerization can proceed in different ways and involve formation of dimers, one-dimensional chains, or two-dimensional structures. The actual type of polymerization is identified by Raman[4] and luminescence[5] spectra, x-ray diffractograms,[6] or atomic-force microscopy[7]. Determination of the degree of polymerization, i.e. of the quantitative ratio of the reacted to unreacted molecules, is a more complex problem, whose solution was approached by Raman and x-ray photoelectron spectroscopy.[8] Polymerization transforms fullerenes to a state resistant to organic solvents. Strictly speaking, only the phase formed in vacuum should be classed among polymerized fullerites, because oxygen quenches the excited molecular state required for the reaction to be initiated. However the transition of fullerites to an insoluble state in the presence of oxygen may likewise be of interest, for example, for lithographic applications. The present work was undertaken to compare the type and degree of polymerization of fullerite films under laser irradiation in vacuum and in the presence of oxygen.

1. EXPERIMENT

Fullerite films 1260 ± 10 Å in thickness were prepared on silicon substrates by discrete evaporation in a quasi-closed volume.[9] This method permits fabrication of highly uniform layers, both in area and in depth. The high degree of purification of the starting material (99.95%), film growth in a dynamic vacuum of 2×10^{-7} Torr, as well as the high rate of growth (60 Å/min) favored a low background impurity concentration.

The polymerization was initiated by He-Cd laser light with photon energy $\hbar\omega = 2.8$ eV. The laser irradiation intensity was $I = 0.5$ W/cm^2. The irradiation dose D was determined as the ratio of the number of photons p absorbed by the film to the molecular density μ. The irradiation dose could be varied by properly varying the exposure time t.

$$D = p/\mu; \quad p = I\alpha t/\hbar\omega; \quad \mu = 4/a^3,$$

where a is the lattice constant, and α is the absorption coefficient.

The film thickness and the complex refractive index were measured on a LÉF-3M laser ellipsometer at $\hbar\omega = 1.96$ eV. It is known that photons of this energy do not produce phototransformation.[2] The measured parameters in an ellipsometric experiment are the ellipsometric angles Ψ and Δ determined by the change in the relative amplitude and phase of a p- and s-polarized electromagnetic wave. These parameters contain information on the thickness of the layers d making up the structure, and on the complex refractive index of each layer $N = n - ik$. The d and N quantities were calculated by the standard technique[10] based on the model chosen.

The Rutherford backscattering method (RBS) was used for independent determination of the thickness and composition of fullerite films. The particles used were 190-keV protons. To achieve a high resolution in energy and, hence, in depth, H^+ ions scattered through 120° were measured with a spherical electrostatic energy analyzer. Because the film under study was sufficiently thin, and signals due to light elements (C and O) were superimposed on those from the silicon substrate, the measurements were carried out in the mode corresponding to ion-beam channeling in the substrate. In this way the silicon signal was suppressed, which im-

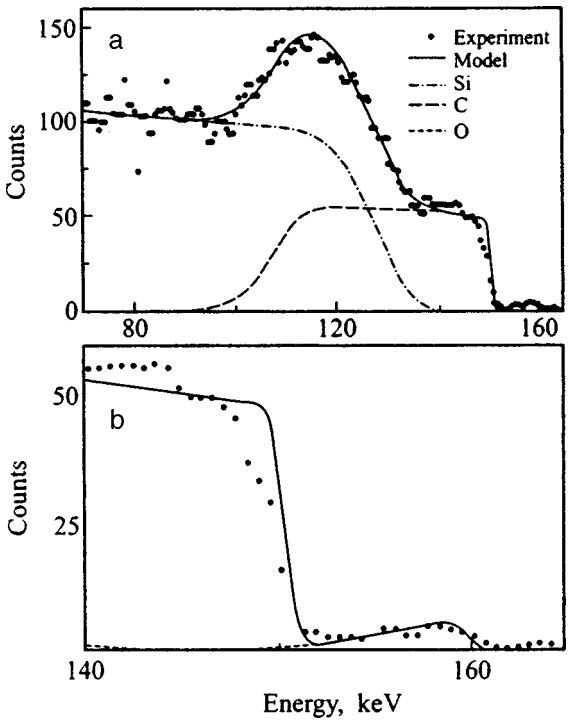

FIG. 1. (a) Rutherford backscattering spectrum of a 1260-Å thick unpolymerized fullerite film, (b) part of the spectrum demonstrating the presence of an upper oxygen-containing layer. Dashed lines: partial spectra of individual elements in the structure, solid line: total spectrum.

proved considerably the relation between the film and substrate signals. Note that no channeling in the fullerite film was observed.

2. RESULTS AND DISCUSSION

Studies performed immediately after the growth (before the light-induced transformation) showed the films to be nonuniform in thickness. The ellipsometric measurements established that the optical parameters of a film can be well described within a model containing two layers with different optical contrast, namely, the layer in contact with the substrate and having a refractive index $N=2.05-i\,0.08$ (for $\hbar\omega=1.96$ eV), and the surface layer with $N=1.50$ $(k=0)$ and thickness $d=150$ Å. This surface layer forms in interaction with the oxygen present in air during a few min, and does not change thereafter. It was shown[11] that the stability with time of the layer contacting the substrate is determined by the quality of the fullerite film, viz. a defect-free crystalline film does not change its properties in storage, whereas a high defect concentration in a film brings about a noticeable gradient of the optical parameters as a result of oxygen diffusion over defects. A Rutherford backscattering spectrum (Fig. 1a and b) also indicates the presence of two layers, namely, of the main one, which directly contacts the substrate, and of a surface one. The main layer contains only carbon atoms, while in the surface layer the carbon/oxygen atom ratio is 10:1. Assuming the surface-layer density to be equal to that of the main one, one obtains 100 Å for the calculated thickness of the surface layer. The ellipsometric value of the geometric thickness, $d=150$ Å, suggests, however, that the surface layer is more loose than the main one (the parameters of both are given in Table I).

To reveal the differences in the nature of the photoinduced changes in fullerite films in the presence of oxygen and without it, which were pointed out earlier,[12] two series of experiments were carried out, namely, with exposure in air and in vacuum of 1×10^{-6} Torr. To remove the surface layer, as well as the oxygen that could penetrate into the film during sample transportation from the growth to measurement chamber, the samples were preheated at 180°C for two hours. The Raman spectra of samples from both series contained features characteristic of one-dimensional polymerization. The spectrum near the pentagonal pinch mode exhibited both the unshifted 1469-cm^{-1} line indicating the presence of the original phase and the lines at 1458 and 1452 cm^{-1} characteristic of the dimers and one-dimensional chains, respectively[13].

The exposed samples were treated with standard organic solvents attacking the unpolymerized phase of the fullerite. The extent of removal of the unpolymerized phase was checked ellipsometrically, with the process of development completed after the ellipsometric parameters of the structure no longer changed following a treatment. The totality of the experimental values of Ψ and Δ obtained on samples subjected to various irradiation doses (see Fig. 2) shows all the

TABLE I. Parameters of pristine C_{60} films and of the films phototransformed in vacuum and in air.

	Pristine film		Polymerized film	
Parameter	Main layer	Surface layer	In air	In vacuum
No. of conventional molecules τ, cm^{-2}	980×10^{15}	80×10^{15}	550×10^{15}	450×10^{15}
Carbon content x	1	0.909	0.813	0.905
Oxygen content $1-x$	0	0.091	0.179	0.090
Composition per C_{60} molecule	C_{60}	$C_{60}O_6$	$C_{60}O_{13.8}$	$C_{60}O_6$
Thickness d, Å	1110	150	1020	1080
Refractive index N	$2.05-i$ 0.08	1.50	1.56	1.44
Void fraction (EMA)	–	–	0.38	0.49
Void fraction (RBS)	0.96	–	0.30	0.47
Density (EMA) ρ, g/cm^3	–	–	1.02	0.81
Density (RBS) ρ, g/cm^3	1.58	1.07	1.16	0.78

Note. The calculations carried out by the effective-medium approximation (EMA) and from Rutherford backscattering spectra (RBS).

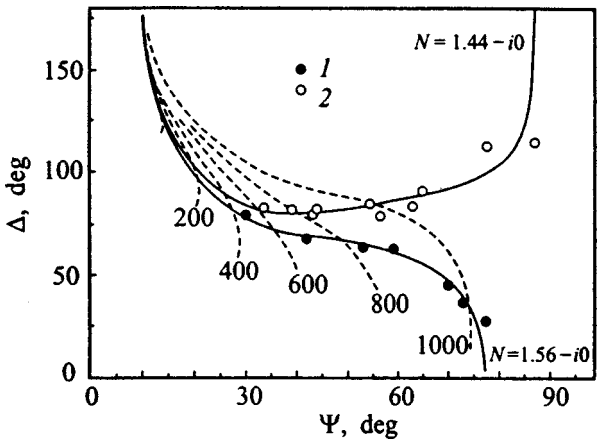

FIG. 2. Ellipsometric nomogram of a polymerized fullerite film on silicon. Points — experimental values obtained on samples exposed in air (*1*) and in vacuum (*2*). Curves: Solid — lines of constant refractive index, dashed — lines of constant thickness. The figures at the lines are thicknesses in Å.

points to fit onto the lines of the same refractive index, which validates the use of the uniform-film model to calculate the film parameters. The results of this calculation are displayed in Fig. 3a and b. In both cases, the insoluble layer starts to form at a threshold irradiation dose of 10^4 photons per fullerene molecule, and the layer thickness begins to change when the dose reaches 10^5 (Fig. 3a). Assuming the complex refractive index $N=2.10-i\,0.35$ (for $\hbar\omega=2.80$ eV), it can be shown that the laser radiation traversing a film with this thickness decreases in intensity tenfold. Hence the saturation of the polymerization process implies that all the molecules received the threshold dose, irrespective of their depth.

The fact that the refractive index of the polymerized layer does not depend on the dose (Fig. 3b) is a nontrivial result. For films exposed in vacuum and in the presence of oxygen, its mean value is, respectively, $n=1.44$ and 1.56, which is substantially smaller than the corresponding value for the starting fullerite films. An increase in the dose does not entail an increase in the extent of polymerization, which may be assigned to the onset of an equilibrium between the reactions of polymerization and depolymerization. Assuming the chemical composition to remain unchanged, and considering the fullerite layers obtained to be a combination of two phases, polymerized fullerite and voids, the dielectric permittivity of such a material can be found in the effective-medium approximation[14]

$$\sum q_i(\varepsilon_i-\varepsilon)/(\varepsilon_i+2\varepsilon)=0\,,$$

where q_i is the volume fraction, and $\varepsilon_i=N^2$ is the dielectric permittivity of each component. Calculations based on the ellipsometric measurements of N yield for the porosity obtained under exposure in the presence of oxygen and in vacuum 0.38 and 0.49, respectively.

The energy spectra of backscattered ions for films polymerized in vacuum and in the presence of oxygen are displayed in Figs. 4a and 4b, respectively. The energy spectrum of the protons scattered from the sample can be used to calculate both the relative amounts of chemical elements in the target and the thickness of the film expressed in units of $\tau=cd$, where c is the volume concentration of the conventional molecules, and d is the geometric thickness.[15] Considered within our model, the film consists of carbon and oxygen, and for the formula of the conventional molecule one can write C_xO_{1-x}. Using the value of d derived from ellipsometric measurements and the values of x and τ extracted from the RBS energy spectra, we calculated the effective density and porosity of the fullerite layers. The results are given in Table I. A good agreement between the values of porosity obtained by this method and in the effective-medium approximation is observed only for the film phototransformed in vacuum. The void fraction is 0.48 ± 0.01. The results for the film subjected to irradiation in the presence of oxygen are essentially different. The volume fraction of voids found in the effective-medium model is 0.38, to be contrasted with 0.30 yielded by RBS data. This difference may be assigned to the fact that oxygen enters a chemical reaction under illumination,[16] thus causing a change in chemical composition and, accordingly, in the refractive index of the material. In this case using the parameters of the starting material in the effective-medium approximation is invalid. In order to reconcile the porosity calculations made by both methods, one has to assume that the refractive index of fullerene polymerized in the presence of oxygen decreases to 1.90–1.95. At the same time the refractive index of fullerene polymerized in vacuum was shown[5] not to change in the IR and red regions of the spectrum, which validates the application of the effective-medium method in these conditions.

A few features in the two RBS spectra are worth mentioning. The extended trailing edge of the partial spectrum of carbon and of the leading edge of the silicon spectrum imply

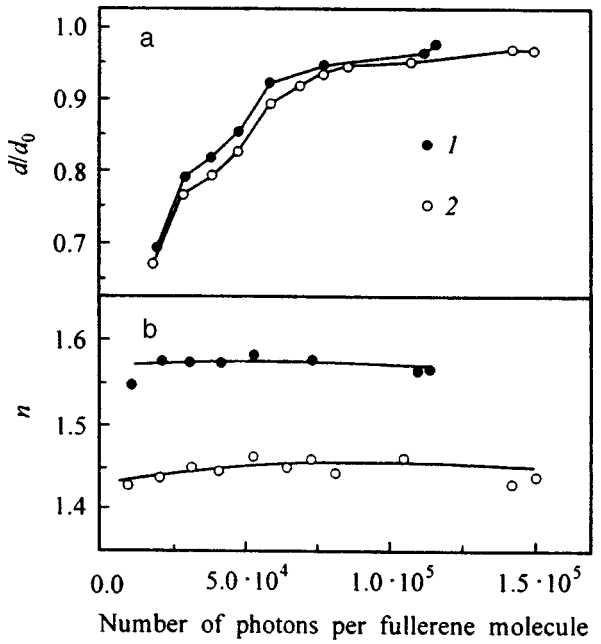

FIG. 3. Dependence of the relative thickness (a) of a polymerized fullerite layer d/d_0 and of its refractive index n (b) on the number of photons absorbed by a fullerene molecule. Exposure (*1*) in air and (*2*) in vacuum.

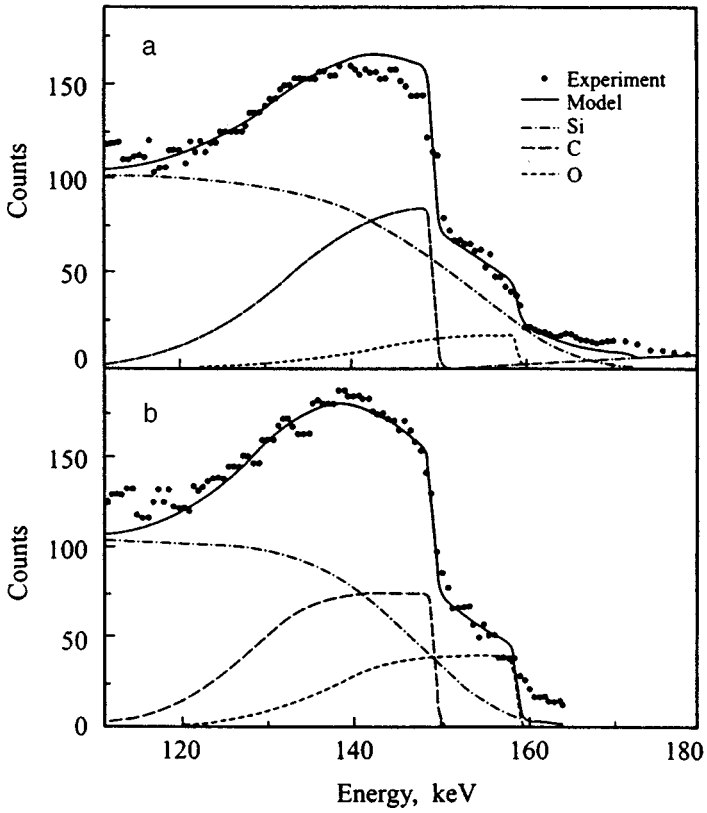

FIG. 4. Rutherford backscattering spectra of fullerite films phototransformed (a) in vacuum and (b) in air.

nonuniformity of the film in thickness within the probed region. For film thicknesses $\tau=(450-550)\times10^{15}$ cm^{-2}, the dispersion in thickness $\sigma=100\times10^{15}$ cm^{-2}. At the same time the sharpness of the carbon-spectrum slope indicates the absence of surface roughness. Hence the apparent change in the thickness of the polymerized fullerene film should be assigned to its porosity, with the pores being of a size comparable to the film thickness along the surface normal and not reaching the surface. The carbon/oxygen ratio, which corresponds to $C_{60}O_6$ and $C_{60}O_{13.8}$ for phototransformation in vacuum and in air, suggests that atmospheric oxygen penetrates easily into the porous matrix of polymerized fullerene.

Thus fullerite films can be polymerized by 2.8-eV laser radiation both in vacuum and in air, but in the second case the process involves formation of oxygen compounds, which results in a change of the refractive index of the phototransformed phase. Both processes give rise to formation of one-dimensional structures, dimers and linear chains. Note that one cannot reach complete phototransformation of the material, although structural changes cease at an irradiation dose of 10^4 photons per fullerene molecule. Dissolution of the starting phase in organic solvents results in formation of a porous structure, with the void fraction being 48% when exposed in vacuum, and 30% under exposure in air.

Support of the Russian Fund for Fundamental Research (Grant 96-02-17926) and of the ''Fullerenes and Atomic Clusters'' program (Grant 98059) is gratefully acknowledged.

[1] Y. Iwasa, T. Arima, R. M. Fleming, T. Siegrist, O. Zhou, R. C. Haddon, L. J. Rothberg, K. B. Lyons, H. L. Carter, Jr., A. F. Hebard, R. Tycko, G. Dabbagh, J. J. Krajewski, G. A. Thomas, and T. Yagi, Science **264**, 1570 (1994).
[2] A. M. Rao, P. K. Zhou, K. A. Wang, G. T. Hager, J. M. Holden, Y. Wang, W. T. Lee, X.-X. Bi, P. C. Eklund, D. C. Cornett, M. A. Duncan, and I. J. Amster, Science **259**, 955 (1993).
[3] Y. B. Zhao, D. M. Poirier, R. J. Pechman, and J. H. Weaver, Appl. Phys. Lett. **64**, 577 (1994).
[4] M. S. Dresselhaus, G. Dresselhaus, and P. C. Eklund, J. Raman Spectrosc. **27**, 351 (1996).
[5] Y. Wang, J. M. Holden, A. M. Rao, P. C. Eklund, U. D. Ventkateswaran, D. Eastwood, R. L. Lidberg, G. Dresselhaus, and M. S. Dresselhaus, Phys. Rev. B **51**, 4547 (1995).
[6] M. Núñes-Regueiro, L. Marques, J.-L. Hodeau, O. Béthoux, and M. Perroux, Phys. Rev. Lett. **74**, 278 (1995).
[7] V. A. Davydov, L. S. Kashevarova, A. V. Rakhmanina, V. N. Agafonov, R. Seolya, and H. Szwarc, JETP Lett. **63**, 818 (1996).
[8] J. Onoe and K. Takeuchi, Phys. Rev. Lett. **79**, 2987 (1997).
[9] T. L. Makarova, N. V. Seleznev, I. B. Zakharova, and T. I. Zubkova, Mol. Mater. **10**, 105 (1998).
[10] R. M. A. Azzam and N. M. Bashara, *Ellipsometry and Polarized Light* (North-Holland, Amsterdam, 1977), p. 583.
[11] T. L. Makarova, Mol. Mater. **7**, 199 (1996).
[12] P. C. Eklund, A. M. Rao, P. Zhou, Y. Wang, and J. M. Holden, Thin Solid Films **257**, 185 (1995).
[13] P. Zhou, A. M. Rao, K.-A. Wang, J. D. Robertson, C. Eloi, M. S. Meier, S. L. Ren, X.-X. Bi, P. C. Eklund, and M. S. Dresselhaus, Appl. Phys. Lett. **60**, 2871 (1992).
[14] D. A. G. Bruggeman, Ann. Phys. **24**, 636 (1935).
[15] W. K. Chu, J. Majer, and M.-A. Nickolet, *Backscattering Spectrometry* (Academic, New York, 1978), 384 pp.
[16] H. Werner, M. Wohlers, D. Bublak, T. Beltz, W. Bensh, and R. Schlögl, in *Electronic Properties of Fullerenes*, edited by H. Kuzmany *et al.*, Springer Series in Solid-State Sciences, Vol. 117 (Berlin, 1993), p. 16.

Translated by G. Skrebtsov